

# THIS WEEK

## EDITORIALS

**WORLD VIEW** No excuses  
scientists, you can  
communicate **p.445**



**TB VACCINE** New candidate  
could offer longer protection  
than BCG **p.446**

**NAUTILUS** 20-year lease under  
the sea to mine marine  
copper and gold **p.449**

## Vive la révolution

*Tunisia's nascent democracy, promoting justice, human rights and intellectual freedom, needs to be celebrated and encouraged.*

**T**he revolution in Tunisia cost more than 100 lives and there is no guarantee at this early stage that the fledgling democracy that has emerged will prosper as many wish it to. But turmoil is to be expected immediately after any revolution, and for the moment there is much to celebrate.

Tunisian scientists are relishing their nation's opportunity as a laboratory, not just for democracy and human rights in the Arab world, but also because the pay-offs from education and science are greatest when fundamental freedoms are respected.

The link between democracy and science as a precondition for progress in the Arab world was clearly articulated in 2003 in a report called *Building a Knowledge Society*, part of the Arab Human Development Reports and "written by Arabs for Arabs" by a group of more than 100 scholars and experts. It made the forceful argument that political deficiencies, such as a lack of respect for human rights, and the guaranteeing of these rights through good governance, were the primary obstacle to building knowledge societies — based on research in science and the humanities — in the Arab world. Poor levels of investment in science and education were secondary. Nader Fergany, lead author of the reports, made the case that knowledge societies could flourish only in open societies with democratic institutions that fully respected human rights such as freedoms of speech and freedom of association (see *Nature* **444**, 33–34; 2006).

### INTERNATIONAL MYOPIA

Tunisia is perhaps a case in point. The ousted regime of President Zine el-Abidine Ben Ali was expert at double speak, and preached the benefits of greater human rights while simultaneously crushing them. Speaking to *Nature* since the revolution, Tunisian researchers tell how it was almost impossible to convince foreign colleagues that the positive image of their country common among outsiders was myopic. The realpolitik embrace of the Tunisian administration by the international community, which saw it as a rock of stability against radical Islam in the Middle East and North Africa, also reinforced its perceived legitimacy.

For years, the regime also projected an image of Tunisia as a country committed to science. From the outside looking in, it was hard to disagree. Tunisia invested more (as a percentage of gross domestic product) than many of its Arab neighbours, and notched up relatively favourable increases in the numbers of researchers and articles published.

So it is both sobering and valuable, particularly given the arguments of the Arab Human Development Reports, to hear the testimony of Tunisian researchers, who argue that much of the claimed success of Tunisian science in the past decade was, on a deeper level, a mirage. And that the achievements that were made, were largely despite the Ben Ali regime rather than because of it. In fact, they tell how through totalitarian governance and the denial of freedoms, the regime imposed an 'intellectual blockage' at every level of university life, which disempowered researchers and stifled the development of a dynamic research

and innovation system (see page 453). Indoctrinated not to criticize the system, young researchers have also failed to develop independent minds. As one Tunisian researcher puts it: "Scientists need the freedom to stand back from dogma if they are to innovate."

Tunisia's science carried other hallmarks of authoritarian regimes, such as the dearth of social-science research. Those who silence critics have little interest in encouraging branches of enquiry that could hold the regime up to scrutiny. Another hallmark was the practice of awarding posts to the politically loyal, rather than on merit. This should not take long to remedy, however, because Tunisia is a small country, and its scientists know who are the best and brightest.

**"Tunisians are optimistic that a new era is at hand."**

Tunisians are optimistic that a new era is at hand, and that the creation of an open society where democracy, human rights and academic freedom flourish is within reach. Researchers there seem convinced, like Fergany, that greater freedoms and good science and education go hand-in-hand. In the heady aftermath of a revolution, such aspirations may sound all too sunny. The road ahead is uncertain, and reforms will take years, but there is every reason to be optimistic that the conditions for change are better now than at any time since the country gained independence in 1956. Many Tunisians are also well educated, and they want their revolution to succeed. Now is not the time for punditry on its chances of success; the hour is one to celebrate what has already been achieved, and to encourage the fledgling democracy, for example, by encouraging scientific cooperation.

### WRONG SIDE OF HISTORY

Most of Tunisia's scientific cooperation and links are with France, its former colonial master across the Mediterranean Sea. A stalwart ally of Ben Ali, the French government utterly discredited itself in the eyes of Tunisians in its response to the revolution — putting itself on the wrong side of history; even offering the dictator the country's expertise in riot control. But the diaspora of Tunisian and Franco-Tunisian academics in France now have an opportunity to speak out and influence what should happen next. So too do the French national research agencies — and the European Union — which have long had formal collaboration programmes with Tunisia.

Last week, *Nature* asked Faouzia Charfi, Tunisia's secretary of state for higher education in the transition government and a well-known human-rights advocate, how researchers elsewhere could help. She said: "When researchers in our country solicit them with solid research proposals, help them. Help our researchers to also have the possibility to take part in conferences and to work outside the country. A Tunisian passport, without a visa, doesn't open doors to many countries. Open up to us your borders, so that we can speak together the same language, the language of science, and the language of human-rights values in which I have always believed." ■

# What comes first?

*An attempt to rework US food-safety regulations will fail without sufficient funds.*

As an example of the absurdity of US food-safety regulations, consider the humble egg. The US Department of Agriculture (USDA) monitors the chickens that produce them and grades the eggs according to their quality. The safety of those (intact) eggs is scrutinized by the Food and Drug Administration (FDA). Once cracked open and used to make a product, the egg comes back under USDA jurisdiction. If that product is then used as an ingredient to make yet another food, responsibility for ensuring its safety again rests with the FDA. Unless, of course, that egg-based food is a meat product — then the USDA remains in charge.

US lawmakers waded into this arcane system late last year when they passed the biggest overhaul of the US food-safety system in more than 70 years. The Food Safety Modernization Act, signed into law on 4 January, aims to shore up the FDA side of food-safety regulation, giving the agency expanded authority to conduct inspections and to pull contaminated products from the market. The law also expands the government's role in the prevention of food-borne illnesses, rather than simply reacting to outbreaks on a case-by-case basis. Farms and food manufacturers will now be required to identify potential hazards in their manufacturing process — anything from bacterial contamination to metal screws that could fall off equipment and into food — and develop plans to prevent them.

But by the time President Barack Obama had signed the act, some in the House of Representatives were already threatening to drag the new law into the budgetary battle brewing on Capitol Hill. Critics, who include Representative Jack Kingston (Republican, Georgia), the lead Republican on the subcommittee that oversees the FDA's budget, have threatened to underfund the law. They argue that the cost of the regulations — US\$1.4 billion over the next five years — outweighs the benefits.

Their sums are short-sighted: the Pew Charitable Trusts in

Washington DC estimates that food-borne illnesses cost the United States \$152 billion a year, not including the cost to industry in lost sales and lawsuits when outbreaks surface. The investment seems a sound strategy.

It is curious that a bill that won bipartisan support should now face starvation at the hands of an appropriations committee, but it is an old story for the FDA. Famously overstretched, the agency's budget has failed to keep pace with the expansion of its mandate.

Without adequate funding for inspectors, the food-safety law will have no teeth. The new law also calls for funds to sponsor food-safety research. In the absence of that money, the underfunded and over-extended National Institute of Food and Agriculture shoulders the

***"It is curious that a bill that won bipartisan support should now face starvation at the hands of an appropriations committee."***

bulk of such projects. That institute faces a budget crisis of its own: its competitive research grants programme is authorized to receive \$700 million. It got \$262 million in 2010, and its budget in 2011 is uncertain.

Meanwhile, improving food safety is not only a question of money. As is often the case between government agencies, communication between the FDA and the USDA is notoriously lacking. Last September, for example, *The Wall Street Journal* reported that USDA inspectors noted filthy conditions at Wright County Egg, a huge producer in Galt, Iowa, when they arrived to grade its eggs, but failed to inform the FDA about the possible food-safety risk. A *Salmonella* outbreak leading to the recall of hundreds of millions of eggs was later traced back to that farm, as well as to another.

The barriers to better communication are clearly surmountable: in 1995, the FDA, USDA and the US Centers for Disease Control and Prevention in Atlanta, Georgia, worked together to create PulseNet, a contaminant alert system that tracks the genetic fingerprints of bacteria found in food. The programme alerts officials when the incidence of any one bacterial strain rises above background levels. PulseNet allowed regulators to track down the spinach behind a 2006 outbreak of *Escherichia coli* O157:H7 food poisoning that made more than 200 people ill. The programme has attracted international collaborators as well. It is a food-safety success story made possible by careful coordination among agencies, and it is a story worth chewing over. ■

# Staring at the Sun

*Solar measurements are better than ever — but that prowess could endanger future efforts.*

Humankind has long marvelled at the Sun and basked in its warmth. So it may be disconcerting to learn that the Sun is not quite as bright as we thought — it now seems that our star gives off 0.34% less radiation than was previously estimated (G. Kopp and J. L. Lean *Geophys. Res. Lett.* **38**, L01706; 2011).

Total solar irradiance, a measure of the Sun's cumulative energy output, is a fundamental, if little-appreciated, number in Earth science. It acts as a baseline for our calculations on climate, and accounts for almost half of our planet's energy balance with impressive simplicity. (It is on the other half of the equation, concerning what happens to that energy once it enters the system, that things get complicated.) The new value should not make calculations trickier: equations representing clouds, for instance, come with enough uncertainty to absorb the effect. But it is important to have an accurate picture of the Sun's output.

Measurements of the Sun from space began in November 1978, and the subsequent continuous record has proved invaluable to the study of solar cycles and the impact of solar variation on the climate system.

Next month, NASA will launch the Glory spacecraft to bolster and extend that record over the coming years (see page 457).

Glory's measurements of the Sun could be the most accurate so far, and they should be the first to match earlier measurements — from NASA's Solar Radiation and Climate Experiment — without adjustment. Indeed, solar researchers are now working to calibrate their systems against an absolute standard before launch, which would make it easier to work with different instrument designs.

The solar physicists who are doing this work have two fears. The first is that the continuous record of solar irradiance measurements will one day come to an end. With the Swiss sensor PREMOS in the air — launched last June on the French satellite PICARD — and Glory on the way, the outlook is bright over the next few years. But so far, only the United States has proposed a follow-on mission, scheduled for 2014.

Physicists' second fear boils down to a moral hazard. Part of the rationale behind the search for an absolute standard is to make the data record resilient enough to withstand future gaps in measurement. But if funders know that the technology has improved to that point, why should they approve missions to plug the gaps? We are not there yet; instrument-makers have yet to prove that their toys are as precise, robust and predictable as they claim.

➔ **NATURE.COM**  
To comment online,  
click on Editorials at:  
[go.nature.com/xhnuq](http://go.nature.com/xhnuq)

But a future where these crucial data are accurate enough to stand on their own, independently of the data record, should be pursued, not feared. ■



## Of course scientists can communicate

**Tim Radford** takes aim at the popular myth that researchers are hopeless at explaining their work to a general audience.

There are several canards about scientists, but one is more pernicious simply because so many scientists themselves repeat it: scientists are not good communicators.

Once again, the allegation is to be the subject of discussions, this time at next month's annual meeting of the American Association for the Advancement of Science in Washington DC. It can be found on *Nature's* website, heard in research councils, it is even occasionally propagated by the public-engagement community, and sometimes endorsed by journalists. In response, I can only say bosh, balderdash and Bronowski, and follow with other intemperate expletives such as Haldane, Hawking and Huxley, Eddington and E. O. Wilson, not to mention, as if in a state of terminal exasperation, Dawkins!

Between 1980 and 2005, I commissioned working scientists to write for *The Guardian* newspaper — from astronomers royal to impoverished doctoral students — and almost all of them delivered high-standard, well-focused newspaper prose and many of them went on to live by the pen. I also encountered distinguished scientists who had already become literary stars.

One was the astronomer Carl Sagan, who told me that his literary hero was Thomas Henry Huxley. Another was the industrial chemist, poet and writer Primo Levi, who when I tried to ask him about the Two Cultures debate — the apparent divide between the humanities and sciences — gently reminded me that Dante Alighieri (himself the subject of at least one paper in *Nature*), was a member of the Florentine guild of physicians and apothecaries. And a third was the Czech poet and dissident Miroslav Holub, who wrote his occasional *Guardian* column in English, and asked that at the end of each I describe him as the author of *Immunology of Nude Mice* (1989). All three were better writers than most writers: two will still be famous as writers a century from now.

They were, of course, exceptions. We all inherit the gift of words; the gift for words, however, is unevenly distributed. Even so, there are reasons why scientists, in particular, should be and often are good communicators. One is that most scientists start with the engaging quality of enthusiasm — to get through a degree course, the PhD and all the research-council hoops, you would need it — and enthusiasm is derived from a Greek term that means divinely intoxicated. Enthusiasm is infectious, but to command an audience of readers, scientists should exploit their other natural gifts. One of these is training in clarity. Another is training in observation. And a third is knowledge.

Those who can think clearly can usually write clearly: thoughts have value only when expressed,

and the more clearly they are expressed, the greater their potential value. Those whose business is to observe are aware of subtle differences that must be described, or the observations would be meaningless. And those who write must have something new or useful to say: if not, why say anything? A novelist who does not publish is not a novelist. A scientist who does not publish remains a scientist — at least for the duration of the research-council grant — but the science performed is of no apparent value until somebody else hears about it.

The problems for the scientist as a public communicator start with academic publishing: the language, form and conventions of the published scientific paper could almost have been devised to conceal information. Even in conversation, scientists start with a communication problem — words that are perfectly ordinary within science are simply never heard on a football terrace or in a tavern or bus queue. So

to be effective communicators, scientists have to learn to stand back from their own work and see it as strangers might do.

It is not a difficult trick: even journalists have learned it. What is the most significant thing about your research? Is it that, at cosmological distances, type Ia supernovae in high redshift galaxies seem insufficiently lustrous? Or is it that you have just realized that you cannot account for 71% of the Universe; make that 96% if you throw in dark matter alongside this newly discovered dark energy? Which is more likely to make people attend? Humphry Davy and Michael Faraday were stars of the lecture halls. Many distinguished scientists — Richard Feynman, J. B. S. Haldane and Peter Medawar among them — knew how to hold a popular audience, and they weren't afraid to address their peers with the same vividness and economy. In fact, their fame became inseparable from their gift for words. So the

case for scientists as inherently bad communicators is a canard.

And while we have our ducks in a row, let me invoke the canard that scientists occasionally propagate about the media: that it does not appreciate scientific uncertainty. That one is especially irritating. It seems to say "I, as a scientist, wish to have it both ways. I want the privilege of knowing better than you, and the indulgence of being wrong without guilt, because science, don't you see, is really about uncertainty." To which the foolish answer might be "In which case, why should we listen?" But alas, people in any case listen selectively, even to the best communicators, which might be why so many Americans think Darwin's theory of evolution is "only a theory". Scientists are not the only people to blame for a problem in communication. ■

**Tim Radford** was science editor of *The Guardian* until 2005.  
e-mail: [tim.radford@guardian.co.uk](mailto:tim.radford@guardian.co.uk)

ENTHUSIASM IS  
**INFECTIOUS,**  
BUT TO COMMAND  
AN AUDIENCE OF  
READERS,  
SCIENTISTS SHOULD  
**EXPLOIT THEIR**  
OTHER NATURAL  
**GIFTS.**

➔ **NATURE.COM**  
Discuss this article  
online at:  
[go.nature.com/uu2spl](http://go.nature.com/uu2spl)

# RESEARCH HIGHLIGHTS

Selections from the  
scientific literature

## CARDIOVASCULAR BIOLOGY

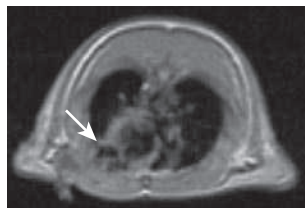
### Fooling the heart into repair

After a heart attack, a type of immune cell can lessen the damaging inflammatory response in the organ by recognizing cells undergoing apoptosis, or programmed cell death. To mimic this protective effect, Smadar Cohen at Ben-Gurion University of the Negev in Beer-Sheva, Israel, and her group designed a liposome — a lipid-based bubble — with the molecule phosphatidylserine on its surface. This is abundant on apoptotic cells, and prompts the immune system's macrophage cells to secrete anti-inflammatory factors.

The authors showed that mouse macrophages took up the liposomes and shifted to an anti-inflammatory mode. Rats injected with liposomes after an induced heart attack showed an accumulation of macrophages in the damaged area after four days (**pictured** with arrow). After four weeks, the rats also had a greater density of heart blood vessels than untreated animals and less remodelling of their left ventricle, a common after-effect of a heart attack.

*Proc. Natl Acad. Sci. USA*  
doi:10.1073/pnas.1015623108  
(2011)

NATL ACAD. SCI.



## IMMUNOLOGY

### TB vaccine with a long view

Tuberculosis (TB) infection can enter an asymptomatic 'latent' phase and re-emerge later. The only approved TB vaccine,

BCG, targets just the disease's early, active stage. A vaccine candidate, H56, that contains an antigen from the latent phase affords mice longer-lasting protection against the disease than does BCG, report Claus Aagaard and Peter Andersen at the Statens Serum Institute in Copenhagen and their co-workers.

The H56 vaccine contains three antigens, including one, Rv2660c, that is expressed during TB's latent stage. When given to mice before infection, H56 generated more diverse T-cell responses than the BCG vaccine, and also yielded a lower bacterial load by 24 weeks post-infection. When administered after the mice

had been infected and treated with antibiotics, H56 protected the animals against developing reactivated infections. The team hopes to test the vaccine in humans.

*Nature Med.* doi:10.1038/nm.2285 (2011)

## METABOLISM

### Bitter aperitifs to aid digestion

The Roman tradition of drinking wine infused with bitter herbs before meals may have been wise: a study in mice reveals that bitter foods can temporarily aid digestion.

Bitter-taste receptors are found in the gut, as well as

turbulence. Using a series of artificial streams, they demonstrated that an increase in mussel species richness is associated with a rise in gravel erosion when population density is high — a result of interactions between species. This shows that biodiversity, and even changes in species abundance, can influence physical processes such as sediment transport.

*Ecology* doi:10.1890/10-0219.1 (2011)



## ECOLOGY

### Mussel mix boosts erosion

Changes in biodiversity can alter not only the interactions between species in ecosystems, but also the physical habitat.

Daniel Allen and Caryn Vaughn at the University of Oklahoma in Norman hypothesized that changes in mussel biodiversity might influence the erosion of riverbed sediments because of species differences in burrowing behaviour and ability to cause water

the mouth. Inge Depoortere and her co-workers at the Catholic University of Leuven in Belgium treated mice with compounds that activate these receptors, and found a rise in a hunger hormone called ghrelin. Over the next half-hour, treated mice ate and digested more food than mice that started out with water. After that, digestion and feeding slowed.

These effects were reduced in mice lacking a protein called  $\alpha$ -gustducin, which is also involved in taste. Tweaking this pathway could provide a new approach to tackling obesity and some digestive disorders.

*Proc. Natl Acad. Sci. USA*  
doi:10.1073/pnas.1011508108  
(2011)

M. DAVIS

## PHYSICAL CHEMISTRY

## Separating water by spin

Water molecules have been separated according to the two possible spin orientations of the molecules' hydrogen atoms.

Water is a mixture of two isomers that differ in the direction of their hydrogen spins. The spins are parallel in 'ortho' water and antiparallel in 'para' water. Little is known about the physical and chemical differences between these two isomers because no viable separation method has been available.

Now Gil Alexandrowicz and his co-workers at the Technion-Israel Institute of Technology in Haifa report a procedure in which they shot a slow beam of water molecules through a strong magnetic field. The field acted like a selective lens for ortho water, which, unlike para water, is sensitive to a magnetic field. Purified ortho water was then collected through a small slit.

The work could pave the way for highly sensitive nuclear magnetic resonance experiments, which rely on the alignment of nuclear spins. *Science* 331, 319–321 (2011)

## CANCER BIOLOGY

## Blood vessels' tumour defence

Tumours rely on the blood vessels that permeate them to survive. However, secretions from the endothelial-cell lining that supports these vessels blunt tumour growth and spread.

Elazer Edelman at the Massachusetts Institute of Technology in Cambridge and his colleagues studied the effect of endothelial cells, which are abundant in tumours, on human breast- and lung-cancer cells. Those grown in media previously occupied by human endothelial cells exhibited a 40% reduction in growth and were also less invasive. Knocking down a key protein expressed by endothelial cells

lowered their ability to block tumour invasion.

Similar anti-tumour effects were seen when the endothelial cells were implanted in mice. *Sci. Transl. Med.* 3, 66ra5 (2011)

## NEUROSCIENCE

## Sleep strengthens memories

Sleep is known to consolidate memories. But what happens to memories if they are reactivated during sleep?

Björn Rasch at the University of Basel in Switzerland, Jan Born at the University of Lübeck in Germany, and their colleagues asked 24 volunteers to learn the locations of pairs of matching cards in an array while being presented with an odour. Half of the volunteers then slept for 40 minutes. During this period, some of the sleeping and wakeful volunteers were exposed to the odour again, to reactivate their memories. Next, the volunteers learned a second task designed to interfere with their memories from the first. They were then asked to recall the original locations of the cards.

Those exposed to the odour during sleep had a higher memory-recall rate than did those who were not exposed. Conversely, in awake volunteers reactivation of the memories with the odour increased forgetfulness.

*Nature Neurosci.* doi:10.1038/nn.2744 (2011)

## BIOCHEMISTRY

## New microbial metabolism

Analysis of a microbe thriving in the harsh salty conditions of the Dead Sea has revealed a novel pathway for metabolizing carbon.

Ivan Berg at the University of Freiburg in Germany and his colleagues discovered the methylaspartate cycle by studying the enzymes and intermediates involved in metabolism when *Haloarcula*

## COMMUNITY CHOICE

The most viewed papers in science

## CLIMATE CHANGE

## More plants, more cooling

**HIGHLY READ**  
on [www.agu.org](http://www.agu.org) the week of 10 January

Vegetation could offset atmospheric warming by around 0.6 °C over land during a projected 30-year period during which atmospheric carbon dioxide levels are double those of pre-industrial times.

Lahouari Bounoua of NASA's Goddard Space Flight Center in Greenbelt, Maryland, and his colleagues ran three long-term climate models simulating various plant feedback effects. These included a response that increases leaf density and decreases photosynthesis at higher CO<sub>2</sub> levels. This caused greater water availability and evaporation from plant surfaces — providing additional cooling not previously accounted for. Average global temperatures rose by 1.68 °C, 0.26 °C less than predicted by conventional models.

The results are in line with observations and suggest that long-term plant responses could moderate global temperatures if CO<sub>2</sub> levels are stabilized.

*Geophys. Res. Lett.* doi:10.1029/2010GL045338 (2010)

*marismortui* is grown on acetate. The pathway converts a molecule called acetyl coenzyme A into the building blocks of sugars, and is only the third such metabolic pathway identified. Among other features, one intermediate of the complex cycle limits the effects of osmosis, helping the microbe to survive in high-salt environments.

The researchers found striking similarities between the enzymes of *H. marismortui* and those found in some ancient bacteria — an indication that the microbe probably acquired components of this pathway by grabbing genes from other species. *Science* 331, 334–337 (2011) For a longer story on this research, see <http://go.nature.com/lbaczj>

## ZOOLOGY

## Fly shows some leg

Males of a recently identified species of dance fly captured on Mount Fuji in Japan may be using strangely enlarged leg segments to court females.

Christophe Daugeron at the National Museum of Natural History in Paris and his colleagues found that some male specimens of *Empis jaschhoforum* caught in their traps had normal limbs (pictured below) but roughly an equal number had one forelimb with a huge final segment (top). One fly even had modifications to both forelimbs.

Such a high prevalence of asymmetry in a population with symmetrical features is unprecedented, say the researchers, who ruled out parasites and genetic differences between cells as causes. The engorged limb-tip is probably a sexual signal and the costs associated with this unwieldy feature may explain why slim-legged flies still exist. *Biol. Lett.* 7, 11–14 (2011)

➔ **NATURE.COM**

For the latest research published by Nature visit:

[www.nature.com/latestresearch](http://www.nature.com/latestresearch)



A. STARK/C. DAUGERON



# SEVEN DAYS

The news in brief

## POLICY

### NASA privacy case

The US Supreme Court has ruled that it is “reasonable” for NASA to make far-reaching background checks on the scientists it employs. A group of 28 researchers at the Jet Propulsion Laboratory (JPL) in Pasadena, California, had sued to stop the investigations (see *Nature* 467, 644; 2010). Robert Nelson, a planetary scientist at JPL and a lead plaintiff in the lost lawsuit, told *Nature* that plaintiffs would accept limited checks that were tailored to NASA’s needs, but might leave the space agency should it “persist in undertaking a fishing expedition into the most intimate details of our private lives”.

### US–China deals

Officials unveiled a raft of agreements last week during the visit of President Hu Jintao of China to Washington DC. The deals included research partnerships in coal technology, energy efficiency and clean vehicles, under the umbrella of the US–China Clean Energy Research Center. The two countries also agreed to establish a centre of excellence in China to promote nuclear security. See [go.nature.com/l7czmr](http://go.nature.com/l7czmr) for more.

### Carbon heist

The European Commission was forced to partially shut down its carbon-trading market — the world’s largest — for a week from 19 January, after carbon credits worth up to €30 million (US\$40 million) were stolen from insecure accounts. The thefts follow earlier scandals, including a massive tax fraud, that have embarrassed Europe’s emissions-trading scheme, a market involving 30 countries,



R. UTRECHT/AFP/GETTY IMAGES

## Dutch protest against university fee hike

The Netherlands saw its largest academic rally in decades on 21 January (pictured), when more than 10,000 Dutch students and around 1,000 professors and rectors protested in The Hague against raised university education fees. As part of budget-saving measures, the coalition government wants to raise €370 million

(US\$500 million) by making students who extend their degrees beyond the standard three years pay an extra €3,000 annually, and by fining their university the same amount. Current standard yearly fees are €1,600, and 16–20% of students on courses at the country’s 14 research universities overextend their studies.

in which companies trade allowances to emit carbon dioxide. See [go.nature.com/ympfmu](http://go.nature.com/ympfmu) for more. Separately, on 21 January, European Union member states voted that, from 1 May 2013, projects that reduce emissions of industrial hydrofluorocarbon gases will be banned from selling carbon-offset credits under the trading scheme. For years, companies have been accused of perversely increasing production of these gases so as to sell more carbon credits (see *Nature* 445, 595–596; 2007).

### Shuttle’s swansong

NASA has added an extra Space Shuttle flight to its schedule of launches this year, even though it has no money to pay for the mission.

The veteran shuttle fleet will be retired after the flight. On 20 January, the space agency said that it would send the *Atlantis* shuttle up to the International Space Station on 28 June. This third shuttle flight of 2011 was mandated by the 2010 NASA Authorization Act, but it has not yet been funded by Congress.

### Italian peer review

The Italian government has set in motion its long-promised university evaluation body, ANVUR (National Agency for Evaluation of the University and Research System). On 21 January, it nominated its board of seven academics. ANVUR will evaluate teaching and research at

universities and distribute budgets accordingly. It will also be responsible for ensuring that all public research funds are distributed through peer review. Scientists hope that ANVUR’s competitive funding process will improve patchy research standards in the country (see *Nature* 468, 1001–1002; 2010).

### Aid corruption

The Global Fund to Fight AIDS, Tuberculosis and Malaria says it is confident that it will not lose support from international donors despite evidence of abuse of its grants in some countries. The corruption, uncovered by the fund’s own Office of the Inspector General last year, was re-reported last week. The fund clarified

that it was demanding the recovery of US\$34 million out of \$13 billion in grants it has disbursed since its creation in 2002. Observers praised the fund for its openness and transparency. See [go.nature.com/cybtcd](http://go.nature.com/cybtcd) for more.

## RESEARCH

## European grants

The European Research Council (ERC) has announced the winners of its third round of Advanced Grants, worth a total of €590 million (US\$800 million). The ERC said on 20 January that 266 leading researchers from 26 countries had been awarded grants; 9% of the recipients were women. See [go.nature.com/arqgku](http://go.nature.com/arqgku) for more. Meanwhile, the European Commission on 24 January adopted three measures — effective immediately — to simplify the process of applying for European Union research funds under the Seventh Framework Programme (see *Nature* **465**, 22; 2010).

## Daisy delisted

Species join the US Endangered Species list much more frequently than they leave it. But the US Fish and Wildlife Service said on 18 January that it is set to remove the Maguire daisy (*Erigeron maguirei*) — a perennial shrub that grows

on flat hills in Utah — from the list in a month's time. The daisy is just the twenty-first species to be 'delisted' owing to recovery. Although habitat protection had a role in the plant's comeback, much of the credit goes to taxonomists who merged two varieties of the daisy into one species, thereby instantly increasing its numbers.

## PEOPLE



## Ecology award

Finnish ecologist Ilkka Hanski (pictured) has won the 2011 Crafoord Prize in Biosciences, worth 4 million Swedish kronor (US\$603,000). Hanski, of the University of Helsinki, Finland, was chosen for his lifetime's work analysing how populations of animals and plants respond to changing and fragmented habitats. His theories have formed the "cornerstones of research on biodiversity", said the Royal Swedish Academy of Sciences,

which awarded the prize on 20 January. See [go.nature.com/tjgdu](http://go.nature.com/tjgdu) for more.

## Climate tzar retreat

Carol Browner, informally known as the 'climate tzar' of US President Barack Obama, is stepping down, White House officials said on 24 January. Her departure from the role of director of the White House Office of Energy and Climate Change leaves Obama's strategy on climate change unclear; as *Nature* went to press, no replacement had been confirmed.

## BUSINESS

## Deep-sea mining

Nautilus Minerals has obtained the world's first lease to mine minerals under the ocean, it said on 17 January. The 20-year lease from Papua New Guinea allows the company, based in Toronto, Canada, to progress with plans to start mining for copper and gold in a 59-square-kilometre area in the Pacific Ocean north of Rabaul, Papua New Guinea, from 2013.

## Antibodies deal

Pfizer has agreed to pay up to US\$632 million to Theraclone Sciences, a biotech firm based in Seattle, Washington, for access to the company's therapeutic antibody technology. Theraclone

## COMING UP

### 30–31 JANUARY

An assembly of the African Union in Addis Ababa follows a week's summit attended by more than 30 heads of state. Climate change and development in the continent are on the agenda.

[go.nature.com/zz9ghv](http://go.nature.com/zz9ghv)

### 2–5 FEBRUARY

The latest advances in DNA sequencing are discussed at the annual Advances in Genome Biology and Technology meeting in Marco Island, Florida.

<http://agbt.org>

will work with Pfizer, headquartered in New York, to identify human antibodies against four targets in infectious disease and cancer. Details of the deal — such as upfront research funding — were not disclosed when it was announced on 19 January, but it marks Pfizer's latest attempt to enter the lucrative field of biological therapies.

## Plastic electronics

Russia's ambitious nanotechnology plans were highlighted by the announcement of a US\$200-million investment in Plastic Logic, a company headquartered in Mountain View, California, that hopes to make flexible electronic readers. The state-owned Russian Corporation of Nanotechnologies (known as Rusnano) in Moscow revealed the sum last week, although the deal, involving a factory to be built in Zelenograd, was trailed last November. Plastic Logic was spun out of research at the University of Cambridge, UK, in 2000. See [go.nature.com/rsv4rk](http://go.nature.com/rsv4rk) for more.

➔ [NATURE.COM](http://NATURE.COM)

For daily news updates see:

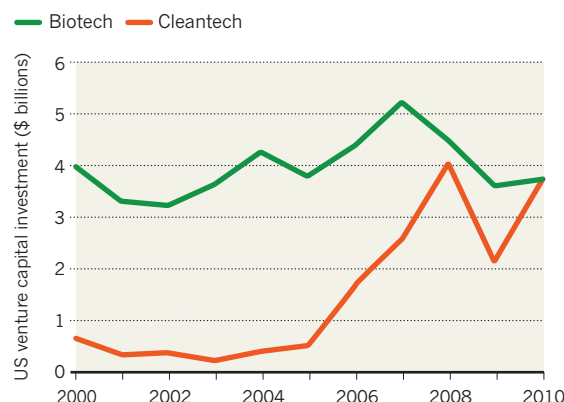
[www.nature.com/news](http://www.nature.com/news)

## BUSINESS WATCH

US venture capitalists spent more money in 2010 than in the previous year — stemming two years of falling investment. Biotechnology saw only a modest increase, but the clean-technology sector improved greatly. Significant investments in the last quarter of the year included US\$110 million for Abound Solar, a Colorado-based photovoltaic manufacturer, and \$100 million for Elevance Renewable Sciences, a California-based start-up that makes chemicals and fuels from renewable feedstocks.

## VENTURE CAPITAL RECOVERY

The cleantech industry was a main beneficiary of increased venture capital spending in 2010.



# NEWS IN FOCUS

**TUNISIA** Stifled for decades, scientists welcome the revolution **p.453**



**SOLAR PHYSICS** High hopes for the Glory probe's mission to watch the Sun **p.457**

**NEUROSCIENCE** Picturing Alzheimer's plaques in the living brain **p.458**

**CHINA** A maverick plots a clear course for marine research **p.460**



Site tests suggest that the superlative observing conditions on Cerro Armazones make it an ideal location for the European Extremely Large Telescope.

## ASTRONOMY

# Brazil ignites telescope race

*Deal boosts Europe's bid to build world's biggest observatory, as US groups compete for funds.*

BY ADAM MANN

To astronomers, Cerro Armazones in Chile's Atacama Desert practically screams for an observatory. Above it is the same dry, stable air that gives the Very Large Telescope (VLT), 20 kilometres away at Cerro Paranal (see map), one of the world's best views of the heavens. But at 3,064 metres, more than 400 metres higher than Paranal, Armazones should make an even better perch for an extraordinary telescope.

The mountain may not have much longer to wait. On 29 December, Brazil announced its intention to join the European Southern Observatory (ESO), which operates the VLT among other sites in Chile. If ratified by Brazil's parliament, the move will make it the consortium's fifteenth, and first non-European,

member. It also significantly improves the odds that the European Extremely Large Telescope (E-ELT), an optical behemoth that would be the world's largest telescope and possibly the most important astronomical tool of the century, will be built on the summit of Armazones, with construction to begin as soon as next year.

"We have the site. We have the design. The addition of Brazil puts the whole funding scenario on a much sounder footing," says Tim de Zeeuw, director-general of ESO, which is headquartered in Garching, Germany.

The deal will give Brazil's astronomers access to ESO's facilities and put the country's burgeoning high-tech sector in a position to bid competitively on building components for the

E-ELT. In return, Brazil will contribute about €300 million (US\$400 million) to ESO over ten years, including a €130-million entry fee. That is enough to tip the scales in favour of the E-ELT being built and to cement ESO's status as the world's leading astronomical research entity. ESO had already selected Armazones as the preferred site for the E-ELT next-generation observatory, which would have a segmented main mirror that is a staggering 42 metres across — giving it 15 times more light-gathering power than the largest telescopes in use today. But until now, it has not been clear whether the organization would secure the estimated €1 billion it needs to make the E-ELT a reality.

The news increases pressure on two US-led efforts of comparable scale: the Thirty Meter Telescope (TMT) project, which also considered Armazones but instead opted for the ▶

**NATURE.COM**  
For more on  
next-generation  
telescopes:  
[go.nature.com/lpcyol](http://go.nature.com/lpcyol)

► advantages of a US location on Mauna Kea in Hawaii, and the Giant Magellan Telescope (GMT), a 24.5-metre instrument planned on the summit of Cerro Las Campanas in Chile. Both are backed by a broad collaboration of US universities and international partners, and are aiming for first light around 2019, about the same time as the E-ELT.

Last year, the US astronomical community's Astro2010 decadal review recommended that the National Science Foundation (NSF) support a giant new observatory. But with resources constrained, the panel said the NSF must choose between the two US-led telescopes.

## GRANDER DESIGN

Both the E-ELT and the TMT are designed along the lines of the two 10-metre Keck Telescopes in Hawaii, but on a grander scale. Their primary mirrors will consist of hundreds of 1.45-metre hexagonal mirrors, the position of which can be controlled individually to optimize image quality. By contrast, the GMT will be composed of six 8.4-metre mirrors arranged around a seventh, central mirror of the same size (see 'Big eyes on the sky').

The scientific case for such enormous instruments is strong, says Ray Carlberg, an astrophysicist at the University of Toronto, Canada, and the Canadian project director of the TMT. They will see to the edge of the visible Universe and discern the formation of the earliest stars, galaxies and black holes. Closer to home, they will image planets in orbit around other stars and probe their atmospheres for constituents that might indicate the presence of life. Any country without access to such a powerful instrument will be at a great disadvantage compared with the rest of the astronomical community, says Carlberg.

Because of their size and cost, such projects require more resources than any single nation can provide. In ESO's case, Brazil's cost of entry is matched by a total of €300 million already committed by the 14 European members.

ESO has also asked members for a further "extraordinary contribution" of €400 million, which should cover the remaining construction costs of the E-ELT, says de Zeeuw. Despite austerity measures, he hopes that the European states will formally agree to provide the extra funding by the middle of this year.

Roger Davies, an astrophysicist at the University of Oxford, UK, and chair of the E-ELT standing review committee, says that Brazil's entry greatly improves the odds that the remaining funds will fall into place. If that happens, ESO's governing council could approve the E-ELT by September, with construction to begin early next year.



For the TMT and GMT, by contrast, momentum has slowed. The decadal review, which recommended that the NSF cover 25% of the cost of one project, urged the agency to make the decision between the two projects "as soon as possible". Researchers are concerned that a prolonged period of uncertainty could drive away other partners.

An informed decision cannot be made without analysing how such a large investment will shape the scientific community in the years to come, says James Ulvestad, division director for astronomical sciences at the NSF. "It's predicting the future," he says. "You have to

evaluate where science will be — not today, not next month, but in ten years." Ulvestad says the agency should be ready to conduct a review of proposals from the GMT and TMT by mid-2011, with a decision to follow by December.

Another complication is that the decadal review lists building the Large Synoptic Sky Telescope (LSST), an 8.4-metre survey instrument that will image wide areas of the sky, as a higher immediate priority than the GMT or TMT. Adhering to this would mean that the NSF would not be free to commit construction funding to other projects before the LSST is built, which could be late in the decade — long after the GMT and TMT project teams hope to be well on the way towards completion.

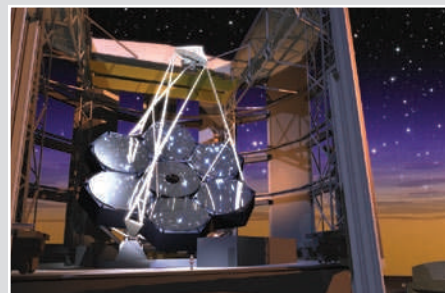
Both projects are making contingency plans in case federal funding does not materialize. "It certainly would be helpful," says GMT director Patrick McCarthy, but the GMT could still go ahead without NSF support, he says, as its international partners, Australia and South Korea, have made their funding commitments.

Similarly, Edward Stone, vice-chair of the TMT's board of directors, says that the TMT aims to get started as planned, "and that will be if the NSF joins or not". But the TMT could soon face a setback. A draft planning document circulated this month by the Canadian astronomical community recommends that Canada pull out of the TMT and seek membership of ESO if, by 2014, the TMT has fallen significantly behind the E-ELT.

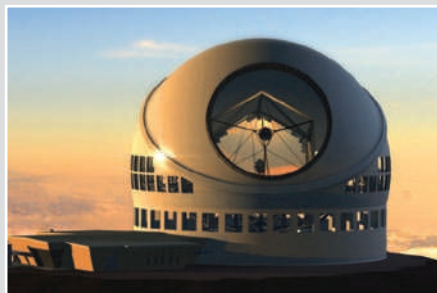
The recommendation is a reminder of the high stakes in the rivalry, as observational astronomy shifts from an era in which a dozen or so major observatories represented the leading edge of the field to a time when just two or three will do so. "People are realizing it will be devastating to be left behind," says Carlberg.

By joining ESO, Brazil, which also considered the GMT and TMT, has apparently decided it will not be left behind. The coming year will determine who else may be in or out of astronomy's next great round of cosmic exploration. ■

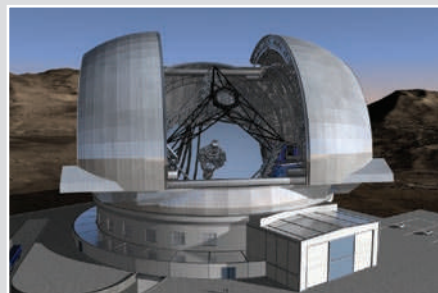
## BIG EYES ON THE SKY | How the megascopes compare



**PROJECT NAME:** Giant Magellan Telescope  
**SELECTED SITE:** Cerro Las Campanas, Chile  
**DIAMETER OF MIRROR ARRAY:** 24.5 metres  
**PARTNERS:** United States, Australia, South Korea  
**ESTIMATED COST:** US\$700 million  
**PROJECTED CONSTRUCTION PERIOD:** 2012–20\*  
 \* Subject to funding



**PROJECT NAME:** Thirty Meter Telescope  
**SELECTED SITE:** Mauna Kea, Hawaii  
**DIAMETER OF MIRROR ARRAY:** 30 metres  
**PARTNERS:** United States, Canada, Japan, India, China  
**ESTIMATED COST:** US\$1 billion  
**PROJECTED CONSTRUCTION PERIOD:** 2012–19\*  
 \* Subject to funding



**PROJECT NAME:** European Extremely Large Telescope  
**SELECTED SITE:** Cerro Armazones, Chile  
**DIAMETER OF MIRROR ARRAY:** 42 metres  
**PARTNERS:** European Southern Observatory members (14 European states and Brazil)  
**ESTIMATED COST:** US\$1.4 billion  
**PROJECTED CONSTRUCTION PERIOD:** 2012–21

GMT: ESO; TMT: ESO



Widespread protests have brought down Tunisia's authoritarian regime.

## POLICY

# Tunisian scientists rejoice at freedom

*As revolution reshapes the country, researchers lay plans for a system that will foster free thinking and innovation.*

BY DECLAN BUTLER

“A historic event, a real revolution,” says one Tunisian researcher. “Proud to find a Tunisia liberated, that has found its freedom of speech, and its dignity,” says another. “Truly the revolution of all a people,” adds a third.

Tunisian scientists contacted by *Nature* could barely contain their emotions about the uprising that this month overthrew President Zine el-Abidine Ben Ali, the dictator who had ruled their country for the past 23 years. Although aware of the challenges ahead, many are convinced that a new era of democracy, human rights and academic freedom will prevail — and help to unleash a surge of creative and entrepreneurial forces among a highly qualified but repressed Tunisian population.

The country has experienced dizzying change since the self-immolation of Mohamed Bouazizi, a poor street vendor, in the southern town of Sidi Bouzid on 17 December triggered a nationwide revolt. Ben Ali was forced to flee

the country on 14 January, ending the de facto single-party rule of his Constitutional Democratic Rally (RDC) party.

Students and intellectuals are often in the vanguard of revolutions, but this was not the case in Tunisia. Instead, broad segments of Tunisia's relatively highly educated youth rose up to protest against high levels of unemployment, government corruption and a dearth of human rights, says Abdelaziz Chikhaoui, an engineering scientist at the University of Provence Aix-Marseille in France, and president of the Association of Tunisian Researchers and Lecturers in France (ACETEF).

“The revolution was unexpected both in intensity and rapidity, we were all surprised

➔ **NATURE.COM**  
For interviews with  
Faouzia Charfi and  
Hamed Ben Dhia see:  
[go.nature.com/wrbxt](http://go.nature.com/wrbxt)  
and [go.nature.com/iomt8e](http://go.nature.com/iomt8e)

by the movement,” says Hamed Ben Dhia, president of Tunisia's University of Sfax, who is considered by colleagues to be relatively independent of the Ben Ali regime. Many academics

and intellectuals soon rallied to the cause and, on 11 January, the regime shut the universities and schools to stop protests spreading there.

Tunisian researchers are now free to express their frustration with the regime's suppression of human rights — and its management of the higher-education and research system. To judge from publication rates and other metrics, the country has a fairly strong science and higher-education base, which compares favourably with its Arab neighbours (see ‘How Tunisia's science measures up’). Although proud of the figures, scientists argue that they mask a reality that is much less upbeat.

## SOLID FOUNDATIONS

Researchers contacted by *Nature* unanimously credit Tunisia's strong science and educational foundations to Ben Ali's predecessor, Habib Bourguiba, who became president in 1957, the year after Tunisia gained independence from France. Bourguiba built a progressive, modern, secular state, and made developing the country's human capital, empowering women and bolstering education top priorities.

At independence, Tunisia had no higher-education system and almost no research base, with the exception of some agricultural research and colonial outposts such as France's Pasteur Institute in Tunis. Bourguiba created the country's universities and got them running with the help of imported French academics. The result has been that Tunisia has long had one of the best-educated populations in the Arab world. Bourguiba was a dictator, but he was a relatively benign and enlightened one, say researchers.

His rule ended in 1987 when, on 7 November, Ben Ali staged a bloodless coup. The new government promised greater freedoms but quickly established a brutal police state. “We went from an honest autocrat to a dishonest and bloody autocrat,” says Ben Dhia.

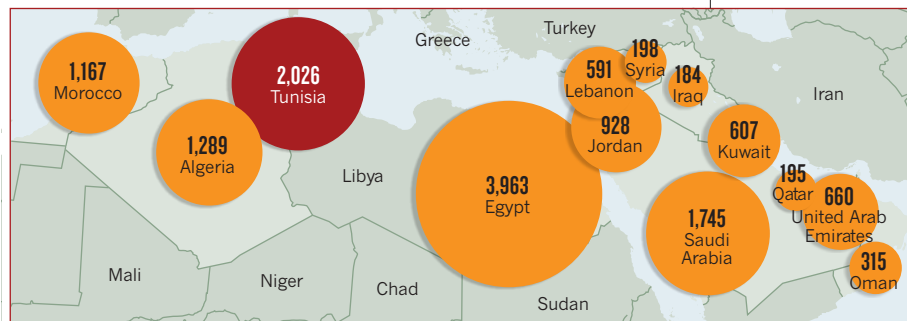
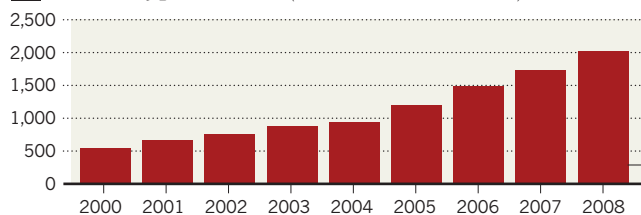
Ben Ali's regime maintained support for education and science, with science funding growing from 0.43% of gross domestic product in 1999 to 1.02% in 2007. Little brain drain took place: scientists who did leave, mostly for France, usually did so for better pay and research conditions. But Tunisia offered a reasonable standard of living, and many preferred to stay, says Ben Dhia. “One got used to living with limited liberty,” he says. But the government's totalitarian reflex to control Tunisia's citizens, including its researchers, stifled the development of a dynamic research and innovation system.

Universities and researchers had little freedom to develop their own strategies, or even to choose who they worked with, says Faouzia Charfi, who was last week appointed secretary of state for higher education in the current transition government. Charfi is a physicist at the Preparatory Institute for Scientific and Technical Studies in Tunis, and the widow of the late Mohamed Charfi, former president of the Tunisian League for the Defense of Human Rights and a former education minister. ▶

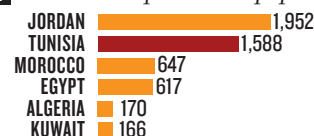
# HOW TUNISIA'S SCIENCE MEASURES UP

Tunisia scores well among nations of the Arab world on research metrics such as its growing number of research publications (1); its relatively high proportion of researchers (2); and the extent of its research funding (3).

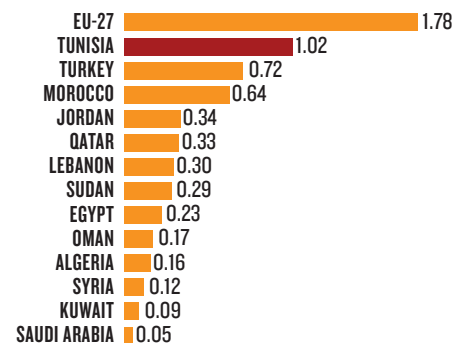
## 1 Number of publications (Science Citation Index)



## 2 Researchers per million population



## 3 Gross domestic expenditure on R&D as a percentage of gross domestic product



Data in 2 and 3 are from 2007 or latest year available. Some of these figures are estimates.

► Multiple permissions were required for almost everything, from leaving the country to meeting with foreign researchers, says Ben Dhia. Tunisians organizing a scientific conference needed to submit to the regime all the presentations that speakers would make, and the regime also required universities to send detailed weekly reports of how all staff spent their time, he says. The regime imposed an “intellectual blockage” at every level of university life, which disempowered researchers and stifled innovation, adds Charfi.

Ben Dhia and Charfi tell similar stories of how regime bureaucrats thwarted any attempts to build independent links with industry. Universities were also prevented from developing their own research strategies. Ben Dhia recalls having to create labs and institutes even when he felt they made little sense. Universities became machines for generating papers and degrees to meet targets, but became disconnected from societal and innovation needs, he says. The administration was scared of letting individuals take the initiative, adds Charfi: “You had no freedom to manage your own institution.”

Now, the revolution has fired people up to make the country succeed. “Scientists will for the first time have the liberty to decide their

own future, and not have it imposed by RDC members,” says Chikhaoui.

A key challenge for reformers is the nepotism that has become ubiquitous in Tunisia’s universities. Ben Ali himself appointed vice-chancellors, and even lower-level faculty members were chosen more for allegiance to the ruling party than for competence. Dorra Cherif, adviser to the director at the Tunis Pasteur Institute, says that scientists, like many Tunisians, often joined the RDC out of pragmatism rather than because they supported the regime.

## LONG ROAD TO REFORM

“It is clear that the system must absolutely change,” Charfi says, adding that the new government intends university presidents and boards to be directly elected — perhaps by academic panels — in the future. But, she adds, the government wants to “avoid a witch-hunt”: those researchers and university administrators who are competent and committed to change will be allowed to share the country’s fresh start.

The transition government is expected to organize elections within the next two months, and Charfi told *Nature* that it hopes to reopen universities and schools “without delay”, possibly as soon as this week. Symbolically,

university chairs named after Ben Ali will be renamed, and students arrested by the regime will be reintegrated into universities so that they can finish their studies, she says.

In the longer term, Charfi and other members of the transition government are supportive of maintaining Tunisia’s science funding, but she emphasizes that university training needs to be revamped to produce creative, entrepreneurial graduates who are better trained to enter the job market. “There is no point in having degrees that lead nowhere,” says Charfi.

This could help to address a key issue that triggered the revolt: many who hold advanced degrees are unemployed. Similarly, a profound rethink of university–industry relations will be needed to help to create jobs, Charfi says. If a stable democracy emerges in Tunisia, foreign investors that were previously discouraged by the regime’s corruption are likely to be more willing to invest there.

Charfi has few illusions that change will come overnight. “We have to be realistic, we won’t have stability within 24 hours, but we must be confident,” she says. “I am profoundly convinced that we will accomplish the success of this revolution, this rupture with the past.” ■ SEE EDITORIAL P.443



**MORE ONLINE**

### LATEST NEWS

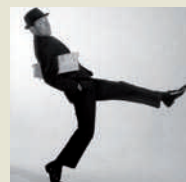


Reefs may simply move house when the oceans heat up  
[go.nature.com/s98hvj](http://go.nature.com/s98hvj)

### MORE STORIES

- Double whammy for HIV [go.nature.com/obftwr](http://go.nature.com/obftwr)
- Ship’s graveyard may be behind West Africa’s toxic problem [go.nature.com/hoxhwb](http://go.nature.com/hoxhwb)
- Slime moulds prosper on the microfarm [go.nature.com/lvltlq](http://go.nature.com/lvltlq)

### VIDEO



Theoretical walker suggests methods for saving energy  
[go.nature.com/hj8m5d](http://go.nature.com/hj8m5d)

## GENETICS

# China spurs quest for human variome

*Population giant weighs in with funds for disease-related genetics project.*

BY DAVID CYRANOSKI

**T**he Human Variome Project (HVP), an ambitious initiative to uncover all of the genetic variations that cause human disease, received a massive boost last week when China announced that it would commit US\$300 million to the effort. The investment, to be paid out over ten years, puts the project on a firm footing for the first time since its launch in 2006, and signals China's intention to take on a bigger role in the medical-genetics field.

The sum is meant to cover roughly 25% of the cost of the HVP, a proportion matching China's share of the world's population and in keeping with its growing economic influence, says Ming Qi, director of the Zhejiang University Center for Genetic and Genomic Medicine, who has led the Chinese initiative. "With the state of our economic development, I felt we could do more," adds Qi.

As part of the agreement, announced on 21 January at the project's headquarters in

Melbourne, Australia, China will set up a genetics institute in Beijing to coordinate activities across the country and to give training in genetic counselling and testing. "The research will be very close to the clinic," says Qi. "It will be a fundamental change for China."

The HVP's goal is to establish "the standards, systems and infrastructure" that will allow sharing of disease-related genetic data between doctors and scientists throughout the world for use in diagnosis and research. Each participating country will have a network, or 'node', that collects information from diagnostic testing laboratories and hospitals.

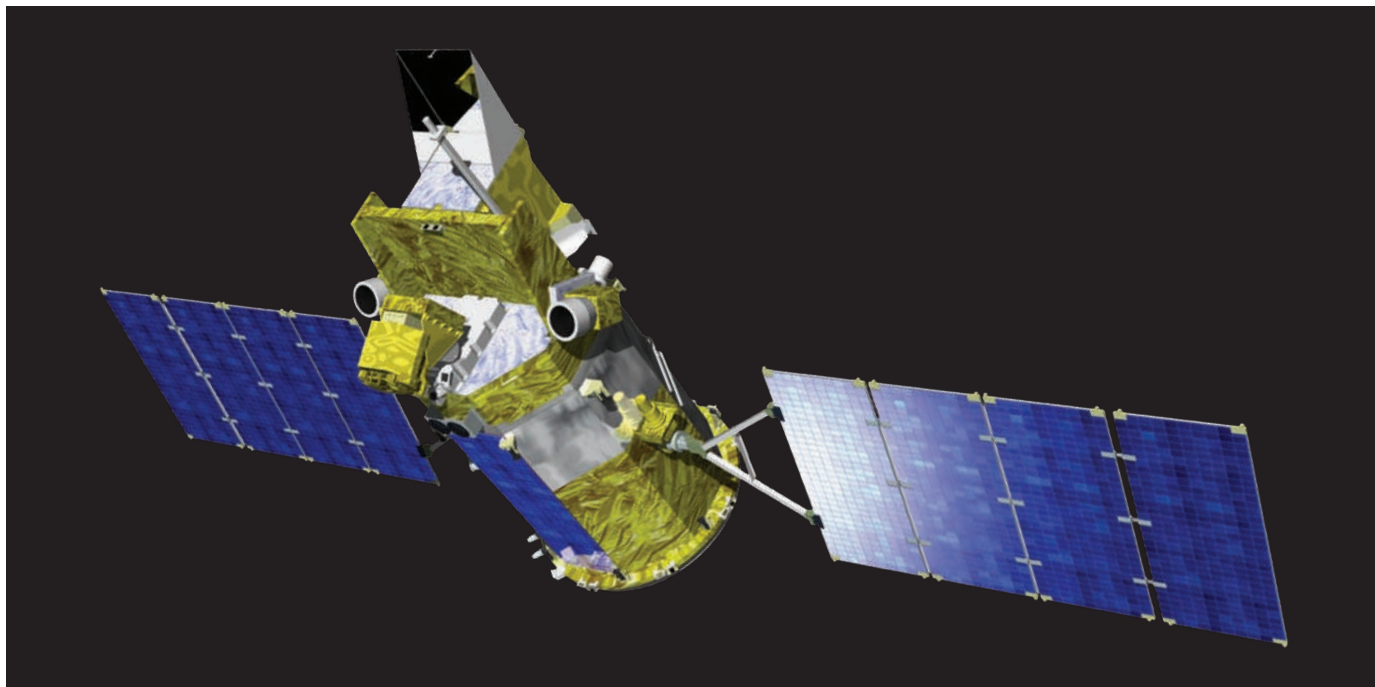
Institutions that have signed up to help develop China's node include Peking Union Medical College Hospital, Tianjin Medical University Cancer Institute and Hospital and hospitals affiliated with Zhejiang University School of Medicine and Peking University. Qi envisages

**"We want to collect every case of each disease."**

the funding bringing many more on board.

China's move offers not only financial resources but also greater access to a vast swathe of human genetic data from a part of the world previously under-represented in genetic studies. Five other nations are also developing nodes for the project — Australia, Kuwait, Malaysia, Egypt and Belgium. "We hope the commitment from the Chinese government will also highlight the need for this work to other countries and their funding bodies," says Richard Cotton, a geneticist at the University of Melbourne and head of the project's coordinating office.

Although other projects, such as the International HapMap Project, have assembled data on single nucleotide polymorphisms — common genetic variations across populations — the HVP is collecting information on all genetic variations related to human disease, including new and rare mutations, large-scale deletions and copy number variations. "We're casting our net wider," says Cotton. "We want to collect every case of each disease." ■



A specially calibrated monitor aboard NASA's Glory satellite will measure how much radiation the Sun emits.

## SOLAR SCIENCE

# Probe keeps keen eye on Sun

*Glory satellite will make more accurate measurements of solar output.*

BY JEFF TOLLEFSON

At some point Greg Kopp just got tired of the questions. Every time the solar physicist showed a plot of the Sun's total radiation output as measured by a succession of satellites since 1978, he had to explain an unexpectedly large offset starting around 2003. That was the year NASA's Solar Radiation and Climate Experiment (SORCE) was launched (see 'Mission control'), carrying a new type of sensor developed by Kopp and his team at the University of Colorado's Laboratory for Atmospheric and Space Physics in Boulder.

Kopp initially thought that there was a problem with the sensor, the Total Irradiance Monitor (TIM), which consistently gave a lower reading than its predecessors. Subsequent analyses now suggest that the sensor's readings offer a truer measure of the Sun's total energy output than others. That accuracy is crucial to understanding the 11-year solar cycle as well as the Sun's small but measurable contribution to global warming. Now, with a second-generation TIM scheduled for launch on 23 February aboard NASA's Glory satellite, Kopp believes he has found a way to avoid a future mismatch

in detector readings. "I decided that with Glory I was going to solve this problem once and for all," he says.

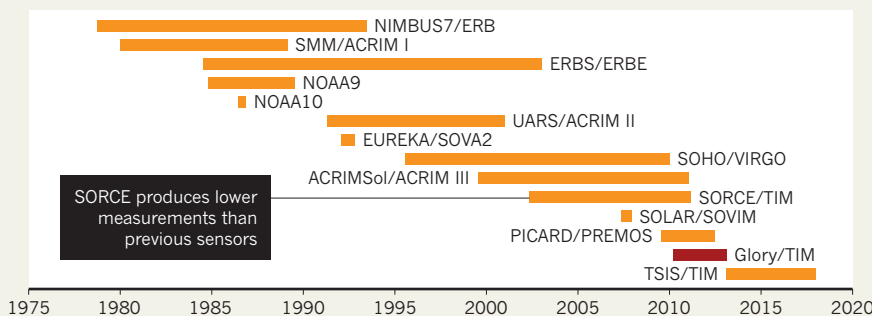
Kopp's solution was to design a facility that can exquisitely calibrate sensors such as TIM before they launch. The facility includes a variable power laser that acts as a light source and a cryogenically cooled radiometer that is almost immune to temperature fluctuations, all inside a space-like vacuum. By calibrating the detector to the radiometer's readings, Kopp hopes to eliminate almost all ambiguity in Glory's measurements of solar radiation, expected to be three

times more precise than those from SORCE.

He has also used the facility to analyse a replica of the SORCE sensor and validate that satellite's readings. On the basis of those and other measurements, Kopp and Judith Lean of the Naval Research Laboratory in Washington DC, calculate that during the 2008 solar minimum, the Sun emitted about 0.34% less energy than previously estimated (G. Kopp and J. L. Lean *Geophys. Res. Lett.* **38**, L01706; 2011). That is not enough to affect estimates of human influence on climate, but it is important for solar physicists. "This is a fundamental ►

## MISSION CONTROL

A series of missions have measured the Sun's energy output continuously since 1978. With the launch of Glory and future satellites, physicists hope to continue the series with even greater accuracy.



► **NATURE.COM**  
For more on the launch of the Glory satellite, see:  
[go.nature.com/mcblind](http://go.nature.com/mcblind)

► quantity that has been pursued for more than 100 years,” Lean says.

The design of TIM explains its consistently lower readings. Other sensors typically use a two-stage aperture to gather incoming light. Kopp and Lean suggest that this can allow light to bounce around within the device and contribute to an overestimate of incoming energy. In Kopp’s TIM, 99.99% of the solar radiation that enters the aperture disappears down a long tube before getting trapped in a chamber full of what he describes as miniature broccoli heads made of a nickel–phosphorus alloy. The device then measures the amount of heat the sensor derives from the incoming radiation.

Solar physicists hope that the increased precision and confidence built into the current

generation of irradiance sensors will compensate for any future lapse in monitoring. Yet continuity remains a high priority. NASA’s goal is to get some overlap between Glory and SORCE, which lost one of the reaction wheels used to aim the instrument in September 2008 and has been running on a back-up system ever since. “Overlap among measurements is essential because absolute accuracy is not guaranteed,” says Kevin Trenberth, a senior climate scientist at the National Center for Atmospheric Research in Boulder.

Preliminary data from PREMOS, a Swiss-built sensor launched in June 2010 on the French PICARD satellite, seem to align well with the SORCE readings. PREMOS was also calibrated against Kopp’s cryogenic radiometer, which

bolstered confidence in its initial readings, says principal investigator Werner Schmutz at the World Radiation Center in Davos. “Without this confirmation, we probably would have hesitated with our new value,” Schmutz adds.

Researchers are counting on another University of Colorado detector to pick up monitoring duties in 2014. While improvements in calibration mean that researchers can probably tolerate a gap in the record and still compare past and future data with reasonable confidence, Kopp says, such a contingency would be a last resort. The truest test of Kopp’s ground-based calibrator will come when Glory begins reporting data later this spring. Kopp says he’s not losing any sleep. “I’m really expecting good agreement,” he says with a smile. ■ [SEE EDITORIAL P.444](#)

## NEUROIMAGING

# Alzheimer’s–disease probe nears approval

*Imaging technique could help to resolve questions about brain plaques associated with the condition.*

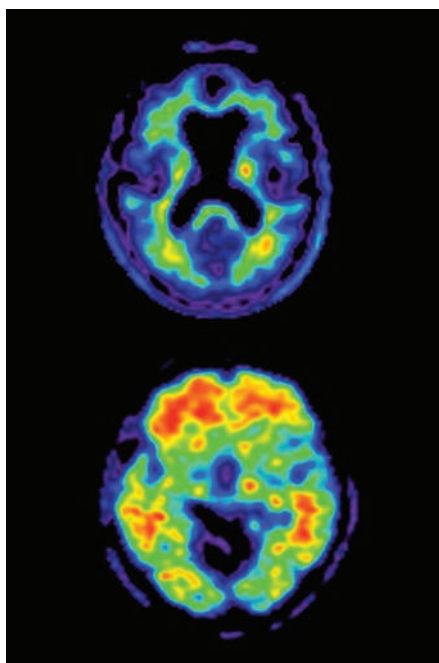
BY HEIDI LEDFORD

An imaging agent that reveals a signature of Alzheimer’s disease in the brain — given conditional support last week by advisers to the US Food and Drug Administration (FDA) — is likely to be more valuable to scientists than to patients.

The agent, called florbetapir (Amyvid), enables physicians to determine whether Alzheimer’s disease is the cause of a patient’s dementia. In the future, it may also help them to catch the disease before obvious symptoms appear, a hope that has sparked fresh debate about the value of early diagnosis for a devastating, untreatable disease. The panel of advisers — whose guidance is usually, but not always, followed by the FDA — also stated that the test should not be given final approval until its developers demonstrate that clinicians can uniformly interpret its results.

“The importance of the decision is probably bigger for research in the near future than it is for clinical practice,” says William Thies, the chief medical and scientific officer of the Alzheimer’s Association based in Chicago, Illinois, a nonprofit organization that funds research on Alzheimer’s disease.

Physicians diagnose Alzheimer’s disease only after memory loss interferes with daily activities. By then, “there’s so much irreversible damage that it might be too late to hope for an effective treatment,” says Gil Rabinovici, a neurologist



**Florbetapir reveals amyloid plaque build-up (red) in the brain of someone with Alzheimer’s disease (bottom), which is absent in a healthy brain (top).**

at the University of California, San Francisco. Definitive confirmation comes from autopsy, with the presence of characteristic lesions in the brain caused by clumps of the peptide

amyloid- $\beta$ . These amyloid plaques are hypothesized to be the cause of the memory loss.

Some researchers already use a reagent called Pittsburgh Compound B to image amyloid plaques in people suspected to have Alzheimer’s disease. The compound binds to the plaques, and its radioactivity can be detected using positron emission tomography. But the reagent is labelled with carbon-11: with a half-life of just 20 minutes, its use is limited to the handful of facilities that have an on-site cyclotron to prepare it.

In contrast, florbetapir is labelled with fluorine-18, which has a half-life of nearly two hours. That would be long enough to allow the compound’s manufacturer, Eli Lilly, based in Indianapolis, Indiana, to send labelled florbetapir directly to users without losing too much of the reagent to radioactive decay. The likely result: more and bigger studies of the relationship between amyloid and disease, says Thies.

A study published last week was crucial to the advisory panel’s decision. It confirmed that brain scans of living patients given florbetapir correlate with amyloid plaques found at autopsy after they died (C. M. Clark *et al.* *J. Am. Med. Assoc.* 305, 275–283; 2011). The Alzheimer’s Disease Neuroimaging Initiative, a project to improve clinical trials of candidate therapies for Alzheimer’s disease, has already incorporated florbetapir in its studies of hundreds of people suspected to have the condition. And Rabinovici hopes to test whether the reagent can distinguish between Alzheimer’s disease and frontotemporal dementia, which causes many of the same symptoms and is often misdiagnosed.

Florbetapir could help to resolve one of the fundamental disputes about Alzheimer’s disease: whether amyloid plaques kill brain tissue or are a side effect of the disease process. “Critics always tell me ‘well we don’t know yet if the amyloid hypothesis is true,’” says William Jagust, a neuroscientist at the University of California, Berkeley. “But this compound will finally allow us to examine just how important amyloid is.” ■

ELI LILLY/AVOID RADIOPHARMACEUTICALS



# China's unsinkable scientist

*After years of struggle on behalf of ocean science, Wang Pinxian is taking a key role in China's plans to expand marine research.*

BY JANE QIU

**W**ang Pinxian began his scientific career in the shabbiest of conditions, spending long winters in an abandoned Shanghai workshop with no heat. He washed and screened samples of sea-floor sediment in a rice bowl, and struggled with a microscope that would barely focus. The most important book on his shelf was a Russian encyclopaedia of palaeontology, which helped him to identify microfossils in the samples pulled up from off the coast of China.

"It's an extraordinary way to start a career in oceanography," says Wang, laughing as he recalls those days half a century ago. He fell in love with the tiny creatures that served as windows to Earth's distant past, and he dreamed of using the fossils to help to develop the scientific capacity of his country.

Wang, now a marine geologist at Tongji University in Shanghai, slowly rose up the ranks. He eventually earned a position in the Chinese

Academy of Sciences and served as a member of the Chinese national legislature. For decades, the 74-year-old, outspoken scientist has used his position to lobby Chinese leaders to devote more resources to marine science, but those arguments have fallen on deaf ears — until recently. With China facing an increasing need for energy and minerals, it is now taking an interest in the deep sea. In its next five-year budget, which will be announced in March, the country will boost funding for oceanography, particularly in exploration, research and deep-sea technologies.

That rising tide has also lifted Wang's fortunes. Last July, he was awarded a US\$22-million grant from China's National Natural Science Foundation to lead studies into the geology and biology of the South China Sea. The project starts this week with an inaugural meeting in Shanghai.

"The South China Sea is a haven for oceanographers and climate researchers," says Wang. Sitting between Asia and the Pacific Ocean (see map), the sea is a crossroads for currents that influence the climate of the entire globe. It also helps to control the Asian monsoon system, which feeds the water supplies for billions of people on the continent. Wang's project aims to uncover information about the prehistoric climate and investigate how the ocean basin formed. At the same time, it will study the microbial community in the deep sea, which has an important role in the cycling of carbon between long-term storage in sediments and its release into the ocean and atmosphere.

Born in 1936 in Shanghai, Wang grew up during a tumultuous period in Chinese history — living first through the Sino-Japanese War and then the Chinese Civil War from 1945 to 1949. After the Communist Party founded the People's Republic of China, the young government began

H. ZHENG

to send promising students to Russian universities, and Wang earned the opportunity in 1955 to attend Moscow State University. There he studied geology, which China regarded as a priority because of its practical value in finding mineral resources and oil.

The experience had an enduring effect on Wang. He excelled in Russian and thrived under the scientific training in Moscow, where he was fairly safe from the severe economic and social turmoil sweeping his home country. But when Wang returned to China in 1960, his tendency to speak his mind drew the ire of officials who publicly rebuked him. He voiced concerns about the widespread famine in China at a time when the economic policy known as the Great Leap Forward was widely portrayed as a great success. “These things just didn’t make sense to me at all,” he says.

Because of the extreme economic hardships at the time, Wang’s training initially seemed irrelevant in China, especially during the Cultural Revolution — a violent political and social movement that began in 1966. But China was eager to find fossil-fuel reserves, so Wang was called up by the government in 1972 to analyse calcareous microfossils in marine samples, in the hope of identifying petroleum deposits.

Although he had access to only basic equipment in his Shanghai workshop, Wang toiled away and eventually published the book *Marine Micropaleontology of China*, first released in Chinese in 1980 and then in English<sup>1</sup>. Wang co-authored all of its 17 papers, and developed an international reputation for his scholarship. The book helped to connect Chinese oceanography to research elsewhere — at a time when little was known about marine geological science in China.

## DEEP CONCERNS

The work also attracted international interest in Chinese marine regions, and Wang helped to convince the international effort known as the Ocean Drilling Program (ODP) to conduct the first deep-sea drilling expedition in the South China Sea. Wang co-led the 1999 effort, known as ODP Leg 184, which drilled 17 holes on the southern and northern continental slopes of the sea to explore the history of the east Asian monsoon.

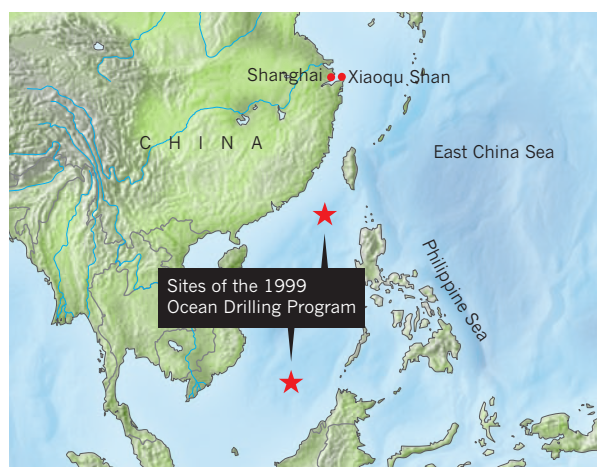
The South China Sea occupies a crucial position between the world’s highest mountains in the Himalayas and the deepest spot on the Earth’s surface, the Mariana Trench in the western Pacific Ocean. Erosion of those nearby mountains causes sediments to accumulate rapidly on the sea floor, providing a detailed record of the regional climate over the past 45 million years, during which time India has collided with Asia and

raised the Himalayas.

“The South China Sea promises some of the most fascinating geological records on Earth,” says Carlo Laj, a palaeoceanographer at the Laboratory of Climate and Environmental Sciences in Gif sur Yvette, France. Laj met Wang during the ODP expedition and the two men have collaborated in subsequent French–Chinese palaeoceanography cruises in the South China Sea.

## EYE ON THE TROPICS

The ODP expedition was a turning point in Wang’s research career. On the basis of the South China Sea records, he and his colleagues found that the chemistry of the region has gone through significant changes in the past 1.6 million years. The sea-floor cores contain fossilized plankton shells that can be used to measure the ratio of the isotopes carbon-13 to carbon-12 in ancient sea water. This can be used to deduce information about different reservoirs of carbon, including atmospheric carbon dioxide and the organic matter from marine organisms. Wang found that the



carbon ratio fluctuated in step with variations in Earth’s orbit — such as the eccentricity of its route around the Sun. And the ratio peaked before two expansions of polar ice sheets, suggesting a possible connection<sup>2</sup>.

These orbital cycles are the pacemakers of Earth’s climate and are thought to trigger ice ages by reducing the amount of sunlight reaching high northern latitudes during summer. But Wang’s work helped to focus attention on the tropics, and raised the possibility that orbital cycles could cool the planet by altering processes in the low-latitudes — such as the weathering of rocks — that in turn cause major changes in the carbon system.

He also conducted research on the East Asian monsoon and its broader connections. He and other researchers have found the fingerprint of orbital cycles within monsoon records from the South China Sea and many other parts of the globe<sup>3</sup>. Instead of regarding monsoons as separate regional phenomena, Wang and others embrace a ‘global monsoon’

concept, which refers to a large-scale churning of the atmosphere throughout the tropics and subtropics. In studies of the palaeoclimate, “Pinxian was one of the first to put monsoon in a global context”, says Laj. “That was extremely original and insightful.” Wang’s work helped to earn him the Milutin Milankovic Medal for long-term climatic research from the European Geosciences Union in 2007.

With the influx of funding and interest from the Chinese government, Wang has big plans for the future. Beyond the eight-year South China Sea project, his team is working with the government to establish a sea-floor observatory off the coast of Xiaoqu Shan, an island south-east of Shanghai. The observatory will record important features of the ocean, including temperature, salinity and sedimentation rates. Wang would ultimately like to build a network of ocean-floor observatories in the South China Sea similar to those off the coasts of the United States and Canada. “This is the only way we can truly understand the oceans,” he says.

Looking back, Wang is surprised that he has managed to thrive under a political regime that usually deals harshly with dissent. Recently, he has openly criticized some entrenched powers in Chinese society. Three years ago, he complained that the election of Chinese Academy members was not based entirely on academic achievements, and that members enjoyed disproportionate authority and privileges. Wang’s remarks sent shock waves across China’s scientific community; even some of his good friends turned against him.

And Wang has not limited his critiques to scientists. He was a member of the National People’s Congress — China’s top legislature — from 1986 to 1992, and has questioned the procedures through which some political decisions are made.

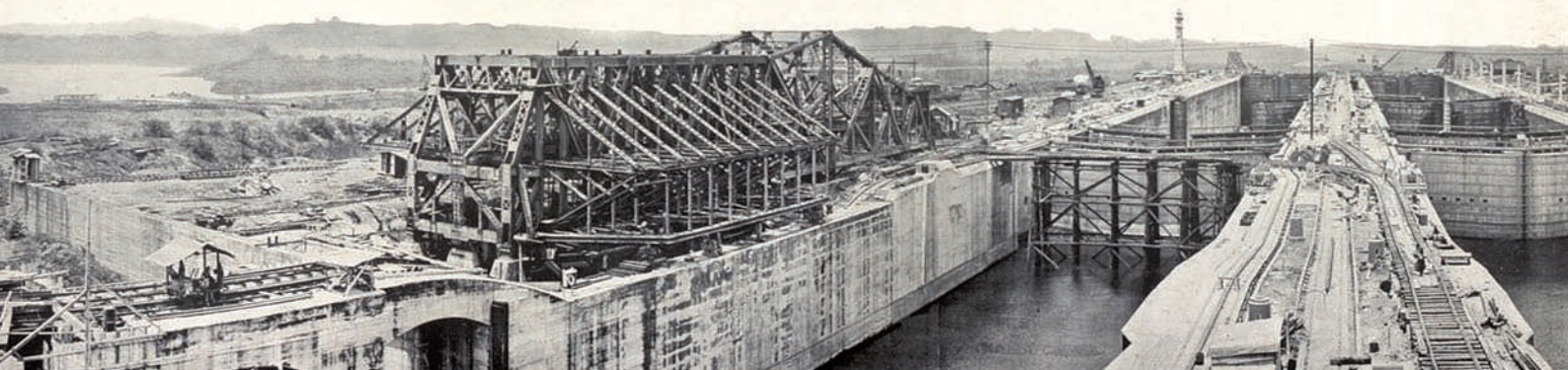
Although he has enjoyed a fruitful career, Wang is concerned about the future of science in a society that has endured so many political upheavals. He says that excessive commercialization and a deficit of moral values have led to rampant scientific misconduct. China, he says, “will need to make some hard decisions and instigate further reforms, especially to its science system”.

Taking the long view, though, Wang recognizes that his country has made tremendous progress since the days he laboured in that frigid Shanghai workshop. “Things will change with time,” he says. “Let’s hope.” ■

Jane Qiu writes for Nature from Beijing.

1. Wang, P. et al. *Marine Micropaleontology of China* (China Ocean Press and Springer-Verlag, 1985).
2. Wang, P., Tian, J., Cheng, X., Liu, C. & Xu, J. *Geology* **31**, 239–242 (2003).
3. Wang, P. *Chin. Sci. Bull.* **54**, 1113–1136 (2009).

**NATURE.COM**  
For more on Chinese science, visit:  
[go.nature.com/kumot7](http://go.nature.com/kumot7)



# PANAMA'S BIG AMBITION

*Researchers in Panama suffered under a dictatorship and were overshadowed by the United States. Now the country is attempting a scientific renaissance.*

BY REX DALTON

**W**hen Carmenza Spadafora Mejía left Panama in 1997, she walked away from a bloody history. In 1985, her brother Hugo had been decapitated by henchmen of the military dictator Manuel Noriega, after Hugo publicly denounced him. For years, Spadafora and her family fought to identify the killers. But the brutal murder helped to spark an uprising that culminated in a US invasion and the imprisonment of Noriega in 1990. After her family won convictions against some of those responsible for the murder, Spadafora felt ready to leave to start a PhD in Spain.

Since 2008, when Spadafora returned to Panama, life for her and her country has been on the up. Now with a US postdoctoral position in infectious diseases under her belt, Spadafora coordinates a cellular and molecular biology centre at INDICASAT-AIP (the Institute of Scientific Advances and High-Technology Services) in Panama City. Last June, she and her colleagues revealed a long-sought receptor that the malaria parasite *Plasmodium falciparum* uses to invade red blood cells<sup>1</sup>, a discovery that could help development of vaccines. A few months later, they won a US\$1-million grant from the Bill & Melinda Gates Foundation in Seattle, Washington, for a scheme that Spadafora concedes may sound outlandish: developing a full-body microwave scanner to cure malaria by killing the parasite. With developments such as these, “we are showing we can compete with anyone worldwide”, she says.

And that is exactly what the Panamanian government wants to do. The country is one of many in Central America that have struggled under dictatorship and political turmoil in the past few decades. Now it is the first to make a significant investment in science part of its recovery, thanks mainly to its past two democratically elected governments, which have seen research as a route to economic growth. “Science and technology are key components for competitiveness,” says Rubén Berrocal Timmons, Panama’s science secretary, adding that he wants to make Panama “an international scientific hub”. To that end, the country’s leaders are intent on increasing investment in science and technology from less than 0.2% of the gross domestic product, as it was in the mid-2000s, to 0.6% by 2014.

The investment is already in evidence. In March, ground is to be broken on a \$20-million science and technology innovation park near Panama City; construction of a \$5-million vivarium for the country’s research animals is planned for this spring; the government is funding

about 100 Panamanians to undertake doctoral studies at universities abroad, with incentives to return to Panama for research careers; and the first complete in-country PhD research programme — in biotechnology — has just begun at INDICASAT-AIP. Observers say that the country’s efforts at a scientific renaissance could even serve as a model for other nations seeking new life after conflicts.

The change in Panamanian science amazes some, including Ira Rubinoff, who led the US Smithsonian Tropical Research Institute in Panama for 34 years until 2008. “If you told me this would happen 25 years ago, I would say you were smoking something illicit,” he says.

## BUILDING AN IDENTITY

Panama is inextricably associated with its canal, which bridges the Atlantic and Pacific oceans. It was built at the start of the twentieth century by the US Army Corps of Engineers, which had to battle malaria and yellow fever to complete its task (see ‘A century in Central America’). Ever since, Panama’s research community has lived in the shadow of the United States, which — in governing the canal — virtually militarily occupied the nation until 1999, when Panama won full control of the waterway under a controversial 1977 US treaty.

During much of the twentieth century, Panama was a US laboratory of sorts for secret military research on mustard and nerve gas, dioxin and depleted-uranium weapons. But after the Second World War, the US presence also allowed the blossoming of the Smithsonian Tropical Research Institute, a branch of the Smithsonian Institution in Washington DC and now a world-class ecological research facility.

Panama’s push to build its own science began with former President Martín Torrijos Espino, who took power in 2004 and saw science as a way to forge a new era independent of the United States. He named Julio Escobar Villarrue, a computer scientist trained at Massachusetts Institute of Technology in Cambridge, as science minister. Escobar’s team initiated a grant programme that awarded at least \$15 million during his 5-year term, provided scholarships for several hundred graduate students to study abroad, and established a system that rewards well-published researchers with stipends worth \$1,000–\$2,000 per month. “He turned things around,” says Rubinoff. Spadafora agrees. “He is awesome,” she says. “He called me to say we are building a new enterprise, please come back.”

CONTRASTO/EYEVINE

L TO R: CORBIS; NEWSCOM; B. GENTILE/CORBIS; K. CALVO/AP; A. FRANCO/AP

**A century  
in Central  
America**

**1910**

Smithsonian Institution starts Biological Survey of Panama, a major inventory of flora and fauna

**1914**

US-financed Panama Canal completed



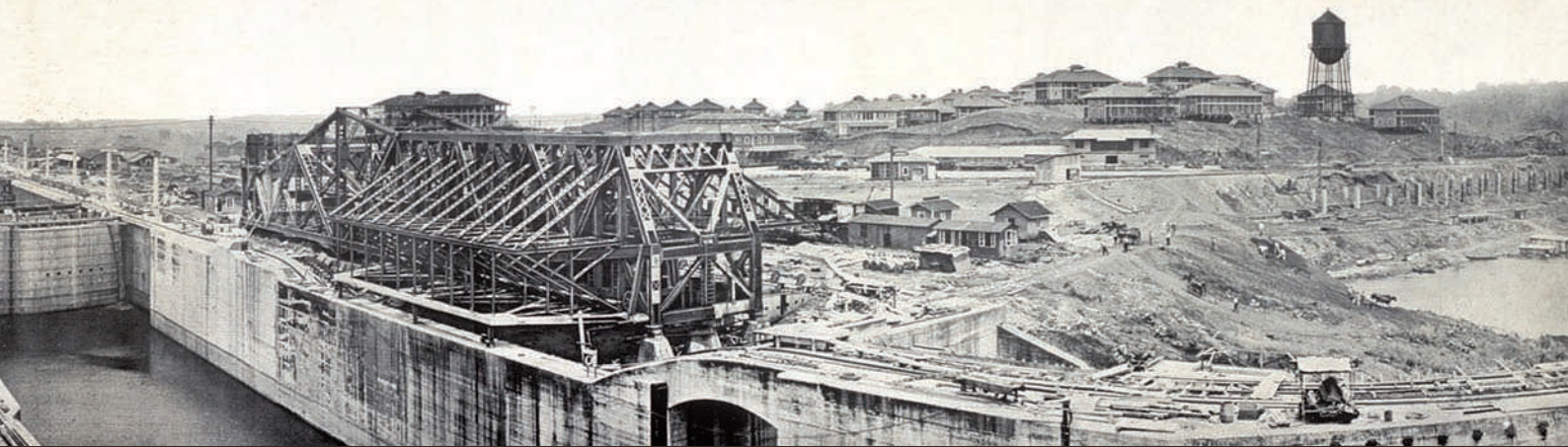
**1923**

A field station starts up on Barro Colorado island; it later becomes the Smithsonian Tropical Research Institute



**1977**

US Senate approves treaty deeding canal to Panama



Construction of the Panama Canal — a huge engineering feat — created a vital shipping shortcut. Canal tolls still help to support the country's economy.

She did — and now can be found in her modern lab in the ‘City of Knowledge’, a former US military base at the Pacific canal entrance that the government is converting into a research centre, housing INDICASAT-AIP and other new agencies. The historic military buildings have been gutted and turned into labs, offices and a conference centre. The new science park and vivarium will be located there.

Spadafora bubbles with excitement when talking about her ‘ray-gun’ idea for curing malaria, devised during a brainstorming session with fellow Panamanian José Stoute Zuriea, a physician at Pennsylvania State University in Hershey. *P. falciparum* invades red blood cells and digests their haemoglobin, then sequesters the iron-rich, toxic remnants in a crystal form called haemozoin. Their idea was to heat these crystals with low-frequency microwaves, fatally releasing their contents.

After the pair won an initial \$100,000 grant from the Gates Foundation in 2009, they demonstrated that the concept would work. They exposed infected red blood cells from mice to 2.45-gigahertz microwaves for four minutes, and showed that the crystals dissolved, killing *P. falciparum* but not the host cells. Now, armed with the new \$1-million Gates grant, the researchers plan to create a mouse-sized microwave device to radiate infected animals.

Meanwhile, the science drive started by the Torrijos administration continued with the 2009 election of President Ricardo Martinelli Berrocal and the appointment of Rubén Berrocal Timmons, his cousin. The Martinelli administration also appointed a new head of INDICASAT-AIP: Jagannatha Rao, a neuroscientist who arrived in summer 2010 from a national lab at India's Council of Scientific and Industrial Research in New Delhi. In Rao, Panama has found a tireless advocate for his adopted nation's scientific community.

Last year, Berrocal and Rao visited Singapore to learn about the country's major science push of recent years. Rao is now initiating a steady stream of conferences featuring international participants, and he has been adding programmes to INDICASAT-AIP's portfolio, including the country's new biotechnology PhD. “Students must have three publications before they can graduate,” says Rao. One of Berrocal's aims is to build up modern labs and recruit high-quality scientists, creating a thriving research atmosphere that can avert a brain drain of new doctorates. “We don't want to lose these people,” he says.

Paul Collier, an economist who studies capacity building at the University of Oxford, UK, says that Panama's science drive “sounds

very positive”. The challenge, he says, is “to concentrate resources in a niche — then be the quality escalator in that niche”. Panama wants its niche to be biotechnology, with a focus on infectious diseases and bioprospecting — the search for drugs developed from its own rich natural resources. (Its neighbour, Costa Rica, has taken a similar tack<sup>2</sup>.) Rao is organizing a drug-discovery meeting in May, which will include discussions of Panama's plans for a Bioprospecting Natural Product Bank, a resource for screening that already includes 8,000 samples of marine bacteria and fungi.

The drive in biomedicine is evident across Panama City. At Hospital Santo Tomás in the city's centre, researchers aim to collaborate with pharmaceutical firms on clinical trials, says Juan Miguel Pascale Bellagamba, a physician who directs programmes at the Gorgas Memorial Institute of Health Studies and Columbus University of Medicine and Science. Pascale is one of several researchers who also want to boost the country's

ability to track and respond to outbreaks of infectious disease or to other public-health concerns.

If there is one thing that might slow down these plans, Panamanians say, it is a lingering resistance to recruiting researchers born outside the country. Few seem concerned that the research investment could dry up; as long as ships continue to traverse the Panama Canal, the country's major revenue source will flow. A \$5.25-billion project for larger locks on the canal, which will markedly increase its capacity, is set for completion in 2014. (Excavations for new locks proved a boon for palaeontologists, who unearthed fossils of camels, horses,

rhinos and pigs<sup>3</sup> that are helping them to understand animal migrations between the North and South American continents.)

Looking back at the Noriega era, Spadafora and Stoute both recall with sadness the country's lost opportunities. After her brother's death, Spadafora chained herself to the Vatican embassy in protest. Stoute, too, was traumatized. “I lost many friends,” he says.

Things are better now, they agree, even if many outside the country are not yet aware of it. “Our US colleagues have told us we're pretty wild down here,” says Spadafora. But if Panama can emerge from the depths of tyranny, maybe a wild idea to fight malaria can emerge here too. ■

Rex Dalton is a writer based in San Diego, California.

1. Spadafora, C. et al. *PLoS Pathog.* **6**, e1000968 (2010).
2. Dalton, R. *Nature* **441**, 567–569 (2006).
3. Macfadden, B. J. et al. *J. Paleont.* **84**, 288–298 (2010).

**“IF YOU TOLD ME THIS  
WOULD HAPPEN 25  
YEARS AGO, I WOULD  
SAY YOU WERE SMOKING  
SOMETHING ILLICIT.”**

**1989–90**

United States  
invades Panama  
and imprisons  
dictator Manuel  
Noriega



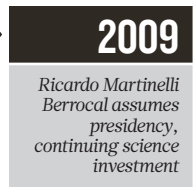
**1999**

Panama  
assumes  
full control  
of canal



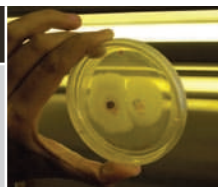
**2004**

President Martin  
Torrijos Espino  
is elected, and  
starts to promote  
research



**2009**

Ricardo Martinelli  
Berrocal assumes  
presidency,  
continuing science  
investment



# COMMENT

**HEALTH** The autism and anti-vaccine saga explored **p.468**



**BIOGRAPHY** The man who turned natural history into an explanatory science **p.470**

**ENERGY** Don't depend on the end of coal supplies to cut emissions **p.472**

**EQUALITY** Why women win fewer scholarly awards and what to do about it **p.472**

K. GEHLE



To aid conservation of the species, volunteers legally plant a Florida torreyia outside its historical range.

## Regulate trade in rare plants

Patrick D. Shirey and Gary A. Lamberti call for action to stem the rising tide of species redistribution caused by Internet sales.

Fewer than ten cabbage-on-a-stick plants (*Brighamia insignis*) are all that remain of the wild population in Hawaii. Yet for US\$29.99, anyone could buy the succulent at online auction. Thanks to loosely regulated Internet commerce and efficient shipping, people are increasingly obtaining endangered or threatened plants, legally and illegally, and moving them outside their native ranges.

The introduction of non-native plant species causes ecological and economic harm — at an estimated cost of more than \$30 billion a year in the United States alone<sup>1</sup> — by damaging crops, pastures and ecosystems. For example, the Australian paperbark tree (*Melaleuca* spp.) is a noxious weed in the United States, causing millions of dol-

**“People are increasingly obtaining endangered or threatened plants, legally and illegally, and moving them outside their native range.”**

lars of damage, even though its habitats are considered threatened in Australia owing to coastal development<sup>2</sup>. Moreover, the trade in endangered plants can severely affect wild populations by introducing plant pathogens or increasing wild-plant harvesting. In the 1980s, for example,

the export of more than 60 million wild bulbs a year from Turkey to the Netherlands significantly depleted wild populations of several rare Turkish species, including snowdrops (*Galanthus* spp.) and cyclamen (*Cyclamen* spp.)<sup>3</sup>.

Environmental agencies and governing bodies must better enforce existing species-protection laws, and establish legal frameworks to monitor and manage this rising tide of species redistribution.

### SELLING OUT

Last year, we searched through thousands of websites containing the phrases ‘seeds for sale’ or ‘plants for sale’ to determine how many of the 753 plants listed as threatened and endangered under the US Endangered Species Act can be purchased online. We found that nearly 10% are being sold or at least advertised online and are available for in-state purchase. Most of these sales are illegal: of the more than 50 sellers we ►



► found offering to ship plants between states, just four had the appropriate interstate commerce permit issued by the US Fish and Wildlife Service (FWS), which costs \$100, involves minimal paperwork and can be obtained in three months.

About half the endangered plants available to buyers in the United States are sold in states outside their native range. Some are even sold overseas. For example, the star cactus (*Astrophytum asterias*) is found in only a few locations in Texas and Mexico, but cultivars can be bought online from at least six states and several countries, including China, Japan, Australia, the United Kingdom and Canada.

**“The purchasers of rare and endangered plants include those trying to protect them.”**

Part of the problem is the failure to enforce existing laws. It is also relatively easy for sellers to exploit weak links in the current legislation.

Under federal law, the FWS can regulate sales between states but not within them. For example, it is legal to sell the endangered Florida torreya (*Torreya taxifolia*) within South Carolina even though the native range of the plant is in Florida and Georgia. If a plant's distribution expands through illegal sales, however, more sellers are likely to start offering it. Because it is legal to transplant plants anywhere in the United States if they are privately owned<sup>4</sup>, subsequent transfers

between states (as well as sales within them) become increasingly difficult to control. Ultimately, state laws may have a bigger effect on trade than federal law, but these vary widely, with most being more lenient towards commerce than the federal law<sup>5</sup>. Although some states such as Connecticut strictly regulate commerce, 25 states, including Alabama, Arkansas, West Virginia and Wyoming, lack laws protecting endangered species or allow trade without restriction, meaning that collection, trade and redistribution can go unchecked.

#### A HELPING HAND

Most online shoppers seem to be amateur horticulturalists seeking flowers for their gardens. But anecdotal evidence from online forums suggests that the purchasers of rare and endangered plants increasingly include those trying to protect them.

Assisted colonization — the movement of species or genetic subtypes to non-native environments where they are expected to thrive — has been proposed by conservationists as a way to preserve species at risk of extinction. This idea has grown in popularity worldwide as the effects of climate change have become more apparent, and scientists have begun to investigate where and when assisted colonization might work<sup>6</sup>. For instance, for the past two years, foresters in British Columbia, Canada, have been moving seedlings of commercially harvested pine and hardwood species to nearly 50 experimental reforestation sites. Historically, the

strains being transferred haven't grown in these sites, but they are expected to flourish under climate change<sup>7</sup>.

In the United States, the FWS allows biologists to conduct assisted colonization of animals only if they can demonstrate that a species' original habitat has been altered irreversibly. Such restrictions don't apply to plants<sup>4</sup>.

Several individuals and citizen groups have already begun to apply the approach to rare plant species. The Torreya Guardians, for example, a group of volunteers including botanists and professional conservationists largely based in Florida, Georgia, North Carolina and South Carolina, have been cultivating seedlings of the Florida torreya since 2005, and planting them outside the plant's formally described historical range (although the Torreya Guardians argue that the species may have thrived there during the last peak interglacial warm period<sup>8</sup>).

It is highly unlikely that the US Congress will change the law on the transport of listed species between states, in part because altering environmental legislation takes such an enormous bipartisan effort. (Also, people have been free to move privately owned plants around for thousands of years.) However, the FWS can tighten trade restrictions without waiting for the government to change the Endangered Species Act.

The agency should work with legitimate sellers to monitor the movement of plants and enforce existing legislation. As a first step, it should establish dedicated surveillance teams

R. NUSSBAUMER/IMAGEBROKER/FLPA; WILDLIFE GMBH/ALAMY; VISUALS UNLIMITED/NATUREPL.COM; R. & N. BOWERS/ALAMY; C. & T. STUART/FLPA



For sale online: the American lotus (far left) is listed as threatened or endangered in three states (Michigan, New Jersey and Pennsylvania) but banned in Connecticut as potentially invasive. The Tennessee coneflower, the Florida *torreya*, the star cactus, and the cabbage-on-a-stick plant (pictured from left to right) are all listed under the US Endangered Species Act.

to monitor online transactions; for instance, low-cost automated search engines could trawl for species names along with phrases such as 'plants for sale' or 'add to cart'.

The agency could also restrict the ability of consumers to buy hybrids bred from endangered species. Currently, these are not formally regulated<sup>9</sup> — allowing breeders to cultivate the unique characteristics of rare plants while evading endangered-species laws. Yet hybrids can have serious implications — good and bad — for the management of wild populations. Take the Tennessee coneflower (*Echinacea tennesseensis*). The FWS proposed delisting this endangered species in August 2010 in part because nursery-propagated plants have helped to re-establish 20 colonies in the species' historical range. The agency also suspects that the commercial availability of plants reduces the poaching threat to wild populations. Yet, in 2003, a commercial grower created a morphologically similar hybrid (*E. tennesseensis* × *Echinacea purpurea*) — a cross between the Tennessee coneflower and the purple coneflower.

**NATURE.COM**  
Threats to the world's plants assessed:  
[go.nature.com/twiob](http://go.nature.com/twiob)

This could further improve the survival of the wild plants by reducing poaching, or it could pose a significant risk if it infiltrates the historical range of the Tennessee coneflower.

A thornier issue is how to regulate the trade and movement of plants in assisted-colonization efforts. The FWS and other government agencies face an enormous challenge in trying to manage biodiversity loss in the face of climate change with inadequate resources.

Individuals and citizen groups should not take the lead on this because of the risks associated with introducing any species. Instead, the FWS should carry out controlled pilot studies first, possibly using the grass-roots resources of volunteers. The agency has begun to make moves in this direction. A five-year review of its Florida *torreya* recovery plan includes a proposal to work with the Torreya Guardians on an assisted-colonization project if other approaches fail.

#### COORDINATE AND CONTROL

The management of natural resources under climate change is at once a local problem, and a national and international one. Ideally, the diverse range of state laws governing the protection for endangered species in the 50 US states, or lack thereof, should be replaced with a uniform and rigorous policy — admittedly a lofty goal for lawmakers. Similarly, worldwide, all exporting and importing countries should coordinate to ensure that domestic laws are enforced and treaties, such as

the Convention on International Trade in Endangered Species of Wild Fauna and Flora, are abided by<sup>10</sup>.

Although the redistribution of plant species around the world is nothing new, the ease with which people can now obtain and transfer specimens is unprecedented. This, combined with a growing interest in assisted colonization, makes it more important than ever for federal and local governments to wrest control of illegal Internet trade, develop a policy for hybrids and ensure that genetic diversity is considered when propagating plants. ■

**Patrick D. Shirey and Gary A. Lamberti**  
are in the Department of Biological Sciences at the University of Notre Dame, Notre Dame, Indiana 46556, USA.  
e-mail: [pshirey@nd.edu](mailto:pshirey@nd.edu)

1. Pimentel, D., Zuniga, R. & Morrison, D. *Ecol. Econ.* **52**, 273–288 (2005).
2. Ricciardi, A. & Simberloff, D. *Trends Ecol. Evol.* **24**, 248–253 (2009).
3. Read, M. *Oryx* **23**, 127–134 (1989).
4. Shirey, P. D. & Lamberti, G. A. *Conserv. Lett.* **3**, 45–52 (2010).
5. Goble, D. D., George, S. M., Mazaika, K., Scott, J. M. & Karl, J. *Environ. Sci. Policy* **2**, 43–59 (1999).
6. Richardson, D. M. et al. *Proc. Natl Acad. Sci. USA* **106**, 9721–9724 (2009).
7. Marris, E. *Nature* **459**, 906–908 (2009).
8. Barlow, C. in *Gaia in Turmoil: Climate Change, Biodepletion, and Earth Ethics in an Age of Crisis* (eds Crist, E. & Rinker, H. B.) Ch. 10 (MIT Press, 2009).
9. Ellstrand, N. C. et al. *Bioscience* **60**, 384–388 (2010).
10. Phelps, J., Webb, E. L., Bickford, D., Nijman, V. & Sodhi, N. S. *Science* **330**, 1752–1753 (2010).



Anti-vaccination protesters in London in 2007.

## EPIDEMIOLOGY

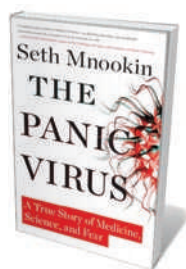
# Epidemic of panic

Autism's broad diagnosis has fuelled fears about vaccines despite no evidence for a link, finds **Melvin Konner**.

Groundless suspicions that vaccines cause autism have an alarmingly long shelf life. The issue flared up again earlier this month, when an investigative report in the *British Medical Journal* documented fraud in a retracted 1998 paper in *The Lancet* by UK gastroenterologist Andrew Wakefield. It had alleged a link between the combined vaccine for measles, mumps and rubella (MMR) and autism. The anti-vaccine community once again defended Wakefield.

In just 50 years, we have moved from experts blaming parents to parents blaming vaccine scientists and paediatricians. As a boy in the 1960s, I worked at a school for children with autism, few of whom had language skills. In those days, parents were often held responsible for autistic behaviour — 'experts' referred to emotionally cold 'refrigerator mothers' and to 'double-bind mothering', which supposedly gave a child conflicting messages. The school where I worked, founded by US educator Carl Fenichel, opposed such theories, and I came to reject them, too.

Some parents of children with autism,



**The Panic Virus:**  
A True Story of  
Medicine, Science,  
and Fear  
SETH MNOOKIN  
Simon & Schuster:  
2011. 410 pp. \$26.99

vaccines being the cause. Yet calls to reduce or ban vaccinations in childhood remain strong. Public insistence on doing unjustified studies of vaccine effects, already well studied, simply diverts funds away from promising avenues such as genetics. Anti-vaccine sentiment also causes the needless spread of deadly diseases, such as measles and whooping cough, by

unable to accept the question mark that science still places over the illness, think that they have found an answer in inoculations. In his disturbing chronicle, *The Panic Virus*, US writer Seth Mnookin looks into the anti-vaccine movement. His analysis is serious and gripping. Although diagnoses of autism are on the increase, all the evidence points away from

reducing the coverage of mass immunization programmes. Immunization with the MMR vaccine peaked at 91% in the United Kingdom in 1997 and began to decline after the Wakefield *Lancet* paper. It was as low as 80% in 2003, but had crept back up to 86% by 2010. A level of 95% is considered adequate to protect those who are not immunized (herd immunity) so outbreaks are not surprising.

Vaccine refusal can cause local immunization rates to fall, as implicated in measles epidemics in Britain, the Netherlands and Germany, and in the current whooping-cough epidemic in California. This epidemic, the state's worst in 50 years, has a dual demographic of undocumented Hispanic immigrants and people from rich white communities in which vaccine refusal is common. The disease has killed at least ten infants who were too young to have been immunized, and will spread to other states.

Possible causal links between vaccines and autism have been extensively studied, and none has been found. Mnookin describes how a panel convened in 2000 by the US Institute of Medicine (IOM) reviewed all the available data. As the finger of blame had shifted from thimerosal, a mercury-containing preservative, to the individual measles or mumps vaccines themselves, the panel carefully considered all possible causes.

The IOM is a respected independent arbiter, but even it took special care to ensure that none of its panellists — authorities on statistics, epidemiology, ethics and various medical fields — had been involved in vaccine development, testing or consulting. In 2004, the panel concluded that there was no evidence of a connection between vaccines and autism. The hate mail that the panel subsequently received led to an FBI investigation.

Among other evidence, the IOM considered a study of more than 530,000 children born in Denmark in 1991–98; a comparable national study in Sweden; large UK and US sampling studies; other well-designed studies; and all the studies on which anti-vaccination claims had been based. None of the studies in the last group was found to have merit, and the properly designed studies led the panel to favour rejection of the claims. There was no greater incidence of autism or autism spectrum disorders (ASDs) in vaccinated versus unvaccinated children, and the removal of thimerosal from vaccines had not reduced diagnoses of ASDs, which continued to increase.

The reasons for the autism increase are uncertain. Changing diagnosis is one possibility — as suggested in the book *Unstrange Minds* (Basic Books, 2007) by Roy Richard Grinker, a social anthropologist whose daughter has autism.

**NATURE.COM**  
For more on the MMR  
vaccine and autism:  
[go.nature.com/qwnmol](http://go.nature.com/qwnmol)

Highlighting autistic traits to physicians, extending its diagnosis to milder and latent

forms and a shift away from descriptions of 'mental retardation' to the less stigmatizing and more treatable ASDs may have increased its recorded incidence.

Mnookin's anti-vaccine cast includes the anguished parents, physicians, lawyers, celebrities and organizations that encouraged scientifically baseless beliefs. The best-known medical figure in the tale is Wakefield. Despite the UK General Medical Council ruling that he can no longer practice medicine in the country because he ordered medically unjustified procedures on children with autism, he is still considered a hero to some.

Citing cognitive research, Mnookin shows how repeating claims makes them seem true even if they are groundless, how belief in a hypothesis biases judgement and how ignorance of statistics breeds false inference. He could also have cited studies on false memories, which are easy to create and may help explain some parents' belated recollection of a temporal link between an inoculation and a child's first autistic symptoms.

Vaccine opponents point out that science can never be absolutely certain, especially about a negative. But it is close to certain that vaccines do not cause autism and that non-vaccination leads to epidemics. This suggests a course of action even if there are small doubts. Mnookin accepts that vaccines do occasionally cause harm; for example, attenuated live viruses can (rarely) cause serious cases of the illness being inoculated against, and an uncontrolled high fever can result in brain damage. Although there is no evidence that these risks include autism, he supports the no-fault system that compensates parents who can show that a child became seriously ill after a vaccination and was left with a listed medical condition, including autism.

Vivid stories about vaccines causing autism must be countered by equally vivid tales of the disability and death wrought by anti-vaccine sentiment. Herd immunity shields children whose parents reject vaccination's tiny risks, up to a point. But if many avoid vaccination, 'herd' protection is lost and others suffer. That includes teenagers and adults whose immunizations have worn off; children who are inoculated but still vulnerable (no vaccine is perfect); and infants who are too young for vaccination. Mnookin's description of the death of a four-week-old baby in Louisiana from whooping cough, caught from an unvaccinated older child, is painful to read.

Mnookin's careful science and compassion for both sides are examples for all journalists, and *The Panic Virus* should be read and pondered. ■

**Melvin Konner** is a professor of anthropology and behavioural biology at Emory University, Atlanta, Georgia, USA. His latest book is *The Evolution of Childhood*.  
e-mail: antmk@emory.edu

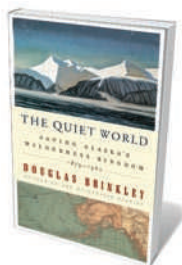
## Books in brief



### Academically Adrift: Limited Learning on College Campuses

Richard Arum and Josipa Roksa UNIVERSITY OF CHICAGO PRESS 256 pp. \$70 (2011)

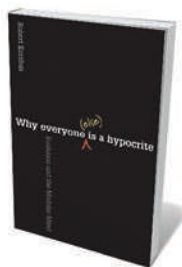
With rising numbers of students paying increasing sums to attend university, two social scientists' finding that they learn little when they get there is sobering. In their study of 2,300 students at 24 institutions in the United States, Richard Arum and Josipa Roksa demonstrate that undergraduates displayed little advancement in a range of skills including critical thinking, complex reasoning and writing. They suggest that the many social distractions of campus culture hinder learning.



### The Quiet World: Saving Alaska's Wilderness Kingdom, 1879-1960

Douglas Brinkley HARPER 592 pp. \$29.99 (2011)

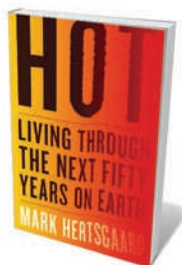
The pristine Alaskan wilderness is at the centre of a tussle between environmentalists and the extraction industries. It has long been so, historian Douglas Brinkley reminds us. He documents attempts by the US federal government from 1879 to 1960 to protect wild areas of the state — including Mount McKinley, the Tongass and Chugach national forests, and the Coastal Plain of the Beaufort Sea. Drawing on new archival material, he describes the colourful characters who established the Arctic National Wildlife Refuge in 1960.



### Why Everyone (Else) Is a Hypocrite: Evolution and the Modular Mind

Robert Kurzban PRINCETON UNIVERSITY PRESS 288 pp. \$27.95 (2011)

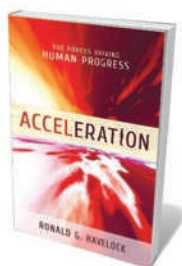
We are all hypocrites, according to psychologist Robert Kurzban. Because of the different ways in which various regions of our brains have evolved, he explains, our actions are riddled with inconsistency. Using humour and anecdotes, he reveals how conflict between the modules of the mind leads to contradictory beliefs, vacillating behaviours, broken moral boundaries and inflated egos. He argues that we should think of ourselves not as 'I' but as 'we' — a collection of interacting systems that are in constant conflict.



### Hot: Living Through the Next Fifty Years on Earth

Mark Hertsgaard HOUGHTON MIFFLIN HARCOURT 352 pp. \$25 (2011)

Concern for his daughter's future drives journalist Mark Hertsgaard to consider the impacts of climate change over the next five decades. Focusing on the United States but including reports from around the world, he explains how Chicago's climate may come to resemble Houston's, how coastal cities such as New York will have to tackle rising sea levels and frequent storm surges, and how water shortages and altered crop yields will affect people around the globe. He argues that human survival will depend on citizens to push for government action.



### Acceleration: The Forces Driving Human Progress

Ronald G. Havelock PROMETHEUS BOOKS 363 pp. \$28 (2011)

Countering fears about humanity's survival, social psychologist and knowledge-transfer consultant Robert Havelock argues that progress is accelerating. His focus is the creation and dispersal of knowledge, the increasing rate of which he tracks from the Stone Age to the present. Rather than worrying about particular threats such as global warming and nuclear proliferation, he argues that in the long term, the sharing of information across global society is a force for good that enhances well-being.

forms and a shift away from descriptions of 'mental retardation' to the less stigmatizing and more treatable ASDs may have increased its recorded incidence.

Mnookin's anti-vaccine cast includes the anguished parents, physicians, lawyers, celebrities and organizations that encouraged scientifically baseless beliefs. The best-known medical figure in the tale is Wakefield. Despite the UK General Medical Council ruling that he can no longer practice medicine in the country because he ordered medically unjustified procedures on children with autism, he is still considered a hero to some.

Citing cognitive research, Mnookin shows how repeating claims makes them seem true even if they are groundless, how belief in a hypothesis biases judgement and how ignorance of statistics breeds false inference. He could also have cited studies on false memories, which are easy to create and may help explain some parents' belated recollection of a temporal link between an inoculation and a child's first autistic symptoms.

Vaccine opponents point out that science can never be absolutely certain, especially about a negative. But it is close to certain that vaccines do not cause autism and that non-vaccination leads to epidemics. This suggests a course of action even if there are small doubts. Mnookin accepts that vaccines do occasionally cause harm; for example, attenuated live viruses can (rarely) cause serious cases of the illness being inoculated against, and an uncontrolled high fever can result in brain damage. Although there is no evidence that these risks include autism, he supports the no-fault system that compensates parents who can show that a child became seriously ill after a vaccination and was left with a listed medical condition, including autism.

Vivid stories about vaccines causing autism must be countered by equally vivid tales of the disability and death wrought by anti-vaccine sentiment. Herd immunity shields children whose parents reject vaccination's tiny risks, up to a point. But if many avoid vaccination, 'herd' protection is lost and others suffer. That includes teenagers and adults whose immunizations have worn off; children who are inoculated but still vulnerable (no vaccine is perfect); and infants who are too young for vaccination. Mnookin's description of the death of a four-week-old baby in Louisiana from whooping cough, caught from an unvaccinated older child, is painful to read.

Mnookin's careful science and compassion for both sides are examples for all journalists, and *The Panic Virus* should be read and pondered. ■

**Melvin Konner** is a professor of anthropology and behavioural biology at Emory University, Atlanta, Georgia, USA. His latest book is *The Evolution of Childhood*. e-mail: antmk@emory.edu

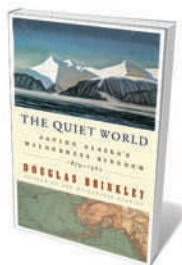
## Books in brief



### Academically Adrift: Limited Learning on College Campuses

Richard Arum and Josipa Roksa UNIVERSITY OF CHICAGO PRESS 256 pp. \$70 (2011)

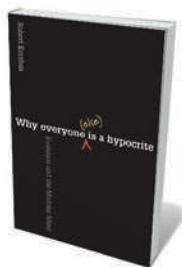
With rising numbers of students paying increasing sums to attend university, two social scientists' finding that they learn little when they get there is sobering. In their study of 2,300 students at 24 institutions in the United States, Richard Arum and Josipa Roksa demonstrate that undergraduates displayed little advancement in a range of skills including critical thinking, complex reasoning and writing. They suggest that the many social distractions of campus culture hinder learning.



### The Quiet World: Saving Alaska's Wilderness Kingdom, 1879-1960

Douglas Brinkley HARPER 592 pp. \$29.99 (2011)

The pristine Alaskan wilderness is at the centre of a tussle between environmentalists and the extraction industries. It has long been so, historian Douglas Brinkley reminds us. He documents attempts by the US federal government from 1879 to 1960 to protect wild areas of the state — including Mount McKinley, the Tongass and Chugach national forests, and the Coastal Plain of the Beaufort Sea. Drawing on new archival material, he describes the colourful characters who established the Arctic National Wildlife Refuge in 1960.



### Why Everyone (Else) Is a Hypocrite: Evolution and the Modular Mind

Robert Kurzban PRINCETON UNIVERSITY PRESS 288 pp. \$27.95 (2011)

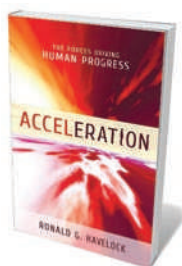
We are all hypocrites, according to psychologist Robert Kurzban. Because of the different ways in which various regions of our brains have evolved, he explains, our actions are riddled with inconsistency. Using humour and anecdotes, he reveals how conflict between the modules of the mind leads to contradictory beliefs, vacillating behaviours, broken moral boundaries and inflated egos. He argues that we should think of ourselves not as 'I' but as 'we' — a collection of interacting systems that are in constant conflict.



### Hot: Living Through the Next Fifty Years on Earth

Mark Hertsgaard HOUGHTON MIFFLIN HARCOURT 352 pp. \$25 (2011)

Concern for his daughter's future drives journalist Mark Hertsgaard to consider the impacts of climate change over the next five decades. Focusing on the United States but including reports from around the world, he explains how Chicago's climate may come to resemble Houston's, how coastal cities such as New York will have to tackle rising sea levels and frequent storm surges, and how water shortages and altered crop yields will affect people around the globe. He argues that human survival will depend on citizens to push for government action.



### Acceleration: The Forces Driving Human Progress

Ronald G. Havelock PROMETHEUS BOOKS 363 pp. \$28 (2011)

Countering fears about humanity's survival, social psychologist and knowledge-transfer consultant Robert Havelock argues that progress is accelerating. His focus is the creation and dispersal of knowledge, the increasing rate of which he tracks from the Stone Age to the present. Rather than worrying about particular threats such as global warming and nuclear proliferation, he argues that in the long term, the sharing of information across global society is a force for good that enhances well-being.



Evelyn Hutchinson in his laboratory at Yale University in 1939.

# BIOGRAPHY

## Ecology's midwife

**John Whitfield** reflects on Evelyn Hutchinson, who transformed natural history into an explanatory science.

**F**oundations tend to be hidden. So it is with the ecologist Evelyn Hutchinson. Little known outside his field, his ideas shaped the discipline of ecology as it is today. In her exhaustive biography, ecologist and science historian Nancy Slack pays tribute to his contribution and, between the lines, shows why he remains in the shadows.

Hutchinson did not make great discoveries. Instead, he made a series of great suggestions, pioneering a variety of approaches to study how plants and animals interact with their environment and with each other, and, in turn, how these interactions affect the diversity and abundance of living things. In

doing so, he helped to turn natural history into ecology, transforming a discipline whose practitioners described what they saw into one where they sought to explain it. Several of his ideas have blossomed into subfields that continue to occupy researchers.

Born in 1903 to a family of scientists, Hutchinson went to university in his home town of Cambridge, UK. He never earned a doctorate; after graduating he spent brief spells in Naples, Italy, where he studied octopus physiology with little success, and South Africa, where he began working on lakes. He then moved to Yale University in New Haven, Connecticut, where he spent

43 years on the faculty. Lake-dwelling insects, an enthusiasm since childhood, became his model system, which he used to devise and test ideas throughout his career. He completed the fourth and final volume of his classic *A Treatise on Limnology* (Wiley) just before his death in 1991.

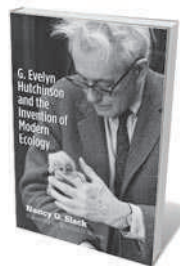
Hutchinson's ecological career can be split into two periods.

From about 1930 until the 1950s, his work focused on how chemical and physical conditions affect living communities. He was among the first to use radioactive elements to trace the movement of nutrients through an ecosystem, and performed some of the first biogeochemical studies, writing a lengthy book on guano.

From the late 1950s on, his interests shifted to population and community ecology — or, as he put it in a famous lecture, “Why are there so many kinds of animals?” He highlighted the conundrum that competing species coexist. If you make them live in close proximity in experimental conditions, he noted, only one will survive. Yet in the wild, many can live together even in apparently homogeneous environments, such as the plankton in lakes.

Hutchinson argued that species occupy different niches, dividing up their environment along axes of space, time, the availability of light, water or food, and so on. He pioneered mathematical approaches to these problems, analysing how species might exert forces on one another through competition for space and resources, or reach equilibrium. The two phases of his work seem very different, but are united by his attempt to find general explanations for structure and patterns in the living world by applying ideas and techniques from chemistry, physics and mathematics.

Hutchinson's appeal lies both in what he did and in the way he did it. His approach was amateurish in the best sense, driven by joy and curiosity. He was interested in everything, and published papers and books on illustration in medieval manuscripts and decoration in Asian art. He was a gifted writer, and his essays in *American Scientist* won him a broad following at the time; a collection of his writing has been reprinted in *The Art of Ecology* (Yale University Press, 2010). He was a brilliant teacher, and had a knack for attracting the brightest graduate students and helping them to realize their potential. He was as much the midwife of modern ecology as the parent.



**G. Evelyn Hutchinson and the Invention of Modern Ecology**

NANCY G. SLACK  
Yale University Press:  
2011. 457 pp. \$40,  
£25

Slack got to know Hutchinson in the last year of his life during a sabbatical at Yale. She has obviously read every available document and interviewed every relevant person willing to talk. Her biography is scholarly and a labour of love. But it is less than the sum of its parts. Some of the details could have been sacrificed in favour of a more coherent narrative or strongly argued thesis — I didn't need to know, for example, how many pages of references *A Treatise on Limnology* contains. Everything Hutchinson did, everywhere he went and everyone he met seems to be here, but the book says little of what it meant. It is difficult to see the wood for the trees.

The picture of Hutchinson beyond his intellectual life is hazy. The letters and papers quoted reveal little of the inner man, and he seems not to have discussed personal matters with friends or family. This was not for a lack of anything to discuss. His life had its share of sorrow, including a divorce and two further wives who predeceased him. We hear little about Hutchinson's politics, even though he declined to accept the President's Medal of Science from the administration of Richard Nixon, and little about his faith, even though he was a churchgoer.

There is no hint of anger, bitterness, feuds or egotism, despite some brutal office politics. Yale's biology department turned its resources away from organismal biology in the 1960s towards molecules and cells, resulting in many of Hutchinson's former students being driven from their jobs. Even for someone

**"Hutchinson's approach was amateurish in the best sense, driven by joy and curiosity."**

of his generation, class, nationality, gender and profession, Hutchinson seems unusually reticent. With so little to work with in creating shades of character, Slack's

book reads more like a tribute to the work than a portrait of the man.

The work however, deserves its tribute. Hutchinson's questions about ecological competition still provoke argument. There is disagreement on whether what we see in nature owes more to predictable forces such as niche differentiation, or if life is structured mainly by chance and history, and whether grand and general theories are applicable to ecology. Hutchinson's concepts are very much alive: they are part of the discipline's furniture. ■

**John Whitfield** is a London-based science writer and author of *In the Beat of a Heart*.  
e-mail: j.a.whitfield@gmail.com

## CULTURE

# Natural colour

**Colin Martin** views a showcase of zoological art — and a dodo painting that misled scientists for 400 years.

A display of rare and fragile illustrations selected from the world's largest collection of natural history paintings and drawings opened this week in a new gallery at London's Natural History Museum.

Restored to its nineteenth-century glory — with terracotta-tiled walls and mahogany display cabinets designed by the museum's original architect, Alfred Waterhouse — the gallery hosts temporary exhibitions of light-sensitive watercolours and prints alongside permanent hangings of oil paintings from the museum's vast collection.

The museum's holdings of 500,000 zoological and botanical illustrations include two copies of John James Audubon's nineteenth-century masterpiece *Birds of America*, containing 435 hand-coloured engravings. The work became the world's most expensive book in December 2010, when another copy was auctioned for £7.3 million (US\$11.5 million).

Owing to the fragility of works on paper and lack of a suitable exhibition space, few items from the collection have been routinely displayed to the public. A different theme will be chosen each year. This year it is China: 96 watercolours drawn from 2,000 natural history paintings from Canton (now Guangzhou) will be shown.

The paintings were commissioned by John Reeves, a tea inspector for the British East India Company and a keen amateur natural historian. Between 1812 and 1831, he employed local Chinese artists to paint plants and animals he found in markets and gardens. Reeves shipped the watercolours to botanical gardens, horticultural societies and other patrons in Britain. A contemporary take on his collection is offered by the gallery's recent artist-in-residence, Shanghai-based Hu Yun, who reflects through drawings and video on the irony that the watercolours that enabled taxonomists to identify and name new species were painted by anonymous Chinese artists.

The displays also juxtapose microscopic views old and new. A small engraving of a human flea, observed under an early compound microscope by Robert Hooke and described in his *Micrographia* (1665) as



A macaw, one of more than 2,000 watercolours commissioned by John Reeves in the 1800s.

"adorn'd with a curiously polish'd suite of sable Armour, neatly jointed", holds its own against a huge image of a bluebottle by contemporary artist Giles Revell, based on scanning electron micrographs.

**Images of Nature Gallery**  
Natural History Museum, London.  
From 21 January 2011.

Another pair of paintings highlights the importance of scientific accuracy in natural history illustration. In a reworked version beside the original, palaeontologist and artist Julian Hume shows how a 1626 oil painting of a dodo, attributed to Flemish artist Roelandt Savery, misled scientists and the public for 400 years. Richard Owen, the Natural History Museum's first superintendent, placed fossil bones over the seventeenth-century painting to determine the layout of the bird's skeleton, and his interpretation, published in 1866, became the recognized scientific description of the dodo. Its rounded body, stout legs, huge head and small wings became a comic cipher for extinction. But Hume shows that the painting was inaccurate. He depicts a more streamlined dodo with longer legs, based on his examination of new fossil finds, contemporary accounts and studies of the anatomy of other flightless birds. ■

**Colin Martin** is a writer based in London.  
e-mail: cmpubrel@aol.com

# CORRESPONDENCE

## Scholars' awards go mainly to men

One area in which female scientists still have to confront sexism (*Nature* 468, 733; 2010) is in scholarly awards: women win fewer. Scientific societies must examine practices for selecting awardees.

The proportion of women receiving service or teaching awards in the past two decades is roughly equivalent to the proportion of women within the cohort-adjusted PhD pool in that discipline, but only half of these have won scholarly awards. Using data in the public domain on 13 disciplinary societies, we found that the proportion of female prizewinners in ten of these was much lower than the proportion of female full professors in each discipline (see also P. Leboy *The Scientist* 22, 67; 2008).

Our investigations reveal that practices for selecting awardees all tend to operate with few guidelines, minimal oversight and little attention to conflict-of-interest issues. Having women on selection committees helps recognition, but many panels have no female members and few have female chairs.

The pool of female nominees for an award is typically small. Their nomination letters tend to contain fewer descriptors of exceptionality, use stereotypically female adjectives (such as 'cooperative' and 'dependable') and mention personal details. Notices soliciting nominations, by contrast, tend to use language that fosters male images, such as 'decisive' or 'confident'. Unsurprisingly, bias thrives under these conditions.

To help push through key changes, the Association for Women in Science in Virginia, with funding from the US National Science Foundation, is collaborating with seven US

science societies and the RAISE Project ([www.raiseproject.org](http://www.raiseproject.org)), which campaigns to raise the status of professional women through better recognition of their achievements.

We urge societies to use gender-neutral descriptors to broaden their candidate pool. Committees should establish selection criteria before reviewing nominees, and committee members need to understand the impact of implicit bias.

**Anne E. Lincoln** *Southern Methodist University, Texas, USA.*

**Stephanie H. Pincus** *The RAISE Project, USA.*

**Phoebe S. Leboy** *Association for Women in Science, USA; University of Pennsylvania, USA. [phoebe@biochem.dental.upenn.edu](mailto:phoebe@biochem.dental.upenn.edu)*

## Pitfalls of coal peak prediction

Richard Heinberg and David Fridley argue that coal reserves may be exhausted within decades (*Nature* 468, 367–369; 2010), basing much of their analysis on fits of cumulative coal production to logistic functions in the style of M. King Hubbert, who famously predicted peak oil supply. But this method is problematic — for example, fitting the decline in production of LP records to a logistic curve would incorrectly indicate that vinyl is a limited resource.

If scarcity were an important determinant of US coal-production history, prices should have increased. Yet they have stayed around US\$34 per tonne for the past 50 years, irrespective of production trends. Alternative explanations could include changes in electricity demand and market structure. There would then be no justification for calculating the limit of coal resources from a logistic graph of

production history.

The logistic fits that drive forecasts of coal exhaustion depend on which years are included in the analysis. Logistic fits using data up to 1989, 1999 or 2009 forecast an ultimate coal reserve of 52, 71 or 96 gigatonnes, respectively, and predict that production should have peaked in 1951, 1967 or 1986. In fact, coal production has increased since 1986 — highlighting the weakness of the scarcity-driven Hubbert model in explaining production.

An exponential fit explains as much of the variation in US production data as does a logistic fit. Yet the interpretation of the two models is different: the logistic model predicts the end of coal; the exponential fit predicts an infinite supply. Supply is obviously not infinite, but without a theoretical framework to support the choice of a logistic fit, its prediction may be just as wrong.

The end of easy oil is driving a shift towards carbon-intensive options, such as oil-sands mining or converting coal to liquid fuel. We must rely on policy changes to ensure a less carbon-intensive future, not the end of cheap coal.

**David Keith, Juan Moreno-Cruz** *University of Calgary, Alberta, Canada. [keith@ucalgary.ca](mailto:keith@ucalgary.ca)*

## Treat ghostwriting as misconduct

Research-funding agencies such as the US National Institutes of Health (NIH) still have no policies in place to prevent either ghostwriting or guestwriting, despite the importance of authorship in career advancement (*Nature* 468, 732; 2010).

Ghostwriting is the unacknowledged authoring of scientific papers by industry,

and guestwriting includes authors who have made little contribution to the work: both affront academic principles.

Cases involving NIH-funded researchers might, the agency confusingly suggests, be regarded as plagiarism and so could be subject to federal regulations on research ([go.nature.com/i5bnzo](http://go.nature.com/i5bnzo)). The University of Pennsylvania School of Medicine's authorship policies also equate ghostwriting with plagiarism. However, neither ghost nor guest plagiarize anyone, and the putative 'victim' — the company — simply invites researchers to publish work under their own names (T. D. Anekwe *Bioethics* 24, 267–272; 2010).

The 2009 Danish law on scientific dishonesty regards misappropriation of authorship as research misconduct, defining it as 'false credit given to the author or authors, misrepresentation of title or workplace' (see [go.nature.com/rj9slh](http://go.nature.com/rj9slh) and [go.nature.com/kqzgscl](http://go.nature.com/kqzgscl)).

The US Office for Research Integrity and others, such as the UK Research Integrity Office and the European Network of Research Integrity Offices, should follow the Danish example by introducing and enforcing regulatory policies on ghost- and guestwriting. Like fabrication and falsification, guest- and ghostwriting should be treated as research misconduct, not plagiarism. **Xavier Bosch** *Department of Internal Medicine, Hospital Clinic, University of Barcelona, Spain.*

[xavbosch@clinic.ub.es](mailto:xavbosch@clinic.ub.es)

### CORRECTION

In Poonam Kaushik Bakhshi's Correspondence (*Nature* 469, 162; 2011), we mistakenly attributed the author's proposed fern bioremediation strategy to the Hungarian government.

## A molecular memory booster

For many — if not all — of us, cognitive enhancement is desirable, but agents that would truly improve memory are hard to find. Unexpectedly, the product of an imprinted gene emerges as a promising candidate. [SEE ARTICLE P.491](#)

JOHANNES GRÄFF & LI-HUEI TSAI

How much do you remember about that article you read just five minutes ago? Wouldn't you like to remember more? A readers' survey by *Nature*<sup>1</sup> showed that one in five respondents already used some form of cognition-enhancing drug. But besides its appeal to healthy individuals, cognitive enhancement is also of help to those with any form of mental impairment, be it due to disease or ageing. Most treatments for cognitive deficits are disease-specific and target-based, or focus on circumstantial factors — such as attention deficits — that constrain the memory's capacity. True enhancers that would increase cognitive capacity irrespective of any given condition are still rare. On page 491 of this issue, Chen *et al.*<sup>2</sup> postulate that insulin-like growth factor II (IGF-II) has such generalized cognition-enhancing qualities in rats. The trick is to apply this signalling molecule during a specific time window after learning.

IGF-II is a well-characterized protein that promotes the growth, development and repair of somatic (non-germ) cells in a variety of tissues<sup>3</sup>. In the brain, this growth factor is highly expressed in the hippocampus<sup>3</sup> — a region important for learning and memory — and its expression decreases with ageing<sup>4</sup>. On the basis of this knowledge, Chen *et al.* hypothesized that IGF-II may also have a role in cognition.

To test this proposition, the authors assessed IGF-II expression in the rat hippocampus for several days after inhibitory avoidance learning. This test of associative memory involves measuring the 'latency' with which rodents enter the darker side of a box, where they previously received an electrical foot-shock. Because rodents normally prefer dark compartments to illuminated ones, their hesitation to re-enter the dark compartment is taken as an indication of how well they have learned to associate the dark side with the foot shock. Chen *et al.* find that levels of IGF-II messenger RNA and protein increased between one and two days (20 and 36 hours) after training, but not immediately, nor three days after training.

Is such increased IGF-II expression functionally relevant to inhibitory avoidance

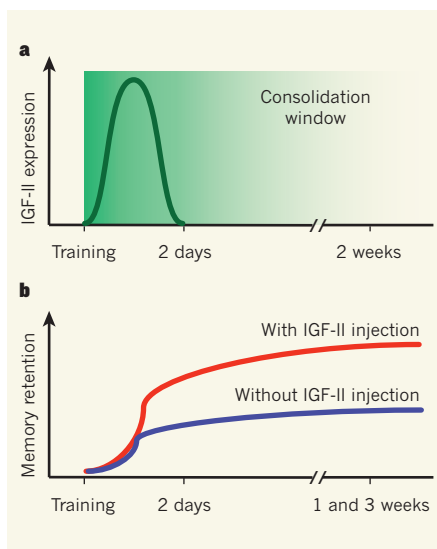


**Figure 1 | IGF-II can promote memory retention.** **a**, Inhibitory avoidance memories are most susceptible to disruption up until two days after training — a period after which their dependence on protein synthesis gradually decreases, allowing memory consolidation. Chen *et al.*<sup>2</sup> find that IGF-II protein and mRNA levels peak after inhibitory avoidance training, precisely during the apex of memory fragility (dark green region), suggesting a role for this molecule in memory consolidation. **b**, When the authors administered IGF-II during the consolidation window, they observed significant improvements in memory retention, compared with control animals, even three weeks after training.

memory? To test this, Chen and co-workers injected antisense oligonucleotides against IGF-II bilaterally into the rats' hippocampi at different time points after training. When examined 24 hours after the injection, memory retention was significantly impaired — but only if the injection had occurred one or two days after training and not later, which is in line with the observed peak of IGF-II expression after training. What's more, these artificially induced deficits could be overcome by simultaneous expression of recombinant IGF-II. These results suggest that IGF-II plays a crucial part in mediating cognitive abilities, specifically during memory consolidation, the process by which fresh, labile memories are stabilized into long-lasting ones<sup>5</sup> (Fig. 1).

Memory consolidation involves protein synthesis. Using anisomycin, an inhibitor of protein synthesis, the same team previously found<sup>6</sup> that newly formed inhibitory avoidance memories are most susceptible to disruption during the first two days after training. Chen and colleagues now show<sup>2</sup> that this consolidation window is also amenable to positive manipulation.

To that end, the authors injected recombinant IGF-II into rat hippocampi immediately after inhibitory avoidance training. On testing the animals 24 hours later, they noted significant enhancement in memory retention — a finding that they could replicate using fear conditioning, another test of associative memory. Remarkably, Chen *et al.* observed the same degree of enhancement one and three weeks after training, which indicates that, if administered during the consolidation window, IGF-II triggers enduring downstream effects that sustain long-lasting memories (Fig. 1). When given outside the peak of the consolidation window (that is, roughly 24 hours after training), IGF-II injection led to no memory improvement.

An immediate question is how IGF-II enhances memory. Chen *et al.* report that this protein acts through its receptor IGF-IIR, and that an antisense oligonucleotide against Arc — a protein found at synaptic connections between neurons that is essential for memory formation — blocks its effects.

Nonetheless, a more comprehensive mechanistic breakdown of the signalling pathways downstream of IGF-II — for example, through genome-wide gene-expression analysis — would be highly beneficial not only to place IGF-II better in the scheme of well-established learning and memory signalling cascades, but also to enable a thorough evaluation of potential side effects. This is particularly necessary, because high levels of IGF-II have been associated<sup>7</sup> with various types of cancer in other tissues.

It should also be determined which cell populations in the brain are most sensitive to IGF-II levels, and whether IGF-II-mediated cognitive enhancement also applies to other forms of learning, such as spatial memory and object memory. Chen and colleagues' results must, therefore, be taken as

a mere first — albeit promising — step on a fresh path in the emerging field of cognitive-enhancement research.

These outstanding questions notwithstanding, the current study<sup>7</sup> has yet another interesting twist. The genes encoding *IGF-II* and *IGF-IIR* are known to be imprinted (they display a dichotomous effect on growth in most tissues studied<sup>8</sup>). The *IGF-II* gene — like many other genes for which only the paternal copy is expressed — favours growth. Conversely, the *IGF-IIR* gene — like most maternally expressed genes — suppresses growth. Chen and co-workers' data are not only the first to attribute a clear-cut function to these genes in the brain, but also to show that, at least in the rat hippocampus, their protein products cooperate to enhance memory. But, given that the spatial and developmental patterns of *IGF-II*

and *IGF-IIR* expression in the brain are highly complex<sup>9</sup>, more work is needed to decipher their exact regulation.

One process by which the expression of maternal and paternal copies of *IGF-II* and *IGF-IIR* is regulated is DNA methylation<sup>8</sup> — an epigenetic mechanism that is dynamically altered after learning<sup>10</sup>. So it would be interesting to know whether learning per se can also trigger epigenetic changes and so the subsequent alterations in the expression of *IGF-II* and *IGF-IIR*. Moreover, 'natural cognition enhancers' such as environmental enrichment, which are known to act through epigenetic mechanisms<sup>11</sup>, might also epigenetically regulate *IGF-II* and *IGF-IIR*. If so, for those in search of a memory boost, natural enhancers would be an attractive alternative to purely pharmacological agents. ■

**Johannes Gräff and Li-Huei Tsai** are at the Picower Institute for Learning and Memory, Department of Brain and Cognitive Sciences, Massachusetts Institute of Technology, Cambridge, Massachusetts 02139, USA. e-mails: jgraeff@mit.edu; lhtsai@mit.edu

1. Maher, B. *Nature* **452**, 674–675 (2008).
2. Chen, D. Y. et al. *Nature* **469**, 491–497 (2011).
3. Russo, V. C. et al. *Endocr. Rev.* **26**, 916–943 (2005).
4. Sonntag, W. E. et al. *Neuroscience* **88**, 269–279 (1999).
5. Dudai, Y. *Annu. Rev. Psychol.* **55**, 51–86 (2004).
6. Milekic, M. H. & Alberini, C. M. *Neuron* **36**, 521–525 (2002).
7. Feinberg, A. P. *Nature* **447**, 433–440 (2007).
8. Reik, W. & Walter, J. *Nature Rev. Genet.* **2**, 21–32 (2001).
9. Gregg, C. et al. *Science* **329**, 643–648 (2010).
10. Day, J. J. & Sweatt, J. D. *Nature Neurosci.* **13**, 1319–1323 (2010).
11. Fischer, A., Sananbenesi, F., Wang, X., Dobbin, M. & Tsai, L.-H. *Nature* **447**, 178–182 (2007).

## QUANTUM INFORMATION

# Entanglement on ice

**The ability to store entangled photons in a solid-state memory, and to retrieve them while preserving the entanglement, is a required step on the way to practical quantum communication. This step has now been taken. SEE LETTERS P.508 & P.512**

JEVON LONGDELL

Communication over long distances needs repeaters — for classical communication these are devices that receive input data and retransmit them. In an important move towards long-distance communication of quantum information, two groups<sup>1,2</sup> (pages 508 and 512 of this issue) have demonstrated the basic building block of a solid-state quantum repeater. The authors have managed to put entangled photons 'on ice'. That is, they were able to show that they could keep a pair of photons entangled, even after storing and retrieving one of the photons in a cryogenically cooled crystal.

Two quantum-mechanical systems are entangled when it is impossible to properly describe the quantum-mechanical state of one of them in isolation. The concept was introduced by Einstein, Podolsky and Rosen in their famous 1935 paper<sup>3</sup>. Quantum mechanics predicts completely random, but perfectly correlated, results for some measurements of the two entangled systems. It also states that the results of these measurements are not determined until one of the systems is measured. However, the fact that these correlations still existed when the systems were too far apart for any signalling between them to be possible, led Einstein and colleagues<sup>3</sup> to conclude that quantum mechanics was not a complete description of entangled systems. They argued that the measurement results must have been

determined by some 'hidden variable' when the entangled pair was created, and not at the time of measurement.

Since 1935, entangled states have been produced, and the strange predictions that quantum mechanics makes about them have been validated. Furthermore, Bell showed<sup>4</sup> that all hidden-variable theories will give predictions that, in certain circumstances, differ from those of quantum mechanics. It was therefore possible to do experiments that supported quantum mechanics over hidden-variable theories. Today, entanglement is at the heart of quantum information. The challenge in achieving secure, long-distance communication of quantum information is entangling systems that are spatially far apart.

In many ways, photons are ideal carriers of quantum information: they are easy to manipulate with optics, can be sent long distances either through optical fibres or in free space, and good single-photon detectors are also available. There are downsides, however. Unless speeding through a vacuum, photons have very short lives. This problem is exacerbated by the fact that most methods for creating, and many methods for manipulating, entangled photons are probabilistic. And this is why the ability to store entangled photons in a memory and then recall them, while preserving the entanglement, which has now been demonstrated by Clausen *et al.*<sup>1</sup> and Saglamyurek *et al.*<sup>2</sup>, is so important. It enables much more sophisticated operations

through synchronization of these probabilistic processes.

An example of these more sophisticated operations is long-distance quantum communication. Entanglement, and therefore secure communication, protected by quantum mechanics<sup>5</sup>, can be achieved over moderate distances (tens of kilometres) by simple propagation of entangled pairs of photons. But at larger distances, photon loss quickly becomes a significant problem, preventing the distribution of entanglement. One way to solve this problem is to break the link between the two parties into a small number of sub-links joined together with quantum repeaters<sup>6</sup>. Entangled photons would then be transmitted between the repeaters. The memories in the repeaters can store entangled photon pairs associated with successful transmission along part of the link until other parts of the link are also successful. In this way, quantum repeaters prevent the effective bit rates for transferring information between the two parties from dropping off exponentially (or worse) with distance. This is because, with repeaters, entanglement can be achieved without one photon having to travel along the whole link, which for long links can be very unlikely.

When implementing quantum repeaters, it has been the memory aspect that has been the most troublesome. But now Clausen *et al.*<sup>1</sup> and Saglamyurek *et al.*<sup>2</sup> have given us proof-of-principle demonstrations. They have produced entangled photons by means of spontaneous parametric downconversion. In this process, an entangled pair of two lower-energy photons is created from a higher-energy photon in an optically nonlinear crystal. The wavelength of the 'pump' lasers that produce the higher-energy photon was chosen by both groups<sup>1,2</sup> such that one member of the entangled photon pair had a suitable wavelength for being stored in a quantum memory based on a cryogenic crystal doped with rare-earth ions; and, as required by quantum repeaters, the wavelength

of the other member of the pair was suitable for long-distance transmission in optical fibre.

Mapping of photonic entanglement into and out of a quantum memory has been demonstrated already with trapped-atom systems<sup>7</sup>. However, the new work<sup>1,2</sup> is the first to achieve it using a solid-state memory. The use of the solid state offers certain practical advantages. For example, Saglamyurek and colleagues<sup>2</sup> formed the memory in an optical waveguide, which could enable integrated devices to be built. More significantly though, the authors' approach<sup>1,2</sup> to quantum memories using cryogenic rare-earth-ion-doped crystals is rapidly developing and has already surpassed the storage bandwidths<sup>2</sup>, capacities<sup>8</sup>, efficiencies<sup>9</sup> and storage times<sup>10</sup> of other approaches.

Such cryogenic rare-earth-ion-doped systems have already been studied for classical optical signal processing because of these systems' large ratio of inhomogeneous to homogeneous broadening<sup>11</sup> for their optical absorption lines. That is, the optical absorption linewidth of each dopant atom is very narrow, whereas the linewidth of the ensemble

of dopants can be very large. This makes them very suitable systems for photon echoes, which is where the dopants emit a pulse of light (echo) in response to earlier applied light pulses. In particular, photon echoes allow signal processing with simultaneous large bandwidth, determined by ensemble linewidth, and high resolution, determined by single-dopant linewidth. The rapid advances of rare-earth quantum memories have been, in large part, due to the development of photon-echo techniques, which are suitable for preserving quantum states of light.

Although the storage of entanglement in a solid is a significant step, the efficiencies and storage times in the entanglement-storage experiments of Clausen *et al.*<sup>1</sup> and Saglamyurek *et al.*<sup>2</sup> need to be improved; they are currently inferior to those that can be achieved in a small spool of optical fibre. And whereas good efficiency, storage time and bandwidth have all been demonstrated by others, in separate demonstrations, the next challenge awaiting researchers is to achieve all these performance metrics for the same memory. This should

open up new capabilities and technologies that will stretch quantum mechanics in a way that we have not yet been able to. Who knows, it might break. ■

**Jevon Longdell** is at the Jack Dodd Centre for Quantum Technology, Department of Physics, University of Otago, Dunedin 9054, New Zealand.

e-mail: jevon@physics.otago.ac.nz

1. Clausen, C. *et al.* *Nature* **469**, 508–511 (2011).
2. Saglamyurek, E. *et al.* *Nature* **469**, 512–515 (2011).
3. Einstein, A., Podolsky, B. & Rosen, N. *Phys. Rev.* **47**, 777–780 (1935).
4. Bell, J. S. *Rev. Mod. Phys.* **38**, 447–452 (1966).
5. Ekert, A. K. *Phys. Rev. Lett.* **67**, 661–663 (1991).
6. Briegel, H.-J., Dür, W., Cirac, J. I. & Zoller, P. *Phys. Rev. Lett.* **81**, 5932–5935 (1998).
7. Choi, K. S., Deng, H., Laurat, J. & Kimble, H. J. *Nature* **452**, 67–71 (2008).
8. Usmani, I., Afzelius, M., de Riedmatten, H. & Gisin, N. *Nature Commun.* **1**, 12 (2010).
9. Hedges, M. P., Longdell, J. J., Li, Y. & Sellars, M. J. *Nature* **465**, 1052–1056 (2010).
10. Longdell, J. J., Fraval, E., Sellars, M. J. & Manson, N. B. *Phys. Rev. Lett.* **95**, 063601 (2005).
11. Barber, Z. W. *et al.* *J. Lumin.* **130**, 1614–1618 (2010).

## CIRCADIAN RHYTHMS

# Redox redux

**Oscillations in gene transcription that occur in response to biological daily clocks coordinate the physiological workings of living organisms. But turnover in cellular energy may be sufficient to make the clock tick. SEE ARTICLE P.498 & LETTER P.554**

JOSEPH BASS & JOSEPH S. TAKAHASHI

Last spring, a visitor at the biennial meeting of the Society for Research on Biological Rhythms in Florida approached the geneticist Sydney Brenner inquiring as to what it was that scientists studying circadian rhythms actually do. With a glimmer in his eye, Brenner responded that the meeting concerned “those things that only happen once each day”. Indeed, all forms of life undergo circadian (roughly 24-hour) fluctuations in energy availability that are tied to alternating cycles of light and darkness. Biological clocks organize such internal energetic cycles through transcription–translation feedback loops. But two papers<sup>1,2</sup> in this issue show that, in both humans and green algae, rhythmic cycles in the activity of peroxiredoxin enzymes can occur independently of transcription.

Biological circadian oscillators have long been recognized as a self-sustained phenomenon, their 24-hour length being both invariant over a wide range of temperatures and responsive to light. Early indications that genes underlie the clocks came<sup>3</sup> from the isolation of mutant fruitflies carrying altered, and yet

heritable, circadian rhythms. This and subsequent work<sup>4,5</sup> established that endogenous molecular clocks consist of a transcription–translation feedback loop that oscillates every 24 hours in cyanobacteria, plants, fungi and animals.

Although the specific clock genes are not evolutionarily conserved across distinct phyla, their architecture is similar. The forward limb of the clock involves a set of transcriptional activators that induce the transcription of a set of repressors. The latter comprise the negative limb, which feeds back to inhibit the forward limb. This cycle repeats itself every 24 hours (Fig. 1).

Energetic cycles are one type of physiological process that shows transcription-dependent circadian periodicity<sup>6,7</sup>; such cycles include the alternating oxygenic and nitrogen-fixing phases of photosynthesis, and the glycolytic and oxidative cycles in eukaryotes (organisms with nucleated cells). The idea that biochemical flux per se may couple circadian and energetic cycles was first suggested by McKnight and colleagues<sup>8</sup>, who showed that varying the redox state of the metabolic cofactor NAD(P) affects the activity of two clock proteins, and it gained further support from subsequent studies<sup>9–14</sup>.

But exactly how transcriptional and non-transcriptional cycles may be interrelated was still not fully understood.

To address this relationship, O'Neill and Reddy<sup>1</sup> (page 498) examined the rhythmic properties of human red blood cells (RBCs). In their mature form, these cells lack both a nucleus and most other organelles, including energy-producing mitochondria. They function mainly as oxygen shuttles, utilizing the protein haemoglobin as the delivery vehicle.

Some of the most abundant proteins in mature RBCs are the evolutionarily conserved enzymes of the peroxiredoxin family, which can inactivate reactive oxygen species (ROS). Class-2 peroxiredoxins contain a cysteine amino-acid residue in their active site that undergoes oxidation when ROS accumulate. This results in the enzyme's transition from a monomeric to a dimeric state. Excess ROS accumulation induces the formation of even higher-order oligomers. Peroxiredoxin function is essential for RBC survival, as defects in the expression or activity of these enzymes lead to the breakdown of the cells.

A previous survey<sup>15</sup> searching for proteins that show circadian rhythms of expression in liver identified peroxiredoxins. In their study, O'Neill and Reddy<sup>1</sup> monitored the monomer–dimer transition of these proteins in RBCs from three humans. They observed two main circadian features in these enucleated cells. First, the oligomerization pattern was self-sustained over several cycles within an approximate 24-hour period and was not affected by temperature. Second, peroxiredoxin oxidation cycles were synchronized in response to temperature cycles, a property called entrainment that is a hallmark of circadian oscillators.

These results, which should be confirmed by replication in larger numbers of individuals, clearly show that circadian patterns of peroxiredoxin oxidation persist even in the absence of gene transcription. To rule out the contribution of other, nucleated, blood cells, the authors show that inhibitors of translation (cycloheximide) and transcription ( $\alpha$ -amanitin) do not interfere with the peroxiredoxin oxidation rhythm.

In seeking to connect the observed peroxiredoxin oxidation rhythm with the broader physiological functions of RBCs, O'Neill and Reddy also examined the oligomeric transitions of haemoglobin. They detected a rhythmic pattern in the dimer–tetramer transition of haemoglobin, which suggests that the oxygen-carrying capacity of an RBC also exhibits circadian variation. Whether cycles of haemoglobin oxidation similarly show temperature compensation and responsiveness — and the robustness of such oscillations — remains unknown.

What drives the rhythmic cycles of oligomerization for peroxiredoxin and haemoglobin? One possibility is flux in metabolic cycles such as glycolysis — the only source of energy in RBCs. Indeed, O'Neill and Reddy report weak oscillations in the levels of ATP, the cellular energy molecule that can be generated by glycolysis. Nonetheless, further analyses are necessary to determine the exact relationship between oxidation-state transitions and energy production.

Rhythmic variation in levels of NAD(P)H, albeit of low amplitude, also corresponded with the variation in oligomerization state of both peroxiredoxin and haemoglobin<sup>1</sup> — a finding that points to this reduced form of NAD(P) as being a cofactor coupling energy flux with changes in the oxidation of these proteins. This observation echoes those of previous studies<sup>8</sup>.

RBCs do not represent a special case for gene–energy coupling. O'Neill and colleagues<sup>2</sup> (page 554) frame their inquiry in a broader context by examining the rhythmic activity of the same family of peroxiredoxins in one of the most primitive eukaryotes known — the green alga *Ostreococcus tauri*.

The authors took advantage of a curious observation — that simply maintaining *O. tauri* out of the light suspends all gene transcription. Shifting this microorganism back into the light reinitiates transcription and restarts the clock. However, the clock does not simply reset following transfer into light at any time of day. Instead, it begins ticking again according to the time when the lights were switched off initially. In other words, the alga seems to keep track of time even in the dark, when transcription has ceased. This implies that other mechanisms in the cell provide a 'sense of time' independent of gene transcription.

To investigate how *O. tauri* senses time, O'Neill *et al.* tested the idea that the persistence

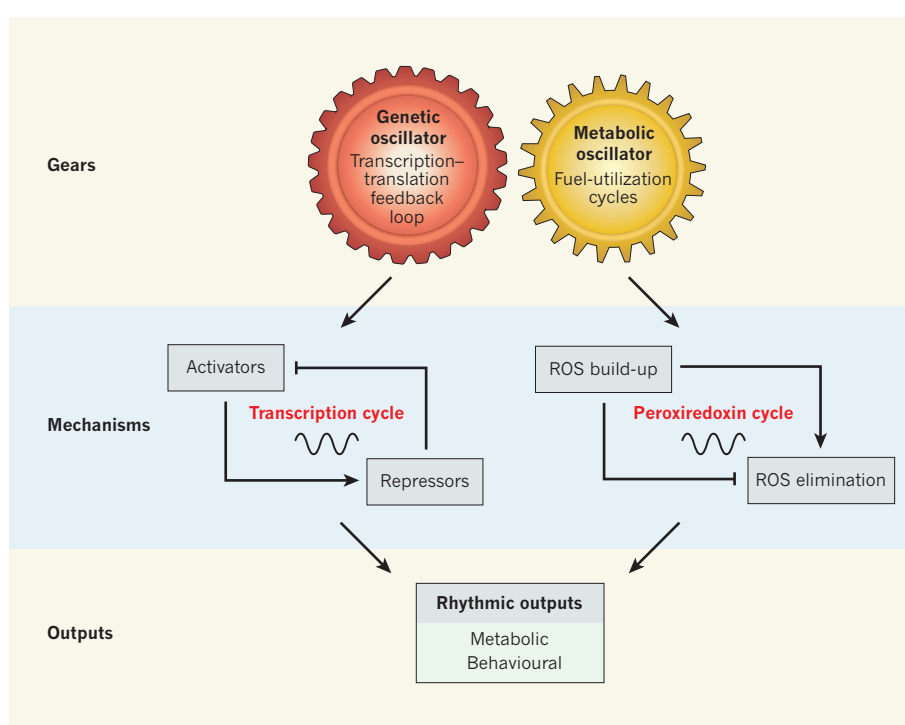


**Figure 1 | Coupling of genetic and metabolic clocks.** Two types of circadian oscillator maintain synchrony between the light–dark environment and internal biochemical processes. These are genetic oscillators, which consist of a transcription–translation feedback loop, and — as two new studies<sup>1,2</sup> show — metabolic oscillators, which are involved in fuel-utilization cycles and consist of the cycle of oxidation and reduction of peroxiredoxin enzymes. The two oscillator types are coupled, both driving rhythmic outputs (such as photosynthetic reaction cycles in plants and the feeding–fasting cycle in animals) in synchrony with Earth's rotation. ROS, reactive oxygen species.

of oscillations in peroxiredoxin oxidation may offer a clue to the 'invisible' factor responsible for keeping time in the absence of transcription. In contrast to the previously established 'transcriptional' oscillator of *O. tauri*, peroxiredoxin oscillation was still detected in the dark, further proving pharmacologically that the enzyme's rhythm is independent of new gene or protein synthesis. Exploring the inter-relationship between transcriptional-feedback oscillators and post-transcriptional mechanisms, the authors show that drugs that inhibit transcription affect circadian oscillation within restricted phases of the daily cycle.

So, are RBCs and *O. tauri* exceptions to the generally accepted idea that the origins of biological clocks can be traced to genetic mechanisms? Intriguingly, O'Neill and Reddy<sup>1</sup> find that peroxiredoxin rhythms were altered in mouse embryonic connective-tissue cells harvested from mutant animals possessing a genetically disrupted clock. This indicates that, in nucleated cells, transcriptional and non-transcriptional oscillators are normally coupled. Similarly, cyclic phosphorylation of the protein KaiC, which can occur in the absence of transcription<sup>16</sup>, is coupled with transcriptional rhythms in intact cyanobacteria<sup>17</sup>.

The provocative models provided by these studies<sup>1,2</sup> return us to the question of the inter-dependence of circadian and energetic systems: just how do these processes communicate

reciprocally? The cofactor signalling molecules that link the two systems remain of great interest, especially given the potential role of circadian disruption in metabolic disorders. Besides, the fact that oscillators exist in the absence of transcription does not negate the selective advantage that circadian genes confer. At the very least, these genes enhance organismal adaptation to the energetic environment. ■

**Joseph Bass** is in the Division of Endocrinology and Molecular Medicine, Department of Medicine, Feinberg School of Medicine, Northwestern University, Chicago, Illinois 60611, USA. He is also at the Center for Sleep and Circadian Biology, Northwestern University, Evanston. **Joseph S. Takahashi** is in the Department of Neuroscience, Howard Hughes Medical Institute, University of Texas Southwestern Medical Center, Dallas, Texas 75390-9111, USA.  
e-mail: j-bass@northwestern.edu

- O'Neill, J. S. & Reddy, A. B. *Nature* **469**, 498–503 (2011).
- O'Neill, J. S. *et al.* *Nature* **469**, 554–558 (2011).
- Konopka, R. J. & Benzer, S. *Proc. Natl Acad. Sci. USA* **68**, 2112–2116 (1971).
- Bell-Pedersen, D. *et al.* *Nature Rev. Genet.* **6**, 544–556 (2005).
- Takahashi, J. S., Hong, H.-K., Ko, C. H. & McDearmon, E. L. *Nature Rev. Genet.* **9**, 764–775 (2008).

6. Harmer, S. L. *Annu. Rev. Plant Biol.* **60**, 357–377 (2009).
7. Bass, J. & Takahashi, J. S. *Science* **330**, 1349–1354 (2010).
8. Rutter, J., Reick, M. & McKnight, S. L. *Annu. Rev. Biochem.* **71**, 307–331 (2002).
9. Nakahata, Y. *et al. Cell* **134**, 329–340 (2008).
10. Asher, G. *et al. Cell* **134**, 317–328 (2008).
11. Ramsey, K. M. *et al. Science* **324**, 651–654 (2009).
12. Nakahata, Y., Sahar, S., Astarita, G., Kaluzova, M. & Sassone-Corsi, P. *Science* **324**, 654–657 (2009).
13. Asher, G. *et al. Cell* **142**, 943–953 (2010).
14. Lamia, K. A. *et al. Science* **326**, 437–440 (2009).
15. Reddy, A. B. *et al. Curr. Biol.* **16**, 1107–1115 (2006).
16. Nakajima, M. *et al. Science* **308**, 414–415 (2005).
17. Kitayama, Y., Nishiwaki, T., Terauchi, K. & Kondo, T. *Genes Dev.* **22**, 1513–1521 (2008).

**J.B. declares competing financial interests.** See online article for details.

## MEDICINE

# Diabetes in India

**With the spread of fast-food outlets and more sedentary lifestyles, the prevalence of diabetes in India is rising alarmingly. But the subpopulations at risk and the symptoms of the disease differ from those in the West.**

JARED DIAMOND

India, the world's second most populous country, now has more people with type 2 diabetes (more than 50 million) than any other nation. The problem has been well documented in a battery of recent papers<sup>1–6</sup>. These publications were foreshadowed by studies of previously Westernized Indian populations elsewhere, and they illuminate distinctive features of diabetes in India.

Type 2 diabetes results from a genetic predisposition and from lifestyle factors, especially those of the so-called Western lifestyle, characterized by high calorie intake and little exercise. Also known as non-insulin-dependent or adult-onset diabetes, this form of the disease is far more common than type 1 (insulin-dependent or juvenile-onset) diabetes. Until recently, type 2 diabetes — henceforth simply

'diabetes' — was viewed as a disease of overfed, sedentary people of European ancestry. But it is now exploding around the world owing to the spread of Western habits.

Hints of trouble ahead came from observations of diabetes epidemics in emigrant Indian communities that achieved affluence long before Indians in India<sup>1–3,7</sup>. Those communities include ones in Fiji, Mauritius, Singapore, South Africa, Surinam, Tanzania and Britain. For instance, in the 1830s, Indians were brought to Mauritius for physically demanding work on sugar plantations. By the 1980s, the decline in world sugar prices had led the Mauritian government to promote industrialization and the export of manufactured goods, which in turn led to increasing affluence and decreasing physical activity for the local population.

As a result, between 1982 and 1986 deaths due to diabetes tripled, and by 1987 reached

13% in the Mauritius Indian community<sup>7,8</sup>. (By contrast, prevalence remained much lower in the even more affluent Mauritius European community, illustrating the role of genetic factors.) Today, Mauritius enjoys a per capita income four times that of India but suffers from the world's second highest national prevalence of diabetes, 24%. Those developments led Zimmet<sup>8</sup> to prophesy in 1996: "If over the next few decades the people in India become modernized to a similar level of those in Mauritius and other countries inhabited by Asian Indians, one could expect dramatically increased diabetes rates in India."

That prophecy has already been grimly fulfilled. In 2010, the average age-adjusted prevalence of diabetes in India was 8%, higher than that in most European countries<sup>1</sup>. By contrast, surveys in 1938 and 1959, in large Indian cities that are today diabetes strongholds, yielded prevalences of just 1% or less. Only in the 1980s did those numbers start to rise, first slowly and now explosively<sup>5,6,9,10</sup>.

The reasons are those behind the diabetes epidemic worldwide. One set of factors is urbanization, a rise in living standards and the spread of calorie-rich, fatty, fast foods cheaply available in cities to rich and poor alike. Another is the increased sedentariness that has resulted from the replacement of manual labour by service jobs, and from the advent of video games, television and computers that keep people seated lethargically watching screens for hours every day. Although the specific role of TV has not been quantified in India, a study in Australia<sup>11</sup> found that each hour per day spent watching TV is associated with an 18% increase in cardiovascular mortality (much of it associated with diabetes), even after controlling for other risk factors such as waist circumference, smoking, alcohol intake and diet. But those factors notoriously increase with TV watching time, so the true figure must be even larger than the 18% estimate.

In India, a wide range of outcomes for different groups<sup>9,10</sup> is buried within the average diabetes prevalence of 8%. Prevalence is only 0.7% for non-obese, physically active, rural Indians. It reaches 11% for obese, sedentary, urban Indians; and it peaks at 20% in the Ernakulam district of Kerala, one of India's most urbanized states. Among lifestyle factors predicting the incidence of diabetes in India, some are familiar from the West, whereas others turn expectations upside down<sup>9,10</sup>. As in the West, diabetes in India is associated with obesity, high blood pressure and sedentariness. But prevalence of the disease is higher among affluent, educated, urban Indians than among poor, uneducated, rural people: exactly the opposite of trends in the West, although similar to the situation in other developing countries. For instance, Indians with diabetes are more likely to have undergone higher education, and less likely to be illiterate, than their healthy compatriots. In 2004, the prevalence of diabetes averaged 16%



**Figure 1 | Raising awareness of diabetes.** Participants on a 'walkathon' in Bangalore, India, in November 2010.

in urban India and only 3% in rural India<sup>10</sup>. That urban concentration of diabetes has also been reported in many other Asian countries.

The likely explanation for these paradoxes is twofold. First, in the West, poor rural people are better able to afford fast foods than their Indian counterparts. Second, educated Westerners with access to fast foods and with sedentary jobs are by now often well aware that fast foods are unhealthy and that one should exercise, whereas that advice has not yet made wide inroads among educated Indians (Fig. 1). Nearly 25% of Indian city dwellers (the sub-population most at risk) haven't even heard of diabetes<sup>9</sup>.

In India, as in the West, diabetes is ultimately due to chronically high levels of blood glucose, and some of the clinical consequences are similar. But whereas Westerners think of type 2 diabetes as an adult-onset disease appearing especially after the age of 50, Indians (and Chinese, Japanese and Aboriginal Australians) with diabetes exhibit symptoms at an age one or two decades younger than that. The age of onset in India has been shifting towards ever-younger people even within the past decade<sup>9</sup> — among Indians in their late teens, 'adult-onset' diabetes already manifests itself more often than does 'juvenile-onset' diabetes. In Britain, the prevalence of type 2 diabetes is 14 times higher in Asian than European children. And although obesity is a risk factor for diabetes both in India and in the West, the disease appears at a lower threshold of obesity in India, as is also the case in China, Japan and other Asian countries<sup>10</sup>.

Symptoms also differ between Indians and Westerners: Indians with diabetes are less likely to develop blindness and kidney disease, but much more likely to suffer coronary artery disease at a relatively young age<sup>9,12</sup>. Just as Indians can't be lumped in with people of European ancestry, differences also appear among Asians: some, but not all, distinctive features of Indian diabetes apply to other Asian populations. For example, by worldwide standards, Chinese people with diabetes experience a low prevalence of coronary artery disease but a high prevalence of retinal and kidney damage. The relative roles of genetic and lifestyle factors in these ethnic differences remain to be teased out.

Although poor Indians are currently at lower risk than affluent Indians, the rapid spread of fast food exposes even urban Indian slum-dwellers to the risk of diabetes. Sandeep and colleagues of the Madras Diabetes Research Foundation<sup>13</sup> summarize the situation as follows: "diabetes [in India] is no longer a disease of the affluent or a rich man's disease. It is becoming a problem even among the middle income and poorer sections of the society. Studies have shown that poor diabetic subjects are more prone to complications as they have less access to quality health care. This presents an alarming picture..." Alas, that's true. ■

**Jared Diamond** is in the Geography Department, University of California, Los Angeles, California 90095-1524, USA. e-mail: [jdiamond@geog.ucla.edu](mailto:jdiamond@geog.ucla.edu)

1. Shaw, J. E., Sicree, R. A. & Zimmet, P. Z. *Diabetes Res. Clin. Practice* **87**, 4–14 (2010).
2. Magliano, D. J. et al. *Diabetes Care* **33**, 1983–1989 (2010).
3. Jowett, J. B. et al. *Twin Res. Hum. Genet.* **12**, 44–52 (2009).
4. Ramachandran, A., Ma, R. C. W. & Snehalatha, C. *Lancet* **375**, 408–418 (2010).
5. Mohan, V. et al. *Indian J. Med. Res.* **131**, 369–372 (2010).

6. Pradeepa, R. et al. *Diabetes Technol. Therapeutics* **12**, 755–761 (2010).
7. Dowse, G. K. et al. *Diabetes* **39**, 390–396 (1990).
8. Zimmet, P. *IDF Bull.* **36**, 29–32 (1996).
9. Mohan, V. et al. *Indian J. Med. Res.* **125**, 217–230 (2007).
10. Mohan, V. et al. *Diabetes Res. Clin. Practice* **80**, 159–168 (2008).
11. Dunstan, D. W. et al. *Circulation* **121**, 384–391 (2010).
12. Unnikrishnan, R. et al. *Diabetes Care* **30**, 2019–2024 (2007).
13. Sandeep, S., Ganesan, A. & Mohan, V. *Development and Updation of the Diabetes Atlas of India* [www.whoindia.org/LinkFiles/NMH\\_Resources\\_Diabetes\\_atlas.pdf](http://www.whoindia.org/LinkFiles/NMH_Resources_Diabetes_atlas.pdf) (2010).

## COSMOLOGY

# A glimpse of the first galaxies

The recently refurbished Hubble Space Telescope reveals a galaxy from a time when the Universe was just 500 million years old, providing insights into the first throes of galaxy formation and the reionization of the Universe. [SEE LETTER P.504](#)

NAVEEN A. REDDY

A central focus of cosmology is to understand how the primordial density fluctuations imprinted by the Big Bang gave rise to the galaxies and larger structures we observe today. Just as archaeologists sift through deeper layers of sand to uncover the past, cosmologists use large telescopes and sensitive detectors to study galaxies at ever greater distances from Earth and, because of the finite speed of light, to peer farther back in time. On page 504 of this issue, Bouwens *et al.*<sup>1</sup> take another step in this direction by exploiting the deepest near-infrared images of the sky, which were obtained with the reserived Hubble Space Telescope and its new Wide Field Camera<sup>2</sup>. On the basis of these data, the authors report the plausible detection of the most distant galaxy yet discovered. The galaxy would have existed when the Universe was just 4% of its current age and when one of the most important phase transitions of gas in the Universe occurred.

Building on previous studies, Bouwens and colleagues used the well-established Lyman break technique<sup>3</sup> to select galaxies at the largest distances, or redshifts. The method relies on the absorption, by neutral hydrogen within a galaxy or by intervening hydrogen clouds, of photons that are more energetic than Lyman- $\alpha$  photons (10.2 eV, corresponding to a wavelength of 1,216 ångströms). The resulting decrease in flux bluewards of the Lyman- $\alpha$  wavelength results in a characteristic 'break' in the spectrum of a galaxy. Galaxies at different redshifts can then be located by searching for

objects that are detected in one filter but that disappear, or are very faint, in a bluer filter.

Until now, the primary obstacle to identifying galaxies beyond redshift 6 — when the Universe was less than 1 billion years old — has been that the Lyman break shifts to the observed near-infrared, where the emission from the sky background is several hundred times higher than it is in the visible range of the spectrum. This higher background inhibits the ability to obtain deep imaging, and has motivated observations from above Earth's atmosphere. A breakthrough came with the installation of the Wide Field Camera on Hubble; the camera's increased field of view and sensitivity over the previous near-infrared instrument on Hubble results in an increase by a factor of more than 30 in its capacity for finding faint galaxies at high redshift.

Using multi-filter imaging from Hubble and the Lyman break technique, Bouwens and collaborators<sup>1</sup> report the discovery of one candidate galaxy at a redshift of about 10 (Fig. 1). Comparing the number density of galaxies at redshift 10, inferred from their observations, with that determined at lower redshifts, they find that the average galaxy increases in luminosity by more than a factor of 10 during the first 2 billion years of galaxy formation. Taken one step further, this finding suggests a close connection between galaxy formation and the assembly of dark matter in the early Universe.

In contrast to the prevailing theory of cold dark matter and its relative success in reproducing the large-scale structure of the Universe, the physics of the development and evolution of visible matter is difficult to model:



## 50 Years Ago

The report of an enquiry into the employment of qualified women scientists and engineers in private manufacturing industry shows clearly that, in general, industry in Britain is a man-dominated world and is likely to remain so for many years to come ... From the survey one conclusion is inescapable. Employers are reluctant to employ educated women scientists and engineers mainly because, on economic grounds, they are a bad risk ... From the employer's point of view, their years of useful service before beginning full-time duties in their homes is very limited. All the well-meaning protestations by women's organizations will not make young women scientists and engineers anything but a bad industrial investment compared with their male counterparts. Most educated women know this and accept this.

From *Nature* 28 January 1961

## 100 Years Ago

In his article on "Sex Relationship", Dr. R. J. Ewart said, in commenting on the present excess of females over males:—"The result of this is to produce in a community a section of women who cannot possibly perform that function for which they were fashioned. Their energies are naturally directed into other spheres, as evidence of which we see the revival of movement for political recognition." ... Dr. Ewart errs in attributing to a purely physical cause a movement which really arises from a mental and moral awakening — and, indeed, his whole article is full of unsupported assertions and loose reasoning; but I should not have ventured to criticise it had he not so clearly allowed his judgment to be warped by his political bias.

Hertha Ayrton

From *Nature* 26 January 1911

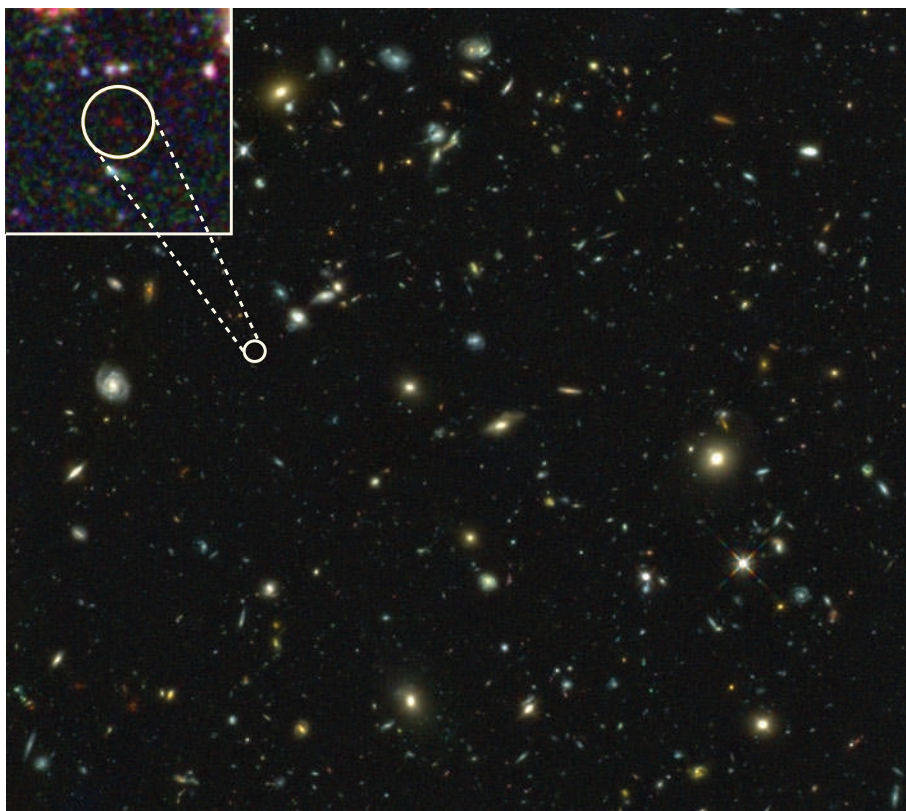


**Figure 1** | A galaxy at redshift 10. Bouwens and colleagues' search<sup>1</sup> for galaxies in the Hubble Ultra Deep Field has resulted in the plausible discovery of the most distant galaxy yet detected. The circle marks the location of the galaxy (red blob in inset).

it depends on complex processes that govern the cooling of gas to form stars, the evolution of the stars themselves, and the feedback of energy and matter from stars and black holes. It is perhaps remarkable, therefore, that at early cosmic times the growth of galaxies seems to mirror that of the dark-matter haloes in which the galaxies reside<sup>4</sup>. This similarity suggests that, despite the seemingly complex physics of star formation, simple gravitational theory — combined with a factor that parametrizes the efficiency of star formation (the fraction of gas that is converted to stars) — can provide a first-order prediction of the luminosity of a galaxy.

Aside from probing the earliest stages of galaxy formation, a topical area of interest in cosmology is to identify the sources responsible for the transition between a neutral state of hydrogen in the Universe (roughly 300,000 years after the Big Bang) to a mostly ionized state at redshift about 6 (950 million years after the Big Bang). Bouwens and colleagues' study<sup>1</sup> probes galaxies at the heart of this 'reionization' epoch. Given some — albeit very uncertain — assumptions of the clumpiness of gas in the Universe and the fraction of ionizing photons that can escape galaxies, they argue that galaxies at redshift 10 may not provide enough ultraviolet flux to reionize the Universe. The dominant contributor to the ionizing flux at early cosmic epochs remains a mystery. Nonetheless, the plausible detection of a galaxy at redshift 10 suggests an onset of

star formation at redshift beyond 12 (about 100 million years earlier), potentially increasing the role of galaxies in the early ionization of the Universe.

Although these results<sup>1</sup> provide a glimpse of the earliest stages of galaxy formation, substantial uncertainties remain and more work is needed. Sample variance remains the dominant uncertainty, as a result of the small number of objects and the small field of view surveyed (equivalent to an area of about 0.6% the size of the Moon). Even more crucial, however, is the need to confirm the redshifts of these objects. The best confirmation of distance would be the detection of a strong emission line in the spectrum, such as the Lyman- $\alpha$  line. Detecting this line may be challenging for these 'primordial' galaxies because they are expected to be gas-rich (having not had enough time to convert a significant fraction of their gas into stars) and to be surrounded by a mostly neutral medium that resonantly scatters Lyman- $\alpha$  photons.

The best hope is the James Webb Space Telescope (JWST). With its larger mirror and near-infrared-sensitive detectors, this facility will dramatically improve the situation: imaging and spectroscopy across a larger swathe of the spectrum will enable the confirmation of a spectral break or the detection of a strong emission line. Scheduled for launch in 2014, the JWST will also have the sensitivity to detect galaxies at redshift 10 that are even fainter than the one reported by Bouwens and

NASA/ESA/G. ILLINGWORTH (UCO/LICK OBS. & UNIV. CALIFORNIA, SANTA CRUZ)/  
R. BOUWENS (UCO/LICK OBS. & LEIDEN UNIV.)/HUDF09 TEAM

collaborators. Studying this faint population will yield a more complete picture of their role in reionizing the Universe. The authors' preliminary foray in studying the first galaxies underscores the important role of facilities such as the JWST in revolutionizing our understanding of galaxy formation at the earliest cosmic epochs, and paves the way for a bright future in studying faint and distant galaxies. ■

**Naveen A. Reddy** is at the National Optical Astronomy Observatory, Tucson, Arizona 85719, USA.  
e-mail: nar@noao.edu

1. Bouwens, R. J. *et al.* *Nature* **469**, 504–507 (2011).
2. Kimble, R. A. *et al.* *Proc. SPIE* **7010**, 1–12 (2008).
3. Steidel, C. C. & Hamilton, D. *Astron. J.* **104**, 941–949 (1992).
4. Bouwens, R. J. *et al.* *Astrophys. J.* **686**, 230–250 (2008).

## ZOOLOGY

# Why are whales big?

**Different groups of diving vertebrates vary greatly in size, with whales being by far the largest. A comparative investigation of the links between swimming speed, size and metabolism provides clues to the reasons.**

GRAEME D. RUXTON

**A**nimals that breathe air but forage under water are highly adapted to the challenges of their extreme lifestyle. The oxygen collected at the surface must be husbanded carefully under water to maximize foraging efficiency. Because the energetic cost of swimming increases rapidly with speed, such divers have long been predicted to ascend and descend at the speed that minimizes the energetic cost (and thus the oxygen burned in aerobic metabolism) for the distance travelled.

In a paper in *Journal of Animal Ecology*, Watanabe *et al.*<sup>1</sup> present the strongest evidence yet in support of such fine-tuned adaptation. Key to their study is the consideration of how we might expect both size and metabolic rate to influence a diver's swimming speed. On the basis of established biomechanical and energetic principles<sup>2</sup>, the authors predicted that larger divers should swim faster (specifically, that swimming speed should increase with mass to the power 0.05). They also predicted that low-metabolism ectotherms (animals, such as turtles, whose temperature is strongly influenced by their environment) should swim more slowly than same-sized, high-metabolism endotherms (which maintain a constant temperature; for example, birds and mammals).

Telemetry studies of free-living animals are becoming increasingly common, making it possible for the researchers<sup>1</sup> to assemble dive-speed data for 37 species encompassing mammals, birds and turtles, and ranging in size from a 500-gram rhinoceros auklet (*Cerorhinca monocerata*) to a 90-tonne blue whale (*Balaenoptera musculus*). They found that dive speed does indeed increase with size, and that the mass exponent of the increase (mean 0.09, 95% confidence interval 0.04–0.14) provided a good match to their

theoretical predictions. They also found that the three turtle species in the data set all had slower swimming speeds than expected on the basis of their mass: just as the authors' theory predicted for ectotherms.

Although fish are the oldest and most diverse group of diving organisms, they do not reach the gigantic size attained by some other marine divers. The largest-known extant fish is the 6-metre-long whale shark (*Rhincodon typus*) and the largest extinct fish the 9-metre-long *Leedsichthys*<sup>3</sup>. Compare these species with the two groups of whales: baleen and toothed. Among the 15 extant baleen whales, only the pygmy right whale (*Caperea marginata*) is as small as the whale shark, and only this species and the common minke (*Balaenoptera acutorostrata*) are smaller than *Leedsichthys*. Among the toothed whales, meanwhile, there are at least five species larger than any extant fish. Turning to extinct marine reptiles<sup>4</sup>, mosasaurs ranged up to 17 m in length, plesiosaurs and plesiosaurs were at least 15 m and 20 m, respectively, and ichthyosaurs were perhaps as large as 21 m.

From these figures, then, explanation is required for the different maximum sizes of the three groups: ectotherms that draw their oxygen from the water (fish); air-breathing endothermic divers (whales); and air-breathing ectothermic divers, both extant and extinct (turtles and species such as mosasaurs). That explanation might run as follows. First, larger divers can stay submerged for longer because oxygen stores increase more rapidly with size than do metabolic rate or the cost of swimming<sup>5</sup>. Second, as Watanabe *et al.*<sup>1</sup> demonstrate, larger divers swim faster.

Taken together, these considerations mean that larger breath-holding divers can exploit deeper waters and search for food more efficiently. However, these selection pressures do not act on fish size. The effect of size on

swimming speed is less drastic in modern-day turtles, probably because their ectothermic metabolism constrains swimming speed. Thus the prediction is that ectothermic breath-holding divers should still face selection for large size, but that this selection will not be as strong as in endotherms such as whales. In agreement with this prediction, the largest extinct marine reptiles were larger than any fish, but not as large as the biggest whales.

This is a thought-provoking study<sup>1</sup>, and there are clear ways in which it could be built upon. Further data on diving ectotherms would be helpful, along with development of the theory to give quantitative predictions for the influence of metabolism. Particularly valuable data would be those that allowed assessment of variation in both resting metabolic rate and dive speed in a given species of turtle across waters of different temperatures (and thus functioning across a range of metabolic rates).

Perhaps the least satisfying aspect of the current theory is that it cannot explain the trend in the empirical data for avian divers to swim faster than mammals of the same mass. Watanabe *et al.*<sup>1</sup> suggest that their assumption that metabolism does not increase to cope with thermoregulation in water may be more valid for mammals than birds. Expansion of the species available for the comparative analyses would help in evaluating such theories: the largest bird considered was the 25-kg Emperor penguin (*Aptenodytes forsteri*) and the smallest mammal was the 33-kg Antarctic fur seal (*Arctocephalus gazella*). Measurements of small diving mammals, such as otters, might be particularly instructive for comparison with those of same-sized birds.

A final puzzle is why gigantic species have not evolved in two groups of extant vertebrate divers (birds and turtles). Perhaps the difference between these and the other vertebrate divers is that birds and turtles must return to land to reproduce, and it is this phase of their existence (in which they lack the buoyancy of water to support much of their weight) that limits their sizes.

Clearly, diving animals still pose many fascinating questions. As Watanabe *et al.*<sup>1</sup> show, however, modern data-collection technologies, combined with biomechanical modelling and comparative approaches, can bring the answers closer to our reach. ■

**Graeme D. Ruxton** is in the College of Medical, Veterinary and Life Sciences, University of Glasgow, Glasgow G12 8QQ, UK.  
e-mail: graeme.ruxton@glasgow.ac.uk

1. Watanabe, Y. Y. *et al.* *J. Anim. Ecol.* **80**, 57–68 (2011).
2. Hansen, E. S. & Ricklefs, R. E. *Am. Nat.* **163**, 358–374 (2004).
3. Friedman, M. *et al.* *Science* **327**, 990–993 (2010).
4. Nicholls, E. L. & Manabe, M. *J. Vert. Paleontol.* **24**, 838–849 (2004).
5. Halsey, L. G., Butler, P. J. & Blackburn, T. M. *Am. Nat.* **167**, 276–287 (2006).

# The challenge of new drug discovery for tuberculosis

Anil Koul<sup>1</sup>, Eric Arnoult<sup>2</sup>, Nacer Lounis<sup>1</sup>, Jerome Guillemont<sup>2</sup> & Koen Andries<sup>1</sup>

Tuberculosis (TB) is more prevalent in the world today than at any other time in human history. *Mycobacterium tuberculosis*, the pathogen responsible for TB, uses diverse strategies to survive in a variety of host lesions and to evade immune surveillance. A key question is how robust are our approaches to discovering new TB drugs, and what measures could be taken to reduce the long and protracted clinical development of new drugs. The emergence of multi-drug-resistant strains of *M. tuberculosis* makes the discovery of new molecular scaffolds a priority, and the current situation even necessitates the re-engineering and repositioning of some old drug families to achieve effective control. Whatever the strategy used, success will depend largely on our proper understanding of the complex interactions between the pathogen and its human host. In this review, we discuss innovations in TB drug discovery and evolving strategies to bring newer agents more quickly to patients.

In 1882, Robert Koch identified *Mycobacterium tuberculosis* as the causative agent of TB, but since his discovery the global TB epidemic seems unabated; this year it is anticipated that there will be about 9.8 million new cases, more than in any other year in history<sup>1</sup>. This situation highlights the relative shortcomings of the current treatment strategies for TB and the limited effectiveness of public health systems, particularly in resource-poor countries where the main TB burden lies. The ease with which TB infection spreads (for example, by inhalation of a few droplet nuclei 2–5 µm in diameter containing as few as 1–3 bacilli<sup>2</sup>), has helped to sustain this scourge at current levels. In spite of half a century of anti-TB chemotherapy, one-third of the world's population asymptomatically still harbour a dormant or latent form of *M. tuberculosis* with a lifelong risk of disease reactivation (Fig. 1). Reactivation of latent TB, even after decades of subclinical persistence, is a high risk factor for

disease development particularly in immunocompromised individuals such as those co-infected with human immunodeficiency virus (HIV), on an anti-tumour necrosis factor therapy or with diabetes<sup>3</sup> (Box 1). In recent years, the TB epidemic has been further fuelled by the emergence

## BOX 1

### Drug resistant TB and mycobacterial latency

Treatment of drug-susceptible (DS)-TB involves an initial phase of isoniazid, a rifamycin, pyrazinamide and ethambutol for the first 2 months followed by a continuation phase of isoniazid and a rifamycin for the last 4 months. Up to 95% of people with DS-TB can be cured in 6 months with this four-drug regimen.

MDR-TB is resistant to at least isoniazid and rifampicin, the two most important first-line drugs used in the treatment of TB. This may result from either primary infection with drug-resistant bacteria or may develop in the course of a patient's treatment when non-optimal treatment durations or regimens are used. Cure rates for MDR-TB are lower, typically ranging from 50% to 70%.

XDR-TB is resistant to isoniazid and rifampicin as well as any fluoroquinolone and any of the second-line anti-TB injectable drugs (amikacin, kanamycin or capreomycin). It has very high mortality rates.

Latent TB is asymptomatic and not infectious; it arises upon immune restriction of the growth of *M. tuberculosis* in hosts. Approximately 5% (higher risk if immunosuppressed; for example, with HIV) of these patients will go on to develop active disease at some stage in life. The term dormancy is used to describe latent TB disease as well as a metabolic state of non-replicative TB bacterium. Of several environmental stresses encountered by the TB bacterium in host cells, hypoxia has been shown to induce non-replicative bacterial phenotypes, leading to tolerance towards certain drugs like cell-wall inhibitors such as isoniazid; and lack of potent drug activity on these bacterial phenotypes may be responsible for prolonging the TB treatment duration<sup>74</sup>.

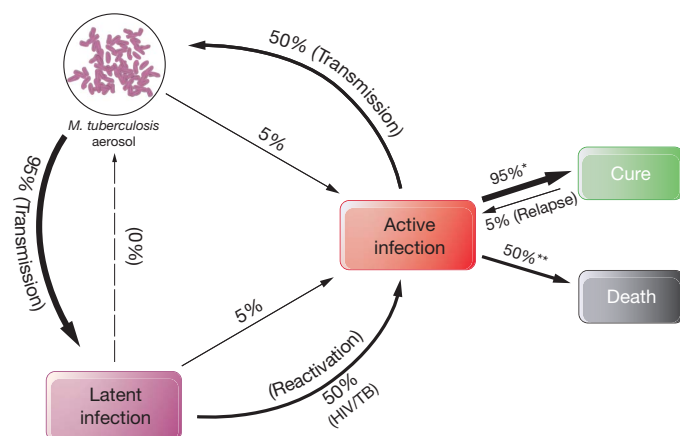


**Figure 1 | Stages of *M. tuberculosis* infection.** *M. tuberculosis* aerosol transmission and progression to infectious TB or non-infectious (latent) disease. A sizeable pool of latently infected people may relapse into active TB, years after their first exposure to the bacterium. Latent TB is commonly activated by immune suppression, as in the case of HIV. In cases of drug-susceptible (DS)-TB (denoted by an asterisk), 95% of patients recover upon treatment, whereas 5% relapse. If untreated (denoted by two asterisks), high mortality results.

<sup>1</sup>Department of Antimicrobial Research, Janssen Research and Development, Johnson & Johnson, Turnhoutseweg 30, B-2340 Beerse, Belgium. <sup>2</sup>Department of Antimicrobial Research, Janssen Research and Development, Johnson & Johnson, Val de Reuil 27106, Cedex, France.

of multi- and extensively-drug-resistant (MDR-TB and XDR-TB) strains and dwindling treatment options that are decades old. The last drug with a new mechanism of action approved for TB was rifampicin (discovered in 1963). Further complicating the situation are drug–drug interactions that preclude the co-administration of some available TB drugs with certain anti-HIV treatments or other chronic disease medications, such as those used in diabetics.

To achieve global control of this epidemic, there is an urgent need for new TB drugs, which can: (1) shorten treatment duration; (2) target MDR or XDR strains; (3) simplify treatment by reducing the daily pill burden; (4) lower dosing frequency (for example, a once-weekly regimen); and (5) be co-administered with HIV medications (Table 1). The challenge of meeting the expectations of this desired target product profile complicates drug discovery efforts. Considering how few drugs from the discovery stage successfully enter the TB clinical pipeline, an increased understanding of the drug discovery hurdles should facilitate development of novel intervention strategies. The situation is further hampered by the unfavourable economics of TB drug development and the lack of proper policy incentives. In this review, we present our perspective on how to refocus discovery and development efforts and identify the underlying knowledge gaps and scientific obstacles in TB drug development. Finally, we highlight some emerging chemical scaffolds, which will hopefully fuel the TB clinical pipeline.

## Emerging challenges in TB treatment

The world's two most populous countries, India and China, account for more than 50% of the world's MDR-TB cases and as such these countries are encountering a high and increasing TB disease burden<sup>4</sup>. The sheer size of their TB case populations results in the highest estimated numbers of MDR-TB cases (about 100,000 each) emerging annually from these two countries. Moreover, the emergence of XDR strains of *M. tuberculosis* (5.4% of MDR-TB cases are found to be XDR-TB<sup>4</sup>) is challenging TB treatment programmes in several other countries and even raises the possibility of a return to a situation akin to the pre-antibiotic TB era. At present, MDR-TB is treated by a combination of eight to ten drugs with therapies lasting up to 18–24 months; only four of these drugs were actually developed to treat TB<sup>5</sup>. Such suboptimal therapy leads to almost 30% of MDR-TB patients experiencing treatment failure<sup>6</sup>. The treatment options for XDR-TB are very limited as XDR-TB bacilli are resistant not only to isoniazid and rifampicin, but also to fluoroquinolones and injectables such as aminoglycosides. In addition, there are serious side effects with most MDR-TB and XDR-TB drugs, including nephrotoxicity and ototoxicity with aminoglycosides, hepatotoxicity with ethionamide and dysglycaemia with gatifloxacin<sup>7</sup>. Thus, the current situation necessitates

the immediate identification of new scaffolds that can address emerging resistance and also demands the conduct of appropriate clinical trials as historically very few clinical studies have been performed to evaluate the efficacy of drugs in MDR-TB or XDR-TB patient groups. Improving the diagnostics with wider coverage of drug susceptibility testing will also help to address the high mortality of MDR/XDR-TB and curb the emergence of resistance.

TB accounts for about one in four of the deaths that occur among HIV-positive people<sup>8</sup>. Of the 9.4 million TB cases in 2009, 11–13% were HIV positive with approximately 80% of these co-infections confined to the African region<sup>8</sup>. The frequent co-infection of TB in HIV patients further complicates the selection of an appropriate treatment regimen because: (1) increased pill burden diminishes compliance; (2) drug–drug interactions lead to sub-therapeutic concentrations of antiretrovirals; and (3) overlapping toxic side effects increase safety concerns. The main interaction between HIV and TB anti-infectives is rifampicin-induced increased expression of the hepatic cytochrome (CYP) P450 oxidase system<sup>9</sup>. This CYP induction results in increased metabolism and decreased therapeutic concentrations of many co-medications such as HIV protease inhibitors<sup>10</sup>. Even in the presence of CYP450 inhibitors such as ritonavir, normal trough levels of various classes of protease inhibitors cannot be rescued and consequently, standard protease inhibitor regimens, whether boosted or not, cannot be given with rifampicin. The only treatments for HIV-infected TB patients with minimal drug–drug interactions are non-nucleoside-reverse-transcriptase-inhibitor (NNRTI) containing regimens. However, there are fewer options for patients with NNRTI-resistant mutations and therefore new chemistry approaches are being used to identify new rifamycins, such as rifabutin, with reduced CYP-induction properties<sup>7</sup>. However, the presence of ritonavir in the protease cocktail increases the serum concentration of rifabutin, thereby increasing its accompanying toxicity<sup>11</sup>.

To discover newer rifamycin analogues with minimal interaction with HIV and other co-medications, the upfront screening of newer molecules in a CYP profiling (pregnane-X receptor) assay can be performed<sup>12</sup>. This receptor drives transcription of CYP genes and can identify chemical analogues with minimal interactions with drug metabolizing enzymes like CYP450. Further, availability of co-crystal structures of rifampicin with bacterial RNA polymerase<sup>13</sup> can help to design molecules with better drug-resistance profiles. In HIV patients harbouring MDR- or XDR-TB strains, drug–drug interaction studies are not well established, as most of these second-line TB drugs (for example, ethionamide, cycloserine, kanamycin, amikacin, capreomycin and para-amino salicylate) were discovered several decades ago<sup>14</sup>. Thus, there is a clear need for new studies to investigate the interaction of antiretrovirals with second-line TB drugs and with those currently in clinical development.

Confounding these issues is the association of TB with other chronic diseases such as diabetes, which is known to increase the risk of developing active TB by threefold<sup>1</sup>. The biological rationale for the slower response of diabetics to anti-TB drugs and for their increased risk of developing MDR-TB is poorly understood, although it is well known that cell-mediated immunity is suppressed in diabetes, which could explain higher TB rates. Attainment of bacterial culture negativity, relapse rates and mortality are significantly higher in diabetic TB patients<sup>15</sup> so we need to identify new TB molecules that are strongly bactericidal and have minimal drug–drug interactions with oral anti-diabetic drugs<sup>16</sup>. Further, diabetics tend to be heavier and more obese, which may in part lead to lower TB drug exposure<sup>17</sup>. Where there is a poor response to TB treatment in diabetic patients, therapeutic drug monitoring may be useful in TB management.

## Identifying new chemical scaffolds

The poor efficiency of identifying new TB drugs by screening pharmaceutical library collections has been linked to the limited chemical diversity within these collections<sup>18</sup>. Additionally, most TB drugs and antibacterials in general do not follow Lipinski's 'rule of 5', which defines the optimal drug-like features; whereas pharmaceutical compound collections are biased towards these properties<sup>19</sup>. In spite of these challenges,

**Table 1 | Desired target product profile for a new TB drug**

Desired target product profile	Biological characteristics
Treat MDR-TB and XDR-TB	New chemical class with a new mechanism of action Existing chemical class covering resistant isolates Drugs with low toxicity issues, like hepatotoxicity
Shorten treatment duration	Strongly bactericidal activity Good activity on latent or dormant or heterogeneous populations More potent and safer regimens of a novel drug and its combinations
Lower dosing frequency	Good pharmacokinetics including longer half-life and target tissue levels Retain potency when administered intermittently (for example, 1–3 times a week)
Reducing pill burden	Novel fixed-dose formulations and delivery technologies Combinations of more efficacious drugs to reduce number of pills taken Child-friendly formulation of newer drugs
Drug–drug interactions	No cytochrome P450 induction liabilities Minimal drug–drug induction particularly with antiretrovirals or oral diabetics

Each target product profile feature is accompanied by the biological characteristics needed to accomplish that respective feature.

the current TB pipeline (Fig. 2) is slowly expanding, although it is inadequate for the development of a completely novel regimen. A key question is: how to search for new TB drugs and where to look for them?

### Novelty in screening

Advances in the identification of new TB drug targets have been driven largely by the availability of the genome sequence of *M. tuberculosis*<sup>20</sup>, but unfortunately this approach has yet to lead to the identification of new drug candidates. Genome-derived, target-based approaches have had little success in the antibacterial therapeutic area in general<sup>18</sup>. The essentiality of a target for replication may be a prerequisite but it does not ensure its druggability; for many essential targets we are unable to identify specific inhibitors with drug-like properties. For example, several high-throughput screening campaigns for identifying inhibitors of isocitrate lyases, which are key glyoxylate-shunt-pathway enzymes found to be essential for mycobacterial intracellular growth and their long-term persistence in mice, were discontinued owing to lack of druggability of these targets<sup>21</sup>. Second, we have often failed to understand how to convert good bacterial enzyme inhibitors into a compound that can easily penetrate the highly impermeable bacterial cell wall. Without proper understanding of the entry mechanisms of antibiotics across bacterial cell walls, any medicinal chemistry approach to engineer (via chemical modifications) a 'permeability property' into an enzymatic inhibitor has proven to be quite challenging.

Over time, it has emerged that shifting the screening strategy from single-enzyme targets to phenotypic screens at a whole bacterial cell level is a much more successful strategy<sup>18</sup>. Such a strategy recognizes the potential holistic interactions of a drug target(s) with one or more components in a bacterial cell and defines its essentiality in a more relevant physiological space. One of the drawbacks of the whole-cell-screening approach is that upfront knowledge regarding the mechanism of action remains largely lacking, thereby preventing any input from structural biology into medicinal chemistry efforts around drug design. Another

challenge of whole-cell screening is to identify the right *in vitro* growth conditions that are relevant for *in vivo* infections, as certain metabolic targets behave differently depending on the composition of the growth medium<sup>22</sup>. Whole-cell screening can deliver many hits, but several of these may work via non-specific mechanisms (such as detergent effects) and have cytotoxic effects. As such, the key in a whole-cell-screening campaign is to identify the 'quality hits' by certain counter-screening assays (for example, cytotoxicity across several cell lines, monitoring non-specific membrane leakage, analysing red-blood-cell haemolysis), so as to account for good selectivity and specificity.

The recent success with the whole-cell-screening approach is particularly exemplified by the identification of new TB drug candidates such as diarylquinolines (TMC207), which target ATP synthesis, and benzothiazines (BTZ043), which target essential cell-wall arabinan synthesis<sup>23–25</sup>. An interesting feature of both these molecules is that they target membrane-associated proteins that may be more easily accessible to drugs from the periplasmic space (that is, the target binding sites are exposed to the periplasm) and this to some extent may overcome certain issues of mycobacterial membrane permeability.

Interestingly, more refined multi-target 'pathway' screens can be initiated to search for inhibitors blocking validated metabolic or signalling pathways. In this regard, respiratory membrane vesicles of *M. tuberculosis*, which have been grown in a variety of conditions in order to simulate the host microenvironment, can be used to screen drug classes or analogues inhibiting respiratory chain components (Fig. 3). For example, such a pathway screen could monitor a drug's influence on diverse mycobacterial respiratory chain functions such as ATP synthesis, redox homeostasis and proton gradients<sup>26</sup>. Modulating external growth stimuli, such as the carbon source, micronutrients, or oxygen levels in such an assay, results in target respiratory proteomes that can be used to screen against functions essential during those metabolic states. For instance, ATP synthase is highly downregulated during hypoxic conditions, and its inhibition by TMC207 indicates an essential role of ATP synthesis in the generation of

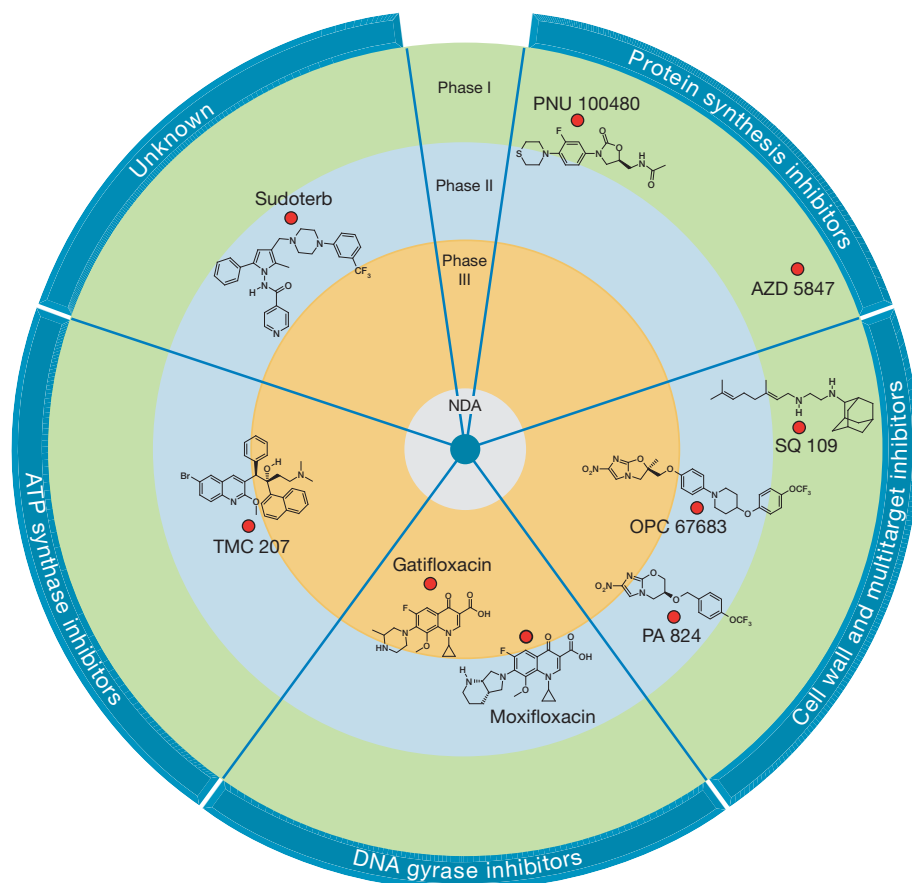


**Figure 2 | A bull's-eye representation of the current clinical pipeline for TB.** Each drug candidate is shown with its current clinical phase of development along with the target family. TMC207 is in phase IIb trials for MDR-TB and in phase IIa trials for DS-TB. The structure of AZD-5847 has not been disclosed. NDA, new drug application (for regulatory approval).

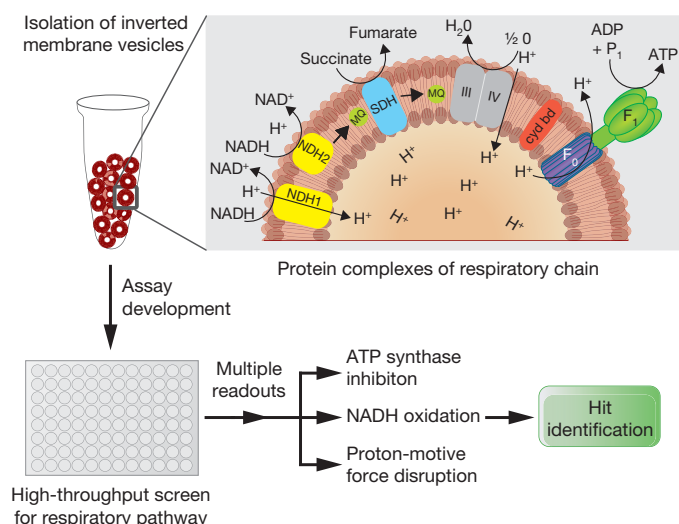


**Figure 3 | Screening for mycobacterial respiratory pathway inhibitors.** Schematic flowchart of a multiple-target screen for the identification of hits targeting the mycobacterial respiratory pathway. Enriched pharmaceutical compound libraries, or compound family analogues, can be used to screen inverted membrane vesicles for inhibition of NADH dehydrogenase, ATP synthase, or other targets impairing electron flow or proton-motive force. The enlargement shows the graphic view of the mycobacterial respiratory chain proteins with menaquinone (MQ) being reduced by NADH dehydrogenase or succinate dehydrogenase (SDH) and oxidized by a supercomplex consisting of complex III and IV (cytochrome *bc*<sub>1</sub> and *aa*<sub>3</sub>)<sup>29</sup>. The transcriptional profiling in infected mice lungs during chronic phase showed downregulation of proton-pumping type-I NADH dehydrogenase (NDH1) and low-affinity *aa*<sub>3</sub>-type cytochrome *c* oxidase, but upregulation of alternative target enzymes such as high-affinity cytochrome *bd* oxidase (*cyd bd*) and non-proton pumping NADH dehydrogenase (NDH2), which can serve as effective targets for latent or persistent infections<sup>68</sup>. Small molecules such as antipsychotic phenothiazine and diarylquinolines (for example, TMC207) have been shown to target NDH2 (ref. 69) and the transmembrane subunit-*c* of ATP synthase<sup>24</sup>, respectively, with potent antimycobacterial activity on actively metabolizing and non-growing cells.

energy in the dormant bacteria, which may explain the potent *in vivo* sterilizing effect of the drug<sup>27</sup>. Dormant *M. tuberculosis* seems to be exceptionally susceptible to inhibition of respiratory chain processes such as ATP synthesis or interference with the cellular redox state<sup>28</sup>, but it still remains to be determined if such inhibition leads to potent sterilization in human lesions with varied microenvironments. Because most TB drugs

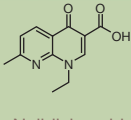
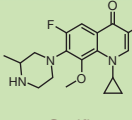
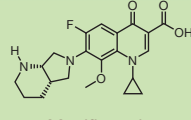
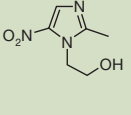
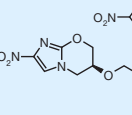
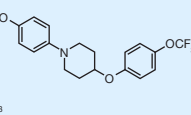
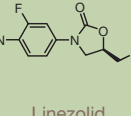
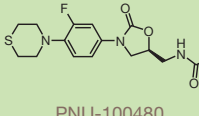
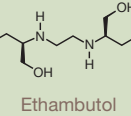
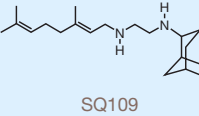
are less efficient in killing slowly replicating or dormant bacilli in the chronic phase of TB infection, a key challenge for identifying sterilizing drugs is to translate information about the chronic state mycobacterial metabolome and proteome adaptations into drug discovery screening platforms. This strategy will not only facilitate development of proper drug discovery tools that might eventually lead to a faster cure, but may also help us to understand the life cycle of mycobacteria in their host (for example, their switch to anaerobic metabolism<sup>29</sup>).

### Engineering existing scaffolds

Many new antibiotic candidates are chemical molecules reengineered from old drug classes discovered decades ago<sup>30</sup>. This approach has identified new TB drugs from existing antibacterial drug classes and either involved the redesign of accessible scaffolds to improve their antimycobacterial potencies or, more directly, the repositioning of known antibacterial drugs with good antimycobacterial activity for testing in TB clinical trials (Fig. 4). During re-engineering of known scaffolds, chemical modifications are introduced into the core structure that may lead to improved bactericidal activities, better resistance profiles, safety, tolerability or superior pharmacokinetic/pharmacodynamic properties.

The modified versions of the oxazolidinones (such as linezolid, a marketed product from this class with activity against Gram-positive infections) have led to new structures such as PNU-100480 and AZD-5847 with better activity against *M. tuberculosis*<sup>31</sup>. These oxazolidinone TB candidates, currently in phase I studies, must address in their clinical development plan the known toxicity issues of linezolid, namely inhibition of mitochondrial protein synthesis, thrombocytopenia and myelosuppression, which has been observed in patients treated for longer than the recommended 14 days<sup>32</sup>. Because TB treatment can take months, safety is of paramount importance with any new tailored oxazolidinone and it will be important to monitor for bone marrow toxicity early in clinical trials. The good human pharmacokinetic profile of linezolid (for example, excellent oral bioavailability, low CYP inhibition and good distribution to lung epithelial lining fluid<sup>33</sup>) raises the hope that this drug class can penetrate the difficult to reach thick-walled lung cavities and lesions where TB bacilli normally hide.

Nitroimidazoles, traditionally used to treat anaerobic bacteria and parasitic infections, represent another established scaffold for which synthetic modifications have been introduced to increase their antimycobacterial potential. An interesting feature of nitroimidazoles relates to their unique mechanism of action, mimicking host defence strategies by producing microbicidal molecules, such as nitric oxide and other reactive

Antibiotic class	Parent scaffold	Derivatized scaffolds
Fluoro-quinolones	 Nalidixic acid	 Gatifloxacin  Moxifloxacin
Nitroimidazoles	 Metronidazole	 PA-824  OPC-67683
Oxazolidinones	 Linezolid	 PNU-100480
1,2-ethylene diamine	 Ethambutol	 SQ109

**Figure 4 | Remodelling the existing antibacterial drug classes.** Chemical tailoring of existing drugs or drug classes has led to the identification of new molecules with potent antimycobacterial activities. The oxazolidinones also include the recently discovered AZD-5847, the structure of which has not been disclosed yet and is therefore not listed here. SQ109, an orally active cell-wall-targeting diamine antibiotic, identified via combinatorial chemistry approaches, is currently being tested in humans.

nitrogen intermediates, which damage multiple targets including respiratory chain cytochrome oxidases<sup>34</sup>. The target specificity of such a mechanism of action is achieved through bioactivation of these prodrugs by flavin-dependent nitroreductases, which are absent in mammalian cells but present in *M. tuberculosis*<sup>35</sup>. Two candidates from this class, PA-824 and OPC-67683, are currently in clinical studies and may potentially shorten treatment duration as this mechanism of action is operational even in hypoxic induced dormant mycobacteria<sup>34</sup> (that are not killed by drugs such as isoniazid). This indicates that in spite of general transcriptional downregulation during mycobacterial dormancy, these nitroreductases are still sufficiently expressed.

For many years, the lack of activity of the natural or semi-synthetic  $\beta$ -lactams against TB was thought to be due to their poor penetration into the organism, with  $\beta$ -lactamase-mediated resistance only a minor confounding factor<sup>36</sup>. However, a recent genetic knockout of *blaC*, encoding the extended-spectrum Ambler class A  $\beta$ -lactamase from *M. tuberculosis*, showed improved sensitivity to  $\beta$ -lactams, particularly carbapenems<sup>37</sup>. By combining a second-generation carbapenem (meropenem) with a  $\beta$ -lactamase inhibitor (clavulanic acid), good *in vitro* bactericidal activity on replicating, non-replicating and resistant clinical isolates of *M. tuberculosis* was obtained<sup>37</sup>. Availability of structural and mechanistic knowledge around BlaC will help researchers design potent and *M. tuberculosis*-specific inhibitors to be used in combination with classical  $\beta$ -lactam antibiotics. At the same time, a newer generation of broad-spectrum  $\beta$ -lactamase inhibitors (for example, current clinical candidates such as NXL104 (ref. 38)) should be explored for mycobacterial BlaC inhibition. Concurrently, medicinal chemistry approaches to improve the antimycobacterial activity of  $\beta$ -lactams, their tissue distribution and oral bioavailability, will be necessary as current drugs such as meropenem require parenteral administration<sup>37</sup>, thereby limiting their use in more serious MDR/XDR-TB cases.

Although incremental improvements of existing scaffolds is a good strategy to fill a drug development pipeline, the increasing resistance to some of these existing drug classes, such as the fluoroquinolones<sup>39</sup>, indicates that discovery of new chemical scaffolds is a more attractive approach. To facilitate the identification of new chemical scaffolds, a proper understanding of the physicochemical features of the existing TB drugs and analysis of their chemical space is desirable.

### The physicochemical space of TB drugs

Antibacterial drugs in general occupy a unique physicochemical space that is markedly different from the space occupied by drugs in other therapeutic areas<sup>40</sup>. Specific physicochemical features in antibiotic drug classes are required because of the unique architecture of bacterial cell walls (especially in Gram negatives), which affects the permeability of drug molecules across these membranes. Antibacterial drugs are unique in a number of physicochemical properties, such as lower lipophilicities, higher molecular weights and increased total polar surface areas when compared to drugs for human host targets<sup>40</sup>. It has been proposed that screening libraries for antibacterial targets should have more polar characteristics to achieve penetration through certain bacterial cell walls<sup>40</sup>.

We studied 14 different physicochemical features, including molecular weight, lipophilicity and polar surface area of first- and second-line TB drugs, and compared these properties to known marketed non-antibacterial compounds (1,663) identified from the Prous Integrity database (<http://integrity.prous.com>) (details in Fig. 5). A mathematical tool called principal component analysis (PCA) was used to study the relationships between various physicochemical properties<sup>41</sup> and to identify regions of physicochemical space required to achieve antimycobacterial activity. A two-dimensional graph indicates that TB drugs actually occupy a broad chemical space and do not fall into any defined chemical area. As expected, natural-product-based molecules such as rifamycins and aminoglycosides occupy a peripheral region of the plotted area, whereas fluoroquinolones, having more 'drug-like' features, are located among the drug bulk (Fig. 5). With no defined optimal physicochemical space for TB drugs, chemistry for the discovery of new scaffolds should

be less restricted and more diverse. At the same time, the wide scatter within the PCA plot may reflect to some extent the fact that most TB drugs were discovered several decades ago without much consideration of optimal physicochemical and other drug-like features.

Although antibacterial agents are generally quite polar, water-soluble molecules, the question is whether TB medicinal chemistry should try to engineer the physicochemical characteristics of newer molecules or screening libraries towards a common parameter such as polarity. In light of this question it is worth considering that TMC207, even with its lipophilic nature (logD at pH 6.0 is 5.14), has potent bactericidal activities. Therefore, biasing our library screens towards compounds with a particular physicochemical parameter could actually be detrimental and decrease the diversity of our screening campaigns and chemistry. Nevertheless, a detailed understanding of the influence of polarity on drug penetration into the highly impermeable mycobacterium cell wall (for example, *Mycobacterium smegmatis* is about 20 times less permeable than *Escherichia coli*<sup>42</sup>) may guide us to improved permeability. An important question is how the unique mycobacterial membrane architecture, with its high lipid content, influences drug uptake and efflux compared to the cell walls of other Gram-positive and Gram-negative bacteria.

### Targeting host–pathogen signalling pathways

Subversion of host-cell signalling pathways is one of the strategies used by pathogenic mycobacteria to survive long term in host cells<sup>43</sup>. As such, targeting the key signalling molecules, either bacterial- or host-derived, may lead to new antimycobacterial therapies.

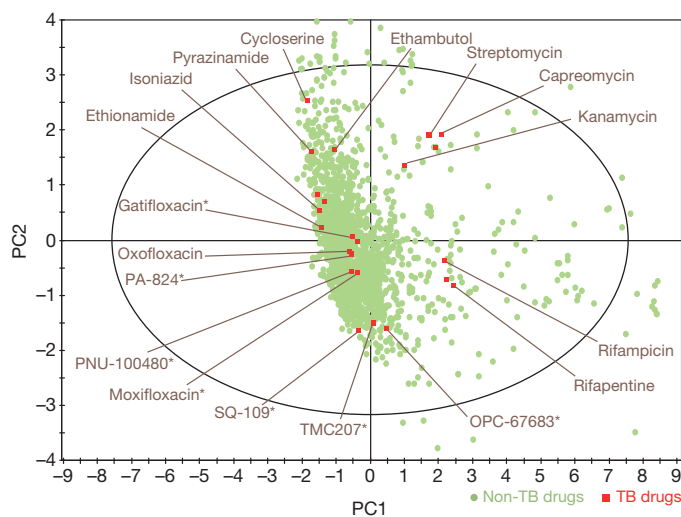


**Figure 5 | Two-dimensional representation of chemical space of the anti-TB drugs.** To understand the physicochemical space occupied by TB compounds, we studied 14 different physicochemical features of TB drugs and compared these properties to 1,663 marketed non-antibacterial unique compounds identified from the Prous Integrity database. The physicochemical parameters calculated using the Molecular Operating Environment software (MOE)<sup>70</sup> were: log of the octanol/water partition coefficient (lipophilicity evaluated by SlogP), molecular weight, number of hydrogen bond donors and hydrogen bond acceptors, number of rotatable bonds, topological polar surface area, solubility, atomic polarizabilities, absolute atomic polarizabilities, connectivity topological index, density, radius, petitjean (diameter – radius)/diameter and molecular refractivity. A PCA analysis, a mathematical procedure that transforms a number of (possibly) correlated variables into a number of uncorrelated variables called principal components, was done using a software program (SIMCA-P+ 12; Umetrics)<sup>71</sup>. A PCA analysis was carried out using the 14 calculated properties mentioned earlier and variation in the properties between the compounds is mapped onto two axes, principal components PC1 and PC2, which contain most of the variance (in this case 70% for PC1 and PC2 combined). The axes are linear combinations of the original 14 properties and each data point in the two-dimensional graph corresponds to one compound. The complete graph shows the chemical space occupied by the different compounds. This figure indicates that TB drugs are widely distributed within the chemical space.

On the basis of the knowledge that *M. tuberculosis* has 11 serine/threonine kinases and several other ATP- (or GTP-)using enzymes, researchers have screened enriched kinase libraries for inhibition of mycobacterial growth *in vitro* or in macrophages, with limited success<sup>44</sup>. However, a recent kinase library screen in *E. coli* led to the identification of a pyridopyrimidine scaffold as a competitive inhibitor of the ATP-binding site of acetyl-coenzyme-A carboxylase<sup>45</sup>. For mycobacteria, the search for kinase inhibitors with potent *in vitro* bactericidal activity has not been successful, although chemical optimization towards the uniquely conserved ATP-binding pockets of protein kinase G did identify a new chemical scaffold, tetra-hydro-benzothiophene (AX20017), but with activity restricted to infected macrophages<sup>46</sup> (Fig. 6). A related concept within bacterial research is to identify inhibitors of bacterial virulence factors or host targets that can modulate pathogen survival inside the infected cells. Recently, it was revealed that the innate immune response within macrophages can be modulated by specifically inhibiting the mycobacterial tyrosine phosphatase (mptpB), which blocks host ERK1/2 and P38 signalling and promotes intramacrophage survival of mycobacteria<sup>47</sup> (Fig. 6). At the same time, genome-wide RNA interference screening has identified key host kinase networks and an autophagic/xenophagic machinery that is severely inhibited on mycobacterial infection<sup>48</sup>. This research showed that pharmacological activation of the xenophagic pathway in infected macrophages by certain drugs led to the killing of intracellular mycobacteria. However, in the absence of any *in vivo* validation and also any extracellular bactericidal activity, such drugs, if proven to be clinically efficacious, would probably be used in an adjunctive therapy along with a direct antibacterial agent. It is not known if the intracellular dwelling of mycobacteria contributes to its prolonged treatment duration and whether strategies targeting host-cell factors will lead to better bactericidal activity and shorter treatment time in patients.

### In vivo screens and preclinical validation

Animal models that mimic various metabolic stages of human infection have proven to be extremely important for TB drug discovery as some

functions deemed to be essential *in vitro* (such as mycobacterial glycolysis) are not essential *in vivo*<sup>49</sup>. However, no animal model is perfect as each model only incompletely reproduces different aspects of human disease. The mouse model is considered imperfect because certain elements of human disease pathogenesis such as organized granulomas, caseous necrosis and hypoxia are not replicated<sup>3</sup>. In the absence of these features, the challenging question is whether the mycobacterial metabolic repertoire present in mice is less heterogeneous than in humans? Despite not exactly replicating the host-tissue microenvironment, the mouse model has served as a cost-effective tool to assess the bactericidal and sterilizing potencies of individual drugs and drug combinations<sup>50</sup>.

The mouse model was recently also used to identify bacterial targets that impair or enhance mycobacterial persistence upon treatment with isoniazid<sup>51</sup>. Such an approach illustrates the potential role of mouse model screens for identifying factors responsible for drug tolerance, which could be easily missed in regular *in vitro* screens. At the same time, a key feature of mouse models that is not properly understood is to what extent the route of administration of TB inocula determines the relapse rates upon drug withdrawal<sup>52</sup>. Alternative animals such as guinea pigs, rabbits and even cynomolgus monkeys have been used as preclinical models as they mimic TB disease pathogenesis better than mice with features such as hypoxic lesions and solid necrotic granulomas. Although guinea pigs do not acquire TB naturally, it was the first TB infection model to be used in 1944, when the efficacy of streptomycin was tested in just four animals before treating patients<sup>53</sup>. We still need rigorous studies comparing the bactericidal and sterilizing efficacy of different drug regimens in different animal models infected by different routes of infection, to enhance our ability to predict treatment outcomes in clinical trials and to validate the models themselves. Only after we have shown for several drug classes that animal model studies are congruent with efficacy seen in clinical trials will we achieve confidence in their predictive power.

Advances in imaging technologies that can map, in real time, the response of individual granulomas to drug treatment will facilitate our understanding of TB pathogenesis and may also help in developing better models to assess relapses. Live imaging tools were recently used to reveal the initial events leading to granuloma formation in a zebrafish model upon infection with *Mycobacterium marinum*<sup>54</sup> and, in another instance, the lungs of patients with pulmonary TB were imaged to study the progression of disease after two months of chemotherapy<sup>55</sup>.

### Evolving science of TB clinical development

A challenge in the clinical development of new TB therapies is the lack of specific biomarkers or surrogate endpoints that are sensitive and specific enough to reliably predict success or failure early in the course of treatment. Historically, clinical development of TB drugs has relied heavily on early bactericidal activity (EBA) trials, which measured reduction in bacterial load in the sputum of patients within 2–5 days of treatment<sup>56</sup>. The EBA kinetics of newer TB drugs such as TMC207 do not seem to follow the fast bactericidal activity observed with isoniazid and rifampicin and therefore studies with treatment durations of less than one week may be less informative for experimental agents showing a delayed bactericidal response<sup>57</sup>. Such delayed responses may be due to time-dependent killing, or a killing mechanism that requires depletion of energy reserves, or to physicochemical properties of the drug that delay its distribution to the bacilli in target sites. On the other hand, EBA studies of more than 2 weeks using monotherapy may be considered unethical because of the likelihood of the emergence of resistance.

In the second phase of clinical development, experimental drugs are administered over 8 weeks, on top of a standardized regimen, to estimate the effect of the drug(s) being tested on time to sputum conversion (positive to negative mycobacterial growth in patient sputum samples). In this setting, strong bactericidal activity and safety is a prerequisite for the further extension of therapy to more than 6–12 months for drug-susceptible (DS-)TB and 12–24 months for MDR-TB. A lengthy follow-up period (up to 2 years after the end of treatment) is needed to access the primary clinical endpoint of sterilization as measured by relapse

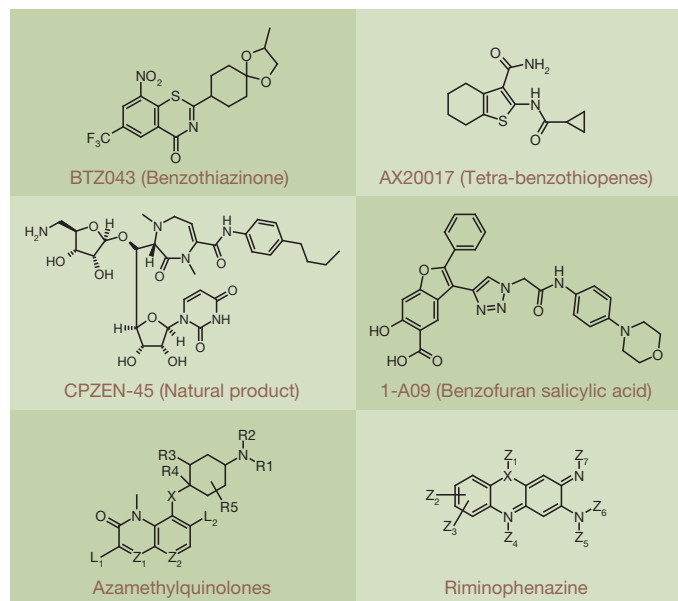


**Figure 6 | Representative underexplored and new chemical scaffolds.** Some of the chemical structures shown are mentioned in the text. CPZEN-45, a streptomycin-derived natural product, is a semi-synthetic nucleoside antibiotic from the caprazamycin family with TB activity<sup>72</sup>. Re-engineering of riminophenazine's chemical scaffold can lead to interesting energy metabolism inhibitors with the potential to kill non-replicating bacilli. Azamethylquinolones have demonstrated activity on mycobacteria and further chemical optimization may lead to interesting lead candidates hopefully with better resistance profiles<sup>73</sup>.

rates. The absence of any other validated surrogate endpoints or biomarkers immensely extends the clinical development timelines and this is preventing any rapid progress in the field and at the same time substantially increasing the costs of running these trials. Sputum conversion to negativity after 2 or 6 months of treatment for DS- or MDR-TB, respectively, may give an early indication of microbiological sterilization<sup>58,59</sup>. Although this sputum conversion rate probably represents the best surrogate marker for estimating the sterilizing efficacy of a regimen, it has been recently observed in mice that bactericidal potency of a regimen does not necessarily predict its sterilizing potency<sup>50</sup> and, as such, culture status after 2 or 6 months of therapy still needs further validation, particularly in diverse patient populations<sup>60</sup>.

One of the factors that might explain the discrepancy between bactericidal and sterilizing activities is the heterogeneous nature of the bacterial population in patients with differential growth rates. Recent clinical trial data confirmed the increased sensitivity of liquid cultures (for example, mycobacteria growth indicator tube) to detect sputum TB bacilli, as compared to solid cultures<sup>61,62</sup>, clearly indicating that even sputum samples may contain different subpopulations of TB bacilli with different growth kinetics. It remains to be seen to what extent cultivation of sputum samples on liquid cultures will allow a more accurate estimation of the sterilizing activity of a regimen.

To accelerate TB drug development and reduce the long clinical development path, research into non-sputum biomarkers, such as bacterial DNA sequences in urine samples or host-derived markers, such as toll-like receptor activation, should be prioritized. The recently identified interferon-inducible blood transcriptional TB signature, which correlates with the extent of disease in active TB and diminishes upon treatment, has great potential as a diagnostic and prognostic tool<sup>63</sup>. This TB signature was also observed in a subset of 10–20% of patients with latent TB and may identify those individuals who will develop active disease, and thereby facilitate targeted preventative therapy. Such biomarkers need further validation to determine if they are sufficiently sensitive and specific to allow monitoring of therapy responses in adults with active TB, or in individuals who are at risk of TB reactivation, or in children with active TB but who often do not excrete mycobacteria in their sputum<sup>60</sup>.

## Drug combination trials and standardization of regimens

At present, the global TB development pipeline has nine candidates, but a key issue is how to develop them concomitantly in combination trials to identify the best regimen in the shortest period of time. In this regard, a recent initiative (Critical Path to New TB Regimens (CPTR)), involving several pharmaceutical companies and nongovernmental organizations, aspires to the development of new regimens of investigational drugs with existing TB drugs or drug candidates to avoid developing each drug sequentially and thereby shortening the development timelines that might otherwise spread over decades<sup>64</sup>. The CPTR approach will undoubtedly lead to improved efficiencies, but only if we can identify drugs that share similar or non-interfering pharmacokinetic features, synergistic or simply additive mechanisms of action, and non-overlapping toxicity profiles. For instance, some TB drugs in clinical development (moxifloxacin) have cardiovascular risks (prolonged QT intervals), and combining them with another drug with a similar liability will raise safety concerns. Even drugs with different mechanisms of action may interact synergistically or antagonistically with each other, and may even induce cross-resistance by common efflux mechanisms.

## Reassessment and time for acceleration

Recent research into the pathogenesis of *M. tuberculosis* has led to the identification of a range of bacterial pathogenic mechanisms that permit it to escape certain host-control measures<sup>65</sup>. To counteract this we need innovative tools including newer drugs, vaccines, and improved diagnostics and biomarkers. The ultimate goal of the TB drug discovery effort is to eradicate both active and latent disease, possibly within a few weeks, like other more common bacterial infections. However, there are tremendous challenges to achieving this goal considering our lack of understanding of

how to target heterogeneous *M. tuberculosis* populations using a single drug or a drug combination. In this regard, it is helpful to consider that TB in humans is a disease of subpopulations, with each population requiring a different drug or therapeutic approach. At the same time, it still remains to be determined to what extent *M. tuberculosis* persists, which are phenotypically and stochastically antibiotic resistant<sup>66</sup>, determine relapse rates following a drug's withdrawal. Any future drug discovery efforts should address the questions of how the goal of shortening the treatment durations can be linked to drug activity on latent or persistent bacterial populations. We still do not know if disrupting their energized membranes or targeting key anaerobic respiratory components such as those involved in energy generation can effectively kill these persisters.

At present, drug treatment developments show some promise owing to a renewed interest from pharmaceutical companies in researching new drugs, coupled with effective support from governmental and non-governmental organizations. The TB vaccine pipeline is also showing progress, with seven vaccine candidates currently in clinical development including candidates being evaluated in paediatric populations<sup>67</sup>. However, we still need more drugs and vaccines to move from discovery into the development pipeline because of the high rate of drug attrition in clinical development and the potential for post-approval failures. Importantly, we also need more drugs from different classes so as to enable the creation of successful drug regimens, and realize the World Health Organization's and United Nations millennium development goal of halting the incidence, prevalence and death rates associated with TB by 2015 and eliminating the disease altogether by 2050<sup>8</sup>. However, any new drug or vaccine for TB will fail to make a significant impact if it is not accompanied by proper support from local healthcare systems. And finally, a key societal and economic challenge will be to ensure the proper access of these drugs or vaccines to the patients most in need in resource-poor countries.

1. Dye, C. & Williams, B. G. The population dynamics and control of tuberculosis. *Science* **328**, 856–861 (2010).
2. Riley, R. L. Aerial dissemination of pulmonary tuberculosis. *Am. Rev. Tuberc.* **76**, 931–941 (1957).
3. Barry, C. E. III et al. The spectrum of latent tuberculosis: rethinking the biology and intervention strategies. *Nature Rev. Microbiol.* **7**, 845–855 (2009).
4. World Health Organization. *Multidrug and Extensive Drug Resistant Tuberculosis: 2010 Global Report on Surveillance and Response* (World Health Organization, 2010).
5. Gandhi, N. R. et al. Multidrug-resistant and extensively drug-resistant tuberculosis: a threat to global control of tuberculosis. *Lancet* **375**, 1830–1843 (2010).
6. Mitnick, C. et al. Community-based therapy for multidrug-resistant tuberculosis in Lima, Peru. *N. Engl. J. Med.* **348**, 119–128 (2003).
7. Ma, Z., Lienhardt, C., McIlleron, H., Nunn, A. J. & Wang, X. Global tuberculosis drug development pipeline: the need and the reality. *Lancet* **375**, 2100–2109 (2010).
8. World Health Organization. *The Global Plan to Stop TB 2011–2015: Transforming the Fight Towards Elimination of Tuberculosis* (World Health Organization, 2010).
9. Niemi, M., Backman, J. T., Fromm, M. F., Neuvonen, P. J. & Kivisto, K. T. Pharmacokinetic interactions with rifampicin: clinical relevance. *Clin. Pharmacokinet.* **42**, 819–850 (2003).
10. L'homme, R. F. et al. Clinical experience with the combined use of lopinavir/ritonavir and rifampicin. *AIDS* **23**, 863–865 (2009).
11. Khachi, H., O'Connell, R., Ladenheim, D. & Orkin, C. Pharmacokinetic interactions between rifabutin and lopinavir/ritonavir in HIV-infected patients with mycobacterial co-infection. *J. Antimicrob. Chemother.* **64**, 871–873 (2009).
12. Goodwin, B., Hodgson, E. & Liddle, C. The orphan human pregnane X receptor mediates the transcriptional activation of CYP3A4 by rifampicin through a distal enhancer module. *Mol. Pharmacol.* **56**, 1329–1339 (1999).
13. Campbell, E. A. et al. Structural mechanism for rifampicin inhibition of bacterial RNA polymerase. *Cell* **104**, 901–912 (2001).
14. Burman, W. J., Gallicano, K. & Peloquin, C. Therapeutic implications of drug interactions in the treatment of human immunodeficiency virus-related tuberculosis. *Clin. Infect. Dis.* **28**, 419–429 (1999).
15. Touré, N. O. et al. Tuberculosis and diabetes [in French with English abstract]. *Rev. Mal. Respir.* **24**, 869–875 (2007).
16. Dooley, K. E. & Chaisson, R. E. Tuberculosis and diabetes mellitus: convergence of two epidemics. *Lancet Infect. Dis.* **9**, 737–746 (2009).
17. Ruslami, R. et al. Pharmacokinetics of antituberculosis drugs in pulmonary tuberculosis patients with type 2 diabetes. *Antimicrob. Agents Chemother.* **54**, 1068–1074 (2010).
18. Payne, D. J., Gwynn, M. N., Holmes, D. J. & Pompliano, D. L. Drugs for bad bugs: confronting the challenges of antibacterial discovery. *Nature Rev. Drug Discov.* **6**, 29–40 (2007).

An excellent review on what is ailing antibacterial research and remedial measures to be taken.

19. Macielag, M. *Chemical Properties of Antibacterial Drugs* (45th Interscience Conference for Antimicrobial Agents and Chemotherapy (ICAAC), December 16–19, 2005).
20. Cole, S. T. *et al.* Deciphering the biology of *Mycobacterium tuberculosis* from the complete genome sequence. *Nature* **393**, 537–544 (1998).  
**A landmark paper describing the genomic sequence of *M. tuberculosis* and thereby identifying several new drug targets.**
21. Working Group on New TB Drugs. The global TB drug pipeline. (<http://www.newtbdrugs.org/project.php?id=183>) (2010).
22. Pethe, K. *et al.* A chemical genetic screen in *Mycobacterium tuberculosis* identifies carbon-source-dependent growth inhibitors devoid of *in vivo* efficacy. *Nature Commun.* **1**, 57 (2010).
23. Andries, K. *et al.* A diarylquinoline drug active on the ATP synthase of *Mycobacterium tuberculosis*. *Science* **307**, 223–227 (2005).  
**Describes the discovery of the novel drug candidate TMC207.**
24. Koul, A. *et al.* Diarylquinolines target subunit c of mycobacterial ATP synthase. *Nature Chem. Biol.* **3**, 323–324 (2007).
25. Makarov, V. *et al.* Benzothiazinones kill *Mycobacterium tuberculosis* by blocking arabinan synthesis. *Science* **324**, 801–804 (2009).
26. Bald, D. & Koul, A. Respiratory ATP synthesis: the new generation of mycobacterial drug targets? *FEMS Microbiol. Lett.* **308**, 1–7 (2010).
27. Koul, A. *et al.* Diarylquinolines are bactericidal for dormant mycobacteria as a result of disturbed ATP homeostasis. *J. Biol. Chem.* **283**, 25273–25280 (2008).
28. Rao, S. P., Alonso, S., Rand, L., Dick, T. & Pethe, K. The protonmotive force is required for maintaining ATP homeostasis and viability of hypoxic, nonreplicating *Mycobacterium tuberculosis*. *Proc. Natl Acad. Sci. USA* **105**, 11945–11950 (2008).  
**Important research demonstrating the effect of inhibition of the respiratory chain for killing dormant TB bacilli.**
29. Boshoff, H. I. & Barry, C. E. III. Tuberculosis—metabolism and respiration in the absence of growth. *Nature Rev. Microbiol.* **3**, 70–80 (2005).  
**This review provides an excellent understanding of how tuberculosis adapts and survives during long-term persistence.**
30. Fischbach, M. A. & Walsh, C. T. Antibiotics for emerging pathogens. *Science* **325**, 1089–1093 (2009).
31. Williams, K. N. *et al.* Promising antituberculosis activity of the oxazolidinone PNU-100480 relative to that of linezolid in a murine model. *Antimicrob. Agents Chemother.* **53**, 1314–1319 (2009).
32. Fortún, J. *et al.* Linezolid for the treatment of multidrug-resistant tuberculosis. *J. Antimicrob. Chemother.* **56**, 180–185 (2005).
33. Conte, J. E. Jr, Golden, J. A., Kipps, J. & Zurlinden, E. Intrapulmonary pharmacokinetics of linezolid. *Antimicrob. Agents Chemother.* **46**, 1475–1480 (2002).
34. Singh, R. *et al.* PA-824 kills nonreplicating *Mycobacterium tuberculosis* by intracellular NO release. *Science* **322**, 1392–1395 (2008).
35. Manjunatha, U., Boshoff, H. I. & Barry, C. E. The mechanism of action of PA-824: novel insights from randomised profiling. *Commun. Integr. Biol.* **2**, 215–218 (2009).
36. Chambers, H. F. *et al.* Can penicillins and other beta-lactam antibiotics be used to treat tuberculosis? *Antimicrob. Agents Chemother.* **39**, 2620–2624 (1995).
37. Hugonnet, J. E., Tremblay, L. W., Boshoff, H. I., Barry, C. E. III & Blanchard, J. S. Meropenem-clavulanate is effective against extensively drug-resistant *Mycobacterium tuberculosis*. *Science* **323**, 1215–1218 (2009).  
**Renewed interest in  $\beta$ -lactams and their combination with broad-spectrum lactamase inhibitors for TB treatment.**
38. Drawz, S. M. & Bonomo, R. A. Three decades of  $\beta$ -lactamase inhibitors. *Clin. Microbiol. Rev.* **23**, 160–201 (2010).
39. Agrawal, D., Udawadia, Z. F., Rodriguez, C. & Mehta, A. Increasing incidence of fluoroquinolone-resistant *Mycobacterium tuberculosis* in Mumbai, India. *Int. J. Tuberc. Lung Dis.* **13**, 79–83 (2009).
40. O'Shea, R. & Moser, H. E. Physicochemical properties of antibacterial compounds: implications for drug discovery. *J. Med. Chem.* **51**, 2871–2878 (2008).  
**A thorough study of the physicochemical properties of antibacterial compounds and accompanying chemical space.**
41. Ritchie, T. J., Luscombe, C. N. & Macdonald, S. J. Analysis of the calculated physicochemical properties of respiratory drugs: can we design for inhaled drugs yet? *J. Chem. Inf. Model.* **49**, 1025–1032 (2009).
42. Hett, E. C. & Rubin, E. J. Bacterial growth and cell division: a mycobacterial perspective. *Microbiol. Mol. Biol. Rev.* **72**, 126–56 (2008).
43. Koul, A., Herget, T., Klebl, B. & Ullrich, A. Interplay between mycobacteria and host signalling pathways. *Nature Rev. Microbiol.* **2**, 189–202 (2004).
44. Székely, R. *et al.* A novel drug discovery concept for tuberculosis: inhibition of bacterial and host cell signalling. *Immunol. Lett.* **116**, 225–231 (2008).
45. Miller, J. R. *et al.* A class of selective antibacterials derived from a protein kinase inhibitor pharmacophore. *Proc. Natl Acad. Sci. USA* **106**, 1737–1742 (2009).
46. Walburger, A. *et al.* Protein kinase G from pathogenic mycobacteria promotes survival within macrophages. *Science* **304**, 1800–1804 (2004).
47. Zhou, B. *et al.* Targeting mycobacterium protein tyrosine phosphatase B for antituberculosis agents. *Proc. Natl Acad. Sci. USA* **107**, 4573–4578 (2010).
48. Kumar, D. *et al.* Genome-wide analysis of the host intracellular network that regulates survival of *Mycobacterium tuberculosis*. *Cell* **140**, 731–743 (2010).
49. Keating, L. A. *et al.* The pyruvate requirement of some members of the *Mycobacterium tuberculosis* complex is due to an inactive pyruvate kinase: implications for *in vivo* growth. *Mol. Microbiol.* **56**, 163–174 (2005).
50. Andries, K., Gevers, T. & Lounis, N. Bactericidal potencies of new regimens are not predictive for their sterilizing potencies in a murine model of tuberculosis. *Antimicrob. Agents Chemother.* **54**, 4540–4544 (2010).
51. Dhar, N. & McKinney, J. D. *Mycobacterium tuberculosis* persistence mutants identified by screening in isoniazid-treated mice. *Proc. Natl Acad. Sci. USA* **107**, 12275–12280 (2010).
52. Ibrahim, M., Truffot-Pernot, C., Andries, K., Jarlier, V. & Veziris, N. Sterilizing activity of R207910 (TMC207)-containing regimens in the murine model of tuberculosis. *Am. J. Respir. Crit. Care Med.* **180**, 553–557 (2009).
53. Feldman, W. H., Karlson, A. G. & Hinshaw, H. C. Streptomycin in experimental tuberculosis: the effects in guinea pigs following infection in intravenous inoculation. *Am. Rev. Tuberc.* **56**, 346–359 (1947).
54. Davis, J. M. & Ramakrishnan, L. The role of the granuloma in expansion and dissemination of early tuberculous infection. *Cell* **136**, 37–49 (2009).
55. Russell, D. G., Barry, C. E. III & Flynn, J. L. Tuberculosis: what we don't know can, and does, hurt us. *Science* **328**, 852–856 (2010).
56. Donald, P. R. & Diacon, A. H. The early bactericidal activity of anti-tuberculosis drugs: a literature review. *Tuberculosis (Edinb.)* **88** (suppl. 1), S75–S83 (2008).
57. Rustonjee, R. *et al.* Early bactericidal activity and pharmacokinetics of the diarylquinoline TMC207 in treatment of pulmonary tuberculosis. *Antimicrob. Agents Chemother.* **52**, 2831–2835 (2008).
58. Wallis, R. S. *et al.* Biomarkers for tuberculosis disease activity, cure, and relapse. *Lancet Infect. Dis.* **10**, 68–69 (2010).
59. Mitchison, D. A. Assessment of new sterilizing drugs for treating pulmonary tuberculosis by culture at 2 months. *Am. Rev. Respir. Dis.* **147**, 1062–1063 (1993).  
**An interesting demonstration of using 2-months culture conversion as a surrogate marker in TB trials.**
60. Wallis, R. S. *et al.* Biomarkers and diagnostics for tuberculosis: progress, needs, and translation into practice. *Lancet* **375**, 1920–1937 (2010).  
**An excellent review on the need for biomarkers and other tools for shortening TB trials.**
61. Diacon, A. H. *et al.* The diarylquinoline TMC207 for multidrug-resistant tuberculosis. *N. Engl. J. Med.* **360**, 2397–2405 (2009).
62. Rustonjee, R. *et al.* A Phase II study of the sterilising activities of ofloxacin, gatifloxacin and moxifloxacin in pulmonary tuberculosis. *Int. J. Tuberc. Lung Dis.* **12**, 128–138 (2008).
63. Berry, M. P. *et al.* An interferon-inducible neutrophil-driven blood transcriptional signature in human tuberculosis. *Nature* **466**, 973–977 (2010).
64. Spigelman, M., Woosley, R. & Gheuens, J. New initiative speeds tuberculosis drug development: novel drug regimens become possible in years, not decades. *Int. J. Tuberc. Lung Dis.* **14**, 663–664 (2010).
65. Pieters, J. *Mycobacterium tuberculosis* and the macrophage: maintaining a balance. *Cell Host Microbe* **3**, 399–407 (2008).
66. Dhar, N. & McKinney, J. D. Microbial phenotypic heterogeneity and antibiotic tolerance. *Curr. Opin. Microbiol.* **10**, 30–38 (2007).
67. Beresford, B. & Sadoff, J. C. Update on research and development pipeline: tuberculosis vaccines. *Clin. Infect. Dis.* **50** (suppl. 3), S178–S183 (2010).
68. Shi, L. *et al.* Changes in energy metabolism of *Mycobacterium tuberculosis* in mouse lung and under *in vitro* conditions affecting aerobic respiration. *Proc. Natl Acad. Sci. USA* **102**, 15629–15634 (2005).
69. Weinstein, E. A. *et al.* Inhibitors of type II NADH:menaquinone oxidoreductase represent a class of antitubercular drugs. *Proc. Natl Acad. Sci. USA* **102**, 4548–4553 (2005).  
**An interesting demonstration of targeting NADH dehydrogenase for identifying new TB drugs or re-purposing old drug classes.**
70. MOE. v. 2009. 10 (<http://www.chemcomp.com>) (Chemical Computing Group Inc/Montreal, Canada) (2010).
71. SIMCA-P+ 12. (<http://www.umetrics.com>) (Umetrics AB, Umeå, Sweden) (2010).
72. Hirano, S., Ichikawa, S. & Matsuda, A. Structure–activity relationship of truncated analogs of caprazamycins as potential anti-tuberculosis agents. *Bioorg. Med. Chem.* **16**, 5123–5133 (2008).
73. Hennessy, A. *et al.* Substituted (Aza)-1 methyl -1H-Quinolin-2-ones as antibacterials. Patent WO2010/046388A1 (2010).
74. Chao, M. C. & Rubin, E. J. Letting sleeping dogs lie: does dormancy play a role in tuberculosis? *Annu. Rev. Microbiol.* **64**, 293–311 (2010).

**Acknowledgements** We thank our colleagues K. Simmen, N. Austin, V. Sinha, H. Van Vlijmen and M. Macleugh for critical reading and providing valuable scientific input for this manuscript. We would also like to thank B. Challis for reviewing this manuscript, S. Mostmans from the Business Intelligence Group for providing TB pipeline updates, and E. Huybrechts for her help with preparing the figures.

**Author Contributions** A.K. wrote the synopsis, conceptualized different topics within the review, wrote and contributed to all sections of the review; coordinated and discussed the content with other co-authors. E.A. did the principal component analysis work on TB drugs, N.L. contributed to the section on animal models, J.G. did the chemistry part of the review including chemical structures and K.A. contributed to different sections of the review with a major focus on TB clinical development.

**Author Information** Reprints and permissions information is available at [www.nature.com/reprints](http://www.nature.com/reprints). The authors declare competing financial interests: details accompany the full-text HTML version of the paper at [www.nature.com/nature](http://www.nature.com/nature). Readers are welcome to comment on the online version of this article at [www.nature.com/nature](http://www.nature.com/nature). Correspondence and requests for materials should be addressed to A.K. ([akoul@its.jnj.com](mailto:akoul@its.jnj.com)).

# A critical role for IGF-II in memory consolidation and enhancement

Dillon Y. Chen<sup>1</sup>, Sarah A. Stern<sup>1</sup>, Ana Garcia-Osta<sup>1†</sup>, Bernadette Saunier-Rebori<sup>2</sup>, Gabriella Pollonini<sup>1</sup>, Dhananjay Bambah-Mukku<sup>1</sup>, Robert D. Blitzer<sup>2,3</sup> & Cristina M. Alberini<sup>1,3</sup>

**We report that, in the rat, administering insulin-like growth factor II (IGF-II, also known as IGF2) significantly enhances memory retention and prevents forgetting. Inhibitory avoidance learning leads to an increase in hippocampal expression of IGF-II, which requires the transcription factor CCAAT enhancer binding protein  $\beta$  and is essential for memory consolidation. Furthermore, injections of recombinant IGF-II into the hippocampus after either training or memory retrieval significantly enhance memory retention and prevent forgetting. To be effective, IGF-II needs to be administered within a sensitive period of memory consolidation. IGF-II-dependent memory enhancement requires IGF-II receptors, new protein synthesis, the function of activity-regulated cytoskeletal-associated protein and glycogen-synthase kinase 3 (GSK3). Moreover, it correlates with a significant activation of synaptic GSK3 $\beta$  and increased expression of GluR1 (also known as GRIA1)  $\alpha$ -amino-3-hydroxy-5-methyl-4-isoxasolepropionic acid receptor subunits. In hippocampal slices, IGF-II promotes IGF-II receptor-dependent, persistent long-term potentiation after weak synaptic stimulation. Thus, IGF-II may represent a novel target for cognitive enhancement therapies.**

Elucidating the mechanisms of memory enhancement is critical for the development of cognitive enhancement therapies. Memory strengthening and persistence depend on consolidation, a process whereby newly learned information, which is initially labile, becomes stronger and resilient to disruption<sup>1</sup>. This process recruits evolutionarily conserved *de novo* RNA and protein syntheses, the function of members of the cAMP response element binding protein (CREB) and CCAAT enhancer binding protein (C/EBP) transcription factor families<sup>2–4</sup>, and correlates with synaptic structural changes<sup>2,5</sup>. Stable memories can again become fragile if retrieved, and undergo a process of reconsolidation that, like the initial consolidation, requires *de novo* RNA and protein synthesis, CREB and C/EBP<sup>6,7</sup> to re-stabilize<sup>8</sup>. The identity of the target genes regulated by CREB and C/EBP is still largely unknown. Studies in liver and other tissues show that C/EBP binding sites are present in promoters of IGF-II<sup>9</sup>, a growth factor that is expressed in the brain but is still poorly characterized.

IGF-II is a mitogenic polypeptide, which together with insulin and insulin-like growth factor 1 (IGF-I, also known as IGF1) belongs to the IGF/IGFBP (IGF/IGF binding protein) system. This system is important in normal somatic growth and development, tissue repair and regeneration throughout the lifespan<sup>10,11</sup>. IGF-II, the less characterized member of the family, is expressed in the brain both during development and in adulthood and declines with ageing<sup>12</sup>. In the adult brain, it is the most abundantly expressed of the IGFs<sup>10</sup>, and its relative concentration is highest in the hippocampus<sup>13</sup>. Given that IGF-II is a putative C/EBP target gene, we investigated its expression and functional role in memory formation.

## C/EBP $\beta$ -dependent IGF-II expression is regulated by training

In previous studies, we showed that inhibitory avoidance (IA) training induces a significant increase in hippocampal C/EBP $\beta$ , which starts between 6 and 9 h after training, lasts for at least 28 h and returns to baseline by 48 h after training<sup>14</sup> (Supplementary Fig. 1). Here we

tested whether C/EBP $\beta$  regulates the expression of the putative target gene IGF-II. The numeric values, and number of animals per group (*n*) of all experiments are shown in Supplementary Tables. Northern blot analysis showed that, compared to controls that were exposed to the box without foot shock and either euthanized immediately after (0 h–) or at paired time points (no shock, –), the hippocampal expression of *IGF-II* mRNA did not change at 6 and 9 h but increased significantly at 20 h and had a strong trend towards an increase at 36 h after training (Fig. 1a).

Quantitative PCR with reverse transcription (qRT-PCR) analyses of mRNA extracts confirmed the significant increase of *IGF-II* mRNA 20 h after training compared to no-shock and 0 h– controls whereas, in the same extracts, *IGF-I* mRNA remained unchanged (Fig. 1b).

Quantitative western blot analyses with an anti-IGF-II antibody that specifically recognizes IGF-II and not IGF-I (Supplementary Fig. 2) showed that hippocampal levels of IGF-II protein significantly increased at 20, but not at 72 or 96 h after training, compared to both time-matched unpaired and 0 h– controls (Fig. 1c). The unpaired control protocol temporally dissociates, within subject, context and foot shock exposure by 1 h, and does not produce long-term IA memory (Supplementary Fig. 3). Thus, IA training leads to an increase in IGF-II that temporally overlaps that of C/EBP $\beta$ <sup>14</sup>.

We next investigated whether the IGF-II increase requires C/EBP $\beta$ . Previous studies have established that hippocampal bilateral injection of C/EBP $\beta$  antisense oligodeoxynucleotide ( $\beta$ -ODN), 5 h after IA training, blocks the training-dependent C/EBP $\beta$  induction and completely disrupts memory consolidation<sup>15</sup>. Using this injection protocol and quantitative western blot analyses we found that, compared to control scrambled ODN (SC-ODN),  $\beta$ -ODN completely disrupted the training-induced IGF-II increase without changing the IGF-II expression in unpaired control rats 24 h after training (Fig. 1d). Chromatin immunoprecipitation of hippocampal extracts confirmed that C/EBP $\beta$  binds *in vivo* to a C/EBP $\beta$  consensus sequence in the promoter region of the rat IGF-II exon 1 (Supplementary Fig. 4). Thus,

<sup>1</sup>Department of Neuroscience, Mount Sinai School of Medicine, New York, New York 10029, USA. <sup>2</sup>Department of Pharmacology and Systems Therapeutics, Mount Sinai School of Medicine, New York, New York 10029, USA. <sup>3</sup>Department of Psychiatry, Mount Sinai School of Medicine, New York, New York 10029, USA. <sup>†</sup>Present address: CIMA, University of Navarra, CIBERNED, Pamplona 31008, Spain.

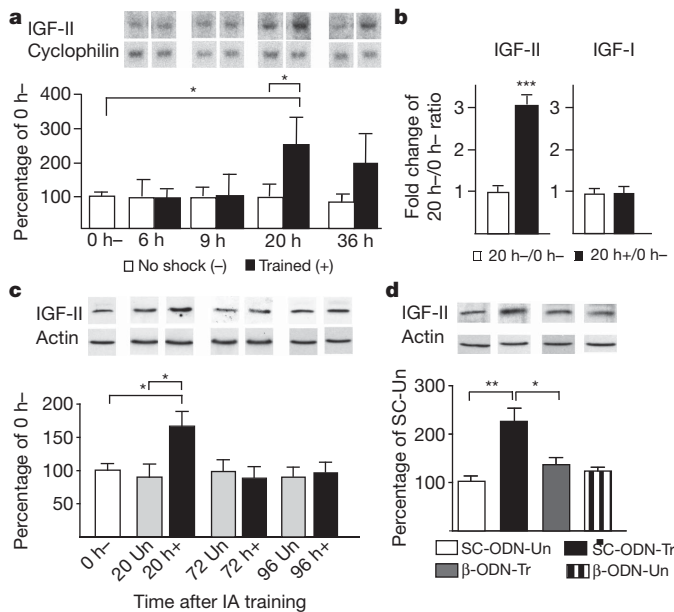


**Figure 1 | C/EBP $\beta$ -dependent IGF-II expression significantly increases following training.** **a**, Northern blot examples and densitometric analyses of IGF-II (cyclophilin-normalized). Data are expressed as mean percentage  $\pm$  s.e.m. of 0 h- (one-way ANOVA comparing all groups  $F_{8,59} = 2.46$ ,  $P = 0.0249$ , post hoc  $t$ -test  $*P < 0.05$ ). **b**, Real-time PCR of hippocampal IGF-II and IGF-I mRNA (18S RNA-normalized). Data are expressed as mean fold change  $\pm$  s.e.m. of 20 h-/0 h- (Student's  $t$ -test  $***P < 0.0001$ ). **c**, Western blot analyses of hippocampal IGF-II from 0 h-, unpaired (Un) and trained (+) rats euthanized 20, 72 or 96 h later (actin-normalized). Data are expressed as mean percentage  $\pm$  s.e.m. of 0 h- (one-way ANOVA comparing 0 h-, 20 Un and 20 h+  $F_{2,29} = 4.69$ ,  $P = 0.0172$ , Newman-Keuls post hoc test,  $*P < 0.05$ ). **d**, Western blot analysis of hippocampal IGF-II from trained or Un rats injected with either SC-ODN or  $\beta$ -ODN 5 h post-training and euthanized 24 h post-training (actin-normalized). Data are expressed as mean percentage  $\pm$  s.e.m. of SC-ODN-Un (two-way ANOVA  $F_{1,19} = 4.62$ ,  $P = 0.0447$  for interaction,  $F_{1,19} = 1.45$ ,  $P = 0.2434$  for ODN-treatment,  $F_{1,19} = 6.46$ ,  $P = 0.0199$  for training-paradigm, Bonferroni post hoc  $**P < 0.01$ ;  $*P < 0.05$ ).

IA training leads to an increase in hippocampal C/EBP $\beta$  that regulates a downstream increase in IGF-II.

### Limited temporal requirement of IGF-II during memory consolidation

We then investigated the functional kinetic of hippocampal IGF-II during IA memory consolidation. Bilateral injections of IGF-II ODN antisense (IGF-II-ODN) were used to selectively knockdown the IGF-II expression in the dorsal hippocampus. Injection either immediately or 8 h after training, or at both time points, showed that double, but not single, injections of IGF-II-ODN significantly disrupted memory retention at 24 h after training, compared to SC-ODN (Fig. 2a, Supplementary Fig. 5). Quantitative RT-PCR confirmed that, compared to SC-ODN, double injections of IGF-II-ODN selectively and significantly decreased the levels of *IGF-II*, but not of *IGF-I* mRNA, 16 h after training (Supplementary Fig. 6). IGF-II-ODN doubly injected at 24 and 32 h after training, compared to SC-ODN, significantly disrupted memory retention at 48 h after training (Fig. 2a) and re-training of the amnesic rats resulted in normal memory retention 24 h after re-training (Fig. 2a), thus excluding hippocampal damage or non-specific effects. However, IGF-II-ODN doubly injected at 96 and 104 h after training did not affect memory retention 24 h later (Fig. 2a). The amnesia caused by IGF-II-ODN double injections was rescued by the co-administration of recombinant IGF-II, but not IGF-I (Fig. 2b), further proving that IGF-II expression is essential for IA memory consolidation. Furthermore, whereas IGF-I had no effect (compare SC-ODN/IGF-I

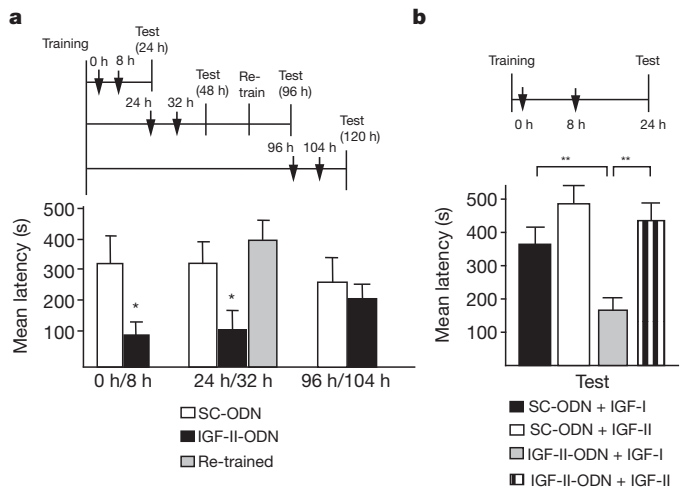


**Figure 2 | Hippocampal IGF-II is required for memory consolidation.** Schedules shown above figures. **a**, Mean latency  $\pm$  s.e.m. of rats given double hippocampal injections ( $\downarrow$ ) of SC-ODN or IGF-II-ODN (one-way ANOVA for treatment  $F_{5,47} = 2.54$ ,  $P = 0.043$ , post hoc Student's  $t$ -test  $*P < 0.05$  for 0 h/8 h and 24 h/32 h). **b**, Mean latency  $\pm$  s.e.m. of rats given double hippocampal injections ( $\downarrow$ ) of SC-ODN or IGF-II-ODN with either IGF-II or IGF-I (two-way ANOVA  $F_{1,33} = 4.29$ ,  $P = 0.0468$  for interaction,  $F_{1,31} = 6.34$ ,  $P = 0.173$  for ODN-treatment,  $F_{1,31} = 11.38$ ,  $P < 0.0021$  for IGF-treatment, Bonferroni post hoc  $**P < 0.01$ ).

from Fig. 2b and SC-ODN from Fig. 2a), IGF-II seemed to enhance memory retention, although the effect was not significant, possibly because the testing latency was cut-off at 540 s.

We concluded that hippocampal IGF-II has a critical role for IA memory consolidation during a limited time window that lasts for more than one but less than 4 days.

### IGF-II significantly enhances memory and prevents forgetting

Because of the tendency towards memory enhancement in our IGF-II rescue experiment (Fig. 2b), we tested whether exogenously administered IGF-II into the hippocampus immediately after training modulates memory strength. The latency cut-off time was raised to 900 s. Bilateral injections of IGF-II immediately after training significantly and persistently enhanced memory retention at 24 h and 7 days, compared to IGF-I or vehicle (Fig. 3a). This enhancement was not due to a non-specific locomotor effect (Supplementary Fig. 7).

The IGF-II-mediated memory enhancement was dose-dependent (Supplementary Fig. 8): hippocampal injections of 25 or 2.5 ng, like 250 ng, immediately after training incrementally enhanced memory retention at 24 h.

Finally, hippocampal injection of IGF-II immediately after training significantly enhanced memory retention tested 3 weeks later when the latency of vehicle-injected rats was not significantly different from acquisition, indicating that IGF-II prevents forgetting (Fig. 3b).

The IGF-II effect generalized to another memory task, contextual fear conditioning. Bilateral hippocampal injection of IGF-II immediately after contextual-auditory fear conditioning training significantly enhanced contextual fear conditioning retention 24 h later, without affecting auditory fear conditioning tested 48 h after training (Fig. 3c). No difference in baseline freezing was found between groups before foot shock delivery (Fig. 3c).

Finally, because IA consolidation also critically involves the amygdala<sup>16</sup>, we tested the effect of bilateral IGF-II injections into the amygdala immediately after training, but found no effect at testing 24 h later (Fig. 3d). Hence, IGF-II in the hippocampus acts as a strong memory enhancer and also prevents forgetting.

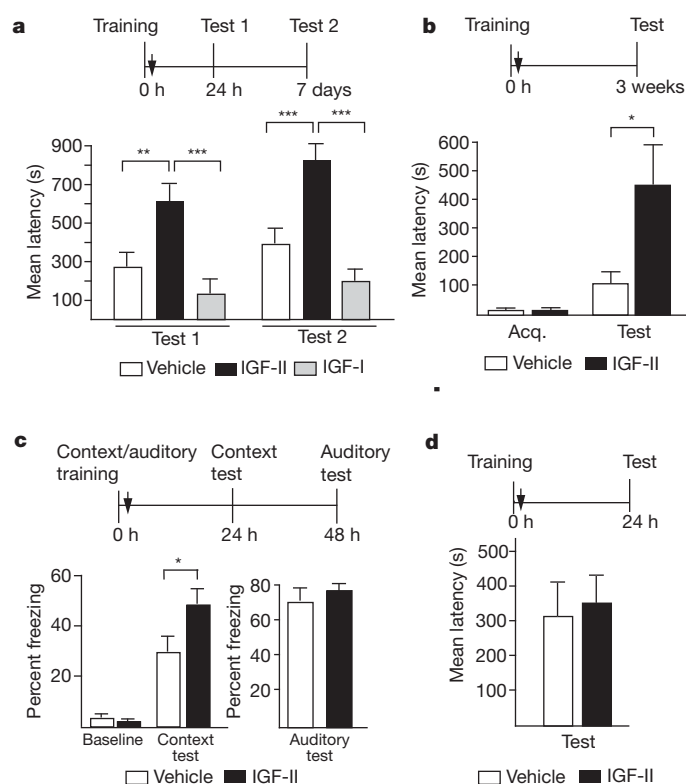


**Figure 3 | Hippocampal post-training IGF-II administration enhances memory and prevents forgetting.** Schedules shown above figures. **a**, Mean latency  $\pm$  s.e.m. of trained rats given hippocampal injection ( $\downarrow$ ) of vehicle, IGF-II or IGF-I and tested 24 h and 7 days later (two-way ANOVA  $F_{2,38} = 0.44$ ,  $P = 0.6463$  for interaction,  $F_{2,38} = 26.7$ ,  $P < 0.0001$  for treatment,  $F_{1,38} = 4.24$ ,  $P = 0.0466$  for test, Bonferroni post hoc test  $^{**}P < 0.01$ ,  $^{***}P < 0.001$ ). **b**, Mean latency  $\pm$  s.e.m. of trained rats given a hippocampal injection ( $\downarrow$ ) of vehicle or IGF-II (acq: acquisition latency; Student's  $t$ -test  $^{*}P = 0.0261$ ). **c**, Mean percentage freezing of trained rats injected with vehicle or IGF-II (Student's  $t$ -test  $^{*}P < 0.0434$ ). **d**, Mean latency  $\pm$  s.e.m. of trained rats given bilateral amygdala injection ( $\downarrow$ ) of vehicle or IGF-II.

### IGF-II-mediated memory enhancement: effect on reconsolidation

An established memory, resilient to disruption, becomes again labile and undergoes another protein-synthesis-dependent reconsolidation process if retrieved<sup>17,18</sup>. Bilateral hippocampal injection of IGF-II 24 h after training had no effect on memory retention tested at 48 h (Fig. 4a). However, if 24 h after training IGF-II was given after memory retrieval (Test 1), memory retention was significantly enhanced 24 h later (Final test, Fig. 4a).

Studies in IA and other types of learning<sup>19–22</sup>, but not all<sup>8,23</sup>, have shown that reconsolidation is temporally limited. IA memory undergoes protein-synthesis-dependent reconsolidation if retrieved 2 or 7 days after training but not 2 or 4 weeks after training<sup>20</sup>. Hence, we asked whether the enhancing effect of IGF-II is also temporally restricted, and coincides with the reconsolidation-sensitive temporal window. Bilateral hippocampal injection of IGF-II immediately after retrieval (Test 1), 2 weeks after training, did not change memory retention tested 1 day later, compared to vehicle (Final test, Fig. 4b). Hence, hippocampal IGF-II-mediated memory enhancement occurs only within the temporal window during which IA memory undergoes reconsolidation.

### Mechanisms underlying IGF-II-mediated memory enhancement

IGF-II activates both IGF-I and IGF-II receptors, but with different affinity<sup>24</sup>. To determine whether IGF-II-mediated memory enhancement recruits one or both of these receptors, we tested the effect of

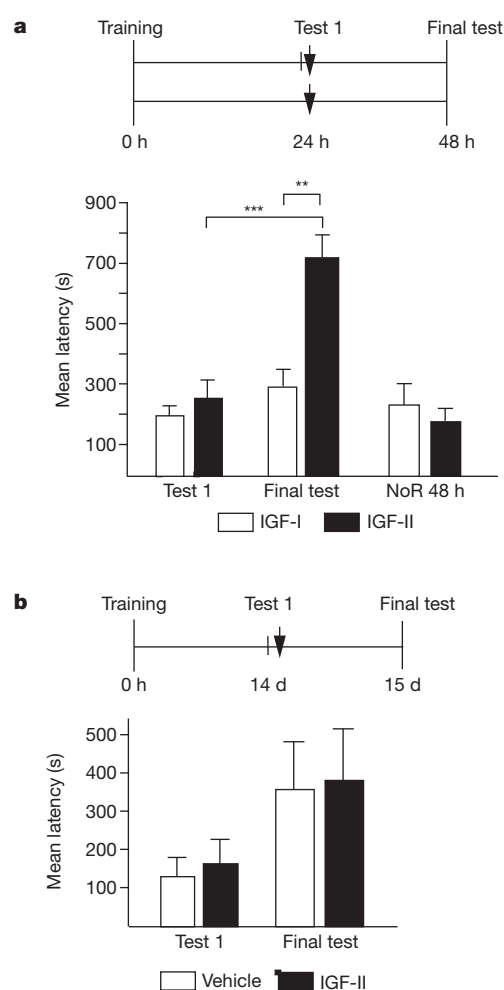


**Figure 4 | Post-retrieval IGF-II administration enhances memory and the effect is temporally limited.** Schedules shown above figures. **a**, Mean latency  $\pm$  s.e.m. of trained rats, tested 24 h post-training and, immediately after, injected ( $\downarrow$ ) with IGF-II or IGF-I. Non-reactivated rats (NoR) were trained and injected ( $\downarrow$ ) without testing. Rats were tested 48 h post-training (two-way ANOVA  $F_{1,26} = 5.67$ ,  $P = 0.0249$  for interaction,  $F_{1,26} = 9.82$ ,  $P = 0.0042$  for treatment,  $F_{1,26} = 13.67$ ,  $P = 0.0001$  for test, Bonferroni post hoc  $^{**}P < 0.01$ ,  $^{***}P < 0.001$ ). **b**, Mean latency  $\pm$  s.e.m. of trained rats, tested 14 days post-training and, immediately after, injected ( $\downarrow$ ) with vehicle or IGF-II; memory was tested 15 days after training.

IGF-I and IGF-II receptor (R) selective inhibitors. Specific inhibitors of IGF-IIR (anti-IGF-IIR antibody) but not IGF-IR (JB1) co-injected with IGF-II completely abolished the memory enhancement compared to respective controls (Fig. 5a). The inhibitors alone did not affect memory retention (Fig. 5a).

Similarly to the antisense experiments, compared to control IgG, a single bilateral hippocampal injection of anti-IGF-IIR antibody immediately after training did not affect memory retention (Fig. 5a), whereas double injections, immediately and 8 h after training, caused a complete amnesia 24 h after training (Fig. 5b).

We next asked whether IGF-II-mediated memory enhancement recruits new protein synthesis. Because memory consolidation *per se* requires new protein synthesis in the hippocampus, blocking protein synthesis in IGF-II-injected rats after training would not be informative. However, because new protein synthesis is not required in the hippocampus for IA reconsolidation<sup>15</sup>, we tested the effect of protein synthesis inhibition on retrieval-dependent IGF-II-mediated memory enhancement.

Bilateral hippocampal co-injection of IGF-II and the protein synthesis inhibitor anisomycin immediately after Test 1, 24 h after training,

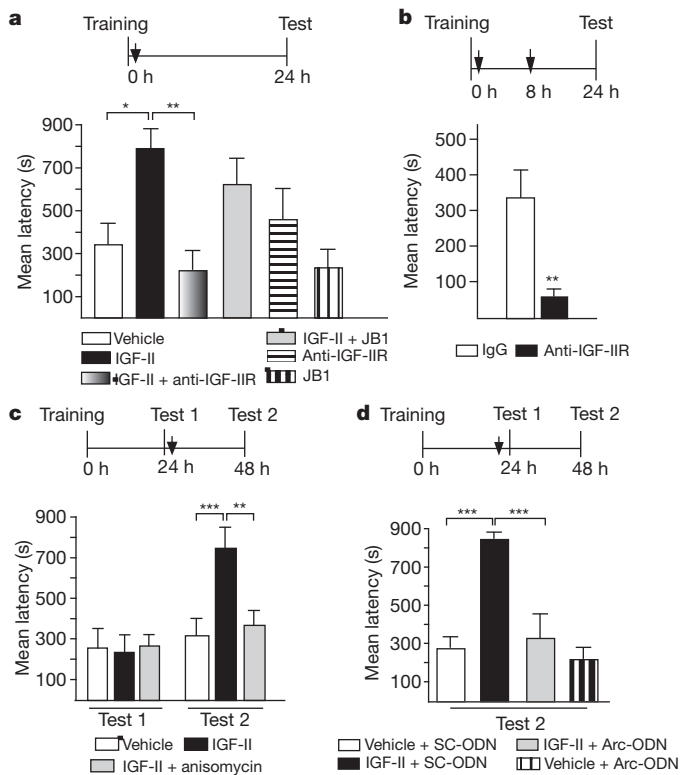


**Figure 5 | The role of IGF-II receptors, *de novo* protein synthesis and Arc in memory consolidation and IGF-II-mediated enhancement.** Schedules shown above figures. **a**, Mean latency  $\pm$  s.e.m. of trained rats injected (i) with vehicle, IGF-II, IGF-II/anti-IGF-IIR, IGF-II/JB1, anti-IGF-IIR or JB1 (one-way ANOVA  $F_{5,40} = 3.82$ ,  $P = 0.0023$ , Newman–Keuls post hoc test  $*P < 0.05$ ,  $**P < 0.01$ ). **b**, Mean latency  $\pm$  s.e.m. of trained rats given double injections of IgG or anti-IGF-IIR antibody (Student's *t*-test  $**P < 0.0041$ ). **c**, Mean latency  $\pm$  s.e.m. of rats trained, tested then injected (i) with vehicle, IGF-II or IGF-II + anisomycin (two-way ANOVA  $F_{2,34} = 5.25$ ,  $P = 0.0103$  for interaction,  $F_{2,34} = 4.68$ ,  $P = 0.0161$  for treatment,  $F_{1,34} = 13.7$ ,  $P = 0.0008$  for test, Bonferroni post hoc  $**P < 0.01$ ,  $***P < 0.001$ ). **d**, Mean latency  $\pm$  s.e.m. of rats trained, tested and injected (i) with vehicle + SC-ODN, vehicle + Arc-ODN, IGF-II + SC-ODN, or IGF-II + Arc-ODN (two-way ANOVA  $F_{1,18} = 7.8$ ,  $P = 0.0119$  for interaction,  $F_{1,18} = 17.3$ ,  $P = 0.0006$  for ODN-treatment,  $F_{1,18} = 12.3$ ,  $P = 0.0025$  for vehicle + IGF-II treatment, Bonferroni post hoc  $***P < 0.001$ ).

showed that anisomycin, compared to vehicle, completely disrupted the IGF-II-mediated memory enhancement tested 24 h later (Fig. 5c) without changing the training-induced retention levels. Hence, memory enhancement, but not reconsolidation, requires hippocampal *de novo* protein synthesis.

To begin identifying which proteins are required for the memory enhancement, we investigated the role of C/EBP $\beta$ . Bilateral hippocampal injection of  $\beta$ -ODN 5 h after retrieval (Test 1) did not affect the IGF-II-mediated memory enhancement tested 48 h after training (Supplementary Fig. 9). The timing of the ODN injections was based on previous kinetics studies showing maximal disruptive effect of  $\beta$ -ODN<sup>7,15</sup>. To test whether a prolonged  $\beta$ -ODN treatment could affect the post-retrieval IGF-II-mediated memory enhancement we injected  $\beta$ -ODNs at both 1 h before and 5 h after reactivation. This treatment, compared to control SC-ODN, also failed to affect the IGF-II-mediated memory enhancement (Supplementary Fig. 9), indicating that, although *de novo* protein synthesis is critical for memory enhancement, C/EBP $\beta$  is not.

We therefore hypothesized that the protein synthesis-mediated enhancement may recruit synaptic rather than cell-wide, transcriptional mechanisms. One rapidly regulated translation known to occur at activated synapses and critical for long-term plasticity and memory

is that of activity-regulated cytoskeletal-associated protein (Arc)<sup>25</sup>. Bilateral hippocampal injection of Arc antisense (Arc-ODN), compared to relative SC-ODN, 1 h before retrieval (Test 1), completely blocked the post-retrieval IGF-II-mediated memory enhancement, without affecting the basal level of the memory 2 days after training (Fig. 5d).

Thus, IGF-II-mediated enhancement requires IGF-II, but not IGF-I receptors. Furthermore, retrieval-dependent IGF-II-mediated enhancement requires *de novo* protein synthesis and Arc but not C/EBP $\beta$ , indicating that it may use synaptic rather than cell-wide-regulatory mechanisms.

Memory consolidation requires the CREB-C/EBP-dependent gene cascade<sup>2</sup>. In IA, both CREB phosphorylation at Ser 133 (pCREB) and the expression of C/EBP $\beta$  are significantly increased in the hippocampus for more than 20 h after training<sup>14</sup>. We examined whether IGF-II-mediated memory enhancement following training correlates with an enhanced hippocampal activation of the CREB-C/EBP pathway. Quantitative western blot analyses confirmed that training significantly increased both pCREB and C/EBP $\beta$  levels in the hippocampus 20 h later<sup>14</sup> (trained-vehicle vs naive-vehicle, Fig. 6a). Compared to vehicle, IGF-II treatment immediately after training resulted in only a tendency towards a further increase in both markers (Fig. 6a). Thus, IGF-II-mediated memory enhancement does not correlate with significant enhancement in the activation of the CREB-C/EBP cascade, strengthening our hypothesis that IGF-II-regulated mechanisms may be synaptic rather than cell-wide. We therefore investigated the synaptic expression levels of GluR1 and GluR2 (also known as GRIA2) AMPA receptor subunits. Synaptic GluR1 AMPA receptors levels have been shown to increase rapidly following IA training and have a critical role in consolidation<sup>26,27</sup>. Furthermore, AMPA receptor subunit trafficking is known to accompany both long-term potentiation (LTP) and long-term depression (LTD)<sup>28</sup>.

Quantitative western blot analyses of synaptoneurosomal extract (see Supplementary Fig. 10 for the biochemical characterization) revealed that there was an increase in synaptic GluR1 30 min after training compared to naive, which, however, was not significant, probably due to the relatively low shock intensity used (Fig. 6b). Importantly, synaptic GluR1 levels were significantly increased in trained rats treated with IGF-II compared to vehicle. This increase was completely abolished by anti-IGF-IIR antibody. On the other hand, GluR2 levels remained unchanged across groups.

Previous studies reported that AMPA receptor trafficking and dendritic expression of GluR1 in neurons are regulated by GSK3 (ref. 29) and, interestingly, IGF-II has been implicated in GSK3 regulation<sup>30</sup>. As depicted in Fig. 6c, the IGF-II-mediated significant increase of GluR1 was paralleled by a significant synaptic activation of GSK3 $\beta$  (measured by its dephosphorylation at Ser 9, ref. 31), which was also completely abolished by anti-IGF-IIR antibody. Furthermore, whereas blocking hippocampal GSK3 function with pretraining injection of the inhibitor SB216763 completely disrupted IA memory retention (data not shown), the same treatment delivered immediately after retrieval (Test 1) selectively eliminated the IGF-II-mediated enhancement tested 2 days after training (Test 2) without affecting memory reconsolidation (Fig. 6d).

Thus, IGF-II-dependent memory enhancement requires the activation of GSK3 $\beta$  and correlates with increased synaptic expression of GluR1.

### IGF-II facilitates long-term potentiation (LTP)

To determine whether the effect of IGF-II was generalized to long-term synaptic plasticity, we tested the effect of IGF-II on hippocampal LTP, which is widely regarded as a cellular correlate of long-term memory<sup>32</sup>. IGF-II was applied to acute hippocampal slices and both LTP in the Schaffer collateral pathway and basal synaptic transmission were investigated. As shown in Fig. 6e, a weak high-frequency stimulation (wHFS) elicited a transient synaptic potentiation that decayed to baseline within 100 min after induction (slope =  $109.4 \pm 9.7\%$ , calculated

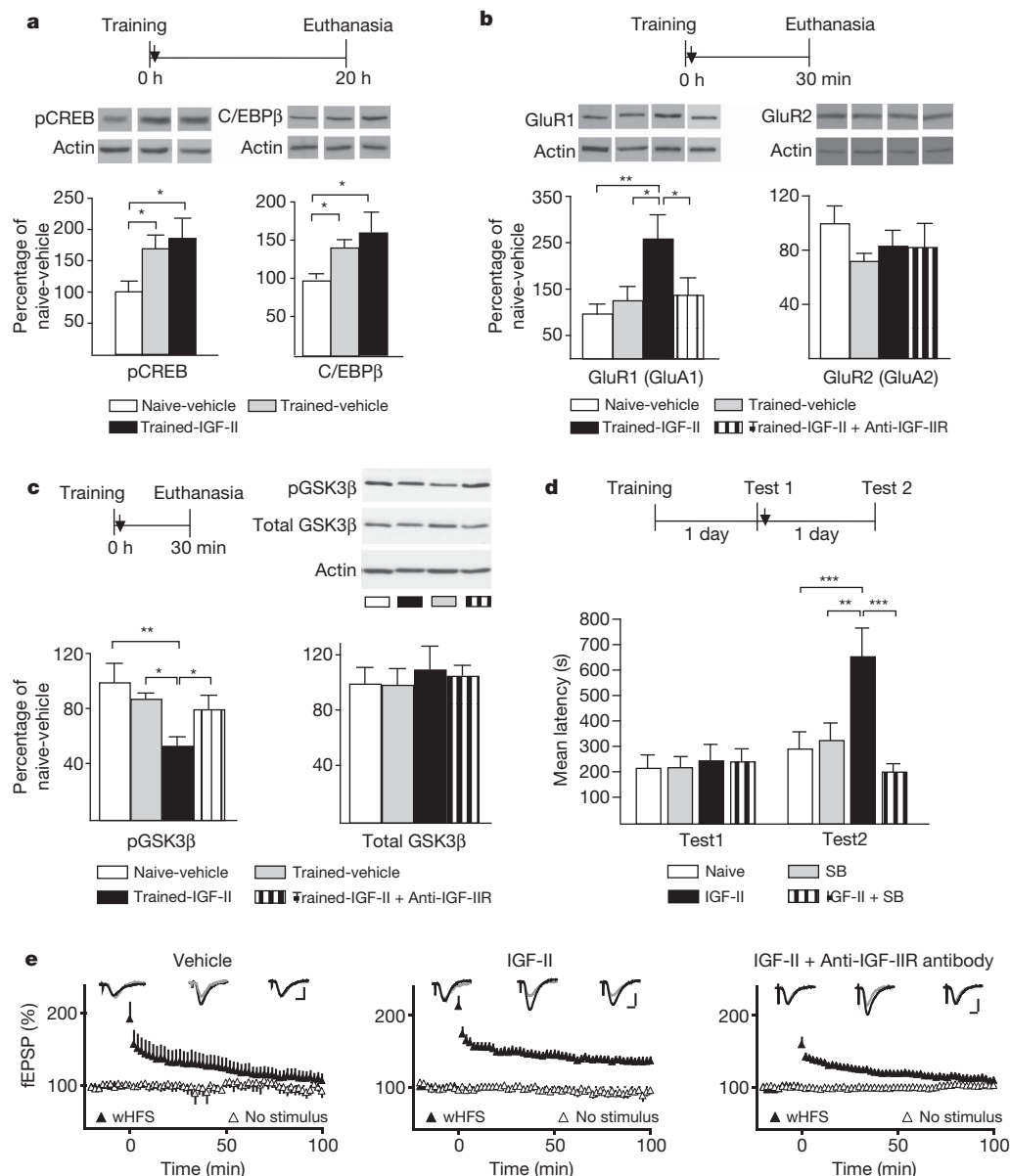


**Figure 6 | Mechanisms of IGF-II-mediated memory enhancement. IGF-II promotes LTP.** **a**, Western blot analysis of hippocampal pCREB and C/EBP $\beta$  from naive or trained rats injected (i) with vehicle or IGF-II and euthanized 20 h later (actin-normalized). Data are expressed as mean percentage  $\pm$  s.e.m. of naive-vehicle (one-way ANOVA, pCREB:  $F_{2,20} = 4.3$ ,  $P = 0.0287$ , C/EBP $\beta$ :  $F_{2,19} = 5.7$ ,  $P = 0.0117$ , Newman-Keuls post hoc test,  $*P < 0.05$ ). **b**, Western blot analysis of hippocampal GluR1 and GluR2 from naive or trained rats injected (i) with vehicle, IGF-II, IGF-II + anti-IGF-IIR antibody (actin-normalized). Data are expressed as mean percentage  $\pm$  s.e.m. of naive-vehicle (one-way ANOVA, GluR1:  $F_{3,19} = 4.24$ ,  $P = 0.0188$ , Newman-Keuls post hoc test  $*P < 0.05$ ,  $**P < 0.01$ ). **c**, Western blot analysis of hippocampal pGSK3 $\beta$  and GSK3 $\beta$  from the same extracts as in **b** (actin normalized). Data are expressed as percentage  $\pm$  s.e.m. of naive-vehicle (one-way ANOVA  $F_{3,19} = 4.93$ ,  $P = 0.130$ , Newman-Keuls post hoc test  $*P < 0.05$ ,  $**P < 0.01$ ). **d**, Mean latency  $\pm$  s.e.m.

of rats trained, tested and injected (i) with vehicle, IGF-II, SB216763 (SB) or IGF-II + SB (two-way ANOVA  $F_{3,56} = 4.44$ ,  $P = 0.0072$  for interaction,  $F_{3,56} = 5.07$ ,  $P = 0.0035$  for treatment,  $F_{1,56} = 9.12$ ,  $P = 0.0038$  for test, Bonferroni post hoc  $**P < 0.01$ ,  $***P < 0.001$ ). **e**, Time-courses of field excitatory postsynaptic potentials (fEPSPs) in area CA1 stratum radiatum are shown with sample traces obtained during the baseline period, 2 min and 100 min after the delivery of weak high frequency stimulation (wHFS) (grey traces, no wHFS; black traces, wHFS). Scale bars, 0.5 mV (y-axis) and 5 ms (x-axis), respectively. Left panel, in vehicle-treated slices, wHFS induced only transient potentiation that returned to baseline levels within 100 min. Middle panel, in the presence of IGF-II, the same protocol induced stable LTP (Student's  $t$ -test  $P < 0.05$ ). Right panel, in slices pretreated with antibodies against the IGFII receptor, IGF-II failed to facilitate the induction of stable LTP.

as the average of the final 10 min of recording normalized to the full baseline period for each slice). When this weak stimulus was delivered in the presence of IGF-II, stable LTP was expressed (slope =  $135.2 \pm 6.6\%$  of baseline). This enabling effect was completely blocked in slices that were pretreated with anti-IGF-IIR antibody ( $112.05 \pm 4.7\%$ ) (Fig. 6e). Neither IGF-II nor the anti-IGF-IIR antibody affected basal synaptic transmission (Supplementary Figs 11 and 12).

## Discussion

Our study shows that memory retention can be enhanced, LTP promoted and forgetting prevented by the administration of IGF-II, a growth factor physiologically regulated following learning. IGF-II is endogenously upregulated following learning as a C/EBP $\beta$  target gene and required in the hippocampus for memory consolidation during the first 1–2 days after training but not at later times, extending previous

conclusions<sup>15</sup> that the transcription- and translation-dependent phase of IA consolidation in the dorsal hippocampus lasts for more than one, but less than 4 days.

The effect of IGF-II as memory enhancer is temporally restricted to active phases induced by either learning or memory retrieval, generalized to different types of hippocampal-dependent memories and occurs with an acute treatment in low doses.

The training-related IGF-II-dependent memory enhancement is restricted to a temporal window that lasts less than a day. However, at later times, the enhancing effect re-emerges if IGF-II is given in combination with memory retrieval, which is known to reactivate the memory and induce reconsolidation<sup>17</sup>. The IGF-II effect following retrieval is also temporally limited and, in fact, restricted to a temporal window that overlaps with the reconsolidation sensitive period of IA<sup>7,15,20</sup>. Both retrieval-induced memory fragility and IGF-II-dependent enhancement require new protein synthesis but in different brain regions: the former in the amygdala<sup>7</sup>, the latter in the hippocampus. Hence, during the first 1–2 weeks after training, IA memory is in a sensitive period during which, if in an active state, it can be either significantly weakened or enhanced. These findings strengthen our previously proposed hypothesis that reconsolidation is a phase of a lingering consolidation process<sup>17,33</sup>. We speculate that the retrieval-induced memory fragility mediated by amygdala mechanisms may be critical for promoting memory enhancement mediated by hippocampal mechanisms and that the temporal boundary of the sensitive period may reflect the hippocampal-cortical redistribution of memory storage<sup>34,35</sup> or the multiple trace distribution of memory<sup>36</sup>.

Intriguingly, the effect of IGF-II as memory enhancer is selectively mediated by IGF-II and not IGF-I receptors. IGF-IIR is identical to the mannose-6-phosphate (M6P) receptor<sup>11</sup> and has a role in lysosomal enzyme trafficking, clearance and endocytosis-mediated degradation of IGF-II and possibly in transmembrane-receptor-mediated signal transduction<sup>11</sup> but, in general, little is known about its function in the brain.

IGF-II-mediated memory enhancement is not paralleled by significant activation of pCREB or C/EBP $\beta$  and does not functionally require C/EBP $\beta$ , but critically depends on GSK3 and Arc and is accompanied by a significant increase in synaptic GSK3 $\beta$  activation and GluR1 expression. Because C/EBP $\beta$  is significantly upregulated for more than 28 h after training<sup>14</sup>, it is possible that this induction is sufficient to also mediate the memory enhancement. Alternatively, the enhancement may use mechanisms either downstream of C/EBP $\beta$  or distinct from those mediating consolidation. Thus, the IGF-II-dependent enhancement might not recruit the activation of new cells, but rather uses those that have been transcriptionally ‘marked’ by training and target synaptic mechanisms, possibly those at activated synapses. One of these mechanisms might be GSK3-regulated GluR1 synaptic mobilization, a hypothesis in line with previous reports of functional links between dendritic trafficking of GluR1 and GSK-3 (ref. 29), as well as between GluR1 and Arc expression, synaptic plasticity and memory consolidation<sup>25</sup>. We cannot exclude that IGF-II-dependent memory enhancement may occur via recruitment of new cell activation, which however would be independently from the activation and function of CREB-C/EBP $\beta$ .

Thus, IGF-II may be a novel target for cognitive enhancement therapies.

## METHODS SUMMARY

Inhibitory avoidance, contextual and auditory fear conditioning: all behavioural procedures were performed as described in refs 15,37,38.

Cannulae implants, hippocampal and amygdala injections were done as described in refs 37,39. Chromatin immunoprecipitation (ChIP) was done as described in ref. 40. Western, northern blot and PCR analyses were carried out as described in ref. 37. Electrophysiology methods were conducted as described in ref. 41.

Statistical analysis: one- or two-way analysis of variance (ANOVA) followed by the Newman–Keuls or Bonferroni post hoc test, and Student’s *t*-test were used.

**Full Methods** and any associated references are available in the online version of the paper at [www.nature.com/nature](http://www.nature.com/nature).

**Received 20 August; accepted 15 November 2010.**

- McGaugh, J. L. Memory—a century of consolidation. *Science* **287**, 248–251 (2000).
- Alberini, C. M. Transcription factors in long-term memory and synaptic plasticity. *Physiol. Rev.* **89**, 121–145 (2009).
- Kandel, E. R. The molecular biology of memory storage: a dialog between genes and synapses. *Biosci. Rep.* **21**, 565–611 (2001).
- Silva, A. J., Kogan, J. H., Frankland, P. W. & Kida, S. CREB and memory. *Annu. Rev. Neurosci.* **21**, 127–148 (1998).
- Bailey, C. H. & Kandel, E. R. Structural changes accompanying memory storage. *Annu. Rev. Physiol.* **55**, 397–426 (1993).
- Kida, S. *et al.* CREB required for the stability of new and reactivated fear memories. *Nature Neurosci.* **5**, 348–355 (2002).
- Milekic, M. H., Pollonini, G. & Alberini, C. M. Temporal requirement of C/EBP $\beta$  in the amygdala following reactivation but not acquisition of inhibitory avoidance. *Learn. Mem.* **14**, 504–511 (2007).
- Nader, K., Schafe, G. E. & LeDoux, J. E. Fear memories require protein synthesis in the amygdala for reconsolidation after retrieval. *Nature* **406**, 722–726 (2000).
- Shamblott, M. J., Leung, S., Greene, M. W. & Chen, T. T. Characterization of a teleost insulin-like growth factor II (IGF-II) gene: evidence for promoter CCAAT/enhancer-binding protein (C/EBP) sites, and the presence of hepatic C/EBP. *Mol. Mar. Biol. Biotechnol.* **7**, 181–190 (1998).
- Russo, V. C., Gluckman, P. D., Feldman, E. L. & Werther, G. A. The insulin-like growth factors system and its pleiotropic functions in brain. *Endocr. Rev.* **26**, 916–943 (2005).
- Hawkes, C. & Kar, S. The insulin-like growth factor-II/mannose-6-phosphate receptor: structure, distribution and function in the central nervous system. *Brain Res. Brain Res. Rev.* **44**, 117–140 (2004).
- Kitraki, E., Bozas, E., Philippidis, H. & Stylianopoulou, F. Aging-related changes in IGF-II and c-fos gene expression in the rat brain. *Int. J. Dev. Neurosci.* **11**, 1–9 (1993).
- Kar, S., Chabot, J. G. & Quirion, R. Quantitative autoradiographic localization of [<sup>125</sup>I]insulin-like growth factor I, [<sup>125</sup>I]insulin-like growth factor II, and [<sup>125</sup>I]insulin receptor binding sites in developing and adult rat brain. *J. Comp. Neurol.* **333**, 375–397 (1993).
- Taubenfeld, S. M. *et al.* Fornix-dependent induction of hippocampal CCAAT enhancer-binding protein  $\beta$  and  $\delta$  co-localizes with phosphorylated cAMP response element-binding protein and accompanies long-term memory consolidation. *J. Neurosci.* **21**, 84–91 (2001).
- Taubenfeld, S. M., Milekic, M. H., Monti, B. & Alberini, C. M. The consolidation of new but not reactivated memory requires hippocampal C/EBP $\beta$ . *Nature Neurosci.* **4**, 813–818 (2001).
- Liang, K. C. *et al.* Post-training amygdaloid lesions impair retention of an inhibitory avoidance response. *Behav. Brain Res.* **4**, 237–249 (1982).
- Alberini, C. M. Mechanisms of memory stabilization: are consolidation and reconsolidation similar or distinct processes? *Trends Neurosci.* **28**, 51–56 (2005).
- Nader, K., Schafe, G. E. & LeDoux, J. E. The labile nature of consolidation theory. *Nature Rev. Neurosci.* **1**, 216–219 (2000).
- Eisenberg, M. & Dudai, Y. Reconsolidation of fresh, remote, and extinguished fear memory in medaka: old fears don’t die. *Eur. J. Neurosci.* **20**, 3397–3403 (2004).
- Milekic, M. H. & Alberini, C. M. Temporally graded requirement for protein synthesis following memory reactivation. *Neuron* **36**, 521–525 (2002).
- Suzuki, A. *et al.* Memory reconsolidation and extinction have distinct temporal and biochemical signatures. *J. Neurosci.* **24**, 4787–4795 (2004).
- Litvin, O. O. & Anokhin, K. V. Mechanisms of memory reorganization during retrieval of acquired behavioral experience in chicks: the effects of protein synthesis inhibition in the brain. *Neurosci. Behav. Physiol.* **30**, 671–678 (2000).
- Debiec, J., LeDoux, J. E. & Nader, K. Cellular and systems reconsolidation in the hippocampus. *Neuron* **36**, 527–538 (2002).
- Nissley, S. P. & Rechler, M. M. Somatomedin/insulin-like growth factor tissue receptors. *Clin. Endocrinol. Metab.* **13**, 43–67 (1984).
- Bramham, C. R., Worley, P. F., Moore, M. J. & Guzowski, J. F. The immediate early gene *Arc/Arg3.1*: regulation, mechanisms, and function. *J. Neurosci.* **28**, 11760–11767 (2008).
- Whitlock, J. R., Heynen, A. J., Shuler, M. G. & Bear, M. F. Learning induces long-term potentiation in the hippocampus. *Science* **313**, 1093–1097 (2006).
- Slipczuk, L. *et al.* BDNF activates mTOR to regulate GluR1 expression required for memory formation. *PLoS ONE* **4**, e6007 (2009).
- Kessels, H. W. & Malinow, R. Synaptic AMPA receptor plasticity and behavior. *Neuron* **61**, 340–350 (2009).
- Wei, J., Liu, W. & Yan, Z. Regulation of AMPA receptor trafficking and function by glycogen synthase kinase 3. *J. Biol. Chem.* **285**, 26369–26376 (2010).
- Scalia, P. *et al.* Regulation of the Akt/glycogen synthase kinase-3 axis by insulin-like growth factor-II via activation of the human insulin receptor isoform-A. *J. Cell. Biochem.* **82**, 610–618 (2001).
- Dajani, R. *et al.* Crystal structure of glycogen synthase kinase 3 $\beta$ : structural basis for phosphate-primed substrate specificity and autoinhibition. *Cell* **105**, 721–732 (2001).
- Cooke, S. F. & Bliss, T. V. Plasticity in the human central nervous system. *Brain* **129**, 1659–1673 (2006).
- Alberini, C. M., Milekic, M. H. & Tronel, S. Mechanisms of memory stabilization and de-stabilization. *Cell. Mol. Life Sci.* **63**, 999–1008 (2006).
- Milner, B., Squire, L. R. & Kandel, E. R. Cognitive neuroscience and the study of memory. *Neuron* **20**, 445–468 (1998).

35. Maviel, T., Durkin, T. P., Menzaghi, F. & Bontempi, B. Sites of neocortical reorganization critical for remote spatial memory. *Science* **305**, 96–99 (2004).
36. Nadel, L. & Land, C. Memory traces revisited. *Nature Rev. Neurosci.* **1**, 209–212 (2000).
37. Garcia-Osta, A. *et al.* Musk expressed in the brain mediates cholinergic responses, synaptic plasticity, and memory formation. *J. Neurosci.* **26**, 7919–7932 (2006).
38. Muravieva, E. V. & Alberini, C. M. Limited efficacy of propranolol on the reconsolidation of fear memories. *Learn. Mem.* **17**, 306–313 (2010).
39. Tronel, S. & Alberini, C. M. Persistent disruption of a traumatic memory by postretrieval inactivation of glucocorticoid receptors in the amygdala. *Biol. Psychiatry* **62**, 33–39 (2007).
40. Tsankova, N. M., Kumar, A. & Nestler, E. J. Histone modifications at gene promoter regions in rat hippocampus after acute and chronic electroconvulsive seizures. *J. Neurosci.* **24**, 5603–5610 (2004).
41. Tsokas, P. *et al.* Local protein synthesis mediates a rapid increase in dendritic elongation factor 1A after induction of late long-term potentiation. *J. Neurosci.* **25**, 5833–5843 (2005).

**Supplementary Information** is linked to the online version of the paper at [www.nature.com/nature](http://www.nature.com/nature).

**Acknowledgments** This work was supported by grants R01-MH065635, R01-MH074736, NARSAD, the Hirschl Foundation and Philoctetes Foundation awarded to C.M.A., F31-MH816213 to D.Y.C., and T32-MH087004 to S.A.S.; R21-DA29298 and R01-GM054508 to R.D.B. We thank M. Baxter for assistance with statistical analyses. We thank J. Feng, J.-W. Koo and C.-Y. Lu for technical assistance. We thank A. Suzuki and A. Arguello for comments on the manuscript. We thank R. Miller and the Center for Comparative Medicine and Surgery Facility at Mount Sinai School of Medicine for technical support.

**Author Contributions** D.Y.C., A.G.-O. and C.M.A. designed and developed this study. D.Y.C., S.A.S. and A.G.-O. carried out the behavioural studies. D.Y.C., A.G.-O., G.P. and D.B.-M. carried out the biochemical studies and analyses. R.D.B. and B.S.-R. designed and conducted the electrophysiology experiments. D.Y.C. and C.M.A. wrote the manuscript.

**Author Information** Reprints and permission information are available at [www.nature.com/reprints](http://www.nature.com/reprints). The authors declare competing financial interests: details accompany the full-text HTML version of the paper at [www.nature.com/nature](http://www.nature.com/nature). Correspondences and requests for materials should be sent to C.M.A. (Cristina.Alberini@mssm.edu).

## METHODS

**Animals.** Long Evans adult male rats (Harlan) weighing between 200 and 250 g at the beginning of the experiments were used. Rats were housed individually on a 12 h light-dark cycle with *ad libitum* access to food and water. All experiments were done during the light cycle between 9 a.m. and 6 p.m. All rats were handled for 2–3 min per day for 5 days before any behavioural procedure. All protocols complied with the National Institute of Health Guide for the Care and Use of Laboratory Animals and were approved by the Mount Sinai School of Medicine Animal Care Committees.

**Inhibitory avoidance (IA).** IA was carried out as described previously<sup>15,37</sup>. The IA chamber (Med Associates) consisted of a rectangular Perspex box divided into a safe compartment and a shock compartment. The safe compartment was white and illuminated, whereas the shock compartment was black and dark. Foot shocks were delivered to the grid floor of the shock chamber via a constant current scrambler circuit. The apparatus was located in a sound-attenuated, non-illuminated room. During training sessions, each rat was placed in the safe compartment with its head facing away from the door. After 10 s, the door separating the compartments was automatically opened, allowing the rat access to the shock compartment; the rats usually enter the shock (dark) compartment within 10–20 s of the door opening. The door closed 1 s after the rat entered the shock compartment, and a brief foot shock (0.6 mA for 2 s for all experiments except for those of Fig. 6a which was done at 0.9 mA) was administered. Latency to enter the shock compartment was taken in seconds as acquisition. The rat was then returned to its home cage and tested for memory retention at the designated time-point(s). Retention tests were done by placing the rat back in the safe compartment and measuring its latency to enter the shock compartment. Foot shocks were not administered on the retention tests, and testing was terminated at 540 s or 900 s as indicated in the figures.

Controls consisted of rats that remained in their home cage (naive), rats exposed to the training apparatus without foot shock (–), or rats exposed to the training apparatus and to foot shock 1 h later (unpaired, Un).

In reactivation (reconsolidation) experiments, rats were trained as described and, at the indicated time points, were tested. This test reactivated the memory. Immediately after or at the designated time-points, rats were injected with the indicated compounds and subsequently tested again for retention.

During testing, the experimenter was blind to the treatments given.

**Contextual and auditory fear conditioning.** Fear conditioning was carried out as described previously<sup>38</sup>. Rats were conditioned in contextual fear conditioning chamber (CFC), which consisted of a rectangular Plexiglass box (30.5 × 24.1 × 21.0 cm) with a metal grid floor (Model ENV-008 Med Associates). All rats were pre-exposed to this chamber for 5 min. On the next day, rats were placed in the CFC chamber for 120 s and then presented with 30 s of the auditory cue consisting of a 5 kHz 75 dB tone that co-terminated with a 0.6 mA 2 s foot shock. One hundred twenty seconds after the first foot shock, another 30 s auditory cue was presented that also co-terminated with another 0.6 mA 2 s foot shock. Rats were returned to their home cage 120 s after the second foot shock. Freezing levels during the first 148 s (before the presentation of the first foot shock) was recorded, scored and reported as baseline freezing. Freezing was defined as lack of movement except for breathing. Twenty-four hour later, rats were placed back in the CFC chamber and their freezing levels recorded for 5 min and scored. Twenty-four hours after CFC test, rats were placed in a different context (the illuminated IA box) for 120 s before being presented with three 30 s auditory cues. The three 30 s auditory cues were separated by 120 s. Freezing levels during the cue presentations was recorded and scored by an experimenter who was blind to the treatment conditions.

**Cannulae implants and hippocampal and amygdala injections.** Hippocampal and amygdala injections were given as described previously<sup>15,37,39</sup>. Rats were anaesthetized with ketamine (65 mg per kg, intraperitoneally (i.p.)) and xylazine (7.5 mg per kg, i.p.), and stainless-steel guide cannulae (22-gauge) were stereotactically implanted to bilaterally target the hippocampus (4.0 mm posterior to the bregma; 2.6 mm lateral from midline; and 2.0 mm ventral). For amygdala injections, 26-gauge guide cannulae were implanted to target the basolateral amygdala bilaterally (2.8 mm posterior to bregma; 5.3 mm lateral from midline; and 6.25 mm ventral). The rats were returned to their home cages and allowed to recover from surgery for 7 days. At the indicated time points before or after training or retrieval, rats received bilateral injections of compounds as specified. All injections are indicated by arrow in the experimental schedule. All hippocampal injections were carried out in 1 µl per side, whereas all amygdala injections were done in 0.5 µl per side. Hippocampal injections used a 28-gauge needle and amygdala injections used 33-gauge needles that extended 1.5 mm beyond the tip of the guide cannula and connected via polyethylene tubing to a Hamilton syringe. The infusions were delivered at a rate of 0.33 µl min<sup>−1</sup> using an infusion pump. The injection needle was left in place for 2 min after the injection to allow complete dispersion of the solution.

To verify proper placement of cannula implants, at the end of the behavioural experiments, rats were anaesthetized and perfused with 4% paraformaldehyde in PBS. Their brains were post-fixed overnight in the same fixative with 30% sucrose. Forty-micrometer coronal sections were cut through the hippocampus, stained with cresyl violet, and examined under a light microscope. Rats with incorrect cannula placement were discarded from the study.

Antisense ODNs and relative scrambled sequences (SC-ODNs) were injected at 2 nmol µl<sup>−1</sup> in all antisense experiments. Sequences: C/EBPβ antisense (β-ODN: 5′-CCAGCAGGCGGTGCATGAAC-3′), C/EBPβ scrambled (SC-ODN: 5′-TCG GAGACTAAGCGCGGCAC-3′); IGF-II antisense (IGF-II-ODN: 5′-CCCATTGGTACCTGAAGTTG-3′); IGF-II scrambled (SC-ODN: 5′-CGCCTTGTGATACGACTTAG-3′); Arc antisense (Arc-ODN: 5′-GTCCAGCTCCATCTGCTCGC-3′); and Arc scrambled (SC-ODN: 5′-CGTGCCCTCTCGCAGCTTC-3′). Vehicle: phosphate-buffered saline (PBS, pH 7.4). The antisense for C/EBPβ has been previously shown to knockdown C/EBPβ in the hippocampus<sup>15</sup>. The antisense for IGF-II mRNA was specific for the sequence that includes the translational start site and was previously used successfully to knockdown IGF-II in other tissues<sup>42</sup>. The antisense for Arc has been previously shown to block Arc protein expression and long-term memory consolidation when injected into the hippocampus<sup>43</sup>. The respective SC-ODNs, which served as control, contained the same base composition but in a random order and show no homology to sequences in the GenBank database. All ODNs were phosphorothioated on the three terminal bases of both 5′ and 3′ ends to produce increased stability. Both ODNs were reverse-phased-cartridge-purified and obtained from Gene Link.

Recombinant IGF-I and IGF-II were purchased from R&D Systems and were dissolved in 0.1% bovine serum albumin (BSA) in 1 × PBS. All experiments with recombinant IGF-II or IGF-I were carried out with 250 ng per injection, except for the dose–response curve (250, 25 or 2.5 ng) and for those in Fig. 5a where 25 ng was used.

The IGF-I receptor (IGF-IR) antagonist JB1 (Bachem Biosciences) was dissolved in PBS. JB1 was injected at 20 ng µl<sup>−1</sup>, a concentration that has been used successfully to block IGF-1 activity in various tissues, including the brain<sup>44,45</sup>. Anti-IGF-II receptor antibody (anti-IGF-IIR, R&D Systems) was dissolved in 1 × PBS and injected at 5 ng µl<sup>−1</sup>. This concentration blocked 95% of IGF-II receptor in an *in vitro* binding assay (R&D).

Anisomycin (Sigma Aldrich) was dissolved in 0.9% saline pH 7.4 and injected at 125 µg µl<sup>−1</sup>. This dose blocks more than 80% of protein synthesis in the dorsal hippocampus for up to 6 h (ref. 46).

GSK3 inhibitor SB216763 was purchased from Sigma and was dissolved in 1% DMSO in PBS and injected at 1 ng µl<sup>−1</sup>. This dose has been shown to block GSK3β activity (as measured by its dephosphorylation levels) in the brain<sup>47</sup>.

**Synaptoneurosomal preparation and western blot analysis.** Synaptoneurosomal preparation was adapted from ref. 48. Briefly, dorsal hippocampi were rapidly dissected in ice-cold cortical dissection buffer followed by homogenization in buffer containing 10 mM HEPES, 2 mM EDTA, 2 mM EGTA, 0.5 mM DTT, phosphatase and protease inhibitor cocktails (Sigma). A glass-Teflon homogenizer was used and homogenates were filtered through 100 µm nylon mesh filter and 5 µm nitrocellulose filters sequentially. Synaptoneurosomes were obtained by centrifuging the filtrate at 1,000g for 10 min. Synaptoneurosomal fraction was enriched for PSD-95 and N-methyl-D-aspartic acid (NMDA) receptor subunit NR-1 (Supplementary Fig. 10).

Western blot analysis was done as reported previously<sup>15,37</sup>. Hippocampal total extracts from rat were obtained by Polytron homogenization in cold lysis buffer with protease and phosphatase inhibitors (0.2 M NaCl, 0.1 M HEPES, 10% glycerol, 2 mM NaF, 2 mM Na<sub>2</sub>P<sub>2</sub>O<sub>7</sub>, 4 U ml<sup>−1</sup> aprotinin, 2 mM DTT, 1 mM EGTA, 1 µM microcystin, 1 mM benzamide). Protein concentrations were determined using the Bio-Rad protein assay (Bio-Rad Laboratories). Equal amounts of total protein (10–20 µg per lane) were resolved on denaturing SDS–PAGE gels and transferred to Hybond-P membranes (Millipore) by electroblotting. Membranes were dried and then reactivated in methanol for 5 min and then washed with three changes of water. The membrane was then blocked in 3% milk/PBS or according to manufacturers' instruction for 1 h at room temperature, then incubated with either anti-IGF-II (1/500, Millipore), or anti-actin (1/5,000, Santa Cruz Biotechnology) antisera in PBS overnight at 4 °C. Anti-phospho-CREB (1/1,000), anti-GluR1 (1/2,000), anti-GluR2 (1/2,000), anti-PSD95 (1/5,000) and anti-NR1 (1/1,000) antibodies were purchased from Millipore. Anti-C/EBPβ antibody was purchased from Santa Cruz Biotechnology (1/1,000). pGSK3β and GSK3β antibodies were purchased from Cell Signaling (1/1,000). pGSK3β was normalized to actin and GSK3β. The colloidal gold total protein stain was purchased from Bio-Rad. The membranes were washed, treated with a secondary horseradish peroxidase-labelled donkey anti-rabbit antibody (1/4,000, GE Healthcare) for 1 h, washed again and incubated with HRP-streptavidin complex and ECL detection reagents

(GE Healthcare). Membranes were exposed to HyBlotCL (Denville Scientific), and quantitative densitometric analysis was performed using NIH ImageJ.

**Real time quantitative RT-PCR.** Hippocampal total RNA was extracted with TRIzol (Invitrogen) and reverse-transcribed using SuperScript II RNase H minus RT (Invitrogen). Real-time PCR was done with an ABI Prism 7900HT (Applied Biosystems). Five hundred picograms of the first-strand cDNA was subjected to PCR amplification using a QuantiTect SYBR Green PCR kit (Qiagen). IGF-II primers (forward: 5'-CCCAGCGAGACTCTGTGCGGA-3'; reverse: 5'-GGAA GTACGGCCTGAGAGGTA-3'); IGF-I primers (forward: 5'-CCTGGGCTTT GTTTCACTTCGG-3'; reverse: 5'-CACAGCTCCGGAAGCAACACTCA-3'). Forty cycles of PCR amplification were performed as follows: denaturation at 95 °C for 30 s, annealing at 55 °C for 30 s and extension for 30 s at 72 °C. Three PCR assays with triplicates were performed for each cDNA sample. 18S rRNA (forward, 5'-CGCCGCTAGAGGTGAAATTCT-3'; reverse, 5'-CAGACCTCC GACTTCGTTCT-3') was used as internal controls. Data were analysed with Sequence Detector System version 2.0 software (Applied Biosystems). The cycle threshold method ( $C_T$ , see Applied Biosystems User Bulletin Number 2, P/N 4303859) was chosen to determine the relative quantification of gene expression in trained and control rats.

**Chromatin immunoprecipitation (ChIP).** ChIP was performed as described in ref. 40. The rat hippocampi were dissected and minced into ~1 mm pieces, and immediately cross-linked in 1% formaldehyde for 17 min at room temperature rotating. The cross-linking reaction was stopped by adding glycine to a final concentration of 0.125 M and incubated for 7 min. The tissue was washed five times in cold PBS containing protease inhibitor (Roche Applied Sciences) and then frozen on dry ice. The chromatin was solubilized and extracted by adding 500 µl of lysis buffer (1% SDS, 50 mM Tris-HCl pH 8.1, 10 mM EDTA), followed by sonication. The homogenate was diluted in 1.1 ml ChIP dilution buffer (1.1% Triton X-100, 167 mM NaCl, 16.7 mM Tris-HCl pH 8.1, 1.2 mM EDTA, 0.01% SDS). The homogenate was used for C/EBPβ ChIP. Magnetic Protein A beads (30 µl, EZ-Magna ChIP A kit; Millipore) and 5 µg of C/EBPβ antibody was added to the homogenate. The mixture was incubated rotating overnight in 4 °C. The wash, elution, and reverse cross-link to free DNA were all performed according to the manufacturer's protocol (EZ-Magna ChIP A kit).

Specific primers were designed to amplify the proximal promoter region of approximately 150 bp 5' of exon one of rat IGF-II (GenBank: X17012.1), which contains a putative C/EBP binding site. Putative C/EBP binding site was predicted using an on-line program AliBaba 2.1. Similar C/EBP binding sites have been identified in other species<sup>49,50</sup>. Primer sequences used: forward 5'-GGTTCCCC ACGTTAGGCTTGAT-3'; reverse 5'-TTGCGGCCCTGGGAATGAGTG-3'. A standard thirty-five cycle PCR was performed as followed: denaturation at 95 °C for 30 s, annealing at 58 °C for 30 s and extension for 30 s at 72 °C. The PCR reaction was resolved on a 2% agarose gel and sequenced. Sequencing confirmed the identity of the fragment. DNA sequencing was performed by W. M. Keck Facility at Yale University.

**Northern blot analysis.** Northern blot analyses were performed as described previously<sup>14</sup>. The rat IGF-II probe consisted of a 224-bp fragment corresponding to nucleotides 1145–1368 of the IGF-II sequence in GenBank accession number NM-031511. The same membrane was stripped and rehybridized with a full-length rat cyclophilin probe that was used as a loading control. Probes were labelled with random oligonucleotide primers (Prime-It II kit, Stratagene) and [ $\alpha$ -<sup>32</sup>P]dCTP (Amersham). Quantitative densitometry analysis was performed using NIH

Image J. Data were expressed as mean percentage  $\pm$  s.e.m. of the 0 h – (100%) control mean values.

**Electrophysiology methods.** Brains were removed from isoflurane-anaesthetized male Long-Evans rats (6–8 weeks old), and chilled in ice-cold ACSF (in mM: 1.25 NaH<sub>2</sub>PO<sub>4</sub>, 1.3 MgSO<sub>4</sub>, 2.5 CaCl<sub>2</sub>, 3.5 KCl, 15 glucose, 24 NaHCO<sub>3</sub>, and 118 NaCl) bubbled with 95% O<sub>2</sub>/5% CO<sub>2</sub> (pH 7.35). Acute transverse slices of dorsal hippocampus (400-µm thick) were recovered in an interface chamber at room temperature, as described previously<sup>41</sup>. Slices were individually transferred to a recirculating submersion recording chamber and superfused with ACSF at 30–32 °C. Field EPSPs (fEPSPs) were recorded with an ACSF-filled pipette (2–4 MΩ) positioned in stratum radiatum of area CA1, and Schaffer collateral inputs were stimulated with 50 µs monophasic pulses using a bipolar concentric electrode placed in area CA3. Weak HFS, which normally induces only transient synaptic potentiation<sup>41</sup>, consisted of two 1-s trains of 100 Hz pulses, delivered 20 s apart, with stimulus intensity set at 20% of the spike threshold.

IGF-II, freshly prepared from stock to a final concentration of 1 nM, was introduced 20 min before HFS was delivered and was present for the remainder of the experiment. The antibody against the IGF-II receptor was used at a final concentration of 16 or 50 µg ml<sup>-1</sup>, prepared fresh before use. As these two concentrations produced indistinguishable results, the data were pooled for analysis and presentation. The antibody was introduced at least 30 min before HFS was delivered, and remained in the superfusate for the rest of the experiment. The numbers for the electrophysiology experiment are: vehicle (wHFS:  $n = 4$ ; no stim.:  $n = 4$ ), IGF-II (wHFS:  $n = 5$ ; no stim.:  $n = 6$ ), IGF-II + anti-IGF-IIR antibody (wHFS:  $n = 5$ ; no stim.:  $n = 5$ ).

**Statistical analysis.** One- or two-way analysis of variance (ANOVA) followed by either the Newman–Keuls, or Bonferroni post hoc test, or Student's  $t$ -test was used for statistical analyses. For the electrophysiology experiments, EPSP slopes were compared by a Student's  $t$ -test.

42. Elizalde, P. V. *et al.* Involvement of insulin-like growth factors-I and -II and their receptors in medroxyprogesterone acetate-induced growth of mouse mammary adenocarcinomas. *J. Steroid Biochem. Mol. Biol.* **67**, 305–317 (1998).
43. Guzowski, J. F. *et al.* Inhibition of activity-dependent Arc protein expression in the rat hippocampus impairs the maintenance of long-term potentiation and the consolidation of long-term memory. *J. Neurosci.* **20**, 3993–4001 (2000).
44. Pietrzowski, Z. *et al.* Inhibition of cellular proliferation by peptide analogues of insulin-like growth factor 1. *Cancer Res.* **52**, 6447–6451 (1992).
45. Quesada, A. & Micevych, P. E. Estrogen interacts with the IGF-1 system to protect nigrostriatal dopamine and maintain motoric behavior after 6-hydroxydopamine lesions. *J. Neurosci. Res.* **75**, 107–116 (2004).
46. Milekic, M. H., Brown, S. D., Castellini, C. & Alberini, C. M. Persistent disruption of an established morphine conditioned place preference. *J. Neurosci.* **26**, 3010–3020 (2006).
47. Xu, C. M. *et al.* Glycogen synthase kinase 3β in the nucleus accumbens core mediates cocaine-induced behavioral sensitization. *J. Neurochem.* **111**, 1357–1368 (2009).
48. Elkobi, A. *et al.* ERK-dependent PSD-95 induction in the gustatory cortex is necessary for taste learning, but not retrieval. *Nature Neurosci.* **11**, 1149–1151 (2008).
49. Lo, J. H. & Chen, T. T. CCAAT/enhancer binding protein β2 is involved in growth hormone-regulated insulin-like growth factor-II gene expression in the liver of rainbow trout (*Oncorhynchus mykiss*). *Endocrinology* **151**, 2128–2139 (2001).
50. van Dijk, M. A., Rodenburg, R. J., Holthuisen, P. & Sussenbach, J. S. The liver-specific promoter of the human insulin-like growth factor II gene is activated by CCAAT/enhancer binding protein (C/EBP). *Nucleic Acids Res.* **20**, 3099–3104 (1992).

# Circadian clocks in human red blood cells

John S. O'Neill<sup>1</sup> & Akhilesh B. Reddy<sup>1</sup>

Circadian (~24 hour) clocks are fundamentally important for coordinated physiology in organisms as diverse as cyanobacteria and humans. All current models of the molecular circadian clockwork in eukaryotic cells are based on transcription–translation feedback loops. Non-transcriptional mechanisms in the clockwork have been difficult to study in mammalian systems. We circumvented these problems by developing novel assays using human red blood cells, which have no nucleus (or DNA) and therefore cannot perform transcription. Our results show that transcription is not required for circadian oscillations in humans, and that non-transcriptional events seem to be sufficient to sustain cellular circadian rhythms. Using red blood cells, we found that peroxiredoxins, highly conserved antioxidant proteins, undergo ~24-hour redox cycles, which persist for many days under constant conditions (that is, in the absence of external cues). Moreover, these rhythms are entrainable (that is, tunable by environmental stimuli) and temperature-compensated, both key features of circadian rhythms. We anticipate that our findings will facilitate more sophisticated cellular clock models, highlighting the interdependency of transcriptional and non-transcriptional oscillations in potentially all eukaryotic cells.

Circadian rhythms are a fundamental property of living cells. When held in temporal isolation, organisms from cyanobacteria to humans exhibit behavioural and physiological rhythms that persist with a period of approximately 24 h (ref. 1). These rhythms are driven by biological clocks, with two key features. First, their free-running period of ~24 h is temperature-compensated: biological clocks do not run slower at lower temperatures or speed up when hot. Second, they can synchronize to temporally relevant stimuli such as light, temperature or feeding schedules and thus their definition of internal time becomes predictive of external (solar) time<sup>2</sup>. Entrained in this way, circadian timing confers selective advantages to organisms by facilitating anticipation of, and thereby adaptation to, the alternating day–night cycle as well as temporally segregating mutually antagonistic processes<sup>3</sup>. The competitive value of circadian clocks has been demonstrated in prokaryotes and higher plants<sup>4,5</sup>, whereas disturbance of circadian timing in humans, as seen in rotational shift workers for example, carries significant long-term health costs<sup>6</sup>.

The molecular clock mechanism is invariably modelled by oscillating transcription–translation feedback, whereby clock proteins feedback to negatively regulate their own transcription, thereby producing rhythmic clock gene expression<sup>3</sup>. This model has recently been challenged by observations in the simplest organism known to exhibit circadian timing, the cyanobacterium *Synechococcus elongatus*, in which biochemical oscillations catalysed by several clock proteins occur even in the absence of transcription and translation<sup>7,8</sup>. Moreover, emerging evidence in multiple eukaryotic systems indicates that assorted cytosolic mechanisms are important to sustain rhythmicity<sup>9–13</sup>. A critical question that remains, therefore, is whether the nucleus is necessary for circadian rhythms in mammals.

Studying the role of the nucleus in circadian oscillations has been challenging, and in mammals, confined to studies using pharmacological inhibitors of transcription<sup>14</sup>. Such approaches are, however, limited by the pleiotropic effects of pharmacological manipulations ('off-target' effects), and because of their deleterious effects on cell survival<sup>14</sup>. To circumvent these issues, we developed a unique model system to study circadian rhythmicity, using naturally occurring anucleate mammalian cells—human red blood cells (RBCs). Conventional clock

gene/protein assays cannot be used in this system because they are not expressed in human RBCs (see Supplementary Table 1). We therefore developed novel indices of circadian rhythmicity that are not dependent on RNA production.

## Peroxiredoxins exhibit circadian redox rhythms

Peroxiredoxins (PRX) comprise a highly conserved family of anti-oxidant proteins that help to control intracellular peroxide levels<sup>15</sup>. They share a common catalytic mechanism whereby reducing peroxide, the catalytic active site cysteine residue (Cys<sub>P</sub>) is oxidized to a sulphenic acid (Cys-SOH), which then forms a disulphide bond with a resolving Cys residue (Cys<sub>R</sub>) that is reduced by thioredoxin. In a subclass of PRXs, namely the classical 2-Cys PRXs, a small fraction of the enzyme becomes catalytically inactive through substrate-mediated hyperoxidation of Cys<sub>P</sub> to the sulphinic and sulphonic acid forms (Cys-SO<sub>2</sub>/H), and is eventually recycled through ATP-dependent reduction by sulphiredoxin<sup>16</sup>. Given this mechanism of action, and that circadian post-translational modification of a PRX family member was observed previously<sup>17</sup>, we hypothesized that PRX oxidation may constitute a novel non-transcriptional rhythmic marker. To test this, we used human RBCs, which lack nuclei and therefore transcriptional capability, to directly test whether rhythms persist without active transcription.

We harvested blood from three age-matched healthy volunteers (subjects A, B and C), and prepared RBC fractions from whole blood. RBCs were then kept in constant conditions of temperature (37 °C) and light (complete darkness) and sampled at 4-hourly intervals for 60 h. Lysates were immunoblotted using an antibody specific to hyper-oxidized peroxiredoxin (PRX-SO<sub>2</sub>/3) to monitor the hyperoxidation status of PRX for each subject (Fig. 1a). For all subjects we observed robust, statistically significant cycling of PRX-SO<sub>2</sub>/3 with a period of ~24 h (Fig. 1a). The clearest and most robust rhythms were exhibited by the dimeric form of PRX (as shown in Fig. 1; a full blot image, illustrating all molecular mass species, is shown in Supplementary Fig. 5). Thus, circadian oscillation of post-translational modification of peroxiredoxins occurs in RBCs that are kept in free-running conditions (that is, in the absence of external time cues), reflecting an endogenous ~24-h (circadian) rhythm.

<sup>1</sup>Department of Clinical Neurosciences, University of Cambridge Metabolic Research Laboratories, Institute of Metabolic Science, University of Cambridge, Addenbrooke's Hospital, Cambridge CB2 0QQ, UK.

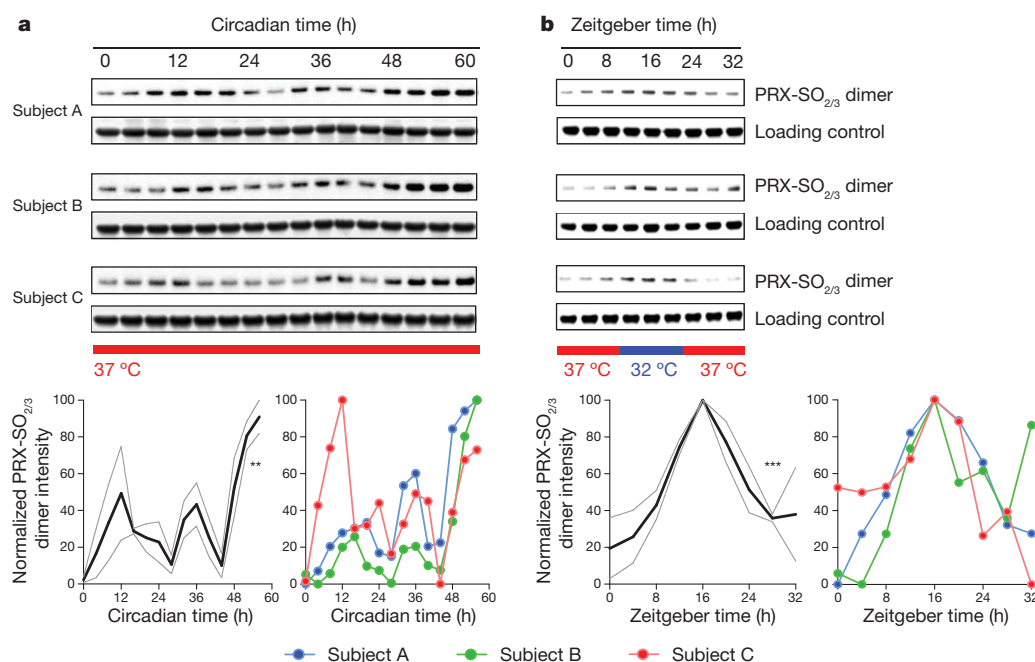


**Figure 1 | Circadian oscillation of peroxiredoxin (PRX) oxidation in human RBCs.** **a**, RBCs from three human subjects (A, B, C) were kept under constant conditions (at 37 °C, in total darkness) and sampled every 4 h. **b**, RBCs incubated in alternating 12-h cycles of high (37 °C) and low (32 °C) temperature. Representative immunoblots showing oxidized/hyperoxidized

To be a useful timing mechanism, or clock, circadian oscillations are tuneable by external cues so that they can be reset when misaligned<sup>18</sup>. When clocks are stably synchronized to an external cycle, they are said to be entrained. Cellular oscillators can be entrained by a variety of stimuli including light, temperature and feeding schedules<sup>3,19</sup>. We used temperature cycles to entrain cultures of RBCs because this is likely to be a physiologically relevant time cue as they circulate through the body over a typical day *in vivo*. Humans experience circadian variation in body temperature, rising to a peak in the late evening (~37.4 °C), and falling to reach a minimum (~36.8 °C) in the early morning<sup>20</sup>. We subjected purified RBCs to alternating 12-h cycles of high (37 °C) and low (32 °C) temperature for 2 cycles (48 h) before sampling every 4 h for a further 32 h. We observed PRX-SO<sub>2/3</sub> rhythms during temperature entrainment, with low levels seen at high temperatures, and higher levels at low temperatures (Fig. 1b). Notably, we observed differential entrainment of samples that started in the same phase, but through temperature entrainment, ended up in opposite phases (Supplementary Fig. 1). Together, these results therefore identify PRX oxidation–reduction rhythms as robust, entrainable circadian rhythms in cells lacking the ability to make new RNA.

### PRX rhythms persist despite synthetic blockade

A possible alternative explanation for rhythmicity in our assays could be due to oscillation of contaminating nucleated white blood cells. However, it was clear that at normal ratios, even in whole blood, the maximum number of white cells that could be present cannot contribute significantly to any signal that we observed (Supplementary Fig. 2). To substantiate this beyond reasonable doubt, we performed experiments in the presence and absence of well described transcriptional and translational inhibitors, which should only have effects if nucleated cells contribute significantly to observed PRX oxidation cycles. RBCs were entrained in temperature cycles, as above, and then placed into free-running conditions at 37 °C in darkness. Those incubated with the potent cell-permeable transcriptional blocker  $\alpha$ -amanitin oleate had highly reproducible circadian rhythms that, surprisingly, were even more robust than vehicle-treated control RBCs (Fig. 2a and Supplementary Fig. 3a). Quantification of PRX-SO<sub>2/3</sub> expression revealed no significant

peroxiredoxin (PRX-SO<sub>2/3</sub>) dimer are shown with loading controls. Quantification by densitometry is shown below. Values were normalized to the maximum for each blot. Solid line represents mean normalized intensity, with grey lines indicating s.e.m. boundaries. \*\**P* < 0.01, \*\*\**P* < 0.001 by 1-way ANOVA (effect of time).

difference between the two treatment groups by 2-way analysis of variance (ANOVA) (Fig. 2a). Similar results were obtained with cycloheximide, a eukaryotic translation inhibitor (Fig. 2b and Supplementary Fig. 3b). Given that the RBCs were cultured in the presence of antibiotics, we strongly believe that the rhythms we observe in peroxiredoxin oxidation arise only from RBCs and that other cell types, eukaryotic or otherwise, do not contribute to the oscillations we observe *in vitro*.

### Temperature compensation of circadian rhythms in RBCs

A key property of circadian clocks is that their free-running period length remains ~24 h despite being held at quite different temperatures under steady-state conditions, that is, they are temperature-compensated. To determine if PRX oxidation rhythms exhibit this property, we entrained RBCs in temperature cycles, and then allowed them to free-run at either 37 °C or 32 °C (Fig. 3). When released into free-run at the two temperatures, oscillations of PRX-SO<sub>2/3</sub> were very similar (Fig. 3). We also attempted to culture the RBCs at a higher temperature (42 °C), but found that this was toxic to the cells after 2 days of incubation (they displayed profound haemolysis), precluding any further assessment of PRX rhythms at this temperature *in vitro*. Together, our findings therefore show that RBCs cultured *in vitro* exhibit free-running, temperature-compensated, entrainable circadian rhythms of peroxiredoxin oxidation, indicative of the presence of a functioning clock in these non-nucleated cells.

### Peroxiredoxin rhythms are complex in their phenotype

Having established robust circadian oscillations of peroxiredoxin oxidation, we next sought to determine further the nature of these oscillations. Peroxiredoxins are highly conserved across the major phylogenetic kingdoms (eukaryotes, archaea and bacteria)<sup>15</sup>. In mammals, there are six PRX paralogues, and they differ in subcellular localization and their antioxidant mechanism<sup>21</sup>. To dissect which peroxiredoxin(s) are relevant to the observed PRX-SO<sub>2/3</sub> rhythms in RBCs, we determined the expression of PRX1–PRX6 (also called PRDX1–PRDX6) in human RBCs and nucleated mouse fibroblast (NIH3T3) cells (Fig. 4a). We focused particularly on PRX2 because of

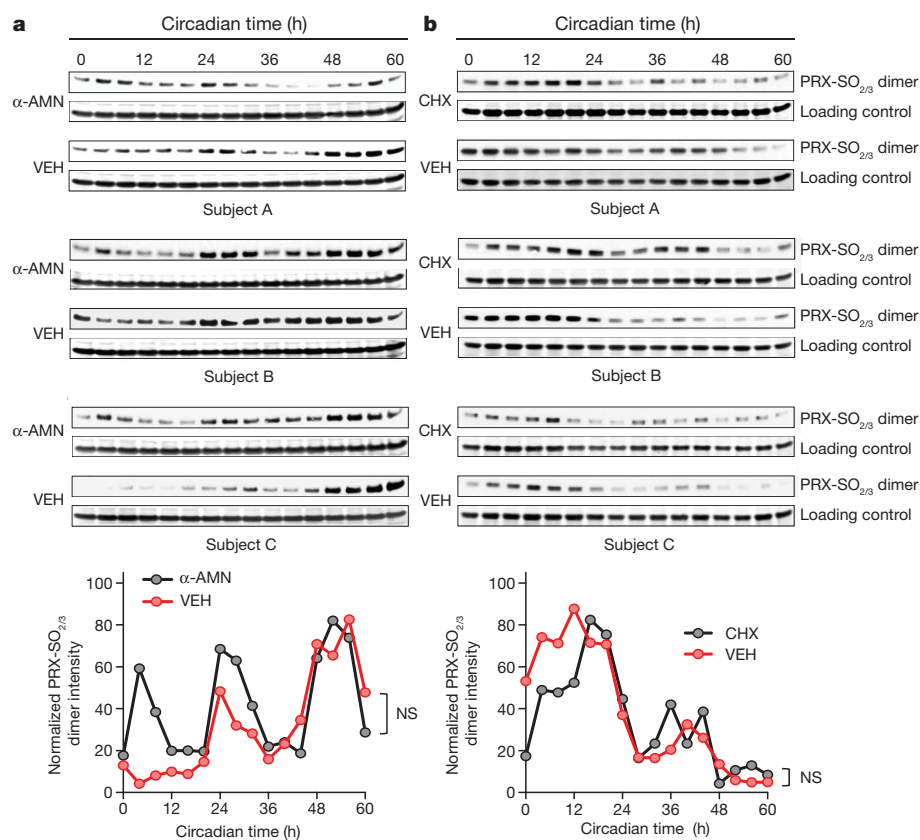


**Figure 2 | Circadian rhythms of peroxiredoxin (PRX) oxidation are not affected by transcriptional and translational inhibition.**

RBCs were entrained under temperature cycles and then kept under constant conditions (at 37 °C, in total darkness) and sampled every 4 h.

**a, b,** Representative immunoblots showing oxidized/hyperoxidized peroxiredoxin (PRX-SO<sub>2/3</sub>) dimer are shown for samples incubated with  $\alpha$ -amanitin (**a**;  $\alpha$ -AMN), or cycloheximide (**b**; CHX) for the entirety of the experiments. Quantification by densitometry is shown below. Values were normalized to the maximum for each blot. Each point represents a mean normalized intensity. NS, not significant; VEH, vehicle. Further details are shown in Supplementary Fig. 3.

its very high expression in RBCs and documented reversible behaviour under oxidizing and reducing conditions<sup>22</sup> (Fig. 4b). As well as the dimeric form of PRX, other electrophoretic forms exist. Interestingly, although clearly rhythmic, different oligomeric forms of PRX1/PRX2 and PRX-SO<sub>2/3</sub> displayed distinct phase relationships, indicating the possibility of ‘shuttling’ between the forms by reversible oligomerization (Supplementary Figs 4c and 5). PRX species thus display complex

and probably interlinked time-varying oligomerization behaviour, some of which is overtly circadian (Fig. 4b–d).

### Circadian rhythms in reversible haemoglobin oxidation

Given the robust circadian rhythms of PRX oxidation, we next explored the possible mechanisms that might underlie them. RBCs transport oxygen in the blood, and haemoglobin is essential for this.

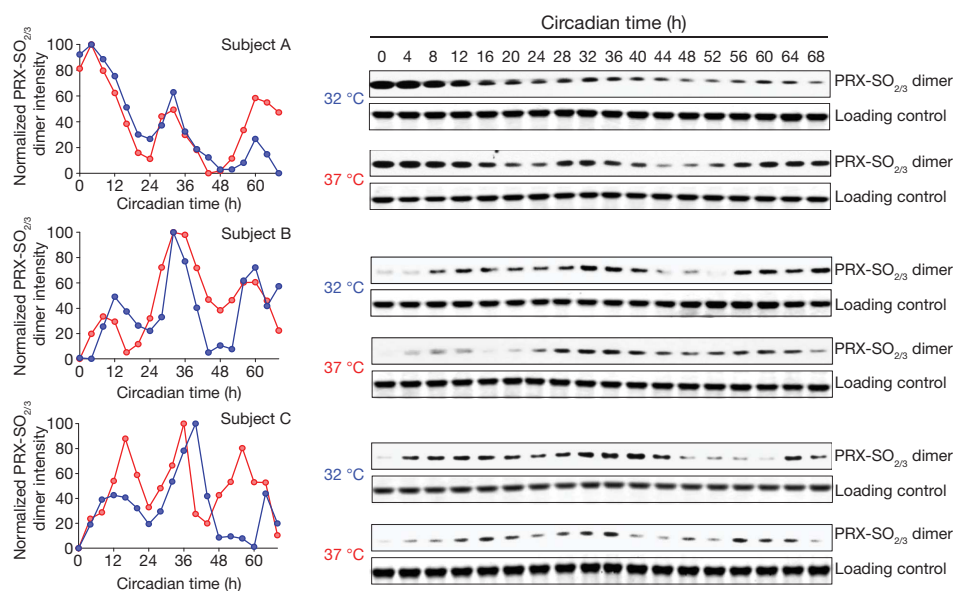


**Figure 3 | Temperature compensation of circadian peroxiredoxin oxidation rhythms.** RBCs were entrained in temperature cycles (12 h at 32 °C, 12 h at 37 °C) for two complete cycles and then kept under a constant temperature of either 32 °C or 37 °C for the rest of the experiment and sampled every 4 h as before. Immunoblots for oxidized/hyperoxidized peroxiredoxin (PRX-SO<sub>2/3</sub>)

dimer from RBC lysates from subjects A, B and C are shown. Loading controls (Coomassie-stained gels showing haemoglobin monomer bands) for each blot are also shown. Quantification of the above immunoblots by densitometry is shown on the left of the figure.

Haemoglobin itself is a source of peroxide intracellularly via auto-oxidation<sup>23</sup>. Because the dimeric form of haemoglobin displays a ~13-fold higher auto-oxidation rate than the tetramer<sup>24</sup>, we hypothesized that circadian modulation of haemoglobin tetramer–dimer equilibrium might be linked with rhythms in PRX state. Unlike the normal haemoglobin tetramer, the dimer displays no cooperativity<sup>25</sup>, and is also far more readily auto-oxidized to methaemoglobin (metHb)<sup>24</sup>, doubly impairing its ability to transport oxygen. Therefore, if the tetramer/dimer ratio, and thus metHb formation rate, were clock-regulated, a circadian variation in oxygen-carrying ability would be expected. Given that blood gas measurements (oxygen concentration) have been shown to be diurnally regulated *in vivo*<sup>26</sup>, this line of enquiry seemed promising. To test our theory, we used intrinsic front-face fluorescence as a real-time assay of rhythmicity<sup>27</sup>. We measured front-face fluorescence from RBCs for more than 60 h under free-running conditions and observed highly reproducible circadian oscillations (Fig. 5a and Supplementary Fig. 6a). This strongly indicates reversible low-amplitude oxidation of haemoglobin in RBCs, even when held *in vitro*.

### Circadian rhythms in red blood cell metabolism

How might rhythms in peroxiredoxins and haemoglobin oxidation interconnect with metabolic pathways in RBCs? The archetypal reducing equivalents NADH and NADPH lie at the core of cellular redox reactions, and thus might be expected to be rhythmic in RBCs<sup>27–29</sup>. We therefore assayed NADH/NADPH in RBCs sampled under free-running conditions, and indeed found ~24-h rhythms of abundance (Fig. 5b and Supplementary Fig. 6b, c).

Given that red blood cells are dependent on glycolysis for ATP synthesis, and that this contributes significantly to NADH flux, we also assayed the levels of ATP in red blood cells. Although levels dampen rapidly over the first 48 h of sampling, we observed two cycles of circadian oscillation of ATP (Supplementary Fig. 6d), supporting the idea that the cycles we observe are metabolic in origin. It is unclear how these low-amplitude circadian oscillations of ATP relate to well-described short period (~10 min) glycolytic cycles<sup>30–32</sup>. A possibility that remains to be tested is whether these rapid oscillations underlie

circadian oscillations of ATP, although red blood cells may not be the ideal platform for resolving this.

### Peroxiredoxin rhythms in nucleated cells

Of particular interest is the circadian oscillation of NADH/NADPH in RBCs, because direct modulation of the DNA-binding activity of the core circadian transcription factors Clock and Bmal1 by NADH/NADPH could couple ‘cytoplasmic’ and ‘nuclear’ rhythms in nucleated cells<sup>33,34</sup> (Supplementary Fig. 8). We therefore mapped the expression of peroxiredoxins in mouse NIH3T3 cells, the best characterized cellular clock model system<sup>14,35</sup>. Prx1 and Prx6 exhibited high-amplitude circadian cycles, as did oxidized Prx-SO<sub>2/3</sub> (Fig. 6a). Thus, anucleate RBCs and nucleated cells share common components displaying circadian rhythms.

To examine cross-talk between cytosolic and nuclear rhythms in modulating peroxiredoxin oxidation, we assayed mouse embryonic fibroblasts (MEFs) from *Cry1 Cry2* double-knockout mice, which lack cyclical expression of known clock genes/proteins<sup>36,37</sup>. Cells were sampled under conditions to mimic conditions used in our RBC experiments (Fig. 6b, c). Although present in *Cry1 Cry2* knockout cells, rhythms in peroxiredoxin oxidation were altered relative to those seen in wild-type MEFs, with an apparently lengthened period of oscillation (Fig. 6b, c). Therefore, in nucleated cells, peroxiredoxin rhythms are influenced by the transcription–translation feedback loop (Supplementary Fig. 9). This implies direct coupling between nuclear and cytoplasmic rhythms in nucleated cells.

Thus far, peroxiredoxins have been treated purely as a rhythmic biomarker, but peroxiredoxins could affect the transcription–translation feedback loop. To assess this, we interrogated a recent genome-wide RNA interference screen which sought to identify genes modifying circadian transcription in human U2OS cells<sup>38</sup>. Knockdown of *PRX2* and *PRX4* resulted in a long-period phenotype, whereas short interfering RNAs directed against *PRX3* and *PRX5* depressed the amplitude of circadian oscillations (Supplementary Fig. 7 and Supplementary Table 2). Therefore, in nucleated cells, there is likely to be an intricate interplay between transcription-dependent processes and non-transcriptional

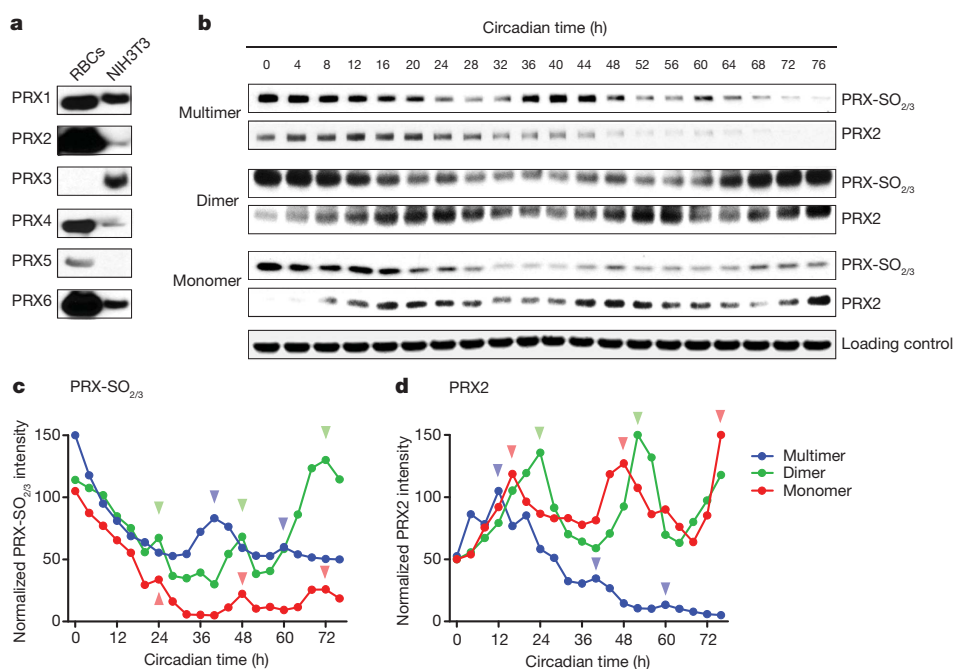


**Figure 4 | Expression patterns and oligomerization of peroxiredoxins.**

**a**, Immunoblots showing expression of the human peroxiredoxin paralogues (PRX1–PRX6) in RBCs and in mouse NIH3T3 cells. Loading of each lane was approximately equal. **b**, Oligomerization patterns of PRX and PRX-SO<sub>2/3</sub> in RBCs. After two cycles of temperature entrainment, cells were kept under

constant temperature (37 °C) for the rest of the experiment, and sampled every 4 h. Representative immunoblots for PRX2 and PRX-SO<sub>2/3</sub> are shown. Whole blot images in Supplementary Fig. 5 illustrate the different oligomeric forms. **c**, **d**, Immunoblots were quantified by densitometry for PRX-SO<sub>2/3</sub> (**c**) and PRX2 (**d**). Arrowheads indicate peaks of abundance.

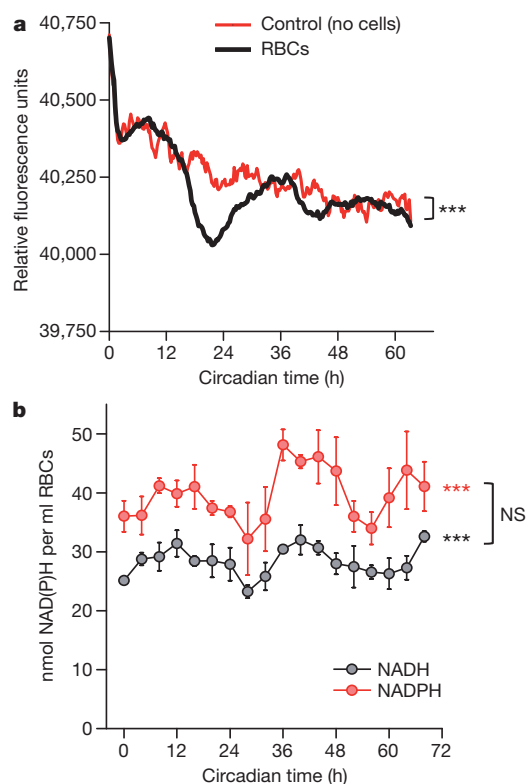


**Figure 5 | Circadian rhythms in haemoglobin oxidation and RBC metabolism.** **a**, Intrinsic front-face fluorescence measurements of RBCs and controls. Experiments were performed under constant conditions (at 37 °C, in total darkness). Mean values for each time point are shown (individual traces and further details are in Supplementary Fig. 6a). Two-way ANOVA (group  $\times$  time) ( $***P < 0.001$ ). **b**, NADH and NADPH concentrations in RBCs. Mean values ( $\pm$  s.e.m.) for three experimental subjects are shown. One-way ANOVA (effect of time) for NADH/NADPH data was significant ( $***P < 0.001$ ). Two-way ANOVA (metabolite  $\times$  time) did not reveal a significant difference between NADH and NADPH profiles. Individual profiles are shown in Supplementary Fig. 6b, c.

oscillations, as there seems to be reciprocal regulation between these systems (Supplementary Fig. 9).

## Discussion

We have shown that human RBCs display robust, temperature-entrainable and temperature-compensated circadian rhythms, consistent with the presence of a circadian clock within these cells. By demonstrating circadian oscillations in a multitude of cytoplasmic redox parameters (peroxiredoxin oxidation–reduction, haemoglobin tetramer–dimer transitions and NADH/NADPH oscillations), some of which are clearly also present in nucleated cells not involved in oxygen transport, we believe that we have uncovered interconnectivity between seemingly distinct cytoplasmic (metabolic) and nuclear circadian processes (Supplementary Fig. 9). Moreover, the interrelationship between post-translational and transcription-dependent oscillations in nucleated cells resembles the emerging model in cyanobacteria<sup>39</sup>. In this regard, peroxiredoxins are extremely interesting from a phylogenetic perspective, as they are found in virtually all known organisms<sup>40</sup>. Thus, a testable and important question is whether they (and similar molecules) constitute a circadian marker that transcends phylogenetic kingdoms. This is of great interest because many classical model organisms that are genetically tractable (for example, yeast and *C. elegans*) have not been found to express any known ‘clock genes’, but do exhibit circadian rhythms<sup>41,42</sup>. In this context, the finding that peroxiredoxin rhythms are exhibited in the alga *Ostreococcus tauri*<sup>43</sup>, a plant-like clock model organism<sup>44</sup>, and that they persist in the absence of transcription, echoes this as a potential underlying principle. Furthermore, it has not escaped our notice that rhythmic peroxiredoxin oligomerization resembles the circadian variation in the formation of hexameric KaiC ring structures in cyanobacteria<sup>45</sup>, and may therefore be a fundamental part of circadian ‘logic’ in divergent organisms.

It remains to be seen whether peroxiredoxins (and their homologues/orthologues) are essential for circadian rhythmicity, but we anticipate that deleting these fundamental and redundant genes will have generally deleterious cellular consequences. We hope that our findings may shed light on a number of apparent paradoxes concerning circadian clocks, such as how they continue to keep time accurately in the absence of transcription, as occurs for example during cell division cycles. Moreover, as we move

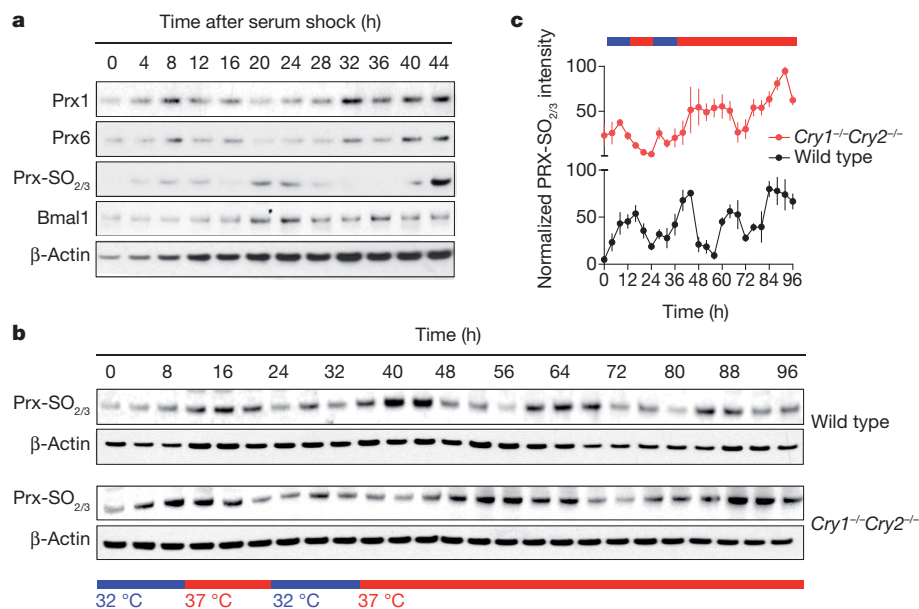


**Figure 6 | Peroxiredoxin rhythms in nucleated cells.** **a**, Peroxiredoxin rhythms in mouse NIH3T3 fibroblasts synchronized by a serum shock. Immunoblots for Prx1, Prx6 and Prx-SO<sub>2/3</sub> dimer are shown, in addition to Bmal1 and a  $\beta$ -actin loading control. **b**, **c**, Peroxiredoxin rhythms in mouse embryonic fibroblasts (MEFs). MEFs from wild-type or *Cry1 Cry2* double-

knockout mice were entrained in temperature cycles and then kept under constant temperature (37 °C) for the rest of the experiment (as shown in the schematic). **b**, Representative immunoblots of oxidized/hyperoxidized peroxiredoxin (Prx-SO<sub>2/3</sub>) dimer. **c**, Quantification of Prx-SO<sub>2/3</sub> immunoblots by densitometry. Mean values ( $\pm$  s.e.m.) for  $n = 4$  biological replicates are shown.

towards a deeper understanding of cellular metabolism and redox status in the context of the clockwork, we anticipate that our findings will aid the development of current clock models and a reassessment of the role of the nucleus in these models.

## METHODS SUMMARY

For red blood cell experiments, ~10 ml of blood was collected from each of three subjects for each experiment by using tubes containing sodium citrate anticoagulant. Red blood cell pellets (and white blood cell fractions) were obtained using gradient centrifugation at 25 °C. After two washes in sterile PBS, the pellet was re-suspended in sterile modified Krebs–Henseleit buffer (pH 7.4, 280 mOsm l<sup>-1</sup>). For all experiments, 100 µl of re-suspended RBCs were dispensed into 0.2-ml PCR tubes, and then placed in a thermal cycler for temperature-entrainment and free-running assessments. When indicated, 100 nM  $\alpha$ -amanitin oleate or 5 µg ml<sup>-1</sup> cycloheximide were added to the RBCs. Dimethyl sulphoxide (DMSO) was used as the vehicle control for those experiments. Samples were lysed in LDS buffer and heated to 70 °C for 10 min with constant shaking (600 r.p.m.) in a thermomixer. Electrophoresis was performed using pre-fabricated 4–12% Bis-Tris gradient gels, using a non-reducing MES SDS buffer system, allowing characterization of proteins between 10 and 260 kDa. Immunoblotting was performed after protein transfer to nitrocellulose membranes. After blocking, membranes were incubated in antibody diluted in blocking buffer (0.5% milk/BSA) overnight at 4 °C. The following day, membranes were washed and bands visualized with chemiluminescence detection. To check protein loading was even in the gels, they were stained with Coomassie blue. Front-face fluorescence measurements were performed in 96-well clear-bottom sterile culture plates, using a PerkinElmer Enspire plate reader held at 37 °C continuously, in its light-tight enclosure. Emission was recorded at 325 nm, using an excitation wavelength of 280 nm, every 15 min for 64 h in total. Colorimetric NADH/NADPH assays were performed using kits purchased from Abcam, following the manufacturer's protocol.

**Full Methods** and any associated references are available in the online version of the paper at [www.nature.com/nature](http://www.nature.com/nature).

**Received 20 May; accepted 22 November 2010.**

- Dunlap, J. C. Molecular bases for circadian clocks. *Cell* **96**, 271–290 (1999).
- Takahashi, J. S., Hong, H. K., Ko, C. H. & McDearmon, E. L. The genetics of mammalian circadian order and disorder: implications for physiology and disease. *Nature Rev. Genet.* **9**, 764–775 (2008).
- Reddy, A. B. & O'Neill, J. S. Healthy clocks, healthy body, healthy mind. *Trends Cell Biol.* **20**, 36–44 (2009).
- Woelfle, M. A., Ouyang, Y., Phanvijhitsiri, K. & Johnson, C. H. The adaptive value of circadian clocks; an experimental assessment in cyanobacteria. *Curr. Biol.* **14**, 1481–1486 (2004).
- Dodd, A. N. *et al.* Plant circadian clocks increase photosynthesis, growth, survival, and competitive advantage. *Science* **309**, 630–633 (2005).
- Barger, L. K., Lockley, S. W., Rajaratnam, S. M. & Landrigan, C. P. Neurobehavioral, health, and safety consequences associated with shift work in safety-sensitive professions. *Curr. Neurol. Neurosci. Rep.* **9**, 155–164 (2009).
- Tomita, J., Nakajima, M., Kondo, T. & Iwasaki, H. No transcription-translation feedback in circadian rhythm of KaiC phosphorylation. *Science* **307**, 251–254 (2005).
- Lakin-Thomas, P. L. Transcriptional feedback oscillators: maybe, maybe not. *J. Biol. Rhythms* **21**, 83–92 (2006).
- Dodd, A. N. *et al.* The *Arabidopsis* circadian clock incorporates a cADPR-based feedback loop. *Science* **318**, 1789–1792 (2007).
- Johnson, C. H. *et al.* Circadian oscillations of cytosolic and chloroplastic free calcium in plants. *Science* **269**, 1863–1865 (1995).
- O'Neill, J. S., Maywood, E. S., Chesham, J. E., Takahashi, J. S. & Hastings, M. H. cAMP-dependent signaling as a core component of the mammalian circadian pacemaker. *Science* **320**, 949–953 (2008).
- Harrisingh, M. C., Wu, Y., Lnenicka, G. A. & Nitabach, M. N. Intracellular Ca<sup>2+</sup> regulates free-running circadian clock oscillation *in vivo*. *J. Neurosci.* **27**, 12489–12499 (2007).
- Woolum, J. C. A re-examination of the role of the nucleus in generating the circadian rhythm in *Acetabularia*. *J. Biol. Rhythms* **6**, 129–136 (1991).
- Dibner, C. *et al.* Circadian gene expression is resilient to large fluctuations in overall transcription rates. *EMBO J.* **28**, 123–134 (2009).
- Hall, A., Karplus, P. A. & Poole, L. B. Typical 2-Cys peroxiredoxins—structures, mechanisms and functions. *FEBS J.* **276**, 2469–2477 (2009).
- Rhee, S. G., Jeong, W., Chang, T. S. & Woo, H. A. Sulfiredoxin, the cysteine sulfenic acid reductase specific to 2-Cys peroxiredoxin: its discovery, mechanism of action, and biological significance. *Kidney Int.* **106** (Suppl.), S3–S8 (2007).
- Reddy, A. B. *et al.* Circadian orchestration of the hepatic proteome. *Curr. Biol.* **16**, 1107–1115 (2006).
- Hastings, M. H., Reddy, A. B. & Maywood, E. S. A clockwork web: circadian timing in brain and periphery, in health and disease. *Nature Rev. Neurosci.* **4**, 649–661 (2003).
- Hastings, M. H., Maywood, E. S. & Reddy, A. B. Two decades of circadian time. *J. Neuroendocrinol.* **20**, 812–819 (2008).
- Wright, K. P. Jr, Hull, J. T. & Czeisler, C. A. Relationship between alertness, performance, and body temperature in humans. *Am. J. Physiol. Regul. Integr. Comp. Physiol.* **283**, R1370–R1377 (2002).
- Barranco-Medina, S., Lazaro, J. J. & Dietz, K. J. The oligomeric conformation of peroxiredoxins links redox state to function. *FEBS Lett.* **583**, 1809–1816 (2009).
- Woo, H. A. *et al.* Reversible oxidation of the active site cysteine of peroxiredoxins to cysteine sulfinic acid. Immunoblot detection with antibodies specific for the hyperoxidized cysteine-containing sequence. *J. Biol. Chem.* **278**, 47361–47364 (2003).
- Cho, C. S. *et al.* Irreversible inactivation of glutathione peroxidase 1 and reversible inactivation of peroxiredoxin II by H<sub>2</sub>O<sub>2</sub> in red blood cells. *Antioxid. Redox Signal.* **12**, 1235–1246 (2010).
- Griffon, N. *et al.* Tetramer-dimer equilibrium of oxyhemoglobin mutants determined from auto-oxidation rates. *Protein Sci.* **7**, 673–680 (1998).
- Hewitt, J. A., Kilmartin, J. V., Eyck, L. F. & Perutz, M. F. Noncooperativity of the dimer in the reaction of hemoglobin with oxygen (human-dissociation-equilibrium-sulphydryl-absorption-x-ray analysis). *Proc. Natl Acad. Sci. USA* **69**, 203–207 (1972).
- Latenkov, V. P. Diurnal rhythm of acid-base equilibrium and blood gas composition [in Russian]. *Biull. Eksp. Biol. Med.* **101**, 614–616 (1986).
- Kennett, E. C. *et al.* Investigation of methaemoglobin reduction by extracellular NADH in mammalian erythrocytes. *Int. J. Biochem. Cell Biol.* **37**, 1438–1445 (2005).
- Ogo, S., Focesi, A. Jr, Cashion, R., Bonaventura, J. & Bonaventura, C. Interactions of nicotinamide adenine dinucleotides with varied states and forms of hemoglobin. *J. Biol. Chem.* **264**, 11302–11306 (1989).
- Jacobsen, M. P. & Winzor, D. J. Characterization of the interactions of NADH with the dimeric and tetrameric states of methaemoglobin. *Biochim. Biophys. Acta* **1246**, 17–23 (1995).
- Ghosh, A. K., Chance, B. & Pye, E. K. Metabolic coupling and synchronization of NADH oscillations in yeast cell populations. *Arch. Biochem. Biophys.* **145**, 319–331 (1971).
- Hess, B., Brand, K. & Pye, K. Continuous oscillations in a cell-free extract of *S. carlsbergensis*. *Biochem. Biophys. Res. Commun.* **23**, 102–108 (1966).
- Betz, A. & Chance, B. Phase relationship of glycolytic intermediates in yeast cells with oscillatory metabolic control. *Arch. Biochem. Biophys.* **109**, 585–594 (1965).
- Rutter, J., Reick, M. & McKnight, S. L. Metabolism and the control of circadian rhythms. *Annu. Rev. Biochem.* **71**, 307–331 (2002).
- Rutter, J., Reick, M., Wu, L. C. & McKnight, S. L. Regulation of clock and NPAS2 DNA binding by the redox state of NAD cofactors. *Science* **293**, 510–514 (2001).
- Nagoshi, E. *et al.* Circadian gene expression in individual fibroblasts: cell-autonomous and self-sustained oscillators pass time to daughter cells. *Cell* **119**, 693–705 (2004).
- Yagita, K., Tamanini, F., van der Horst, G. T. J. & Okamura, H. Molecular mechanisms of the biological clock in cultured fibroblasts. *Science* **292**, 278–281 (2001).
- van der Horst, G. T. J. *et al.* Mammalian *Cry1* and *Cry2* are essential for maintenance of circadian rhythms. *Nature* **398**, 627–630 (1999).
- Zhang, E. E. *et al.* A genome-wide RNAi screen for modifiers of the circadian clock in human cells. *Cell* **139**, 199–210 (2009).
- Qin, X., Byrne, M., Xu, Y., Mori, T. & Johnson, C. H. Coupling of a core post-translational pacemaker to a slave transcription/translation feedback loop in a circadian system. *PLoS Biol.* **8**, e1000394 (2010).
- Wood, Z. A., Schroder, E., Robin Harris, J. & Poole, L. B. Structure, mechanism and regulation of peroxiredoxins. *Trends Biochem. Sci.* **28**, 32–40 (2003).
- Eldereink-Chen, Z. *et al.* A circadian clock in *Saccharomyces cerevisiae*. *Proc. Natl Acad. Sci. USA* **107**, 2043–2047 (2010).
- Kippert, F., Saunders, D. S. & Blaxter, M. L. *Caenorhabditis elegans* has a circadian clock. *Curr. Biol.* **12**, R47–R49 (2002).
- O'Neill, J. S. *et al.* Circadian rhythms persist without transcription in a eukaryote. *Nature* doi:10.1038/nature09654 (this issue).
- Corellou, F. *et al.* Clocks in the green lineage: comparative functional analysis of the circadian architecture of the picoeukaryote *Ostreococcus*. *Plant Cell* **21**, 3436–3449 (2009).
- Johnson, C. H., Mori, T. & Xu, Y. A cyanobacterial circadian clockwork. *Curr. Biol.* **18**, R816–R825 (2008).

**Supplementary Information** is linked to the online version of the paper at [www.nature.com/nature](http://www.nature.com/nature).

**Acknowledgements** This work was supported by the Wellcome Trust (083643/Z/07/Z), the MRC Centre for Obesity and Related metabolic Disorders (MRC CORD) and the NIHR Cambridge Biomedical Research Centre. We thank M. Jain and R. Edgar for discussions about the manuscript, A. Coles and J. Jones for providing access to samples, and G. van der Horst and F. Tamanini for providing access to *Cry1 Cry2* knockout (and wild-type) mouse embryonic fibroblasts.

**Author Contributions** A.B.R. and J.S.O.N. conceived, designed and performed the experiments, and wrote the manuscript.

**Author Information** Reprints and permissions information is available at [www.nature.com/reprints](http://www.nature.com/reprints). The authors declare no competing financial interests. Readers are welcome to comment on the online version of this article at [www.nature.com/nature](http://www.nature.com/nature). Correspondence and requests for materials should be addressed to A.B.R. ([areddy@cantab.net](mailto:areddy@cantab.net)).

## METHODS

**Participants.** Studies were conducted in accordance with the principles of the Declaration of Helsinki, with ethical approval from the Local Research Ethics Committee (Cambridge, UK). Participants in the study were screened for health (by history, physical examination, and standard biochemistry and haematology), and did not suffer from sleep disorders or excessive daytime sleepiness. All participants provided written, informed consent after having received a detailed explanation of the study procedures.

**Red blood cell culture.** Approximately 10 ml of blood was collected from each of three subjects for each experiment by using tubes containing sodium citrate anticoagulant (Sarstedt). Red cell pellets (and white cell fractions) were obtained using gradient centrifugation at 25 °C with Accuspin Histopaque-1077 columns (Sigma-Aldrich), following the manufacturer's protocol. After two washes in approximately 50 ml of sterile phosphate-buffered saline (PBS), the pellet (approximately 8 ml volume) was re-suspended to a total volume of 30 ml with sterile modified Krebs-Henseleit Buffer (Sigma-Aldrich). Krebs buffer was made up in 500-ml batches with sterile water, and adding 0.1% w/v bovine serum albumin (Sigma-Aldrich), with antibiotics added (100 units ml<sup>-1</sup> penicillin, 100 mg ml<sup>-1</sup> streptomycin) and the osmolarity adjusted to 280 mOsm l<sup>-1</sup>, and pH to 7.4, to match conditions normally found in human plasma. For all experiments, 100 µl of re-suspended RBCs were dispensed into 0.2-ml PCR tubes (Thermo), and then placed in a thermal cycler (Bio-Rad Tetrad) for temperature-entrainment and free-running assessments. When indicated, 100 nM  $\alpha$ -amanitin oleate or 5 µg ml<sup>-1</sup> cycloheximide, purchased from Sigma-Aldrich, were added to the RBCs before aliquoting, and thus the drugs were present for the entirety of the experiment. Drugs were made up in sterile dimethyl sulphoxide (DMSO), which was also used therefore as the vehicle control for those experiments. Samples were taken directly from the thermal cycler and either flash-frozen (with liquid nitrogen) or 75 µl immediately lysed in 250 µl 2× LDS buffer (Life Technologies) and heated to 70 °C for 10 min with constant shaking (600 r.p.m.) in a thermomixer (Grant). Samples and lysates were stored at -80 °C until use.

**NIH3T3 cell culture.** NIH3T3 cells were obtained from the American Type Culture Collection (ATCC) and used at passage 6 for these experiments. Cells plated into 35-mm circular standard cell culture dishes, with at least  $n = 3$  replicates for each time point to be assayed. Cells were cultured in high-glucose Dulbecco's modified Eagle's medium (DMEM, Sigma-Aldrich), supplemented with 10% fetal bovine serum (Hyclone), 100 units ml<sup>-1</sup> penicillin and 100 mg ml<sup>-1</sup> streptomycin, and Glutamax (Life Technologies). Cultures were maintained under standard sterile cell culture conditions, at 37 °C and in 5% CO<sub>2</sub>, in a humidified incubator. Experiments were performed when cultures were fully confluent (100%). Serum starvation was instituted for 24 h, before serum shock with 50% horse serum for 2 h, and then incubated in standard supplemented high-glucose DMEM for subsequent sampling. Dishes were taken from the incubator 0–44 h after the serum shock, and cells lysed immediately in LDS buffer (Life Technologies). Lysates were immediately heated to 70 °C for 10 min with constant shaking (600 r.p.m.) in a thermomixer (Grant). Samples and lysates were stored at -80 °C until use. For MEF experiments, temperature cycles were imposed on fully confluent cells growing in 12-well plates using an automated temperature-cycling incubator. Sampling at each time point was performed on four biological replicates, and lysates prepared as above, after initial lysis in non-reducing CHAPS/urea buffer to facilitate protein loading correction<sup>46</sup>.

**Flow cytometry and cell viability assays.** Cells were stained with Vybrant DyeCycle Ruby (Life Technologies), at 1:500 dilution for 60 min at 25 °C, and then assessed by flow cytometry using a FACScalibur system (BD Biosciences). Data were analysed with the CellQuest Pro software.  $2 \times 10^4$  cells were counted for each of the three experimental subjects. For quantification, a FL3 (red) channel cutoff level of >100 (determined empirically) was used to classify cells as being nucleated. For cell viability assays, either whole blood or purified red cell fractions were subjected to haemolysis by re-suspending respective pellets (approximately 200 µl volume) in 800 µl hypotonic solution (50% PBS, pH 7.2) for 1 min at 25 °C.

After incubation with hypotonic solution (which lyses red cells but not white cells), the tonicity is brought back to 100% PBS by adding 110 µl of 10× PBS concentrate (Life Technologies). Aliquots of the haemolysed samples from each subject were then assayed, using 0.4% trypan blue, with the automated Countess system (Life Technologies) following the manufacturer's instructions.

**Real-time intrinsic front-face fluorescence measurements.** Red blood cells were prepared as above and then diluted 1:100 for front-face fluorescence. Fluorescence measurements were performed in 96-well, black, clear-bottomed sterile culture plates, using an Enspire plate reader (PerkinElmer) held at 37 °C continuously, in its light-tight enclosure. Emission was recorded at 325 nm, using an excitation wavelength of 280 nm, every 15 min for 64 h in total. The excitation/emission wavelength is optimal for detecting maximal fluorescence in RBCs<sup>47</sup>.

**NADH and NADPH assays.** Colorimetric assays were performed using commercial kits from Abcam (ab65348, ab65349). Cell pellets (100 µl per time point, per biological replicate) were processed following the instructions in the kit. NADH/NADPH were extracted in the recommended extraction buffer, and all samples were processed in a single run to aid quantification and comparability. Colorimetric measurements were made at 25 °C using optical density at 450 nm (OD<sub>450</sub>) measurements on a Packard Fusion plate-reader. We performed  $n = 3$  technical replicates for each of  $n = 3$  biological replicates (subjects A, B, C) at each time point. OD<sub>450</sub> measurements were converted to nmol per ml RBCs using a standard curve for both NADH and NADPH.

**ATP assays.** We used the Promega ENLITEN ATP assay system, following the manufacturer's protocol. ATP was extracted from cell pellets (100 µl per time-point, per biological replicate) with an equal volume of 0.38N (6%) trichloroacetic acid (Sigma). Samples were then diluted/neutralized 1:50 with Tris-acetate buffer to final pH 7.75. This step brought the samples into an appropriate pH range for the bioluminescence assay, and also decreased the trichloroacetic acid concentration to 0.1%, both of which are necessary to avoid inhibition of the luciferase reaction. Luminescence measurements were performed in triplicate for each biological replicate using a Berthold Centro LB 960 high-sensitivity system, integrating photon counts over 2 s per well.

**Gel electrophoresis and immunoblotting.** We used NuPAGE Novex 4–12% Bis-Tris gradient gels (Life Technologies), and ran them using the manufacturer's protocol with a non-reducing MES SDS buffer system, allowing characterization of proteins between 10–260 kDa. Protein transfer to nitrocellulose for blotting was performed using the iBlot system (Life Technologies), with a standard (P3, 7 min) protocol. Nitrocellulose was then washed briefly, and then blocked for 30 min in 0.5% w/w BSA/non-fat dried milk (Marvel) in Tris buffered saline/0.05% Tween-20 (TBST). After three brief washes in TBST, membranes were incubated in antibody diluted in blocking buffer (0.5% milk/BSA) overnight at 4 °C. The following day, membranes were washed for 5 min three times (in TBST) and then incubated with 1:10,000 HRP-conjugated secondary antibody (Sigma-Aldrich) for 30 min. Four more 10-min washes were then performed before performing chemiluminescence detection using ECL Plus reagent (GE Healthcare). To check protein loading was even in the gels, they were stained with Coomassie SimplyBlue (Life Technologies). Antisera against peroxiredoxins were obtained from Abcam (Cambridge) and used at the recommended dilutions (PRX-SO<sub>2/3</sub>, ab16830; PRX1, ab59538; PRX2, ab15572; PRX3, ab16751; PRX4, ab16943; PRX5, ab16944; PRX6, ab16947; 2-Cys PRX, ab16765). Rabbit anti-Bmal1 antiserum was used at 1:2,000 in 0.5% BSA<sup>46</sup>. A mouse  $\beta$ -actin antibody (Santa Cruz Antibodies) was used at 1:5,000 in 0.5% milk/BSA.

**Image and statistical analysis.** Coomassie-stained gel images were obtained using a Licor Odyssey system, and immunoblot films were scanned using a back-illuminated flat-bed scanner. Densitometric quantification of images was performed using NIH ImageJ software. Parametric statistics (1-way and 2-way ANOVA) were performed using Graphpad Prism v5 software.

46. Reddy, A. B. *et al.* Circadian orchestration of the hepatic proteome. *Curr. Biol.* **16**, 1107–1115 (2006).

47. Hu, T. *et al.* PEGylation of Val-1( $\alpha$ ) destabilizes the tetrameric structure of hemoglobin. *Biochemistry* **48**, 608–616 (2009).

# A candidate redshift $z \approx 10$ galaxy and rapid changes in that population at an age of 500 Myr

R. J. Bouwens<sup>1,2</sup>, G. D. Illingworth<sup>1</sup>, I. Labbe<sup>3</sup>, P. A. Oesch<sup>4</sup>, M. Trenti<sup>5</sup>, C. M. Carollo<sup>4</sup>, P. G. van Dokkum<sup>6</sup>, M. Franx<sup>2</sup>, M. Stiavelli<sup>7</sup>, V. González<sup>1</sup>, D. Magee<sup>1</sup> & L. Bradley<sup>7</sup>

Searches for very-high-redshift galaxies over the past decade have yielded a large sample of more than 6,000 galaxies existing just 900–2,000 million years (Myr) after the Big Bang (redshifts  $6 > z > 3$ ; ref. 1). The Hubble Ultra Deep Field (HUDF09) data<sup>2,3</sup> have yielded the first reliable detections of  $z \approx 8$  galaxies<sup>3–9</sup> that, together with reports of a  $\gamma$ -ray burst at  $z \approx 8.2$  (refs 10, 11), constitute the earliest objects reliably reported to date. Observations of  $z \approx 7$ –8 galaxies suggest substantial star formation at  $z > 9$ –10 (refs 12, 13). Here we use the full two-year HUDF09 data to conduct an ultra-deep search for  $z \approx 10$  galaxies in the heart of the reionization epoch, only 500 Myr after the Big Bang. Not only do we find one possible  $z \approx 10$  galaxy candidate, but we show that, regardless of source detections, the star formation rate density is much smaller ( $\sim 10\%$ ) at this time than it is just  $\sim 200$  Myr later at  $z \approx 8$ . This demonstrates how rapid galaxy build-up was at  $z \approx 10$ , as galaxies increased in both luminosity density and volume density from  $z \approx 10$  to  $z \approx 8$ . The 100–200 Myr before  $z \approx 10$  is clearly a crucial phase in the assembly of the earliest galaxies.

The detection of galaxies at very high redshift from deep imaging data depends on the absorption (by intervening neutral hydrogen) of much of the flux in the spectrum at wavelengths below the wavelength

of Lyman  $\alpha$  (121.6 nm). These ‘spectral breaks’ shift to longer wavelengths for more distant, redshifted galaxies seen at earlier times. A distinguishing characteristic of  $z \approx 10$  galaxies would be, first, a detection in the  $H_{160}$  band, and, second, the absence of flux in the  $J_{125}$  band, and in all other shorter-wavelength Hubble Space Telescope (HST) Wide Field Camera 3 (WFC3/IR) and Advanced Camera for Surveys (ACS) filters blueward of the  $J_{125}$  band (hence they are called ‘ $J_{125}$ -dropouts’). The new, powerful HST WFC3/IR camera is  $\sim 40$  times more efficient at finding  $z \approx 7$  galaxies<sup>2,4–9</sup> than the previous near-infrared NICMOS camera owing to its wider field of view and greater sensitivity in its  $Y_{105}$ ,  $J_{125}$  and  $H_{160}$  filters. It provides us with the capability to explore to  $z \approx 10$ .

A thorough search of the deep WFC3/IR HUDF09 data set strong limits at  $z \approx 10$ , and also resulted in the detection of a candidate  $z \approx 10$   $J_{125}$ -dropout galaxy UDFj-39546284 at  $5.4\sigma$  in our  $0.26''$ -diameter selection aperture (Fig. 1). The signal-to-noise ratio grows to  $5.8\sigma$  in a larger  $0.35''$ -diameter aperture. The candidate is  $28.92 \pm 0.18$  mag in the WFC3/IR  $H_{160}$  band ( $(1.01 \pm 0.18) \times 10^{-31} \text{ erg s}^{-1} \text{ cm}^{-2} \text{ Hz}^{-1}$ ), has a likely redshift of  $z \approx 10.3$  (Fig. 2), and appears to be slightly extended. Given the importance of the limits that we set, and of the candidate  $z \approx 10$  galaxy, we perform extensive tests and simulations.

UDFj-39546284 ( $H = 28.9$ ,  $J-H > 2.0$ )

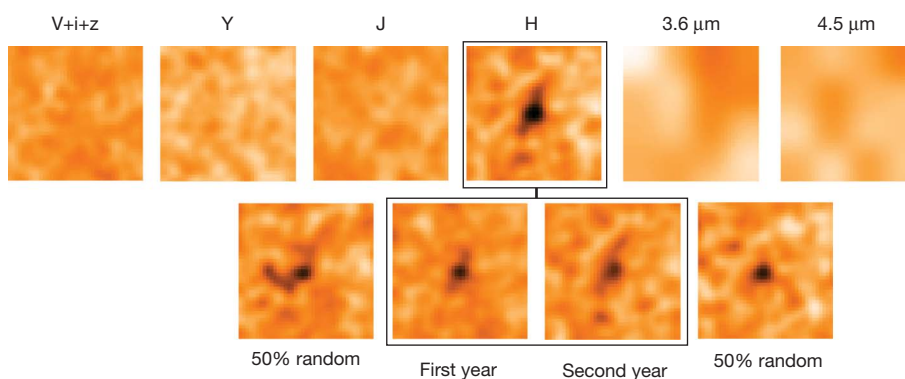


**Figure 1 | Optical and near-infrared images of the candidate  $z \approx 10$  galaxy, UDFj-39546284, from the HUDF.** Top row: the leftmost panel shows the HUDF ACS ( $V_{606} + i_{775} + z_{850}$ ) data<sup>26</sup>; the next three panels show the similarly deep HUDF09 (HST GO 11563), near-infrared WFC3/IR ( $Y_{105}$ ,  $J_{125}$ ,  $H_{160}$ ) data (reaching to  $5\sigma$  depths of  $\sim 29.8$  AB mag)<sup>2,3,9</sup>; and the last two panels show the longer wavelength Spitzer IRAC 3.6 and  $4.5 \mu\text{m}$  observations. Bottom row: the two middle panels show images of our  $z \approx 10$  candidate in the first and second year of  $H_{160}$ -band observations (each representing  $\sim 50\%$  of the total); the two outer panels show two random  $50\%$  subsets of the data (see also Supplementary Fig. 2). Each cutout is  $2.4'' \times 2.4''$  on a side, and is orientated with north at the top. For our selection criteria, we require our  $z \approx 10$  candidates to be detected at  $5\sigma$  in the  $H_{160}$  band, to have  $J_{125} - H_{160}$  colours redder than 1.2 AB mag, and to

be undetected ( $< 2\sigma$ ) in all imaging observations blueward of the  $J_{125}$  band. Also, candidates must not be detected at  $> 1.5\sigma$  in more than one band blueward of the  $J_{125}$  band, and have  $\chi^2 < 2.5$  in the extremely-deep image obtained by combining the  $B_{435}$ ,  $V_{606}$ ,  $i_{775}$ ,  $z_{850}$  and  $Y_{105}$  imaging data. All of these requirements place very strong limits on the optical flux from our  $z \approx 10$  candidates and provide strong discrimination against contamination by low-redshift sources (see ref. 9, Appendix C). The candidate is significant at  $> 3\sigma$  in each year of observations and therefore not likely to be spurious. It is detected at  $5.4\sigma$  in the  $H_{160}$  band, which is much more significant than the next possible candidates (seen at  $4.0\sigma$  and  $4.9\sigma$ ). In addition, our  $z \approx 10$  candidate is not detected in the IRAC data, as expected given the IRAC flux limits. The position and other properties of this candidate are given in Supplementary Table 1.

<sup>1</sup>Department of Astronomy, University of California Santa Cruz, Santa Cruz, California 95064, USA. <sup>2</sup>Leiden Observatory, Leiden University, Leiden NL-2333, The Netherlands. <sup>3</sup>Carnegie Observatories, Pasadena, California 91101, USA. <sup>4</sup>Institute for Astronomy, ETH Zurich, Zurich CH-8093, Switzerland. <sup>5</sup>University of Colorado, Center for Astrophysics and Space Astronomy, Boulder, Colorado 80303, USA. <sup>6</sup>Department of Astronomy, Yale University, New Haven, Connecticut 06520, USA. <sup>7</sup>Space Telescope Science Institute, Baltimore, Maryland 21218, USA.

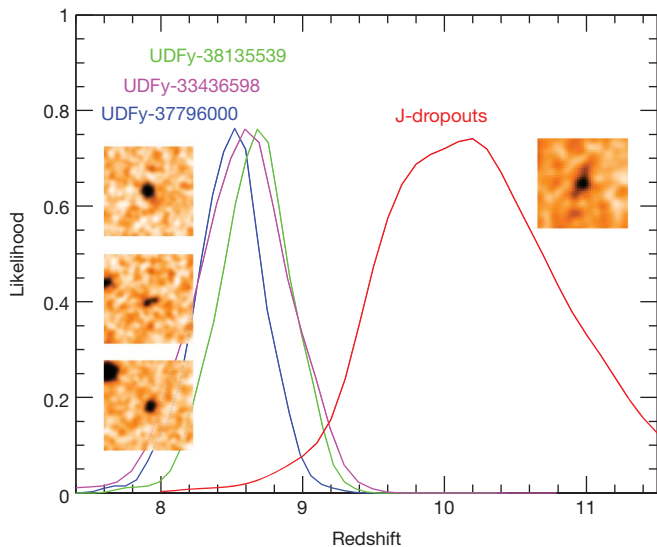


**Figure 2 | Predicted redshift distributions for our  $z \approx 8.5$  and  $z \approx 10$  galaxy candidates.** The red line gives the redshift distribution for our  $z \approx 10$   $J_{125}$ -dropout candidate, while the blue, green and magenta lines give the redshift distributions for our  $z \approx 8.5$   $Y_{105}$ -dropout candidates. The  $H_{160}$ -band source images that correspond to the redshift distributions are shown for the  $z \approx 8.7$ ,  $8.6$  and  $z \approx 8.5$  sources (labels arranged in same order as images), and for our  $z \approx 10.3$  candidate. Each source image is  $2.4'' \times 2.4''$ , with north at the top. The selection criteria for the  $z \approx 8$ – $9$  sources have been published elsewhere<sup>3,9</sup> (see also Supplementary Information section 5). However, the detailed redshift distributions are shown here for the first time. The redshift distributions were derived by adding artificial sources to the HUDF09 WFC3/IR data, and re-selecting them in the same way as the actual galaxy candidates (see Supplementary Information sections 4, 5 and 9). The mean redshifts of these distributions are 8.7, 8.6, 8.5 and 10.3. The  $z \approx 8.7$  source has a tentative spectroscopic confirmation at  $z \approx 8.6$  (ref. 14). For these simulations, the ultraviolet luminosity function was used. The luminosity function describes the number density of galaxies versus luminosity and is usually parameterized as  $\phi * e^{-1/L * (L/L^*)^\alpha}$ , where  $\phi *$  is the normalization,  $L^*$  is the characteristic luminosity, and  $\alpha$  is the faint end slope (see Fig. 3). The luminosity function was assumed to have an  $M^*_{UV}$  of  $-19.5$  and  $-18.8$  at  $z \approx 8$  and  $z \approx 10$ , respectively (based on predictions from our  $z \approx 4$ – $6$  fitting relation<sup>9,22</sup>), while  $\alpha$  was taken to be  $-1.74$ .

These are described in Supplementary Information sections 4 and 7, while the candidate properties are given in Supplementary Table 1.

The existence of galaxies at  $z > 8.2$  (the  $\gamma$ -ray burst redshift<sup>10,11</sup>) is strengthened by three additional sources that have been detected in recent searches<sup>3–9</sup>, one of which has a tentative spectroscopic confirmation at  $z = 8.6$  (ref. 14). The updated redshift distributions from our simulations show that these three sources<sup>3</sup> are most likely to be at  $z \approx 8.7$ ,  $8.5$  and  $8.6$  (Fig. 2). The expectation of finding galaxies at  $z \approx 10$ , just  $\sim 120$  Myr earlier, is enhanced by these strong detections at  $z \approx 8.5$ , especially since the  $z \approx 7$ – $8$  Spitzer and HST data suggest that substantial star formation is likely at  $z > 9$ – $10$  (refs 12, 13).

The photometric-selection ‘dropout’ approach has been verified through numerous spectroscopic confirmations at redshifts from  $z \approx 2$  to  $z \approx 6$  (refs 15–19), and possibly also now at  $z \approx 8.6$  (ref. 14). For our candidate  $z \approx 10$  galaxy, however, its single band ( $H_{160}$  band) detection increases the risk of contamination compared to the  $z \approx 7$  and  $z \approx 8$  samples, where two (or more) bands are used to measure the source magnitudes and colours. Fortunately, we can test the robustness of the single-band detection process by selecting  $z \approx 8$  galaxy candidates using the  $J_{125}$ -band data alone. Analogous to the  $z \approx 10$   $J_{125}$ -dropouts,  $z \approx 8$  galaxies are  $Y_{105}$ -band dropouts. We compare this single-band selection against the more robust  $z \approx 8$  detections using two bands<sup>3</sup> ( $J_{125}$  and  $H_{160}$ ). We are very encouraged that we select the same eight  $z \approx 8$   $Y_{105}$ -dropouts with the  $J_{125}$ -band data alone, as we do with the normal selection using both the  $J_{125}$ - and  $H_{160}$ -band data. The primary

reason for the robustness is the non-detection in all shorter wavelength filters. The  $\chi^2_{\text{opt}}$  test that we have developed<sup>9</sup> largely eliminates contaminating objects.

Our  $z \approx 10$  candidate was also checked for any Spitzer IRAC flux in the  $3.6 \mu\text{m}$  band (see Fig. 1). It is quite isolated and is not detected to  $\sim 27$  AB mag ( $2\sigma$ ), further enhancing the case that this  $z \approx 10$  candidate corresponds to a very-high-redshift galaxy rather than a highly reddened, lower-redshift contaminant. Contamination from spurious sources is also an important concern for such faint sources. We verified that the source is present in a wide variety of subsets of the  $H_{160}$ -band data (Fig. 1, Supplementary Fig. 2), suggesting that the candidate is not spurious. Although these tests make a case for this source being a  $z \approx 10$  galaxy, deeper observations—involving both imaging (with, for example, WFC3/IR) and spectroscopy (with the James Webb Space Telescope)—will be required to confirm it.

Using the results of these tests and Monte Carlo simulations, we estimate there is an  $\sim 20\%$  probability that our candidate is a contaminant or is spurious. Of that 20%, 10% was estimated to be from photometric scatter. Contamination from spurious sources is uncertain, and our estimates range from 1% to 10% probability; to be conservative we adopt 10%. Contamination from lower-redshift red sources is also possible, but the above single-filter  $z \approx 8$   $Y_{105}$ -dropout test suggests that the probable contamination is small, consistent with the totals we estimate from our other tests ( $\sim 20\%$ ).

Fortunately, the depth of the data and the thoroughness of our analysis for contamination allow us to set very strong constraints on the volume density of  $z \approx 10$  galaxies, regardless of the uncertainties associated with our candidate  $z \approx 10$  galaxy. Thus we evaluate our constraints based on the limit set if no galaxies were found, and based on the candidate  $z \approx 10$  galaxy, whose volume density is corrected by 20% to account for the estimated contamination rate.

Large-scale structure uncertainties are important for small area searches. We estimate the field-to-field variance on the present  $z \approx 10$   $J_{125}$ -dropout searches in the HUDF09 field to be 39% (see Supplementary Information)<sup>20</sup>. Even at this level, the cosmic variance (‘large-scale structure’) is not the dominant source of uncertainty for our single candidate galaxy.

These  $z \approx 10$  results have far-reaching implications for estimating the role of galaxies in reionization (using the luminosity density), and for establishing the star formation rate density at very early times, as  $z \approx 10$  is just 480 Myr after the Big Bang and just a few hundred million years since the first galaxies formed. Strikingly, the upper limits and our candidate allow us to do this through quantitative constraints we place on the  $z \approx 10$  luminosity function.

The extent of the changes at  $z \approx 10$  can be demonstrated by first contrasting what we see at  $z \approx 10$  with expectations based on a ‘no-evolution’ scenario: that is, the galaxy populations stay unchanged with time. We compute the ‘no-evolution’ estimate by using our ‘galaxy cloning’ software<sup>21</sup> to artificially redshift the observed  $z \approx 6$  and  $z \approx 7$  galaxy population to  $z \approx 10$ , add them at random positions within our HUDF data, and then repeat the object selection process just as for the observed  $z \approx 10$  galaxies. We estimated that we would find  $12 \pm 4$   $z \approx 10$  galaxies using our  $z \approx 7$  detections as the baseline, and  $23 \pm 5$   $z \approx 10$  galaxies using our  $z \approx 6$  detections as a baseline. These ‘no-evolution’ estimates are substantially higher than our (contamination-corrected) estimate of  $\sim 0.8$   $z \approx 10$  galaxies. For simple Poissonian statistics, our observed number of  $\sim 0.8$  galaxies is inconsistent with no-evolution at  $4\sigma$  and  $5\sigma$  confidence, respectively (and sets even stronger limits on any ‘upturn’ in the star formation rate<sup>6</sup>). Although striking, this is not wholly unexpected. Extrapolating the trends seen by us at lower redshifts<sup>22</sup> would lead us to expect  $3 \pm 2$   $z \approx 10$  sources. Thus our results reaffirm that the significant evolution seen in galaxies at lower redshift continues to  $z \approx 10$  (in contrast with other studies<sup>6</sup>).

The present search results can also be expressed as constraints on the luminosity function at  $z \approx 10$ . The luminosity function describes

the number density of galaxies versus luminosity, and is important for estimating the ultraviolet flux from galaxies and their expected role in reionizing the Universe. The high-redshift-galaxy ultraviolet luminosity function maintains a nearly constant form and evolves in a largely self-similar manner, with the characteristic luminosity ( $L^*$ ) increasing smoothly over about 1,300 Myr from  $z \approx 7$  to  $z \approx 3$ , that is, from  $\sim 750$  Myr to  $\sim 2,000$  Myr. Assuming the same form for the ultraviolet luminosity function at  $z \approx 10$ , we find that  $L^*$  at  $z \approx 10$  is fainter, indicating that the evolution in the bright end of the ultraviolet luminosity function seen from  $z \approx 7$  to  $z \approx 4$  (refs 1, 9, 22) continues to  $z \approx 10$  (Fig. 3). Definitive measurements of  $L^*$  at  $z \approx 10$  will, of course, require deep, wide-area data to define the luminous end of the  $z \approx 10$  luminosity function.

The existence of a steep slope  $\alpha$  to the faint end of the ultraviolet luminosity function found at  $z \approx 6-7$  (refs 1, 2, 9) highlights the importance of low luminosity galaxies in providing the flux needed to reionize the Universe. It is of great interest to estimate the ultraviolet luminosity density at  $z \approx 7-10$  where reionization most probably occurred, given its apparent completion at  $z \approx 6$  (ref. 23) and its onset at  $z \approx 11$  as deduced from Wilkinson Microwave Anisotropy Probe (WMAP)<sup>24</sup> observations. The recent results from the HUDF09 data set provide estimates for the ultraviolet luminosity density at  $z \approx 7$  and at  $z \approx 8$  (ref. 9). We can now also do so at  $z \approx 10$ . We compute the luminosity density implied by our sample by assuming a faint-end slope of  $-1.7$  (the same slope as found for the  $z \approx 2-7$  luminosity functions) and extending the integration down to a very plausible limit of  $-12$  AB mag. We find that the ultraviolet flux that is available from

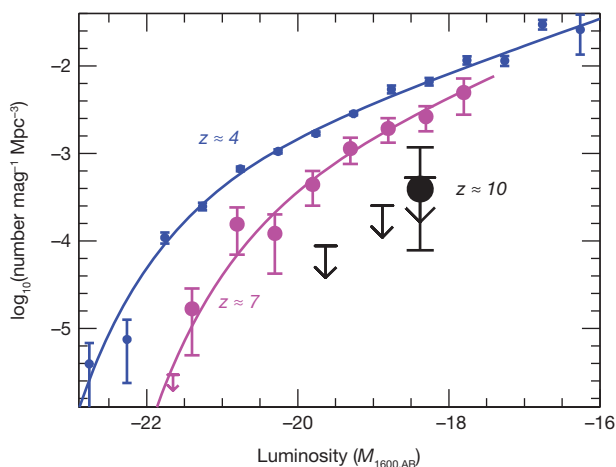


**Figure 3 | Ultraviolet luminosity functions at  $z \approx 4$ ,  $z \approx 7$  and constraints for  $z \approx 10$ .** The present constraints on the stepwise ultraviolet luminosity function at  $z \approx 10$  (black points and upper limits) are new and are derived from the  $J_{125}$ -dropout candidate galaxies over our ultra-deep HUDF WFC3/IR field. These luminosity functions are a function of the absolute magnitude (that is, luminosity) of galaxies ( $M_{1600,AB}$ ) in the rest-frame far-ultraviolet. All error bars are  $1\sigma$ . The stepwise luminosity function at  $z \approx 10$  is also presented as a  $1\sigma$  upper limit, given the uncertainty of our  $z \approx 10$  candidate. The lowest luminosity point has been corrected for incompleteness. The ultraviolet luminosity functions<sup>1,9</sup> at  $z \approx 4$  (blue) and at  $z \approx 7$  (magenta) are shown for comparison. The luminosity functions fitted here are of the form  $\phi^* e^{-L/L^*} (L/L^*)^\alpha$  (see Fig. 2 legend). This analytic representation has recently been shown<sup>9</sup> to fit well at  $z \approx 7$  and later times. The present search results also allow us to estimate the value of  $L^*$  at  $z \approx 10$ —assuming that the luminosity function at  $z \approx 10$  has the same values of  $\phi^*$  and  $\alpha \approx -1.7$  as have been found to describe ultraviolet luminosity function results from  $z \approx 7$  to  $z \approx 4$  (refs 1, 2, 9, 27–29). Doing so allows us to constrain the evolution in the luminosity function out to  $z \approx 10$ , nearly 500 Myr earlier than at  $z \approx 6$  (and so halving the time difference between the first galaxies at  $z \approx 15-20$  and those seen at  $z \approx 6$ ). We find  $L^*$  at  $z \approx 10$  to be  $-18.3 \pm 0.5$  AB mag, or  $L^* > -18.3$  in the limit of no detected sources—although obviously very uncertain, this is consistent with the evolution in the bright end of the ultraviolet luminosity function seen from  $z \approx 7$  to  $z \approx 4$  continuing to  $z \approx 10$ .

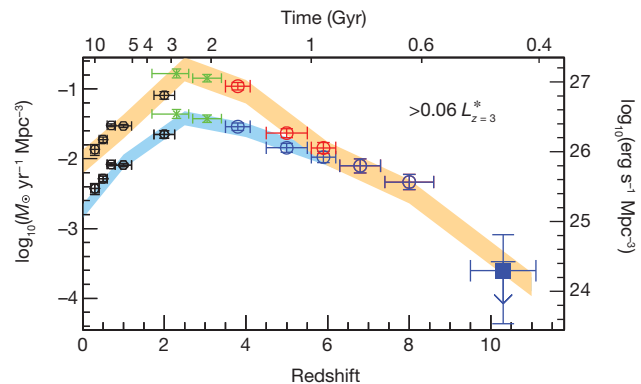


**Figure 4 | The luminosity density and star formation rate density in the Universe over 13.2 Gyr.** The rest-frame continuum ultraviolet luminosity density (right axis, blue points) at  $z \approx 10$ , and the star formation rate density (left axis, red points) derived from the extinction-corrected luminosity density<sup>1,25</sup>, are integrated down to the approximate magnitude limit  $M_{AB} \approx -18$  ( $0.06 L^*$ ) of our  $z \approx 10$   $J_{125}$ -dropout search. The conversion from ultraviolet luminosity to star formation rate assumes a Salpeter initial mass function. The upper horizontal axis gives the time after the Big Bang and the lower axis the redshift. As before, we assume that the ultraviolet luminosity function has the same faint-end slope (and normalization) as at  $z \approx 6$  and  $z \approx 7$ . The star formation rate density ( $1.9^{+4.5}_{-1.5} \times 10^{-4} M_\odot \text{ yr}^{-1} \text{ Mpc}^{-3}$ ) from the contamination-corrected sample is shown at  $z \approx 10$  from the current  $J_{125}$ -dropout search, as is the  $1\sigma$  upper limit ( $< 3 \times 10^{-4} M_\odot \text{ yr}^{-1} \text{ Mpc}^{-3}$ ) if we assume no  $z \approx 10$  sources are detected. All error bars are  $1\sigma$ . Also included here are the recent star formation rate determinations at  $z \approx 7$  and  $z \approx 8$  from our HUDF09 WFC3/IR  $z_{850}$ -dropout and  $Y_{105}$ -dropout searches<sup>9</sup>, and from the literature at  $z < 4$  (green and black points: refs 27, 30) and at  $z \approx 4-6$  (ref. 1). The dust corrections at  $z \approx 4$  are based on the estimated ultraviolet-continuum slopes  $\beta$ , and are already negligible by  $z \approx 7$  (refs 2, 3, 25). There is no evidence for any substantial change in the star formation rate density trends established at lower redshift.

galaxies at  $z \approx 10$  is only  $\sim 12^{+26}_{-10}\%$  of what is needed for galaxies to be the reionizing source, with typical assumptions of an escape fraction of  $\sim 0.4$ , a clumping factor of  $\sim 3$  and a Salpeter initial mass function (see, for example, ref. 9). This result is tantalizing, suggesting that galaxies are contributing to reionization, but the enigma remains: where are most of the needed ultraviolet photons coming from? Observations to significantly fainter levels will be central to characterizing the role of galaxies in reionization.

The star formation rate (SFR) density is derived from the luminosity density (see Fig. 4). The SFR density increases systematically and monotonically at early times from  $z \approx 10$  (500 Myr) to  $z \approx 4$  (1,600 Myr), peaking at  $z \approx 2-3$  (at  $\sim 2,500$  Myr), before decreasing at  $z < 2$  (Fig. 4). This suggests that the luminosity function and star formation rate density evolution found at lower redshifts<sup>1,25</sup> continues to  $z \approx 10$  when the universe was just 480 Myr old. The limits established here even suggest that the trends in star formation rate density established at lower redshifts could be steepening.

This is clearly an era when galaxies were evolving very rapidly. The star formation rate density increased by a factor of  $\sim 10$  in less than 200 Myr, from  $z \approx 10$  to  $z \approx 8$ . This dramatic change in such a short period of time suggests that the first phases of galaxy formation and their build-up could be unveiled by observations that penetrate just 200 Myr earlier, to redshifts  $z \approx 15$ . However, only when the James Webb Space Telescope is launched will these first phases of galaxy build-up between  $z \approx 15$  and  $z \approx 10$  be revealed.

Received 21 December 2009; accepted 30 November 2010.

- Bouwens, R. J., Illingworth, G. D., Franx, M. & Ford, H. UV luminosity functions at  $z \approx 4, 5$ , and 6 from the Hubble Ultra Deep Field and other deep Hubble Space Telescope ACS fields: evolution and star formation history. *Astrophys. J.* **670**, 928–958 (2007).
- Oesch, P. A. *et al.*  $z \approx 7$  Galaxies in the HUDF: first epoch WFC3/IR results. *Astrophys. J.* **709**, L16–L20 (2010).

3. Bouwens, R. J. *et al.* Discovery of  $z \sim 8$  galaxies in the HUDF from ultra-deep WFC3/IR observations. *Astrophys. J.* **709**, L133–L137 (2010).
4. McLure, R. *et al.* Galaxies at  $z \sim 6$ –9 from the WFC3/IR imaging of the HUDF. *Mon. Not. R. Astron. Soc.* **403**, 960–983 (2010).
5. Bunker, A. *et al.* The contribution of high redshift galaxies to cosmic reionization: new results from deep WFC3 Imaging of the Hubble Ultra Deep Field. *Mon. Not. R. Astron. Soc.* **409**, 855–866 (2010).
6. Yan, H. *et al.* Galaxy formation in the reionization epoch as hinted by Wide Field Camera 3 observations of the Hubble Ultra Deep Field. *Res. Astron. Astrophys.* **10**, 867–904 (2010).
7. Finkelstein, S. *et al.* On the stellar populations and evolution of star-forming galaxies at  $6.3 < z < 8.6$ . *Astrophys. J.* **719**, 1250–1273 (2010).
8. Robertson, N., Ellis, R. S., Dunlop, R. S., McLure, R. J. & Stark, D. P. Early star-forming galaxies and the reionization of the Universe. *Nature* **468**, 49–55 (2010).
9. Bouwens, R. J. *et al.* UV luminosity functions from 113  $z \sim 7$  and  $z \sim 8$  Lyman-break galaxies in the ultra-deep HUDF09 and wide-area ERS WFC3/IR observations, 2010. *Astrophys. J.* (submitted); preprint at (<http://arxiv.org/abs/1006.4360>) (2010).
10. Tanvir, N. *et al.* A  $\gamma$ -ray burst at a redshift of  $z \approx 8$ . *Nature* **461**, 1254–1257 (2009).
11. Salvaterra, R. *et al.* GRB090423 at a redshift of  $z \approx 8.1$ . *Nature* **461**, 1258–1260 (2009).
12. Labbé, I. *et al.* Ultra-deep IRAC observations of sub- $L^*$   $z \sim 7$  and  $z \sim 8$  galaxies in the HUDF: the contribution of low-luminosity galaxies to the stellar mass density and reionization. *Astrophys. J.* **708**, L26–L31 (2010).
13. González, V. *et al.* Stellar mass density and specific star formation rates of the Universe at  $z \sim 7$ . *Astrophys. J.* **713**, 115–130 (2010).
14. Lehnert, M. *et al.* Spectroscopic confirmation of a galaxy at  $z = 8.6$ . *Nature* **467**, 940–942 (2010).
15. Steidel, C. C., Giavalisco, M., Pettini, M., Dickinson, M. & Adelberger, K. L. Spectroscopic confirmation of a population of normal star-forming galaxies at redshifts  $z > 3$ . *Astrophys. J.* **462**, L17–L21 (1996).
16. Vanzella, E. *et al.* Spectroscopic observations of Lyman break galaxies at redshifts  $\sim 4$ , 5, and 6 in the GOODS-South Field. *Astrophys. J.* **695**, 1163–1182 (2009).
17. Popesso, P. *et al.* The great observatories origins deep survey. VLT/VIMOS spectroscopy in the GOODS-south field. *Astron. Astrophys.* **494**, 443–460 (2009).
18. Steidel, C. C. *et al.* Lyman break galaxies at redshift  $z \sim 3$ : survey description and full data set. *Astrophys. J.* **592**, 728–754 (2003).
19. Reddy, N. *et al.* A spectroscopic survey of redshift  $1.4 < z < 3.0$  galaxies in the GOODS-North Field: survey description, catalogs, and properties. *Astrophys. J.* **653**, 1004–1026 (2006).
20. Trenti, M. & Stiavelli, M. Cosmic variance and its effect on the luminosity function determinations in deep high- $z$  surveys. *Astrophys. J.* **676**, 767–780 (2008).
21. Bouwens, R. J., Broadhurst, T. J. & Silk, J. Cloning Hubble Deep Fields. I. A model-independent measurement of galaxy evolution. *Astrophys. J.* **506**, 557–578 (1998).
22. Bouwens, R. J., Illingworth, G. D., Franx, M. & Ford, H.  $z \sim 7$ –10 galaxies in the HUDF and GOODS Fields: UV luminosity functions. *Astrophys. J.* **686**, 230–250 (2008).
23. Fan, X. *et al.* Evolution of the ionizing background and the epoch of reionization from the spectra of  $z \sim 6$  quasars. *Astron. J.* **123**, 1247–1257 (2002).
24. Komatsu, E. *et al.* Seven-Year Wilkinson Microwave Anisotropy Probe observations: cosmological interpretation. *Astrophys. J.* (in the press); preprint at (<http://arxiv.org/abs/1001.4538>) (2010).
25. Bouwens, R. *et al.* UV-continuum slope and dust obscuration from  $z \sim 6$  to  $z \sim 2$ : the star formation rate density at high redshift. *Astrophys. J.* **705**, 936–961 (2009).
26. Beckwith, S. W. *et al.* The Hubble Ultra Deep Field. *Astrophys. J.* **132**, 1729–1755 (2006).
27. Reddy, N. & Steidel, C. C. A steep faint-end slope of the UV luminosity function at  $z \sim 2$ –3: implications for the global stellar mass density and star formation in low-mass halos. *Astrophys. J.* **692**, 778–803 (2009).
28. Yoshida, M. *et al.* Luminosity functions of Lyman break galaxies at  $z \sim 4$  and  $z \sim 5$  in the Subaru Deep Field. *Astrophys. J.* **653**, 988–1003 (2006).
29. McLure, R., Cirasuolo, M., Dunlop, J. S., Foucaud, S. & Almaini, O. The luminosity function, halo masses, and stellar masses of luminous Lyman-break galaxies at  $5 < z < 6$ . *Mon. Not. R. Astron. Soc.* **395**, 2196–2209 (2009).
30. Schiminovich, D. *et al.* The GALEX-VDS measurement of the evolution of the far-ultraviolet luminosity density and the cosmic star formation rate. *Astrophys. J.* **619**, L47–L50 (2005).

**Supplementary Information** is linked to the online version of the paper at [www.nature.com/nature](http://www.nature.com/nature).

**Acknowledgements** We are grateful to all those at NASA, STScI and throughout the community who have worked to make the Hubble Space Telescope the observatory that it is today, and we acknowledge the importance of the servicing missions and those who organised them. We acknowledge our program coordinator W. Januszewski for his care in helping to set up our program and observing configuration. We acknowledge support from NASA and the Swiss National Science Foundation.

**Author Contributions** R.J.B. carried out the most of the data analysis and calculations for this paper, and wrote most of the Supplementary Information; G.D.I. wrote most of the text in the Letter and iterated on the initial science results and content with R.J.B.; I.L., P.A.O., M.T., C.M.C., P.G.v.D., M.F., M.S. and L.B. provided significant feedback on the science content and on the drafts; I.L. and V.G. were involved with processing the Spitzer IRAC data; P.A.O. contributed to the data analysis; M.T. made the cosmic variance estimates; and D.M. was involved in data processing and pipeline generation for the WFC3/IR data.

**Author Information** Reprints and permissions information is available at [www.nature.com/reprints](http://www.nature.com/reprints). The authors declare no competing financial interests. Readers are welcome to comment on the online version of this article at [www.nature.com/nature](http://www.nature.com/nature). Correspondence and requests for materials should be addressed to R.J.B. ([bouwens@ucolick.org](mailto:bouwens@ucolick.org)).

# Quantum storage of photonic entanglement in a crystal

Christoph Clausen<sup>1\*</sup>, Imam Usmani<sup>1\*</sup>, Félix Bussi eres<sup>1</sup>, Nicolas Sangouard<sup>1</sup>, Mikael Afzelius<sup>1</sup>, Hugues de Riedmatten<sup>1,2,3</sup> & Nicolas Gisin<sup>1</sup>

Entanglement is the fundamental characteristic of quantum physics—much experimental effort is devoted to harnessing it between various physical systems. In particular, entanglement between light and material systems is interesting owing to their anticipated respective roles as ‘flying’ and stationary qubits in quantum information technologies (such as quantum repeaters<sup>1–3</sup> and quantum networks<sup>4</sup>). Here we report the demonstration of entanglement between a photon at a telecommunication wavelength (1,338 nm) and a single collective atomic excitation stored in a crystal. One photon from an energy–time entangled pair<sup>5</sup> is mapped onto the crystal and then released into a well-defined spatial mode after a predetermined storage time. The other (telecommunication wavelength) photon is sent directly through a 50-metre fibre link to an analyser. Successful storage of entanglement in the crystal is proved by a violation of the Clauser–Horne–Shimony–Holt inequality<sup>6</sup> by almost three standard deviations ( $S = 2.64 \pm 0.23$ ). These results represent an important step towards quantum communication technologies based on solid-state devices. In particular, our resources pave the way for building multiplexed quantum repeaters<sup>7</sup> for long-distance quantum networks.

Although single atoms<sup>8,9</sup> and cold atomic gases<sup>10–15</sup> are currently some of the most advanced light–matter quantum interfaces, there is a strong motivation to control light–matter entanglement with more practical systems, such as solid-state devices<sup>16</sup>. Solid-state quantum memories for photons can be implemented with cryogenically cooled crystals doped with rare-earth-metal ions<sup>17</sup>, which have impressive coherence properties at temperatures below 4 K. They have the advantage of simple implementation because rare-earth-metal-doped crystals are widely produced for solid-state lasers, and closed-cycle cryogenic coolers are commercially available. Important progress has been made over the last years in the context of light storage into solid-state memories, including long storage times<sup>18</sup>, high efficiency<sup>19</sup> and storage of light at the single photon level with high coherence and negligible noise<sup>19–23</sup>. Yet these experiments were realized with classical bright pulses or weak coherent states of light. Although this is sufficient to characterize the performance of the memory, and even to infer the quantum characteristics of the device<sup>19,20</sup>, it is not sufficient for the implementation of more sophisticated experiments involving entanglement, as required for most applications in quantum information science. For this purpose, it is necessary to store non-classical light, in particular individual photons that are part of an entangled state (generated, for example, through spontaneous parametric down-conversion, SPDC), similar to previous demonstrations using electromagnetically induced transparency in cold atomic gases<sup>14,15</sup>. In addition, for quantum communication applications, the other part of the entangled state should be a photon at telecommunication wavelength in order to minimize loss during transmission in optical fibres.

In this Letter, we report on an experiment in which a photon from an entangled pair is stored in a quantum memory based on a rare-earth-metal-doped crystal. More specifically, we show that non-classical

intensity correlations between the two photons still exist after storage and retrieval. We then show, through a violation of a Bell inequality, that the storage process creates a light–matter entangled state. In addition, these results represent the first successful mapping of energy–time entangled photons onto a quantum memory.

Our experiment consists of a coherent solid-state quantum memory and a source of entangled photons. A schematic of the experiment is shown in Fig. 1. The source is based on non-degenerate SPDC in a nonlinear waveguide pumped by continuous wave light at 532 nm. This yields energy–time entangled photons with the signal photon at

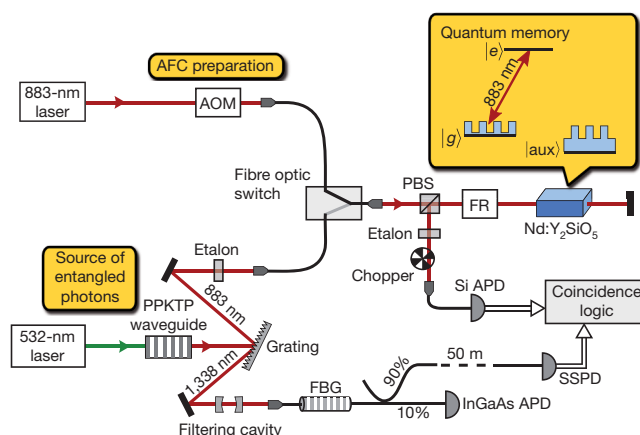


**Figure 1 | Experimental set-up.** The experimental set-up can be divided into three parts: the Nd:Y<sub>2</sub>SiO<sub>5</sub> crystal serving as quantum memory, the laser system for the preparation of the AFC in the crystal, and the source of entangled photons with associated spectral filtering. During the experiment we periodically switch between 15 ms of AFC preparation and frequency stabilization and a 15-ms measurement phase, in which single photons are stored. During the preparation, the comb structure is prepared by frequency-selective optical pumping of atoms from the ground state  $|g\rangle$  to the auxiliary state  $|aux\rangle$  using light from an 883-nm diode laser in combination with an acousto-optic modulator (AOM). The fibre optic switch is in the upper position, and the silicon avalanche photodiode (Si APD) is protected from the bright light by a chopper. During the measurement phase, the positions of switch and chopper are reversed. Now, photon pairs are generated in the periodically poled potassium titanyl phosphate (PPKTP) waveguide via SPDC. The two photons in a pair are spatially separated by a diffraction grating and then strongly filtered by two etalons, a cavity and a fibre Bragg grating (FBG). Photons at 883 nm are sent through the crystal in a double-pass configuration to increase the absorption probability, and are afterwards detected by the Si avalanche photodiode. Photons at 1,338 nm are directed towards a superconducting single photon detector (SSPD) located in another laboratory 50 m away. All relevant quantities are extracted from the coincidence statistics of the two detectors. Details of the frequency stabilization and the filtering system are given in the Methods. PBS, polarizing beam splitter; FR, Faraday rotator.

<sup>1</sup>Group of Applied Physics, University of Geneva, CH-1211 Geneva 4, Switzerland. <sup>2</sup>ICFO—Institut de Ci ncies F toniques, Mediterranean Technology Park, 08860 Castelldefels, Barcelona, Spain. <sup>3</sup>ICREA—Institut Catal  de Recerca i Estudis Avan ats, 08015 Barcelona, Spain.

\*These authors contributed equally to this work.

the memory wavelength of 883 nm, and the idler photon at the telecom wavelength of 1,338 nm. Both photons initially have a spectral width of approximately 1.5 THz, a factor of  $10^4$  larger than the 120-MHz bandwidth of the memory. Hence, strong filtering is crucial<sup>14</sup> to achieve signal-to-noise ratios sufficiently large to reveal the presence of entanglement during storage. After filtering, the signal photon is sent to the memory, and the idler photon is coupled into a fibre leading to a detector in another laboratory 50 m away. Owing to the low loss at telecommunication wavelengths, this distance could, in principle, be extended to several kilometres without significantly affecting the results presented here.

The quantum memory is a 1-cm-long  $\text{Y}_2\text{SiO}_5$  crystal, impurity-doped with neodymium ions having a resonance at 883 nm with good coherence properties<sup>23</sup>. It is based on a photon-echo-type interaction using an atomic frequency comb (AFC) (see ref. 24 and Supplementary Information). In an AFC, the absorption profile of the atomic ensemble is shaped into a comb-like structure by optical pumping. A photon is then, with some efficiency, absorbed and re-emitted into a well-defined spatial mode due to a collective rephasing of the atoms in the comb structure. The time of re-emission depends on the period of the comb and is predetermined. We have previously shown that this kind of memory can store multiple temporal modes<sup>23</sup> and is therefore perfectly suited for storing energy-time entangled photons. For the work presented here, we have significantly improved the storage efficiency to obtain sufficiently large signal-to-noise ratios. Indeed, using a new optical pumping scheme for the preparation of the AFC (see Supplementary Information), the efficiency was increased by a factor of three for storage times below 200 ns, now reaching values up to 21% (see results below).

In a first experiment we verified that the non-classical nature of the intensity correlations between the signal (883 nm) and idler (1,338 nm) modes is preserved after the storage and retrieval process. If we assume second-order auto-correlations of signal and idler  $g_x^{(2)}$  (where  $x = 's'$  for signal or  $'i'$  for idler) satisfying  $1 \leq g_x^{(2)} \leq 2$ , then non-classicality is proved by measuring a cross-correlation  $g_{si}^{(2)} = P_{si}/P_s P_i$  greater than 2 (see ref. 25). Here,  $P_s$  (or  $P_i$ ) is the probability of detecting a signal (or idler) photon, and  $P_{si}$  the probability of a coincidence detection (see Methods).

We first measured  $g_{si}^{(2)}$  as a function of the pump power of the source, as shown in Fig. 2a. We find an optimum around a pump power of 3 mW, where  $g_{si}^{(2)} \approx 115$  without the AFC memory, and  $g_{si}^{(2)} \approx 30$  after a 25-ns storage, thus proving the quantum character of the storage (note that all results presented in this Letter are without any subtraction of background noise). The reduction in the cross-correlation with

the storage is due to limited efficiency (21%), which effectively increases the contribution of accidental coincidences stemming from dark counts and multiple pair emissions. Next, we measured the memory efficiency and the cross-correlation for different storage times, as shown in Fig. 2b and c.

We now turn our attention towards a particular kind of quantum correlation, namely entanglement. By performing a two-photon quantum interference experiment, we show that the entanglement of the photon pair is preserved when the signal photon is stored in the crystal.

Photon pairs generated by our source are energy-time entangled, that is, the two photons in a pair are created simultaneously to ensure energy conservation, but the pair-creation time is uncertain to within the coherence time of the pump laser. We wish to reveal the presence of this entanglement using a Franson-type set-up<sup>5</sup>. As detailed in the Supplementary Information, the correlations can be interpreted as stemming from local measurements performed on a post-selected time-bin entangled state:  $\frac{1}{\sqrt{2}}(|E_s E_i\rangle + |L_s L_i\rangle)$ , where the early and late time bins  $|E_{s,i}\rangle$  and  $|L_{s,i}\rangle$  are separated by a time of 25 ns set by the analysing interferometer (see Fig. 3a). In our experiment, however, the state of the signal photon is stored as a collective atomic excitation in the quantum memory before the measurement. Moreover, using a double AFC scheme<sup>20,23</sup>, the memory is used not only to store the entangled photon, but also to analyse it as part of the measurement. More precisely, the incident time-bins  $|E_s\rangle$  and  $|L_s\rangle$  are mapped to distinct AFC modes  $|E_{QM}\rangle$  and  $|L_{QM}\rangle$ , respectively (where subscript QM denotes quantum memory). Storage of the entangled signal photon then creates a light-matter entangled state:

$$\frac{1}{\sqrt{2}}(|E_{QM} E_i\rangle + |L_{QM} L_i\rangle) \quad (1)$$

The predetermined storage times of  $|E_{QM}\rangle$  and  $|L_{QM}\rangle$  are 75 ns and 50 ns, respectively. After absorption, both AFCs coherently re-emit the stored excitation into the same well-defined temporal and spatial mode with a relative phase  $\Delta\phi_s$ . This re-emission, followed by detection, constitutes the measurement of the state of the memory. The idler photon is measured using a fibre-based time-bin qubit analyser with a 25-ns delay and a relative phase  $\Delta\phi_i$  between the short and long arms. The coincidence detection probability is given by:

$$P_{si} \propto 1 + V \cos(\Delta\phi_s + \Delta\phi_i) \quad (2)$$

where  $V$  is the visibility of interference. Figure 3b shows the measured coincidence rate as a function of  $\Delta\phi_s$  for two values of  $\Delta\phi_i$ . The raw visibilities are  $V = (84 \pm 4)\%$  and  $(78 \pm 4)\%$ .

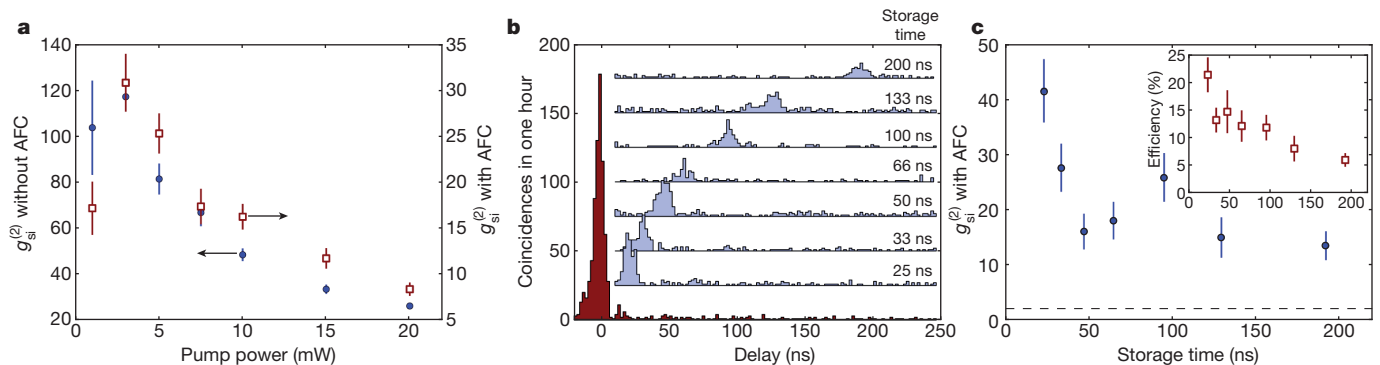


**Figure 2 | Non-classical correlations and storage efficiency.** **a**, Cross-correlation  $g_{si}^{(2)}$  as a function of the pump power incident on the wave guide. Data points shown were taken with an AFC memory storage time of 25 ns (brown square symbols), and for comparison, with the crystal prepared with a 120-MHz-wide transmission window, that is, without AFC (blue circle symbols). The size of the coincidence window is 10 ns. **b**, Coincidence histograms for different predetermined storage times, vertically offset for clarity. For comparison, the lowest histogram was taken without AFC. The pump power was 3 mW. **c**, Cross-

correlation  $g_{si}^{(2)}$  as a function of storage time with 10-ns coincidence window, extracted from **b**. For storage times up to 200 ns the correlations stay well above the classical limit of  $g_{si}^{(2)} = 2$  (dashed line). The inset shows the storage efficiency for the same range of storage times. With increasing storage times, limiting factors in the storage medium degrade the comb shape and reduce the efficiency and cross-correlation (see Supplementary Information). However, the latter stays well above the classical limit for storage times up to 200 ns. Error bars show  $\pm 1$  standard deviation (s.d.).

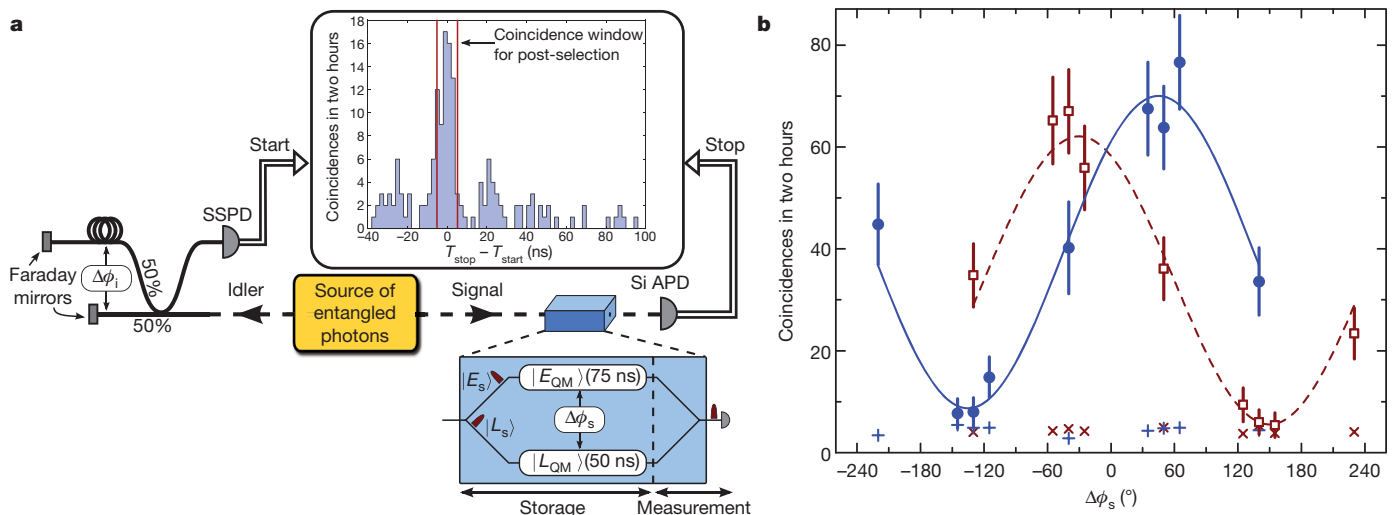


**Figure 3 | Storage of photonic entanglement in a crystal.** **a**, Franson-type set-up used to reveal the entanglement. A qubit analyser consisting of an unbalanced, fibre-based Michelson interferometer with 25-ns delay and relative phase  $\Delta\phi_i$  is inserted before the SSPD used to detect the idler photon (see also Fig. 1). The signal photon is stored in the crystal, yielding a light-matter entangled state. The state of the memory is measured through re-emission and detection of the photon in the time-window at zero-time delay (central peak) of the coincidence histogram (inset). This post-selects measurement on the entangled state of equation (1). The relative phase  $\Delta\phi_s$  can

be reliably set to any desired value (see the Supplementary information). **b**, Number of coincidences in the central peak in two hours as a function of the relative phase  $\Delta\phi_s$  for two values of  $\Delta\phi_i$ . The pump power was 5 mW, and the size of the coincidence window 10 ns. The solid and dashed lines result from fits to equation (2) and respectively give visibilities of  $V = (78 \pm 4)\%$  and  $(84 \pm 4)\%$ . The visibilities are mainly limited by the level of accidental coincidences (cross symbols). The fit also gives a difference between the two values of  $\Delta\phi_i$  of  $75^\circ \pm 10^\circ$ . These values closely match settings necessary for a maximal violation of the CHSH inequality. Error bars are  $\pm 1$  s.d.

Quantum entanglement can be revealed by a violation of the Clauser–Horne–Shimony–Holt (CHSH) inequality<sup>6</sup>. The possibility of violating this inequality, that is, of finding a CHSH parameter  $S > 2$ , can be inferred indirectly from a visibility larger than  $1/\sqrt{2} \approx 70.7\%$ . Nevertheless, we performed the measurements necessary for a direct violation of the inequality and obtained  $S = 2.64 \pm 0.23$ . This proves the presence of entanglement between the idler photon and the matter qubit in the crystal, provided the effect of the memory on single photons is appropriately described as storage followed by measurement (see Supplementary Information). This description is correct within the theory of AFC memories<sup>24</sup>, which is supported by experiments storing weak coherent states of light<sup>11,21–23</sup>. Note also that we do not claim any demonstration of nonlocal correlations. Indeed, besides the usual locality and detection loopholes, here the measurement setting has to be chosen before the photonic qubit is mapped onto the crystal. This could have been avoided by adding an interferometer after the memory, the latter being used for storage only. We did not do so because we think that it is elegant and simple to use the memory also as a small quantum processor that performs the measurement.

A particularly intriguing situation arises when post-selecting on the case where only  $|E_s\rangle$  is stored in the crystal for 25 ns using a single AFC scheme, while  $|L_s\rangle$  is directly transmitted. Indeed, the imbalance between the storage efficiency and the transmission probability offers a well-suited qubit analyser for a violation of the CHSH inequality using bases lying in the  $x$ - $z$  plane of the Bloch sphere. We performed such a measurement and observed  $S = 2.62 \pm 0.15$  (see Supplementary Information). This implies that the initial photon–photon entangled state is mapped onto a state of the form:

$$\sqrt{\eta_{\text{abs}}} |E_{\text{QM}} E_i\rangle + |L_s L_i\rangle \quad (3)$$

where  $\eta_{\text{abs}}$  is the absorption efficiency. This is an entangled state between a telecommunication-wavelength qubit and a light-matter hybrid qubit. We note that this kind of hybrid qubit is the key ingredient of an efficient quantum repeater protocol based on atomic ensembles and linear optics<sup>3</sup>.

This work is part of the effort towards implementing a quantum repeater, which could provide a solution to the distance limit (due to intrinsic loss) for entanglement distribution and quantum cryptography

using optical fibres<sup>3</sup>. To achieve this long-term goal, several future advances are required. The user must be able to trigger the re-emission of the memory, whereas in our experiment the duration of the storage is pre-determined. We have proposed<sup>24</sup> and demonstrated<sup>26</sup> a method for achieving on-demand re-emission using so-called spin-wave storage. This has the additional benefit of allowing longer storage times owing to the more robust spin coherence. Another crucial aspect is the efficiency, which is directly linked to the optical depth of the material<sup>24</sup>. It can be increased by using longer crystals<sup>19</sup> or optical cavities<sup>27,28</sup>.

The creation of entanglement between a single photon and a macroscopic object—in this case a single collective atomic excitation delocalized over a 1-cm-long crystal—is fascinating in itself. Beyond its fundamental interest, we believe that our demonstration of storage of entanglement in a crystal represents an important step towards quantum repeaters based on solid-state quantum memories.

We note that, parallel to this work, Saglamyurek *et al.* have demonstrated storage and retrieval of an entangled photon using a thulium-doped lithium niobate waveguide<sup>29</sup>.

**METHODS SUMMARY**

**Spectral filtering and detection.** The bandwidth of the photon pairs is reduced by a factor of  $10^4$  in several steps. Pump, signal and idler photons are spatially separated by a diffraction grating (see Fig. 1). In combination with coupling into single-mode fibres, this reduces the bandwidth to tens of gigahertz. A subsequent passage through a Fabry–Perot cavity reduces the bandwidth of the idler photon to 45 MHz (corresponding to a coherence time of about 4 ns), and a fibre Bragg grating blocks all but one of the longitudinal cavity modes. The signal photon is filtered by two etalons with a linewidth of 600 MHz each, and different free spectral ranges. The detector efficiency is 8% for the idler photon with 10-Hz dark counts, and 30% with 100-Hz dark counts for the signal photon.

**Frequency stabilization.** We must ensure, for the whole duration of a measurement, that the central frequency of the optical filtering system at 1,338 nm and of the AFC at 883 nm both satisfy the energy conservation of the SPDC process. To do this, a small fraction of the light at 883 nm is overlapped with the light of the 532-nm laser that pumps the PPKTP waveguide. This leads to the creation of light at 1,338 nm by difference frequency generation (DFG). Using this DFG signal, the frequency of the 532-nm light is adjusted such that the detection rate on a separate InGaAs avalanche photodiode (see Fig. 1) stays constant, which means that the 1,338-nm DFG light is in resonance with the filtering cavity. Long-term stability of the 883-nm laser itself is achieved by continuously referencing it to a Fabry–Perot cavity.

**Full Methods** and any associated references are available in the online version of the paper at [www.nature.com/nature](http://www.nature.com/nature).

**Received 24 August; accepted 9 November 2010.**

**Published online 12 January 2011.**

- Briegleb, H.-J., Dür, W., Cirac, J. I. & Zoller, P. Quantum repeaters: the role of imperfect local operations in quantum communication. *Phys. Rev. Lett.* **81**, 5932–5935 (1998).
- Duan, L.-M., Lukin, M. D., Cirac, J. I. & Zoller, P. Long-distance quantum communication with atomic ensembles and linear optics. *Nature* **414**, 413–418 (2001).
- Sangouard, N., Simon, C., de Riedmatten, H. & Gisin, N. Quantum repeaters based on atomic ensembles and linear optics. Preprint at (<http://arxiv.org/abs/0906.2699>) (2009).
- Kimble, H. J. The quantum internet. *Nature* **453**, 1023–1030 (2008).
- Franson, J. D. Bell inequality for position and time. *Phys. Rev. Lett.* **62**, 2205–2208 (1989).
- Clauser, J. F., Horne, M. A., Shimony, A. & Holt, R. A. Proposed experiment to test local hidden-variable theories. *Phys. Rev. Lett.* **23**, 880–884 (1969).
- Simon, C. *et al.* Quantum repeaters with photon pair sources and multimode memories. *Phys. Rev. Lett.* **98**, 190503 (2007).
- Blinov, B. B., Moehring, D., Duan, L.-M. & Monroe, C. Observation of entanglement between a single trapped ion and a single photon. *Nature* **428**, 153–157 (2004).
- Volz, J. *et al.* Observation of entanglement of a single photon with a trapped atom. *Phys. Rev. Lett.* **96**, 030404 (2006).
- Matsukevich, D. N. *et al.* Entanglement of a photon and a collective atomic excitation. *Phys. Rev. Lett.* **95**, 040405 (2005).
- de Riedmatten, H. *et al.* Direct measurement of decoherence for entanglement between a photon and stored atomic excitation. *Phys. Rev. Lett.* **97**, 113603 (2006).
- Chen, S. *et al.* Demonstration of a stable atom-photon entanglement source for quantum repeaters. *Phys. Rev. Lett.* **99**, 180505 (2007).
- Sherson, J. F. *et al.* Quantum teleportation between light and matter. *Nature* **443**, 557–560 (2006).
- Akiba, K., Kashiwagi, K., Arikawa, M. & Kozuma, M. Storage and retrieval of nonclassical photon pairs and conditional single photons generated by the parametric down-conversion process. *N. J. Phys.* **11**, 013049 (2009).
- Jin, X.-M. *et al.* Quantum interface between frequency-uncorrelated down-converted entanglement and atomic-ensemble quantum memory. Preprint at (<http://arxiv.org/abs/1004.4691>) (2010).
- Togan, E. *et al.* Quantum entanglement between an optical photon and a solid-state spin qubit. *Nature* **466**, 730–734 (2010).
- Tittel, W. *et al.* Photon-echo quantum memory in solid state systems. *Laser Photon. Rev.* **4**, 244–267 (2010).
- Longdell, J. J., Fraval, E., Sellars, M. J. & Manson, N. B. Stopped light with storage times greater than one second using electromagnetically induced transparency in a solid. *Phys. Rev. Lett.* **95**, 063601 (2005).
- Hedges, M. P., Longdell, J. J., Li, Y. & Sellars, M. J. Efficient quantum memory for light. *Nature* **465**, 1052–1056 (2010).
- de Riedmatten, H., Afzelius, M., Staudt, M. U., Simon, C. & Gisin, N. A solid-state light-matter interface at the single-photon level. *Nature* **456**, 773–777 (2008).
- Chanelière, T., Ruggiero, J., Bonarota, M., Afzelius, M. & Gouët, J.-L. Efficient light storage in a crystal using an atomic frequency comb. *N. J. Phys.* **12**, 023025 (2010).
- Sabooni, M. *et al.* Storage and recall of weak coherent optical pulses with an efficiency of 25%. *Phys. Rev. Lett.* **105**, 060501 (2010).
- Usmani, I., Afzelius, M., de Riedmatten, H. & Gisin, N. Mapping multiple photonic qubits into and out of one solid-state atomic ensemble. *Nature Commun.* **1**, 12 (2010).
- Afzelius, M., Simon, C., de Riedmatten, H. & Gisin, N. Multimode quantum memory based on atomic frequency combs. *Phys. Rev. A* **79**, 052329 (2009).
- Kuzmich, A. *et al.* Generation of nonclassical photon pairs for scalable quantum communication with atomic ensembles. *Nature* **423**, 731–734 (2003).
- Afzelius, M. *et al.* Demonstration of atomic frequency comb memory for light with spin-wave storage. *Phys. Rev. Lett.* **104**, 040503 (2010).
- Afzelius, M. & Simon, C. Impedance-matched cavity quantum memory. *Phys. Rev. A* **82**, 022310 (2010).
- Moiseev, S. A., Andrianov, S. N. & Gubaidullin, F. F. Efficient multimode quantum memory based on photon echo in an optimal QED cavity. *Phys. Rev. A* **82**, 022311 (2010).
- Saglamyurek, E. *et al.* Broadband waveguide quantum memory for entangled photons. *Nature* doi:10.1038/nature09719 (this issue).

**Supplementary Information** is linked to the online version of the paper at [www.nature.com/nature](http://www.nature.com/nature).

**Acknowledgements** We thank R. Locher for help during the early stages of the experiment. We are grateful to A. Beveratos and W. Tittel for lending us avalanche photodiodes. This work was supported by the Swiss NCCR Quantum Photonics, the Science and Technology Cooperation Program Switzerland–Russia, as well as by the European projects QuRep and ERC-Qore. F.B. was supported in part by FQRNT.

**Author Contributions** All authors contributed extensively to the work presented in this paper.

**Author Information** Reprints and permissions information is available at [www.nature.com/reprints](http://www.nature.com/reprints). The authors declare no competing financial interests. Readers are welcome to comment on the online version of this article at [www.nature.com/nature](http://www.nature.com/nature). Correspondence and requests for materials should be addressed to M.A. ([mikael.afzelius@unige.ch](mailto:mikael.afzelius@unige.ch)).

## METHODS

**Spectral filtering and detection.** The narrowband filtering of the SPDC photons consists of several steps (see Fig. 1). First, a diffraction grating spatially separates the pump, signal and idler photons and, in combination with coupling into single-mode fibres, reduces the bandwidth of the photons at 883 nm (or 1,338 nm) to 90 GHz (or 60 GHz). Photons at 1,338 nm are then coupled through a Fabry–Perot cavity with linewidth 45 MHz and free spectral range of 23.9 GHz. Subsequently, a fibre Bragg grating with 16 GHz bandwidth ensures that only a single longitudinal cavity mode remains.

Filtering one of the photons in the pair is the same as filtering the photon pair as a whole, because energy conservation guarantees that photons measured in coincidence have the same bandwidth. However, uncorrelated photons would then contribute significantly to the accidental coincidences. Therefore, complementary filtering at 883 nm was necessary. To do this, we used one solid and one air-spaced etalon, both with bandwidths around 600 MHz. Different free spectral ranges of 42 and 50 GHz eliminate uncorrelated longitudinal modes. Additionally, outside the 120-MHz bandwidth of the AFC, the absorption of the crystal with an inhomogeneous linewidth of 6 GHz provides a final filtering step.

We used detectors with 30% detection efficiency and approximately 100 Hz dark counts at 883 nm, and detectors with 8% detection efficiency and approximately 10 Hz at 1,338 nm. Together with a transmission of the filtering system for the signal (or idler) photon of 45% (or 14%), and 4% (or 14%) for the remainder of the optical set-up, we reached an overall detection efficiency of 0.5% (or 0.15%) (see also Supplementary Information). These numbers could, in principle, be significantly improved through optimized optical alignment, the use of anti-reflection-coated elements, and so on.

**Frequency stabilization.** In the experiment, coincidence rates are typically a few per minute. With accumulation times thus reaching several hours, a high degree of frequency stability of the lasers and filtering elements is indispensable. In particular, frequency drifts of the AFC preparation laser with respect to the pump laser of the

SPDC source have to be eliminated. Otherwise, the photon-pair frequencies  $\omega_{883} + \omega_{1338} = \omega_{532}$  imposed by energy conservation in the SPDC would not simultaneously match the centre of the AFC and that of the filtering system at 1,338 nm. Drifts were eliminated using the following method. First, the long-term stability of the 883-nm laser was dramatically increased by locking it to a temperature-stabilized Fabry–Perot cavity. Second, during the 15-ms preparation cycle, we injected a fraction of the 883-nm light into the waveguide. The frequency of the light created at 1,338 nm via difference frequency generation (DFG) was tuned by controlling the frequency of the pump laser at 532 nm. Using a side-of-fringe technique, we could then lock the frequency of the DFG signal to the transmission peak of the filtering cavity. As a result, long-term frequency deviations between the centre of the AFC structure and the filtered photon pairs were reduced to about 1 MHz over several hours.

For measurements involving the unbalanced Michelson interferometer for the idler photon, the phase of the interferometer was also stabilized using the highly coherent DFG light.

**Photon correlations in SPDC.** Neglecting the exact frequency dependence, the state of the photons created in the SPDC process is described by  $|0_s, 0_i\rangle + \sqrt{p}|1_s, 1_i\rangle + O(p)$ , where the subscript 's' (or 'i') indicates the signal (or idler) mode at 883 nm (or 1,338 nm). Here, the pair creation probability  $p$  is assumed to be small and proportional to the pump power. In such a state, the signal and idler modes individually exhibit the statistics of a classical thermal field, that is, their auto-correlations are  $g_x^{(2)} = 2$  for  $x = s$  or  $i$ . We stress, however, that the criterion for non-classicality of the cross-correlation that we used, namely  $g_{si}^{(2)} = P_{si}/P_s P_i > 2$ , requires only that  $1 \leq g_x^{(2)} \leq 2$ , which is always fulfilled by non-degenerate photon pairs created through SPDC. In practice,  $P_{si}$  (or  $P_s P_i$ ) is determined by the number of coincidences in a certain time window centred on (or away from) the coincidence peak. For low pump powers, the measured cross-correlation is usually limited by detector dark counts, and at high pump powers it is reduced by the contribution of multiple pairs, that is, higher-order terms in  $p$ .

# Broadband waveguide quantum memory for entangled photons

Erhan Saglamyurek<sup>1</sup>, Neil Sinclair<sup>1</sup>, Jeongwan Jin<sup>1</sup>, Joshua A. Slater<sup>1</sup>, Daniel Oblak<sup>1</sup>, Félix Bussi eres<sup>1†</sup>, Mathew George<sup>2</sup>, Raimund Ricken<sup>2</sup>, Wolfgang Sohler<sup>2</sup> & Wolfgang Tittel<sup>1</sup>

The reversible transfer of quantum states of light into and out of matter constitutes an important building block for future applications of quantum communication: it will allow the synchronization of quantum information<sup>1</sup>, and the construction of quantum repeaters<sup>2</sup> and quantum networks<sup>3</sup>. Much effort has been devoted to the development of such quantum memories<sup>1</sup>, the key property of which is the preservation of entanglement during storage. Here we report the reversible transfer of photon–photon entanglement into entanglement between a photon and a collective atomic excitation in a solid-state device. Towards this end, we employ a thulium-doped lithium niobate waveguide in conjunction with a photon-echo quantum memory protocol<sup>4</sup>, and increase the spectral acceptance from the current maximum<sup>5</sup> of 100 megahertz to 5 gigahertz. We assess the entanglement-preserving nature of our storage device through Bell inequality violations<sup>6</sup> and by comparing the amount of entanglement contained in the detected photon pairs before and after the reversible transfer. These measurements show, within statistical error, a perfect mapping process. Our broadband quantum memory complements the family of robust, integrated lithium niobate devices<sup>7</sup>. It simplifies frequency-matching of light with matter interfaces in advanced applications of quantum communication, bringing fully quantum-enabled networks a step closer.

Quantum communication is founded on the encoding of information, generally referred to as quantum information, into quantum states of light<sup>8</sup>. The resulting applications of quantum physics at its fundamental level offer cryptographic security through quantum key distribution without relying on unproved mathematical assumptions<sup>8</sup> and allow for the disembodied transfer of quantum states between distant places by means of quantum teleportation<sup>6</sup>. Reversible mapping of quantum states between light and matter is central to advanced applications of quantum communication such as quantum repeaters<sup>2</sup> and quantum networks<sup>3</sup>, in which matter constitutes nodes that hold quantum information until needed, and thereby synchronize the information flow through the communication channel or network. Furthermore, such a quantum interface allows the generation of light–matter entanglement through the mapping of one of two entangled photons into matter. To determine whether and how different physical systems can be entangled, and to localize the fundamental or technological boundaries where this fascinating quantum link breaks down, are central goals in quantum physics and have received much attention over the past decades<sup>6</sup>.

The reversible light–matter interface can be realized through the direct transfer of quantum states from light onto matter and back, or through the generation of light–matter entanglement followed by teleportation of quantum information from an externally provided photon into matter, and eventually back. Experimental capabilities have advanced rapidly over the past years and quantum state transfer between light and atomic vapour<sup>9–13</sup>, solid-state ensembles<sup>4,14</sup>, or single absorbers<sup>15</sup>, as well as the generation of light–matter entanglement

through the absorption of photons<sup>16–18</sup>, or the emission of photons from atomic ensembles<sup>19–21</sup> or single emitters<sup>22,23</sup> have all been reported.

For quantum memory to become practical, it is important to reduce the complexity of experimental implementations, and the recent addition of rare-earth-ion-doped crystals<sup>4,14</sup> to the set of storage materials has been a valuable step towards this goal. The promise of such crystals is further enhanced through potentially long storage times—up to several seconds in Pr:Y<sub>2</sub>SiO<sub>5</sub> (ref. 24). In addition, given the large inhomogeneous broadening of optical zero-phonon lines, up to ~100-gigahertz (GHz), rare-earth-ion-doped crystals in principle offer storage of photons with less than 100-picosecond duration when being used in conjunction with a suitable quantum memory protocol<sup>4</sup>. Yet, the reversible state transfer between light and solid-state devices has so far not been shown to preserve entanglement. This is largely due to the limited spectral bandwidth of current implementations, 100 megahertz (MHz) at most<sup>5</sup>, which is orders of magnitude smaller than that of entangled photon pairs generated in the widely used process of spontaneous parametric down-conversion<sup>6</sup>. In this work, we approach the problem from both ends: we increase the acceptance bandwidth of our storage device to 5 GHz and narrow the bandwidths of our entangled photons to similar values. Furthermore, by using a wave-guiding storage medium, we move fundamental quantum memory research further towards application.

The layout of our experiment is depicted in Fig. 1. Short pulses of 523-nm wavelength light travel through an unbalanced interferometer. For sufficiently small pulse energies, subsequent spontaneous parametric down-conversion yields, to a good approximation, individual pairs of photons, centred at wavelengths around 795 nm and 1,532 nm, in the time-bin entangled qubit state<sup>25</sup>:

$$|\phi^+\rangle = \frac{1}{\sqrt{2}}(|e,e\rangle + |l,l\rangle) \quad (1)$$

Here,  $|e\rangle$  and  $|l\rangle$  denote early and late temporal modes and replace the usual spin-down and spin-up notation for spin-half particles. More specifically,  $|i,j\rangle$  denotes a quantum state in which the 795-nm photon has been created in the temporal mode  $i$ , and the 1,532-nm photon has been created in the temporal mode  $j$ . We point out that, owing to the spectral filtering, our source generates frequency-uncorrelated entangled photons at wavelengths that match the low-loss windows of free-space and standard telecommunication fibre. It can thus be readily used in real-world applications of quantum communication that involve quantum teleportation and entanglement swapping.

The 1,532-nm photon is directed to a qubit analyser. It consists of either a fibre delay line followed by a single-photon detector that monitors the photon's arrival time, or a fibre-optical interferometer that is unbalanced in the same way as the pump interferometer, followed by single-photon detectors. The role of the delay line is to perform projection measurements of the photon's state onto early and late qubit states. Alternatively, the interferometer enables projections onto

<sup>1</sup>Institute for Quantum Information Science, and Department of Physics and Astronomy, University of Calgary, 2500 University Drive NW, Calgary, Alberta. T2N 1N4, Canada. <sup>2</sup>Department of Physics—Applied Physics, University of Paderborn, Warburger Strasse 100, 33095 Paderborn, Germany. <sup>†</sup>Present address: GAP-Optique, University of Geneva, Rue de l' cole-de-M decine 20, 1211 Geneva 4, Switzerland.

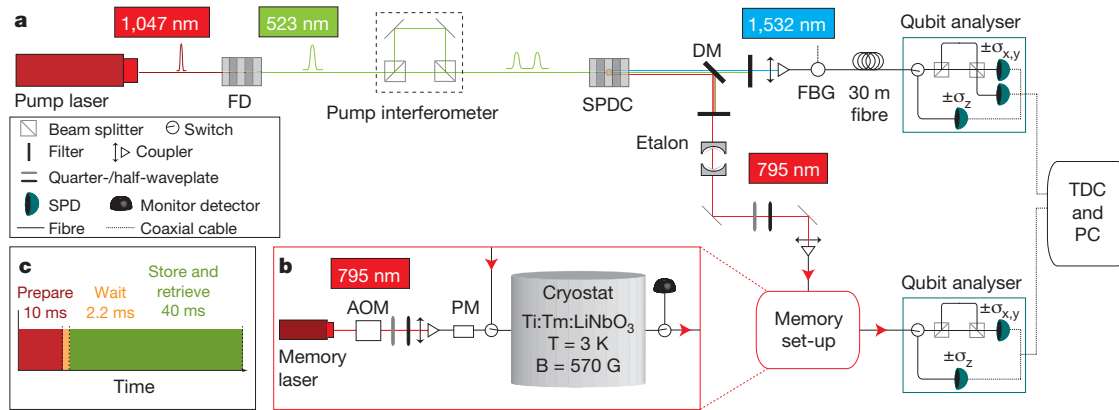


**Figure 1 | Schematics of the experimental set-up.** **a**, Generating and measuring entanglement. Six-picosecond-long pump laser pulses (1,047.328 nm wavelength, 80 MHz repetition rate) are frequency doubled (FD) in a periodically poled lithium niobate (PPLN) crystal. Each resulting 16-ps-long pulse (523.664 nm wavelength, 90 mW average power) is coherently split into two by the unbalanced pump interferometer, featuring a 1.4-ns travel-time difference. Spontaneous parametric down-conversion (SPDC) in a second PPLN crystal followed by frequency filtering using an etalon and a fibre Bragg grating (FBG) (bandwidths of 6 GHz and 9 GHz, respectively), yields maximally entangled pairs of photons centred at 795.506 nm and 1,532.426 nm wavelength (DM, dichroic mirror). The 1,532-nm photon travels through a 30-m telecommunication fibre, and the 795-nm photon is either stored in the memory or sent through a fibre delay line (not pictured). To characterize the bi-photon state, we use qubit analysers consisting of delay lines or unbalanced interferometers connected to single-photon detectors. Detection events are

equal superpositions of early and late modes<sup>25</sup>. Using the language of spin-half systems, this corresponds to projections onto  $\sigma_z$  and, for appropriately chosen phases,  $\sigma_x$  and  $\sigma_y$ , respectively.

The 795-nm photon is transmitted to the quantum memory where its state—specifically that it is entangled with the 1,532-nm photon—is mapped onto a collective excitation of millions of thulium ions. Some time later, the state is mapped back onto a photon that exits the memory through a fibre in well-defined spatio-temporal modes and is probed by a second qubit analyser.

collected with a time-to-digital converter (TDC) connected to a personal computer (PC). All interferometers are phase-locked to stable reference lasers (not shown). **b**, Memory set-up. The 795.506-nm continuous-wave memory laser beam is intensity- and phase/frequency-modulated using an acousto-optic modulator (AOM) and a phase modulator (PM). The waveguide is cooled to 3 K and exposed to a 570-G magnetic field aligned with the crystal's  $C_3$ -axis. Waveplates allow adjusting the polarization of the beam to the waveguide's transverse magnetic (TM) mode, and optical switches combine and separate the optical pump beam and the 795-nm photons. **c**, Timing sequence. We use three continuously repeated phases: the 10 ms 'prepare' phase for optical pumping, the 2.2-ms 'wait' phase, which ensures stored photons are not polluted by fluorescence from the excited state, and the 40-ms 'store and retrieve' phase, during which many 795-nm photons are successively stored in the waveguide and recalled after 7 ns.

To reversibly map the 795-nm photon onto matter, we use a photon-echo quantum memory protocol based on atomic frequency combs (AFC)<sup>4</sup>. It is rooted in the interaction of light with an ensemble of atomic absorbers (so far rare-earth-ion-doped crystals cooled to cryogenic temperatures) with an inhomogeneously broadened absorption line that has been tailored into a series of equally spaced absorption peaks (see Fig. 2). The absorption of a single photon leads to a collective excitation shared by many atoms. Owing to the particular shape of the tailored absorption line, the excited collective coherence rapidly dephases and repeatedly recovers after multiples of the storage time  $T_s$ . This results in the re-emission of a photon in the state encoded into the original photon.

In our implementation the moment of photon re-emission is pre-determined by the spacing of the teeth in the comb,  $T_s = 1/\Delta$ , and the storage process can be described as arising from the linear response of an optical filter made by spectral hole burning. Yet, readout on demand can be achieved by temporarily mapping the optically excited coherence onto ground-state coherence where the comb spacing is smaller or the comb structure is washed out<sup>4</sup>, or by combining the AFC protocol with controlled reversible inhomogeneous broadening of each absorption line, similar to the storage mechanism used in another photon-echo quantum memory protocol<sup>1</sup>.

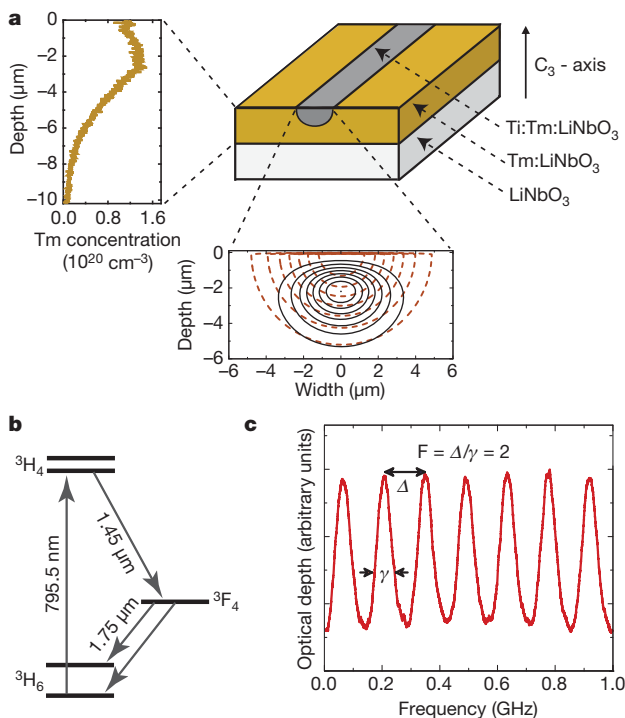


**Figure 2 | The storage medium.** **a**, Waveguide geometry. The measured thulium (Tm) concentration profile is given on the left and the calculated intensity distribution of the fundamental TM-mode at the 795-nm wavelength is shown below. Iso-intensity lines are plotted corresponding to 100%, 87.5%, 75% and so on of the maximum intensity. **b**, Simplified energy level diagram of thulium ions. The optical coherence time of the  $^3\text{H}_6 \leftrightarrow ^3\text{H}_4$  transition at 3 K is 1.6 μs, the radiative lifetimes of the  $^3\text{H}_4$  and  $^3\text{F}_4$  levels are 82 μs and 2.4 ms, respectively, and the branching ratio from the  $^3\text{H}_4$  to the  $^3\text{F}_4$  level is 44%. Upon application of a magnetic field of 570 G, the ground and excited levels split into magnetic sublevels with lifetimes exceeding one second<sup>27</sup>. **c**, Atomic frequency comb. The bandwidth of our AFC is 5 GHz (shown here is a 1-GHz broad section). The separation between the teeth is  $\Delta \approx 143$  MHz, resulting in 7 ns storage time. The line width of the peaks is  $\gamma \approx 75$  MHz, yielding a finesse  $F = 2$ , as expected for the sinus-type comb.

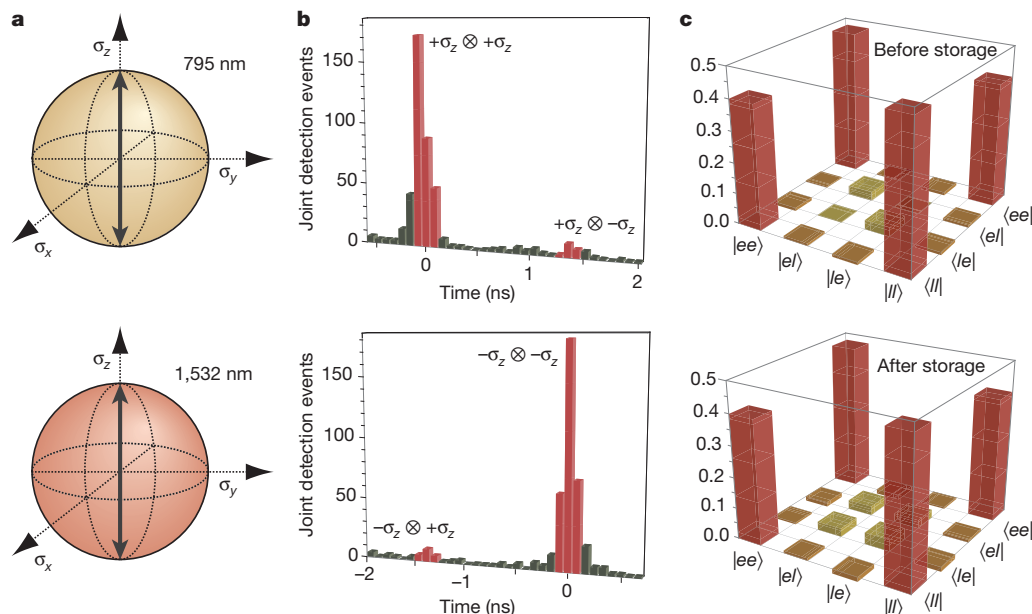


**Figure 3 | Measurement of density matrices.** **a**, Visualization of projection measurements. The measurement settings for the 795-nm (or 1,532-nm) qubit analyser are depicted on the upper (or lower) Bloch sphere. The example shows joint settings that enable calculating normalized probabilities for projections onto  $\sigma_z \otimes \sigma_z$  and  $\sigma_z \otimes -\sigma_z$ . **b**, Results for joint projection measurement after storage. The top (bottom) histogram displays joint detection events for the projection onto  $\sigma_z \otimes \sigma_z$  and  $\sigma_z \otimes -\sigma_z$  ( $-\sigma_z \otimes \sigma_z$  and  $-\sigma_z \otimes -\sigma_z$ ) as a function of the time difference between detections of the 795-nm and the 1,532-nm

photons. The desired events are those within the red-highlighted time windows. This allows us to calculate the joint-detection probabilities for projections onto  $\sigma_z \otimes \sigma_z$  and  $\sigma_z \otimes -\sigma_z$  (for results with other joint settings see the Supplementary Information). **c**, Density matrices. Density matrices were calculated using a maximum-likelihood estimation for the bi-photon states before and after storage. Only the real parts are shown—the absolute values of all imaginary components are below 0.04.

Our storage device, a Ti:TM:LiNbO<sub>3</sub> optical waveguide cooled to 3 K, is detailed in Fig. 2. It was previously characterized to establish its suitability as a photon-echo quantum memory material<sup>26</sup>. It combines interesting properties from the specific rare-earth element (795-nm storage wavelength), the host crystal (allowing for controlled dephasing and rephasing by means of electric fields), and from the waveguiding structure (ease-of-use). Lithium niobate waveguides have also been doped with neodymium, praseodymium and erbium<sup>7</sup>, and we conjecture that other rare-earth ions could also be used. This could extend the properties of LiNbO<sub>3</sub> and allow an integrated approach to other storage wavelengths, ions with different level structures, and so on.

To generate the AFC, we use a sideband-chirping technique (see Supplementary Information) to transfer atomic population between magnetic sublevels and create troughs and peaks in the inhomogeneously broadened absorption line. They form a 5-GHz-wide comb with tooth spacing of 143 MHz, setting the storage time to 7 ns. The system efficiency in our implementation is currently about 0.2%. This is in part due to the 90% fibre-to-waveguide input and output coupling loss, which we attribute to imperfect mode overlap. In addition, owing to the specific level structure of thulium under current experimental conditions, the finesse of the comb in the broadband approach is two, which limits the memory efficiency to about 10%. However, imperfections in the creation of the comb decrease this efficiency to around 2%. The system efficiency can be increased by improving the spectral tailoring of the AFC, and triggering photon re-emission in the backward direction. By also optimizing the mode overlap, we anticipate that it could reach

approximately 15%. Furthermore, if the two long-lived atomic levels between which population is transferred during the optical pumping procedure (in our case the two magnetic ground states; see Fig. 2) are spaced by more than the storage bandwidth, the memory efficiency can theoretically reach unity (see Supplementary Information).

To assess the quantum nature of our light-matter interface, we first make projection measurements with the 795-nm photons and the 1,532-nm photons onto time-bin qubit states characterized by Bloch vectors aligned along **a** and **b**, respectively, where **a**, **b**  $\in [\pm\sigma_x, \pm\sigma_y, \pm\sigma_z]$  (see Fig. 3). Experimentally, this is done by means of suitably adjusted qubit analysers, and by counting the number  $C(\mathbf{a}, \mathbf{b})$  of detected photon pairs. From two such spin-measurements, we calculate the normalized joint-detection probability:

$$P(\mathbf{a}, \mathbf{b}) = \frac{C(\mathbf{a}, \mathbf{b})}{C(\mathbf{a}, \mathbf{b}) + C(\mathbf{a}, -\mathbf{b})} \quad (2)$$

The measurement and the results with the fibre delay line, as well as the memory, are detailed in Fig. 3 and the Supplementary Information. From this data, we reconstruct the bi-photon states before and after storage in terms of their density matrices  $\rho_{\text{in}}$  and  $\rho_{\text{out}}$ , depicted in Fig. 3, using a maximum likelihood estimation<sup>27</sup>. This, in turn, allows us to examine the entanglement of formation<sup>28</sup>, a measure that indicates entanglement if it exceeds zero; it is upper-bounded by one. The results, listed in Table 1, clearly show the presence of entanglement in  $\rho_{\text{in}}$  and  $\rho_{\text{out}}$  and, within experimental uncertainty, establish that the storage process preserves entanglement without measurable degradation.

**Table 1 | Entanglement measures, purities and fidelities**

	Entanglement of formation (%)	Purity (%)	Fidelity with $ \phi^+\rangle$ (%)	Input/output fidelity (%)	Expected $S_{\text{th}}$	Measured $S$
$\rho_{\text{in}}$	64.4 $\pm$ 4.2	75.7 $\pm$ 2.4	86.2 $\pm$ 1.5		2.235 $\pm$ 0.085	2.379 $\pm$ 0.034
$\rho_{\text{out}}$	65 $\pm$ 11	76.3 $\pm$ 5.9	86.6 $\pm$ 3.9	95.4 $\pm$ 2.9	2.2 $\pm$ 0.22	2.25 $\pm$ 0.06

Entanglement of formation (normalized with respect to the entanglement of formation of  $|\phi^+\rangle$ ), purity  $P = \text{tr}(\rho^2)$ , fidelity with  $|\phi^+\rangle$ , input-output fidelity  $F = \left( \text{tr} \sqrt{\sqrt{\rho_{\text{out}}} \rho_{\text{in}} \sqrt{\rho_{\text{out}}}} \right)^2$  (referring to the fidelity of  $\rho_{\text{out}}$  with respect to  $\rho_{\text{in}}$ ), and expected and experimentally obtained  $S$  values for tests of the CHSH Bell inequality (measured for  $\mathbf{a} = \sigma_x$ ,  $\mathbf{a}' = \sigma_y$ ,  $\mathbf{b} = \sigma_x + \sigma_y$ , and  $\mathbf{b}' = \sigma_x - \sigma_y$ ). The correlation coefficients used to compute  $S$  and the calculation of  $S_{\text{th}}$  are detailed in the Supplementary Information. We note that the original state (and hence the recalled state) has limited purity and fidelity with  $|\phi^+\rangle$ . This is due to the probabilistic nature of our spontaneous parametric down-conversion source, which features a non-negligible probability of generating more than two photons simultaneously<sup>26</sup>. Uncertainties indicate one-sigma standard deviations and are estimated from Poissonian detection statistics and using a Monte Carlo simulation.

Furthermore, we note that the fidelity  $F$  between  $\rho_{\text{in}}$  and  $\rho_{\text{out}}$  is close to one, and hence the unitary transformation introduced by the storage process is almost the identity transformation.

In addition, as a second entanglement measure, we perform tests of the Clauser–Horne–Shimony–Holt (CHSH) Bell inequality<sup>6</sup>. This test indicates non-local correlations and thus the possibility of using the bi-photons for entanglement-based quantum key distribution<sup>8</sup> if the sum:

$$S = |E(\mathbf{a}, \mathbf{b}) + E(\mathbf{a}', \mathbf{b}) + E(\mathbf{a}, \mathbf{b}') - E(\mathbf{a}', \mathbf{b}')| \quad (3)$$

of four correlation coefficients

$$E(\mathbf{a}, \mathbf{b}) = \frac{C(\mathbf{a}, \mathbf{b}) - C(\mathbf{a}, -\mathbf{b}) - C(-\mathbf{a}, \mathbf{b}) + C(-\mathbf{a}, -\mathbf{b})}{C(\mathbf{a}, \mathbf{b}) + C(\mathbf{a}, -\mathbf{b}) + C(-\mathbf{a}, \mathbf{b}) + C(-\mathbf{a}, -\mathbf{b})} \quad (4)$$

with appropriately chosen settings  $\mathbf{a}, \mathbf{a}'$  and  $\mathbf{b}, \mathbf{b}'$  exceeds the classical bound of two; quantum mechanically it is upper-bounded by  $2\sqrt{2}$ . As detailed in Table 1, we find  $S_{\text{in}} = 2.379 \pm 0.034 > 2$  before the memory and, crucially,  $S_{\text{out}} = 2.25 \pm 0.06 > 2$ , which is in agreement with the value  $S_{\text{th}} = 2.2 \pm 0.22$  predicted from the reconstructed density matrix  $\rho_{\text{out}}$ . This validates the suitability of our set-up for quantum communication.

Our investigation provides an example of entanglement being transferred between physical systems of different nature, thereby adding evidence that this fundamental quantum property is not as fragile as is often believed. Furthermore, our broadband integrated approach permits the linkage of a promising quantum storage device with extensively used, high-performance sources of photons in bi- and multi-partite entangled states<sup>6</sup>. Although the storage efficiency and the storage time need to be significantly increased, and the moment of recall was pre-set, this study opens the way to new investigations of fundamental and applied aspects of quantum physics. Having increased the storage bandwidth also significantly facilitates the building of future quantum networks, because mutual frequency matching of photons and distant quantum memories will be simple. In addition, a large storage bandwidth—that is, the possibility to encode quantum information into short optical pulses—allows us to increase the number of temporal modes that can be stored during a given time. This enhances the flow of quantum information through a network and decreases the time needed to establish entanglement over a large distance using a quantum repeater<sup>1,2</sup>.

We note that, parallel to this work, Clausen *et al.* have demonstrated the storage of an entangled photon using a neodymium-doped crystal<sup>29</sup>.

Received 1 September; accepted 6 December 2010.

Published online 12 January 2011.

1. Lvovsky, A. I., Sanders, B. C., & Tittel, W. Optical quantum memory. *Nature Photon.* **3**, 706–714 (2009).
2. Sangouard, N., Simon, C., de Riedmatten, H. & Gisin, N. Quantum repeaters based on atomic ensembles and linear optics. Preprint at (<http://arxiv.org/abs/0906.2699>) (2009).
3. Kimble, H. J. The quantum Internet. *Nature* **453**, 1023–1030 (2008).
4. de Riedmatten, H., Afzelius, M., Staudt, M. U., Simon, C. & Gisin, N. A solid-state light–matter interface at the single-photon level. *Nature* **456**, 773–777 (2008).
5. Usmani, I., Afzelius, M., de Riedmatten, H. & Gisin, N. Mapping multiple photonic qubits into and out of one solid-state atomic ensemble. *Nature Commun.* **1**, 1–7 (2010).
6. Pan, J.-W., Chen, Z.-B., Żukowski, M., Weinfurter, H. & Zeilinger, A. Multi-photon entanglement and interferometry. Preprint at (<http://arxiv.org/abs/0805.2853>) (2008).

7. Sohler, W. *et al.* Integrated optical devices in lithium niobate. *Opt. Photon. News* 24–31 (January 2008).
8. Gisin, N., Ribordy, G., Tittel, W. & Zbinden, H. Quantum cryptography. *Rev. Mod. Phys.* **74**, 145–195 (2002).
9. Julsgaard, B., Sherson, J. & Cirac, J. I. J. Fűrřšek, J. & Polzik, E. S. Experimental demonstration of quantum memory for light. *Nature* **432**, 482–486 (2004).
10. Chanelière, T. *et al.* Storage and retrieval of single photons transmitted between remote quantum memories. *Nature* **438**, 833–836 (2005).
11. Eisaman, M. D. *et al.* Electromagnetically induced transparency with tunable single-photon pulses. *Nature* **438**, 837–841 (2005).
12. Honda, K. *et al.* Storage and retrieval of a squeezed vacuum. *Phys. Rev. Lett.* **100**, 093601 (2008).
13. Appel, J., Figueroa, E., Korystov, D., Lobino, M. & Lvovsky, A. Quantum memory for squeezed light. *Phys. Rev. Lett.* **100**, 093602 (2008).
14. Hedges, M. P., Longdell, J. J., Li, Y. & Sellars, M. J. Efficient quantum memory for light. *Nature* **465**, 1052–1056 (2010).
15. Boozer, A. D. *et al.* Reversible state transfer between light and a single trapped atom. *Phys. Rev. Lett.* **98**, 193601 (2007).
16. Choi, C. S. & Deng, H. Laurat, J. & Kimble, H. J. Mapping photonic entanglement into and out of a quantum memory. *Nature* **452**, 67–71 (2008).
17. Akiba, K. & Kashiwagi, K. Arikawa, M. & Kozuma, M. Storage and retrieval of non-classical photon pairs and conditional single photons generated by the parametric down-conversion process. *N. J. Phys.* **11**, 013049 (2009).
18. Jin, X.-M. *et al.* Quantum interface between frequency-uncorrelated down-converted entanglement and atomic-ensemble quantum memory. Preprint at (<http://arxiv.org/abs/1004.4691>) (2010).
19. Chou, C. W. *et al.* Measurement-induced entanglement for excitation stored in remote atomic ensembles. *Nature* **438**, 828–832 (2005).
20. Matsukevich, D. N. *et al.* Entanglement of a photon and a collective atomic excitation. *Phys. Rev. Lett.* **95**, 040405 (2005).
21. Yuan, Z.-S. *et al.* Experimental demonstration of a BDCZ quantum repeater node. *Nature* **454**, 1098–1101 (2008).
22. Blinov, B. B., Moehring, D. L., Duan, L.-M. & Monroe, C. Observation of entanglement between a single trapped atom and a single photon. *Nature* **428**, 153–157 (2004).
23. Togan, E. *et al.* Quantum entanglement between an optical photon and a solid-state spin qubit. *Nature* **466**, 730–734 (2010).
24. Longdell, J., Fraval, E., Sellars, M. & Manson, N. Stopped light with storage times greater than one second using electromagnetically induced transparency in a solid. *Phys. Rev. Lett.* **95**, 063601 (2005).
25. Marcikic, I. *et al.* Time-bin entangled qubits for quantum communication created by femtosecond pulses. *Phys. Rev. A* **66**, 062308 (2002).
26. Sinclair, N. *et al.* Spectroscopic investigations of a Ti:TM:LiNbO<sub>3</sub> waveguide for photon-echo quantum memory. *J. Lumin.* **130**, 1586–1593 (2010).
27. Altepeter, J. B., Jeffrey, E. R., & Kwiat, P. G. Photonic state tomography. *Adv. At. Mol. Opt. Phys.* **52**, 105–159 (2005).
28. Plenio, M. B. & Virmani, S. An introduction to entanglement measures. *Quant. Inf. Comput.* **7**, 1–51 (2007).
29. Clausen, C. *et al.* Quantum storage of photonic entanglement in a crystal. *Nature* doi:10.1038/nature09662 (this issue).

**Supplementary Information** is linked to the online version of the paper at [www.nature.com/nature](http://www.nature.com/nature).

**Acknowledgements** This work is supported by NSERC, QuantumWorks, General Dynamics Canada, iCORE (now part of Alberta Innovates), CFI, AAET and FQRNT. We thank C. La Mela, T. Chanelière, T. Stuart, V. Kiselyov and C. Dascalos for help during various stages of the experiment, C. Simon, K. Rupavatham and N. Gisin for discussions, and A. Lvovsky for lending us a single-photon detector.

**Author Contributions** The Ti:TM:LiNbO<sub>3</sub> waveguide was fabricated and characterized at room temperature by M.G., R.R. and W.S. The photon-pair source was built by J.J., J.A.S. and F.B., the AFC memory set-up was developed by E.S. and N.S., and the complete experiment was conceived and directed by W.T. The measurements and the analysis were done by E.S., N.S., J.J., J.A.S., D.O. and W.T., and W.T., E.S., N.S., J.J., J.A.S. and D.O. wrote the paper. E.S., N.S., J.J. and J.A.S. contributed equally to this work.

**Author Information** Reprints and permissions information is available at [www.nature.com/reprints](http://www.nature.com/reprints). The authors declare no competing financial interests. Readers are welcome to comment on the online version of this article at [www.nature.com/nature](http://www.nature.com/nature). Correspondence and requests for materials should be addressed to W.T. ([wtittel@ucalgary.ca](mailto:wtittel@ucalgary.ca)).

# Hard-tip, soft-spring lithography

Wooyoung Shim<sup>1,2</sup>, Adam B. Braunschweig<sup>2,3†</sup>, Xing Liao<sup>1,2</sup>, Jinan Chai<sup>2,3</sup>, Jong Kuk Lim<sup>2,3</sup>, Gengfeng Zheng<sup>2,3†</sup> & Chad A. Mirkin<sup>1,2,3</sup>

Nanofabrication strategies are becoming increasingly expensive and equipment-intensive, and consequently less accessible to researchers. As an alternative, scanning probe lithography has become a popular means of preparing nanoscale structures, in part owing to its relatively low cost and high resolution, and a registration accuracy that exceeds most existing technologies<sup>1–6</sup>. However, increasing the throughput of cantilever-based scanning probe systems while maintaining their resolution and registration advantages has from the outset been a significant challenge<sup>7–17</sup>. Even with impressive recent advances in cantilever array design, such arrays tend to be highly specialized for a given application, expensive, and often difficult to implement. It is therefore difficult to imagine commercially viable production methods based on scanning probe systems that rely on conventional cantilevers. Here we describe a low-cost and scalable cantilever-free tip-based nanopatterning method that uses an array of hard silicon tips mounted onto an elastomeric backing. This method—which we term hard-tip, soft-spring lithography—overcomes the throughput problems of cantilever-based scanning probe systems and the resolution limits imposed by the use of elastomeric stamps and tips: it is capable of delivering materials or energy to a surface to create arbitrary patterns of features with sub-50-nm resolution over centimetre-scale areas. We argue that hard-tip, soft-spring lithography is a versatile nanolithography strategy that should be widely adopted by academic and industrial researchers for rapid prototyping applications.

Molecular printing capabilities<sup>1</sup>, where molecules and materials can be directly delivered to a surface in the form of nanometre-scale features, have been dramatically accelerated through the invention of micro-contact printing<sup>18,19</sup> and dip-pen nanolithography<sup>2,20</sup>, two micro- and nanofabrication techniques that have complementary strengths and weaknesses. The former allows a master to be duplicated repeatedly over large areas with 200-nm resolution in a rapid fashion<sup>21,22</sup>. It is limited with respect to registration, requires a mask for every new master, and is not well-suited for making closely spaced structures with different chemical inks. The latter provides sub-50-nm resolution, custom nanostructure generation capabilities, high registration capabilities, and with cantilever arrays, a modest ability to generate structures made of different chemical compositions simultaneously<sup>23,24</sup>. It does not have the throughput of contact printing and requires substantially higher cost and cumbersome cantilever array technology. Attempts to combine the capabilities of dip-pen nanolithography and micro-contact printing have led to the development of polymer pen lithography<sup>25,26</sup>, a low cost scanning probe approach that utilizes an elastomeric stamp made of pyramids to generate arbitrary patterns over surfaces by using the tips of the pyramids as compressible point sources of molecules or materials to be delivered to an underlying substrate. Polymer pen lithography is a significant advance in that it eliminates most of the drawbacks of the two techniques and combines almost all of their attributes. However, it does not offer the sub-50-nm resolution<sup>25</sup> afforded by high resolution scanning probe lithography or alternative electron-beam technologies.

Ideally, one would like an array of hard tips resting on springs made of soft materials to create a technique that provides the high resolution of a single-tip scanning probe lithography experiment and the scalability of polymer pen lithography. Here we describe a new tip array architecture that achieves this goal and provides a way of engaging and aligning as many as 4,750 ultrasharp Si tips on a surface over an area of one square centimetre (in principle, the arrays could be much larger).

Major advances in scanning probe lithography are often the result of novel tip designs and fabrication procedures. The key innovation that enables hard-tip, soft-spring lithography (HSL) is a new protocol for fabricating arrays of ultra-sharp Si tips on a spring-like elastomer layer that allows all of the tips to be brought into contact with a surface over large areas (Fig. 1a). The HSL tip array architecture is composed of thousands of Si tips attached to a layer of elastomer that coats a glass slide. The elastomeric backing significantly reduces the cost of fabrication because it circumvents the necessity for micromachined cantilevers, and enables a levelling protocol without requiring a complex feedback scheme<sup>26</sup>. The Si tips, prepared by an established self-sharpening wet etching protocol<sup>27</sup>, have an average diameter of  $22 \pm 3$  nm. Because the tip arrays are prepared on a glass slide, they can be easily mounted onto the piezoelectric actuators of a conventional atomic force microscope, which provides precise tip positioning and registration, hallmarks of scanning probe lithographies. Both the elastomer and the glass onto which the arrays are mounted are transparent, which enables the visual observation of the compression of the elastomer that occurs when the tips touch the surface of a substrate (see Supplementary Video 1), thereby enabling a straightforward, optical method for levelling the plane of the tip array with respect to the substrate surface.

Depending on the intended use, the pitch of a tip array is deliberately set between 100 and 200  $\mu\text{m}$ , corresponding to tip densities of  $10,000\text{ cm}^{-2}$  and  $2,500\text{ cm}^{-2}$ , respectively, and the density can be as high as  $110,000\text{ cm}^{-2}$  (9,007,700 tips in 4-inch wafer) with a pitch of 30  $\mu\text{m}$ . To make the tip arrays (Fig. 1b), a  $1\text{ cm} \times 1\text{ cm}$  piece of a 50- $\mu\text{m}$ -thick (100)Si wafer with a 1- $\mu\text{m}$ -thick layer of  $\text{SiO}_2$  on each side of the wafer was placed onto the uncured elastomer. The top layer of the  $\text{SiO}_2$  eventually serves as an etching mask, while the oxygen-plasma-treated bottom  $\text{SiO}_2$  layer of the wafer in contact with the hydrophilic surface of the elastomer increases adhesion between the two surfaces, so that the tips do not fall off the array once the wafer has been etched (Supplementary Fig. 1). Following the curing of the elastomer, photolithography was used to define  $150\text{ }\mu\text{m} \times 150\text{ }\mu\text{m}$  square features of exposed  $\text{SiO}_2$ , each of which can be used to prepare an ultrasharp tip. HF is used to remove the exposed  $\text{SiO}_2$ , and aqueous KOH (40% w/v) is used to anisotropically etch the underlying Si. An array of square  $\text{SiO}_2$  masks along the  $\langle 110 \rangle$  direction exposes the (311) and (100) planes of the wafer during KOH etching at rates of 88 and  $50\text{ }\mu\text{m h}^{-1}$ , respectively. To achieve self-sharpening,  $R_w/\cos\theta$  (where  $R_w$  is the sidewall etching rate and  $\theta$  is the slope of the tip sidewall) must exceed the surface etching rate,  $R_f$  (ref. 27). Thus the critical anisotropy ratio  $\eta_c$  and the condition for self-sharpening  $\eta$  are

<sup>1</sup>Department of Materials Science and Engineering, Northwestern University, 2220 Campus Drive, Evanston, Illinois 60208, USA. <sup>2</sup>International Institute for Nanotechnology, Northwestern University, 2145 Sheridan Road, Evanston, Illinois 60208, USA. <sup>3</sup>Department of Chemistry, Northwestern University, 2145 Sheridan Road, Evanston, Illinois 60208, USA. †Present addresses: Department of Chemistry, New York University, 100 Washington Square East, New York, New York 10003, USA (A.B.B.); Laboratory of Advanced Materials & Department of Chemistry, Fudan University, 2205 Song-Hu Road, Shanghai, 200438, China (G.Z.).

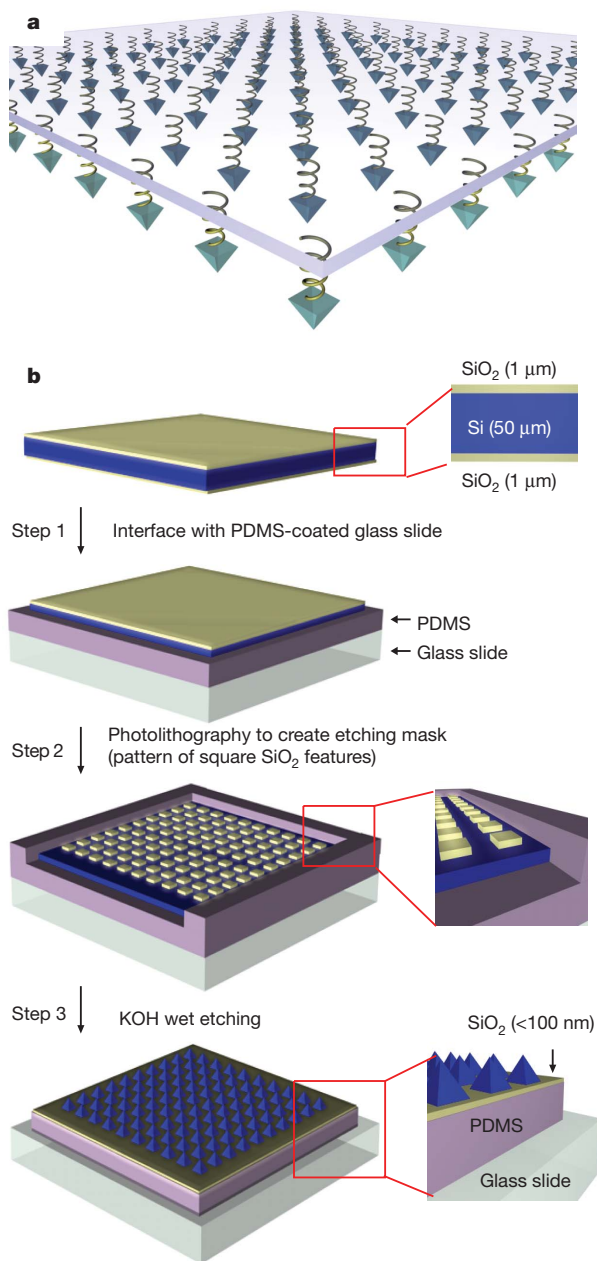


**Figure 1 | Fabrication of an HSL tip array.** **a**, Schematic illustration of an HSL tip array supported by a transparent, soft backing layer that provides mechanical flexibility to each tip. **b**, Experimental procedure to fabricate the tip arrays: 50- $\mu\text{m}$ -thick (100)Si wafers with thermally oxidized  $\text{SiO}_2$  (1- $\mu\text{m}$  thick) on each side were used. Step 1, an oxygen-plasma-treated Si wafer is placed onto uncured polydimethylsiloxane (PDMS) on a glass slide, followed by curing. Step 2, an array of square  $\text{SiO}_2$  masks of different edge lengths (100–200  $\mu\text{m}$  with 5  $\mu\text{m}$  separation) along the  $\langle 110 \rangle$  direction is defined by conventional photolithography and an isotropic buffered hydrofluoric acid (HF) etch. An additional PDMS passivation layer on the edge of the Si wafer protects the sides of the wafer from exposure to the etching solution, thereby preventing the (110) crystal face on the sides of the wafer from etching faster than the (100) face on the surface. Step 3, the arrays of tips are formed by etching the Si in a 40 wt% KOH (aq.) solution at 75 °C. After a defined time (60–65 min) when the sample became transparent owing to the removal of the opaque Si, the sample was removed from the etchant, rinsed with water, dried using a nitrogen stream, and if necessary, further  $\text{SiO}_2$  etching was conducted in HF to increase the flexibility of the backing layer.

expressed as  $\eta = R_t/R_w \leq 1/\cos\theta = \eta_c$ , which indicates that sidewall etching must be faster than etching of the tip base in order to form a sharp tip. For the HSL tip array made here, the experimental

$\eta = R_{(100)}/R_{(311)}$  is 0.56 in 40 wt% KOH at 75 °C, while the theoretical  $\eta_c$  required for self-sharpening conditions is 3.33 (ref. 27).

Optical and scanning electron microscopy (SEM) analysis of the resulting tip arrays reveal that this fabrication protocol does, indeed, yield an array of uniform Si nanotips (Fig. 2). The Si wafer, before KOH etching, is immobilized onto a glass slide using uncured polydimethylsiloxane (PDMS; Fig. 2a); curing results in adhesion and the generation of a rigid support for the Si substrate and eventually the tip array, which is made from the KOH etching procedure. This protocol allows one to handle and manipulate the fragile tip array without damaging it, and the glass-supported structure serves as a platform that can be easily mounted onto an AFM scanner. The glass-supported tip array is transparent (Fig. 2b), which enables the visual levelling of the tips with respect to a surface. An SEM image of the tips with a 150  $\mu\text{m}$  centre-to-centre separation shows that they adhere well to the elastomer surface and are remarkably uniform, with an average bottom diameter of  $30 \pm 0.6 \mu\text{m}$  (Supplementary Fig. 2) and an average tip height of  $47 \pm 0.9 \mu\text{m}$  (Fig. 2c). The tip height variation may cause a few tens of milliseconds difference in contact time between a tip and the surface, but not vary the feature size significantly. SEM analysis also shows that the surface intersection angles,  $\alpha_1$  and  $\alpha_2$ , and the rotation of the intersection of the planes to the  $\langle 100 \rangle$  direction of the wafer,  $\phi$ , are 127°, 143° and 18° (Fig. 2d), respectively, which shows that the sidewalls of the tips are (311) planes; indeed the angle values correspond well with the theoretical values of the intersection angles for (311) planes of Si, which are 126.9°, 143.1° and 18.4°, respectively<sup>27</sup>. Importantly, this procedure results in a tip yield >99%, and the average Si tip diameter is  $22 \pm 3 \text{ nm}$  (Fig. 2e), demonstrating that self-sharpening

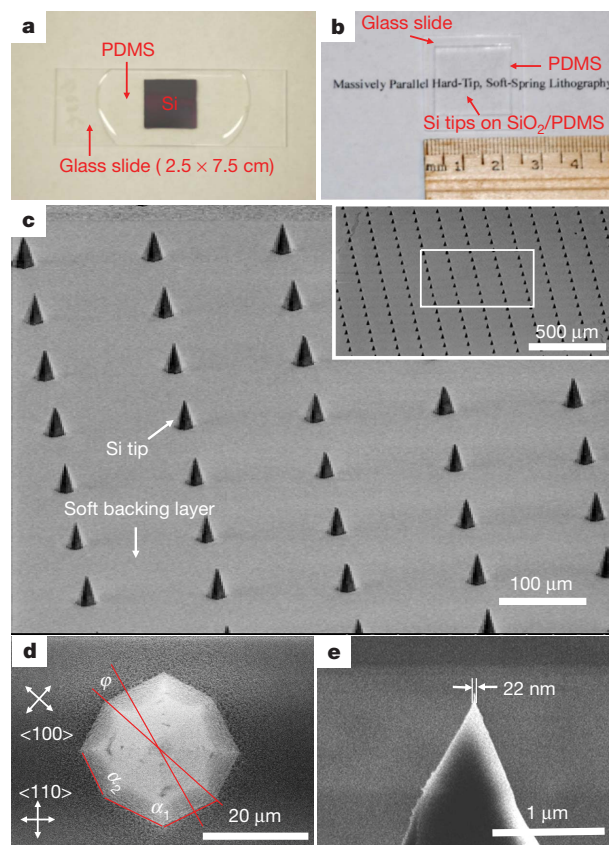


**Figure 2 | HSL tip arrays.** **a**, Si wafer (2 × 2 cm) on a cured PDMS surface rests on a glass slide before KOH etching. **b**, A transparent Si tip array after etching in KOH. **c**, An SEM image of the Si tip array on  $\text{SiO}_2$ /PDMS/glass with a 150- $\mu\text{m}$  pitch between tips. The inset shows a large area of the array to demonstrate the homogeneity of the tips. **d**, The (311) planes of Si were exposed during the wet etching with [110] oriented masks on a (100)Si surface. **e**, SEM image of a tip with diameter 22 nm.

has been realized. Note that the tip diameter, in principle, could be reduced down to 5 nm by optimizing etching conditions<sup>28</sup>, but these tips are sufficient to evaluate the potential for sub-50-nm lithography. Finally, because the wafer thickness has a variation of  $\sim 10\%$  ( $50 \pm 5 \mu\text{m}$ , NOVA Electronic Materials), the tip height can also vary up to 10%.

The molecular printing capabilities of HSL—including the ability to make arbitrary patterns, reproducibility, and time-dependent feature size control—were evaluated in the context of printing poly(ethylene glycol) (PEG) and 16-mercaptohexadecanoic acid (MHA) onto a hexamethyldisilazane-coated Si surface and a thermally evaporated polycrystalline Au surface, respectively. The tip arrays were inked by spin-coating an ethanol solution of PEG or MHA onto the tip arrays, which were subsequently mounted onto an XE-150 AFM platform (Park Systems) that was specially equipped with a tilt stage, an environmental humidity control chamber, a specialized scanning head (Fig. 3a), and lithography software capable of controlling the position, dwell time, and vertical-axis piezo ( $z$ -piezo) extension for each feature in a pattern. In a departure from dip-pen nanolithography and all cantilever-based lithography approaches, there is no need for laser feedback during writing: rather, the compression of the elastomer backing as the tips push against the surface is used to indicate that the tips are in contact with the surface and that writing is occurring (Fig. 3b and Supplementary Fig. 3). This optical signal is also used to level the plane of the tip array with respect to the plane of the surface: the tilt angle of the tip array is adjusted until, upon  $z$ -piezo extension, all of the tips contact the surface (see Supplementary Video 1 of the tips being aligned). As a way of evaluating the resiliency of the tip architecture, the  $z$ -motor was extended as far as  $100 \mu\text{m}$  after the tips have touched the surface, and the array structure was subsequently analysed. Significantly, upon retraction the tips rebound without breaking off the support (see Supplementary Video 2).

In polymer pen lithography, there is a linear relationship between the force between the tip array and the surface and the resulting feature edge length because of the compression of the polymeric tips<sup>25</sup>, however in HSL, no such relationship is observed because the Si tips do not deform under pressure. PEG was written with a dwell time of 0.5 s, at a humidity of 80%, and with  $z$ -piezo extension values ranging from 4 to  $12 \mu\text{m}$  without any significant deviation in the size of the features ( $564 \pm 23 \text{ nm}$ ) written by any single tip (Fig. 3c and d). This lack of feature diameter dependence on the force exerted between the tip array and the surface suggests that all tips in HSL can be brought into contact with a surface by extending the  $z$ -piezo without consequences on the resulting feature sizes, even though the force exerted on each tip may differ. In dip-pen nanolithography, precise control of feature diameter is achieved because the ink diffuses through the meniscus that forms between the tip and the surface, thereby resulting in a linear relationship between feature area  $A$  and the square root of the dwell time  $t$ ,  $A \propto \sqrt{t}$  (ref. 23). This relationship between feature and dwell time was investigated in the context of an HSL experiment by writing an MHA pattern on an Au polycrystalline surface, and varying the feature dwell times. The dots were written at dwell times from 1 to 15 s at 50% humidity and resulted in etched Au features with diameters from  $261 \pm 22$  to  $1,002 \pm 32 \text{ nm}$ , respectively (Fig. 3e), showing that this linear relationship is maintained (Fig. 3d), although there seems to be a saturation of feature size above dwell times of 13 s. When the humidity is lowered to 15%, etched Au dot features with diameters as small as  $34 \pm 5 \text{ nm}$  can be reproducibly obtained with a dwell time of 0.01 s (Fig. 3f; also see Supplementary Fig. 4 for an MHA pattern on Au), showing that dwell time and humidity can be used to effectively control the resulting feature size from several micrometres to less than 50 nm (Fig. 3d).

The ability to use the HSL tip arrays to transfer energy, rather than materials (ink), to a surface was also evaluated (Supplementary Fig. 5). For example, HSL was used to make a pattern of holes in a 30-nm-thick PMMA film. The tip arrays were lowered into the polymer at 30% humidity and a 0.5 s contact time, which resulted in  $38 \pm 4 \text{ nm}$  diameter

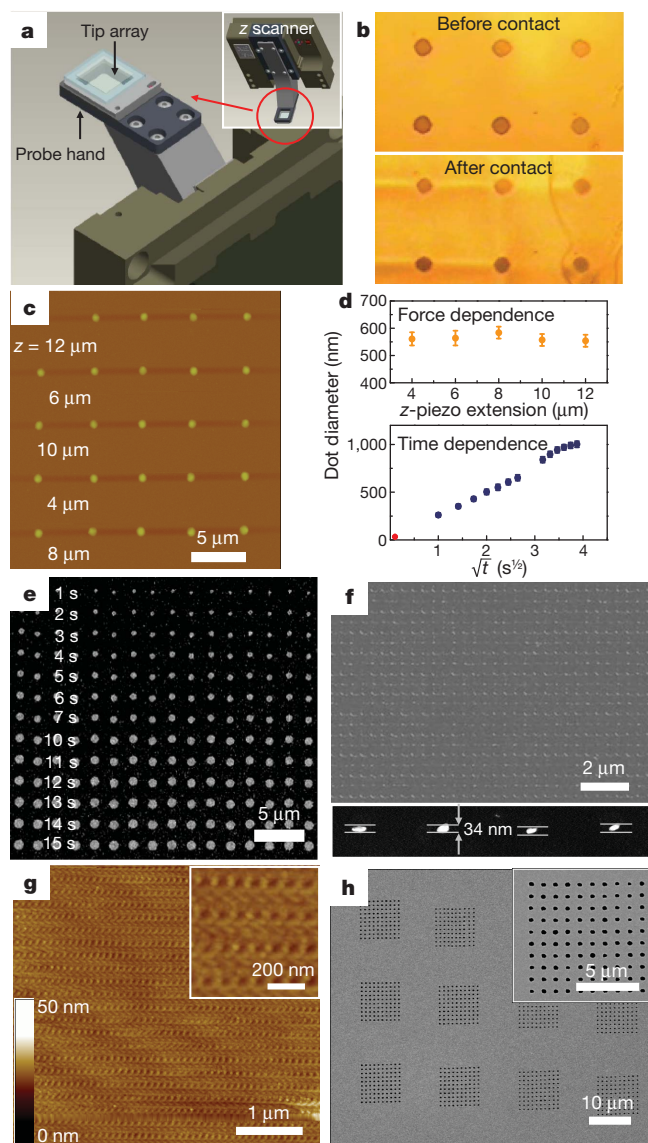


**Figure 3 | Operating principles and single tip capabilities.** **a**, A tip array attached to the probe hand of a 25- $\mu\text{m}$   $z$ -scanner that provides a  $10 \text{ mm} \times 10 \text{ mm}$  panning optical view for levelling the tips with a surface on the tilting stage. **b**, Optical images showing compression of the elastomer backing as the tips come in contact with the surface (see Supplementary Video 1). **c**, AFM image indicating the lack of force dependence of the PEG feature diameters when patterned onto a hexamethyldisilazane-coated Si surface with varying  $z$ -piezo extension and a constant dwell time of 0.5 s (humidity of 90%). The  $z$ -piezo extensions and measured diameters of the PEG dots are as follows:  $12 \mu\text{m}$ ,  $554 \pm 22 \text{ nm}$ ;  $10 \mu\text{m}$ ,  $557 \pm 22 \text{ nm}$ ;  $8 \mu\text{m}$ ,  $584 \pm 22 \text{ nm}$ ;  $6 \mu\text{m}$ ,  $564 \pm 27 \text{ nm}$ ;  $4 \mu\text{m}$ ,  $561 \pm 24 \text{ nm}$ . **d**, Time and force dependence of feature size variation (orange dots from **c**, blue dots from **e**, and red dot from **f**). **t**, contact time. **e**, SEM image of a pattern of etched Au dots of different sizes on an Si surface created by intentionally varying the dwell time (shown in panel) of MHA-coated tips at a humidity of 50%. The time of MHA deposition and measured diameter of the Au dots are as follows: 15 s,  $1,002 \pm 32 \text{ nm}$ ; 14 s,  $990 \pm 30 \text{ nm}$ ; 13 s,  $970 \pm 28 \text{ nm}$ ; 12 s,  $942 \pm 30 \text{ nm}$ ; 11 s,  $897 \pm 30 \text{ nm}$ ; 10 s,  $840 \pm 31 \text{ nm}$ ; 7 s,  $651 \pm 31 \text{ nm}$ ; 6 s,  $606 \pm 29 \text{ nm}$ ; 5 s,  $551 \pm 31 \text{ nm}$ ; 4 s,  $503 \pm 28 \text{ nm}$ ; 3 s,  $429 \pm 24 \text{ nm}$ ; 2 s,  $352 \pm 22 \text{ nm}$ ; 1 s,  $261 \pm 22 \text{ nm}$ . **f**, Main panel, SEM image of a pattern of etched Au dots on a Si surface patterned with a dwell time of 0.01 s and at a humidity of 15%. Inset (bottom), a magnified SEM image of the Au dots. **g**, Main panel, AFM topographical image of the dot pattern of PMMA prepared by indentation with a Si tip at room temperature. Inset, a magnified image. **h**, Main panel, SEM image of Au hole patterns created by Au etching after removing MHA SAM at a bias voltage of  $-5 \text{ V}$  with a dwell time of 5 s and at a humidity of 30%. Inset, a magnified image.

holes at a pitch distance of 100 nm (Fig. 3g; see also Supplementary Fig. 4). To show that these tip arrays could also transfer electrical energy to a surface, the tip arrays were coated with Au (50 nm Au, 5 nm Ti adhesion layer), attached to a voltage source, and brought into contact

with an Au surface coated with MHA<sup>29</sup>. Following the application of  $-5$  V with a contact time of 5 s at a humidity of 30%, the MHA self-assembled monolayer (SAM) was removed selectively from the points where voltage had been applied, leaving an array of holes with an average diameter of  $274 \pm 20$  nm (Fig. 3h).

HSL is distinguished from all other lithographic techniques by the ability to form arbitrary patterns in massively parallel (over a  $1\text{-cm}^2$  area) and mask-less fashion at a feature resolution of less than 50 nm. The record for feature resolution with a cantilever array over a  $1\text{-cm}^2$  area still stands at 80 nm (ref. 8). The ability to generate arbitrary patterns with HSL tip arrays was evaluated in the context of reproducing a bitmap representation of the pyramid on the US \$1 bank-note. The resolution limits of this first HSL tip array were also evaluated in this experiment. The pyramid image was loaded into the Park AFM custom XEL software, which converted the image into a dot-matrix representation. The computer generated pattern is composed of 6,982 dots with the corresponding position coordinates for each dot (Fig. 4A). The 4,750 HSL tip array ( $1\text{ cm} \times 1\text{ cm}$ ) was inked with MHA and then subsequently used to generate the etched Au dots (0.01 s contact time, 40% humidity) that comprise the pyramid and surrounding letters (Fig. 4B; see also Supplementary Fig. 6). In this initial proof-of-concept, the resulting etched Au pattern is an accurate miniaturized duplication ( $30 \times 33\text{ }\mu\text{m}$ ) of the bitmap image. Each dot is connected to the others in the structure to make the observed pyramid and letters (the intended pitch was 150 nm). In order to resolve individual dots, the image size was increased to  $55 \times 60\text{ }\mu\text{m}$  with a 270-nm dot pitch while maintaining the number of dots (6,982). The tip-substrate contact time was kept constant at 0.01 s but the humidity was lowered to 30% to decrease the molecule transport rate and, as a consequence, feature size. A representative portion of the  $\sim 19,000$  replicas (yield  $>99\%$ ) generated across the  $1\text{-cm}^2$  substrate show the quality and high resolution of this novel nanofabrication technique (Fig. 4C). Importantly, at the edge of the etched Au patterns (Fig. 4D), individual dots can be clearly seen, allowing us to determine the average feature diameter ( $41 \pm 7$  nm across the  $1\text{-cm}^2$  area; Supplementary Fig. 7). The standard deviation of the etched Au dot diameters for features generated by HSL was 17% across the  $1\text{-cm}^2$  area, which is a combined result of minor variations in surface etching, tip morphology, ink coating, and the polycrystallinity of the Au surface. These results confirm that registry and levelling of the tip array are maintained within the field of view of each tip and between tips as well, showing the flexibility and robustness of this technique. The total time required to fabricate this large-area, high-resolution pattern ( $1.32 \times 10^8$  dots) was about 200 min with the custom Park XEL lithography software.

In conclusion, this is to our knowledge the first time a hard-tip-based approach has been realized in the context of a cantilever-free system, and it offers significant advantages in terms of resolution, scalability and decreased complexity compared to many previous approaches<sup>30</sup>. Importantly, the cost of each tip array is comparable to the cost of a single AFM tip, and the HSL approach could be implemented with the now common conventional AFM equipment.

## METHODS SUMMARY

Si wafers (NOVA Electronic Materials; resistivity,  $1\text{--}10\text{ }\Omega\text{ cm}$ , (100) orientation,  $50 \pm 5\text{ }\mu\text{m}$  thick) with a  $10,000\text{ }\text{\AA}$  ( $\pm 5\%$ )  $\text{SiO}_2$  layer on each side were used for fabricating the tip arrays. For etch mask fabrication, the square mask along the  $\langle 110 \rangle$  direction was transferred into the  $\text{SiO}_2$  layer by photolithography with photoresist (AZ 1518, MicroChem) and isotropic etching with buffered hydrofluoric acid (HF, Transene) for 9 min. The sample was transferred to 40 wt % KOH solution at  $75^\circ\text{C}$  and held in the centre of the etchant in a Teflon holder. It is worth noting that the use of the bottom  $\text{SiO}_2$  layer contacting PDMS significantly increases the adhesion of tips to PDMS during etching. In a typical patterning experiment, HSL was performed with a Park System XE-150 AFM equipped with a tilt stage and an environmental chamber (that is, active humidity control) at a relative humidity of 15–50% and a temperature of  $\sim 25^\circ\text{C}$ . The statistics used to evaluate the patterned features are based on one standard deviation. A summary of the statistics is presented in Supplementary Fig. 8.

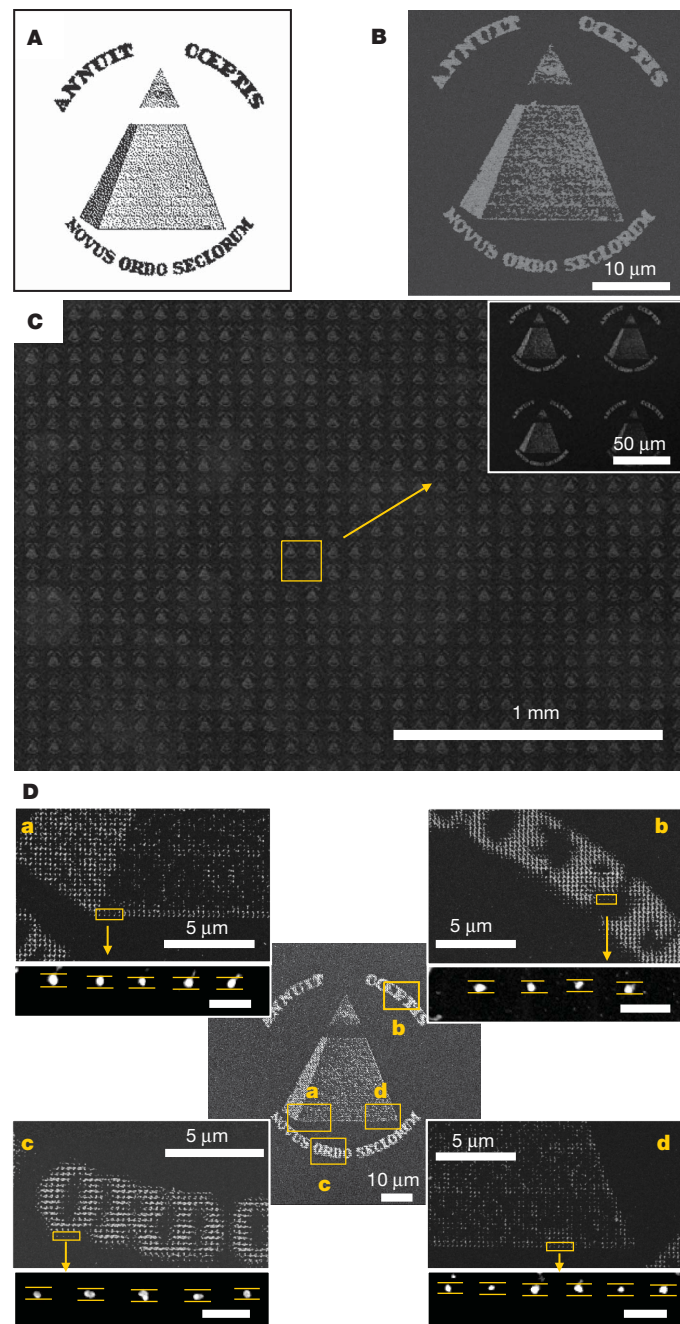


**Figure 4 | High-resolution parallel HSL writing.** A, Dot matrix map of the pyramid on the US \$1 bank-note. The image consists of 6,982 dots. B, SEM image of the resulting etched Au pattern produced by writing the image with a dwell time of 0.01 s per dot at a humidity of 40%. The image size is  $30 \times 33\text{ }\mu\text{m}$  and the distance between dots is 150 nm (a large area pattern is shown in Supplementary Fig. 5). C, Main panel, SEM image of a representative region of  $\sim 19,000$  duplicates of the pyramid from the US \$1 bank-note. The size of each duplicate is  $55 \times 60\text{ }\mu\text{m}$  with a 270-nm dot-centre-to-dot-centre distance. Inset, magnified SEM image of four pyramid replicas. D, Central panel, SEM image of a single pyramid,  $55 \times 60\text{ }\mu\text{m}$  in size. Also shown are magnified images of the bottom-left corner of pyramid (a), the top-right letters 'COEPTIS' (b), the bottom letters 'ORDO' (c), and the bottom-right corner of a pyramid (d). Each sub-panel a–d shows at bottom a magnified image of the marked regions with individual dots ( $41 \pm 7$  nm in diameter). Scale bars in sub-panel insets are 270 nm.

**Full Methods** and any associated references are available in the online version of the paper at [www.nature.com/nature](http://www.nature.com/nature).

**Received 30 August; accepted 24 November 2010.**

- Braunschweig, A. B., Huo, F. & Mirkin, C. A. Molecular printing. *Nature Chem.* **1**, 353–358 (2009).
- Salaita, K., Wang, Y. & Mirkin, C. A. Applications of dip-pen nanolithography. *Nature Nanotechnol.* **2**, 145–155 (2007).
- Quate, C. F. Scanning probes as a lithography tool for nanostructures. *Surf. Sci.* **386**, 259–264 (1997).
- Tseng, A. A., Notargiacomo, A. & Chen, T. P. Nanofabrication by scanning probe microscope lithography: A review. *J. Vac. Sci. Technol. B* **23**, 877–894 (2005).
- Rosa, L. G. & Liang, J. Atomic force microscope nanolithography: dip-pen nanoshaving, nanografting, tapping mode, electrochemical and thermal nanolithography. *J. Phys. Condens. Matter* **21**, 483001 (2009).
- Saavedra, H. M. *et al.* Hybrid strategies in nanolithography. *Rep. Prog. Phys.* **73**, 036501 (2010).
- Bullen, D. *et al.* Parallel dip-pen nanolithography with arrays of individually addressable cantilevers. *Appl. Phys. Lett.* **84**, 789–791 (2004).
- Hong, S. H. & Mirkin, C. A. A nanoplotter with both parallel and serial writing capabilities. *Science* **288**, 1808–1811 (2000).
- Zhang, M. *et al.* MEMS nanoplotter with high-density parallel dip-pen nanolithography probe arrays. *Nanotechnology* **13**, 212–217 (2002).
- Salaita, K. *et al.* Sub-100 nm, centimeter-scale, parallel dip-pen nanolithography. *Small* **1**, 940–945 (2005).
- Lenhart, S., Sun, P., Wang, Y. H., Fuchs, H. & Mirkin, C. A. Massively parallel dip-pen nanolithography of heterogeneous supported phospholipid multilayer patterns. *Small* **3**, 71–75 (2007).
- Mirkin, C. A. The power of the pen: development of massively parallel dip-pen nanolithography. *ACS Nano* **1**, 79–83 (2007).
- Eigler, D. M. & Schweizer, E. K. Positioning single atoms with a scanning tunneling microscope. *Nature* **344**, 524–526 (1990).
- Leung, O. M. & Goh, M. C. Orientational ordering of polymer by atomic force microscope tip-surface interaction. *Science* **255**, 64–66 (1992).
- Xia, Y. & Whitesides, G. M. Soft lithography. *Angew. Chem. Int. Edn* **37**, 550–575 (1998).
- Gates, B. D. *et al.* New approaches to nanofabrication: molding, printing, and other techniques. *Chem. Rev.* **105**, 1171–1196 (2005).
- Ginger, D. S., Zhang, H. & Mirkin, C. A. The evolution of dip-pen nanolithography. *Angew. Chem. Int. Edn* **43**, 30–45 (2004).
- Kumar, A. & Whitesides, G. M. Features of gold having micrometer to centimeter dimensions can be formed through a combination of stamping with an elastomeric stamp and an alkanethiol “ink” followed by chemical etching. *Appl. Phys. Lett.* **63**, 2002–2004 (1993).
- Zheng, Z., Jang, J.-W., Zheng, G. & Mirkin, C. A. Topographically flat, chemically patterned PDMS stamps made by dip-pen nanolithography. *Angew. Chem. Int. Edn* **47**, 9951–9954 (2008).
- Piner, R. D., Zhu, J., Xu, F., Hong, S. H. & Mirkin, C. A. “Dip-pen” nanolithography. *Science* **283**, 661–663 (1999).
- Hong, S. H., Zhu, J. & Mirkin, C. A. Multiple ink nanolithography: toward a multiple-pen nano-plotter. *Science* **286**, 523–525 (1999).
- Huo, F. *et al.* Polymer pen lithography. *Science* **321**, 1658–1660 (2008).
- Liao, X., Braunschweig, A. B. & Mirkin, C. A. “Force-feedback” leveling of massively parallel arrays in polymer pen lithography. *Nano Lett.* **10**, 1335–1340 (2010).
- Liu, J., Betzner, T. M. & Henderson, H. T. Etching of self-sharpening {338} tips in (100) silicon. *J. Micromech. Microeng.* **5**, 18–24 (1995).
- Yun, M. H., Burrows, V. A. & Kozicki, M. N. Analysis of KOH etching of (100) silicon on insulator for the fabrication of nanoscale tips. *J. Vac. Sci. Technol. B* **16**, 2844–2848 (1998).
- Jang, J., Maspoch, D., Fujigaya, T. & Mirkin, C. A. A “Molecular eraser” for dip-pen nanolithography. *Small* **3**, 600–605 (2007).
- Nie, Z. & Kumacheva, E. Patterning surfaces with functional polymers. *Nature Mater.* **7**, 277–290 (2008).

**Supplementary Information** is linked to the online version of the paper at [www.nature.com/nature](http://www.nature.com/nature).

**Acknowledgements** C.A.M. acknowledges the US Air Force Office of Scientific Research (AFOSR), the US Defense Advanced Research Projects Agency (DARPA) and the US NSF (NSEC program) for support of this research. C.A.M. is grateful for a NSSEF Fellowship from the US Department of Defense. A.B.B. is grateful for a NRSA fellowship from the US NIH. We thank Z. Zheng for discussions.

**Author Contributions** W.S. and C.A.M. designed all experiments. W.S., A.B.B. and C.A.M. contributed to this work in analysing results and drafting the manuscript. W.S., A.B.B., X.L., J.C., J.K.L. and G.Z. also performed experiments and helped with revisions.

**Author Information** Reprints and permissions information is available at [www.nature.com/reprints](http://www.nature.com/reprints). The authors declare no competing financial interests. Readers are welcome to comment on the online version of this article at [www.nature.com/nature](http://www.nature.com/nature). Correspondence and requests for materials should be addressed to C.A.M. ([chadnano@northwestern.edu](mailto:chadnano@northwestern.edu)).

## METHODS

**Fabrication of the Si etching masks.** Si wafers (NOVA Electronic Materials; resistivity 1–10  $\Omega\text{cm}$ , (100) orientation,  $50 \pm 5 \mu\text{m}$  thick) with a 10,000-Å ( $\pm 5\%$ )  $\text{SiO}_2$  layer on each side were used for fabricating the tip arrays. The wafers were cleaned in acetone, ethanol, then rinsed with water before use. In preparing the elastomer base, PDMS and a curing agent (Sylgard 184 Silicone) were mixed in 20:1 ratio (w/w), and then degassed under vacuum ( $10^{-3}$  torr). Oxygen-plasma-treated (1 min at 60 W at a pressure of 100 mtorr) wafers were then placed on uncured PDMS on clean glass slides, followed by curing at 70 °C for 24 h. This wafer/PDMS/glass slide sample is easier to handle and less fragile than the 50- $\mu\text{m}$ -thick wafer alone. The choice of a particular mask material depends on a number of considerations. The main issues are availability of materials, ease of the process (processing time, complexity of the process, and reliability), and selectivity of the etching process. Metals such as Au, Cr, Pt, Ag, Cu and Ti are known to be resistant to KOH etching. In our case, however, thermally evaporated Au/Ti was used as an etching mask and found to be vulnerable to KOH degradation. Indeed, the use of an Au (500 nm)/Ti (100 nm) mask (instead of  $\text{SiO}_2$ ) followed by KOH etching for 1 h at 75 °C resulted in a significant failure in tip fabrication due to pinholes in the mask. Thermally grown  $\text{SiO}_2$  is a better mask material as it provides a greater etching selectivity than many metal materials with respect to Si (of the order of 500:1). As the etching rate of Si (100) in 40 wt% KOH at 75 °C is  $50 \mu\text{m h}^{-1}$ , the minimum required thickness of  $\text{SiO}_2$  is 250 nm for an experimentally viable fabrication procedure, which justifies the use of the 1- $\mu\text{m}$ -thick  $\text{SiO}_2$  coating. For etch mask fabrication, the square mask along the  $\langle 110 \rangle$  direction was transferred into the  $\text{SiO}_2$  layer by photolithography with photoresist (AZ 1518, MicroChem) and isotropic buffered hydrofluoric acid (9% HF, Transene) etch for 9 min. To remove the photoresist, the wafer was cleaned in acetone, then ethanol, and subsequently dried with flowing nitrogen. The wafer was finally cleaned in an oxygen plasma. These cleaning procedures before Si etching were found to improve the uniformity of the tips (1 min at 60 W at a pressure of 100 mtorr).

**Fabrication of Si tip arrays.** Following photolithography, the wafer was etched for 1 min using ammonium fluoride (20%  $\text{NH}_4\text{F}$ , Time Etch, Transene) to remove the native oxide from the surface of the Si regions, which was followed by rinsing in water and drying with a nitrogen stream. The sample was immediately transferred to 40 wt% KOH solution at 75 °C and held in the centre of the etchant in a Teflon holder. The solution was continuously stirred to reduce the effect of micro-masking by hydrogen bubbles generated in the reaction at the Si surface. After 60–65 min, the sample was removed from the etchant, rinsed in water and dried under a nitrogen stream. It is worth noting that the use of the bottom  $\text{SiO}_2$  layer contacting PDMS significantly increases the adhesion of tips to PDMS during etching. For example, it was observed that a number of tips fell off of the PDMS surface during etching when no interfacial  $\text{SiO}_2$  layer was used (Supplementary Fig. 1).

**Fabrication of nanopatterns by material and energy delivery.** In a typical experiment, HSL was performed with a Park System XE-150 AFM equipped with a tilt stage and an environmental chamber (that is, active humidity control, error

range  $\sim 5\%$ ) at a relative humidity of 15–80% and a temperature of  $\sim 23$ –26 °C. Environmental parameters that affect feature size include relative humidity, temperature, substrate, and ink concentration. In the temperature range of 23–26 °C, MHA transport from a tip to a surface is less sensitive to temperature. The arrays were driven by the custom XEL lithography software (Park System) capable of controlling the position, dwell time, and  $z$ -piezo extension at every point in an arbitrary pattern. To pattern MHA (Sigma-Aldrich) on an Au surface, MHA (5–10 mM) was spin-coated (1 ml, 1,000 r.p.m., 30 s) onto an oxygen-plasma-cleaned HSL tip array (1 min). The tip array was aligned with respect to the surface by varying the tilt of the surface until all tips were observed by optical microscopy to contact the surface on  $z$ -piezo extension. The inked Si tip array was used for generating MHA dot patterns on a thermally evaporated polycrystalline Au surface (20–25 nm Au with a 5 nm Ti adhesion layer coated on Si) by bringing the tip array repeatedly into contact with the Au surface. The exposed Au on this MHA patterned surface was subsequently etched (the substrate was immersed in 20 mM thiourea (aq.), 30 mM  $\text{FeNO}_2$  (aq.), 20 mM HCl (aq.), and 2 mM octanol (aq.) and gently shaken by hand) for 4–5 min to yield raised structures that are approximately 20–25 nm in height and easily imaged by SEM (3–5 kV in SE mode at a pressure of  $10^{-5}$  torr; Hitachi S4800). Before imaging the etched Au features, the MHA SAM was removed by oxygen plasma. We inspected the Au surface (20-nm thick on 5-nm thick Ti) before patterning and after patterning and etching (Supplementary Fig. 9). To pattern PEG, a 5 mg  $\text{ml}^{-1}$  poly(ethylene glycol) (PEG) solution ( $M_w = 2,000$ ) was prepared in pure ethanol and sonicated at room temperature for 10 min until the PEG dissolved. The tip array was cleaned by oxygen plasma for 1 min at 60 W at a pressure of 100 mtorr. 1 ml of the PEG solution was dropped onto the tip array and allowed to settle for 1 min before spin coating at 1,000 r.p.m. for 1 min. The tip array was mounted onto the patterning platform and then levelled. The environmental chamber was sealed, and a humidifier was used to increase the relative humidity to at least 80%. To pattern nano-holes by the transfer of mechanical energy, PMMA (495 PMMA C3, MicroChem) diluted in chlorobenzene (1 g PMMA: 2.5 g chlorobenzene) was spin-coated onto the Si substrate at 3,000 r.p.m. for 45 s, and thermally annealed at 180 °C for 1 min. The thickness of the resulting film was  $31 \pm 3$  nm, and the surface roughness (r.m.s. value) was about  $1.1 \pm 0.4$  nm. Patterns were generated by indentation of the film by the tip array at room temperature by controlling the position and extension of the  $z$ -piezo scanner. After patterning, the surface roughness was about  $1.30 \pm 0.05$  nm and peak-to-peak roughness (highest point minus lowest point) was about  $11.69 \pm 0.99$  nm. To electrically pattern nano-holes, the Si tip array was first coated with Au (50 nm) / Ti (5 nm) to become conductive. SAMs of MHA molecules were prepared on Au thin films by immersing the substrate in a 1 mM ethanolic MHA solution for 1 h, followed by rinsing with ethanol and water, and drying with nitrogen. An Au-coated Si tip array with a bias voltage of  $-5$  V contacted the MHA SAM surface to selectively desorb portions of the MHA SAM surface under ambient conditions ( $\sim 30\%$  humidity, 23 °C). The resulting indentations were characterized by topographical AFM.

# Melt-induced speed-up of Greenland ice sheet offset by efficient subglacial drainage

Aud Venke Sundal<sup>1</sup>, Andrew Shepherd<sup>1</sup>, Peter Nienow<sup>2</sup>, Edward Hanna<sup>3</sup>, Steven Palmer<sup>1</sup> & Philippe Huybrechts<sup>4</sup>

Fluctuations in surface melting are known to affect the speed of glaciers and ice sheets<sup>1–7</sup>, but their impact on the Greenland ice sheet in a warming climate remains uncertain<sup>8</sup>. Although some studies suggest that greater melting produces greater ice-sheet acceleration<sup>7,9</sup>, others have identified a long-term decrease in Greenland's flow despite increased melting<sup>3</sup>. Here we use satellite observations of ice motion recorded in a land-terminating sector of southwest Greenland to investigate the manner in which ice flow develops during years of markedly different melting. Although peak rates of ice speed-up are positively correlated with the degree of melting, mean summer flow rates are not, because glacier slow-down occurs, on average, when a critical run-off threshold of about 1.4 centimetres a day is exceeded. In contrast to the first half of summer, when flow is similar in all years, speed-up during the latter half is  $62 \pm 16$  per cent less in warmer years. Consequently, in warmer years, the period of fast ice flow is three times shorter and, overall, summer ice flow is slower. This behaviour is at odds with that expected from basal lubrication alone<sup>7,9</sup>. Instead, it mirrors that of mountain glaciers<sup>10–12</sup>, where melt-induced acceleration of flow ceases during years of high melting once subglacial drainage becomes efficient. A model of ice-sheet flow that captures switching between cavity and channel drainage modes<sup>13</sup> is consistent with the run-off threshold, fast-flow periods, and later-summer speeds we have observed. Simulations of the Greenland ice-sheet flow under climate warming scenarios should account for the dynamic evolution of subglacial drainage; a simple model of basal lubrication alone misses key aspects of the ice sheet's response to climate warming.

Recent studies addressing the mass balance of the Greenland Ice Sheet (GrIS) show that snowfall-driven thickening of the interior<sup>14</sup> is more than offset by near-coastal mass loss caused by increased surface melting<sup>15</sup> and accelerated glacier flow<sup>16</sup>. Enhanced basal sliding due to the penetration of surface melt-water to the base of the ice sheet is one proposed mechanism for the observed increase in glacier flow<sup>7</sup>. Theoretical work<sup>9</sup> suggests that the direct coupling between increased surface melting and ice-sheet flow may substantially hasten the mass loss of the GrIS. However, our ability to incorporate surface melt-induced acceleration into ice-sheet models is limited by a lack of knowledge of the extent and characteristics of the hydrological forcing. In consequence, the potential impact of surface melting on ice dynamics has not been incorporated into the ice-sheet models that form the basis of the Intergovernmental Panel on Climate Change sea level projections<sup>8</sup>. This study provides an improved understanding of the relationship between ice-sheet dynamics and hydrology through a comparison of inter-annual, altitudinal, and seasonal variations in ice velocity and modelled run-off rates across the land-terminating section of the GrIS draining westwards between  $66^{\circ} 39' \text{ N}$  to  $67^{\circ} 56' \text{ N}$  (Fig. 1). The analysis is based on data from 1993 and 1995–1998 (see Methods Summary).

We explored spatial and temporal variations in ice flow by comparing velocities recorded in all five years along the centre-lines of the six major glaciers in the study area (Fig. 1 and Fig. 2). The average winter

(days 330 to 60) speed of the six glaciers in this part of the ice sheet is  $122 \text{ m yr}^{-1}$ , ranging from  $80 \text{ m yr}^{-1}$  (glacier 5) to  $207 \text{ m yr}^{-1}$  (glacier 3). During the height of summer speed-up (May–June), average speeds range from  $138 \text{ m yr}^{-1}$  (glacier 5) to  $314 \text{ m yr}^{-1}$  (glacier 3). Overall, there is a significant flow increase in summer relative to winter at all six glaciers, with average speed-ups of 50% to 125% that are similar to earlier observations<sup>1</sup>. There is also a marked decrease in the variance of ice speed in winter compared to summer (shaded areas, Fig. 2). The seasonal velocity fluctuations are broadly coincident with fluctuations in the degree of surface melting (Fig. 3), adding further support to hypotheses that seasonal surface melting drives seasonal cycles in ice-sheet

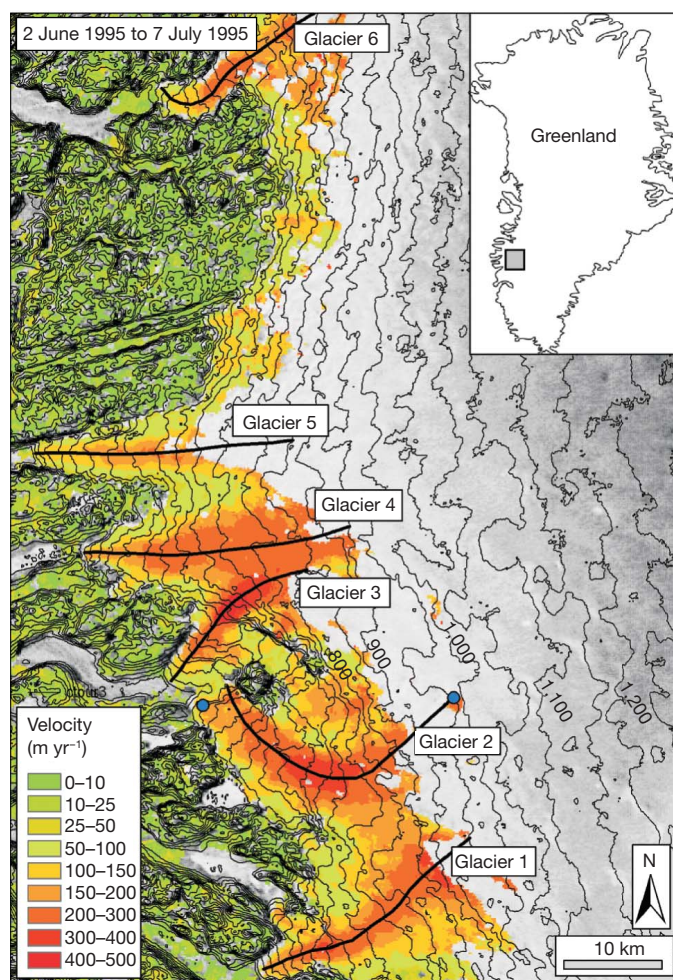


**Figure 1 | Ice-velocity map of the study area.** Example of a two-dimensional ice-velocity map for the selected study area derived using intensity tracking between two European Remote Sensing satellite synthetic aperture radar images separated by 35 days (2 June 1995 to 7 July 1995).

<sup>1</sup>School of Earth and Environment, University of Leeds, Woodhouse Lane, Leeds, LS2 9JT, UK. <sup>2</sup>School of Geosciences, University of Edinburgh, Drummond Street, Edinburgh, EH8 9XP, UK. <sup>3</sup>Department of Geography, University of Sheffield, Winter Street, Sheffield, S10 2TN, UK. <sup>4</sup>Earth System Sciences & Departement Geografie, Vrije Universiteit Brussel, Pleinlaan 2, B-1050 Brussels, Belgium.

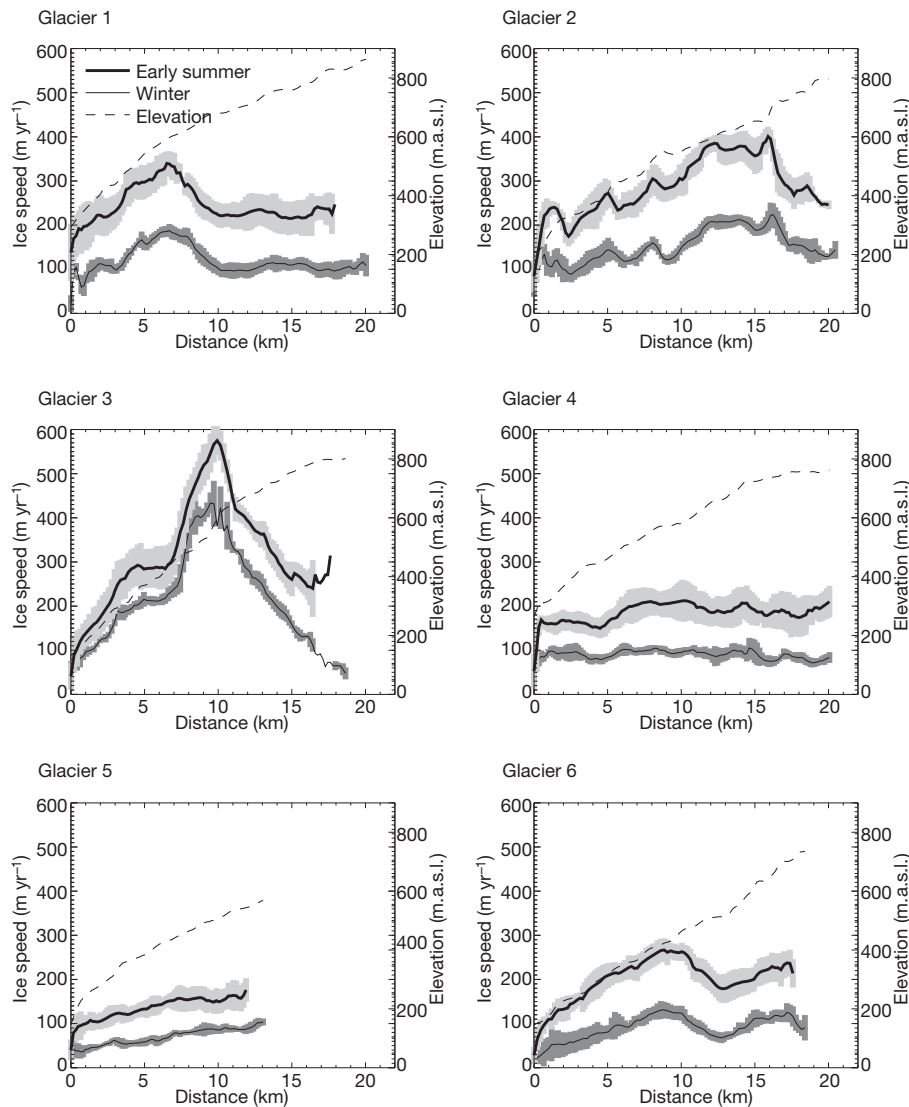


**Figure 2 | Ice-velocity profiles along six glaciers in the study area.** Average ice velocities during winter (days 330 to 60) and during the height of summer speed-up (May–June) on all five years along the centre-lines of the six major glaciers in the study area, with one standard deviation shown as shaded area.

flow<sup>1–4,7</sup>. To explore this relationship further, we compared velocity data at two distinct altitudes at glacier 2 (see Fig. 1) to assess the impact of delays in melting on ice speed-up. Using a lag-correlation of monthly averaged velocity data (see Supplementary Information and Supplementary Fig. 1), we estimate that summer speed-up at 950 m above sea level is delayed by 18 days compared to the changes recorded at 250 m above sea level. This speed-up delay is in close agreement with the  $\sim 20$ -day delay in the onset of surface melting between the same altitudes recorded in the temperature data set at Kangerlussuaq (Danish Meteorological Institute, station 04231) modified by a local atmospheric lapse rate<sup>17</sup>. Within the range of elevations encompassed by our survey, summer speed-up closely follows the rate at which melting propagates inland.

It is well known that variations in the degree of melting affect the rate at which coastal sectors of the GrIS flow<sup>1–7</sup>. Factors contributing to the manner in which seasonal velocity cycles may evolve include variations in the timing, extent and quantity of surface run-off, and potential variations in the routing of water to and at the ice-sheet base. In the absence of details of the englacial and subglacial hydraulic network, we investigated the extent to which fluctuations in surface run-off affected the ice flow by contrasting ice velocity observations during the years with highest (1995 and 1998) and lowest (1993, 1996, and 1997) run-off

The median error of the data set is  $17 \text{ m yr}^{-1}$ . The elevation data set is derived from the ASTER Global Digital Elevation Model (<http://www.ersdac.or.jp/GDEM/E/index.html>). We note that local ice-velocity maxima generally correspond to areas of steeper ice surface slopes. m.a.s.l., metres above sea level.

and melt extent<sup>18</sup> (see Supplementary Table 1). For the purpose of these calculations, we define summer as the period of surface run-off (see Fig. 3 and Table 1), and divide it further into equally long early-summer and late-summer periods. Peak summer is defined as the period when ice flow exceeds the winter rate by more than 100%, and winter encompasses the common period when no significant temporal flow variation occurs. Data from all five years were included when calculating the average winter velocity. The velocity data used in our comparison were extracted from locations with a continuous record across all years. Four glaciers (glaciers 2, 4, 5 and 6) exhibit a marked difference in the pattern of seasonal speed-up on years of low and high melting (Fig. 3). Although glacier 3 showed similar behaviour, the degree of speed-up was small in relation to other glaciers—possibly owing to the steep slopes and high speeds in the region of our comparison (Fig. 2), which may complicate glacier 3's response to fluctuations in surface melting—so we excluded it from our inter-annual comparison.

In contrast to the early-summer period, when flow is similar in all years, the average speed-up of glaciers 2, 4, 5 and 6 during late-summer was  $39 \pm 14\%$  in years of high melting and  $102 \pm 9\%$  in years of lower melting (Table 1 and Fig. 3). Although the peak rate of speed-up is greater during years of high melting ( $123 \pm 8\%$  versus  $104 \pm 9\%$ ), the period of peak flow is far shorter ( $\sim 30$  days versus  $\sim 90$  days). The

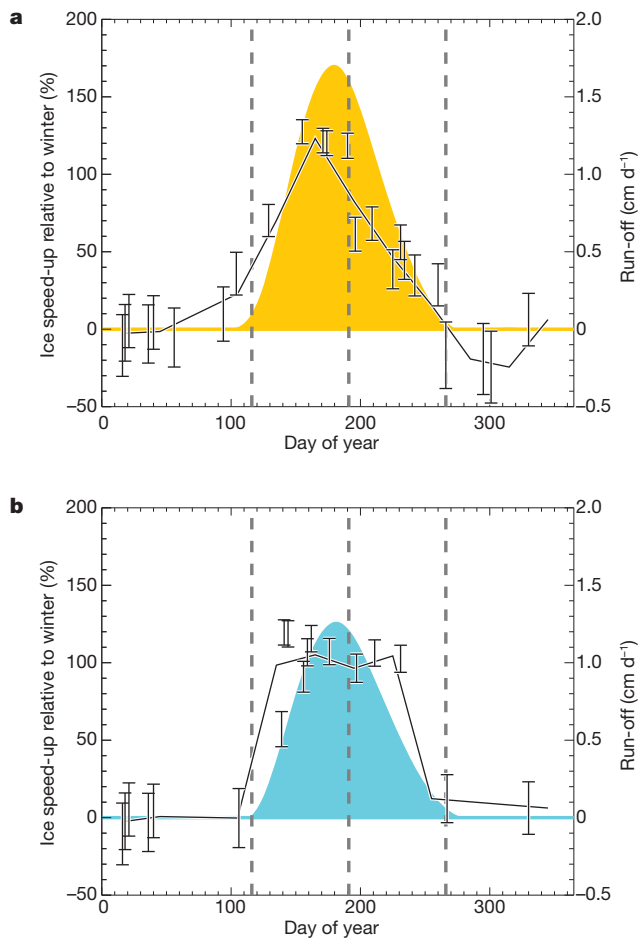


**Figure 3 | Ice speed-up relative to winter during years of high and low surface melting.** **a**, Speed-up in years of high melting (1995 and 1998). **b**, Speed-up in years of low melting (1993, 1996 and 1997). Point data are 35-day ice-velocity averages relative to the winter mean within the elevation band 500–600 m above sea level on glaciers 2, 4 and 6 and the elevation band 400–500 m above sea level on glacier 5. Glacier 1 was excluded owing to paucity of data. Error bars show the one-sigma uncertainty of speed-up measurements at each epoch. Monthly averaged data are shown as solid lines. Also shown (in colour) are model estimates of daily surface run-off rates within the study area averaged during the years of high (orange) and low (blue) melting. Vertical dashed lines indicate the shoulders and midway-point of the run-off period, which are used to define the summer period over which average speed-up is calculated.

ratio of peak speed-up to positive degree days (R. van de Wal, personal communication) recorded in our catchment ( $\sim 0.3\%$  per positive degree day) are similar to those measured elsewhere ( $\sim 0.2\%$  per positive degree day from the data of ref. 7). To calculate the integrated effect of these fluctuations, we computed the average degree of speed-up during the entire period of summer melting (days 116 to 266). On average, summer ice flow was  $67 \pm 12\%$  and  $102 \pm 9\%$  greater than during winter in years of high and low melting, respectively. Overall, summer ice flow was  $34 \pm 15\%$  slower in warmer years. There is some evidence of flow variability at times beyond the run-off period (Fig. 3). For example, in warm years, a small ( $\sim 25\%$ ) degree of speed-up occurs

**Table 1 | Glacier speed-up**

Period	Start day	End day	$\Delta V_{\text{warm}}$ (%)	$\Delta V_{\text{cold}}$ (%)	$\Delta V_{\text{cold}}$ minus $\Delta V_{\text{warm}}$ (%)
Early summer	116	191	$112 \pm 8$	$102.2 \pm 9$	$-9 \pm 12$
Late summer	191	266	$39 \pm 14$	$101.8 \pm 9$	$62 \pm 16$
Summer	116	266	$67 \pm 12$	$102.1 \pm 9$	$34 \pm 15$

Average speed-up ( $\Delta V$ ) (with one-sigma uncertainty) of glaciers 2, 4, 5 and 6 at an altitude of 400–600 m above sea level in warm (1995 and 1998) and cold (1993, 1996 and 1997) years during fixed time periods relative to winter (days 330 to 60). The periods of early and late summer are defined using model estimates of run-off (see Fig. 3). We point out that the similarity of  $\Delta V_{\text{cold}}$  during early summer, late summer and all summer is a coincidence of the data.

before run-off begins and a comparable degree of slowdown occurs after run-off ceases. We are, however, not able to make inter-annual comparisons over these periods owing to the paucity of data in colder years.

Although the lower degree of late-summer speed-up we observe in years of high melting is at odds with that expected due to basal lubrication alone<sup>2</sup>, the behaviour can be explained by inter-annual differences in the evolution of subglacial drainage. Abundant melt-water can trigger a switch from inefficient (cavity<sup>19</sup>) to efficient (channelized<sup>20</sup>) modes of drainage and, consequently, to a reduction in subglacial water pressure and ice speed. Such events have been observed at High Arctic<sup>10</sup> and Alaskan valley glaciers<sup>11</sup>, where summer speed-up is of shorter duration during years of high melting. A numerical simulation of idealized ice-sheet flow that incorporates dynamic switching between drainage modes<sup>13</sup> is able to capture the key aspects of flow variations we observe in southwest Greenland. This model<sup>13</sup> predicts that glacier slowdown occurs above a critical rate of water flow in the range 1–2 cm per day. It also predicts that the period of speed-up is shorter than the period of melt-supply by a factor proportional to the intensity of melting. Imposing a melt-supply of  $\sim 10$  cm per day or  $\sim 20$  cm per day for  $\sim 100$  days, for example, leads to overall speed-up periods of  $\sim 70$  days or  $\sim 40$  days, respectively, and late-summer speeds that are about half those in early summer. Our observations show that in warm years, slowdown occurs when the monthly run-off rate exceeds about 1.4 cm per day (see Fig. 3 and Supplementary Table 1) and that, in consequence, the period of fast-flow (double the winter rate) is about three times shorter and late-summer speeds are  $73 \pm 16\%$  lower than in early summer.

The effect of melt-induced velocity fluctuations on the GrIS remains a subject of debate<sup>1–9,21</sup>. Although some studies have shown that greater melting produces greater ice-sheet acceleration<sup>7,9</sup>, others have identified a long-term (17-year) decrease in Greenland's flow during a period of increased melting<sup>3</sup>. Our data reconcile these contradictory findings: although the peak rate of flow increases during years of high melting, the associated faster transition to a period of more efficient subglacial drainage reduces both the duration of rapid flow and the average summer speed when compared to years of low melting. In regions where the critical run-off threshold<sup>13</sup> is not breached, we would not expect to see the effects of efficient drainage on flow. On the basis of our data set, we are not able to establish whether the transition between distinct modes of flow is an abrupt or gradual process. Furthermore, we recognize that the classification of our data into two discrete categories could mask intermediate behaviour, and that changes in flow associated with shorter period melting variability<sup>2</sup> cannot be captured by our satellite observations. The small speed-up observed before the summer period in warm years, for example, may be driven by brief melting events that are not recorded by our run-off model. These changes are, however, small in comparison to the overall speed-up during summer, and are not central to our analysis of how flow responds to drainage mode switching. Altogether, our data show that the subglacial drainage system in southwest Greenland evolves in response to variable surface melting in a way similar to that of mountain glaciers<sup>10–12</sup>.

Rates of surface melting at the Greenland ice sheet are predicted to double over the course of the twenty-first century<sup>22</sup>. One model of the ice-sheet response to climate warming<sup>9</sup> has estimated that melt-induced acceleration could add between 0.15 m and 0.40 m to global sea levels by 2500. However, several authors<sup>11,21</sup> have cautioned against the notion<sup>7,9</sup> that increases in ice flow are simply proportional to increases in surface melting. Our data are the first to reveal a drop in summer speed-up of the GrIS in years of high melting compared to years of low melting, and support views<sup>3,11,21</sup> that the ice-sheet subglacial drainage system may adjust to accommodate increased melting in a way that does not lead to proportionate increases in flow. The net effect of melt-induced speed-up and efficient drainage remains uncertain; numerical experiments<sup>13</sup> suggest that their combined impact depends upon how both the mean supply and short-period spikes in

melting develop over time. According to our data set, which covers a range of melting conditions<sup>23</sup> that is small in comparison to predicted changes over the next century<sup>22</sup>, increases in surface melting lead to a reduction in rates of summertime ice flow in the lower ablation zone of southwest Greenland. An improved understanding of subglacial drainage is therefore an essential step towards developing numerical models that capture the link between ice-sheet hydrology and ice motion. Until the influence of changes in melting on ice-sheet velocity are more firmly established, the response of the cryosphere to climate change and its ultimate contributions to sea level will remain uncertain.

## METHODS SUMMARY

We used synthetic aperture radar intensity tracking<sup>24</sup> to determine ice velocity within our study area (see Supplementary Information). We applied the method to 37 European Remote Sensing satellite synthetic aperture radar 35-day repeat-track pairs acquired between 1993 and 1998. The median velocity error was estimated to be  $17 \text{ m yr}^{-1}$  by measuring the mean difference from zero of large samples of data over areas of static rock present within each image<sup>25</sup>. Run-off data were extracted from a monthly degree-day surface melt-water run-off/retention model<sup>23</sup> adapted from an annual degree-day run-off/retention model<sup>26</sup> using the European Centre for Medium-Range Weather Forecasts as input parameters (see Supplementary Information). On the basis of their combination of anomalously high run-off and melt-extent<sup>18</sup>, we classified 1995 and 1998 as high-melt years, and 1993, 1996 and 1997 as low-melt years (see Supplementary Information).

Received 12 May; accepted 1 December 2010.

- Joughin, I. *et al.* Seasonal speedup along the western flank of the Greenland Ice Sheet. *Science* **320**, 781–783 (2008).
- Shepherd, A. *et al.* Greenland ice sheet motion coupled with daily melting in late summer. *Geophys. Res. Lett.* **36**, L01501 (2009).
- van de Wal, R. S. W. *et al.* Large and rapid melt-induced velocity changes in the ablation zone of the Greenland Ice Sheet. *Science* **321**, 111–113 (2008).
- Palmer, S. J., Shepherd, A., Nienow, P. W. & Joughin, I. Seasonal speedup of the Greenland Ice Sheet linked to routing of surface water. *Earth Planet. Sci. Lett.* (in the press).
- Bartholomew, I. *et al.* Seasonal evolution of subglacial drainage and acceleration in a Greenland outlet glacier. *Nature Geosci.* **3**, 408–411 (2010).
- Das, S. B. *et al.* Fracture propagation to the base of the Greenland Ice Sheet during supraglacial lake drainage. *Science* **320**, 778–781 (2008).
- Zwally, H. J. *et al.* Surface melt-induced acceleration of Greenland ice-sheet flow. *Science* **297**, 218–222 (2002).
- Meehl, G. A. *et al.* in *Climate Change 2007: The Physical Science Basis. Contribution of Working Group I to the Fourth Assessment Report of the Intergovernmental Panel on Climate Change* (eds Solomon, S. *et al.*) 747–846 (Cambridge University Press, 2007).
- Parizek, B. R. & Alley, R. B. Implications of increased Greenland surface melt under global-warming scenarios: ice-sheet simulations. *Quat. Sci. Rev.* **23**, 1013–1027 (2004).
- Bingham, R. G., Nienow, P. W. & Sharp, M. J. Intra-annual and intra-seasonal flow dynamics of a high Arctic polythermal valley glacier. *Ann. Glaciol.* **37**, 181–188 (2003).
- Truffer, M., Harrison, W. D. & March, R. S. Record negative glacier balances and low velocities during the 2004 heatwave in Alaska, USA: implications for the interpretation of observations by Zwally and others in Greenland. *J. Glaciol.* **51**, 663–664 (2005).
- Bartholomew, T. C., Anderson, R. S. & Anderson, S. P. Response of glacier basal motion to transient water storage. *Nature Geosci.* **1**, 33–37 (2008).
- Schoof, C. Ice-sheet acceleration driven by melt supply variability. *Nature* **468**, 803–806 (2010).
- Johannessen, O. M. & Khvorostovsky, K. Bobylev, & Leonid P. Recent ice-sheet growth in the interior of Greenland. *Science* **310**, 1013–1016 (2005).
- Hanna, E. *et al.* Increased runoff from melt from the Greenland ice sheet: a response to global warming. *J. Clim.* **21**, 331–341 (2008).
- Rignot, E. & Kanagaratnam, P. Changes in the velocity structure of the Greenland ice sheet. *Science* **311**, 986–990 (2006).
- Steffen, K. & Box, J. Surface climatology of the Greenland ice sheet: Greenland climate network 1995–1999. *J. Geophys. Res.* **106**, 33951–33964 (2001).
- Abdalati, W. & Steffen, K. Greenland ice sheet melt extent: 1979–1999. *J. Geophys. Res.* **106**, 33983–33988 (2001).
- Schoof, C. The effect of cavitation on glacier sliding. *Proc. R. Soc. Lond. A* **461**, 609–627 (2005).
- Rothlisberger, H. Water pressure in intra- and subglacial channels. *J. Glaciol.* **11**, 177–203 (1972).
- Price, S., Payne, A. J., Catania, G. & Neumann, T. A. Seasonal acceleration of inland ice via longitudinal coupling to marginal ice. *J. Glaciol.* **54**, 213–219 (2008).
- Mernild, S. H., Liston, G. E., Hiemstra, C. A. & Christensen, J. H. Greenland ice sheet surface mass-balance modeling in a 131-yr perspective, 1950–2080. *J. Hydrometeorol.* **11**, 3–25 (2010).
- Hanna, E. *et al.* Runoff and mass balance of the Greenland ice sheet: 1958–2003. *J. Geophys. Res.* **110**, D13108 (2005).
- Strozzi, T., Luckman, A., Murray, T., Wegmuller, U. & Werner, C. L. Glacier motion estimation using SAR offset-tracking procedures. *IEEE Trans. Geosci. Rem. Sens.* **40**, 2384–2391 (2002).
- Pritchard, H., Murray, T., Luckman, A., Strozzi, T. & Barr, S. Glacier surge dynamics of Sortebrae, east Greenland, from synthetic aperture radar feature tracking. *J. Geophys. Res.* **110**, F03005 (2005).
- Janssens, I. & Huybrechts, P. The treatment of meltwater retention in mass-balance parameterizations of the Greenland ice sheet. *Ann. Glaciol.* **31**, 133–140 (2000).

**Supplementary Information** is linked to the online version of the paper at [www.nature.com/nature](http://www.nature.com/nature).

**Acknowledgements** This work was supported by the UK NERC National Centre for Earth Observation, a Philip Leverhulme Prize to A.S. and by the EU FP7 Ice2Sea project (publ. no. 026). European Remote Sensing satellite synthetic aperture radar data were provided by the European Space Agency Vectra Consortium. We thank R. van de Wal for providing positive degree-day data.

**Author Contributions** A.S. designed the research. A.V.S. produced the ice velocity data. E.H. and P.H. produced the run-off data. A.V.S. and A.S. analysed the data sets and produced the results. A.V.S. and A.S. wrote the manuscript. All authors discussed the results and commented on the manuscript.

**Author Information** Reprints and permissions information is available at [www.nature.com/reprints](http://www.nature.com/reprints). The authors declare no competing financial interests. Readers are welcome to comment on the online version of this article at [www.nature.com/nature](http://www.nature.com/nature). Correspondence and requests for materials should be addressed to A.S. ([a.shepherd@leeds.ac.uk](mailto:a.shepherd@leeds.ac.uk)).

# Ependymal cells of chordate larvae are stem-like cells that form the adult nervous system

Takeo Horie<sup>1</sup>, Ryoko Shinki<sup>1</sup>, Yosuke Ogura<sup>1</sup>, Takehiro G. Kusakabe<sup>2</sup>, Nori Satoh<sup>3</sup> & Yasunori Sasakura<sup>1</sup>

In ascidian tunicates, the metamorphic transition from larva to adult is accompanied by dynamic changes in the body plan. For instance, the central nervous system (CNS) is subjected to extensive rearrangement because its regulating larval organs are lost and new adult organs are created<sup>1</sup>. To understand how the adult CNS is reconstructed, we traced the fate of larval CNS cells during ascidian metamorphosis by using transgenic animals and imaging technologies with photoconvertible fluorescent proteins<sup>2</sup>. Here we show that most parts of the ascidian larval CNS, except for the tail nerve cord, are maintained during metamorphosis and recruited to form the adult CNS. We also show that most of the larval neurons disappear and only a subset of cholinergic motor neurons and glutamatergic neurons are retained. Finally, we demonstrate that ependymal cells of the larval CNS contribute to the construction of the adult CNS and that some differentiate into neurons in the adult CNS. An unexpected role of ependymal cells highlighted by this study is that they serve as neural stem-like cells to reconstruct the adult nervous network during chordate metamorphosis. Consequently, the plasticity of non-neuronal ependymal cells and neuronal cells in chordates should be re-examined by future studies<sup>3,4</sup>.

Among chordates, urochordate ascidians perform dramatic metamorphosis, which converts swimming larvae to sessile adults<sup>5</sup>. The larva of ascidians contains a well-organized tripartite brain<sup>6</sup>. The traditional view, based on morphological studies, is that most of the larval brain is destroyed during metamorphosis. The adult CNS is then formed from the neurohypophyseal duct, which is located in the anterior-most part of the larval brain connecting to the stomodeum<sup>7,8</sup>. However, more recent work using yellow fluorescent protein has suggested that, for *Ciona* at least, a part of the larval CNS, notably the neck region, is an important source of adult neurons<sup>9</sup>. Our intent here is to extend this earlier study to address more definitively how much of the larval CNS is lost and how much of it contributes to form the adult CNS during ascidian metamorphosis.

To address this, we used Kaede fluorescent protein because Kaede fluorescence can be irreversibly converted from green to red by irradiation with ultraviolet light<sup>2</sup> (Fig. 1a). Consequently, we can label cells in the larval CNS with red fluorescence and trace them during metamorphosis (Fig. 1). The newly formed neural cells can be distinguished from the larval neural cells because of their exclusive transmission of green fluorescence. We have established a transgenic line of *Ciona intestinalis* that expresses Kaede in the entire larval nervous system with the *cis* regulatory element of the *Ci-β2tubulin* gene<sup>10</sup> (Fig. 1b). Ultraviolet irradiation was applied to larvae of the transgenic line (Fig. 1c), which were observed during and after metamorphosis. We found that red-labelled cells derived from the larval CNS were located in the entire region of the cerebral ganglion and ciliated funnel, two major parts of the adult CNS (Fig. 1d). This indicates that cells in the adult CNS are inherited from the larval CNS. Most red-labelled cells also expressed green fluorescence (Fig. 1d), suggesting their continuous expression of Kaede from the *β2tubulin* regulatory element. In contrast,

cells around pigment cells, which were located in the middle part of the cerebral ganglion, showed strong red fluorescence but only background levels of green fluorescence (Fig. 1d, asterisk). This suggests that these cells terminated their expression of the Kaede protein from the *β2tubulin* regulatory element during metamorphosis. Support for this notion

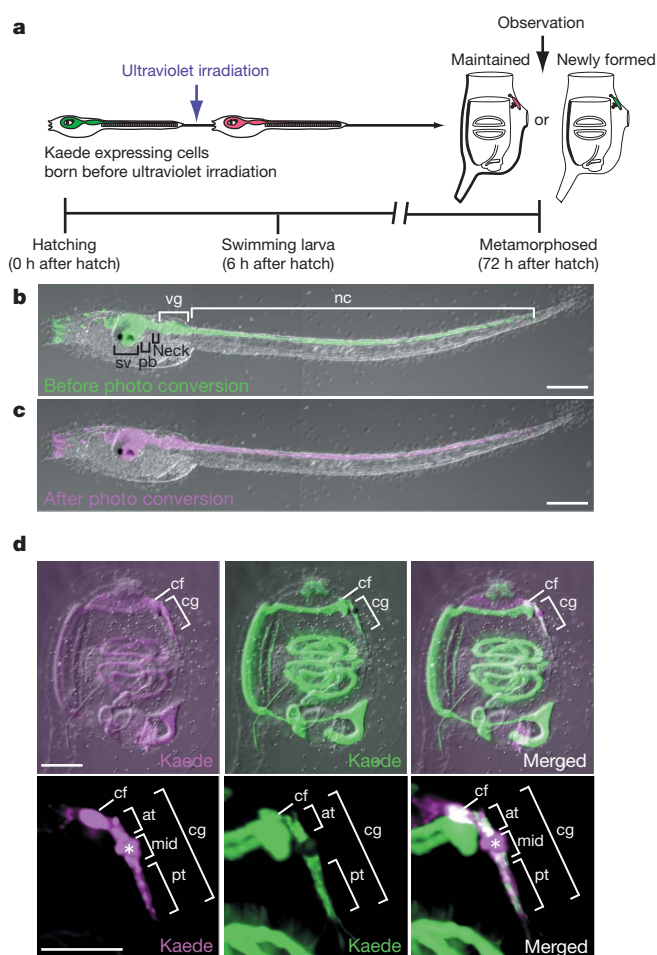


**Figure 1 | Tracing of cells in the larval CNS.** **a**, The tracing experiment. **b**, Kaede expression in the larval CNS of the *β2tubulin*-Kaede line; sv, sensory vesicle; pb, posterior brain; vg, visceral ganglion; nc, nerve cord. **c**, A larva after ultraviolet irradiation. Red fluorescence is shown in magenta. **d**, Distribution of larval neural cells in the adult CNS. Upper, photographs of a whole juvenile; lower, magnified images of the adult CNS. Left, Kaede red fluorescence; middle, Kaede green fluorescence; right, merged images. Cells with red fluorescence are distributed throughout the cerebral ganglion (cg) and ciliated funnel (cf). Asterisk indicates cells around pigment cells. The cerebral ganglion is divided into anterior (at), middle (mid) and posterior (pt) parts. Kaede green fluorescence is also observed in the mesodermal and endodermal tissues. Scale bars, 100 μm.

<sup>1</sup>Shimoda Marine Research Center, University of Tsukuba, Shimoda, Shizuoka 415-0025, Japan. <sup>2</sup>Department of Biology, Konan University, Kobe, Hyogo 658-8501, Japan. <sup>3</sup>Marine Genomics Unit, Okinawa Institute of Science and Technology Promotion Corporation, Onna, Okinawa 904-0412, Japan.

comes from a previous report that cells around the pigment cells are subjected to programmed cell death during metamorphosis<sup>11</sup>. Therefore the red cells around the pigment cells are highly likely to be dead larval cells, so we excluded these from subsequent analyses. The cerebral ganglion contained not only red-labelled cells but also cells with only green fluorescence that were newly born after the larval stage (Fig. 1d). However, such new cells were evidently fewer than larval neural cells, suggesting that most of the cells composing the adult CNS were derived from the larval CNS.

The larval CNS is largely divided into five parts: the sensory vesicle (the anterior part of the brain), posterior brain, neck, visceral ganglion and nerve cord (Fig. 1b). Using ultraviolet irradiation of specific parts of the larval CNS in the *β2tubulin*-Kaede line, we examined which of these five parts was maintained to participate in adult CNS formation. When cells in the sensory vesicle and posterior brain were traced, red-labelled cells were present in the entire cerebral ganglion and ciliated funnel (Supplementary Fig. 1a). This suggests that cells in the sensory vesicle/posterior brain are the major source of cells composing the adult CNS. When non-neuronal cells in the posterior brain and neck were traced separately from those of the sensory vesicle (by expressing Kaede with the *cis* element of *CiPhox2* (ref. 9); Supplementary Fig. 1b), the cells remained to form the relatively posterior part of the cerebral ganglion (Supplementary Fig. 1b); this suggests the conservation of the anterior–posterior axis between the larval and adult CNS. When cells in the visceral ganglion were traced, a few red-labelled cells were present in the middle and posterior parts of the cerebral ganglion (Supplementary Fig. 1c). In contrast, cells in the tail nerve cord disappeared completely after metamorphosis, indicating no contribution of these cells to adult CNS formation (Supplementary Fig. 1d).

The larval CNS of *Ciona* is composed of approximately 350 cells, including five sensory receptor cells, approximately 100 neurons and approximately 245 ependymal cells<sup>12,13</sup>. Because most of the larval neurons are cholinergic, glutamatergic or GABAergic/glycinergic<sup>14–16</sup>, we determined which type of neuron contributes to the adult CNS. To trace the location of larval cholinergic neurons, we used our previously established transgenic line that expresses Kaede in cholinergic neurons with the upstream regulatory region of *Ci-VACHT*, a specific marker gene of the neurons<sup>17,18</sup>. Larvae of the *VACHT*-Kaede line expressed Kaede in the posterior brain and the motor neurons in the visceral ganglion (Fig. 2a). When larval cholinergic neurons were traced during metamorphosis, red-labelled, larval cholinergic neurons were found in the posterior part of the cerebral ganglion (Fig. 2b). Red-coloured cholinergic neurons extended long axons posteriorly, suggesting that they are functional neurons in the adult CNS. We then examined whether the cholinergic neurons in the posterior brain or the visceral ganglion were linked to the adult neurons. We found that only the cholinergic motor neurons in the visceral ganglion remained in the posterior part of the cerebral ganglion (Supplementary Fig. 2).

We then traced glutamatergic neurons during metamorphosis. Again, we used a previously established transgenic line that expresses Kaede in glutamatergic neurons by the promoter of *Ci-VGLUT*, a gene expressed specifically in glutamatergic neurons<sup>14</sup> (Supplementary Fig. 3a). When larval glutamatergic neurons were traced, the anterior-most part of the ciliated funnel showed both red and green fluorescence, suggesting that this part contains larval glutamatergic neurons (Supplementary Fig. 3b). Therefore most of the larval glutamatergic neurons were lost during metamorphosis, although a few of them remained and formed the ciliated funnel.

We found a different result when tracing GABAergic/glycinergic neurons. GABAergic/glycinergic neurons were labelled with the upstream regulatory region of their marker gene *Ci-VGAT*<sup>18</sup> (Supplementary Fig. 3c). When the larval GABAergic/glycinergic neurons were traced during metamorphosis, a conspicuous red fluorescence was detected in dead cells around the pigmented cells (Supplementary Fig. 3d). This suggests that larval GABAergic/glycinergic neurons disappeared during metamorphosis.

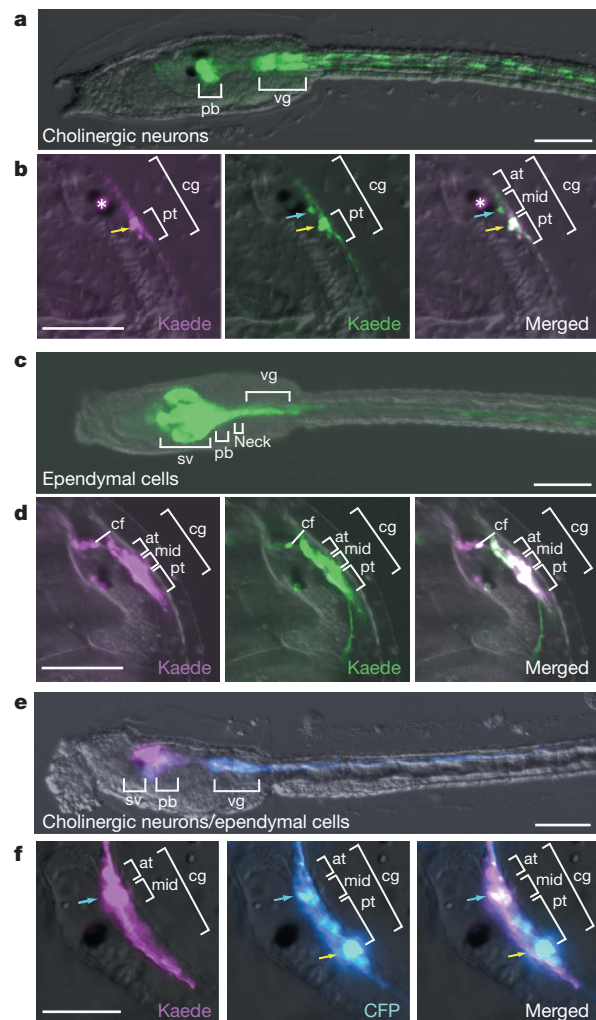


**Figure 2 | Tracing of larval cholinergic neurons and ependymal cells, and differentiation of larval ependymal cells to adult cholinergic neurons.**

**a**, Kaede expression in the posterior brain (pb) and visceral ganglion (vg) of a larva of the *VACHT*-Kaede line. **b**, Tracing of cholinergic neurons. Larval cholinergic neurons are located in the posterior (pt) part of the cerebral ganglion (cg) (yellow arrow). The asterisk indicates dead cells around the pigmented cells. Newly born neural cells are present in the middle part (blue arrow). **c**, A larva into which the *Ci-opsin3* promoter and Kaede fusion construct was introduced by electroporation. Kaede is expressed in the sensory vesicle (sv), posterior brain (pb), neck and visceral ganglion (vg). **d**, Tracing of ependymal cells. Red-coloured cells are present in the entire region of the cerebral ganglion (cg) and ciliated funnel (cf). **e**, Expression of CFP and photoconverted Kaede in the larval cholinergic neurons and ependymal cells, respectively. **f**, Kaede and CFP fluorescence in the adult cerebral ganglion after metamorphosis. Cholinergic neurons in the anterior to middle part of the cerebral ganglion (blue arrow) showed Kaede red fluorescence, suggesting that they were derived from larval ependymal cells. Cholinergic neurons in the posterior part (yellow arrow) did not show Kaede red fluorescence. Scale bars, 100  $\mu$ m.

We also followed the outcome of glial cells. Ependymal cells, which line the cavity of the sensory vesicle and constitute the entire nerve cord<sup>12,19</sup>, are the only glial cell type found in the ascidian CNS. The *Ciona* larval brain has approximately 70% of these cells<sup>13</sup>. Kaede was expressed in ependymal cells through the upstream regions of *Ci-opsin3* and *Ci-CRALBP*, marker genes of ependymal cells<sup>20</sup> (Fig. 2c). The trace of larval ependymal cells revealed the distribution of red-labelled cells throughout the cerebral ganglion and ciliated funnel (Fig. 2d). When ependymal cells in the visceral ganglion were specifically traced (by *DiI* labelling), these cells remained after metamorphosis in the posterior part of the adult cerebral ganglion (Supplementary Fig. 4).

This finding supports the notion that there is conservation of the anterior–posterior axis between the larval and adult CNS. Next, to determine whether adult neurons are produced from larval ependymal cells, their fate after metamorphosis was traced by the co-expression of Kaede in the larval ependymal cells and a cyan fluorescent protein (CFP) with neuron subtype-specific promoters (Supplementary Fig. 5a). When cholinergic neurons were examined, it was found that the CFP-positive cholinergic neurons located in the anterior part of the cerebral ganglion showed red Kaede fluorescence, the marker of larval ependymal cells (Fig. 2e, f, blue arrow). This indicates that they were derived from larval ependymal cells. Posterior cholinergic neurons were negative for Kaede fluorescence (Fig. 2f, yellow arrow), confirming that they are derived from larval cholinergic neurons. Likewise, GABAergic/glycinergic neurons in the middle part of the cerebral ganglion were derived from larval ependymal cells (Supplementary Fig. 5). Glutamatergic neurons were not examined because only a few of them were found in the cerebral ganglion of juveniles immediately after metamorphosis. We therefore concluded that an abundance of larval ependymal cells are maintained and that some of them differentiate into adult neurons.

Furthermore, in light of a previous report suggesting that the cerebral ganglion is formed from the neurohypophyseal duct<sup>7,8</sup>, we conducted tracing experiments on this region. We introduced a promoter of *Ci-otp*, a gene encoding a homeodomain transcription factor that is expressed in the anterior part of the larval sensory vesicle including the neurohypophyseal duct<sup>21</sup>, and a Kaede fusion construct into *Ciona* embryos. Larvae that expressed Kaede exclusively in the neurohypophyseal duct were selected to trace this specific region (Supplementary Fig. 6a). We found red-labelled larval cells located in the anterior tip of

the ciliated funnel (Supplementary Fig. 6b), whereas no red-coloured cells were present in the cerebral ganglion. This result suggests that the cells in the neurohypophyseal duct comprise the anterior tip of the ciliated funnel, but they are not a major source of cells for the adult CNS.

Based on these results, we conclude that the anterior parts of the ascidian larval CNS, namely the sensory vesicle, posterior brain, neck and visceral ganglion, contribute to the formation of the adult CNS (Fig. 3). Thus components of the larval and adult CNS are maintained even though their body plan is subjected to extensive rearrangement during metamorphosis to form sessile adults in ascidians. In addition, the anterior–posterior axis of the larval CNS is also inherited to form the adult CNS. This indicates that the anterior–posterior axis of the adult CNS is already determined by developmental regulatory genes that are known to play essential roles in anterior–posterior axis formation of the larval CNS<sup>6,22</sup>. The conservative mode of adult CNS formation is completely different from the destructive mode seen in lower deuterostomes. Rather, such a conservative system is observed in vertebrate metamorphosis<sup>23</sup>, suggesting that urochordates and vertebrates share a similar system of adult CNS formation.

In contrast to the overall maintenance of the CNS during metamorphosis, most larval neurons, except for a few motor neurons and glutamatergic neurons, disappear during the process of adult CNS formation (Fig. 3b). Most adult CNS cells are supplied from larval ependymal cells (Fig. 3a). In addition, a subset of adult neurons unambiguously originates from larval ependymal cells. Thus ascidian larval ependymal cells can act as neural stem-like cells that can give rise to several types of adult neuron during metamorphosis. In support of this idea, it has been shown that ependymal cells in vertebrates can act as neural stem cells during recovery from injury and that they also generate olfactory bulb neurons<sup>24,25</sup>. However, it is still controversial whether ependymal cells act as neural stem cells<sup>26</sup>. Indeed, the role of ependymal cells in the chordate CNS in general warrants further investigation<sup>3,4</sup>.

## METHODS SUMMARY

Transgenic lines of *Ciona intestinalis* were created with *Minos* transposon-mediated transgenesis<sup>27</sup>. The photoconversion of Kaede was performed by illuminating larvae with an ultraviolet light using a fluorescence microscope (Axio10, Carl Zeiss). The illuminated larvae were cultured under dark conditions until observation.

**Full Methods** and any associated references are available in the online version of the paper at [www.nature.com/nature](http://www.nature.com/nature).

Received 20 September; accepted 27 October 2010.

Published online 2 January 2011.

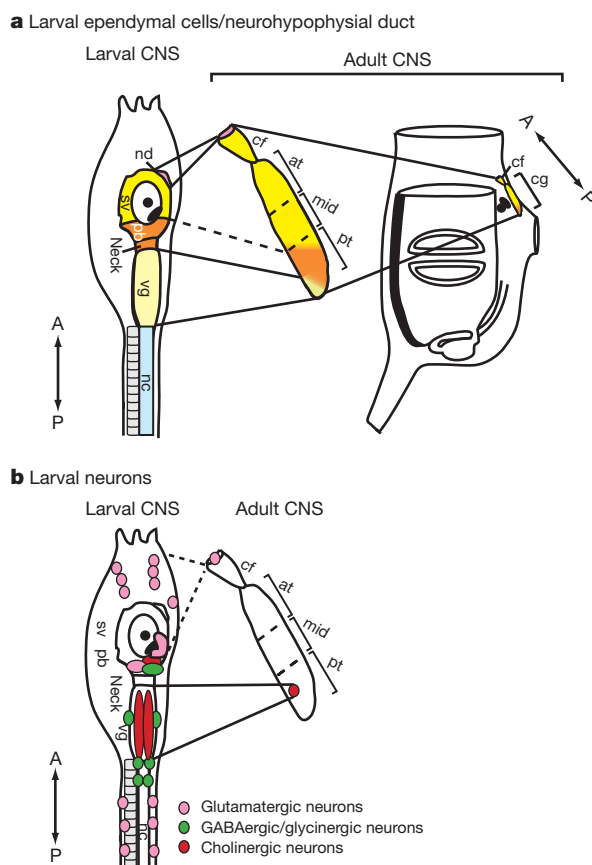


**Figure 3 | Adult CNS is constructed from the larval CNS.** The relationship between the larval and adult CNS with respect to larval ependymal cells (a) and larval neurons (b); nd, neurohypophyseal duct; sv, sensory vesicle; pb, posterior brain; vg, visceral ganglion; nc, nerve cord; cf, ciliated funnel; at, mid and pt, anterior, middle and posterior parts of the cerebral ganglion, respectively; cg, cerebral ganglion; A, anterior; P, posterior.

- Nielsen, C. Larval and adult brains. *Evol. Dev.* **7**, 483–489 (2005).
- Ando, R., Hama, H., Yamamoto-Hino, M., Mizuno, H. & Miyawaki, A. An optical marker based on the UV-induced green-to-red photoconversion of a fluorescent protein. *Proc. Natl Acad. Sci. USA* **99**, 12651–12656 (2002).
- Barres, B. A. The mystery and magic of glia: a perspective on their roles in health and disease. *Neuron* **60**, 430–440 (2008).
- Allen, N. J. & Barres, B. A. Glia – more than just brain glue. *Nature* **457**, 675–677 (2009).
- Satoh, N. *Developmental Biology of Ascidians* (Cambridge University Press, 1994).
- Wada, H., Saiga, H., Satoh, N. & Holland, P. W. Tripartite organization of the ancestral chordate brain and the antiquity of placodes: insight from ascidian *Pax-2/5/8*, *Hox* and *Otx* genes. *Development* **125**, 1113–1122 (1998).
- Manni, L. et al. Neurogenic and non-neurogenic placodes in ascidians. *J. Exp. Zool. B* **302**, 483–504 (2004).
- Manni, L., Agnoletto, A., Zaniolo, G. & Burighel, P. Stomodaeal and neurohypophyseal placodes in *Ciona intestinalis*: insights into the origin of the pituitary gland. *J. Exp. Zool. B* **304**, 324–339 (2005).
- Dufour, H. D. et al. Precranial origin of cranial motoneurons. *Proc. Natl Acad. Sci. USA* **103**, 8727–8732 (2006).
- Kusakabe, T., Yoshida, R., Ikeda, Y. & Tsuda, M. Computational discovery of DNA motifs associated with cell type-specific gene expression in *Ciona*. *Dev. Biol.* **276**, 563–580 (2004).
- Tarallo, R. & Sordino, P. Time course of programmed cell death in *Ciona intestinalis* in relation to mitotic activity and MAPK signaling. *Dev. Dyn.* **230**, 251–262 (2004).
- Katz, M. J. Comparative anatomy of the tunicate tadpole *Ciona intestinalis*. *Biol. Bull.* **164**, 1–27 (1983).

13. Nicol, D. & Meinertzhagen, I. A. Cell counts and maps in the larval central nervous system of the ascidian *Ciona intestinalis* (L.). *J. Comp. Neurol.* **309**, 415–429 (1991).
14. Horie, T., Kusakabe, T. & Tsuda, M. Glutamatergic networks in the *Ciona intestinalis* larva. *J. Comp. Neurol.* **508**, 249–263 (2008).
15. Horie, T., Nakagawa, M., Sasakura, Y. & Kusakabe, T. G. Cell type and function of neurons in the ascidian nervous system. *Dev. Growth Differ.* **51**, 207–220 (2009).
16. Horie, T., Nakagawa, M., Sasakura, Y., Kusakabe, T. G. & Tsuda, M. Simple motor system of the ascidian larva: neuronal complex comprising putative cholinergic and GABAergic/glycinergic neurons. *Zool. Sci.* **27**, 181–190 (2010).
17. Takamura, K., Egawa, T., Ohnishi, S., Okada, T. & Fukuoka, T. Developmental expression of ascidian neurotransmitter synthesis genes. I. Choline acetyltransferase and acetylcholine transporter genes. *Dev. Genes Evol.* **212**, 50–53 (2002).
18. Yoshida, R. *et al.* Identification of neuron-specific promoters in *Ciona intestinalis*. *Genesis* **39**, 130–140 (2004).
19. Konno, A. *et al.* Distribution and structural diversity of cilia in tadpole larvae of the ascidian *Ciona intestinalis*. *Dev. Biol.* **337**, 42–62 (2010).
20. Tsuda, M. *et al.* Origin of the vertebrate visual cycle: II. Visual cycle proteins are localized in whole brain including photoreceptor cells of a primitive chordate. *Vision Res.* **43**, 3045–3053 (2003).
21. Moret, F. *et al.* Regulatory gene expressions in the ascidian ventral sensory vesicle: evolutionary relationships with the vertebrate hypothalamus. *Dev. Biol.* **277**, 567–579 (2005).
22. Imai, K. S., Stolfi, A., Levine, M. & Satou, Y. Gene regulatory networks underlying the compartmentalization of the *Ciona* central nervous system. *Development* **136**, 285–293 (2009).
23. Gilbert, S. F. *Developmental Biology* 8th edn (Sinauer Associates, 2006).
24. Johansson, C. F. *et al.* Identification of a neural stem cell in the adult mammalian central nervous system. *Cell* **96**, 25–34 (1999).
25. Coskun, V. *et al.* CD133<sup>+</sup> neural stem cells in the ependyma of mammalian postnatal forebrain. *Proc. Natl Acad. Sci. USA* **105**, 1026–1031 (2008).
26. Chojnacki, A. K., Mak, G. K. & Weiss, S. Identity crisis for adult periventricular neural stem cells: subventricular zone astrocytes, ependymal cells or both? *Nature Rev. Neurosci.* **10**, 153–163 (2009).
27. Sasakura, Y., Awazu, S., Chiba, S. & Satoh, N. Germ-line transgenesis of the Tc1/*mariner* superfamily transposon *Minos* in *Ciona intestinalis*. *Proc. Natl Acad. Sci. USA* **100**, 7726–7730 (2003).

**Supplementary Information** is linked to the online version of the paper at [www.nature.com/nature](http://www.nature.com/nature).

**Acknowledgements** We acknowledge the members of the Shimoda Marine Research Center at the University of Tsukuba for their cooperation with our study. We also thank National Bio-resource Project, Ministry of Education, Culture, Sports, Science and Technology, Japan (MEXT), S. Fujiwara and all members of the Maizuru Fishery Research Station of Kyoto University and the Education and Research Center of Marine Bioresources of Tohoku University for providing us with *Ciona* adults, and C. Savakis for providing *Minos*. This study was supported by Grants-in-Aid for Scientific Research from the Japan Society for the Promotion of Science and MEXT to T.H., T.G.K., N.S. and Y.S. Y.S. was supported by the National Institute of Genetics Cooperative Research Program.

**Author Contributions** T.H. and Y.S. designed the experiments. T.H., R.S. and Y.O. performed most of the experiments. T.H. and T.G.K. isolated *cis* regulatory elements. T.G.K. and N.S. were advisors for the experiments and evaluated the data. T.H., N.S. and Y.S. wrote the manuscript.

**Author Information** Reprints and permissions information is available at [www.nature.com/reprints](http://www.nature.com/reprints). The authors declare no competing financial interests. Readers are welcome to comment on the online version of this article at [www.nature.com/nature](http://www.nature.com/nature). Correspondence and requests for materials should be addressed to T.H. ([horie@kurofune.shimoda.tsukuba.ac.jp](mailto:horie@kurofune.shimoda.tsukuba.ac.jp)).

## METHODS

**Biological materials.** Wild-type *Ciona intestinalis* were collected from or cultivated in Onagawa Bay (Miyagi), Maizuru Bay (Kyoto) and Usa Bay (Kochi). Sperm and eggs were collected by dissecting the sperm and gonadal ducts. Transgenic lines<sup>27</sup> were cultured by an island system<sup>28</sup>.

**Constructs.** To generate pSPCi $\beta$ 2tubulin(TB)K, pSPCiVGLUTK, pSPCiVGATK, pSPCiVACHTK, pSPCiPhox2K, pSPCiopsin3K, pSPCiCRALBPK and pSPCiCtptK, the 5' upstream region of *Ci- $\beta$ 2tubulin*, *CiPhox2*, *Ci-VGLUT*, *Ci-VGAT*, *Ci-VACHT*, *Ci-opsin3*, *Ci-CRALBP* and *Ci-otp*<sup>9,10,14,18</sup> were amplified by polymerase chain reaction (PCR) using thermostable DNA polymerases and gene-specific oligonucleotide primers (5'-ACGTGGATCCGATCAAGCACTGAGG GTGCT-3' and 5'-GGGGATCCATGATGAATAGAACTAAAGAT-3' for *Ci- $\beta$ 2tubulin*; 5'-AGGGATCCCCGAAAAACAAGTCTTCTG-3' and 5'-CCGGA TCCATCGGTGGCTGGCAGTTTCC-3' for *CiPhox2*; 5'-GATCGGATCCCCG GTATGTCCACAGCATTC-3' and 5'-GGGGATCCAATATCCTAAATACCC TCC-3' for *Ci-VGLUT*; 5'-TATAGGATCCTGATGGAAGATGGGACAC-3' and 5'-TGCGGATCCACTAACAGAAGGTACCTATTC-3' for *Ci-VGAT*; 5'-TATGGGATCCAGGCTTAAGCACACGTTTC-3' and 5'-GCCGGGATCCG ATGAACAATAAAGTAGA-3' for *Ci-VACHT*; 5'-AGGGATCCGTTGTTTG TACCAATGTGAG-3' and 5'-CCGGATCCATCTTGAAATGTGTCTTCT-3' for *Ci-opsin3*; 5'-AGGGATCCTATTGTAATTACAGTTTAAA-3' and 5'-CCG GATCCATTGCAGATGTCGTCTGTGTA-3' for *Ci-CRALBP*; and 5'-AGGGA TCCTTCCTGAAATGCCGCTTC-3' and 5'-GGGGATCCATCTTTACTTAA AAAACT-3' for *Ci-otp*). The PCR products were digested with BamHI and inserted in the BamHI site of pSP-Kaede<sup>29</sup>. To generate pMiCi $\beta$ 2TBK, pMiCiVGLUTK, pMiCiVGATK and pMiCiVACHTK, promoter-Kaede cassettes were amplified by PCR using a thermostable DNA polymerase and vector-specific oligonucleotide primers (5'-GGGGACAAGTTTGTACAAAAAGCAGGCTG AACTCGAGCAGCTGAAGCTTG-3' and 5'-GGGGACCACTTTGTACAAGA AAGCTGGGTGCAGATCTGATGGCCGCTTTGAC-3'). The PCR products were subcloned into pMiDestF<sup>29</sup> with the Gateway system (Invitrogen). To generate pSPCiVACHTK and pSPCiVGATC, 5' upstream regions of *Ci-VACHT* and *Ci-VGAT* were amplified with primers described above, digested with BamHI and inserted into the BamHI site of pSPCFP. To generate pSPCiVACHTKCCiCRA-LBPK, the CiVACHTK-CFP cassette was amplified with vector-specific primers (5'-GAACTCGAGCAGCTGAAGCTTG-3' and 5'-GCAGATCTGATGGCCGC TTTGAC-3'), digested with HindIII and inserted into HindIII and blunted PstI sites of pSPCiCRALBPK. To generate pSPCiVGATCCiCRA-LBPK, the CiVGAT-CFP cassette was amplified with vector-specific primers, digested with XhoI and inserted into XhoI and blunted PstI sites of pSPCiCRALBPK.

**Generation of Kaede transgenic lines.** Kaede transgenic lines were created by co-electroporation of 80  $\mu$ g of *in vitro* synthesized transposase messenger RNA (mRNA) and 60  $\mu$ g of pMiCi $\beta$ 2TBK, pMiCiVGLUTK, pMiCiVGATK and pMiCiVACHTK constructs<sup>27,30</sup>. The specificities of the expression of Kaede in the glutamatergic neurons, GABAergic/glycinergic neurons and cholinergic neurons in the transgenic lines were confirmed by double-fluorescence *in situ* hybridization of Kaede mRNA and *Ci-VGLUT*, *Ci-VGAT* and *Ci-VACHT* mRNAs, respectively. For synthesis of digoxigenin-labelled RNA probes, complementary DNA (cDNA) fragments of *Ci-VGLUT*, *Ci-VGAT* and *Ci-VACHT* were obtained from cDNA in the larval stage by reverse transcription PCR with gene-specific primers (5'-TATGGCGGCCGCCCTCCCTTCCAGTATGGG-3' and 5'-TTAATGCTTGAATATTTCTCATCTTCC-3' for *Ci-VGLUT*; 5'-TATGGC GGCCGCCGAAAGACGTGGTACC-3' and 5'-TTAACTATAGTGCTCGAT GCTCTGTC-3' for *Ci-VGAT*; 5'-TATGGCGGCCGCCGTTCTGCCCCATCT TT-3' and 5'-CTATTTTCGTTGGTATGTATGTCC-3' for *Ci-VACHT*). The cDNA fragments were cloned into the pBluescript SK II Vector (Stratagene) and used as templates for the synthesis of the digoxigenin-labelled antisense RNA probe. Fluorescence *in situ* hybridization was performed as described previously<sup>31</sup>. The photoconversion of Kaede was performed by illuminating larvae with an ultraviolet light using a fluorescence microscope (Axio10, Carl Zeiss). The illuminated larvae were cultured under dark conditions until observation.

**Dil labelling.** Dil labelling of the A9.15 blastomere, which gives rise to ependymal cells of the visceral ganglion<sup>32</sup>, was performed as described previously<sup>33</sup>. Dil (Celltracker CM-Dil, Molecular Probes) was dissolved in soybean oil at a concentration of 5 mg ml<sup>-1</sup>. Dil-labelled animals were observed with a fluorescent microscope (Axio10, Carl Zeiss).

28. Joly, J. S. *et al.* Culture of *Ciona intestinalis* in closed systems. *Dev. Dyn.* **236**, 1832–1840 (2007).
29. Hozumi, A. *et al.* Efficient transposition of a single *Minos* transposon copy in the genome of the ascidian *Ciona intestinalis* with a transgenic line expressing transposase in the egg. *Dev. Dyn.* **239**, 1076–1088 (2010).
30. Matsuoka, T., Awazu, S., Shoguchi, E., Satoh, N. & Sasakura, Y. Germline transgenesis of the ascidian *Ciona intestinalis* by electroporation. *Genesis* **41**, 67–72 (2005).
31. Ikuta, T. & Saiga, H. Dynamic change in the expression of developmental genes in the ascidian central nervous system: revisit to the tripartite model and the origin of midbrain–hindbrain boundary region. *Dev. Biol.* **312**, 631–643 (2007).
32. Cole, A. G. & Meinertzhagen, I. A. The central nervous system of the ascidian larva: mitotic history of cells forming the neural tube in late embryonic *Ciona intestinalis*. *Dev. Biol.* **271**, 239–262 (2004).
33. Satou, Y., Imai, K. S. & Satoh, N. The ascidian *Mesp* gene specifies heart precursor cells. *Development* **131**, 2533–2541 (2004).

# Comparative and demographic analysis of orang-utan genomes

Devin P. Locke<sup>1</sup>, LaDeana W. Hillier<sup>1</sup>, Wesley C. Warren<sup>1</sup>, Kim C. Worley<sup>2</sup>, Lynne V. Nazareth<sup>2</sup>, Donna M. Muzny<sup>2</sup>, Shiaw-Pyng Yang<sup>1</sup>, Zhengyuan Wang<sup>1</sup>, Asif T. Chinwalla<sup>1</sup>, Pat Minx<sup>1</sup>, Makedonka Mitreva<sup>1</sup>, Lisa Cook<sup>1</sup>, Kim D. Delehaunty<sup>1</sup>, Catrina Fronick<sup>1</sup>, Heather Schmidt<sup>1</sup>, Lucinda A. Fulton<sup>1</sup>, Robert S. Fulton<sup>1</sup>, Joanne O. Nelson<sup>1</sup>, Vincent Magrini<sup>1</sup>, Craig Pohl<sup>1</sup>, Tina A. Graves<sup>1</sup>, Chris Markovic<sup>1</sup>, Andy Cree<sup>2</sup>, Huyen H. Dinh<sup>2</sup>, Jennifer Hume<sup>2</sup>, Christie L. Kovar<sup>2</sup>, Gerald R. Fowler<sup>2</sup>, Gerton Lunter<sup>3,4</sup>, Stephen Meader<sup>3</sup>, Andreas Heger<sup>3</sup>, Chris P. Ponting<sup>3</sup>, Tomas Marques-Bonet<sup>5,6</sup>, Can Alkan<sup>5</sup>, Lin Chen<sup>5</sup>, Ze Cheng<sup>5</sup>, Jeffrey M. Kidd<sup>5</sup>, Evan E. Eichler<sup>5,7</sup>, Simon White<sup>8</sup>, Stephen Searle<sup>8</sup>, Albert J. Vilella<sup>9</sup>, Yuan Chen<sup>9</sup>, Paul Flicek<sup>9</sup>, Jian Ma<sup>10</sup>, Brian Raney<sup>10</sup>, Bernard Suh<sup>10</sup>, Richard Burhans<sup>11</sup>, Javier Herrero<sup>9</sup>, David Haussler<sup>10</sup>, Rui Faria<sup>6,12</sup>, Olga Fernando<sup>6,13</sup>, Fleur Darré<sup>6</sup>, Domènec Farré<sup>6</sup>, Elodie Gazave<sup>6</sup>, Meritxell Oliva<sup>6</sup>, Arcadi Navarro<sup>6,14</sup>, Roberta Roberto<sup>15</sup>, Oronzo Capozzi<sup>15</sup>, Nicoletta Archidiacono<sup>15</sup>, Giuliano Della Valle<sup>16</sup>, Stefania Purgato<sup>16</sup>, Mariano Rocchi<sup>15</sup>, Miriam K. Konkel<sup>17</sup>, Jerilyn A. Walker<sup>17</sup>, Brygg Ullmer<sup>18</sup>, Mark A. Batzer<sup>17</sup>, Arian F. A. Smit<sup>19</sup>, Robert Hubley<sup>19</sup>, Claudio Casola<sup>20</sup>, Daniel R. Schrider<sup>20</sup>, Matthew W. Hahn<sup>20</sup>, Victor Quesada<sup>21</sup>, Xose S. Puente<sup>21</sup>, Gonzalo R. Ordoñez<sup>21</sup>, Carlos López-Otin<sup>21</sup>, Tomas Vinar<sup>22</sup>, Brona Brejova<sup>22</sup>, Aakrosh Ratan<sup>11</sup>, Robert S. Harris<sup>11</sup>, Webb Miller<sup>11</sup>, Carolin Kosiol<sup>23</sup>, Heather A. Lawson<sup>24</sup>, Vikas Taliwal<sup>25</sup>, André L. Martins<sup>25</sup>, Adam Siepel<sup>25</sup>, Arindam RoyChoudhury<sup>26</sup>, Xin Ma<sup>25</sup>, Jeremiah Degenhardt<sup>25</sup>, Carlos D. Bustamante<sup>27</sup>, Ryan N. Gutenkunst<sup>28</sup>, Thomas Mailund<sup>29</sup>, Julien Y. Dutheil<sup>29</sup>, Asger Hobolth<sup>29</sup>, Mikkel H. Schierup<sup>29</sup>, Oliver A. Ryder<sup>30</sup>, Yuko Yoshinaga<sup>31</sup>, Pieter J. de Jong<sup>31</sup>, George M. Weinstock<sup>1</sup>, Jeffrey Rogers<sup>2</sup>, Elaine R. Mardis<sup>1</sup>, Richard A. Gibbs<sup>2</sup> & Richard K. Wilson<sup>1</sup>

‘Orang-utan’ is derived from a Malay term meaning ‘man of the forest’ and aptly describes the southeast Asian great apes native to Sumatra and Borneo. The orang-utan species, *Pongo abelii* (Sumatran) and *Pongo pygmaeus* (Bornean), are the most phylogenetically distant great apes from humans, thereby providing an informative perspective on hominid evolution. Here we present a Sumatran orang-utan draft genome assembly and short read sequence data from five Sumatran and five Bornean orang-utan genomes. Our analyses reveal that, compared to other primates, the orang-utan genome has many unique features. Structural evolution of the orang-utan genome has proceeded much more slowly than other great apes, evidenced by fewer rearrangements, less segmental duplication, a lower rate of gene family turnover and surprisingly quiescent Alu repeats, which have played a major role in restructuring other primate genomes. We also describe a primate polymorphic neocentromere, found in both *Pongo* species, emphasizing the gradual evolution of orang-utan genome structure. Orang-utans have extremely low energy usage for a eutherian mammal<sup>1</sup>, far lower than their hominid relatives. Adding their genome to the repertoire of sequenced primates illuminates new signals of positive selection in several pathways including glycolipid metabolism. From the population perspective, both *Pongo* species are deeply diverse; however, Sumatran individuals possess greater diversity than their Bornean counterparts, and more

species-specific variation. Our estimate of Bornean/Sumatran speciation time, 400,000 years ago, is more recent than most previous studies and underscores the complexity of the orang-utan speciation process. Despite a smaller modern census population size, the Sumatran effective population size ( $N_e$ ) expanded exponentially relative to the ancestral  $N_e$  after the split, while Bornean  $N_e$  declined over the same period. Overall, the resources and analyses presented here offer new opportunities in evolutionary genomics, insights into hominid biology, and an extensive database of variation for conservation efforts.

Orang-utans are the only primarily arboreal great apes, characterized by strong sexual dimorphism and delayed development of mature male features, a long lifespan (35–45 years in the wild, more than 55 years in captivity) and the longest interbirth interval among mammals (8 years on average)<sup>2</sup>. Orang-utans create and adeptly use tools in the wild, and while long presumed socially solitary, dense populations of Sumatran orang-utans show complex social structure and geographic variability in tool use indicative of cultural learning<sup>3</sup>. Both species have been subject to intense population pressure from loss of habitat, deforestation, hunting and disease. A 2004 study estimated that 7,000–7,500 Sumatran individuals and 40,000–50,000 Bornean individuals remained in the wild in fragmented subpopulations<sup>4,5</sup>. The International Union for Conservation of Nature lists Sumatran orang-utans as critically endangered and Bornean orang-utans as endangered.

<sup>1</sup>The Genome Center at Washington University, Washington University School of Medicine, 4444 Forest Park Avenue, Saint Louis, Missouri 63108, USA. <sup>2</sup>Human Genome Sequencing Center, Department of Molecular and Human Genetics, Baylor College of Medicine, One Baylor Plaza, Houston, Texas 77030, USA. <sup>3</sup>MRC Functional Genomics Unit and Department of Physiology, Anatomy and Genetics, University of Oxford, Le Gros Clark Building, South Parks Road, Oxford OX1 3QX, UK. <sup>4</sup>Wellcome Trust Centre for Human Genetics, Oxford OX3 7BN, UK. <sup>5</sup>Department of Genome Sciences, University of Washington School of Medicine, Seattle, Washington 98195, USA. <sup>6</sup>IBE, Institut de Biologia Evolutiva (UPF-CSIC), Universitat Pompeu Fabra, PRBB, Doctor Aiguader, 88, 08003 Barcelona, Spain. <sup>7</sup>Howard Hughes Medical Institute, 1705 NE Pacific Street, Seattle, Washington 98195, USA. <sup>8</sup>Wellcome Trust Sanger Institute, Wellcome Trust Genome Campus, Cambridge CB10 1SA, UK. <sup>9</sup>European Bioinformatics Institute, Wellcome Trust Genome Campus, Hinxton, Cambridge CB10 1SD, UK. <sup>10</sup>Center for Biomolecular Science and Engineering, University of California, Santa Cruz, California 95064, USA. <sup>11</sup>Center for Comparative Genomics and Bioinformatics, Penn State University, University Park, Pennsylvania 16802, USA. <sup>12</sup>CIBIO, Centro de Investigação em Biodiversidade e Recursos Genéticos, Universidade do Porto, Campus Agrário de Vairão, 4485-661 Vairão, Portugal. <sup>13</sup>Instituto de Tecnologia Química e Biológica, Universidade Nova de Lisboa, Oeiras 2780-157, Portugal. <sup>14</sup>ICREA (Institució Catalana de Recerca i Estudis Avançats) and INB (Institut Nacional de Bioinformàtica) PRBB, Doctor Aiguader, 88, 08003 Barcelona, Spain. <sup>15</sup>Department of Biology, University of Bari, Via Orabona 4, 70125, Bari, Italy. <sup>16</sup>Department of Biology, University of Bologna, Via Selmi 3, 40126, Bologna, Italy. <sup>17</sup>Department of Biological Sciences, Louisiana State University, Baton Rouge, Louisiana 70803, USA. <sup>18</sup>Center for Computation and Technology, Department of Computer Sciences, Louisiana State University, Baton Rouge, Louisiana 70803, USA. <sup>19</sup>Institute for Systems Biology, Seattle, Washington 98103, USA. <sup>20</sup>Department of Biology and School of Informatics and Computing, Indiana University, Bloomington, Indiana 47405, USA. <sup>21</sup>Instituto Universitario de Oncología, Departamento de Bioquímica y Biología Molecular, Universidad de Oviedo, Oviedo 33006, Spain. <sup>22</sup>Faculty of Mathematics, Physics and Informatics, Comenius University, Mlynska Dolina, Bratislava 84248, Slovakia. <sup>23</sup>Institut für Populationsgenetik, Vetmeduni Vienna, Veterinärplatz 1, A-1210 Wien, Austria. <sup>24</sup>Department of Anatomy and Neurobiology, Washington University School of Medicine, Saint Louis, Missouri 63110, USA. <sup>25</sup>Department of Biological Statistics and Computational Biology, Cornell University, Ithaca, New York 14853, USA. <sup>26</sup>Department of Biostatistics, Columbia University, New York, New York 10032, USA. <sup>27</sup>Department of Genetics, Stanford University, Stanford, California 94305, USA. <sup>28</sup>Department of Molecular and Cellular Biology, University of Arizona, Tucson, Arizona 85721, USA. <sup>29</sup>Bioinformatics Research Centre, Aarhus University, DK-8000 Aarhus C, Denmark. <sup>30</sup>San Diego Zoo's Institute for Conservation Research, Escondido, California 92027, USA. <sup>31</sup>Children's Hospital Oakland Research Institute, Oakland, California 94609, USA. †Present address: Department of Bioengineering, University of Illinois at Urbana-Champaign, Urbana, Illinois 61801, USA.

**Table 1 | Sumatran orang-utan assembly statistics**

Total contig bases	3.09 Gb
Total contig bases >Phred Q20	3.05 Gb (98.5%)
Ordered/oriented contigs and scaffolds	3.08 Gb
Number of contigs >1 kb	410,172
N50 contig length	15.5 kb
N50 contig number	55,989
Number of scaffolds >2 kb	77,683
N50 scaffold length	739 kb
N50 scaffold number	1,031
Average read depth	5.53 ×

Q20 refers to a score of 20 on the Phred scale of base quality scores; here we present the total number of bases in the assembly with a Phred score greater than 20 (3.05 Gb, which is 98.5% of assembled bases). N50 refers to a length-weighted median such that 50% of the genome is contained in contigs or scaffolds of the indicated size or greater.

We sequenced the genome of a female Sumatran orang-utan using a whole-genome shotgun strategy. The assembly provides 5.5-fold coverage on average across 3.08 gigabases (Gb) of ordered and oriented sequence (Table 1) (Supplementary Information section 1). Accuracy was assessed by several metrics, including comparison to 17 megabases (Mb) of finished bacterial artificial chromosome (BAC) sequences and a novel method of detecting spurious insertions and deletions (Supplementary Information section 2). Further validation resulted from orang-utan–human divergence estimates based on alignment of whole-genome shotgun reads to the human reference (Hs.35; Fig. 1, Supplementary Information section 3). We also sequenced the genomes of 10 additional unrelated wild-caught orang-utans, five Sumatran and five Bornean, using a short read sequencing platform (297 Gb of data in total; Supplementary Information section 4). The orang-utan gene set was constructed using a combination of human gene models and orang-utan complementary DNA data generated for this project (available at [www.ensembl.org/Pongo\\_pygmaeus/Info/StatsTable](http://www.ensembl.org/Pongo_pygmaeus/Info/StatsTable); see also Supplementary Information section 5).

Among hominids, the orang-utan karyotype is the most ancestral<sup>6</sup>, and sequencing the orang-utan genome allowed a comprehensive assessment of conservation among the wide range of rearrangement types and sequence classes involved in structural variation. We characterized orang-utan synteny breaks in detail cytogenetically in concert with an *in silico* approach that precisely tracked rearrangements between primate (human, chimpanzee, orang-utan and rhesus macaque) and other mammalian assemblies (mouse, rat and dog) (Supplementary Information section 6). Alignment-level analyses at 100 kilobase (kb) and 5 kb resolution found that the orang-utan genome underwent fewer rearrangements than the chimpanzee or human genomes, with a bias for large-scale events (>100 kb) on the chimpanzee branch (Table 2). Orang-utan large-scale rearrangements were further enriched for segmental duplications (52%) than

**Table 2 | Number of genome rearrangements by species**

Species	Rearrangements >100 kb	Rearrangements >5 kb
Orang-utan	38	861
Chimpanzee	85 (+124%)	1,095 (+27%)
Human	54 (+42%)	1,238 (44%)

The number in parentheses indicates the percentage change with respect to the orang-utan genome. Note 40 events >100 kb and 532 events >5 kb were assigned to the human-chimpanzee ancestor by ancestral reconstruction (Supplementary Information section 6).

for small-scale events (27%), suggesting that mechanisms other than non-allelic homologous recombination may have made a greater contribution to small rearrangements. Genome-wide, we estimated less segmental duplication content (3.8% total) in the orang-utan genome compared to the chimpanzee and human genomes (5%) using equivalent methods (Supplementary Information section 11). We also assessed the rate of turnover within gene families as an additional measure of genome restructuring (Supplementary Information section 12). Our analysis indicated that the human and chimpanzee lineages, as well as their shared ancestral lineage after the orang-utan split, had the highest rates of gene turnover among great apes (0.0058 events per gene per Myr)—more than twice the rate of the orang-utan and macaque lineages (0.0027)—even as the nucleotide substitution rate decreased<sup>7</sup>. Collectively, these data strongly suggest that structural evolution proceeded much more slowly along the orang-utan branch, in sharp contrast to the acceleration of structural variation noted for the chimpanzee and human genomes<sup>8,9</sup>.

One structural variant that we characterized in detail was a previously described polymorphic ‘pericentric inversion’ of orang-utan chromosome 12 (ref. 10). Surprisingly, both forms of this chromosome showed no difference in marker order by fluorescence *in situ* hybridization (FISH) despite two distinct centromere positions—the hallmark of a neocentromere (Fig. 2; Supplementary Information section 8). Neocentromere function was confirmed by chromatin immunoprecipitation with antibodies to centromeric proteins CENP-A and CENP-C and subsequent oligo array hybridization (ChIP-on-chip), which narrowed the neocentromere to a ~225 kb gene-free window devoid of  $\alpha$  satellite-related sequences. Our observations bore similarity to a recently described centromere repositioning event in the horse genome<sup>11</sup>; however, this is to our knowledge the first observation of such a variant among primates, with the additional complexity of polymorphism in two closely related species. Potentially related, orang-utan chromosome 12 did not show any appreciable centromeric alphoid FISH signal in comparison to other autosomes. The neocentromere most probably arose before the Bornean/Sumatran split as it is found in both species, and represents a unique opportunity to study the initial stages of centromere formation

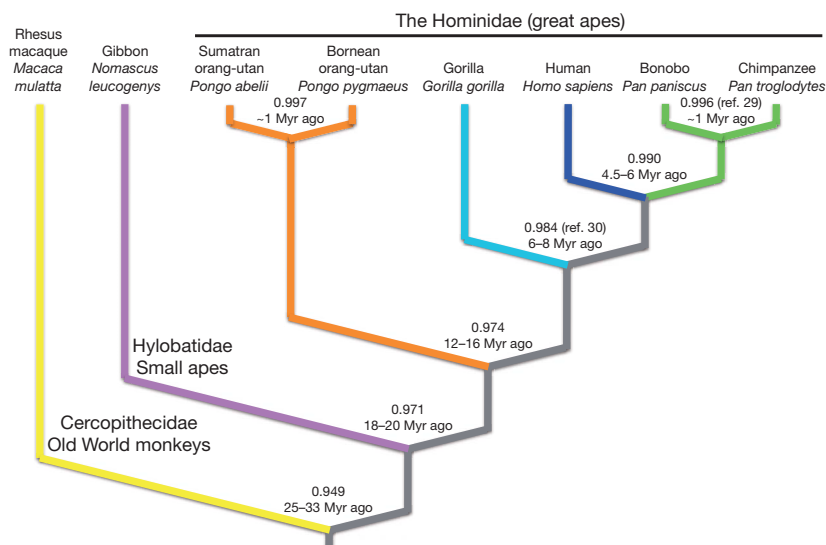


**Figure 1 | Divergence among great apes, a small ape, and an Old World monkey with respect to humans.** We estimated nucleotide divergence in unique gap-free sequence, indicated at each node, from the alignment of rhesus macaque (yellow), gibbon (purple), orang-utan (orange), gorilla (aqua), chimpanzee (green) and human (blue) whole genome shotgun reads to the human reference (Hs.35; Supplementary Information section 3). Note that the Bornean (*P. pygmaeus*) and Sumatran (*P. abelii*) orang-utan species showed nucleotide identity comparable to that of bonobo (*Pan paniscus*) and chimpanzee (*Pan troglodytes*). Estimates of divergence time based on sequence identity are indicated at each node, ~1 Myr implies approximately 1 Myr or less. Values taken from refs 29 and 30 where indicated.

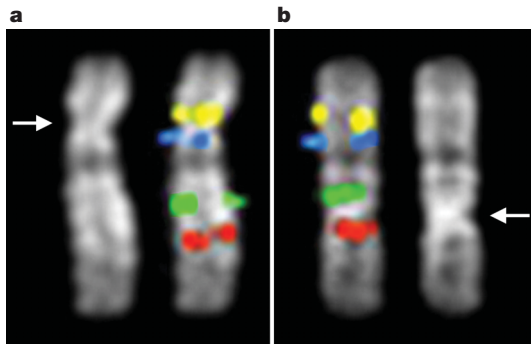


**Figure 2 | The neocentromere of orang-utan chromosome 12.** Note the identical order of four sequentially arranged BAC-derived FISH probes indicated in yellow, blue, green and red (given in Supplementary Information section 8) between the normal (a) and neocentromere-bearing (b) configurations of orang-utan chromosome 12, despite discordant centromere positions. The left image of a and the right image of b are DAPI-only images that show the primary constriction of both chromosomal forms, indicated by the arrows. The neocentromere recruits centromeric proteins CENP-A and CENP-C and lies within a ~225 kb gene-free and  $\alpha$  satellite-free region. The neocentromere-bearing variant is polymorphic in both Bornean and Sumatran populations, suggesting the neocentromere arose before the Bornean/Sumatran split, yet has not been fixed in either species.

and the impact of such a large chromosomal variant on population variation and recombination.

The orang-utan genome has a comparable cadre of mobile elements to that of other primates, comprising roughly half the genome<sup>12–14</sup>. Orang-utan long interspersed element 1 (LINE1; L1) and SVA (SINE-R, VNTR and Alu) element expansions were expectedly broad, with roughly 5,000 and 1,800 new insertions respectively, consistent with other primates (Supplementary Information section 9). Surprisingly, Alu elements were relatively quiescent, with only ~250 recent insertions identified by computational and laboratory approaches (Fig. 3). By comparison, 5,000 human-specific and 2,300 chimpanzee-specific Alu elements were identified by similar methods. The rate of processed pseudogene formation, which like Alu insertion requires functional L1 machinery<sup>15</sup>, was similar for the human (8.0 per Myr), chimpanzee (12.7 per Myr) and orang-utan (11.6 per Myr) lineages (Supplementary Information section 10). We identified a small number of polymorphic Alu elements exclusive to *P. abelii*

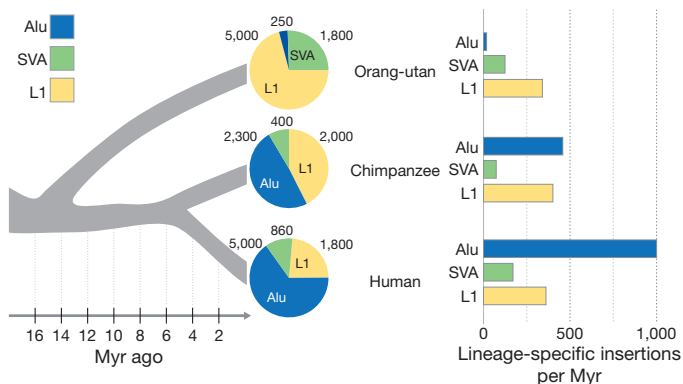


**Figure 3 | Alu quiescence in the orang-utan lineage.** We identified only ~250 lineage-specific Alu retroposition events in the orang-utan genome, a dramatically lower number than that of other sequenced primates, including humans. The total number of lineage-specific L1, SVA and Alu insertions is shown (pie chart) at the terminus of each branch of the phylogeny of sequenced great apes shown in grey at left, along with the rate of insertion events per element type (bar graph). Reduced Alu retroposition potentially limited the effect of a wide variety of repeat-driven mutational mechanisms in the orang-utan lineage that played a major role in restructuring other primate genomes.

(Supplementary Information section 19), indicating that Alu retroposition has been strongly limited, but not eliminated. This dramatic Alu-specific repression represents an unprecedented change in primate retrotransposition rates<sup>16,17</sup>. Possible explanations include L1 source mutations that lowered Alu affinity and *cis* mobilization preference<sup>18</sup>, pressure against Alu retroposition from the APOBEC RNA editing family<sup>19</sup>, or fixation of less effectively propagated Alu 'master' variants.

It is tempting to propose a correlation between reduced Alu retroposition and the greater structural stability of the orang-utan genome. More than 10<sup>6</sup> Alu elements exist within primate genomes. Because of their large copy number and high sequence identity, Alu repeats play a crucial role in multiple forms of structural variation through insertion and post-insertion recombination<sup>20</sup>. By virtue of reduced Alu retroposition, the orang-utan lineage experienced fewer new insertions and a putative decrease in the number of regions susceptible to post-insertion Alu-mediated recombination events genome-wide, limiting the overall mobile element threat to the genome.

The unique phylogenetic position of *Pongo* species also offered the opportunity to detect signals of positive selection with increased power. We assessed positive selection in 13,872 human genes with high-confidence orthologues in the orang-utan genome, and in one or more of the chimpanzee, rhesus macaque and dog genomes, using branch-site likelihood ratio tests (Supplementary Information section 15)<sup>14,21</sup>. Two new Gene Ontology categories were statistically enriched for positive selection in primates: 'visual perception' and 'glycolipid metabolic processes'<sup>22</sup>. The enrichment for visual perception includes strong evidence from two major visual signalling proteins: arrestin (SAG,  $P = 0.007$ ) and recoverin (RCVRN,  $P = 0.008$ ), as well as the opsin, *OPN1SW1* ( $P = 0.020$ ), associated with blue colour vision<sup>23</sup>. The enrichment for glycolipid metabolism is particularly intriguing owing to medium-to-strong evidence for positive selection (nominal  $P < 0.05$ ) from six genes expressed in nervous tissue that cluster in the cerebroside-sulphatid region of the sphingolipid metabolism pathway (Fig. 4). This pathway

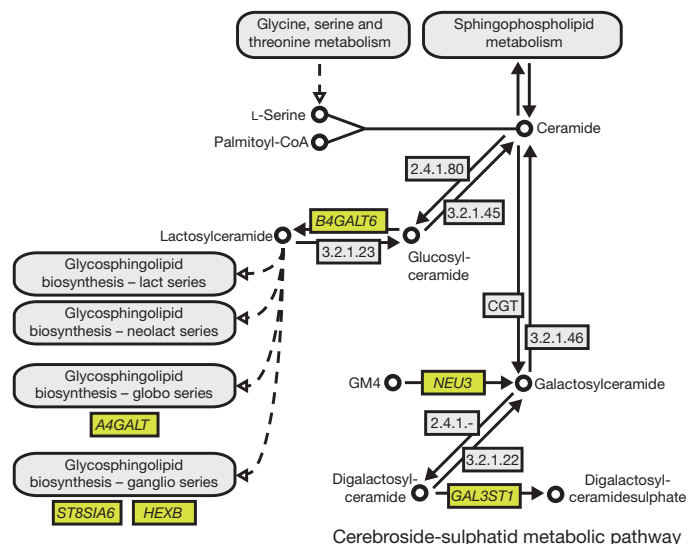


**Figure 4 | Enrichment for positive selection in the cerebroside-sulphatid metabolism pathway.** We identified six genes (indicated in yellow) under moderate to strong positive selection in primates ( $P < 0.05$ ) that fall within the cerebroside-sulphatid region of the sphingolipid metabolism pathway (adapted from human KEGG pathway 00600). This pathway is associated with several human lysosomal storage disorders, such as Gaucher's disease, Sandhoff's disease, Tay-Sachs disease and metachromatic leukodystrophy. Abbreviations, annotations and connections are presented in accordance with KEGG standards: solid lines represent direct relationships between enzymes (boxes) and metabolites (circular nodes), dashed lines represent indirect relationships, arrowheads denote directionality (see [http://www.genome.jp/kegg-bin/show\\_pathway?map00600](http://www.genome.jp/kegg-bin/show_pathway?map00600) for further details).

is associated with human neurodegenerative diseases such as Gaucher's, Sandhoff's, Tay-Sachs, and metachromatic leukodystrophy. Variation in lipid metabolism may have affected neurological evolution among primates, and diversity of diets and life history strategies, as apes—especially orang-utans—have slower rates of reproduction and dramatically lower energy usage than other primates and mammals<sup>1</sup>.

Ancestral orang-utan species ranged broadly across southeast Asia, including the mainland, while modern species are geographically restricted to their respective islands owing to environmental forces and human population expansion. Historically, protein markers, restriction fragment length polymorphisms, and small sets of mitochondrial and nuclear markers have been used to estimate the divergence and diversity of orang-utan species. We used short read sequencing to address this question from a genome-wide perspective. We first estimated average Bornean/Sumatran nucleotide identity genome-wide (99.68%) based on the alignment of 20-fold coverage of short read data from a Bornean individual to the Sumatran reference (Supplementary Information section 16). We then called single nucleotide polymorphisms (SNPs) from the alignment of all short read data from 10 individuals (five Bornean, including the 20-fold coverage mentioned above, and five Sumatran) (Supplementary Information section 4). We analysed each species separately using a Bayesian approach with 92% power to detect SNPs (Supplementary Information section 20). Because of relatively deep sequencing, allele frequency spectra were estimated accurately, but with an overestimation of singletons compared to other allele frequency categories of approximately 7.8% based on re-sequencing a subset of SNPs ( $n = 108$ ) (Supplementary Information section 20). This level of error had only a marginal effect on downstream population genetic analyses (Supplementary Information section 21). Overall, 99.0% (931/940) of genotypes were accurately called within the re-sequenced subset of SNPs.

In total, we identified  $13.2 \times 10^6$  putative SNPs across 1.96 Gb of the genome, or 1 SNP every 149 base pair (bp) on average. Within the Bornean and Sumatran groups we detected  $6.69 \times 10^6$  ( $3.80 \times 10^6$  Bornean-exclusive) and  $8.96 \times 10^6$  ( $5.19 \times 10^6$  Sumatran-exclusive) SNPs, respectively (Fig. 5). Observing 36% more SNPs among Sumatran individuals strongly supports a larger  $N_e$ . In addition, independent analysis of 85 polymorphic retroelement loci among 37 individuals (19 Sumatran, 18 Bornean) also showed more complex Sumatran population structure (Supplementary Information section 19). Using Watterson's approach<sup>24</sup>, we estimated nucleotide diversity from the SNP data as  $\theta_w = 1.21$  and  $\theta_w = 1.62$  per kb for the Bornean and Sumatran species, respectively, and  $\theta_w = 1.89$  per kb for the orang-utan species combined, roughly twice the diversity of modern humans<sup>25</sup>.

The modal category of SNPs were singletons, with  $2.0 \times 10^6$  and  $3.7 \times 10^6$  SNPs observed as single heterozygous sites in a Bornean or Sumatran individual, consistent with the expectation that most genetic variation for an outcrossing population ought to be rare due to mutation-drift equilibrium. We observed little correlation between Bornean and Sumatran SNPs in the allele frequency spectra (that is, the 'heat' of the map is not along the diagonal as expected for populations with similar allele frequencies, but rather along the edges) (Fig. 5b). This was further supported by principal component analysis, in which PC1 corresponded to the Bornean/Sumatran population label and explained 36% of the variance (Supplementary Information section 20).

On the basis of these data, our demographic model consisted of a two-population model with divergence and potential migration, growth and difference in population size (Supplementary Information section 21). Among several models tested, we found very strong statistical support ( $10^5$  log-likelihood units) for the most complex model, which included a split with growth and subsequent low-level migration. We estimated a relative  $N_e$  of 210% for Sumatran orang-utans relative to the ancestral and 49% for Bornean orang-utans, noting a fourfold difference for the derived populations (Fig. 5c). Assuming a mutation rate of  $2.0 \times 10^{-8}$  and 20 years per generation, we estimated an ancestral  $N_e$  of 17,900 and a split time of 400,000 years ago.

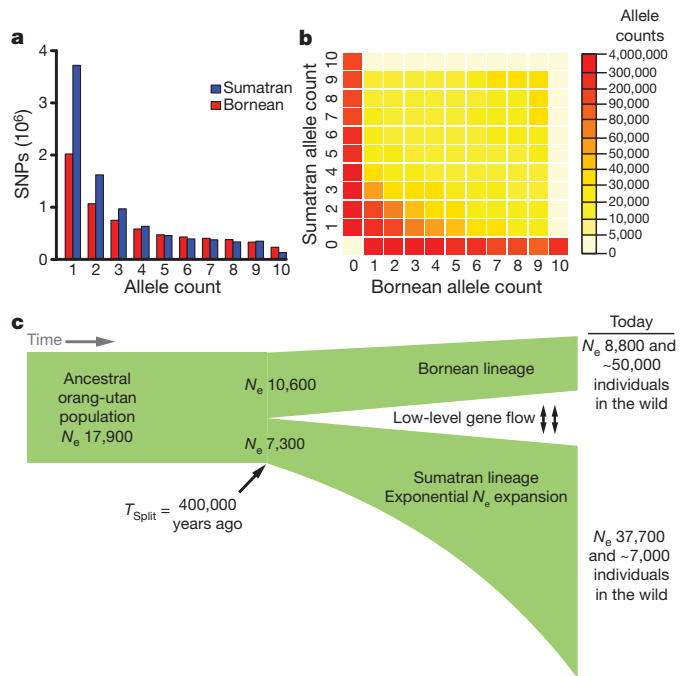


**Figure 5 | Orang-utan population genetics and demographics.** **a**, Site-frequency spectra for  $13.2 \times 10^6$  Bornean (red) and Sumatran (blue) SNPs are shown based on the ascertainment of 10 chromosomes per species; note the enrichment of low-frequency SNPs among Sumatran individuals. **b**, The majority of SNPs were restricted to their respective island populations as the 'heat' of the two-dimensional site-frequency spectra, representing high allele counts, lay along the axes. **c**, Our demographic model estimated that the ancestral orang-utan population ( $N_e = 17,900$ ) split approximately 400,000 years ago, followed by exponential expansion of Sumatran  $N_e$  and a decline of Bornean  $N_e$ , culminating in higher diversity among modern Sumatran orang-utans despite a lower census population size. The model also supported low-level gene flow ( $<1$  individual per generation), indicated by arrows.

Parallel to the SNP-based effort, we employed a coalescent hidden Markov model (coal-HMM) approach to estimate speciation time, recombination rate and ancestral  $N_e$  from the alignment of 20-fold coverage of a Bornean individual to the Sumatran reference (Supplementary Information section 17). This method also supported a relatively recent Bornean/Sumatran speciation time ( $334 \pm 145$  kyr ago), and estimated a recombination rate of  $0.95 \pm 0.72$  cM Mb<sup>-1</sup>. We independently estimated the ancestral  $N_e$  of the autosomes ( $26,800 \pm 6,700$ ) and the X chromosome ( $20,400 \pm 7,400$ ), which was consistent with the theoretical 3/4 effective population size of X chromosomes compared to autosomes. The Bornean and Sumatran X chromosomes thus diverged as expected, in contrast to the human-chimpanzee speciation process<sup>26,27</sup>.

The orang-utan story is thus a tale of two islands with distinct evolutionary histories. Our high-resolution population studies explored the counter-intuitive nature of orang-utan diversity—greater variation among Sumatran orang-utans than their Bornean counterparts despite a smaller population size (approximately sevenfold lower by recent estimates). Further dissection of the orang-utan speciation process will require a broader survey, incorporating representatives from additional orang-utan subpopulations.

Finally, even though we found deep diversity in both Bornean and Sumatran populations, it is not clear whether this diversity will be maintained with continued habitat loss and population fragmentation. Evidence from other species suggests fragmentation is not the death knell of diversity<sup>28</sup>, but their slow reproduction rate and arboreal lifestyle may leave orang-utan species especially vulnerable to rapid dramatic environmental change. It is our hope that the genome assembly and population variation data presented here provide a valuable resource to the community to aid the preservation of these precious species.

## METHODS SUMMARY

Whole-genome sequencing was performed as described previously<sup>12–14</sup>. The genome assembly was constructed with a custom computational pipeline (Supplementary Information section 1). Assembly source DNA was derived from a single Sumatran female (Susie; Studbook no. 1044; ISIS no. 71), courtesy of the Gladys Porter Zoo, Brownsville, Texas. Short fragment sequencing libraries for population studies (Supplementary Information section 4) were constructed in accordance with standard Illumina protocols and sequenced on the Illumina GAlIx platform. The resulting data were processed with Illumina base-calling software and analysed using custom computational pipelines. See Supplementary Information for additional details.

Received 11 March; accepted 19 November 2010.

- Pontzer, H., Raichlen, D. A., Shumaker, R. W., Ocozbek, C. & Wich, S. A. Metabolic adaptation for low energy throughput in orangutans. *Proc. Natl Acad. Sci. USA* **107**, 14048–14052 (2010).
- van Noordwijk, M. A. & van Schaik, C. P. Development of ecological competence in Sumatran orangutans. *Am. J. Phys. Anthropol.* **127**, 79–94 (2005).
- van Schaik, C. P. *et al.* Orangutan cultures and the evolution of material culture. *Science* **299**, 102–105 (2003).
- Singleton, I. *et al.* Orangutan Population and Habitat Viability Assessment: Final Report (IUCN/SSC Conservation Breeding Specialist Group, Apple Valley, 2004).
- Meijaard, E. & Wich, S. Putting orang-utan population trends into perspective. *Curr. Biol.* **17**, R540 (2007).
- Stanyon, R. *et al.* Primate chromosome evolution: ancestral karyotypes, marker order and neocentromeres. *Chromosome Res.* **16**, 17–39 (2008).
- Yi, S., Ellsworth, D. L. & Li, W. H. Slow molecular clocks in Old World monkeys, apes, and humans. *Mol. Biol. Evol.* **19**, 2191–2198 (2002).
- Hahn, M. W., Demuth, J. P. & Han, S. G. Accelerated rate of gene gain and loss in primates. *Genetics* **177**, 1941–1949 (2007).
- Marques-Bonet, T. *et al.* A burst of segmental duplications in the genome of the African great ape ancestor. *Nature* **457**, 877–881 (2009).
- Seuanez, H., Fletcher, J., Evans, H. J. & Martin, D. E. A chromosome rearrangement in orangutan studied with Q-, C-, and G-banding techniques. *Cytogenet. Cell Genet.* **17**, 26–34 (1976).
- Wade, C. M. *et al.* Genome sequence, comparative analysis, and population genetics of the domestic horse. *Science* **326**, 865–867 (2009).
- The Chimpanzee Sequencing and Analysis Consortium. Initial sequence of the chimpanzee genome and comparison with the human genome. *Nature* **437**, 69–87 (2005).
- International Human Genome Sequencing Consortium. Initial sequencing and analysis of the human genome. *Nature* **409**, 860–921 (2001).
- Gibbs, R. A. *et al.* Evolutionary and biomedical insights from the rhesus macaque genome. *Science* **316**, 222–234 (2007).
- Esnault, C., Maestre, J. & Heidmann, T. Human LINE retrotransposons generate processed pseudogenes. *Nature Genet.* **24**, 363–367 (2000).
- Liu, G. *et al.* Analysis of primate genomic variation reveals a repeat-driven expansion of the human genome. *Genome Res.* **13**, 358–368 (2003).
- Lee, J. *et al.* Different evolutionary fates of recently integrated human and chimpanzee LINE-1 retrotransposons. *Gene* **390**, 18–27 (2007).
- Kulpa, D. A. & Moran, J. V. Cis-preferential LINE-1 reverse transcriptase activity in ribonucleoprotein particles. *Nature Struct. Mol. Biol.* **13**, 655–660 (2006).
- Bogerd, H. P. *et al.* Cellular inhibitors of long interspersed element 1 and Alu retrotransposition. *Proc. Natl Acad. Sci. USA* **103**, 8780–8785 (2006).
- Cordaux, R. & Batzer, M. A. The impact of retrotransposons on human genome evolution. *Nature Rev. Genet.* **10**, 691–703 (2009).
- Kosiol, C. *et al.* Patterns of positive selection in six Mammalian genomes. *PLoS Genet.* **4**, e1000144 (2008).
- Ashburner, M. *et al.* Gene ontology: tool for the unification of biology. *Nature Genet.* **25**, 25–29 (2000).
- Makino, C. L. *et al.* Recoverin regulates light-dependent phosphodiesterase activity in retinal rods. *J. Gen. Physiol.* **123**, 729–741 (2004).
- Watterson, G. A. On the number of segregating sites in genetical models without recombination. *Theor. Popul. Biol.* **7**, 256–276 (1975).
- Li, W. H. & Sadler, L. A. Low nucleotide diversity in man. *Genetics* **129**, 513–523 (1991).
- Hobolth, A., Christensen, O. F., Mailund, T. & Schierup, M. H. Genomic relationships and speciation times of human, chimpanzee, and gorilla inferred from a coalescent hidden Markov model. *PLoS Genet.* **3**, e7 (2007).
- Patterson, N., Richter, D. J., Gnerre, S., Lander, E. S. & Reich, D. Genetic evidence for complex speciation of humans and chimpanzees. *Nature* **441**, 1103–1108 (2006).
- Alcaide, M. *et al.* Population fragmentation leads to isolation by distance but not genetic impoverishment in the philopatric Lesser Kestrel: a comparison with the widespread and sympatric Eurasian Kestrel. *Heredity* **102**, 190–198 (2009).
- Yu, N. *et al.* Low nucleotide diversity in chimpanzees and bonobos. *Genetics* **164**, 1511–1518 (2003).
- Chen, F. C. & Li, W. H. Genomic divergences between humans and other hominoids and the effective population size of the common ancestor of humans and chimpanzees. *Am. J. Hum. Genet.* **68**, 444–456 (2001).

Supplementary Information is linked to the online version of the paper at [www.nature.com/nature](http://www.nature.com/nature).

**Acknowledgements** The orang-utan genome project was funded by the National Human Genome Research Institute (NHGRI), including grants U54 HG003079 (R.K.W.) and U54 HG003273 (R.A.G.), with further support from National Institutes of Health R01 GM59290 (M.A.B.), PO1 AG022064 (M.A.B.), HG002385 (E.E.E.) and HG002238 (W.M.), National Science Foundation DBI-0644111 (A.S. and B.B.), David and Lucile Packard Foundation (A.S., V.T. and T.V.), Cornell University Provost's Fellowship (A.L.M.), UK Medical Research Council (C.P.P., G.L., S.M. and A.H.), Marie Curie Fellowship (T.M.-B.), Ministerio de Ciencia e Innovación-Spain (MCI-Spain) and Fundación M. Botín (V.Q., X.S.P., G.R.O. and C.L.-O.), MCI-Spain BFU2006-15413-C02-01 and BFU2009-13409-C02-02 (A.N.), Spanish National Institute for Bioinformatics (INAB) and Fundação para a Ciência e a Tecnologia (Portugal), SFRH/BPD/26384/2006 (R.F.) and SFRH/BD/15856/2005 (O.F.), PRIN and CEGBA (M.R., N.A. and G.D.V.), and the Commission of the European Communities IRG-224885 (T.V.), IRG-231025 (B.B.). We thank the Gladys Porter Zoo, and S. O'Brien and S. Pääbo for use of orang-utan samples. D.P.L. thanks S. D. McGrath, A. Wollam, R. M. Abbott and L. Chemnick for technical assistance. We acknowledge all the important work that could not be cited owing to space limitations. Resources for exploring the orang-utan genome are available at UCSC (<http://genome.ucsc.edu>), Ensembl (<http://www.ensembl.org>), NCBI (<http://ncbi.nlm.nih.gov>) and The Genome Center at Washington University ([http://genome.wustl.edu/genomes/view/pongo\\_abelii/](http://genome.wustl.edu/genomes/view/pongo_abelii/)).

**Author Contributions** D.P.L. led the project and manuscript preparation. D.P.L., A.S., T.M.-B., C.P.P., M.A.B., A.N., E.E.E., M.W.H., C.L.-O., C.D.B., J.M. and M.H.S. led the analyses. Sanger data production, assembly construction, testing and submission: L.W.H., W.C.W., S.-P.Y., Z.W., A.T.C., P.M., M.M., L.A.F., R.A.F., J.O.N., C.P., K.C.W., L.V.N., D.M.M., A.C., H.H.D., J.H., C.L.K., G.R.F. and J.R. BAC sequencing: T.A.G. 454 cDNA sequencing: V.M. and C.M. Illumina sequencing: L.C., K.D.D. and C.F. SNP validation: H.S. Indel assessment: G.L., S.M., A.H. and C.P.P. Segmental duplication, divergence and structural variation studies: T.M.-B., C.A., L.C., Z.C., J.M.K. and E.E.E. Gene models: S.W., S.S. and A.J.V. Assembly-based SNPs: Y.C. and P.F. Ancestral reconstruction and rearrangement analyses: J.M., B.R., B.S., R.B., J.H., D.H., R.S.H. and W.M. Regional variation in nucleotide divergence analyses: R.F., O.F., F.D., D.F., E.G., M.O. and A.N. Cytogenetics and neocentromere characterization: R.R., O.C., N.A., G.D.V., S.P. and M.R. Repeat analyses: M.K.K., J.A.W., B.U., M.A.B., A.F.A.S. and R.H. Gene family evolution analyses: C.C., D.R.S. and M.W.H. Protease gene family studies: V.Q., X.S.P., G.R.O. and C.L.-O. Orthologue and defensin analyses: T.V., B.B., A.R. and W.M. Positive selection analyses: C.K., T.V., H.A.L., V.T., A.L.M. and A.S. Short read alignments, SNP calling and population genetics: A.R., X.M., J.D. and C.D.B. Demographic analyses: R.N.G. Coalescent-HMM analyses: T.M., J.Y.D., A.H. and M.H.S. Orang-utan samples for diversity sequencing: O.A.R. BAC library construction: Y.Y. and P.J.d.J. Principal investigators: G.M.W., E.R.M., R.A.G. and R.K.W.

**Author Information** The *P. abelii* whole-genome shotgun project has been deposited in DDBJ/EMBL/GenBank under the project accession ABGA00000000. The version described in this Letter is ABGA00000000.1. Assembly-based SNPs and SNPs derived from short read sequence data have been deposited in dbSNP. All short read data have been deposited into the Short Read Archive (<http://www.ncbi.nlm.nih.gov/sra>) under accessions listed in Supplementary Information. Reprints and permissions information is available at [www.nature.com/reprints](http://www.nature.com/reprints). This paper is distributed under the terms of the Creative Commons Attribution-Non-Commercial-Share Alike Licence, and is freely available to all readers at [www.nature.com/nature](http://www.nature.com/nature). The authors declare no competing financial interests. Readers are welcome to comment on the online version of this article at [www.nature.com/nature](http://www.nature.com/nature). Correspondence and requests for materials should be addressed to D.P.L. ([dlocke@wustl.edu](mailto:dlocke@wustl.edu)) or W.C.W. ([wwarren@wustl.edu](mailto:wwarren@wustl.edu)).

# Distinct physiological and behavioural functions for parental alleles of imprinted *Grb10*

Alastair S. Garfield<sup>1,2,†</sup>, Michael Cowley<sup>1,†</sup>, Florentia M. Smith<sup>1</sup>, Kim Moorwood<sup>1</sup>, Joanne E. Stewart-Cox<sup>1</sup>, Kerry Gilroy<sup>2</sup>, Sian Baker<sup>2</sup>, Jing Xia<sup>3</sup>, Jeffrey W. Dalley<sup>3,4</sup>, Laurence D. Hurst<sup>1</sup>, Lawrence S. Wilkinson<sup>2</sup>, Anthony R. Isles<sup>2</sup> & Andrew Ward<sup>1</sup>

**Imprinted genes, defined by their preferential expression of a single parental allele, represent a subset of the mammalian genome and often have key roles in embryonic development<sup>1</sup>, but also postnatal functions including energy homeostasis<sup>2</sup> and behaviour<sup>3,4</sup>. When the two parental alleles are unequally represented within a social group (when there is sex bias in dispersal and/or variance in reproductive success)<sup>5,6</sup>, imprinted genes may evolve to modulate social behaviour, although so far no such instance is known. Predominantly expressed from the maternal allele during embryogenesis, *Grb10* encodes an intracellular adaptor protein that can interact with several receptor tyrosine kinases and downstream signalling molecules<sup>7</sup>. Here we demonstrate that within the brain *Grb10* is expressed from the paternal allele from fetal life into adulthood and that ablation of this expression engenders increased social dominance specifically among other aspects of social behaviour, a finding supported by the observed increase in allogrooming by paternal *Grb10*-deficient animals. *Grb10* is, therefore, the first example of an imprinted gene that regulates social behaviour. It is also currently alone in exhibiting imprinted expression from each of the parental alleles in a tissue-specific manner, as loss of the peripherally expressed maternal allele leads to significant fetal and placental overgrowth. Thus *Grb10* is, so far, a unique imprinted gene, able to influence distinct physiological processes, fetal growth and adult behaviour, owing to actions of the two parental alleles in different tissues.**

To characterize expression and investigate functions of the two parental *Grb10* alleles we have generated a mutant mouse strain (*Grb10KO*), derived by insertion of a *LacZ:neomycin*<sup>r</sup> gene-trap cassette within *Grb10* exon 8 (Fig. 1a). Transmission of the *Grb10KO* allele separately through the two parental lines generated heterozygous progeny in which either the maternal (*Grb10KO*<sup>ml/+</sup>) or paternal (*Grb10KO*<sup>+p</sup>) *Grb10* allele was disrupted by the  $\beta$ -geo cassette and allowed us to examine *Grb10* expression in an allele-specific manner. Northern blot analysis of RNA samples prepared from whole fetuses (Fig. 1b) showed that endogenous *Grb10* transcripts were readily detected in wild-type animals and in heterozygotes that inherited a mutant *Grb10KO*<sup>+p</sup> allele. In contrast, *Grb10* transcripts were found at relatively low levels in heterozygous animals with a mutant *Grb10KO*<sup>ml/+</sup> allele, an observation consistent with previous demonstrations that most *Grb10* expression is maternally derived (for example, ref. 8). We next conducted more refined *in situ* analyses of allele-specific expression, using the integrated *LacZ* reporter gene. During fetal development, *LacZ* expression from the maternal allele was widespread in tissues of mesodermal and endodermal origin, but absent from the central nervous system (CNS) proper (Fig. 1d, f). At embryonic day (E) 14.5, expression of the maternal *Grb10* allele within the brain was seen only in the ventricular ependymal layers, the epithelium of the choroid plexus and the meninges, presumably identifying sources of maternal brain expression that have been reported by

others<sup>9–13</sup> (Supplementary Fig. 1a, b). In contrast, expression from the paternal allele was predominant within the developing CNS, with only a few discrete sites of relatively low-level expression seen in other tissues (Figs 1e, g, 2a and Supplementary Fig. 1c, d). The CNS expression starts between E11.5 and E14.5, consistent with the onset of neurogenesis, and correlates with the brain-specific loss of a repressive histone modification (H3K27me3) from the paternal *Grb10* allele during development and during neural precursor cell differentiation *in vitro*<sup>14</sup>. This loss of H3K27me3 from the promoter region of the *Grb10* paternal allele-specific transcripts (see Fig. 1a) leaves a permissive histone mark on the paternal allele (H3K4me2), whereas this region of the maternal allele is constitutively associated with two repressive histone modifications (H3K9me3 and H4K20me3)<sup>14</sup>.

Our analysis showed paternal allele expression within the developing CNS was restricted to specific regions of both the brain and spinal cord, with reporter signal identified within select areas of the diencephalon, ventral midbrain and the medulla oblongata extending caudally along the ventral spinal cord. There was no expression detected within the presumptive neocortex, dorsal midbrain or the cerebellar primordium (Fig. 2a). Embryonic *Grb10* expression within the CNS proper was entirely paternal in origin, a fact that was not evident from previous expression studies that identified a promoter and brain-specific transcripts associated with the paternal allele, but relied on techniques involving RNA extraction from tissue homogenates<sup>9–12</sup>. Thus our *Grb10* expression analysis provides striking evidence of reciprocal imprinted expression from the two parental alleles in different tissues. Several imprinted genes exhibit tissue-specific and/or temporal regulation, such that their expression is biallelic (non-imprinted) at some of their sites of expression. However, the reciprocal parent-of-origin expression described here is unprecedented, suggesting new and intriguing possibilities for imprinted gene function and evolution.

Consistent with our previous studies of *Grb10* $\Delta$ 2–4 mice<sup>8,15</sup>, *Grb10KO*<sup>ml/+</sup> animals displayed a disproportionate overgrowth phenotype apparent from E12.5 onwards (Fig. 1h, i and Supplementary Fig. 2). At birth, the mean body weight of *Grb10KO*<sup>ml/+</sup> pups was  $25 \pm 2.5\%$  greater than that of wild-type littermates. The liver was disproportionately enlarged ( $117 \pm 9.8\%$  heavier), but there was sparing of the brain and kidney, such that the weights of these organs were not significantly different to those of wild types (Fig. 1i). The cranial sparing is consistent with limited *Grb10* maternal allele expression within the developing CNS. Body weight and proportions of *Grb10KO*<sup>+p</sup> mutants did not differ from wild-type controls and no function has yet been ascribed to the paternally inherited *Grb10* allele, despite evidence of its expression within the neonatal brain<sup>9</sup>. Both *Grb10KO*<sup>ml/+</sup> and *Grb10KO*<sup>+p</sup> mutants were present at the expected Mendelian frequencies ( $\chi^2$  values,  $P = 0.737$  and  $P = 0.395$ , respectively) when animals were genotyped at 3–4 weeks of age, indicating that survival to weaning was unimpaired. Observations of *Grb10KO*<sup>+p</sup> pups before weaning, including analysis

<sup>1</sup>Department of Biology & Biochemistry and Centre for Regenerative Medicine, University of Bath, Claverton Down, Bath BA2 7AY, UK. <sup>2</sup>Behavioural Genetics Group, MRC Centre for Neuropsychiatric Genetics and Genomics, Neuroscience and Mental Health Research Institute, Schools of Medicine and Psychology, Cardiff University, Cardiff CF14 4XN, UK. <sup>3</sup>Behavioural and Clinical Neuroscience Institute and Department of Experimental Psychology, University of Cambridge, Downing Street, Cambridge CB2 3EB, UK. <sup>4</sup>Department of Psychiatry, University of Cambridge, Addenbrooke's Hospital, Hill's Road, Cambridge CB2 2QQ, UK. <sup>†</sup>Present addresses: Department of Pharmacology, University of Cambridge, Tennis Court Road, Cambridge CB2 1PD, UK. (A.S.G.); Department of Medical and Molecular Genetics, King's College London, 8th Floor Tower Wing, Guy's Hospital, London SE1 9RT, UK (M.C.).

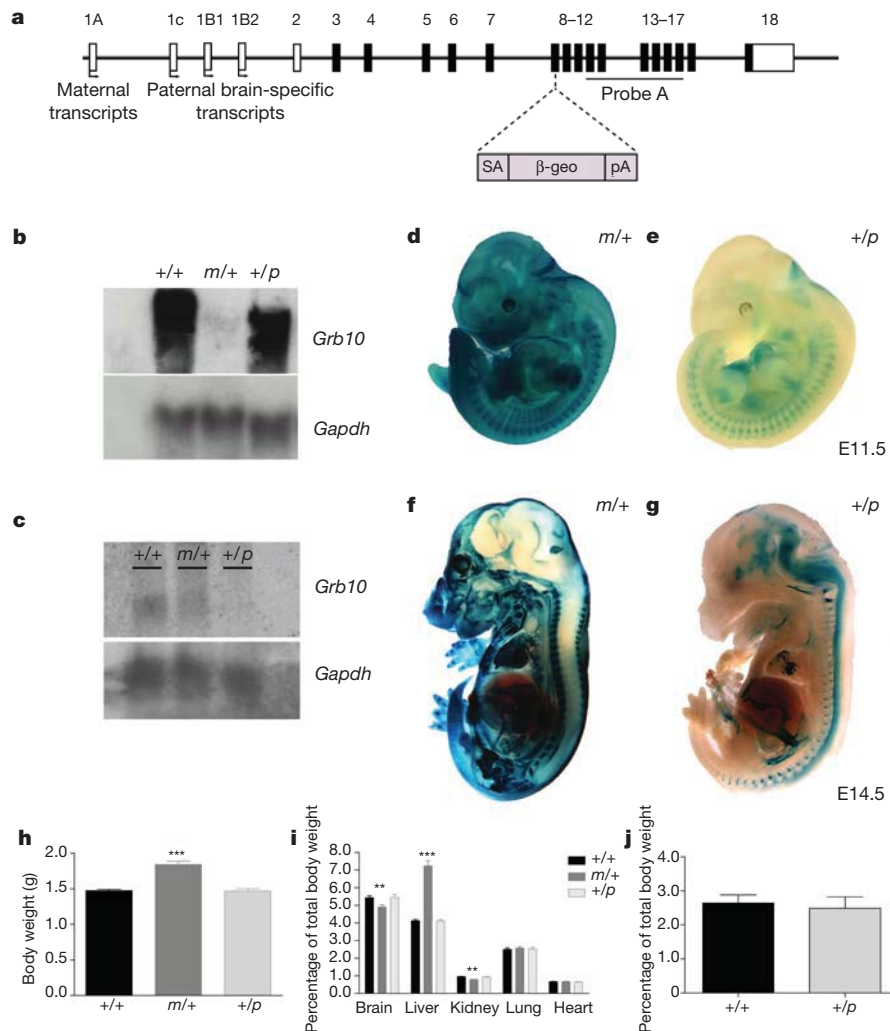


**Figure 1 | Generation and characterization of *Grb10*KO mutants.** **a**, The mouse *Grb10* locus showing the *LacZ:neomycin<sup>r</sup>* ( $\beta$ -geo) insertion in the *Grb10*KO allele (not to scale), showing transcriptional start-sites (arrows), numbered exons (boxes), translated regions (filled boxes) and heterologous splice acceptor (SA) and polyadenylation (pA) signals. **b**, Northern (RNA) blot analysis of *Grb10* expression in whole E14.5 embryos. *Grb10* transcripts (approximately 5.5 kilobases) were readily detected in wild-type (+/+) and *Grb10*KO<sup>+/*p*</sup> (+/p) but not *Grb10*KO<sup>m/+</sup> (m/+) samples. **c**, Northern blot analysis of *Grb10* expression in adult brain. *Grb10* transcripts were evident in wild-type (+/+) and *Grb10*KO<sup>+/*m*</sup> (m/+) but not *Grb10*KO<sup>+/*p*</sup> (+/p) samples. **d–g**, *LacZ* reporter expression in E11.5 (**d–e**) and E14.5 (**f–g**) heterozygous

*Grb10*KO embryos showing opposite imprinting of the two parental alleles in different tissues. **h**, Neonatal body weight analysis revealed that *Grb10*KO<sup>m/+</sup>, but not *Grb10*KO<sup>+/*p*</sup> neonates were overgrown compared with wild-type littermates on the day of birth ( $F_{(2,90)} = 41.69$ ;  $P < 0.001$ ). **i**, Analysis of dissected organs showed that growth enhancement in *Grb10*KO<sup>m/+</sup> neonates was proportional within most tissues, except the liver, which was disproportionately overgrown ( $F_{(2,87)} = 118.60$ ;  $P < 0.001$ ), and the kidneys and brain, which were spared. **j**, Stomach weights of wild-type and *Grb10*KO<sup>+/*p*</sup> neonates were not significantly different, suggesting that feeding was not impaired in the mutants ( $t_{(36)} = 0.38$ ;  $P = 0.70$ ). **h–j**, Values represent means  $\pm$  s.e.m.

of stomach weights (Fig. 1j), suggested that suckling behaviour was normal.

*Grb10* expression in the adult brain was consistent with that observed during embryogenesis in being predominately paternally derived. Northern blot analysis demonstrated the presence of *Grb10* transcripts in the wild-type and *Grb10*KO<sup>m/+</sup> brains but not in the *Grb10*KO<sup>+/*p*</sup> brain (Fig. 1c), with no effects observed on expression of the adjacent *Ddc* gene (data not shown). Consistent with this, expression of the *LacZ* reporter was derived exclusively from the *Grb10*KO<sup>+/*p*</sup> allele (Fig. 2a–d and Supplementary Fig. 3). Histological analysis of *LacZ* expression in the adult *Grb10*KO<sup>+/*p*</sup> brain revealed a discrete pattern of paternal allele expression (Fig. 2k–m). Reporter expression was observed within thalamic, hypothalamic, midbrain and hindbrain nuclei, with no cortical expression detected at any point throughout the brain. Forebrain expression was also evident within the septal nuclei and specifically the cholinergic inter-neurons of the caudate putamen. Within the midbrain and hindbrain sites of expression

included almost all monoaminergic cell populations (for a complete list of sites of paternal allele expression see Supplementary Table 1). *In situ* hybridization analysis of endogenous *Grb10* messenger RNA (mRNA) expression was in close accordance with the observed *LacZ* expression profile, indicating that it was not an artefact of reporter insertion (Fig. 2e–j and Supplementary Fig. 4). *Grb10* maternal allele expression is dramatically downregulated from late gestation and persists postnatally in only a subset of peripheral tissues<sup>16</sup>. Consistent with this, ependymal and choroid plexus epithelial expression observed in the embryo was no longer apparent in the *Grb10*KO<sup>m/+</sup> adult. *In situ* hybridization analysis of *Grb10*KO<sup>+/*p*</sup> brains revealed an almost complete absence of maternal *Grb10* expression. A low level of maternal allele expression was detected in a few brain regions, including the median preoptic nucleus, medial habenular, medial amygdaloid nuclei and ventromedial hypothalamus (Supplementary Fig. 4), therefore representing sites of biallelic *Grb10* expression. These sites within the brain mirror the situation outside the CNS where expression from

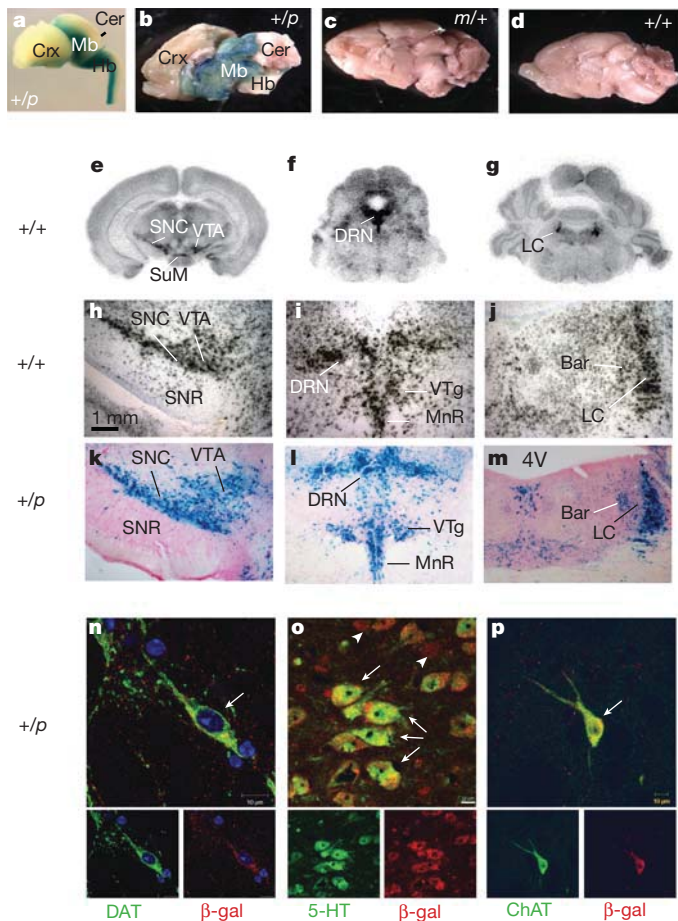


**Figure 2 | *Grb10* expression in the mouse brain.** **a**, A *Grb10*KO<sup>+/-</sup> brain dissected from an E14.5 embryo, showing *LacZ* reporter expression within the ventral midbrain (Mb), hindbrain (Hb) and ventral spinal cord, but not cortex (Crx) or cerebellum (Cer). **b–d**, Adult brains, bisected longitudinally, showing *LacZ* reporter expression, in *Grb10*KO<sup>+/-</sup> (b), but not *Grb10*KO<sup>ml/+</sup> (c) and wild-type (d) samples, demonstrating exclusively paternal *Grb10* allele expression. **e–g**, *In situ* hybridization autoradiographs of endogenous *Grb10* mRNA expression (using probe A, see Fig. 1a) within the substantia nigra pars compacta (SNC), supramammillary nucleus (SuM), ventral tegmental area (VTA) (e), dorsal raphe nucleus (DRN) (f) and locus coeruleus (LC) (g) of the adult brain. **h–j**, Higher-resolution microscope images from hybridized slides dipped in photographic emulsion; positive signal (black grains) demonstrates cellular localization of *Grb10* mRNA at the level of **e–g**. **k–m**, *LacZ* expression from the paternal *Grb10* allele in the brain of *Grb10*KO<sup>+/-</sup> mice faithfully recapitulates endogenous *Grb10* expression as reported by *in situ* hybridization (in **h–j**; 4V indicates fourth ventricle). **n–p**, Histological sections of *Grb10*KO<sup>+/-</sup> adult brain showing co-localization of immunofluorescence staining for  $\beta$ -galactosidase ( $\beta$ -gal), expressed from the *Grb10* paternal allele, with markers specific for dopaminergic neurons (dopamine transporter; DAT) within the SNC (n), serotonergic neurons (serotonin; 5-HT) within the DRN (o) and cholinergic inter-neurons (choline acetyltransferase; ChAT) within the caudate putamen (p). Arrows indicate co-localized cells. Arrowheads indicate cells positive for  $\beta$ -galactosidase but negative for the neurochemical marker. SNR, substantia nigra pars reticulata; Bar, Barrington's nucleus; MnR, median raphe nucleus; VTg, ventral tegmental nucleus.

the maternal allele predominates, but there are also discrete sites of biallelic expression (Fig. 1e, g). Expression from the paternal allele in the CNS followed a pattern suggesting that expression established during embryogenesis was maintained into adulthood, as demonstrated by analysis of endogenous *Grb10* expression in *Grb10*KO<sup>ml/+</sup> brains (Supplementary Fig. 4).

The distribution of *LacZ*-positive cells within expressing regions of the adult brain suggested expression from the paternal allele was predominantly neuron specific. Supporting this, immunofluorescent

co-localization experiments performed within three discrete brain regions, the substantia nigra pars compacta, dorsal raphe nucleus and caudate putamen, demonstrated that paternal *Grb10* expression was detectable in dopaminergic (Fig. 2n), serotonergic (Fig. 2o) and cholinergic (Fig. 2p) neurons, respectively.

Despite having established a role for maternal *Grb10* as a major regulator of both fetal and placental growth<sup>8,15</sup> (Fig. 1 and Supplementary Fig. 2), we found no evidence of brain overgrowth in neonatal *Grb10*KO<sup>+/-</sup> mutant animals (Fig. 1i). Several genes show imprinted expression in the brain and knockout mouse studies have shown that some of these genes regulate specific behaviours. Notably, these include paternally expressed genes important for maternal nurturing of young (*Mest* and *Peg3*, reviewed in ref. 4), but also genes regulating other behavioural functions, including exploratory behaviour (maternally expressed *Nesps55* (ref. 17)) and circadian rhythm output (paternally expressed *Magel2* (ref. 18)). We therefore sought to assay *Grb10*KO<sup>+/-</sup> mutant animals by using standard tests of different behavioural parameters. In most of these assays *Grb10*KO<sup>+/-</sup> mice were essentially indistinguishable from wild-type littermate controls, including tests of anxiety-related behaviour, locomotor activity, olfaction and aggression (Supplementary Fig. 5). However, in an assay of social dominance in which a forced encounter was observed between two unfamiliar animals, using the tube test<sup>19</sup>, *Grb10*KO<sup>+/-</sup> mutants were found to be significantly less likely to back down than their wild-type 'opponents' (Fig. 3a). This was not the case for *Grb10*KO<sup>ml/+</sup> mice (Supplementary Fig. 5i). In the context of all of our behavioural testing, the outcome of the tube test was interpreted as a specific change in the behaviour of *Grb10*KO<sup>+/-</sup> mutant animals. Moreover, this behavioural change was found to correlate with observations of socially housed mice, where there was a significantly elevated incidence of facial barbering in cages containing at least one *Grb10*KO<sup>+/-</sup> mutant (Fig. 3b, c). Typically, these cages contained a single unbarbered *Grb10*KO<sup>+/-</sup> mutant (81% of cages), suggesting this animal was responsible for allogrooming of cage-mates. Consistent with this, isolation of barbered animals facilitated complete regrowth of missing hair and vibrissae. Barbering was observed in both male and female animals (Supplementary Fig. 5j). Allogrooming is regarded as a robust correlate of social dominance, as its assessment is independent of exogenous confounds<sup>20</sup>. Rigorous testing of additional aspects of social behaviour in *Grb10*KO<sup>+/-</sup> mice revealed no further differences in comparison with wild-type littermate controls (Fig. 3d, e). Specifically, habituation–dishabituation studies designed to probe aspects of social recognition, pertinent to the interpretation of the tube-test data, indicated that *Grb10*KO<sup>+/-</sup> animals reacted normally by exhibiting a general habituation to the olfactory cue, urine, followed by subsequent dishabituation when presented with a novel odour. Consistent with this outcome, *Grb10*KO<sup>+/-</sup> mutant mice exhibited normal olfactory responses when tested in their latency to investigate two different odours (Supplementary Fig. 5e, f).

Our study identifies *Grb10* as the first imprinted gene to have a role in the modulation of a specific social behaviour (as distinct from parental care). This function is predicted to be subject to the effects of intragenomic conflict within social groups when the two parental alleles are unequally represented, notably when there is sex bias in dispersal and/or variance in reproductive success<sup>5,6</sup>. In mice, as in other mammals<sup>6</sup>, there is probably greater variance in reproductive success in males than in females and unequal representation is thus very likely. However, whether the association of the phenotypes with the sex-of-origin that we observe is consistent with the theory is unclear. For species such as humans, in which there is greater variation between males in reproductive success and (most probably) female dispersal, the involvement of paternally derived genes in promoting more altruistic behaviours is expected<sup>6</sup>. For mice, however, the necessary parameters are not well enough described to enable confident prediction as to whether paternal or maternal alleles should be the more 'altruistic'<sup>6</sup>. We note that our finding might also be considered consistent with the co-adaptation theory of imprinted gene evolution<sup>21,22</sup>. Similarly, the

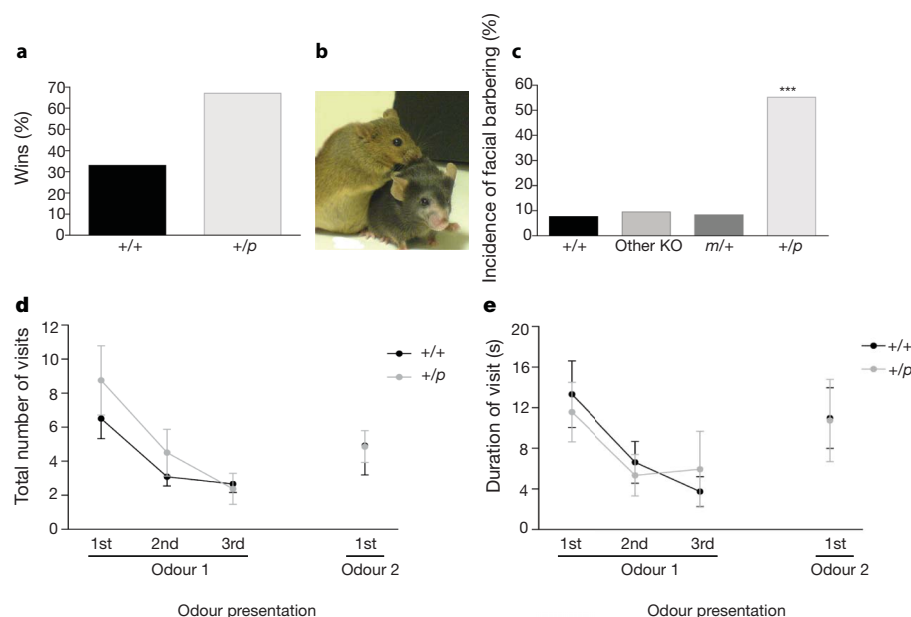


**Figure 3 | Increased social dominance in *Grb10*KO<sup>+/-</sup> mice.** **a**, Assessment of social dominance using the tube test revealed that *Grb10*KO<sup>+/-</sup> mutants were significantly more likely to prevail in a forced encounter than wild-type controls ( $P < 0.05$ , significance determined by non-parametric Monte Carlo permutation test at the individual level: see Methods for details). **b**, A typical example of a barbed animal (black mouse), pictured with an unbarbed cage-mate. **c**, The incidence of facial barbering within cages containing one or more *Grb10*KO<sup>+/-</sup> (+/-) mutants was significantly greater than in control cages containing wild-type animals (+/+), other genetically modified strains

(Other KO) or *Grb10*KO<sup>m/+</sup> mutants ( $m/+$ ) ( $\chi^2 = 24.86$ ;  $P < 0.001$ ).

**d, e**, Assessment of social recognition used a urinary odour habituation–dishabituation test. *Grb10*KO<sup>+/-</sup> mutants were indistinguishable from wild-type controls in the number of visits made to the odour source (**d**; ANOVA, no effect of genotype  $F_{(1,10)} = 0.513$ ,  $P = 0.49$ ) and duration of these investigations (**e**; ANOVA, no effect of genotype  $F_{(1,10)} = 0.011$ ,  $P = 0.92$ ). Mutant and control animals exhibited the significant but comparable increases in both measures on presentation of a second novel odour (visits,  $P = 0.015$ ; duration,  $P = 0.032$ ). **d, e**, Values represent means  $\pm$  s.e.m.

effect of *Grb10* on placental growth<sup>8,15</sup> is potentially consistent both with the parental conflict and co-adaptation theories.

It has also been suggested that differences in parental genome representation within social groups could engender differential tolerance to risk-taking behaviours<sup>4</sup>. Tempering of socially dominant behaviour can be viewed as a risk-averse phenotype aimed at maximizing reproductive success by avoiding the potentially detrimental consequences of challenging for social status. Expression of *Grb10* within several monoaminergic nuclei may be relevant to the possible underlying mechanism, as cerebrospinal fluid levels of serotonin and dopamine metabolites have been independently correlated with dominant/submissive behaviour<sup>23,24</sup>. However, no changes in the levels of dopamine, serotonin, noradrenalin and acetylcholine (and associated metabolites) were detected from macro-dissected brain regions of *Grb10*KO<sup>+/-</sup> mice (Supplementary Fig. 6). The imprinted *Nesp55* gene has been associated with the promotion of risk tolerance, notable because *Nesp55* is expressed from the maternal allele within discrete brain regions that overlap sites of *Grb10* paternal allele expression, including the serotonergic raphe nucleus and noradrenergic neurons of the locus coeruleus<sup>4,17</sup>. This raises the possibility that these two genes might represent antagonistic components within the same neurological systems. Moreover, a recent genome-wide screen has indicated that over 1,300 loci could be subject to parent-of-origin allelic expression bias within the mouse brain<sup>13</sup>, suggesting the influence of genomic imprinting within the brain may be much greater than previously thought. However, verification of this will require extensive validation of allelic expression bias together with functional testing of the identified genes.

Many imprinted genes are found in clusters that can contain genes expressed from either parental allele as well as non-imprinted genes<sup>25</sup>. However, the demonstration of opposite imprinting within a single mouse gene, most likely conserved in humans<sup>26</sup>, represents a highly provocative situation, whereby the two parental alleles of *Grb10* have evolved distinct patterns of imprinted expression according to their functions in different tissues.

## METHODS SUMMARY

***Grb10*KO mice.** Chimaeric animals were generated by microinjection of a gene-trap ES cell line (XC302; Baygenomics) into F<sub>2</sub> (C57BL/6  $\times$  CBA) strain blastocysts, using standard methods<sup>27</sup>. Mice were maintained on a C57BL/6:CBA mixed genetic background and kept as previously described<sup>28</sup>. Behavioural phenotyping and statistical methods are detailed in Methods.

**Northern blot analysis.** Total RNA was extracted using TRI Reagent (Sigma Aldrich), with 20–50  $\mu$ g run on denaturing agarose gels and transferred to a nylon membrane for hybridization with a *Grb10*-specific radiolabelled probe<sup>8</sup>.

**In situ hybridization.** Adult brain tissue was collected from animals transcardially perfused with 4% paraformaldehyde, cryoprotected in 20% sucrose and sectioned at 30  $\mu$ m on a freezing microtome. Tissue was processed for *in situ* hybridization<sup>29</sup> and a [<sup>35</sup>S]riboprobe specific to exons 11–16 of the mouse *Grb10* mRNA sequence was used to detect endogenous *Grb10* expression.

**LacZ expression analysis.** Dissected embryos were fixed in 2% formaldehyde/0.2% glutaraldehyde in PBS for 2 h at room temperature, stained at 37  $^{\circ}$ C for approximately 2 h in freshly prepared X-gal solution, post-fixed overnight at 4  $^{\circ}$ C using 4% paraformaldehyde in PBS, then cleared in 80% glycerol. Adult brains were longitudinally bisected and stained, as above, without fixation. For adult brain sections, animals were first perfused with chilled 9.25% (w/v) sucrose solution, followed by approximately 100 ml of chilled 3% paraformaldehyde in 0.1% PBS. Brains were sectioned at 50  $\mu$ m on a vibratome (VT1000S; Leica), with the tissue kept ice-cold. Free-floating sections were collected and immersed in X-gal staining solution at 28  $^{\circ}$ C overnight. *Grb10*KO samples were co-terminally stained alongside wild-type controls.

**Immunofluorescent analysis of adult brain sections.** Brain sections (50  $\mu$ m) were collected from animals perfused with 4% paraformaldehyde and the sections post-fixed in 4% paraformaldehyde at 4  $^{\circ}$ C overnight before antibody staining, as described<sup>30</sup>.

**Full Methods** and any associated references are available in the online version of the paper at [www.nature.com/nature](http://www.nature.com/nature).

Received 14 December 2009; accepted 4 November 2010.

- Reik, W. & Walter, J. Genomic imprinting: parental influence on the genome. *Nature Rev. Genet.* **2**, 21–32 (2001).
- Smith, F. M., Garfield, A. S. & Ward, A. Regulation of growth and metabolism by imprinted genes. *Cytogenet. Genome Res.* **113**, 279–291 (2006).
- Davies, W., Isles, A. R. & Wilkinson, L. S. Imprinted gene expression in the brain. *Neurosci. Biobehav. Rev.* **29**, 421–430 (2005).

4. Isles, A. R., Davies, W. & Wilkinson, L. S. Genomic imprinting and the social brain. *Phil. Trans. R. Soc. B* **361**, 2229–2237 (2006).
5. Haig, D. Genomic imprinting, sex-biased dispersal, and social behavior. *Ann. NY Acad. Sci.* **907**, 149–163 (2000).
6. Ubeda, F. & Gardner, A. A model for genomic imprinting in the social brain: juveniles. *Evolution* **64**, 2587–2600 (2010).
7. Holt, L. J. & Siddle, K. Grb10 and Grb14: enigmatic regulators of insulin action—and more? *Biochem. J.* **388**, 393–406 (2005).
8. Charalambous, M. *et al.* Disruption of the imprinted Grb10 gene leads to disproportionate overgrowth by an Igf2-independent mechanism. *Proc. Natl Acad. Sci. USA* **100**, 8292–8297 (2003).
9. Arnaud, P. *et al.* Conserved methylation imprints in the human and mouse GRB10 genes with divergent allelic expression suggests differential reading of the same mark. *Hum. Mol. Genet.* **12**, 1005–1019 (2003).
10. Hikichi, T., Kohda, T., Kaneko-Ishino, T. & Ishino, F. Imprinting regulation of the murine Meg1/Grb10 and human GRB10 genes; roles of brain-specific promoters and mouse-specific CTCF-binding sites. *Nucleic Acids Res.* **31**, 1398–1406 (2003).
11. Monk, D. *et al.* Reciprocal imprinting of human GRB10 in placental trophoblast and brain: evolutionary conservation of reversed allelic expression. *Hum. Mol. Genet.* **18**, 3066–3074 (2009).
12. Yamasaki-Ishizaki, Y. *et al.* Role of DNA methylation and histone H3 lysine 27 methylation in tissue-specific imprinting of mouse Grb10. *Mol. Cell. Biol.* **27**, 732–742 (2007).
13. Gregg, C. *et al.* High-resolution analysis of parent-of-origin allelic expression in the mouse brain. *Science* **329**, 643–648 (2010).
14. Sanz, L. A. *et al.* A mono-allelic bivalent chromatin domain controls tissue-specific imprinting at Grb10. *EMBO J.* **27**, 2523–2532 (2008).
15. Charalambous, M. *et al.* Maternally-inherited Grb10 reduces placental size and efficiency. *Dev. Biol.* **337**, 1–8 (2010).
16. Smith, F. M. *et al.* Mice with a disruption of the imprinted Grb10 gene exhibit altered body composition, glucose homeostasis, and insulin signaling during postnatal life. *Mol. Cell. Biol.* **27**, 5871–5886 (2007).
17. Plagge, A. *et al.* Imprinted Nesp55 influences behavioral reactivity to novel environments. *Mol. Cell. Biol.* **25**, 3019–3026 (2005).
18. Kozlov, S. V. *et al.* The imprinted gene *Magel2* regulates normal circadian output. *Nature Genet.* **39**, 1266–1272 (2007).
19. Spencer, C. M. *et al.* Altered anxiety-related and social behaviors in the Fmr1 knockout mouse model of fragile X syndrome. *Genes Brain Behav.* **4**, 420–430 (2005).
20. Sarna, J. R., Dyck, R. H. & Whishaw, I. Q. The Dalila effect: C57BL6 mice barber whiskers by plucking. *Behav. Brain Res.* **108**, 39–45 (2000).
21. Keverne, B. Monoallelic gene expression and mammalian evolution. *Bioessays* **31**, 1318–1326 (2009).
22. Wolf, J. B. & Hager, R. A maternal–offspring coadaptation theory for the evolution of genomic imprinting. *PLoS Biol.* **4**, 2238–2243 (2006).
23. Kaplan, J. R., Manuck, S. B., Fontenot, M. B. & Mann, J. J. Central nervous system monoamine correlates of social dominance in cynomolgus monkeys (*Macaca fascicularis*). *Neuropsychopharmacology* **26**, 431–443 (2002).
24. Raleigh, M. J. *et al.* Serotonergic mechanisms promote dominance acquisition in adult male vervet monkeys. *Brain Res.* **559**, 181–190 (1991).
25. Edwards, C. A. & Ferguson-Smith, A. C. Mechanisms regulating imprinted genes in clusters. *Curr. Opin. Cell Biol.* **19**, 281–289 (2007).
26. Blagitko, N. *et al.* Human GRB10 is imprinted and expressed from the paternal and maternal allele in a highly tissue- and isoform-specific fashion. *Hum. Mol. Genet.* **9**, 1587–1595 (2000).
27. Nagy, A., Gertsenstein, K., Vintersten, K. & Behringer, R. *Manipulating the Mouse Embryo: A Laboratory Manual* 3rd edn (Cold Spring Harbor Laboratory Press, 2003).
28. Bennett, W. R., Crew, T. E., Slack, J. M. & Ward, A. Structural-proliferative units and organ growth: effects of insulin-like growth factor 2 on the growth of colon and skin. *Development* **130**, 1079–1088 (2003).
29. Przydzial, M. J. *et al.* Nutritional state influences Nociceptin/Orphanin FQ peptide receptor expression in the dorsal raphe nucleus. *Behav. Brain Res.* **206**, 313–317 (2009).
30. Rousseau, S. J., Jones, I. W., Pullar, I. A. & Wonnacott, S. Presynaptic  $\alpha 7$  and non- $\alpha 7$  nicotinic acetylcholine receptors modulate [3H]D-aspartate release from rat frontal cortex *in vitro*. *Neuropharmacology* **49**, 59–72 (2005).

**Supplementary Information** is linked to the online version of the paper at [www.nature.com/nature](http://www.nature.com/nature).

**Acknowledgements** We thank S. Wonnacott for reagents, the University of Bath Biological Services Unit and S. Routley for technical assistance, I. Jones and P. Mitchell for advice and C. Tickle for comments on the manuscript. We acknowledge funding of the work from the Biotechnology and Biological Sciences Research Council, Medical Research Council, Wellcome Trust and external benefactors.

**Author Contributions** A.W. and A.S.G. conceived the project and interpreted the data, with input from L.D.H., A.R.I. and L.S.W.; K.M. and J.E.S.-C. generated the *Grb10KO* mice; A.S.G. performed most of the experiments with contributions from M.C., J.W.D., S.B., K.G., A.R.I., F.M.S., J.X. and A.W.; A.S.G. and A.W. jointly wrote the manuscript.

**Author Information** Reprints and permissions information is available at [www.nature.com/reprints](http://www.nature.com/reprints). The authors declare no competing financial interests. Readers are welcome to comment on the online version of this article at [www.nature.com/nature](http://www.nature.com/nature). Correspondence and requests for materials should be addressed to A.W. ([bssaw@bath.ac.uk](mailto:bssaw@bath.ac.uk)).

## METHODS

**Grb10KO mice.** Chimaeric animals were generated by microinjection of a gene-trap ES cell line (XC302; Baygenomics) into F<sub>2</sub> (C57BL/6 × CBA) strain blastocysts, using standard methods<sup>27</sup>. Mice were maintained on a C57BL/6:CBA mixed genetic background and kept as previously described<sup>28</sup>. We note that *Grb10KO* mice were derived using the XC302 gene-trap ES cell line and are distinct from our previously published *Grb10A2-4* model<sup>8</sup>. The XC302  $\beta$ -geo gene-trap insertion has replaced 12 base pairs (bp) of endogenous *Grb10* sequence (the 3' terminal 11 bp from exon 8 plus the 5'–most 1 bp from intron 8; data not shown). The mutant allele might, therefore, express the amino (N)-terminal 248 amino acids of Grb10 that would include two of the five recognized domains of the Grb10 adaptor protein (the Ras-association-like and proline-rich domains). Using an antibody raised to the N terminus of Grb10, we have been unable to detect any novel protein products in *Grb10KO* tissue (we examined protein from E14.5 embryo and placenta when Grb10 expression is strong and widespread; data not shown), either in the form of a distinct short peptide or a long *Grb10*: $\beta$ -geo fusion product. *Grb10KO* mice were derived in addition to our previously published *Grb10A2-4* model<sup>8</sup> which did not recapitulate fully the expression profile of endogenous *Grb10*, most likely because of the loss of a brain-specific enhancer element within a 36-kilobase deletion mapped to the *Grb10A2-4* allele (ref. 8 and M.C., A.S.G. and A.W., unpublished observations).

**Mouse genotyping and weight analyses.** *Grb10KO*<sup>ml/+</sup> and *Grb10KO*<sup>+/-p</sup> study animals were generated separately by transmission of the *Grb10KO* locus from heterozygous females and males, respectively. Animals were genotyped by PCR using primers specific to the  $\beta$ -geo insertion ( $\beta$ geoF2 5'-CCGAGCGAAACGG TCTGCG-3' and  $\beta$ geoR2 5'-CTTCCGCTTAGTGACAACG-3'). Analysis of neonatal body and dissected organ weights was performed on postnatal day 1 (*Grb10KO*<sup>+/+</sup> *n* = 43; *Grb10KO*<sup>ml/+</sup> *n* = 23; *Grb10KO*<sup>+/-p</sup> *n* = 27), as was analysis of stomach weight (*Grb10KO*<sup>+/+</sup> *n* = 23; *Grb10KO*<sup>+/-p</sup> *n* = 16).

**Probes for northern blot analysis.** Total RNA was extracted using TRI Reagent (Sigma Aldrich), with 20–50  $\mu$ g run on denaturing agarose gels and transferred to a nylon membrane for hybridization with a radiolabelled Grb10 probe. Grb10 probes were generated from mouse complementary DNA (cDNA) by PCR with reverse transcription using primers specific to *Grb10* (probe A, Fig. 1) (F, 5'-CTG ACCTGGAAGAAAGCAGC-3' and R, 5'-GATCCTGTGAGACTCCTCGC-3'). The Grb10 probe corresponds to nucleotides 1,353–1,858 of the mouse *Grb10* gene (accession number NM\_010345). Purified PCR products were cloned into pGEM-T Easy (Promega), excised from the vector backbone and gel-purified. Isolated probes were labelled with [ $\alpha$ -<sup>32</sup>P]dCTP and hybridized to blots, as previously described<sup>8</sup>.

**In situ hybridization.** Adult brain tissue was collected from animals transcardially perfused with 4% paraformaldehyde, cryoprotected in 20% sucrose and sectioned at 30  $\mu$ m on a freezing microtome. Tissue was processed for *in situ* hybridization as previously described<sup>29</sup>. A [<sup>35</sup>S]riboprobe specific to exons 11–16 of the mouse *Grb10* mRNA sequence was used to detect endogenous Grb10 expression (probe A, Fig. 1). The Grb10 riboprobe was synthesized by PCR using cDNA obtained from normal mouse brain and was the same as described above. The recombinant plasmid was linearized by restriction digest and subjected to *in vitro* transcription with a T7 RNA polymerase (antisense) or SP6 RNA polymerase (sense) in the presence of <sup>35</sup>S-labelled UTP, according to the manufacturer's instructions (Ambion). The [<sup>35</sup>S]Grb10 riboprobe was diluted to 2 × 10<sup>7</sup> c.p.m. ml<sup>-1</sup> in a hybridization solution composed of 50% formamide, 20 mM Tris-HCl pH 7.5, 0.02% sheared single-stranded DNA (Sigma), 0.1% total yeast RNA (Sigma), 0.01% yeast tRNA (Gibco), 20% dextran sulphate, 0.3 M NaCl, 2 mM EDTA pH 8.0, Denhardt's solution (Sigma), 100 mM DTT, 0.2% SDS and 0.2% sodium thiosulphate (Sigma). Before hybridization, brain sections were fixed in 4% formaldehyde in DEPC-treated PBS for 20 min at 4 °C, dehydrated in ascending concentrations of ethanol, cleared in xylene for 15 min, rehydrated in descending concentrations of ethanol and permeabilized by heating in prewarmed sodium citrate buffer (95–100 °C, pH 6.0), before being dehydrated in ascending concentrations of ethanol, and air-dried. Hybridization solution (containing radiolabelled riboprobe) and a coverslip were applied to each slide, and sections were incubated for 12–16 h at 57 °C. After this time the coverslips were removed, and slides were washed with 2× sodium chloride/sodium citrate buffer (SSC). Sections were then incubated in 0.002% RNase A (Qiagen) for 30 min, followed by sequential washes in decreasing concentrations of SSC. The sections were dehydrated in ascending concentrations of ethanol with 0.3 M ammonium acetate (NH<sub>4</sub>OAc) followed by 100% ethanol. Slides were air-dried and placed in X-ray film cassettes with BMR-2 film (Kodak) for 72 h. Films were developed on an OPTIMAX X-ray film processor (Protec). Slides were subsequently dipped in photographic emulsion (GE Healthcare) and stored at 4 °C for 2 weeks before being developed in D-19 developer and fixer (Kodak).

**LacZ expression analysis.** Dissected embryos were fixed in 2% formaldehyde/0.2% glutaraldehyde in PBS for 2 h at room temperature, stained at 37 °C for approximately 2 h in freshly prepared X-gal solution<sup>31</sup>, post-fixed overnight at 4 °C using 4% paraformaldehyde in PBS, then cleared in 80% glycerol. Adult brains were longitudinally bisected and stained, as above, without fixation. For adult brain sections, animals were first perfused with chilled 9.25% (w/v) sucrose solution, followed by approximately 100 ml of chilled 3% paraformaldehyde in 0.1% PBS. Brains were sectioned at 50  $\mu$ m on a vibratome (VT1000S; Leica), with the tissue kept ice-cold. Free-floating sections were collected and immersed in X-gal staining solution at 28 °C overnight. *Grb10KO* samples were coetaneously stained alongside wild-type controls.

**$\beta$ -galactosidase immunohistochemistry.** Free floating 50- $\mu$ m sections from *Grb10KO* mice transcardially perfused with 4% paraformaldehyde were processed for immunohistochemistry analysis of  $\beta$ -galactosidase expression. Tissue was washed extensively in PBS and endogenous peroxidases quenched with a 30 min 0.3% H<sub>2</sub>O<sub>2</sub> incubation. Sections were blocked in 10% normal donkey serum, 0.5% BSA and 0.5% Tirtan-X 100 in PBS for 1 h at room temperature. The  $\beta$ -galactosidase antibody ( $\alpha$ -rabbit, Cappel) was diluted 1/10,000 in antibody buffer (1% normal donkey serum, 0.5% BSA and 0.5% Triton-X 100 in PBS) overnight at 4 °C. Sections were washed in PBS and a biotinylated donkey anti-rabbit secondary antibody (Vector Laboratories) applied at 1/1,000 in antibody buffer for 1 h at room temperature. Sections were then washed in PBS and incubated for 1 h at room temperature in Vectastain ABC Reagent (Vector Laboratories) according to the manufacturer's instructions. Chromogenic detection of positive labelling was conducted using 3,3'-diaminobenzidine (DAB) reagent (Vector Laboratories) according to the manufacturer's instructions. Sections were then rinsed extensively in PBS, mounted onto glass microscope slides, dehydrated along an ascending series of alcohol, cleared in xylene and coverslipped for viewing.

**Immunofluorescence histochemistry.** Brain sections (50  $\mu$ m) were collected from animals perfused with 4% paraformaldehyde and the sections post-fixed in 4% paraformaldehyde at 4 °C overnight before antibody staining, as described<sup>30</sup>. Adult brain sections were processed as described above with the exclusion of the hydrogen peroxide step. Primary antibodies were diluted as follows in antibody buffer:  $\beta$ -galactosidase ( $\alpha$ -rabbit, 1/500, Cappel), choline-acetyltransferase ( $\alpha$ -mouse, 1/1,000)<sup>32</sup>, dopamine transporter ( $\alpha$ -rat, 1/1000, Abcam), serotonin (1/1,000, Immunostar). Secondary antibodies (Alex Fluor, Molecular Probes) were diluted to 1/750 in antibody buffer and applied to the tissue for 1 h. Sections were then immediately viewed and images captured under a confocal microscope (Zeiss, LSM-510).

**Behavioural phenotyping.** Male wild-type and *Grb10KO*<sup>+/-p</sup> littermates between the ages of 10 and 12 months and *Grb10KO*<sup>ml/+</sup> at 3 months were tested. We note that although *Grb10KO*<sup>ml/+</sup> mice are a good genetic control for *Grb10KO*<sup>+/-p</sup> mice, their altered body size and proportions may confound behavioural comparisons with wild-type and *Grb10KO*<sup>+/-p</sup> littermates. Thus wild-type littermates were the preferred controls in most tests and the use of younger *Grb10KO*<sup>ml/+</sup> mice allowed body size to be better matched across all of the tested genotypes. Unless otherwise stated, tests were performed during daylight hours using socially housed animals that were removed from their home cages, and therefore isolated, only for the duration of each test. Where possible, tests and subsequent analyses were performed blind for animal genotype.

**Light/dark box.** Dimensions were 46 cm × 27 cm × 30 cm (length × breadth × height) with the dark compartment comprising one-third of the length. Animals were placed in the light compartment facing away from the dark side and allowed to explore freely for 10 min (*Grb10KO*<sup>+/+</sup> *n* = 16; *Grb10KO*<sup>+/-p</sup> *n* = 16).

**Open field test.** Arena diameter was 76 cm, with eight central and eight peripheral segments demarked with non-tactile paint. Animals were individually placed in the same segment facing towards the centre and allowed to explore freely for 10 min (*Grb10KO*<sup>+/+</sup> *n* = 15; *Grb10KO*<sup>+/-p</sup> *n* = 16).

**Locomotor activity (beam-break apparatus).** Animals were socially isolated and allowed to acclimatize to test cages/apparatus (Linton Instrumentation) for 1 week before analysis. Daytime (08:00–18:00) and night-time (19:00–05:00) readings were made on three consecutive days with data recorded in 5 min bins by a computer running AmlLogger software (Linton Instrumentation; *Grb10KO*<sup>+/+</sup> *n* = 15; *Grb10KO*<sup>+/-p</sup> *n* = 15).

**Assessment of olfaction.** Small squares of filter paper soaked with 10  $\mu$ l of vanilla extract or urine (collected from four 8-week-old F<sub>1</sub> females and pooled) were attached to one corner of the 14 test cages at a height that required animal rearing to be reached. Socially housed animals were placed in the test cage and allowed to explore freely for 2 min (*Grb10KO*<sup>+/+</sup> *n* = 8; *Grb10KO*<sup>+/-p</sup> *n* = 8). The time for each animal to touch its snout to the filter paper was recorded.

**Resident-intruder test.** Socially isolated *Grb10KO*<sup>+/-p</sup> animals (residents) were confronted with the introduction of a weight matched, socially housed wild-type male of the same genetic background (intruders). Each *Grb10KO*<sup>+/-p</sup> mutant was

assessed against three different wild-type animals on three consecutive days. Animals were allowed to explore freely for 10 min (*Grb10KO*<sup>+/+</sup> *n* = 8; *Grb10KO*<sup>+/-</sup> *n* = 8).

**Tube test.** Test apparatus comprised a 30-cm smooth, transparent acrylic tube with an internal diameter of 3.5 cm. Socially isolated *Grb10KO* animals were challenged with at least three different socially isolated wild-type animals on consecutive days. Animals were placed at opposite ends of the tube and released simultaneously. Losers were scored as those animals that retreated from the tube; a full retreat was determined by the absence of any paws within the tube. Tests in which crossing over or turning of animals occurred were not scored (*Grb10KO*<sup>+/+</sup> *n* = 7; *Grb10KO*<sup>+/-</sup> *n* = 8). Light/dark box, open field and resident-intruder tests were videotaped for analysis.

**Urinary odour habituation–dishabituation test.** The test protocol was adapted from Isles *et al.*<sup>33</sup> and took place in a Perspex testing arena divided into two equal-sized chambers and linked by a small opening. The arena was lit in low-level white light (15 lux). Male animals were habituated to the whole arena for 10 min (*Grb10KO*<sup>+/+</sup> *n* = 12; *Grb10KO*<sup>+/-</sup> *n* = 8). The test period was divided into four separate 5-min trials, with a gap of 2 min between each trial during which the test animals were placed in a separate holding cage. During a trial, 15 µl of urine was applied to a disc of filter paper in one of the two chambers (alternated between subjects). This was secured to the arena floor with a 4-cm plastic washer, but the test animal could have contact with the urine. Contact with the urine was deemed important as both volatile and involatile urinary cues are thought to be important for recognition<sup>34</sup>. The animal was placed in the chamber not containing the urine, and the time an animal spent in either chamber and investigated the odour cue itself was measured using Ethovision software (Noldus) linked to a digital camera. Several other measures indicative of locomotor activity were also obtained. In trials 1–3 the same odour cue was presented (habituation); however, in trial 4, urine from a different individual animal, of differing background strain, was presented (dishabituation). The urine was collected from individual female mice, and within any given test the two odour cues were matched for oestrus cycle, which was determined by vaginal smear<sup>33</sup>.

**Neurochemical analysis.** Animals were killed by exposure to a rising concentration of carbon dioxide and cervical dislocation (*Grb10KO*<sup>+/+</sup> *n* = 5; *Grb10KO*<sup>+/-</sup> *n* = 5). The brains were rapidly removed and dissected according to four key regions of interest: the frontal cortex, striatum, hypothalamus and brainstem. Tissue aliquots were derived from both hemispheres and homogenized in 200 µl of 0.2 M perchloric acid by an ultrasonic cell disruptor (Microson). Levels of noradrenaline, dopamine, 5-hydroxytryptamine and acetylcholine and associated metabolites (DOPAC and 5HIAA) were determined in the supernatant by reversed-phase, high-performance liquid chromatography (HPLC), as described

previously<sup>35</sup>. Levels of ACh were assessed by microbore HPLC with an acetylcholinesterase/choline oxidase IMER and a wired peroxidase glassy carbon electrode<sup>36</sup>. **Statistical analyses.** Body and organ weights (Fig. 1h, i) were analysed using one-way ANOVA with Tukey's post-hoc test. Stomach weights (Fig. 1j), HPLC analysis of neurotransmitter levels (Supplementary Fig. 6) and most of the behavioural tests (Supplementary Fig. 1a–h) were analysed using the two-tailed Student's *t*-test. *Grb10KO* survival and whisker barbering were analysed using  $\chi^2$  tests.

Non-parametric statistical analysis assessed the significance of winning tendency in the tube test (Fig. 3a) and was based on assigning a +1 value for animals that won more than 50% of their bouts, –1 for animals that lost more than 50% of their bouts and 0 for those animals that won as many as they lost. Next, the net effect of each genotype was determined by addition of the individual scores (+/+ = –4, +/- = +4) and the difference between the genotypes calculated from the difference between these summed values (+8). The same number of animals tested in reality (*Grb10KO*<sup>+/+</sup> *n* = 7, *Grb10KO*<sup>+/-</sup> *n* = 8) was used to run 100,000 randomizations so as to estimate significance of the observed data, by estimating how commonly, if the null of no difference between genotypes was correct, we would expect to see a deviation as large as or larger than that observed. In each randomization the number of winners, losers and neutrals was held constant, the same as in the observed data, with the first seven results assigned to a pseudo-wild-type class and the last eight to a pseudo-*Grb10KO*<sup>+/-</sup> class. We asked, across these 100,000 randomizations, whether a difference of +8 or greater was seen between the summed genotypic scores. Three thousand one hundred and thirty-seven randomizations with a difference of +8 or greater were observed. If this value is assigned as *r* and *N* is the number of randomizations (in this case 100,000), then the unbiased estimator of  $P = r + 1/N + 1$ .

For the urinary odour habituation–dishabituation test (Fig. 3d, e), a repeated-measure ANOVA determined an interaction between odour and genotype.

31. Ainscough, J. F. *et al.* Imprinting of Igf2 and H19 from a 130 kb YAC transgene. *Development* **124**, 3621–3632 (1997).
32. Morales, M. A. *et al.* Localization of choline acetyltransferase in rat peripheral sympathetic neurons and its coexistence with nitric oxide synthase and neuropeptides. *Proc. Natl Acad. Sci. USA* **92**, 11819–11823 (1995).
33. Isles, A. R. *et al.* Urinary odour preferences in mice. *Nature* **409**, 783–784 (2001).
34. Nevison, C. M. *et al.* The ownership signature in mouse scent marks is involatile. *Proc. R. Soc. Lond. B* **270**, 1957–1963 (2003).
35. Doe, C. M. *et al.* Loss of the imprinted snoRNA mbii-52 leads to increased 5htr2c pre-RNA editing and altered 5HT2CR-mediated behaviour. *Hum. Mol. Genet.* **18**, 2140–2148 (2009).
36. Dalley, J. W. *et al.* Distinct changes in cortical acetylcholine and noradrenaline efflux during contingent and noncontingent performance of a visual attentional task. *J. Neurosci.* **21**, 4908–4914 (2001).

# Exome sequencing identifies frequent mutation of the SWI/SNF complex gene *PBRM1* in renal carcinoma

Ignacio Varela<sup>1</sup>, Patrick Tarpey<sup>1</sup>, Keiran Raine<sup>1</sup>, Dachuan Huang<sup>2</sup>, Choon Kiat Ong<sup>2</sup>, Philip Stephens<sup>1</sup>, Helen Davies<sup>1</sup>, David Jones<sup>1</sup>, Meng-Lay Lin<sup>1</sup>, Jon Teague<sup>3</sup>, Graham Bignell<sup>1</sup>, Adam Butler<sup>1</sup>, Juok Cho<sup>1</sup>, Gillian L. Dalgliesh<sup>1</sup>, Danushka Galappaththige<sup>1</sup>, Chris Greenman<sup>1</sup>, Claire Hardy<sup>1</sup>, Mingming Jia<sup>1</sup>, Calli Latimer<sup>1</sup>, King Wai Lau<sup>1</sup>, John Marshall<sup>1</sup>, Stuart McLaren<sup>1</sup>, Andrew Menzies<sup>1</sup>, Laura Mudie<sup>1</sup>, Lucy Stebbings<sup>1</sup>, David A. Largaespada<sup>3</sup>, L. F. A. Wessels<sup>4</sup>, Stephane Richard<sup>5,6</sup>, Richard J. Kahnoski<sup>7</sup>, John Anema<sup>7</sup>, David A. Tuveson<sup>8</sup>, Pedro A. Perez-Mancera<sup>8</sup>, Ville Mustonen<sup>9</sup>, Andrej Fischer<sup>9,10</sup>, David J. Adams<sup>11</sup>, Alistair Rust<sup>11</sup>, Waraporn Chan-on<sup>2</sup>, Chutima Subimerb<sup>2</sup>, Karl Dykema<sup>12</sup>, Kyle Furge<sup>12</sup>, Peter J. Campbell<sup>1</sup>, Bin Tean Teh<sup>2,13,14</sup>, Michael R. Stratton<sup>1,15</sup> & P. Andrew Futreal<sup>1</sup>

The genetics of renal cancer is dominated by inactivation of the *VHL* tumour suppressor gene in clear cell carcinoma (ccRCC), the commonest histological subtype. A recent large-scale screen of ~3,500 genes by PCR-based exon re-sequencing identified several new cancer genes in ccRCC including *UTX* (also known as *KDM6A*)<sup>1</sup>, *JARID1C* (also known as *KDM5C*) and *SETD2* (ref. 2). These genes encode enzymes that demethylate (*UTX*, *JARID1C*) or methylate (*SETD2*) key lysine residues of histone H3. Modification of the methylation state of these lysine residues of histone H3 regulates chromatin structure and is implicated in transcriptional control<sup>3</sup>. However, together these mutations are present in fewer than 15% of ccRCC, suggesting the existence of additional, currently unidentified cancer genes. Here, we have sequenced the protein coding exome in a series of primary ccRCC and report the identification of the SWI/SNF chromatin remodelling complex gene *PBRM1* (ref. 4) as a second major ccRCC cancer gene, with truncating mutations in 41% (92/227) of cases. These data further elucidate the somatic genetic architecture of ccRCC and emphasize the marked contribution of aberrant chromatin biology.

Exome sequencing based on a solution phase capture approach<sup>5</sup> was performed on seven cases of ccRCC, three of which carry *VHL* mutations, and matching normal DNAs (See Supplementary Information and Supplementary Table 1). Captured material was sequenced using 76 base pair paired-end reads on the Illumina GAIIX platform. After read alignment, variant calling was performed using a naive Bayesian classifier algorithm for substitutions and a split-read mapping approach (PinDel<sup>6</sup> with substantial cancer-aware output filtering) for insertion/deletions (See Supplementary Material for details). These algorithms aim to identify somatically acquired coding and splice-site variants (that is, present in the tumour but not in the matching normal), and all mutations reported here were confirmed by PCR-based capillary sequencing. In total 156 somatic mutations were identified, of which 92 were missense, 9 nonsense, 1 canonical splice site, 1 stop codon read-through, 11 frameshift and 42 synonymous (Supplementary Table 2).

In four cases truncating mutations were identified in *PBRM1*. *PBRM1* maps to chromosome 3p21 and encodes the BAF180 protein, the chromatin targeting subunit of the PBAF SWI/SNF chromatin remodelling complex<sup>7</sup>. The gene is comprised of six bromodomains involved in binding acetylated lysine residues on histone tails, two bromo-adjacent homology domains important in protein–protein

interaction and an HMG DNA-binding domain<sup>4</sup>. PBAF complex-mediated chromatin remodelling is implicated in replication, transcription, DNA repair and control of cell proliferation/differentiation<sup>4,7</sup>. The *SMARCB1* and *BRG1* components of this complex have inactivating mutations in rhabdoid tumours<sup>8,9</sup> and *BRG1* mutations have been reported in several tumour types<sup>10</sup>. The *PBRM1* mutations included three frame-shifting insertions and a nonsense mutation; all judged to be homozygous from SNP array and mutant allele read count data. *PBRM1* was not included in our previous PCR-based sequencing screen<sup>2</sup> and was the only gene, apart from *VHL*, with recurrent truncating mutations in the seven cases screened. We next sequenced *PBRM1* in a further 257 RCC cases, including 36 cases of papillary, chromophobe and other non-ccRCC cancers. Truncating mutations were identified in a remarkable 88/257 (34%) (Fig. 1) of cases, all diagnosed as ccRCC (for full data see Supplementary Tables 3 and 4). *PBRM1* mutations were all found in the context of chromosome 3p loss of heterozygosity (38/38) where SNP array data was available (<http://www.sanger.ac.uk/cgi-bin/genetics/CGP/cghviewer/CghHome.cgi>). Two in-frame deletion mutations were identified—a predicted 6-amino-acid deletion (p.M1209\_E1214delMFYKKE) in the second BAH (bromo-adjacent homology) domain likely to be involved in protein–protein interactions within the SWI/SNF complex<sup>4</sup> and deletion of an isoleucine codon (Ile 57) in the first bromodomain (Fig. 1). Both deletions remove amino acids conserved to *Caenorhabditis elegans* and both were in cases with 3p LOH. The ratio of nine missense to zero silent mutations suggests that a proportion of the missense mutations are likely to be pathogenic. Six of nine missense mutations occur in bromodomains and one in the second BAH domain (Fig. 1).

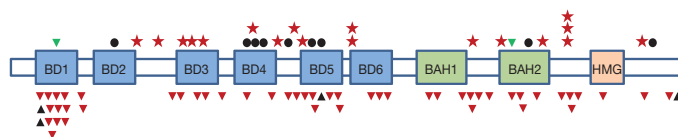


**Figure 1 | *PBRM1* somatic mutations.** Representation of *PBRM1* transcript with boxes BD1–BD6, BAH1, BAH2 and HMG indicating the positions of the bromodomains 1–6, bromo-adjacent homology domains and high-mobility group domain, respectively. Relative positions of mutations are indicated by symbols. Stars, nonsense; dots, missense; red triangles, frameshift deletions; black triangles, frameshift insertions; and green triangles, in-frame deletions. Splice-site mutations are not depicted.

<sup>1</sup>Cancer Genome Project, Wellcome Trust Sanger Institute, Hinxton CB10 1SA, UK. <sup>2</sup>NCCS-VARI Translational Research Laboratory, National Cancer Centre Singapore, 11 Hospital Drive, 169610, Singapore. <sup>3</sup>Masonic Cancer Center, University of Minnesota, Minneapolis, Minnesota 55455, USA. <sup>4</sup>Bioinformatics and Statistics, Department of Molecular Biology, The Netherlands Cancer Institute, Plesmanlaan 121, 1066 CX Amsterdam, The Netherlands. <sup>5</sup>Génétique Oncologique EPHE-INSEEM U753, Faculté de Médecine Paris-Sud and Institut de Cancérologie Gustave Roussy, 94805 Villejuif, France. <sup>6</sup>Centre Expert National Cancer Rares INCA “PREDIR”, Service d’Urologie, Hôpital de Bicêtre, AP-HP, 94276 Le Kremlin-Bicêtre, France. <sup>7</sup>Department of Urology, Spectrum Health Hospital, Grand Rapids, Michigan 49503, USA. <sup>8</sup>Li Ka Shing Centre, Cambridge Research Institute, Cancer Research UK, Robinson Way, Cambridge CB2 0RE, UK. <sup>9</sup>Bioinformatics, Wellcome Trust Sanger Institute, Hinxton CB10 1SA, UK. <sup>10</sup>Institut für Theoretische Physik, Universität zu Köln, Zùlpicherstrasse 77, 50937 Köln, Germany. <sup>11</sup>Experimental Cancer Genetics, Wellcome Trust Sanger Institute, Hinxton CB10 1SA, UK. <sup>12</sup>Laboratory of Computational Biology, Van Andel Research Institute, Grand Rapids, Michigan 49503, USA. <sup>13</sup>Laboratory of Cancer Therapeutics, DUKE-NUS Graduate Medical School, Singapore. <sup>14</sup>Laboratory of Cancer Genetics, Van Andel Research Institute, Grand Rapids, Michigan, 49503, USA. <sup>15</sup>Institute of Cancer Research, Sutton, Surrey SM2 5NG, UK.

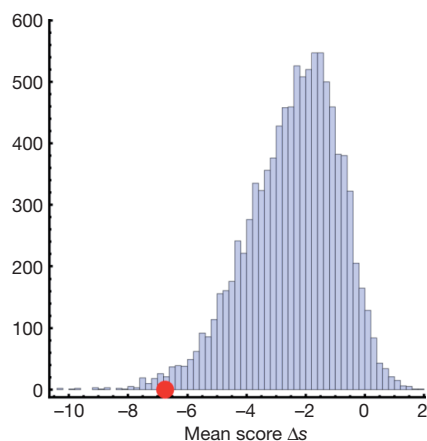


**Figure 2 | Analysis of *PBRM1* missense mutations.** Bars represent histogram of the mean score of *in silico* generated random missense mutations (10,000 sets of three mutations that can be scored) and the red disk denotes the mean score of the somatic mutations that could be scored (T232P  $\Delta s = -7.78$ , A597D  $\Delta s = -9.69$ , H1204P  $\Delta s = -2.76$ ). The somatic set is significantly different from the null set ( $P$ -value = 0.01). They have a higher negative mean score and are thus predicted to be more deleterious on average.

The bromodomains of *PBRM1* have been shown to have preferential binding to different acetylated lysine configurations of histone tails, indicating they may contribute to 'reading' of the histone code<sup>11</sup>. The likelihood of the missense mutations having functional impact was assessed using a scoring system calibrated with protein domain alignments from Pfam (see Supplementary Methods). Three missense mutations (p.T232P, p.A597D and p.H1204P) could be scored with these alignments. This set of mutations was predicted to be deleterious, having a significantly lower mean score than a typical null set of *in silico* generated random missense mutations falling onto the scorable parts of the gene ( $P$ -value = 0.01 Fig. 2), making these mutations interesting candidates for functional studies.

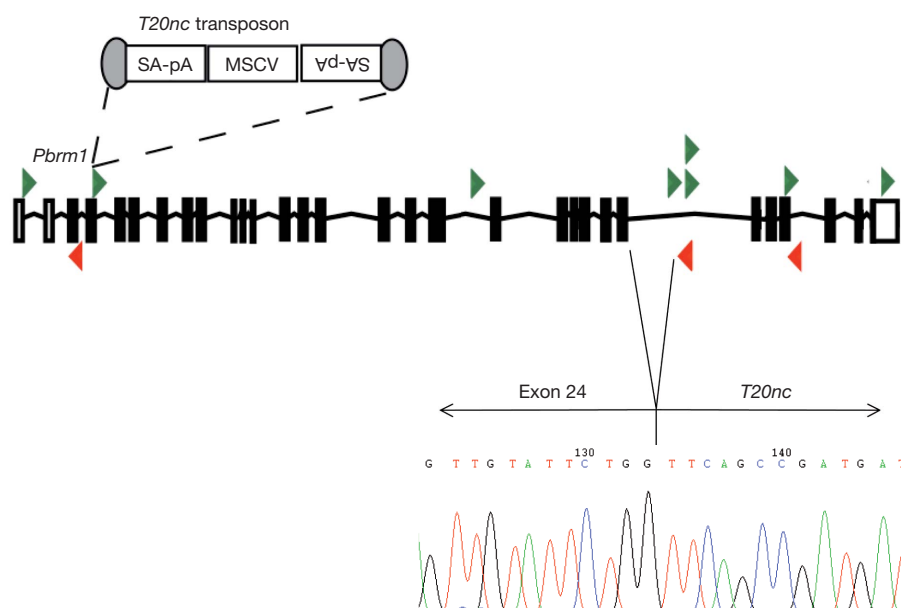


**Figure 3 | *Pbrm1* is frequently mutated in a mouse model of pancreatic cancer.** To identify genes that co-operate with *Kras* in the formation of pancreatic cancer a conditional allele of *Kras*<sup>G12D</sup> and *Pdx1*-Cre were combined with a conditional *Sleeping Beauty* transposase driver and the *T20nc*<sup>8</sup> transposon donor allele<sup>29</sup>. Expression of Cre results in expression of *Kras*<sup>G12D</sup> and transposon mobilization within the epithelial compartment of the pancreas. Isolation of the transposon insertion sites from a panel of 153 pancreatic cancers and pre-neoplastic lesions generated from this model

Four *PBRM1* truncating mutations have been described in breast cancer previously<sup>12</sup>. Although there is frequent 3p21 LOH in small-cell lung cancer, no evidence for *PBRM1* inactivation was found<sup>13</sup>. To further evaluate the contribution of *PBRM1* mutation in human cancer, copy number was evaluated and the coding exons were sequenced through a series of 727 cancer cell lines of various histologies. SNP array copy number analysis (<http://www.sanger.ac.uk/cgi-bin/genetics/CGP/cghviewer/CghHome.cgi>) identified one homozygous deletion in the HCC-1143 breast cancer cell line, described previously<sup>12</sup>. Sequencing analysis identified five homozygous truncating mutations (Supplementary Table 5). Frame-shifting deletions were identified in the *VHL*-mutant A704 renal cancer, NCI-H2196 small-cell lung cancer and TGBC24TKB gall bladder cancer lines. Nonsense mutations were identified in the NCI-H226 squamous-cell lung cancer and PANC-10-05 pancreatic adenocarcinoma lines. Interestingly, a *PBRM1* truncating mutation has been reported in a comprehensive pancreatic cancer mutational screen<sup>14</sup>.

To obtain further support that *PBRM1* can act as a cancer gene, we examined data from several insertional mutagenesis screens in mice. Analyses of transposon insertion sites from a forward genetic screen performed using a conditional *Sleeping Beauty* transposon system<sup>15</sup> in a mouse pancreatic cancer model<sup>16</sup> revealed a significant enrichment of insertion events in *Pbrm1* amongst all genes hit using Monte Carlo simulation analyses as described previously<sup>17</sup>. Insertions were found in pancreatic dysplasia, intraductal (panIN) and high grade invasive tumours, indicating *Pbrm1* inactivation is an early event in this model. The mixed forward and reverse pattern of insertions is indicative of inactivation, as demonstrated by RT-PCR showing premature termination of the *Pbrm1* cDNA via splicing into the inserted transposon (Fig. 3). These data suggest that loss of *Pbrm1* cooperates with *Kras* in driving pancreatic tumour development in this model. Intriguingly, *Setd2*, previously implicated human ccRCC, was also found to rank significantly in frequency among all insertion sites and two tumours had both *Setd2* and *Pbrm1* insertions. These comparative oncogenic data provide independent support for *PBRM1* as a cancer gene

revealed a common insertion site in *Pbrm1* suggesting that loss of *Pbrm1* co-operates with *Kras*<sup>G12D</sup> in pancreatic cancer development. Statistical analysis was performed as described previously<sup>30</sup>. Transposon insertions in the forward strand of *Pbrm1* are shown in green. Insertions in the reverse orientation are shown in red. A chromatogram from sequencing of RT-PCR products from one tumour is shown demonstrating splicing of exon 24 of *Pbrm1* into the inserted transposon, thus truncating the transcript.

and suggest further investigation of the role of *PBRM1* (and *SETD2*) in human pancreatic cancer is warranted.

Abrogation of *PBRM1* expression via small interfering RNA (siRNA) knockdown in ccRCC cell lines was investigated to assess possible consequences of *PBRM1* loss. Greater than 60% knockdown of *PBRM1* RNA and protein resulted in a significant increase in proliferation 4/5 RCC lines (Fig. 4a, b and Supplementary Information). No effect was seen, however, in A704 which carries a homozygous truncating *PBRM1* mutation and expresses no *PBRM1*, confirming the specificity of the assay. Further, knockdown of *PBRM1* resulted in significantly increased colony formation in soft-agar and increased cell migration (Fig. 4c, d), indicative of an increase in transformed phenotype. Taken together, these data support *PBRM1* having a tumour suppressor role in ccRCC.

Transcriptional profiling before and after *PBRM1* knockdown was performed using gene expression microarrays. Gene set enrichment analysis following *PBRM1* knockdown showed that *PBRM1* activity regulates pathways associated with chromosomal instability and cellular proliferation (Fig. 4e and Supplementary Table 6), the latter being consistent with previous studies identifying *PBRM1* as critical transcriptional regulator of p21 (also known as *CDKN1A*) in breast cancer cell lines<sup>12</sup> and work showing that *PBRM1* is implicated in regulating TP53-mediated replicative senescence<sup>18</sup>. The PBAF complex has been shown to localize at kinetochores during mitosis<sup>19</sup> and *SMARCB1* has been implicated in spindle checkpoint control<sup>20</sup>, which would support the loss of *PBRM1* giving rise to a chromosomal instability/spindle checkpoint expression phenotype. It may be of interest to explore further spindle checkpoint control in *PBRM1*-mutated ccRCC as a potential therapeutic opportunity.

Previous work has demonstrated that *VHL* loss alone is insufficient for ccRCC tumorigenesis, arguing the need for additional genetic events<sup>21,22</sup> (B. T. Teh, unpublished) and has further suggested the existence of a 3p21 'gatekeeper' ccRCC mutation on the basis of LOH studies<sup>23</sup>. The data presented here strongly suggest that inactivation of *PBRM1* comprises this second major mutation in ccRCC development. Nearly all (36/38) *PBRM1* mutant cases fall into the hypoxia signature group as described previously<sup>2</sup>, including 13/14 cases without demonstrable *VHL* point mutations where expression data are available—further indicating the importance of *PBRM1* in typical ccRCC development. The SWI/SNF complex has been implicated in the normal cellular response to hypoxia, with impairment of the complex rendering cells resistant to hypoxia-induced cell cycle arrest<sup>24</sup>, which would be consistent with selection for frequent loss of *PBRM1* in ccRCC. Multiple cancers have apparently concomitant *VHL*, *PBRM1* and *SETD2* mutations, with all three genes mapping to chromosome 3p, indicating that the mutations are non-redundant functionally. Half (55/107) of cases in this series with a demonstrable *VHL* mutation<sup>2</sup> have a *PBRM1* mutation. Strikingly, all nine cases with a *SETD2* mutation have a mutation in either *PBRM1* or *VHL*, with 6 of 9 cases having mutations in all three genes. Physical linkage of these three ccRCC cancer genes together with their potential interaction may be the key driver for the large scale 3p LOH seen in most cases of ccRCC—being particularly parsimonious in requiring only four genetic events to unmask three tumour suppressor genes as opposed to six if the genes were on different chromosomes.

Several other mutated genes of potential interest were identified. In particular, *ARID1A* encoding the BAF250A subunit of the SWI/SNF complex was found to have two heterozygous missense mutations:

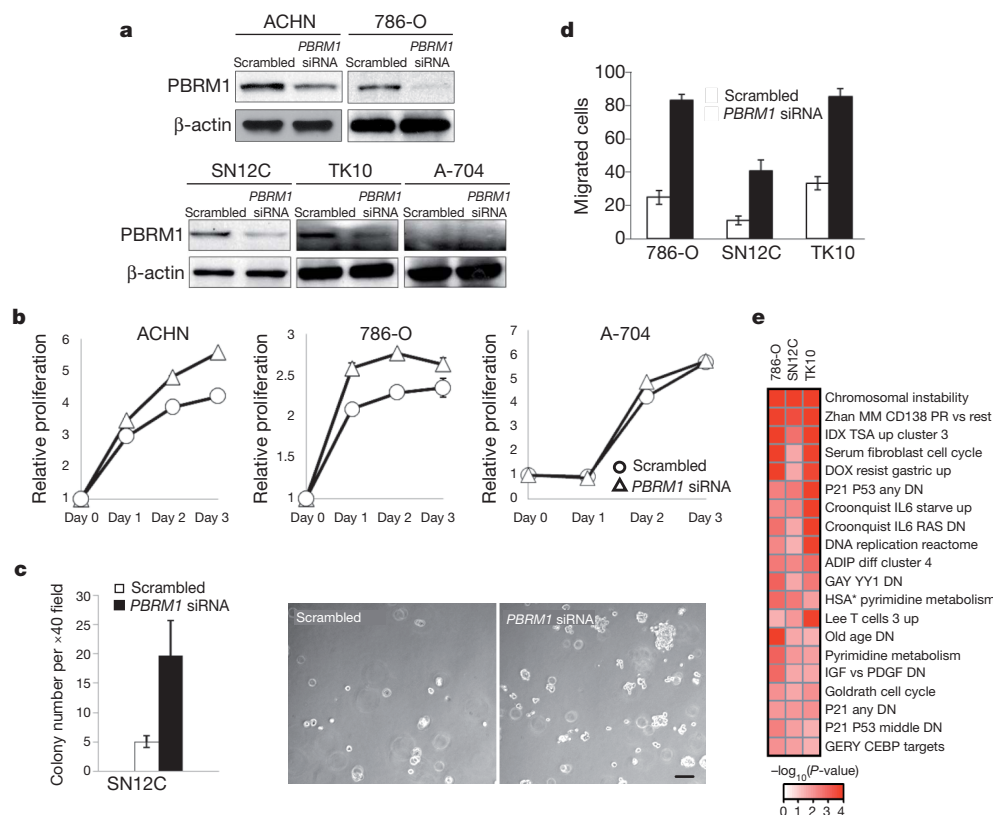


**Figure 4 | Knockdown of *PBRM1* expression in RCC cell lines.**

**a**, Verification of *PBRM1* knockdown by western blotting. **b**, Silencing *PBRM1* increased the proliferation of ACHN and 786-O with wild-type *PBRM1*, but not A704 with a homozygous *PBRM1* truncating mutation. Data represent means of triplicate experiments with standard deviation,  $P < 0.01$ .

**c**, Knockdown of *PBRM1* enhanced colony formation in SN12C cells. Data represent means of triplicate experiments with standard deviation,  $P < 0.01$ .

Scale bar, 100  $\mu$ m. **d**, Knockdown of *PBRM1* enhanced cell migration in 786-O, SN12C and TK10 cells. Data represent means of triplicate experiments with standard deviation,  $P < 0.01$ . **e**, Gene sets that are most significantly deregulated following *PBRM1* knockdown in three RCC cell lines using curated gene sets obtained from MSigDB (<http://www.broadinstitute.org/gsea/msigdb/>) and additional curated gene sets obtained from the PGSEA package (see Supplementary Information for details).

p.R1020K,c.3059G>A and p.L1872P,c.5615T>C. Both cases (PD2126, PD2127) have a PBRM1 truncating mutation. Two homozygous *ARID1A* deletions were found in SNP 6.0 data (<http://www.sanger.ac.uk/cgi-bin/genetics/CGP/conan/search.cgi>) in the LB1047-RCC ccRCC and NCI-SNU-5 gastric carcinoma cell lines and loss of *ARID1A* expression has been reported in RCC<sup>25</sup>. Frequent truncating *ARID1A* mutations have recently been reported in clear cell ovarian carcinoma<sup>26,27</sup>. These data all point to *ARID1A* being a cancer gene, likely to be operative in ccRCC. PD2127 was also found to have a heterozygous truncating mutation in *ARID5B*, related to *ARID1A* and recently implicated in childhood acute lymphoblastic leukaemia susceptibility<sup>28</sup>. The extent to which the other mutated genes identified here contribute to ccRCC will await large-scale follow-up screens. Similarly, exome and whole genome sequencing on a large number of cases is likely to yield further insights.

The identification of a second major cancer gene in ccRCC further defines the genetic and molecular architecture of this tumour type. It is remarkable that *PBRM1*, like the majority of the other non-VHL mutated cancer genes identified in ccRCC, is involved in chromatin regulation—again at least in part at the level of histone H3 modification and recognition. Understanding the contribution of *PBRM1* mutation to clinical disease progression and outcome as well the potential for exploiting SWI/SNF complex abrogation therapeutically are important future areas of renal cancer research.

## METHODS SUMMARY

DNA samples from ccRCC patients tumour and matching normal were all obtained under local IRB and LREC approvals for this study and processed as described previously<sup>2</sup>. DNA fragmentation, library preparation and solution phase hybrid capture were according to manufacturer instructions (Agilent Technologies) and modified from protocols published previously<sup>3</sup>. Capillary-based Sanger sequencing for confirmations and *PBRM1* follow-up were done as described previously<sup>2</sup> with manual inspection of all sequencing traces. mRNA was extracted from snap-frozen mouse pancreatic lesions and subjected to RT-PCR using a nested PCR approach using primers of mouse *Pbrm1* exon 23/24 and the Carp- $\beta$ -Actin Splice acceptor sequence of the T2Onc transposon cassette. Resulting bands were gel-purified and subjected to capillary-based Sanger sequencing. *PBRM1* or scrambled control siRNAs (Santa Cruz) were transfected into ccRCC cell lines using Lipofectamine 2000 (Invitrogen) according to the manufacturer's conditions. Real-time PCR and western blotting were all done using standard protocols essentially as described<sup>1</sup>. Expression analyses were carried out as described previously<sup>2</sup>.

Received 28 July; accepted 2 November 2010.

Published online 19 January 2011.

- van Haaften, G. *et al.* Somatic mutations of the histone H3K27 demethylase gene *UTX* in human cancer. *Nature Genet.* **41**, 521–523 (2009).
- Dagliesh, G. L. *et al.* Systematic sequencing of renal carcinoma reveals inactivation of histone modifying genes. *Nature* **463**, 360–363 (2010).
- Kouzarides, T. Chromatin modifications and their function. *Cell* **128**, 693–705 (2007).
- Thompson, M. Polybromo-1: the chromatin targeting subunit of the PBAF complex. *Biochimie* **91**, 309–319 (2009).
- Gnirke, A. *et al.* Solution hybrid selection with ultra-long oligonucleotides for massively parallel targeted sequencing. *Nature Biotechnol.* **27**, 182–189 (2009).
- Ye, K., Schulz, M. H., Long, Q., Apweiler, R. & Ning, Z. Pindel: a pattern growth approach to detect break points of large deletions and medium sized insertions from paired-end short reads. *Bioinformatics* **25**, 2865–2871 (2009).
- Reisman, D., Glaros, S. & Thompson, E. A. The SWI/SNF complex and cancer. *Oncogene* **28**, 1653–1668 (2009).
- Schneppenheimer, R. *et al.* Germline nonsense mutation and somatic inactivation of *SMARCA4/BRG1* in a family with rhabdoid tumor predisposition syndrome. *Am. J. Hum. Genet.* **86**, 279–284 (2010).
- Versteeg, I. *et al.* Truncating mutations of hSNF5/INI1 in aggressive paediatric cancer. *Nature* **394**, 203–206 (1998).
- Wong, A. K. C. *et al.* *BRG1*, a component of the SWI-SNF complex, is mutated in multiple human tumor cell lines. *Cancer Res.* **60**, 6171–6177 (2000).
- Chandrasekaran, R. & Thompson, M. Polybromo-1-bromodomains bind histone H3 at specific acetyl-lysine positions. *Biochem. Biophys. Res. Commun.* **355**, 661–666 (2007).
- Xia, W. *et al.* BAF180 is a critical regulator of p21 induction and a tumor suppressor mutated in breast cancer. *Cancer Res.* **68**, 1667–1674 (2008).

- Sekine, I. *et al.* The 3p21 candidate tumor suppressor gene BAF180 is normally expressed in human lung cancer. *Oncogene* **24**, 2735–2738 (2005).
- Jones, S. *et al.* Core signaling pathways in human pancreatic cancers revealed by global genomic analyses. *Science* **321**, 1801–1806 (2008).
- Keng, V. W. *et al.* A conditional transposon-based insertional mutagenesis screen for genes associated with mouse hepatocellular carcinoma. *Nature Biotechnol.* **27**, 264–274 (2009).
- Hingorani, S. R. *et al.* Preinvasive and invasive ductal pancreatic cancer and its early detection in the mouse. *Cancer Cell* **4**, 437–450 (2003).
- Starr, T. K. *et al.* A transposon-based genetic screen in mice identifies genes altered in colorectal cancer. *Science* **323**, 1747–1750 (2009).
- Burrows, A. E., Smogorzewska, A. & Elledge, S. J. Polybromo-associated BRG1-associated factor components BRD7 and BAF180 are critical regulators of p53 required for induction of replicative senescence. *Proc. Natl Acad. Sci. USA* **107**, 14280–14285 (2010).
- Xue, Y. *et al.* The human SWI/SNF-B chromatin-remodeling complex is related to yeast Rsc and localizes at kinetochores of mitotic chromosomes. *Proc. Natl Acad. Sci. USA* **97**, 13015–13020 (2000).
- Vries, R. G. J. *et al.* Cancer-associated mutations in chromatin remodeler hSNF5 promote chromosomal instability by compromising the mitotic checkpoint. *Genes Dev.* **19**, 665–670 (2005).
- Mandriota, S. J. *et al.* HIF activation identifies early lesions in VHL kidneys: evidence for site-specific tumor suppressor function in the nephron. *Cancer Cell* **1**, 459–468 (2002).
- Young, A. P. *et al.* VHL loss actuates a HIF-independent senescence programme mediated by Rb and p400. *Nature Cell Biol.* **10**, 361–369 (2008).
- Clifford, S. C., Prowse, A. H., Affara, N. A., Buys, C. H. C. M. & Maher, E. R. Inactivation of the von Hippel-Lindau (VHL) tumour suppressor gene and allelic losses at chromosome arm 3p in primary renal cell carcinoma: evidence for a VHL-independent pathway in clear cell renal tumorigenesis. *Genes Chromosom. Cancer* **22**, 200–209 (1998).
- Kenneth, N. S., Mudie, S., van Uden, P. & Rocha, S. SWI/SNF regulates the cellular response to hypoxia. *J. Biol. Chem.* **284**, 4123–4131 (2009).
- Wang, X. *et al.* Expression of p270 (ARID1A), a component of human SWI/SNF complexes, in human tumors. *Int. J. Cancer* **112**, 636–642 (2004).
- Jones, S. *et al.* Frequent mutations of chromatin remodeling gene *ARID1A* in ovarian clear cell carcinoma. *Science* **330**, 228–231 (2010).
- Wiegand, K. C. *et al.* *ARID1A* mutations in endometriosis-associated ovarian carcinomas. *N. Engl. J. Med.* **363**, 1532–1543 (2010).
- Papaemmanuil, E. *et al.* Loci on 7p12.2, 10q21.2 and 14q11.2 are associated with risk of childhood acute lymphoblastic leukemia. *Nature Genet.* **41**, 1006–1010 (2009).
- Collier, L. S., Carlson, C. M., Ravimohan, S., Dupuy, A. J. & Largaespada, D. A. Cancer gene discovery in solid tumours using transposon-based somatic mutagenesis in the mouse. *Nature* **436**, 272–276 (2005).
- Uren, A. G. *et al.* Large-scale mutagenesis in *p19<sup>ARF</sup>*- and *p53*-deficient mice identifies cancer genes and their collaborative networks. *Cell* **133**, 727–741 (2008).

**Supplementary Information** is linked to the online version of the paper at [www.nature.com/nature](http://www.nature.com/nature).

**Acknowledgements** P.A.F. and M.R.S. would like to acknowledge the Wellcome Trust for support under grant reference 077012/Z/05/Z and A. Coffey, D. Turner and L. Mamanova for assistance with the exon capture. K.F., K.D. and B.T.T. acknowledge the support of the Van Andel Research Institute. B.T.T. would like to acknowledge support from the Lee Foundation. I.V. is supported by a fellowship from The International Human Frontier Science Program Organization. D.J.A. acknowledges the support of Cancer Research UK. D.A.T. and P.A.P.-M. acknowledge the support of the University of Cambridge, Cancer Research UK and Hutchison Whampoa and thank W. Howatt, A. Hazelhurst and colleagues in the CRI core facilities for their support. B.T.T. would like to dedicate this work to Tat Hock Teh.

**Author Contributions** I.V. and P.T. performed the main analytical aspects of the study. P.S., H.D., G.L.D., M.-L.L., G.B., C.H., L.M., S.M. performed the follow-up sequencing and analyses. K.R., D.J., J.T., A.B., C.G., D.G., M.J., C.L., J.M., A.M., L.S. contributed to the data processing, mapping and variant calling informatics. C.G. and K.W.L. performed statistical analyses. S.R., R.J.K., J.A. contributed samples and data for the clinical series. D.J.A., A.R., D.A.L., L.F.A.W., D.A.T., P.A.P.-M. performed the transposon screening and analyses. D.H., C.K.O., W.C., C.S. performed the siRNA and functional work. V.M., A.F. performed the missense mutation analysis. K.D., K.F. and J.C. performed the expression analyses. P.J.C., B.T.T., M.R.S., P.A.F. directed the study and wrote the manuscript, which all authors have approved.

**Author Information** Exome sequence data have been deposited at the European Genome-Phenome Archive (<http://www.ebi.ac.uk/ega/>) hosted by the European Bioinformatics Institute under accession EGAS00001000006 and expression data has been deposited with Gene Expression Omnibus (<http://www.ncbi.nlm.nih.gov/geo/>) under accession GEO22316. Reprints and permissions information is available at [www.nature.com/reprints](http://www.nature.com/reprints). The authors declare no competing financial interests. Readers are welcome to comment on the online version of this article at [www.nature.com/nature](http://www.nature.com/nature). Correspondence and requests for materials should be addressed to B.T.T. (Bin.Teh@vai.org), M.R.S. (mrs@sanger.ac.uk) or P.A.F. (paf@sanger.ac.uk).

# Bifidobacteria can protect from enteropathogenic infection through production of acetate

Shinji Fukuda<sup>1,2</sup>, Hidehiro Toh<sup>3</sup>, Koji Hase<sup>1</sup>, Kenshiro Oshima<sup>4</sup>, Yumiko Nakanishi<sup>1,2,5</sup>, Kazutoshi Yoshimura<sup>6</sup>, Toru Tobe<sup>7</sup>, Julie M. Clarke<sup>8</sup>, David L. Topping<sup>8</sup>, Tohru Suzuki<sup>9</sup>, Todd D. Taylor<sup>3</sup>, Kikui Itoh<sup>6</sup>, Jun Kikuchi<sup>2,5,10</sup>, Hidetoshi Morita<sup>11</sup>, Masahira Hattori<sup>4</sup> & Hiroshi Ohno<sup>1,2,12</sup>

The human gut is colonized with a wide variety of microorganisms, including species, such as those belonging to the bacterial genus *Bifidobacterium*, that have beneficial effects on human physiology and pathology<sup>1–3</sup>. Among the most distinctive benefits of bifidobacteria are modulation of host defence responses and protection against infectious diseases<sup>4–6</sup>. Nevertheless, the molecular mechanisms underlying these effects have barely been elucidated. To investigate these mechanisms, we used mice associated with certain bifidobacterial strains and a simplified model of lethal infection with enterohaemorrhagic *Escherichia coli* O157:H7, together with an integrated ‘omics’ approach. Here we show that genes encoding an ATP-binding-cassette-type carbohydrate transporter present in certain bifidobacteria contribute to protecting mice against death induced by *E. coli* O157:H7. We found that this effect can be attributed, at least in part, to increased production of acetate and that translocation of the *E. coli* O157:H7 Shiga toxin from the gut lumen to the blood was inhibited. We propose that acetate produced by protective bifidobacteria improves intestinal defence mediated by epithelial cells and thereby protects the host against lethal infection.

Enterohaemorrhagic *Escherichia coli* (EHEC) causes illnesses ranging from mild diarrhoea to severe diseases such as haemorrhagic colitis and haemolytic uraemic syndrome<sup>7,8</sup>. EHEC O157:H7, which produces Shiga toxin (Stx), is the major EHEC serotype responsible for public health problems worldwide<sup>9</sup>. Germ-free mice are a suitable model for analysing the mechanism of infection with this bacterium, which is denoted *E. coli* O157 throughout. Studies using this model have shown previously that Stx (both Stx1 and Stx2) produced by *E. coli* O157 is a crucial factor in lethal infection<sup>10</sup> and that pretreatment with certain probiotics, including bifidobacteria, protects mice against death<sup>11–13</sup>. However, the protective mechanism of bifidobacteria remains unknown.

When germ-free mice were fed *E. coli* O157, they died within 7 days. However, mice survived if they had been colonized, 7 days before inoculation with *E. coli* O157, with *Bifidobacterium longum* subsp. *longum* JCM 1217<sup>T</sup> (denoted BL) (Fig. 1a and Supplementary Table 1). By contrast, another strain of bifidobacteria, *Bifidobacterium adolescentis* JCM 1275<sup>T</sup> (BA), failed to prevent *E. coli* O157-induced death under the same conditions. In these two groups of mice—denoted BL+O157 mice and BA+O157 mice—there was no significant difference in several physiological and pathological markers in the gut: the number of *E. coli* O157 and the number of bifidobacteria, the concentration of Stx2 protein (the type of Stx produced by the *E. coli* strain studied), the expression level of *E. coli* O157 virulence genes, the amounts of mucin and immunoglobulin A (IgA), and the pH (Fig. 1b–d and

Supplementary Fig. 1). Nevertheless, the serum concentration of Stx2 was markedly lower in BL+O157 mice than in BA+O157 mice (Fig. 1e), suggesting that BL, but not BA, promotes epithelial defence functions that prevent the translocation of Stx2 into the blood.

Consistent with this idea, histological analysis showed a slight inflammation, characterized by a reduction in the number of goblet cells and an infiltration with inflammatory cells, only in the distal colon of the dying mice that been administered *E. coli* O157 alone (O157 mice) and in the BA+O157 mice but not in the surviving BL+O157 mice (Supplementary Fig. 2a, b). Gene expression profiling of the distal colonic epithelium, followed by multivariate partial least squares-discriminant analysis (PLS-DA), also showed substantial upregulation of inflammation-related genes in O157 and BA+O157 mice, even as early as 1 day after administration of *E. coli* O157, when no obvious microscopic inflammation was evident (Supplementary Figs 2c and 3 and Supplementary Tables 2 and 3). This upregulation of inflammation-related genes coincided with increased epithelial cell apoptosis in O157 and BA+O157 mice (Supplementary Fig. 2d), suggesting that *E. coli* O157 provokes apoptosis of these cells before mucosal inflammation can occur and that such inflammation does not occur if BL has been administered.

It was unclear how BL, but not BA, prevents *E. coli* O157-induced epithelial cell apoptosis. We thought that differential metabolite production by BL and BA in the gut environment might be involved in this process. To address this possibility, we performed PLS-DA of the metabolic profiles of faeces from mice that had been monoassociated with each of four bifidobacterial strains: BL (which prevents infection with *E. coli* O157); *B. longum* subsp. *infantis* 157F (BF)<sup>13</sup> (preventive); BA (non-preventive); and *B. longum* subsp. *infantis* JCM 1222<sup>T</sup> (BT)<sup>13</sup> (non-preventive). We found a striking difference in the faecal metabolite composition between mice that had been administered the preventive strains and those that had received the non-preventive strains (Fig. 2a). Loading-plot analysis and <sup>1</sup>H–<sup>13</sup>C correlation NMR measurement identified carbohydrates as the main metabolites that differed between mice associated with the preventive bifidobacterial strains and the non-preventive ones (Supplementary Fig. 4 and Supplementary Table 4). The efficiency of carbohydrate consumption by bifidobacteria correlated with their ability to prevent *E. coli* O157-induced death.

Short-chain fatty acids are the major end products of carbohydrate metabolism in bifidobacteria. Indeed, the concentration of acetate, but not lactate or formate, was significantly higher in the faeces of mice associated with the preventive strains than in those associated with the non-preventive strains (Fig. 2b). Butyrate and propionate were not

<sup>1</sup>Laboratory for Epithelial Immunobiology, RIKEN Research Center for Allergy and Immunology, 1-7-22 Suehiro-cho, Tsurumi-ku, Yokohama, Kanagawa 230-0045, Japan. <sup>2</sup>Graduate School of Nanobioscience, Yokohama City University, 1-7-29 Suehiro-cho, Tsurumi-ku, Yokohama, Kanagawa 230-0045, Japan. <sup>3</sup>MetaSystems Research Team, RIKEN Advanced Science Institute, 1-7-22 Suehiro-cho, Tsurumi-ku, Yokohama, Kanagawa 230-0045, Japan. <sup>4</sup>Graduate School of Frontier Sciences, The University of Tokyo, 5-1-5 Kashiwanoha, Kashiwa, Chiba 277-8561, Japan. <sup>5</sup>Advanced NMR Metabonomics Research Team, RIKEN Plant Science Center, 1-7-22 Suehiro-cho, Tsurumi-ku, Yokohama, Kanagawa 230-0045, Japan. <sup>6</sup>Graduate School of Agricultural and Life Sciences, The University of Tokyo, 1-1-1 Yayoi, Bunkyo-ku, Tokyo 113-8657, Japan. <sup>7</sup>Graduate School of Medicine, Osaka University, 2-2 Yamada-oka, Suita, Osaka 565-0871, Japan. <sup>8</sup>Preventative Health National Research Flagship, CSIRO Food and Nutritional Sciences, Adelaide, South Australia 5000, Australia. <sup>9</sup>The United Graduate School of Agricultural Science, Gifu University, 1-1 Yanagido, Gifu 501-1193, Japan. <sup>10</sup>Graduate School of Bioagricultural Sciences, Nagoya University, Furo-cho, Chikusa-ku, Nagoya, Aichi 464-8601, Japan. <sup>11</sup>School of Veterinary Medicine, Azabu University, 1-17-71 Fuchinobe, Sagamihara, Kanagawa 229-8501, Japan. <sup>12</sup>Graduate School of Medicine, Chiba University, 1-8-1 Inohana, Chuo-ku, Chiba 260-8670, Japan.

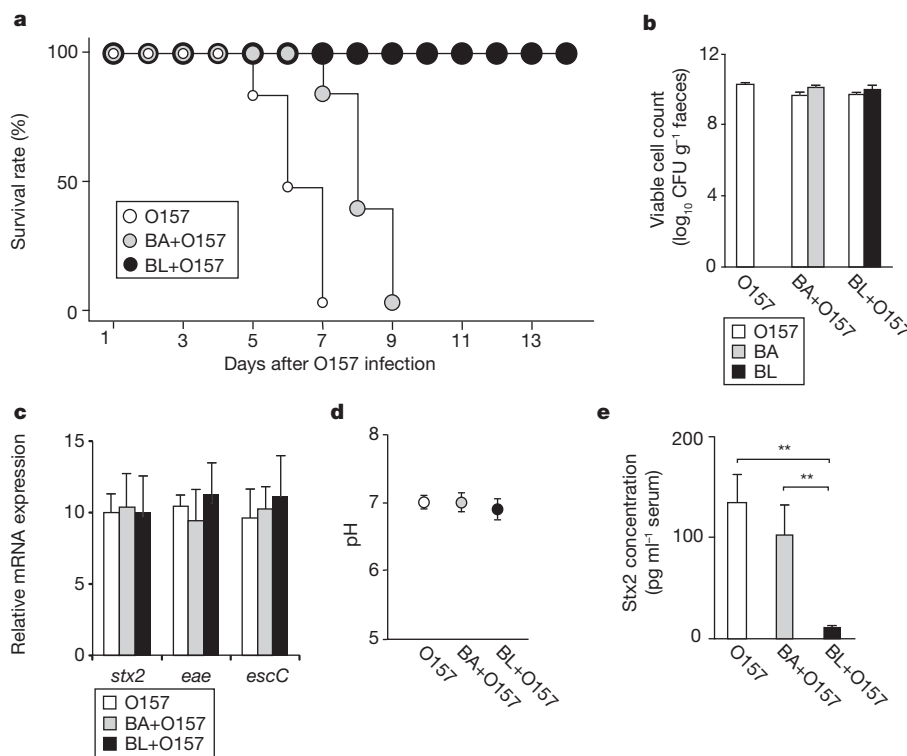


**Figure 1 | Effect of preventive and non-preventive bifidobacteria against lethal infection with *E. coli* O157.** **a**, Survival rate of mice after infection with *E. coli* O157: germ-free BALB/c mice (O157); mice associated with the preventive *B. longum* subsp. *longum* JCM 1217<sup>T</sup> (BL+O157); and with the non-preventive *Bifidobacterium adolescentis* JCM 1275<sup>T</sup> (BA+O157). *n* = 10. **b**, Number of *E. coli* O157 and bifidobacteria in faeces. CFU, colony-forming unit. **c**, Quantitative RT-PCR (PCR with reverse transcription) analysis of

expression of the *E. coli* O157 virulence genes encoding Stx2 (*stx2*), intimin (*eae*) and a type III secretion system component (*escC*) in these mice. Messenger RNA expression values are expressed relative to the percentage of *E. coli* O157 16S ribosomal RNA. **d**, pH of the caecal contents. **e**, Stx2 concentration in the serum. *P* value was determined using the Kruskal–Wallis test followed by the Scheffé test. \*\*, *P* < 0.01. **b–e**, Error bars, s.e.m. (*n* = 3).

detected in the faeces of any of these groups of mice (data not shown). These results suggest a positive correlation between the amount of faecal acetate and the resistance of mice to infection with *E. coli* O157. Covariation analysis of the transcriptome of the colonic epithelium (Supplementary Figs 5 and 6 and Supplementary Table 5) and the faecal metabolome of BL-monoassociated mice and BA-monoassociated mice (Supplementary Fig. 7) indicated that the expression level of mouse genes such as *Apoe*, *C3* and *Pla2g2a* strongly correlates with the amount of faecal acetate. The transcription of *Apoe*, *C3* and *Pla2g2a* is known to be upregulated by activation of retinoid X receptor, which has a central role in the transcriptional control of cellular energy metabolism<sup>14–16</sup> and in the anti-inflammatory response<sup>17–20</sup>. Experiments using human colonic epithelial (Caco-2) cells confirmed that acetate could induce the expression of these three genes (Fig. 2c). Additionally, acetate prevented the reduction in transepithelial electrical resistance resulting from *E. coli* O157-induced cell death and the translocation of Stx2 from the apical to the basolateral side of colonic epithelial cells, without affecting the growth rate of *E. coli* O157 or the expression level of several virulence genes of *E. coli* O157 (Fig. 2d–f and Supplementary Fig. 8). These data strongly suggest that acetate produced in large amounts by the preventive bifidobacteria exerts its action on the colonic epithelium by inducing anti-inflammatory and/or anti-apoptotic effects, blocking the translocation of the lethal dose of Stx2 to the blood.

To gain genetic insight into how the preventive strains efficiently consume carbohydrates and produce acetate, we determined the complete genome sequences of BL, BF and BT<sup>21</sup> and compared them with the sequences of BA and another preventive strain, *B. longum* subsp. *longum* NCC 2705 (BN)<sup>22</sup> (which were available from public databases) (Supplementary Tables 1 and 6). Reciprocal BLASTP comparison between the gene sets of these five genomes identified five syntenic loci

that are present in the preventive bifidobacteria (BL, BF and BN) but absent from the non-preventive ones (BA and BT) (Supplementary Table 7). All five loci contained genes encoding ATP-binding cassette (ABC)-type carbohydrate transporters. Among them, the genes assigned to COG1879, COG1172 and COG1129 (the clusters of orthologous groups from the NCBI COGs database) at loci 1 and 5 were specific to the preventive bifidobacteria (Fig. 3a). At the other three loci, by contrast, paralogous genes were also present in the genomes of the non-preventive bifidobacteria (Supplementary Table 8).

Substrates for the preventive-bifidobacteria-specific transporters were predicted, by *in silico* analysis by another research group, to be ribose, fructose, mannose and many other sugars<sup>23,24</sup>. Substrates for the transporters commonly expressed in the preventive and non-preventive bifidobacteria were predicted to be fructo-oligosaccharide and lactose<sup>23</sup> (Supplementary Table 7). Correspondingly, *in vitro* metabolic profiling using <sup>13</sup>C-labelled glucose and fructose, followed by PLS-DA, revealed both a significantly higher rate of consumption of fructose and production of acetate in the preventive strains than in the non-preventive strains (Fig. 3b, c and Supplementary Table 9). Consistent with the predicted substrate specificity of the transporters, mannose, but not fructo-oligosaccharide or lactose, was also a specific substrate for the preventive bifidobacteria (Supplementary Table 10). Of the two preventive bifidobacteria-specific carbohydrate transporters (those encoded at loci 1 and 5) (Fig. 3a), the expression of the genes BL0033 and BL0034 by BN has been reported to be highly induced by fructose<sup>24</sup>. We confirmed that fructose upregulated expression of BL0033–BL0036, but not BL1691–BL1696, in BN (Supplementary Fig. 9a), and we found that BL0033 was expressed by the preventive bifidobacteria in the mouse distal colon (Supplementary Fig. 9b). These data suggest that the genes BL0033–BL0036 are involved in preventing *E. coli* O157-induced death of mice by, at least, BN.

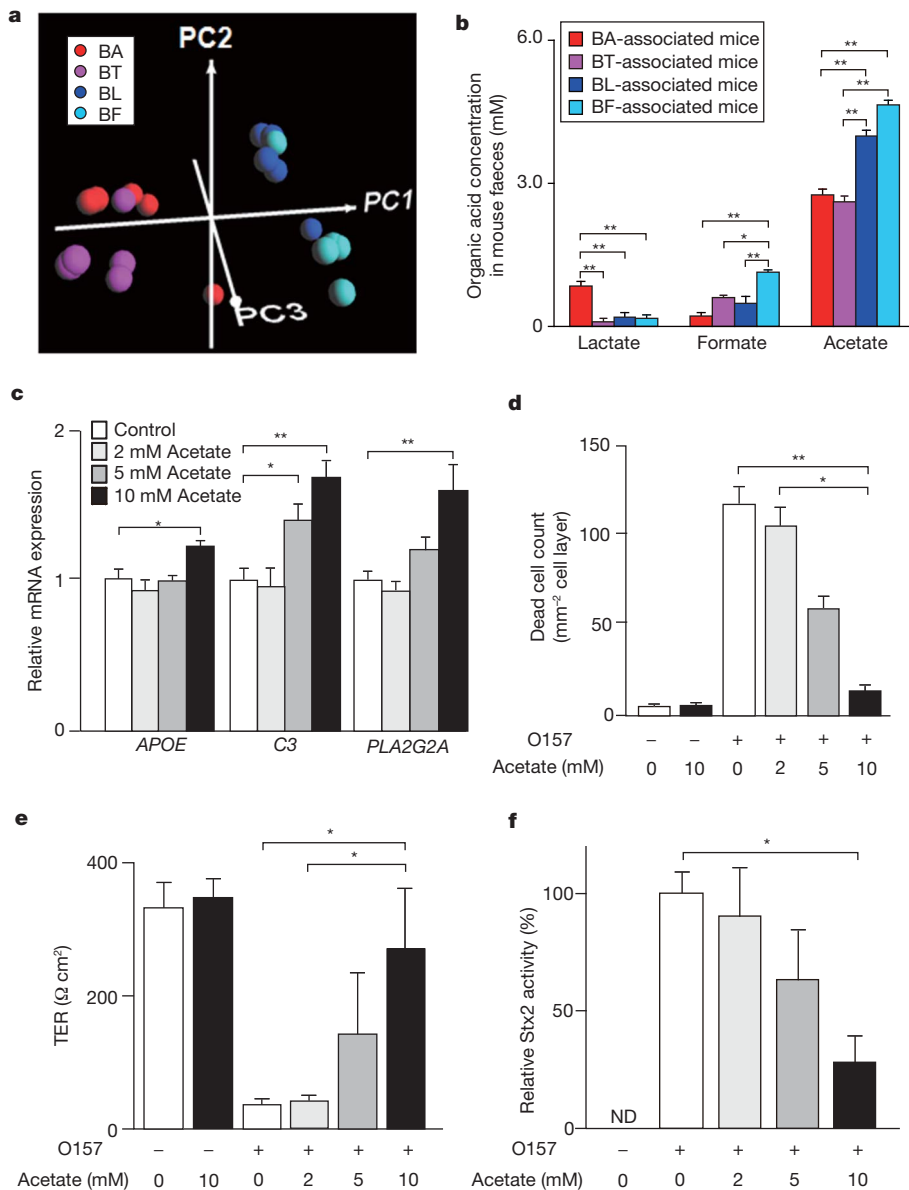


**Figure 2 | Identification of acetate as causative substance for protection provided by preventive bifidobacteria.** **a**, PLS-DA on metabolome data from mouse faeces 7 days after inoculation of each preventive and non-preventive bifidobacterial strain into germ-free mice ( $n = 5$ ). Proportions of the first (PC1), second (PC2) and third (PC3) components are 66.5%, 11.2% and 9.1%, respectively. **b**, Organic acid concentrations in mouse faeces, as determined by high-performance liquid chromatography. **c**, Quantitative RT-PCR analysis of *APOE*, *C3* and *PLA2G2A* gene expression in Caco-2 cells in the absence or presence of the indicated concentration of acetate. The orthologues of these genes were upregulated in the colonic epithelium of mice associated with preventive bifidobacteria (Supplementary Table 5). Gene expression levels are expressed as values relative to the control (0 mM acetate). **d**, The number of dead cells in polarized Caco-2 cells 8 h after infection with *E. coli* O157 in the absence or presence of the indicated concentration of acetate. **e**, Transepithelial electrical resistance (TER) of polarized Caco-2 cells 16 h after infection with *E. coli* O157 in the absence or presence of the indicated concentration of acetate. **f**, Relative Stx2 activity in the basolateral side of polarized Caco-2 cell culture media 16 h after infection with *E. coli* O157 in the absence or presence of the indicated concentration of acetate. Activity is expressed as a percentage of activity in control cells (infected with *E. coli* O157 and treated with 0 mM acetate). **b–f**, Error bars, s.e.m. ( $n = 3$ ). *P* values were determined using the one-way analysis of variance (ANOVA) test followed by Tukey's test (**b**, **c**) or the Kruskal–Wallis test followed by the Scheffé test (**d–f**). \*,  $P < 0.05$ ; \*\*,  $P < 0.01$ . ND, not detected.

To test this, we generated a strain of BN in which BL0033 had been knocked out (denoted BNKO) using homologous recombination (Supplementary Figs 9a and 10). *In vitro* culture of BNKO showed a significant reduction in capacity to catabolize fructose and in acetate production compared with BN (Fig. 4a). Accordingly, BNKO did not prevent Caco-2 cell death induced by *E. coli* O157 (Supplementary Fig. 11). More importantly, the survival rate of BNKO-associated mice after infection with *E. coli* O157 was also significantly less than that of BN-associated mice, consistent with the lower acetate concentration in the faeces of BNKO-associated mice (Fig. 4b, c).

We also generated a strain of BA strain that exogenously expressed BL0033–BL0036 (denoted BATg). After infection with *E. coli* O157, BATg-associated mice survived slightly (but significantly) longer than BA-associated mice (Fig. 4d). The moderate effect of BATg is probably caused by a modest increase in acetate produced from fructose because of the lower expression of BL0033–BL0036 in BATg than in BN, in the presence of fructose (Fig. 4e and Supplementary Fig. 9a). Finally, we asked whether an increased amount of acetate in the distal colon could protect mice against *E. coli* O157-induced death. We fed BA+O157 mice a diet supplemented with acetylated starch, which is gradually hydrolysed, releasing acetate in the intestinal tract<sup>25</sup>. Administration of

the acetylated starch significantly increased the amount of acetate in the faeces and improved the survival rate of BA-associated mice in response to *E. coli* O157, suggesting that the amount of acetate is crucial for this protection (Fig. 4f, g).

Short-chain fatty acids generated by commensal bacteria have long been implicated in having a variety of beneficial effects on the host, including trophic and anti-inflammatory effects on the gut *in vitro*<sup>1,5,12,26,27</sup> and *in vivo*<sup>28</sup>. Our findings suggest that bacterial acetate acts *in vivo* to promote the defence functions of host epithelial cells. Of more importance is the identification of carbohydrate transporters that confer a probiotic effect on bifidobacterial strains. These 'probiotic transporters' are likely to be present in only a subset of *B. longum*, and genes encoding proteins that are highly similar to these probiotic transporters were also identified in several human gut microbiomes<sup>29</sup> (Supplementary Table 11). Both the preventive and non-preventive bifidobacteria can produce enough acetate in the presence of glucose, and this is probably what takes place in the proximal part of the colon. In the distal colon, however, the glucose supply has been exhausted, and only the bifidobacteria equipped with probiotic transporters can produce enough acetate, through catabolizing the fructose that is present (Supplementary Fig. 12). As demonstrated in this study, a simplified

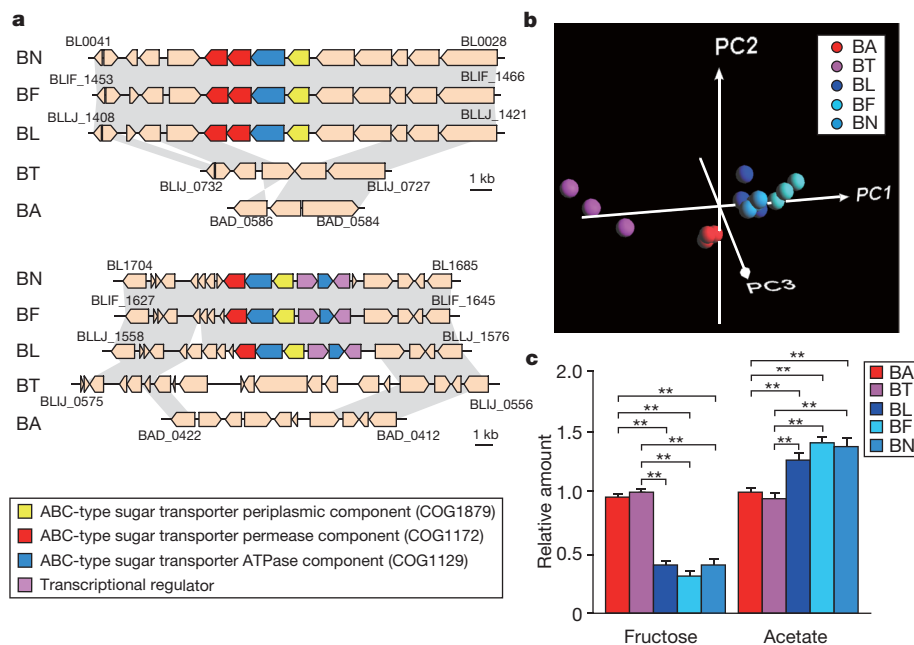


**Figure 3 | Genomic and metabolic profiling of the bifidobacterial strains.** **a**, Comparison of the regions containing the genes that encode specific ABC-type carbohydrate transporters in the sequenced bifidobacterial strains. Genes and their orientations are depicted with arrows. Grey bars indicate orthologous regions. **b**, PLS-DA on metabolome data from bifidobacterial strains cultured for 12 h in  $^{13}\text{C}$ -labelled medium *in vitro*. Proportions of the first (PC1), second (PC2) and third (PC3) components are 73.1%, 16.8% and 4.0%, respectively. The top five loading coefficients of  $^1\text{H}$ - $^{13}\text{C}$  correlation NMR cross peaks are shown in Supplementary Table 9. **c**, Relative amount of fructose or acetate present in the medium for the five bifidobacterial strains after 12 h incubation *in vitro* ( $n = 3$ ). The amounts of fructose and acetate are shown as values relative to those for BA. Error bars, s.e.m.  $P$  values were determined using the one-way ANOVA test followed by Tukey's test. \*\*,  $P < 0.01$ .

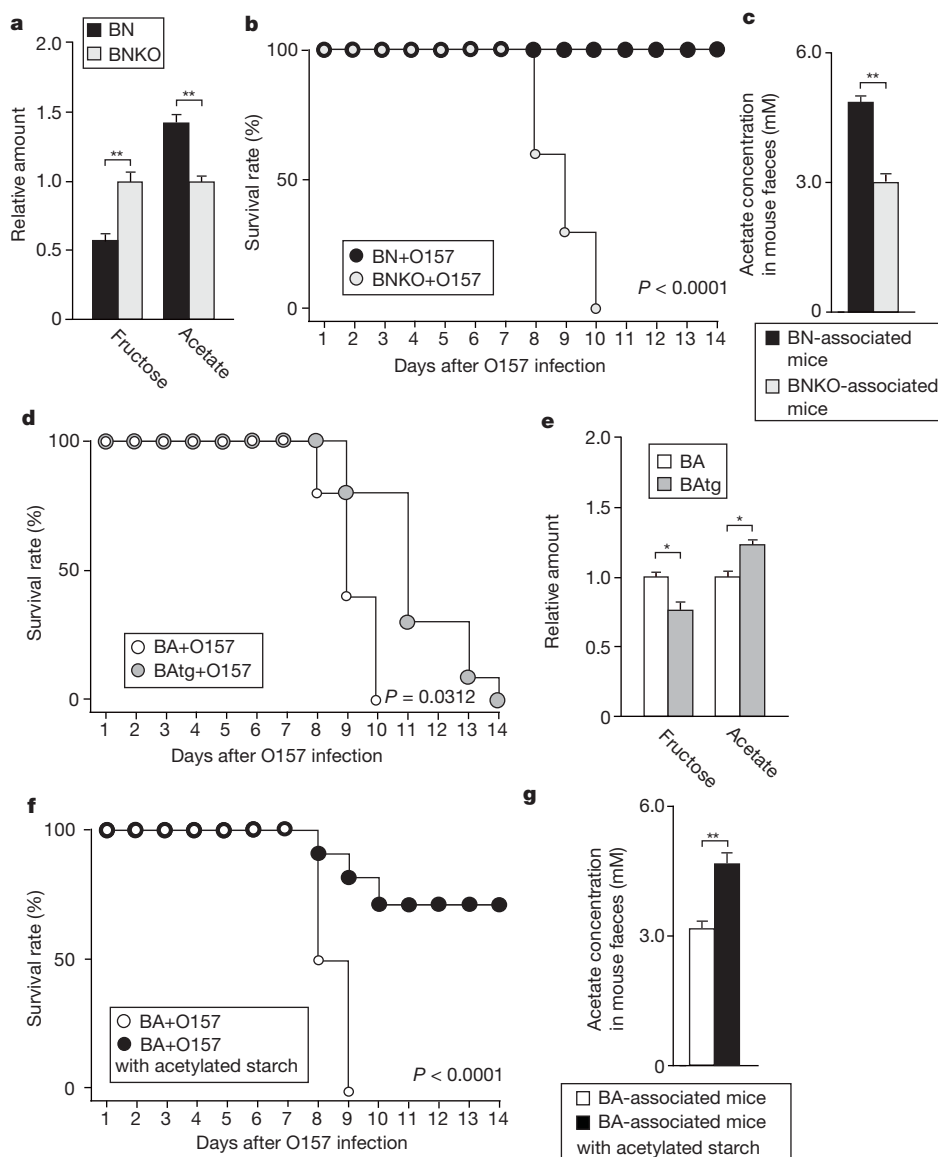


**Figure 4 | Functional analysis of the ABC-type carbohydrate transporter.** **a**, Amount of fructose and acetate present in the medium for BN and BNKO after 12 h incubation *in vitro* ( $n = 5$ ). Data are expressed relative to the amount for BNKO. **b**, Survival rate of BN- and BNKO-associated mice after infection with *E. coli* O157 ( $n = 10$ ). **c**, Acetate concentration in the faeces of BN- and BNKO-associated mice ( $n = 5$ ). **d**, Survival rate of BA- and BAAtg-associated mice after infection with *E. coli* O157 ( $n = 10$ ). **e**, Amount of fructose and acetate present in the medium for BA and BAAtg after 12 h incubation *in vitro* ( $n = 5$ ). Data are expressed relative to the amount for BA. **f**, Survival rate of BA+O157 mice fed with a control synthetic diet or a modified synthetic diet—in which 15% starch was replaced with acetylated starch—for 1 week before infection with *E. coli* O157 ( $n = 10$ ). **g**, Acetate concentration in the faeces of BA-associated mice fed on a control diet or starch-modified diet ( $n = 5$ ). **a**, **c**, **e**, **g**, Error bars, s.e.m.  $P$  values were determined using Student's  $t$ -test. \*,  $P < 0.05$ ; \*\*,  $P < 0.01$ . **b**, **d**, **f**,  $P$  values were determined using the Kaplan-Meier method followed by the log-rank test.

animal model system coupled with multiple 'omics' technologies can provide a powerful strategy for dissecting host–microbe cross-talk in the complex gut ecosystem.

## METHODS SUMMARY

**Animals.** Germ-free BALB/c mice were housed in gnotobiotic isolators and fed an autoclaved standard rodent chow diet (CMF, Oriental Yeast). All experiments were performed using protocols approved by the University of Tokyo Animal Studies Committee. Male or female germ-free mice of 8–16 weeks of age were colonized with a single gavage of  $10^8$  colony-forming units (CFU) of bifidobacteria. For infection with *E. coli* O157, mice that were germ free or had been monoassociated with bifidobacteria (for 7 days) were orally inoculated with a single gavage of  $10^4$  CFU of *E. coli* O157:H7 strain 44<sup>Rf</sup>.

**Metabolic profiling.** Faecal metabolites were extracted by gentle shaking of faeces with 100 mM potassium phosphate buffer containing 90% deuterium oxide and 1 mM sodium 2,2-dimethyl-2-silapentane-5-sulphonate as the chemical-shift reference compound ( $\delta = 0.0$  p.p.m.). They were then analysed by  $^1\text{H}$ -NMR and  $^1\text{H}$ - $^{13}\text{C}$  correlation NMR spectroscopy. PLS-DA, a regression extension of the classical principal component analysis that is appropriate to the metabolome data set, was run with R software using the PLS package (v2.0) and the 'SIMPLS' method. Briefly, the normalized metabolome data set was imported into the R software. Variance and regression were computed in a class-supervised manner, and principal component (PC) scores were determined. Data were visualized as PC score plots, with the PC1 axis showing most of the differences among the samples, whereas PC2 and PC3 corresponded to factors with decreasing contribution to the differences.

**Full Methods** and any associated references are available in the online version of the paper at [www.nature.com/nature](http://www.nature.com/nature).

Received 11 September 2009; accepted 4 November 2010.

- Picard, C. *et al.* Bifidobacteria as probiotic agents—physiological effects and clinical benefits. *Aliment. Pharmacol. Ther.* **22**, 495–512 (2005).
- Ventura, M. *et al.* Genome-scale analyses of health-promoting bacteria: probiogenomics. *Nature Rev. Microbiol.* **7**, 61–71 (2009).
- Jia, W., Li, H., Zhao, L. & Nicholson, J. K. Gut microbiota: a potential new territory for drug targeting. *Nature Rev. Drug Discov.* **7**, 123–129 (2008).
- Mazmanian, S. K. & Kasper, D. L. The love–hate relationship between bacterial polysaccharides and the host immune system. *Nature Rev. Immunol.* **6**, 849–858 (2006).
- Saulnier, D. M., Spinler, J. K., Gibson, G. R. & Versalovic, J. Mechanisms of probiosis and prebiotics: considerations for enhanced functional foods. *Curr. Opin. Biotechnol.* **20**, 135–141 (2009).
- Sonnenburg, J. L., Chen, C. T. & Gordon, J. I. Genomic and metabolic studies of the impact of probiotics on a model gut symbiont and host. *PLoS Biol.* **4**, e413 (2006).
- Garmendia, J., Frankel, G. & Crepin, V. F. Enteropathogenic and enterohemorrhagic *Escherichia coli* infections: translocation, translocation, translocation. *Infect. Immun.* **73**, 2573–2585 (2005).
- Tarr, P. I., Gordon, C. A. & Chandler, W. L. Shiga-toxin-producing *Escherichia coli* and haemolytic uraemic syndrome. *Lancet* **365**, 1073–1086 (2005).
- Kitajima, H., Ida, S. & Fujimura, M. Daily bowel movements and *Escherichia coli* O157 infection. *Arch. Dis. Child.* **87**, 335–336 (2002).
- Eaton, K. A. *et al.* Pathogenesis of renal disease due to enterohemorrhagic *Escherichia coli* in germ-free mice. *Infect. Immun.* **76**, 3054–3063 (2008).
- Asahara, T. *et al.* Probiotic bifidobacteria protect mice from lethal infection with Shiga toxin-producing *Escherichia coli* O157:H7. *Infect. Immun.* **72**, 2240–2247 (2004).
- Gagnon, M., Kheadr, E. E., Dabour, N., Richard, D. & Fliss, I. Effect of *Bifidobacterium thermacidophilum* probiotic feeding on enterohemorrhagic *Escherichia coli* O157:H7 infection in BALB/c mice. *Int. J. Food Microbiol.* **111**, 26–33 (2006).
- Yoshimura, K., Matsui, T. & Itoh, K. Prevention of *Escherichia coli* O157:H7 infection in gnotobiotic mice associated with *Bifidobacterium* strains. *Antonie Van Leeuwenhoek* **97**, 107–117 (2010).
- Li, J., Pircher, P. C., Schulman, I. G. & Westin, S. K. Regulation of complement C3 expression by the bile acid receptor FXR. *J. Biol. Chem.* **280**, 7427–7434 (2005).
- Lafitte, B. A. *et al.* LXRs control lipid-inducible expression of the apolipoprotein E gene in macrophages and adipocytes. *Proc. Natl Acad. Sci. USA* **98**, 507–512 (2001).
- Antonio, V., Janvier, B., Brouillet, A., Andreani, M. & Raymondjean, M. Oxysterol and 9-*cis*-retinoic acid stimulate the group IIA secretory phospholipase A<sub>2</sub> gene in rat smooth-muscle cells. *Biochem. J.* **376**, 351–360 (2003).
- Zelcer, N. & Tontonoz, P. Liver X receptors as integrators of metabolic and inflammatory signaling. *J. Clin. Invest.* **116**, 607–614 (2006).
- Sethi, S. *et al.* Oxidized omega-3 fatty acids in fish oil inhibit leukocyte–endothelial interactions through activation of PPAR $\alpha$ . *Blood* **100**, 1340–1346 (2002).
- Staels, B. *et al.* Activation of human aortic smooth-muscle cells is inhibited by PPAR $\alpha$  but not by PPAR $\gamma$  activators. *Nature* **393**, 790–793 (1998).
- Delerive, P., Gervois, P., Fruchart, J. C. & Staels, B. Induction of I $\kappa$ B $\alpha$  expression as a mechanism contributing to the anti-inflammatory activities of peroxisome proliferator-activated receptor- $\alpha$  activators. *J. Biol. Chem.* **275**, 36703–36707 (2000).
- Sela, D. A. *et al.* The genome sequence of *Bifidobacterium longum* subsp. *infantis* reveals adaptations for milk utilization within the infant microbiome. *Proc. Natl Acad. Sci. USA* **105**, 18964–18969 (2008).
- Schell, M. A. *et al.* The genome sequence of *Bifidobacterium longum* reflects its adaptation to the human gastrointestinal tract. *Proc. Natl Acad. Sci. USA* **99**, 14422–14427 (2002).
- Parche, S. *et al.* Sugar transport systems of *Bifidobacterium longum* NCC 2705. *J. Mol. Microbiol. Biotechnol.* **12**, 9–19 (2007).
- Yuan, J. *et al.* A proteomic reference map and proteomic analysis of *Bifidobacterium longum* NCC 2705. *Mol. Cell. Proteomics* **5**, 1105–1118 (2006).
- Annisson, G., Illman, R. J. & Topping, D. L. Acetylated, propionylated or butyrylated starches raise large bowel short-chain fatty acids preferentially when fed to rats. *J. Nutr.* **133**, 3523–3528 (2003).
- Tedelind, S., Westberg, F., Kjerrulf, M. & Vidal, A. Anti-inflammatory properties of the short-chain fatty acids acetate and propionate: a study with relevance to inflammatory bowel disease. *World J. Gastroenterol.* **13**, 2826–2832 (2007).
- Kles, K. A. & Chang, E. B. Short-chain fatty acids impact on intestinal adaptation, inflammation, carcinoma, and failure. *Gastroenterology* **130**, S100–S105 (2006).
- Maslowski, K. M. *et al.* Regulation of inflammatory responses by gut microbiota and chemoattractant receptor GPR43. *Nature* **461**, 1282–1286 (2009).
- Kurokawa, K. *et al.* Comparative metagenomics revealed commonly enriched gene sets in human gut microbiomes. *DNA Res.* **14**, 169–181 (2007).

**Supplementary Information** is linked to the online version of the paper at [www.nature.com/nature](http://www.nature.com/nature).

**Acknowledgements** We thank H. Kitamura and M. E. Mariotti-Ferrandiz for discussions and for reading the manuscript; T. Morita for suggestions; and C. Nishigaki, M. Ohmae, Y. Chiba, T. Kato, H. Shima, A. Nakano, K. Sakaguchi, K. Furuya, C. Yoshino, H. Inaba, E. Iioka, K. Motomura and Y. Hattori for technical support. This research was supported in part by grants from the Ministry of Education, Culture, Sports, Science and Technology of Japan: a Grant-in-Aid for Scientific Research on Priority Areas 'Comprehensive Genomics' (M.H.), 'Membrane Traffic' (H.O.) and 'Matrix of Infectious Phenomena' (K.H.); Young Scientists (S.F., K.H. and J.K.); Challenging Exploratory Research (J.K.); Scientific Research (H.O.); and Scientific Research on Innovative Areas 'Intracellular Logistics' (H.O.). This work was also supported in part by a RIKEN President's Special Research Grant (J.K.); a RIKEN DRI Research Grant (S.F.); a CREST grant from the Japan Science and Technology Agency (J.K.); the Danone Institute of Japan (H.O.); the Institute for Fermentation, Osaka (S.F.); the Kieikai Research Foundation (S.F.); the Naito Foundation (S.F.); the Nestlé Nutrition Council, Japan (S.F.); the Sasakawa Scientific Research Grant from the Japan Science Society (S.F. and Y.N.); the Yakult Bio-Science Foundation (S.F.); the Academic Frontier Project for Private Universities (Matching Fund Subsidy (H.M.)); and the Private University Scientific Foundation (H.M.).

**Author Contributions** S.F., K.I., M.H. and H.O. conceived and designed the experiments. S.F., Y.N., K.H., K.Y., K.O., H.M. and K.I. performed the experiments. S.F., H.T. and Y.N. analysed the data. T.T., J.M.C., D.L.T., T.S., T.D.T., J.K. and M.H. contributed reagents, materials and analysis tools. S.F., H.T., K.H., T.D.T., M.H. and H.O. wrote the paper.

**Author Information** Microarray data have been deposited in the NCBI Gene Expression Omnibus under accession number GSE13061. Sequences for the *B. longum* genomes have been deposited in the DNA Data Bank of Japan, GenBank and the EMBL Nucleotide Sequence Database under accession numbers AP010888 (BL), AP010889 (BT) and AP010890–AP010892 (BF). Reprints and permissions information is available at [www.nature.com/reprints](http://www.nature.com/reprints). The authors declare no competing financial interests. Readers are welcome to comment on the online version of this article at [www.nature.com/nature](http://www.nature.com/nature). Correspondence and requests for materials should be addressed to H.O. ([ohno@rcai.riken.jp](mailto:ohno@rcai.riken.jp)) or M.H. ([hattori@k.u-tokyo.ac.jp](mailto:hattori@k.u-tokyo.ac.jp)).

## METHODS

**Bacterial strains, cell lines and culture conditions.** *B. longum* subsp. *longum* JCM 1217<sup>T</sup> (BL), *B. longum* subsp. *infantis* JCM 1222<sup>T</sup> (BT) and *B. adolescentis* JCM 1275<sup>T</sup> (BA) were purchased from the Japan Collection of Microorganisms. *B. longum* subsp. *longum* NCC 2705 (BN) was provided by the Nestlé Research Center. *B. longum* subsp. *infantis* 157F (BF) was isolated from the faeces of a human infant<sup>13</sup>. *E. coli* O157:H7 strain 44<sup>Rf</sup> (*E. coli* O157), a rifampicin-resistant mutant, was originally derived from bovine faeces<sup>13</sup>. This strain does not produce Stx1. Bifidobacteria and *E. coli* O157 were cultured anaerobically in blood liver (BL) agar (Nissui) and tryptic soy (TS) agar (BBL, Becton Dickinson), respectively<sup>13</sup>.

Vero cells and Caco-2 cells were purchased from the American Type Culture Collection. They were grown as a monolayer in the medium DMEM (GIBCO) supplemented with 10% FBS and 1% penicillin-streptomycin-glutamine (GIBCO). Cultures were maintained in plastic dishes at 37 °C in a 5% CO<sub>2</sub> atmosphere.

**Counting the number of bacteria in faeces.** Unless stated otherwise, the faecal samples were directly collected from mice just after a bowel movement. These samples were then immediately used for several analyses. Faecal suspensions were homogenized with anaerobic solution A (4.5 g l<sup>-1</sup> KH<sub>2</sub>PO<sub>4</sub>, 6.0 g l<sup>-1</sup> Na<sub>2</sub>HPO<sub>4</sub>, 12.5 g l<sup>-1</sup> L-cysteine-HCl, 0.5 g l<sup>-1</sup> Tween 80 and 0.75 g l<sup>-1</sup> Bacto Agar (BBL)) (1:50 dilution). Serial tenfold dilutions were prepared, and a 50 µl aliquot of each dilution was spread on TS agar plates (for *E. coli* O157) or BL agar plates (for bifidobacteria). The plates were incubated at 37 °C anaerobically, and the CFU were enumerated<sup>13</sup>.

**Vero cell bioassay for Stx2 cytotoxicity.** Stx2 cytotoxicity was determined in 96-well microtitre plates, as previously described<sup>30</sup>. Cell morphology was observed under a phase contrast microscope. Shiga toxin (100 ng ml<sup>-1</sup>; VTEC-RPLA test, Denka Seiken) was used as a standard.

**Measurement of mucin, total IgA, pH and organic acids.** Crude mucin was isolated from mouse caecal contents and analysed by SDS-PAGE<sup>31</sup>. Caecal IgA was determined using the mouse IgA ELISA quantitation set (Bethyl Laboratories). Caecal pH was measured with a compact pH meter (Model C-1, Horiba). Organic acid concentrations of faecal contents were determined by NMR spectroscopy (DRX-700 spectrometer, Bruker BioSpin) and high-performance liquid chromatography (L-7000, Hitachi)<sup>31</sup>.

**Immunohistochemistry.** Paraformaldehyde-fixed, frozen sections of mouse large intestine were stained with anti-mouse CD4, CD11b and CD11c monoclonal antibodies (BD Biosciences) and anti-Ki67 antiserum (Novocastra), as described previously<sup>32</sup>. For the TdT-mediated dUTP nick end labelling (TUNEL) staining, sections of mouse large intestine were fixed in 4% paraformaldehyde, frozen and then stained with the *in situ* cell death detection kit, fluorescein (Roche). For haematoxylin and eosin staining, sections of mouse large intestine were fixed in 10% formalin (Richard-Allan Scientific) and stained according to standard protocols.

**Gene expression profiling of colonic epithelium.** The colonic epithelium was isolated from the distal colon, as previously described<sup>33</sup>. Epithelial samples obtained from the colon of two mice from each group were combined, and total RNA was extracted according to standard protocols (Affymetrix). Targets were then prepared and hybridized to the GeneChip Mouse Genome 430 2.0 Array (Affymetrix) according to standard protocols. GeneChip data sets were analysed using GeneSpring GX 7.3.1 (Agilent). Array data were normalized using robust multi-array analysis considering guanine and cytosine content (GC-RMA) algorithms<sup>34</sup>. Probe sets categorized to A or B, which both target specific transcripts in the databases NCBI Reference Sequence (RefSeq) and NCBI GenBank, were used<sup>35</sup>.

**Self-organized mapping and hierarchical clustering analysis.** Genes that were upregulated or downregulated twofold or more in O157, BA+O157 or BL+O157 mice compared with germ-free mice were selected (approximately 4,000 genes). Self-organized mapping and hierarchical clustering analysis were performed using GeneSpring GX 7.3.1. Briefly, in each experimental group, genes with similar relative expression values were clustered together, forming a cell. The resultant map allows easy visualization of the clusters. Hierarchical clustering analysis was then computed for the resultant maps to determine the similarity distances among the experimental groups.

**PLS-DA on transcriptome data.** The transcriptomic profiling data set that had been subjected to self-organized mapping analysis was imported into R software (R Foundation for Statistical Computing). Variance and regression were computed in a class-supervised manner, and principal component (PC) scores were determined<sup>36</sup>. Data were visualized as PC score plots, with the PC1 axis showing most of the differences among the samples, whereas PC2 and PC3 corresponded to factors with decreasing contribution to the differences.

**Real-time quantitative RT-PCR.** Total RNA was extracted and reverse-transcribed by using an RNeasy kit (QIAGEN) and RevaTra Ace (TOYOBO), respectively. Real-time PCR was performed using SYBR Premix Ex Taq (Takara) and primers specific

for each gene (Supplementary Table 12). Assays were performed in triplicate using a Thermal Cycler Dice Real Time System (Takara).

**<sup>1</sup>H-NMR and <sup>1</sup>H-<sup>13</sup>C correlation NMR measurements.** For all '*in vivo*' experiments, faecal metabolites were extracted by gentle shaking of faeces in 100 mM potassium phosphate buffer containing 90% deuterium oxide and 1 mM sodium 2,2-dimethyl-2-silapentane-5-sulphonate as the chemical-shift reference compound ( $\delta = 0.0$  p.p.m.). They were then analysed by <sup>1</sup>H-NMR and <sup>1</sup>H-<sup>13</sup>C correlation NMR spectroscopy<sup>37</sup>. By contrast, all '*in vitro*' experiments were carried out using direct measurements of bacterial culture by <sup>1</sup>H-NMR and <sup>1</sup>H-<sup>13</sup>C correlation NMR spectroscopy. Bacterial cells were cultivated in uniformly <sup>13</sup>C-labelled rich media (Spectra) supplemented with 0.5% (w/v) <sup>13</sup>C<sub>6</sub>-D-glucose (Spectra), 0.5% (w/v) <sup>13</sup>C<sub>6</sub>-D-fructose (Spectra) and 0.5% (w/v) <sup>13</sup>C<sub>15</sub>N Algal Amino Acid Mixture (Chlorella Industry). All *in vivo* and *in vitro* NMR experiments were conducted using a DRX-700 spectrometer equipped with a cryogenically cooled probe. The NMR spectra were processed with a procedure similar to that described previously<sup>36-39</sup>. Briefly, <sup>1</sup>H-NMR data were reduced by subdividing the spectra into sequential 0.04 p.p.m. designated regions between <sup>1</sup>H chemical shifts of 0.5–9.0 p.p.m. <sup>1</sup>H-<sup>13</sup>C correlation NMR data were reduced by subdividing spectra into sequential bins of 0.3 p.p.m. in the f1 direction and 0.03 p.p.m. in f2 designated regions between <sup>1</sup>H chemical shifts of 0.5–9.0 p.p.m. and <sup>13</sup>C chemical shifts of 40–90 p.p.m., respectively. After exclusion of water resonance, each region was integrated and normalized to the total of all resonance integral regions (Supplementary Tables 13 and 14). Metabolite annotations were performed using our standard database<sup>40,41</sup>.

***E. coli* O157 infection experiment in Caco-2 cells.** Caco-2 cells were grown on collagen-coated Transwell filter inserts (6.5 mm diameter, 0.4 µm pore size; Costar). During culture, transepithelial electrical resistance (TER) was monitored with an EVOM resistance reader (WPI)<sup>42</sup>. The cells were cultured for 7–12 days until stable TER values of 400 Ω cm<sup>2</sup> were obtained, indicating establishment of epithelial barrier function. The polarized Caco-2 cells were then pre-incubated with acetate for 72 h before infection with *E. coli* O157. Bacteria were added to the upper Transwell compartment at a multiplicity of infection (MOI) of 10 in complete medium without antibiotics. After the indicated incubation periods at 37 °C in 5% CO<sub>2</sub>, the TER and Stx activity of the lower Transwell compartment were determined.

To count the dead cells, Caco-2 cells were grown on 6-well plastic plates for 7–12 days and treated with acetate at concentrations of 0–10 mM for 72 h before infection with *E. coli* O157 at an MOI of 10. After the indicated incubation periods, dead cells were stained with 0.5% (w/v) trypan blue and enumerated under a phase contrast microscope. In the co-culture experiments with bifidobacteria, polarized Caco-2 cells were pre-incubated with BN or BNKO for 12 h before infection with *E. coli* O157 at an MOI of 10. In these experiments, fructose was added at a final concentration of 3 mg ml<sup>-1</sup> to glucose-free DMEM (D5030, Sigma-Aldrich) before culturing.

**Genome sequencing.** The genome sequences of BF, BT and BL were determined by a whole-genome shotgun strategy. We constructed small-insert (2 kb) and large-insert (10 kb) genomic libraries for the three genomes. We generated 26,880 (BF), 30,720 (BT) and 28,416 (BL) reads, each using 3730xl DNA Analyzers (Applied Biosystems), giving 7.8-, 6.3- and 7.6-fold coverage from both ends of the genomic clones, respectively. Sequence reads were assembled with the Phred-Phrap-Consed program<sup>43</sup>, and gaps were closed by direct sequencing of clones that spanned the gaps or of PCR products amplified with oligonucleotide primers designed to anneal to each end of neighbouring contigs. The overall accuracy of the finished sequences was estimated to have an error rate of less than 1 in 10,000 bases (Phrap score, ≥ 40).

**Genome informatics.** An initial set of predicted protein-coding genes was identified using the program Glimmer 3.0 (ref. 44). Genes that were overlapping or <120 base pairs were eliminated. All predicted proteins were searched against a non-redundant protein database (nr, NCBI) using BLASTP (NCBI) with a bit-score cutoff of 60. The start codon of each protein-coding gene was manually refined from BLASTP alignments. Transfer RNA genes were predicted by the program tRNAscan-SE<sup>45</sup>, and ribosomal RNA genes were detected by BLASTN analysis using known bifidobacterial rRNA sequences as queries. Orthology across whole genomes was determined using BLASTP reciprocal best hits with a bit-score cutoff of 60 in all-against-all comparisons of amino acid sequences.

**Generation of BNKO, a BN strain deficient in the ABC-type carbohydrate transporter gene BL0033.** A target vector containing two 1-kb genomic fragments flanking the spectinomycin-resistant gene was constructed with the plasmid pBlueScript II SK (+). The targeting vector was introduced into BN by electroporation, and spectinomycin-resistant colonies were selected, as described previously<sup>46</sup>. The homologous recombination event in BNKO was confirmed by genomic PCR. Southern blotting further confirmed the absence of random integration of the targeting vector. The probes indicated in Supplementary Fig. 10a were

amplified by PCR using BN genomic DNA and the plasmid pKKT427 as templates, and the following primers: 5'-AACCAGCAGAAGGTGCTCATTG-3' (forward) and 5'-AATGCGACGATCGACCAGGTC-3' (reverse) for probe A; and 5'-TTGGTATGATTTTACCCGTGTC-3' (forward) and 5'-TTGGATCAGGAGTTGAGAGTGG-3' (reverse) for probe B.

**Generation of BATg, a BA strain exogenously expressing the ABC-type carbohydrate transporter BL0033–BL0036.** A 3.9-kb *Bifidobacterium–E. coli* shuttle vector, pKKT427 (ref. 47), carrying a spectinomycin-resistance gene, a multi-cloning site and two replication origins (including *repB* from *B. longum* and ColEI ori), was used to generate BATg. DNA containing the ABC-type carbohydrate transporter (BL0033–BL0036) and the histone-like protein (HU) promoter, which was reported to be a high-level expression promoter in bifidobacteria<sup>46</sup>, was cloned from BN. The regions encoding the ABC-type carbohydrate transporter and the HU promoter were amplified by PCR using the following primers: ABC-type carbohydrate transporter sense primer 5'-ATGAAGAATTGGAAGAAGGCC-3' and antisense primer 5'-caactttgtatatacaagttgCTATTTTATCTCCG CCGACC-3'; and HU promoter sense primer 5'-caagttgtacaaaaagcagTGGGC GCGGCGGCCATGAAG-3' and antisense primer 5'-cttccaattctcatAAAGCA TCCTCTTGGGTCAGG-3'. Lower-case letters indicate pDONR vector sequences. The PCR products and linearized pDONR was ligated using the In-Fusion Advantage PCR Cloning Kit (Clontech). The pKKT427 plasmid containing the HU promoter and the ABC transporter gene (pKKT427-HU+BN) was constructed by using the Gateway system (Invitrogen) with the above pDONR vector. The pKKT427-HU+BN plasmid was transferred directly into BA by electroporation with a Gene Pulser apparatus (Bio-Rad)<sup>46</sup>. Transfected BA was grown under anaerobic conditions at 37 °C in BL agar containing 100 µg ml<sup>-1</sup> spectinomycin. **Animal experiments with BATg.** Spectinomycin-resistant BA and *E. coli* O157 were generated by electroporation of a pKKT427 plasmid. To maintain a high copy number of pKKT427-HU+BN in BATg, drinking water containing 1 mg ml<sup>-1</sup> spectinomycin had been given to spectinomycin-resistant BA+O157 mice and spectinomycin-resistant BATg+O157 mice 1 week before infection with spectinomycin-resistant *E. coli* O157.

**Animal experiments with BA-associated mice fed on a starch-modified diet.** BA+O157 mice were fed a control diet (AIN-93G synthetic diet) or a modified AIN-93G synthetic diet in which 15% (w/w) starch was replaced with acetylated starch (Starplus A, CSIRO) 1 week before infection with *E. coli* O157.

**Statistical analyses.** Differences between two or more groups were analysed by Student's *t*-test or the one-way analysis of variance (ANOVA) test followed by Tukey's test. When variances were not homogeneous, the data were analysed by the non-parametric Mann–Whitney *U* test or the Kruskal–Wallis test followed by the Scheffé test. The survival rate of mice associated with different bacteria was

analysed using the Kaplan–Meier method. All statements indicating significant differences show at least a 5% level of probability.

30. Kongmuang, U., Honda, T. & Miwatani, T. Enzyme-linked immunosorbent assay to detect Shiga toxin of *Shigella dysenteriae* and related toxins. *J. Clin. Microbiol.* **25**, 115–118 (1987).
31. Morita, T., Tanabe, H., Takahashi, K. & Sugiyama, K. Ingestion of resistant starch protects endotoxin influx from the intestinal tract and reduces D-galactosamine-induced liver injury in rats. *J. Gastroenterol. Hepatol.* **19**, 303–313 (2004).
32. Hase, K. *et al.* Activation-induced cytidine deaminase deficiency causes organ-specific autoimmune disease. *PLoS ONE* **3**, e3033 (2008).
33. Hase, K. *et al.* Distinct gene expression profiles characterize cellular phenotypes of follicle-associated epithelium and M cells. *DNA Res.* **12**, 127–137 (2005).
34. Irizarry, R. A. *et al.* Summaries of Affymetrix GeneChip probe level data. *Nucleic Acids Res.* **31**, e15 (2003).
35. Hijikata, A. *et al.* Construction of an open-access database that integrates cross-reference information from the transcriptome and proteome of immune cells. *Bioinformatics* **23**, 2934–2941 (2007).
36. Tian, C. *et al.* Top-down phenomics of *Arabidopsis thaliana*: metabolic profiling by one- and two-dimensional nuclear magnetic resonance spectroscopy and transcriptome analysis of albino mutants. *J. Biol. Chem.* **282**, 18532–18541 (2007).
37. Fukuda, S. *et al.* Evaluation and characterization of bacterial metabolic dynamics with a novel profiling technique, real-time metabolotyping. *PLoS ONE* **4**, e4893 (2009).
38. Kikuchi, J., Shinozaki, K. & Hirayama, T. Stable isotope labeling of *Arabidopsis thaliana* for an NMR-based metabolomics approach. *Plant Cell Physiol.* **45**, 1099–1104 (2004).
39. Sekiyama, Y., Chikayama, E. & Kikuchi, J. Profiling polar and semi-polar plant metabolites throughout extraction processes using a combined solution-state and HR-MAS NMR approach. *Anal. Chem.* **82**, 1643–1652 (2010).
40. Akiyama, K. *et al.* PRIME: a Web site that assembles tools for metabolomics and transcriptomics. *In Silico Biol.* **8**, 339–345 (2008).
41. Chikayama, E. *et al.* Statistical indices for simultaneous large-scale metabolite detections for a single NMR spectrum. *Anal. Chem.* **82**, 1653–1658 (2010).
42. Schuller, S., Frankel, G. & Phillips, A. D. Interaction of Shiga toxin from *Escherichia coli* with human intestinal epithelial cell lines and explants: Stx2 induces epithelial damage in organ culture. *Cell. Microbiol.* **6**, 289–301 (2004).
43. Gordon, D., Desmarais, C. & Green, P. Automated finishing with Autofinish. *Genome Res.* **11**, 614–625 (2001).
44. Delcher, A. L., Harmon, D., Kasif, S., White, O. & Salzberg, S. L. Improved microbial gene identification with GLIMMER. *Nucleic Acids Res.* **27**, 4636–4641 (1999).
45. Lowe, T. M. & Eddy, S. R. tRNAscan-SE: a program for improved detection of transfer RNA genes in genomic sequence. *Nucleic Acids Res.* **25**, 955–964 (1997).
46. Nakamura, T. *et al.* Cloned cytosine deaminase gene expression of *Bifidobacterium longum* and application to enzyme/pro-drug therapy of hypoxic solid tumors. *Biosci. Biotechnol. Biochem.* **66**, 2362–2366 (2002).
47. Yasui, K. *et al.* Improvement of bacterial transformation efficiency using plasmid artificial modification. *Nucleic Acids Res.* **37**, e3 (2009).

# Interferon- $\gamma$ links ultraviolet radiation to melanomagenesis in mice

M. Raza Zaidi<sup>1</sup>, Sean Davis<sup>2</sup>, Frances P. Noonan<sup>3</sup>, Cari Graff-Cherry<sup>4</sup>, Teresa S. Hawley<sup>5</sup>, Robert L. Walker<sup>2</sup>, Lionel Feigenbaum<sup>4</sup>, Elaine Fuchs<sup>6</sup>, Lyudmila Lyakh<sup>7</sup>, Howard A. Young<sup>7</sup>, Thomas J. Hornyak<sup>8</sup>, Heinz Arnheiter<sup>9</sup>, Giorgio Trinchieri<sup>7</sup>, Paul S. Meltzer<sup>2</sup>, Edward C. De Fabo<sup>3</sup> & Glenn Merlino<sup>1</sup>

Cutaneous malignant melanoma is a highly aggressive and frequently chemoresistant cancer, the incidence of which continues to rise. Epidemiological studies show that the major aetiological melanoma risk factor is ultraviolet (UV) solar radiation, with the highest risk associated with intermittent burning doses, especially during childhood<sup>1,2</sup>. We have experimentally validated these epidemiological findings using the hepatocyte growth factor/scatter factor transgenic mouse model, which develops lesions in stages highly reminiscent of human melanoma with respect to biological, genetic and aetiological criteria, but only when irradiated as neonatal pups with UVB, not UVA<sup>3,4</sup>. However, the mechanisms underlying UVB-initiated, neonatal-specific melanomagenesis remain largely unknown. Here we introduce a mouse model permitting fluorescence-aided melanocyte imaging and isolation following *in vivo* UV irradiation. We use expression profiling to show that activated neonatal skin melanocytes isolated following a melanomagenic UVB dose bear a distinct, persistent interferon response signature, including genes associated with immunoevasion. UVB-induced melanocyte activation, characterized by aberrant growth and migration, was abolished by antibody-mediated systemic blockade of interferon- $\gamma$  (IFN- $\gamma$ ), but not type-I interferons. IFN- $\gamma$  was produced by macrophages recruited to neonatal skin by UVB-induced ligands to the chemokine receptor Ccr2. Admixed recruited skin macrophages enhanced transplanted melanoma growth by inhibiting apoptosis; notably, IFN- $\gamma$  blockade abolished macrophage-enhanced melanoma growth and survival. IFN- $\gamma$ -producing macrophages were also identified in 70% of human melanomas examined. Our data reveal an unanticipated role for IFN- $\gamma$  in promoting melanocytic cell survival/immunoevasion, identifying a novel candidate therapeutic target for a subset of melanoma patients.

Mechanisms associated with UV-mediated alterations to melanocytes and their microenvironment have been inscrutable because they cannot be adequately studied in cultured cells. Moreover, melanocytes represent only ~1% of skin cells, and bear few specific cell-surface markers permitting efficient isolation. To enable detailed study of melanocyte biology *in vivo*, we generated a mouse model in which expression of the reverse tetracycline-activated transactivator rtTA2s-M2, characterized by minimal leakiness and background, was regulated by the melanocyte-specific dopachrome tautomerase (*Dct*) gene promoter (Supplementary Fig. 1a). Dct-rtTA mice bred with transgenic mice bearing a histone H2B-GFP fusion construct controlled by the tetracycline response element (TRE) created Dct-rtTA/TRE-H2B-GFP bi-transgenic mice (hereafter iDct-GFP) (Supplementary Fig. 1b). iDct-GFP mice showed an inducible GFP profile from embryonic to adult stages consistent with known *Dct* expression patterns. GFP expression was observed in embryonic neural crest, retinal pigment epithelium and telencephalon, as expected (Fig. 1a and Supplementary

Fig. 2). Neonatal and adult skin GFP<sup>+</sup> cells were strictly localized to hair follicles, where most GFP<sup>+</sup> cells were in bulb regions, with smaller numbers in the outer root sheath and bulge regions, harbouring melanocyte precursors<sup>5</sup> (Fig. 1b). Co-localization of GFP and anti-Dct antibody by immunohistochemistry unequivocally identified GFP<sup>+</sup> cells as melanocytes (Fig. 1c). No background GFP expression was detectable without doxycycline. Full GFP induction was achieved within 12–18 h of a single intraperitoneal injection of a non-toxic doxycycline dose in neonatal or adult mice (Supplementary Fig. 1c).

Reasoning that new clues to the molecular mechanism(s) underlying UV-induced melanomagenesis would be found within the genomic response of melanocytes to UV radiation, we used the iDct-GFP mouse to examine the responses to UVB versus UVA of melanocytes residing *in situ*, within their natural morphological and physiological microenvironment. Precisely defined wideband wavelengths and physiologically relevant doses<sup>4</sup> (see Methods) of UV (Supplementary Fig. 3) were used to irradiate postnatal day 1 (PD1) iDct-GFP mice, and skins were harvested at certain time points after irradiation. To avoid potential toxicity from chronic expression and interference with UV absorption, GFP was doxycycline-induced after UV irradiation, 24 h before skin harvest. GFP<sup>+</sup> melanocytes were phenotypically activated, characterized by raised melanocyte numbers and migration towards the epidermis as previously reported<sup>6</sup>, 24–48 h after exposure to UVB, but not UVA, peaking at 3 days and lasting at least 10 days after irradiation (Fig. 1d and Supplementary Fig. 4a). UVB-induced melanocyte activation was specific to neonatal irradiation; adult mice irradiated at PD29 did not show this response (Supplementary Fig. 4b).

We performed an expression microarray study on melanocytes isolated from dorsal skin of iDct-GFP pups irradiated at PD1 with UVB or UVA (Fig. 1e). Doxycycline-induced GFP-labelled melanocytes were isolated via fluorescence-activated cell sorting (FACS) at 1 day and 6 days after irradiation (ages PD2 and PD7, respectively); arrays from 1 day post-UV would reflect the acute UV stress response of *in vivo* melanocytes, whereas the 6 days post-UV time point should uncover responses persisting after the acute stress response subsides. FACS isolation consistently yielded >95% melanocyte enrichment (Supplementary Fig. 5). Gene expression profiling produced robust data with good reproducibility among biological triplicates (Fig. 2a), and confirmed the absence of detectable levels of contaminating skin cell types, including keratinocytes, fibroblasts and adipocytes (Supplementary Fig. 6).

UVB elicited a potent, transient, acute stress response in melanocytes, including increased expression of p53 target genes (for example, *p21<sup>Waf1/Cip1</sup>*, cyclin G1 and reprimin), whereas UVA-associated changes were subtle (Fig. 2a and Supplementary Fig. 7). Intriguingly, a small subset of genes showed a delayed response evident at 6 days after UVB exposure (Fig. 2a), including a putative IFN-responsive gene signature<sup>7</sup>

<sup>1</sup>Laboratory of Cancer Biology and Genetics, National Cancer Institute, Bethesda, Maryland 20892, USA. <sup>2</sup>Genetics Branch, National Cancer Institute, Bethesda, Maryland 20892, USA. <sup>3</sup>Laboratory of Photobiology and Photoimmunology, Department of Microbiology, Immunology and Tropical Medicine, George Washington University Medical Center, Washington, District of Columbia 20037, USA.

<sup>4</sup>Laboratory Animal Sciences Program, National Cancer Institute, Frederick, Maryland 21702, USA. <sup>5</sup>Flow Cytometry Core, George Washington University Medical Center, Washington, District of Columbia 20037, USA. <sup>6</sup>Rockefeller University, New York, New York 10021, USA. <sup>7</sup>Cancer and Inflammation Program, National Cancer Institute, Frederick, Maryland 21702, USA. <sup>8</sup>Dermatology Branch, National Cancer Institute, Bethesda, Maryland 20892, USA. <sup>9</sup>National Institute of Neurological Disorders and Stroke, Bethesda, Maryland 20892, USA.

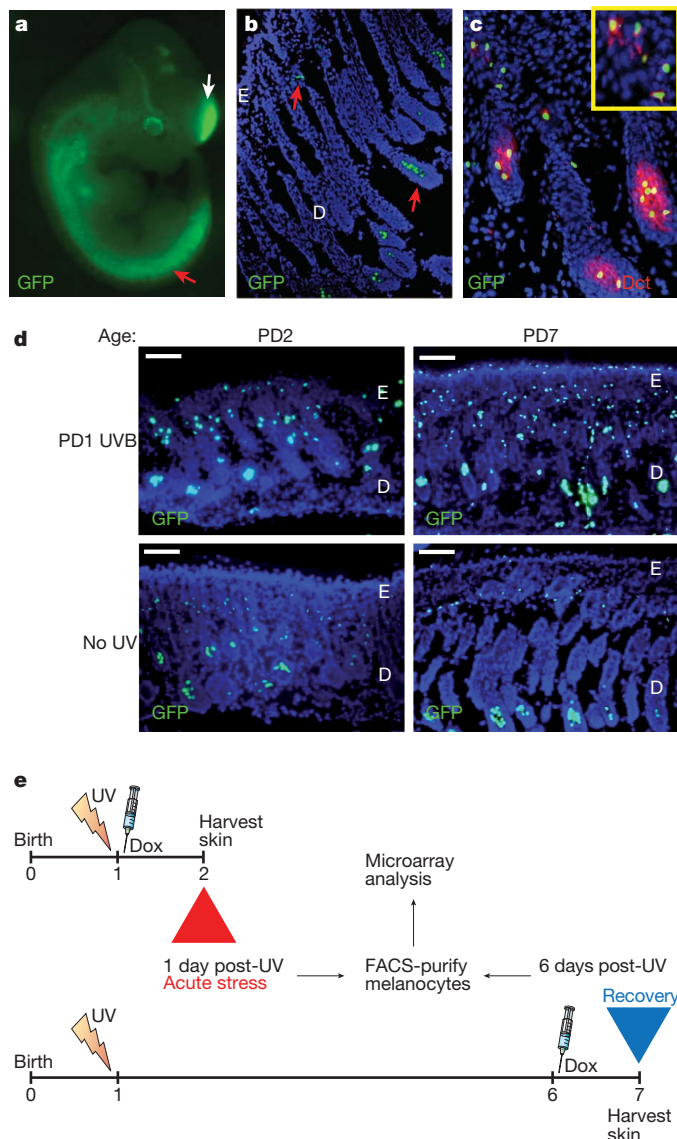


**Figure 1 | Melanocyte-specific GFP expression reveals UVB-induced activation.** **a**, Embryonic day 11.5 iDct-GFP embryo showing GFP<sup>+</sup> cells in neural crest (red arrow) and telencephalon (white arrow); magnification,  $\times 10$ . **b**, In 7-day old pup skin GFP<sup>+</sup> cells are located in the bulb (lower arrow) and bulge (upper arrow) regions of hair follicles. Blue, 4',6-diamidino-2-phenylindole (DAPI); magnification,  $\times 40$ . D, dermis; E, epidermis. **c**, Immunohistochemistry with anti-Dct antibody shows co-localization with GFP in iDct-GFP skin; magnification,  $\times 100$ . **d**, UVB-induced activation of melanocytes, characterized by proliferation and migration towards epidermis. Dorsal skins were examined at 1 day (at age PD2) and 6 days (PD7) after irradiation. Scale bars, 40  $\mu$ m. **e**, Schematic of the regime for isolating GFP<sup>+</sup> melanocytes by FACS. Pups are irradiated at PD1, and dorsal skins harvested at either PD2 (24 h post-UV) or PD7 (6 days post-UV). Doxycycline (Dox) injections are always given after irradiation, 24 h before skin harvest.

(Fig. 2a and Supplementary Table 1). Four upregulated genes (*Ccl8*, *Ctla4*, *H2-K1* and *H2-T23*) from this group were validated by quantitative reverse transcription-polymerase chain reaction (qRT-PCR) (Fig. 2b). The response was neonate specific (Supplementary Fig. 8), and included genes implicated in conferring immunoevasiveness (that is, *Ctla4*, *H2-T23*, *H2-M3*, *Cfb* (also known as *H2-Bf*) and *C4a* (also known as *Slp*)).

To determine whether IFN signalling has a biologically significant role in UVB-induced melanocyte activation, we blocked both type-I (IFN- $\alpha$  and IFN- $\beta$ ) and type-II (IFN- $\gamma$ ) interferons by neonatal administration of anti-IFN- $\alpha$  receptor 1 (IFN- $\alpha$ R1) and anti-IFN- $\gamma$

antibodies, respectively. Melanocytes from 6-day post-UVB skin were activated in the presence of isotype control antibody, whereas the anti-IFN- $\alpha$ R1 + anti-IFN- $\gamma$  antibody combination completely abolished this response (Fig. 2c). Moreover, although antibody-mediated blockade of type-I IFN- $\alpha/\beta$  signalling alone failed to overtly affect UVB-mediated activation, blockade of IFN- $\gamma$  alone markedly inhibited this response (Fig. 2c). These results were corroborated by flow cytometric quantification of GFP<sup>+</sup> skin cells from each antibody-treated group (Supplementary Fig. 9). We next isolated GFP<sup>+</sup> melanocytes from UV-irradiated neonates blocked with either anti-IFN- $\gamma$  or anti-IFN- $\alpha$ R1, and compared their expression patterns to control. Anti-IFN- $\gamma$  and anti-IFN- $\alpha$ R1 antibodies repressed expression of a common gene set associated with the IFN response (Supplementary Fig. 10). However, IFN- $\gamma$  inhibition also more potently repressed expression of several non-classical major histocompatibility complex (MHC) class Ib antigens (for example, *H2-T23* and *H2-Q2*), as well as *Psmb9*, *Gbp2*, *Icam*, *Irf1* and *Fosb*; members of this gene subset should be responsible for the observed melanocytic phenotypes. Notably, IFN- $\gamma$  blockade exclusively and potently inhibited expression of chemokine *Ccl8* (also known as MCP-2).

We determined the IFN- $\gamma$  source by interrogating 6-day post-UVB-irradiated skin for immune-cell infiltration. Immunohistochemistry failed to detect T cells, B cells, dendritic cells, natural killer (NK), or NK-T cells; however, CD11b<sup>+</sup> cells of myeloid origin were evident (Supplementary Fig. 11). Anti-F4/80 and anti-Gr-1 antibodies identified these as macrophages (F4/80<sup>+</sup>Gr-1<sup>-</sup>), not neutrophils (Fig. 3a, upper panel). Nearly 90% of CD11b<sup>+</sup> cells were also F4/80<sup>+</sup> (Supplementary Fig. 12). Notably, the adult response was distinct; dorsal skins from PD35 mice 2 days after UVB showed predominant Gr-1<sup>+</sup> cell infiltration, and minimal F4/80<sup>+</sup> cells (Fig. 3a, lower panel), as reported<sup>8</sup>.

To determine if infiltrating macrophages expressed IFN- $\gamma$ , as has been suggested<sup>9</sup>, type-I and type-II interferon mRNAs were quantified from FACS-purified CD11b<sup>+</sup> and F4/80<sup>+</sup> cells. Both had upregulated IFN- $\alpha$  and IFN- $\gamma$  expression, and to a lesser extent IFN- $\beta$  (Fig. 3b). Flow cytometry demonstrated that 28% of both CD11b<sup>+</sup> and F4/80<sup>+</sup> cells expressed IFN- $\gamma$  (Fig. 3c). Our data support the notion that UVB-recruited, infiltrating macrophages secrete IFN- $\gamma$ , inducing the IFN signature detected in activated melanocytes. Although we were unable to detect NK cell markers in FACS-isolated CD11b<sup>+</sup> cells by qRT-PCR (Supplementary Fig. 13), we cannot rule out a possible contribution by undetectably low numbers of NK or other inflammatory cells.

That UVB-induced chemokines were responsible for neonatal macrophage recruitment, particularly *Ccr2*/*Ccr5* ligands, was indicated by our melanocyte microarray data and confirmed by qRT-PCR (Supplementary Fig. 14a, b). These results were further corroborated through treatment of cultured melan-c normal immortalized melanocyte cell line with non-cytotoxic UV (Supplementary Fig. 14c). In contrast, upregulation of these chemokines was not detected in UV-irradiated whole skin (Supplementary Fig. 15) or isolated keratinocytes<sup>10</sup>. *Ccr2* and *Ccr5* were highly expressed in skin-infiltrating macrophages, but not in non-activated RAW264.7 macrophages (Supplementary Fig. 16). Finally, mice deficient in *Ccr2* were significantly inhibited in their ability to recruit F4/80<sup>+</sup> macrophages into neonatal skin (Fig. 3d); in contrast, *Ccr5*-deficient mice showed no significant difference (data not shown).

The arrival of IFN- $\gamma$ -expressing macrophages coincided with a >100-fold upregulation in melanocyte expression of the *Ccr2* ligand *Ccl8*, a known IFN- $\gamma$ -response gene<sup>11</sup>, whereas expression of other *Ccr2* ligands had returned to baseline. We propose that recruited IFN- $\gamma$ <sup>+</sup> macrophages enhance melanocyte *Ccl8* expression, reinforcing macrophage-melanocyte interactions and fueling an inflammatory positive feedback loop. To confirm its ability to potently chemoattract macrophages, *Ccl8* was ectopically expressed in F5061 cells—established from a UV-induced melanoma from an immunocompetent hepatocyte

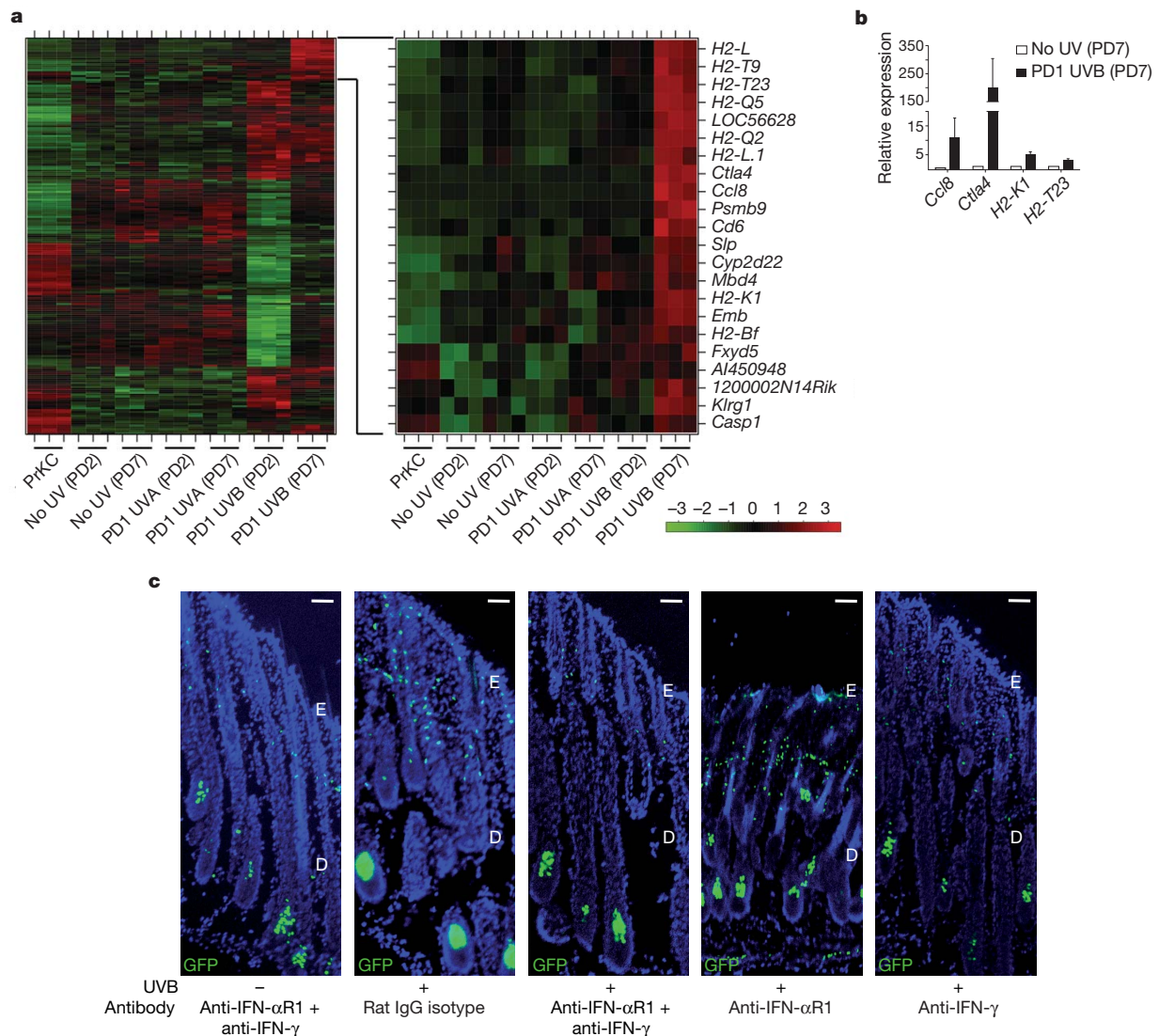


**Figure 2 | UVB-induced melanocyte activation is mediated by IFN- $\gamma$ .** **a**, Unsupervised clustering of complementary DNA (cDNA) microarray analysis of gene expression in FACS-sorted melanocytes from 1 day (PD2) or 6 days (PD7) after UVB or UVA irradiation, and respective unirradiated controls. The expanded heatmap (right) shows the delayed induced gene subset, which includes multiple genes known to be induced by IFN- $\gamma$ . Primary mouse keratinocytes (PrKC) were included as controls. All groups included

biological triplicates. **b**, qRT-PCR validation of expression of 4 genes ( $n = 3$  samples each) from IFN signature (error bars = s.e.m.). **c**, Antibody-mediated blockade of interferons by treating pups with intraperitoneal injections of anti-IFN- $\alpha$ R1, anti-IFN- $\gamma$ , or both in combination, 1 h before and 3 days after UVB irradiation at PD1. The dorsal skins were harvested ( $n = 3$  each group) and analysed for melanocyte activation. Representative images are shown. D, dermis; E, epidermis. Scale bars, 18  $\mu$ m.

growth factor/scatter factor (HGF/SF)-transgenic mouse. F5061-Ccl8 cells were subcutaneously inoculated into syngeneic FVB/N mice, markedly enhancing macrophage infiltration into the transplantation site (Fig. 3e). Conditioned media from F5061-Ccl8 cells also significantly elevated transmembrane migration of RAW264.7 macrophages (Supplementary Fig. 17).

Macrophages show either anti- or pro-tumorigenic properties<sup>12</sup>. F4/80<sup>+</sup> macrophages were isolated from 6-day post-UVB neonatal skin, admixed at a ratio of 1:5 with F5061 melanoma cells and transplanted subcutaneously into FVB/N mice. Admixed transplants showed significantly increased growth relative to controls (Fig. 4a and Supplementary Fig. 18), indicating that these activated macrophages were pro-tumorigenic. In contrast, macrophages isolated from spleens of unirradiated control pups did not affect tumour growth (Supplementary Fig. 19). Ki-67 immunohistochemistry showed no difference in proliferation between admixed tumours versus controls (Supplementary Fig. 20); however, TdT-mediated dUTP nick end labelling (TUNEL) assays revealed significantly less apoptosis in admixed tumours (Fig. 4b

and Supplementary Fig. 21), demonstrating that UVB-recruited macrophages promote melanoma cell survival. Immunohistochemistry confirmed that a subset of tumour-associated macrophages maintained IFN- $\gamma$  expression (Supplementary Fig. 22). Moreover, macrophage presence strongly correlated with enhanced Ctla4 expression in F5061 melanoma cells (Supplementary Fig. 23), recapitulating the functional consequence of macrophage infiltration observed in neonatal skin melanocytes (Fig. 2a, b).

Despite its well-documented anti-tumorigenic activity<sup>13</sup>, IFN- $\gamma$  has also been implicated as a pro-tumorigenic factor<sup>14,15</sup>. To determine if macrophage-secreted IFN- $\gamma$  was responsible for the enhanced melanoma growth observed in admixed tumours, we included intraperitoneal administration of either anti-IFN- $\gamma$  or control antibodies. Whereas admixed melanomas in the control group showed the expected enhanced growth, those in mice given anti-IFN- $\gamma$  antibody showed significantly reduced growth (Fig. 4c). Immunophenotyping of tissue microarrays containing UVB-induced mouse melanomas showed that most (66%) were macrophage-rich, with fewer having T cells (59%) and B cells (32%)

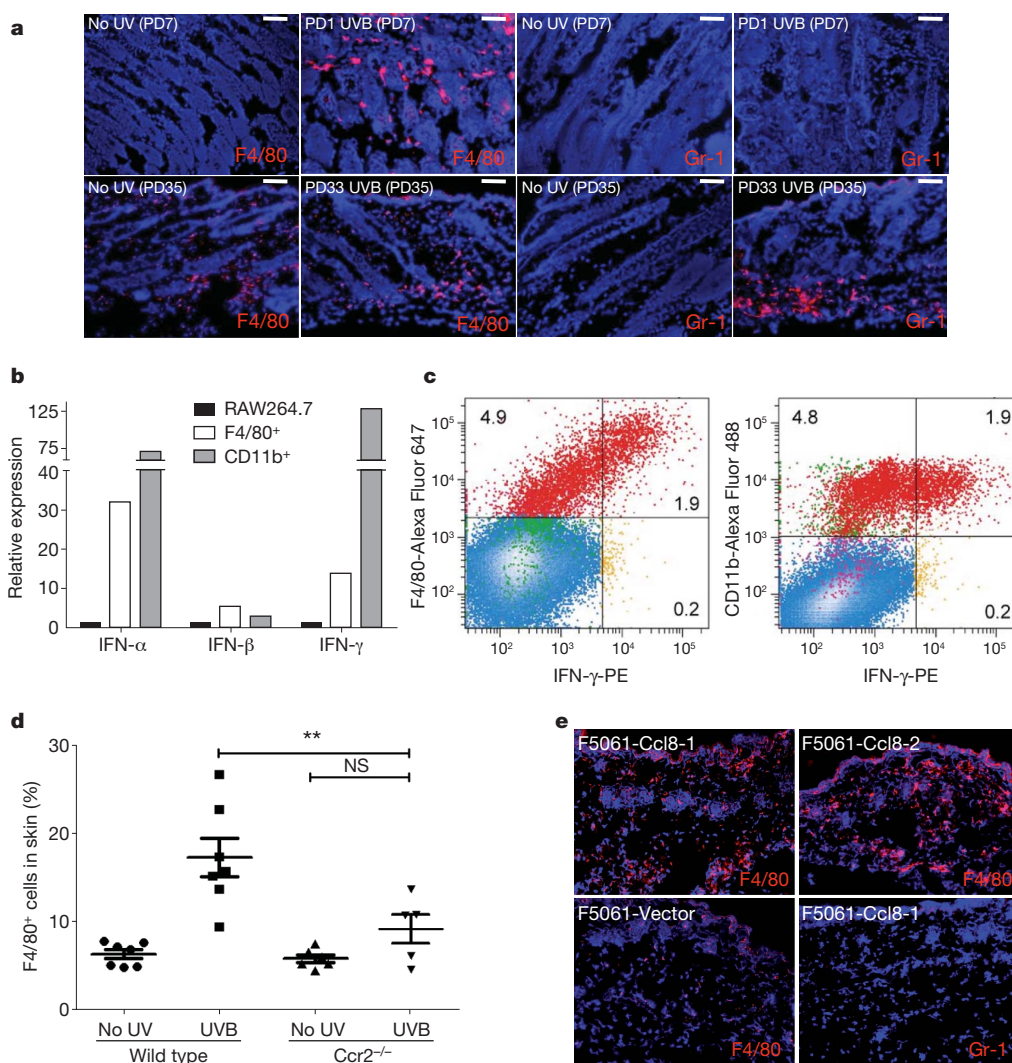


**Figure 3 | UVB induces chemoattraction of IFN- $\gamma$ -producing macrophages into neonatal skin.** **a**, Immunohistochemistry with anti-F4/80 and anti-Gr-1 antibodies in dorsal skins of UVB-irradiated and unirradiated neonatal (upper panel) and adult (lower panel) mice. Scale bars, 40  $\mu$ m. **b**, qRT-PCR for IFN- $\alpha$ , IFN- $\beta$  and IFN- $\gamma$  expression in F4/80<sup>+</sup> and CD11b<sup>+</sup> cells FACS-isolated from neonatal dorsal skins UVB-irradiated at PD1 and examined at PD7, compared with non-activated RAW264.7 macrophages. **c**, Flow cytometric analysis of PD1 UVB-irradiated (PD7 examined) skin-cell-suspension-identified IFN- $\gamma$ <sup>+</sup>

macrophages. PE, phycoerythrin. **d**, Flow cytometric analysis of macrophage (F4/80<sup>+</sup>) infiltration into skin, 2 days after UVB irradiation in Ccr2-deficient pups (irradiated at PD1), as compared to wild-type pups. \*\* $P < 0.01$ ; one-way ANOVA test with post-hoc Tukey analysis. NS, not significant. **e**, F5061 melanoma cells ectopically expressing Ccl8 chemoattract F4/80<sup>+</sup> macrophages (red), but not Gr-1<sup>+</sup> cells, to sites of subcutaneous inoculation in syngeneic FVB/N mice. One vector-transfected and two Ccl8-transfected clone cells were used. Blue, DAPI.

(Supplementary Fig. 24). To determine if human melanoma-associated macrophages produce IFN- $\gamma$ , we performed dual immunohistochemistry for CD68 and IFN- $\gamma$  using human melanoma tissue microarrays. We discovered that 19 of 27 (70%) melanomas examined contained abundant macrophages (CD68<sup>+</sup>), of which all 19 demonstrated CD68<sup>+</sup> IFN- $\gamma$ <sup>+</sup> dual positivity (Fig. 4d and Supplementary Fig. 25).

In this study we show that UV incites melanomagenesis not only through DNA mutagenesis, but also by altering interactions between melanocytes and their microenvironment to regulate remodelling of UV-damaged skin. On the basis of our results, a model implicating a neonatal-specific UV-induced pro-melanomagenic inflammatory cascade emerges (Fig. 4e). In accordance with their relative tumorigenicity in albino HGF/SF-transgenic mice<sup>4</sup>, UVB not UVA induces melanocytic expression of multiple chemoattracting Ccr2 ligands (Ccl2, Ccl7, Ccl8, Ccl12), recruiting Ccr2<sup>+</sup> macrophages into neonatal skin. IFN- $\gamma$  from recruited macrophages stimulates melanocyte proliferation and migration, and the expression of genes implicated in immunoevasion/survival.

Erythematous neonatal UVB causes robust macrophage infiltration and is melanomagenic; adult skin responds with a rapid, short-lived neutrophil influx, but no melanoma. We propose that mechanisms underlying neonatal UVB-induced melanomagenesis operate within the immunoeediting paradigm<sup>13</sup>: UVB-activated mutant neonatal melanocytes—particularly progenitors<sup>16</sup>—exposed to inflammation evade immune-mediated elimination, persisting through an extended equilibrium phase before evolving into clinically significant melanoma. Macrophage-induced melanocyte proliferation would more efficiently fix UV-induced mutations in prospective melanoma cells, whereas enhanced melanocyte migration could facilitate UVB-associated long-term tolerance to melanocytic antigens<sup>17</sup> by promoting aberrant melanocyte-immune-cell interactions. Moreover, enduring inflammation-associated epigenetic alterations occur in transformed cells<sup>18</sup>, and perhaps in long-lived macrophage subpopulations<sup>19</sup>, indefinitely extending their biological effects.

Notably, our systemic antibody blockade experiments demonstrating the importance of physiologically relevant IFN- $\gamma$  in UVB-induced melanocyte activation and melanoma cell survival strongly support the

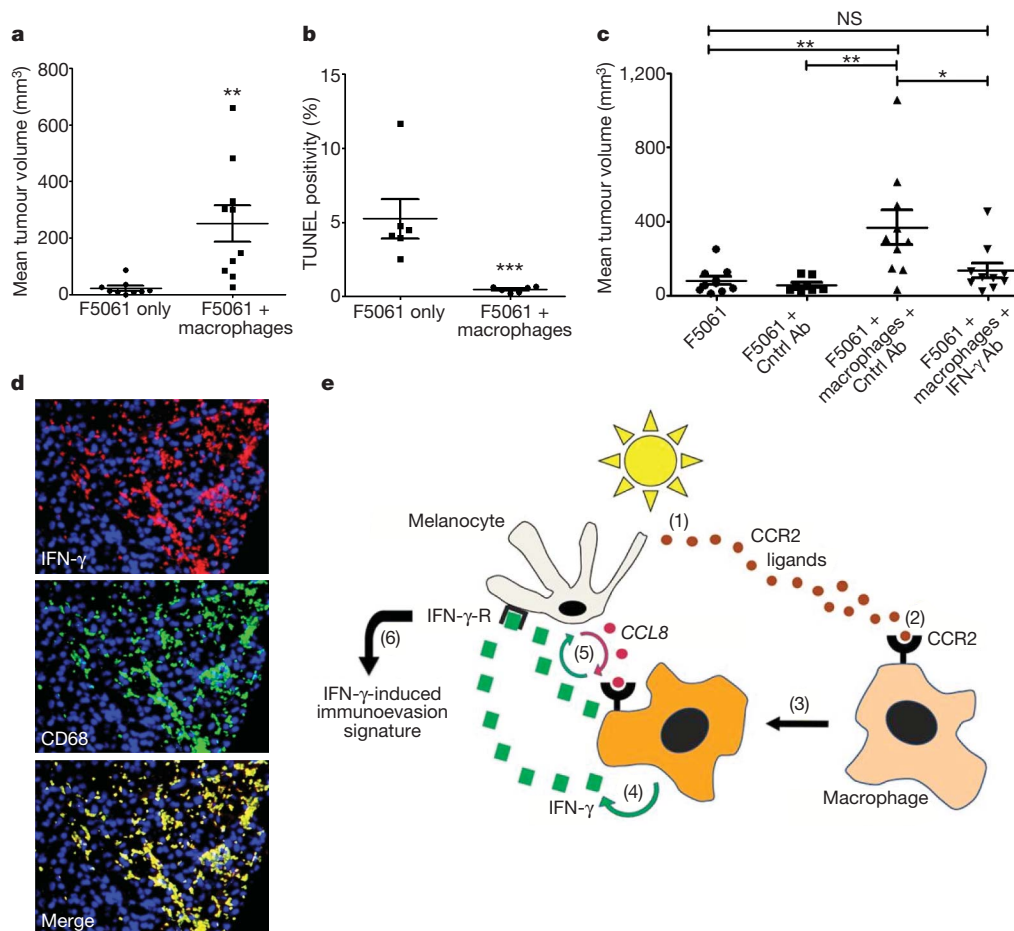


**Figure 4 | IFN- $\gamma$  mediates pro-tumorigenic effects of UVB-recruited skin macrophages.** **a**, Mean volumes ( $\pm$  s.e.m.) of F5061 melanomas admixed with skin macrophages isolated from PD1 UVB-irradiated (PD7-examined) pups ( $n = 10$ ), versus F5061-only controls ( $n = 9$ ), following subcutaneous transplantation in syngeneic FVB/N mice.  $**P < 0.01$ . **b**, Percentages of TUNEL plus cells ( $\pm$  s.e.m.) in admixed and control tumours ( $n = 6$  each).  $***P < 0.001$ . **c**, Antibody-mediated blockade of IFN- $\gamma$  significantly inhibits pro-tumorigenic effects of macrophages. Cntrl Ab, control antibody.  $*P < 0.05$ ;  $**P < 0.01$ ; NS, not significant. One-Way ANOVA test with post-hoc Tukey analysis. **d**, Dual immunohistochemistry with anti-IFN- $\gamma$  (red) and anti-CD68

(green) antibodies on a human melanoma tissue microarray shows IFN- $\gamma$ -expressing macrophages (yellow). Representative tumour is shown.

**e**, Schematic representation of the UVB-induced inflammatory cascade leading to IFN- $\gamma$ -mediated immunoevasion and survival of melanocytes during sunburn-associated remodelling. UV induces release of CCR2 ligands (1); that activate CCR2<sup>+</sup> macrophages (2); which are recruited to neonatal skin (3); macrophages secrete IFN- $\gamma$  (4); which activates melanocytes, inducing expression of genes that include *CCL8*, fueling inflammation (5); and immunoevasion (6).

notion that IFN- $\gamma$  can be pro-tumorigenic as well as anti-tumorigenic, depending on the context, intensity and durability of the IFN- $\gamma$  signal<sup>14</sup>. In fact, an association between IFN- $\gamma$ -induced genes and early mouse melanocytic lesions has been reported<sup>15</sup>, and serum IFN- $\gamma$  has been implicated as an independent prognostic indicator for melanoma recurrence<sup>20</sup>. We propose that IFN- $\gamma$ -associated survival mechanisms operational in neonatal melanocytes are recapitulated in melanoma, contributing to the selection of more aggressive, therapeutically resistant phenotypes. Relevance to human melanoma is supported by the detection of macrophage-associated IFN- $\gamma$  expression in most patient samples examined, and a clinical trial showing that IFN- $\gamma$  may have adverse effects regarding melanoma patient relapse and mortality<sup>21</sup>. We provide the first evidence, to our knowledge, that IFN- $\gamma$ -R signalling can facilitate melanoma progression, a remarkable discovery considering that high-dose IFN- $\alpha$  is used to treat melanoma, albeit with limited success<sup>22</sup>. Non-overlapping functions of type-I and type-II interferons are well described<sup>13</sup>, and strongly supported by our data.

The IFN 'survival signature' associated with UVB-activated mouse melanocytes contains genes involved in human melanoma immunoevasion, including non-classical MHC class Ib antigens (mouse H2-M3/human HLA-G; mouse H2-T23 (also known as Qa-1)/human HLA-E)<sup>23,24</sup>. HLA-E suppresses NK and cytotoxic T lymphocytes<sup>25,26</sup>.

This IFN signature also features complement isoforms C4a and C4b, implicated in systemic autoimmunity suppression<sup>27</sup>, and CTLA4, a potent immune evasion facilitator. CTLA4 is also highly upregulated in mouse melanoma cells admixed with neonatal macrophages, and expressed on human melanoma cells, where it may be involved in immune escape<sup>28,29</sup>.

Here we identify novel cellular/molecular inflammatory mechanisms centred on IFN- $\gamma$  signalling that may underlie the initiation, survival and/or outgrowth of UVB-induced melanoma cells. We propose that such mechanisms are highly relevant to strategies used by melanoma cells to evade immunosurveillance in patients. In what could prove to be a paradigm shift, our data strongly suggest that IFN- $\gamma$ /IFN- $\gamma$ -R or its downstream pathway members represent promising prognostic markers and/or efficacious therapeutic targets in an appropriate subset of melanoma patients.

## METHODS SUMMARY

All mouse studies were performed under the strict guidelines of Animal Study Protocols approved by the Animal Care and Use Committees at the National Cancer Institute/National Institutes of Health and the George Washington University Medical Center. The Dct-rtTA transgenic mice express rtTA2s-M2 under the control of the *Dct* (*Trp2*) gene promoter. Thirty-one founder transgenic mice were generated by standard microinjection techniques, individually crossed

with the TRE-H2B–GFP transgenic mice, and screened for a line that produced no leaky background expression of GFP without doxycycline and quickly responded to a single intraperitoneal doxycycline injection. One such line was selected to make a double homozygous Dct-rtTA/TRE-H2B–GFP transgenic mouse line in albino FVB/N background, and males were crossed with wild-type FVB/N females to produce litters that were 100% double heterozygous (iDct–GFP). One day after birth, the pups were irradiated with UV radiation (UVB, UVA, or sham)<sup>4</sup> (Supplementary Fig. 3). Dorsal skins were harvested at 24 h and 6 days after irradiation (or sham irradiation). Twenty-four hours before mice were killed and dorsal skins harvested, neonates were injected intraperitoneally with doxycycline at 80 µg g<sup>−1</sup> body weight to activate GFP expression. Skins from 6–8 pups of a litter were pooled to prepare single-cell suspensions using a published protocol<sup>30</sup>, followed by isolation of GFP<sup>+</sup> melanocytes via FACS. RNA samples isolated from these melanocytes were subjected to cDNA microarray on Illumina Murine Beadchips v. 2.0 (Illumina). qRT–PCR validation was performed using primers listed in Supplementary Table 2. Immunohistochemical and flow cytometric analyses were performed using antibodies listed in Supplementary Table 3.

**Full Methods** and any associated references are available in the online version of the paper at [www.nature.com/nature](http://www.nature.com/nature).

**Received 26 March; accepted 9 November.**

**Published online 19 January 2011.**

- Garibyan, L. & Fisher, D. E. How sunlight causes melanoma. *Curr. Oncol. Rep.* **12**, 319–326 (2010).
- Whiteman, D. C., Whiteman, C. A. & Green, A. C. Childhood sun exposure as a risk factor for melanoma: a systematic review of epidemiologic studies. *Cancer Causes Control* **12**, 69–82 (2001).
- Noonan, F. P. et al. Neonatal sunburn and melanoma in mice. *Nature* **413**, 271–272 (2001).
- De Fabo, E. C., Noonan, F. P., Fears, T. & Merlino, G. Ultraviolet B but not ultraviolet A radiation initiates melanoma. *Cancer Res.* **64**, 6372–6376 (2004).
- Nishimura, E. K. et al. Dominant role of the niche in melanocyte stem-cell fate determination. *Nature* **416**, 854–860 (2002).
- Walker, G. J. et al. Murine neonatal melanocytes exhibit a heightened proliferative response to ultraviolet radiation and migrate to the epidermal basal layer. *J. Invest. Dermatol.* **129**, 184–193 (2009).
- Schroder, K., Hertzog, P. J., Ravasi, T. & Hume, D. A. Interferon- $\gamma$ : an overview of signals, mechanisms and functions. *J. Leukoc. Biol.* **75**, 163–189 (2004).
- Wolnicka-Glubisz, A. et al. Deficient inflammatory response to UV radiation in neonatal mice. *J. Leukoc. Biol.* **81**, 1352–1361 (2007).
- Darwich, L. et al. Secretion of interferon- $\gamma$  by human macrophages demonstrated at the single-cell level after costimulation with interleukin (IL)-12 plus IL-18. *Immunology* **126**, 386–393 (2009).
- Li, D. et al. Rays and arrays: the transcriptional program in the response of human epidermal keratinocytes to UVB illumination. *FASEB J.* **15**, 2533–2535 (2001).
- Proost, P., Wuyts, A. & Van Damme, J. Human monocyte chemotactic proteins-2 and -3: structural and functional comparison with MCP-1. *J. Leukoc. Biol.* **59**, 67–74 (1996).
- DeNardo, D. G. et al. CD4<sup>+</sup> T cells regulate pulmonary metastasis of mammary carcinomas by enhancing protumor properties of macrophages. *Cancer Cell* **16**, 91–102 (2009).
- Dunn, G. P., Koebel, C. M. & Schreiber, R. D. Interferons, immunity and cancer immunoeediting. *Nature Rev. Immunol.* **6**, 836–848 (2006).
- He, Y. F. et al. Sustained low-level expression of interferon- $\gamma$  promotes tumor development: potential insights in tumor prevention and tumor immunotherapy. *Cancer Immunol. Immunother.* **54**, 891–897 (2005).
- Aoki, H. & Moro, O. Upregulation of the IFN- $\gamma$ -stimulated genes in the development of delayed pigmented spots on the dorsal skin of F1 mice of HR-1 x HR/De. *J. Invest. Dermatol.* **124**, 1053–1061 (2005).
- Hirobe, T. Histochemical survey of the distribution of the epidermal melanoblasts and melanocytes in the mouse during fetal and postnatal periods. *Anat. Rec.* **208**, 589–594 (1984).
- Wolnicka-Glubisz, A. & Noonan, F. P. Neonatal susceptibility to UV induced cutaneous malignant melanoma in a mouse model. *Photochem. Photobiol. Sci.* **5**, 254–260 (2006).
- Iliopoulos, D., Jaeger, S. A., Hirsch, H. A., Bulyk, M. L. & Struhl, K. STAT3 activation of miR-21 and miR-181b-1 via PTEN and CYLD are part of the epigenetic switch linking inflammation to cancer. *Mol. Cell* **39**, 493–506 (2010).
- Murphy, J., Summer, R., Wilson, A. A., Kotton, D. N. & Fine, A. The prolonged lifespan of alveolar macrophages. *Am. J. Respir. Cell Mol. Biol.* **38**, 380–385 (2008).
- Porter, G. A. et al. Significance of plasma cytokine levels in melanoma patients with histologically negative sentinel lymph nodes. *Ann. Surg. Oncol.* **8**, 116–122 (2001).
- Meyskens, F. L. Jr et al. Randomized trial of adjuvant human interferon gamma versus observation in high-risk cutaneous melanoma: a Southwest Oncology Group study. *J. Natl. Cancer Inst.* **87**, 1710–1713 (1995).
- Ascierto, P. A. & Kirkwood, J. M. Adjuvant therapy of melanoma with interferon: lessons of the past decade. *J. Transl. Med.* **6**, 62 (2008).
- Rebmann, V., Wagner, S. & Grosse-Wilde, H. HLA-G expression in malignant melanoma. *Semin. Cancer Biol.* **17**, 422–429 (2007).
- Derre, L. et al. Expression and release of HLA-E by melanoma cells and melanocytes: potential impact on the response of cytotoxic effector cells. *J. Immunol.* **177**, 3100–3107 (2006).
- Lee, N. et al. HLA-E is a major ligand for the natural killer inhibitory receptor CD94/NKG2A. *Proc. Natl. Acad. Sci. USA* **95**, 5199–5204 (1998).
- Wischhusen, J., Waschbisch, A. & Wiendl, H. Immune-refractory cancers and their little helpers—an extended role for immunotolerogenic MHC molecules HLA-G and HLA-E? *Semin. Cancer Biol.* **17**, 459–468 (2007).
- Chen, Z., Koralov, S. B. & Kelsoe, G. Complement C4 inhibits systemic autoimmunity through a mechanism independent of complement receptors CR1 and CR2. *J. Exp. Med.* **192**, 1339–1352 (2000).
- Hodi, F. S. et al. Improved survival with ipilimumab in patients with metastatic melanoma. *N. Engl. J. Med.* **363**, 711–723 (2010).
- Shah, K. V., Chien, A. J., Yee, C. & Moon, R. T. CTLA-4 is a direct target of Wnt/ $\beta$ -catenin signaling and is expressed in human melanoma tumors. *J. Invest. Dermatol.* **128**, 2870–2879 (2008).
- Wolnicka-Glubisz, A., King, W. & Noonan, F. P. SCA-1<sup>+</sup> cells with an adipocyte phenotype in neonatal mouse skin. *J. Invest. Dermatol.* **125**, 383–385 (2005).

**Supplementary Information** is linked to the online version of the paper at [www.nature.com/nature](http://www.nature.com/nature).

**Acknowledgements** We would like to thank the following individuals for their support: S. Yuspa for primary keratinocytes; C. Toniatti and H. Bujard for the rTA2sM2 construct; V. Hearing for melan-c cell line; S. Hewitt for the human melanoma tissue microarray; M. Anver for immunohistochemical staining and production/analysis of mouse melanoma tissue microarray; K. Blas and E. Vega-Valle for technical help; N. Restifo and A. Hurwitz for suggestions and discussions. This research was supported in part by the Intramural Research Program of the NIH, National Cancer Institute, Center for Cancer Research. M.R.Z. was supported by a National Cancer Institute Director's Innovation Career Development Award. E.C.D. and F.P.N. were supported by grants from the National Institutes of Health (awards CA53765 and CA92258), and the Melanoma Research Foundation.

**Author Contributions** M.R.Z. designed and performed experiments, interpreted data and wrote the manuscript. S.D. performed statistical analysis of microarray data and generated heatmaps. F.P.N. interpreted data and reviewed the manuscript. C.G.-C. managed mouse colonies. T.S.H. performed flow cytometry and FACS. R.L.W. performed cDNA microarrays. L.F. produced Dct-rtTA transgenic mice. E.F. provided TRE-H2B–GFP mice. L.L. helped design interferon blockade experiments. H.A.Y. interpreted data and reviewed the manuscript. T.J.H. evaluated GFP expression in skin and reviewed the manuscript. H.A. evaluated embryonic expression of GFP and reviewed the manuscript. G.T. designed interferon blockade experiments, provided antibodies, and reviewed the manuscript. P.S.M. designed and performed analysis of microarray data and reviewed manuscript. E.C.D. designed, measured and performed UV irradiation experiments, supervised project, and reviewed manuscript. G.M. designed experiments, interpreted data, supervised the project and wrote the manuscript.

**Author Information** The microarray data have been deposited in the Gene Expression Omnibus (GEO) database (<http://www.ncbi.nlm.nih.gov/geo>) under accession number GSE25164. Reprints and permissions information is available at [www.nature.com/reprints](http://www.nature.com/reprints). The authors declare no competing financial interests. Readers are welcome to comment on the online version of this article at [www.nature.com/nature](http://www.nature.com/nature). Correspondence and requests for materials should be addressed to G.M. (gmerlino@helix.nih.gov) and E.C.D. (drmecc@gwumc.edu).

## METHODS

**Generation of Dct-rtTA and iDct-GFP mice.** DNA fragments from the following plasmids were used to construct the plasmid pDct-rtTA- $\beta$ Glo, which harbours the transgene fragment used to make the Dct-rtTA transgenic mice. Firstly, pH $\beta$ Globin: the vector backbone is pBluescript II KS+ and the insert is a BamHI/PstI genomic fragment from the human  $\beta$ -globin gene, which is comprised of partial exon 2, full intron 2, full exon 3 and poly A signal. Secondly, pPDct: this plasmid contains the 3.4-kb BamHI/Eco47III fragment from the *Dct* gene promoter<sup>31</sup>. Thirdly, pBS/IRES-M2: this plasmid contains the rtTA2s-M2 fragment. It is a variant of pUHRt62-1<sup>32</sup>, and was obtained from C. Toniatti and H. Bujard. The Dct-rtTA transgenic mice were generated using standard microinjection techniques in a FVB/N background strain. Dct-rtTA mice were bred with the TRE-H2B-GFP transgenic mice<sup>33</sup> to generate the bi-transgenic iDct-GFP mice.

**Mice.** Wild-type FVB/N female breeders, *Ccr2*<sup>-/-</sup> mice (strain B6.129S4-Ccr2<sup>tm1Jf</sup>/J), and *Ccr5*<sup>-/-</sup> mice (strain B6.129P2-Ccr5<sup>tm1Kuz</sup>/J) were obtained from Jackson Laboratories and housed under the strict guidelines of the Institutional Animal Care and Use Committee (IACUC)-approved protocols. Transportation of mice between National Cancer Institute-Frederick and George Washington University Medical Center (GWUMC) animal facilities was performed by special animal courier service approved by IACUC.

**In vivo UV irradiation.** iDct-GFP pups were irradiated with UV radiation (UVB, UVA, or sham) as previously described<sup>4</sup> (Supplementary Fig. 3). The standard erythral dose (SED) is used to compare the sunburning effectiveness of different UV-emitting sources. These sources include UV-emitting lamps in sunbathing beds, welder's arcs and sunlight among others. By determining the SED one is able to compare how efficient the UV-emitting sources are at inducing sunburn or reddening in skin relative to each other. In experimental UV studies, many laboratories use different types of UV sources for a variety of experiments. Thus, determining the SED allows one to produce equivalent amounts of 'sunburning' radiation regardless of the UV spectral output of the different sources used. The SED is produced by multiplying the spectral output or irradiance ( $\text{W m}^{-2}$  of the UV-emitting source) with the Commission Internationale de l'Eclairage (CIE) standard erythral action spectrum (note that  $1 \text{ W} = 1 \text{ J s}^{-1}$ ). The CIE standard erythral action spectrum is thus used to 'weight' the incoming UV radiation on an erythral wavelength basis. The product curve produced from this convolution will give the 'erythral effective' irradiance ( $\text{W}_{\text{erythral effective}} \text{ m}^{-2}$ ) upon integration of the area under this curve. The erythral effective irradiance is used to calculate the erythral or sunburning dose by the equation:  $\text{dose}_{\text{erythral effective}} = \text{irradiance}_{\text{erythral effective}} \times \text{time (s)}$ . By definition,  $1 \text{ SED} = 100 \text{ J m}^{-2}$ .

Thus, our UVB source, which consists of a UVB bandpass interference filter with a half-band width of  $\pm 5 \text{ nm}$  (dimensions:  $5.1 \text{ cm} \times 5.1 \text{ cm}$ ) blocked to  $10^{-3}$  to  $10^{-4}$  outside the main bandpass (280–320 nm). This custom-made filter when coupled to our 2.5 kW Xenon arc allows for very clean wavelength resolution. The 100 cm<sup>2</sup> exposure area is large enough to accommodate up to 12 neonates (1–3 days old), which are situated in a three-chambered animal holder covered with a quartz lid that allows for UV transmission. Holes are drilled into the sides to allow for air exchange. This unit sits on top of a turntable rotating at approximately 3 r.p.m. to average out beam uniformity. The irradiance is measured with a spectroradiometer (StellarNet) and under standard conditions regularly produces an irradiance of approximately 0.30 CIE-effective  $\text{W m}^{-2}$ . The exposure time is constant at 90 min. These conditions regularly produce a CIE-effective dose of approximately 14–16 SED. This level of CIE-effective irradiance agrees well with our previous calculations using a radiation transfer algorithm over a global latitude/longitude grid at Northern or Southern summer mid-latitudes<sup>34</sup>. Direct terrestrial measurements at these latitudes indicate that under summer sunlight conditions on clear days in the Northern or Southern Hemisphere between 11:00 and 15:00 local time one can measure SEDs in the range of 10 to 20 depending on exposure conditions. As an example and as part of a project to estimate the number of SEDs one might receive during the day using, in this case, cyclists training in Spain during summer and winter, a recent paper shows just such levels in good agreement with our measurements<sup>35</sup>.

**FACS.** Single-cell suspensions from pooled skin samples were prepared using a published protocol<sup>30</sup>. FACS was performed on a FACSaria flow cytometer (BD Biosciences) equipped with a fixed-alignment cuvette flow cell and a Coherent Sapphire solid state laser providing 13 mW of 488-nm excitation wavelength. Processing rates averaged about 5,000 events per second at 20 psi. Cells of interest were gated by a combination of forward and orthogonal light scatter, and GFP fluorescence was captured in the detector with a 530/30 bandpass filter. GFP-positive cells suspended in PBS plus 1% bovine serum albumin (BSA) were sorted as bulk populations into  $12 \times 75 \text{ mm}$  polypropylene tubes. Dorsal skins from a combined litter of 6–8 pups gave a disaggregated cell suspension containing about  $30\text{--}50 \times 10^6$  cells. FACS resulted in collection of  $1\text{--}3 \times 10^5$  GFP-positive melanocytes per litter. Following FACS collection of cells into PBS plus 1% BSA

solution, the cells were centrifuged at  $4^\circ\text{C}$ , and the pelleted cells were lysed in Trizol Reagent (Invitrogen) for isolation of RNA. Total RNA was isolated from cells by Trizol organic extraction followed by RNeasy Micro Kit (Qiagen Sciences) procedure. Skin macrophages were isolated by immunostaining with anti-F4/80-Alexa Fluor 647 antibody (BioLegend).

**Microarray analysis of gene expression.** Three biological replicates for each group were used for cDNA microarray analyses. RNA was quantified fluorimetrically and assayed for integrity using the Agilent Bioanalyzer (Agilent Technologies). One-hundred nanograms of RNA was converted to biotinylated cRNA using one round of amplification with the Illumina Labelling Kit (Illumina) and one round of T7 polymerase amplification and hybridized to Illumina Murine Beadchips v. 2.0. After hybridization and staining, the arrays were scanned in an Illumina Bead Station, and the images processed using Illumina Bead Studio software.

**Statistical analysis of microarray data.** The raw microarray data were extracted from the BeadStudio software and imported into the R statistical programming environment (R Development Core Team)<sup>36</sup> and Bioconductor<sup>37</sup>. A variance stabilization transformation<sup>38</sup> followed by quantile normalization and quality assessment were performed using the lumi package<sup>38</sup>. Differential expression between groups was calculated using a linear model and empirical Bayes-moderated false discovery rates (FDR) for each treated versus untreated line were calculated using the limma package<sup>39</sup>. A heatmap including probes showing differential expression between UVB-treated and untreated with a FDR of 0.05 was generated (Fig. 2a and Supplementary Fig. 7). Hierarchical clustering of genes was performed using single linkage and Pearson correlation distance metric. Samples were simply ordered naturally.

**qRT-PCR.** The most highly significant genes identified through the statistical analysis of microarray data were validated by qRT-PCR. Reverse transcription was performed on 0.1–1.0  $\mu\text{g}$  RNA with Superscript III RT system (Invitrogen) following the manufacturer's protocol. Real-time PCR was performed with Quantitect SYBR Green PCR system (Qiagen Sciences) on a 7900HT Real-Time PCR machine (Applied Biosystems). 18S ribosomal RNA was used as the normalizer. The primers used in qRT-PCR are listed in Supplementary Table 2.

**Histology and immunohistochemistry.** Skin and tumour samples were preserved in optimal cutting temperature (OCT) compound and stored frozen at  $-80^\circ\text{C}$ . Five-micrometre sections were cut using a cryostat (Leica Microsystems) and were observed under a fluorescence microscope (Nikon Instruments) with DAPI (Vectashield, Vector Laboratories) counterstaining. The antibodies for fluorescence immunohistochemistry were obtained as listed in Supplementary Table 3. Haematoxylin and eosin stainings were performed using standard protocols. Select haematoxylin and eosin stained sections are shown in Supplementary Figure 26.

**In vivo antibody-mediated blockade.** For the IFN-blockade experiment in pups, the anti-murine IFN- $\gamma$  neutralizing antibody was the rat IgG clone XMG-6 ( $3.19 \text{ mg ml}^{-1}$ )<sup>40</sup>. The anti-murine IFN- $\alpha$ 1 antibody was the mouse IgG1 clone MARI-5A3 (purified monoclonal antibodies,  $4 \text{ mg ml}^{-1}$ )<sup>41</sup>. The control antibodies were rat IgG1 clone GL113 ( $1.52 \text{ mg ml}^{-1}$ ) ascites. The *in vivo* applications of these antibodies have been described<sup>42,43</sup>. 0.1–0.2 mg antibody was injected per pup intraperitoneally, 1–2 h before and 3 days after UVB irradiation. For IFN- $\gamma$  blockade in the tumorigenesis experiment, the anti-IFN- $\gamma$  antibody was XMG-6. The control antibody was rat IgG1 against horseradish peroxidase (HRPN; BioXcell). Antibodies were administered intraperitoneally as follows: 1 mg per mouse on days –1, 0, 1, 3, 6; and 0.5 mg per mouse on days 9, 12, and 15 after inoculation. Tumours were harvested at day 18.

**Immunofluorescence flow cytometry and FACS.** The immunofluorescence-based flow cytometry and FACS sorting were done using antibodies listed in Supplementary Table 3, using standard procedures.

**In vitro UV irradiation.** The melan-c melanocyte cell line (gift from V. Hearing) was irradiated with the Junggust Box, a hand-made enclosed module that houses two F20 sunlamps outputting 60% UVB and 38% UVA wavebands. A total UV dose of  $175 \text{ J m}^{-2}$  was given at a dose rate of  $2.0 \text{ W m}^{-2}$ . The cells were irradiated in 10-cm culture dishes at 80% confluence overlaid with 3 ml PBS and the dish covered with plastic saran wrap to filter out any UVC. Following irradiation, the cells were incubated for the desired time in normal media (RPMI1640, 10% FBS,  $100,000 \text{ U l}^{-1}$  penicillin,  $100 \text{ mg l}^{-1}$  streptomycin sulphate, 2 mM glutamine and 200 nM 12-O-tetradecanoylphorbol-13-acetate (TPA)).

**Chemotactic assays for Ccl8.** The cDNA for mouse Ccl8 was amplified by RT-PCR and cloned into the pcDNA3.1 expression vector (Clontech). F5061 cells were transfected using FuGene HD (Roche). Empty pcDNA3.1 vector was transfected as control. *In vitro* chemotactic assay was performed on the RAW264.7 macrophage cell line in a Transwell system with 8- $\mu\text{m}$  pore size (Corning).  $1 \times 10^5$  cells were seeded in the top well, and the migrant cells were counted following haematoxylin staining. The experiment was done in duplicate. Five random microscopic fields from each replicate were counted for the number of migrant cells. For the *in vivo* chemotactic assay,  $2.5 \times 10^5$  F5061-Ccl8 or F5061-vector cells were inoculated

subcutaneously in syngeneic FVB/N mice. Skin samples from the area of the inoculation were harvested two days after inoculation, preserved in OCT compound, cryosectioned, and immunohistochemistry with anti-F4/80 antibody was performed to assess macrophage infiltration.

**Tumorigenicity assay.** F4/80<sup>+</sup> macrophages were FACS-isolated from dorsal skins of pups 6 days after UVB irradiation at PD1. Macrophages were admixed with F5061 melanoma cells at a 1:5 ratio ( $0.5 \times 10^5$  macrophages:  $2.5 \times 10^5$  F5061) and inoculated subcutaneously in syngeneic FVB/N mice ( $n = 10$ ). Control mice were inoculated with  $2.5 \times 10^5$  F5061 cells without macrophages ( $n = 10$ ). Tumours were harvested after three weeks and were measured in three dimensions. Tumour volumes were calculated by the formula:  $V = \text{length} \times \text{width} \times \text{depth} \times \pi \times 1/6$ . For the tumorigenicity experiment with IFN- $\gamma$  blockade, for each of the two groups with macrophages, four mice had  $0.5 \times 10^5$  macrophages but another 6 mice from each group had  $0.42 \times 10^5$  macrophages mixed with  $2.5 \times 10^5$  F5061 cells. No differences in tumour growth were detected between the mice with these differing numbers of macrophages. All four groups contained ten mice, but two mice from the F5061 plus control-antibody group died prematurely and were taken out of the analysis.

**TUNEL assay.** The TUNEL assay was performed using TACS TdT Fluorescein kit (R&D Systems) following the manufacturer's protocol.

**Human and mouse melanoma tissue microarrays.** The human melanoma tissue microarray was obtained from S. Hewitt at the National Cancer Institute/National Institutes of Health. Antigen retrieval was performed by microwave boiling in citrate buffer (pH 6). Immunohistochemistry with anti-CD68 and anti-IFN- $\gamma$  antibodies (Supplementary Table 3) was performed serially with appropriate fluorescence-tagged secondary antibodies. The mouse melanoma tissue microarray has been generated by our laboratory and contains melanoma tissues from our HGF/SF transgenic mouse model, induced by a single neonatal UV radiation dose. Anti-F4/80 (macrophages), anti-CD3 (pan T cells) and anti-B220 (B cells) antibodies were used in conjunction with the Vectastain Elite ABC system (Vector Laboratories) following the manufacturer's protocol.

**Statistical analyses.** All statistical analyses were performed using Graphpad Prism software. Two-tailed Student's  $t$ -test and ANOVA with post-hoc Tukey analyses

were performed as indicated to validate significant differences. Means  $\pm$  s.e.m. are indicated for all statistical analyses. A  $P$  value of  $<0.05$  was considered statistically significant.

31. Budd, P. S. & Jackson, I. J. Structure of the mouse tyrosinase-related protein-2/dopachrome tautomerase (*Tyrp2/Dct*) gene and sequence of two novel slaty alleles. *Genomics* **29**, 35–43 (1995).
32. Urlinger, S. *et al.* Exploring the sequence space for tetracycline-dependent transcriptional activators: novel mutations yield expanded range and sensitivity. *Proc. Natl Acad. Sci. USA* **97**, 7963–7968 (2000).
33. Tumber, T. *et al.* Defining the epithelial stem cell niche in skin. *Science* **303**, 359–363 (2004).
34. De Fabo, E. C., Noonan, F. P. & Frederick, J. E. Biologically effective doses of sunlight for immune suppression at various latitudes and their relationship to changes in stratospheric ozone. *Photochem. Photobiol.* **52**, 811–817 (1990).
35. Serrano, M. A., Canada, J. & Moreno, J. C. Erythral ultraviolet exposure of cyclists in Valencia, Spain. *Photochem. Photobiol.* **86**, 716–721 (2010).
36. Team, R. D. C. R. *A Language and Environment for Statistical Computing*. (R Foundation for Statistical Computing, 2008).
37. Gentleman, R. C. *et al.* Bioconductor: open software development for computational biology and bioinformatics. *Genome Biol.* **5**, R80 (2004).
38. Du, P., Kibbe, W. A. & Lin, S. M. lumi: a pipeline for processing Illumina microarray. *Bioinformatics* **24**, 1547–1548 (2008).
39. Gentleman, R. *Bioinformatics and Computational Biology Solutions using R and Bioconductor* (Springer, 2005).
40. Cherwinski, H. M., Schumacher, J. H., Brown, K. D. & Mosmann, T. R. Two types of mouse helper T cell clone. III. Further differences in lymphokine synthesis between Th1 and Th2 clones revealed by RNA hybridization, functionally monospecific bioassays, and monoclonal antibodies. *J. Exp. Med.* **166**, 1229–1244 (1987).
41. Sheehan, K. C. *et al.* Blocking monoclonal antibodies specific for mouse IFN- $\alpha$ /beta receptor subunit 1 (IFNAR-1) from mice immunized by *in vivo* hydrodynamic transfection. *J. Interferon Cytokine Res.* **26**, 804–819 (2006).
42. Goldszmid, R. S. *et al.* TAP-1 indirectly regulates CD4<sup>+</sup> T cell priming in *Toxoplasma gondii* infection by controlling NK cell IFN- $\gamma$  production. *J. Exp. Med.* **204**, 2591–2602 (2007).
43. Gramzinski, R. A. *et al.* Interleukin-12- and gamma interferon-dependent protection against malaria conferred by CpG oligodeoxynucleotide in mice. *Infect. Immun.* **69**, 1643–1649 (2001).

# Circadian rhythms persist without transcription in a eukaryote

John S. O'Neill<sup>1,2\*</sup>, Gerben van Ooijen<sup>1\*</sup>, Laura E. Dixon<sup>1</sup>, Carl Troein<sup>3</sup>, Florence Corellou<sup>4,5</sup>, François-Yves Bouget<sup>4,5</sup>, Akhilesh B. Reddy<sup>2</sup> & Andrew J. Millar<sup>1,3</sup>

Circadian rhythms are ubiquitous in eukaryotes, and coordinate numerous aspects of behaviour, physiology and metabolism, from sleep/wake cycles in mammals to growth and photosynthesis in plants<sup>1,2</sup>. This daily timekeeping is thought to be driven by transcriptional-translational feedback loops, whereby rhythmic expression of 'clock' gene products regulates the expression of associated genes in approximately 24-hour cycles. The specific transcriptional components differ between phylogenetic kingdoms<sup>3</sup>. The unicellular pico-eukaryotic alga *Ostreococcus tauri* possesses a naturally minimized clock, which includes many features that are shared with plants, such as a central negative feedback loop that involves the morning-expressed *CCA1* and evening-expressed *TOC1* genes<sup>4</sup>. Given that recent observations in animals and plants have revealed prominent post-translational contributions to time-keeping<sup>5</sup>, a reappraisal of the transcriptional contribution to oscillator function is overdue. Here we show that non-transcriptional mechanisms are sufficient to sustain circadian timekeeping in the eukaryotic lineage, although they normally function in conjunction with transcriptional components. We identify oxidation of peroxiredoxin proteins as a transcription-independent rhythmic biomarker, which is also rhythmic in mammals<sup>6</sup>. Moreover we show that pharmacological modulators of the mammalian clock mechanism have the same effects on rhythms in *Ostreococcus*. Post-translational mechanisms, and at least one rhythmic marker, seem to be better conserved than transcriptional clock regulators. It is plausible that the oldest oscillator components are non-transcriptional in nature, as in cyanobacteria<sup>7</sup>, and are conserved across kingdoms.

Over the past two decades, great progress has been made towards delineating the molecular basis of eukaryotic circadian rhythms using model organisms such as *Arabidopsis thaliana* (plant), *Mus musculus* (mammal) and *Drosophila melanogaster* (insect)<sup>5,8</sup>. In each case, mechanistic models of the cellular clock have relied heavily on networks of transcriptional/translational feedback loops and can successfully account for a wide range of experimental data<sup>9</sup>. Although the identified 'clock genes' differ widely across taxa, a growing number of ubiquitous post-translational mechanisms, such as casein kinase II activity<sup>5,10,11</sup>, have been shown to contribute to timing. Similarly, signal transduction pathways, for example,  $\text{Ca}^{2+}$ /cAMP, previously viewed as clock inputs have been shown also to be clock outputs, thus becoming indistinguishable from the 'core' mechanisms<sup>5,12</sup>. As a result it is presently unclear whether transcription, per se, is necessary to sustain the eukaryotic cellular clock<sup>13,14</sup>, especially in light of observations that prokaryotic timekeeping can be reconstituted *in vitro* using the gene expression products of the cyanobacterial *kaiBC/kaiA* operons<sup>7</sup>. We hypothesized that non-transcriptional mechanisms would be competent to sustain cellular rhythms without a transcriptional contribution, and so set out to test this using the pico-eukaryote *Ostreococcus tauri*. This single-celled eukaryote has several advantages. It is readily cultured,

possesses a small genome (~12 Mb), and yet its light-entrainable clock shares the transcriptional architecture of the clock in higher plants, namely a negative feedback loop between the morning-expressed *CCA1* and evening-expressed *TOC1* genes<sup>4</sup>.

Recently, bioluminescent luciferase (LUC) reporter lines for transcription and translation of *O. tauri* clock genes were developed to enable non-invasive interrogation of clock mechanisms<sup>4</sup>. After entrainment in 12 h light/12 h dark cycles, circadian rhythms of bioluminescence from a translational (*CCA1*-LUC) and transcriptional (*pCCA1::LUC*) reporter were observed to persist for >4 days in constant light (Fig. 1a), indicating the presence of an underlying circadian clock, able to keep time without reference to any external time cues. Although many cellular processes in photosynthetic organisms are light-dependent<sup>4,15,16</sup>, the cyanobacterial clock was recently shown to persist in darkness<sup>7</sup>. We therefore determined whether circadian rhythms might similarly persist in *O. tauri* without light. When placed in constant darkness, bioluminescent traces rapidly damped to background levels (Fig. 1a). After 96 h in constant darkness, no incorporation of [ $\alpha$ -<sup>32</sup>P]UTP was observed (Fig. 1b), meaning that no nascent RNA was being transcribed. Upon transfer of these transcriptionally incompetent cultures into constant light, circadian rhythms in bioluminescence began at a phase that was not dictated solely by the time of transfer into light (Fig. 1c and Supplementary Fig. 1a, b). If no cellular oscillation had persisted in the dark, we would expect the clock to restart with its phase determined solely by when it was transferred into the light (that is, complete phase resetting). In contrast, the cultures' new phase suggested that the response to light was modulated by a pre-existing oscillation, instead of being completely reset by light (Fig. 1c)<sup>17</sup>. These observations indicate that *O. tauri* is competent to keep time in the absence of transcription.

To confirm this, we used a novel post-translational biomarker for rhythmicity: peroxiredoxin oxidation. The peroxiredoxins (PRXs) are a ubiquitous family of antioxidant enzymes that scavenge reactive oxygen species, such as hydrogen peroxide, catalysing their own oxidation at a conserved redox-active cysteine (Cys) group to sulphenic acid followed by hyperoxidation through to sulphonic acid<sup>18</sup>. In plants, a subtype of peroxiredoxins (the 2-Cys group) is targeted to chloroplasts where they protect the photosynthetic membrane against photo-oxidative damage<sup>19</sup>. Oxidation of PRX drives the formation of higher molecular mass multimers with reported chaperone and signalling functions<sup>18</sup>. Circadian cycles of post-translational modification of PRX have previously been reported in mouse liver<sup>6</sup> and recently shown to persist in human red blood cells *in vitro*<sup>20</sup>. *Ostreococcus tauri* expresses at least one 2-Cys PRX<sup>15</sup> (GenBank accession CAL55168.1) sharing 61% sequence identity with human PRX2 and 100% sequence identity around the catalytic cysteine residue (Supplementary Fig. 2a, b). Immunoblots using an antibody targeting this highly conserved region<sup>20</sup> revealed diurnal regulation of PRX oxidation that was highest during

<sup>1</sup>Centre for Systems Biology at Edinburgh, C.H. Waddington Building, Mayfield Road, Edinburgh EH9 3JD, UK. <sup>2</sup>Department of Clinical Neurosciences, University of Cambridge Metabolic Research Laboratories, Institute of Metabolic Science, Addenbrooke's Hospital, Cambridge CB2 0QQ, UK. <sup>3</sup>School of Biological Sciences, University of Edinburgh, Mayfield Road, Edinburgh EH9 3JH, UK. <sup>4</sup>UPMC Univ Paris 06, UMR7621 Laboratoire d'Océanographie Microbienne, Observatoire Océanologique, F-66651 Banyuls/mer, France. <sup>5</sup>CNRS, UMR7621, Laboratoire d'Observatoire d'Océanographie Microbienne, Observatoire Océanologique, F-66651 Banyuls/mer, France.

\*These authors contributed equally to this work.

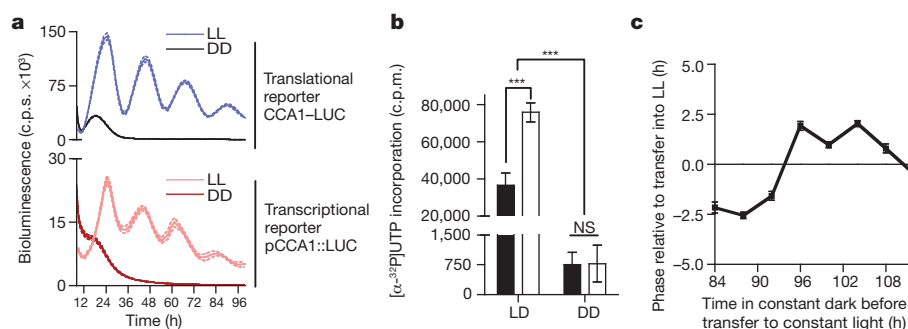


**Figure 1 | Transcriptionally inactive cells show a phase-dependent response to re-illumination.** **a**, Grouped data showing bioluminescent transcriptional (pCCA1::LUC) and translational (CCA1-LUC) reporter activity in constant darkness (DD) or constant light (LL) ( $n = 16$ , dotted lines  $\pm$  s.e.m.). c.p.s., counts per second. **b**, After 96 h in darkness there is no significant (NS) incorporation of radiolabelled UTP; 10 min UTP treatment (black,  $\pm$  s.e.m.)

compared with 30 min treatment (white,  $\pm$  s.e.m.) (2-way ANOVA interaction,  $P < 0.001$  for time, condition and interaction,  $n = 3$ ; Bonferroni post-tests: \*\*\* $P < 0.001$ ; for DD groups,  $P = 0.95$ ). c.p.m., counts per minute. **c**, Upon transfer from darkness, the phase of CCA1-LUC ( $\pm$  s.e.m.) deviates significantly from the time of transfer into light (2-way ANOVA interaction,  $P < 0.001$ ,  $n \geq 16$ ).

subjective day, in advance of ribulose 1,5-bisphosphate carboxylase-oxygenase (RUBISCO) large chain expression (RbcL; a highly expressed plant/algal protein) (Fig. 2a). Moreover, in constant darkness, circadian rhythms persisted without transcription (Fig. 2b). PRX oxidation rhythms even persisted in constant darkness in the presence of inhibitors of cellular RNA synthesis (cordycepin) and cytosolic translation (cycloheximide), at concentrations that abolish clock reporter bioluminescence (Fig. 2c and Supplementary Fig. 3c, d), providing strong evidence that new RNA and/or protein synthesis is indeed not required for sustained rhythmicity. RbcL was used as a loading control, because although this protein was rhythmically expressed in a diurnal cycle, its

levels were high and stable under constant conditions. Furthermore, rhythms in PRX oxidation are altered in a long period mutant (TOC1-LUC)<sup>4</sup>, relative to controls (CCA1-LUC), under constant light; this indicates that post-translational oscillations are coupled with transcriptional/translational cycles under more physiological conditions (Supplementary Fig. 2c, d). Thus, PRX oxidation constitutes the first example, as far as we are aware, of a post-translational circadian biomarker shared between the animal (mouse/human) and green (plant) lineages.

Although experimentally useful for dissecting the algal clockwork, constant darkness potentially represents an exotic environmental

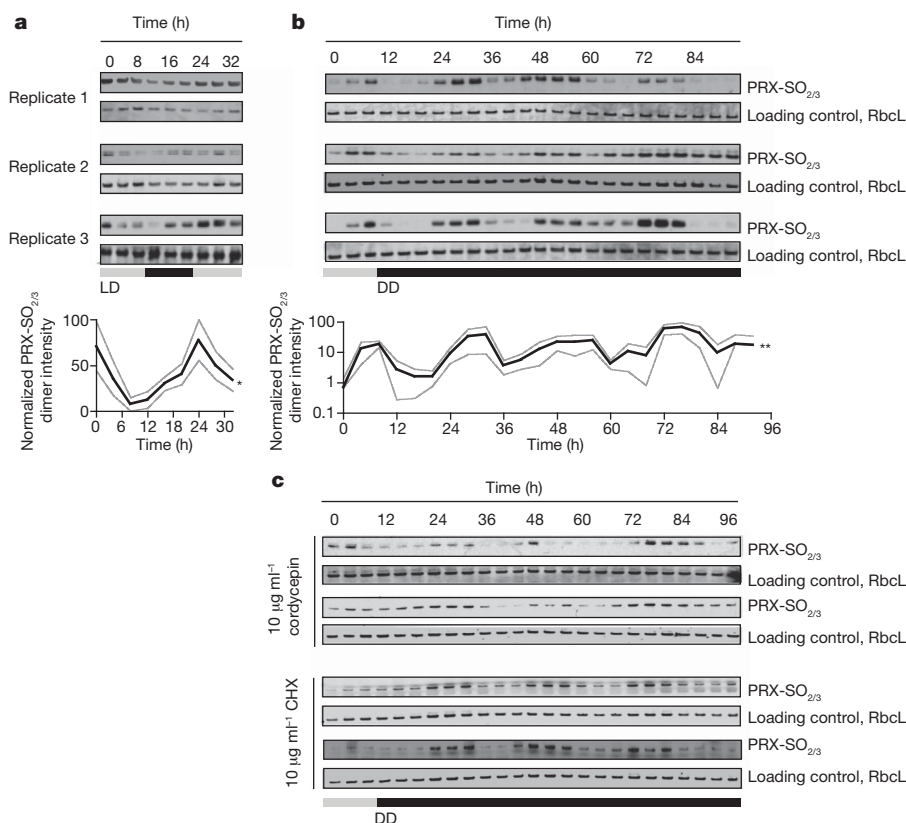


**Figure 2 | Circadian cycles of PRX oxidation are detected during light/dark cycles and in constant darkness, and persist during drug inhibition of gene expression.** **a**, Individual blots and grouped mean intensities for three *O. tauri* time series sampled under 12/12 h light/dark cycles (\*Friedman test,  $P = 0.04$  for time effect). **b**, Individual blots and grouped mean intensities for three *O.*

*tauri* time series sampled under constant darkness (\*\*Friedman test,  $P = 0.005$  for time effect). **c**, PRX-SO<sub>2/3</sub> immunoblots of *O. tauri* time series sampled under constant darkness in the presence of inhibitors of transcription (cordycepin) and translation (cycloheximide (CHX)).

challenge to *O. tauri*, and hence we sought to also examine non-transcriptional rhythms in constant light using real-time bioluminescence reporter assays. CCA1-LUC and pCCA1::LUC reporter lines were incubated with a range of concentrations of cordycepin and cycloheximide during bioluminescent recordings, to assay the effects of inhibiting cellular RNA synthesis and cytosolic translation, respectively. At lower concentrations we observed dose-dependent damping of rhythmic amplitude with both drugs, and a robust increase in circadian period with increasing cordycepin concentration (Supplementary Fig. 3a, b), in agreement with observations in the marine mollusc *Bulla*<sup>21</sup>. At saturating doses, both drugs resulted in immediate damping and arrhythmia in the transcriptional reporter lines (Supplementary Fig. 3c). Notably, the translational reporter exhibited an additional cycle of CCA1-LUC synthesis in the presence of saturating transcriptional inhibitor (Supplementary Fig. 3d), which was not observed in the transcriptional reporter line. We interpret this to mean that when CCA1-LUC messenger RNA is present, post-transcriptional mechanisms are sufficient to drive an additional cycle of correctly timed protein accumulation.

Clearly in the context of a living cell, transcription is ultimately required for any biological process, including circadian rhythms, as the mRNAs have limited half-lives and can only be replaced through transcription. In a biological clock context, it seems natural that some mRNAs are cyclically expressed in anticipation of cellular need. Microarray studies in several organisms have shown that >10% of the transcriptome is regulated on a daily basis<sup>6,15,22</sup>. This implies that circadian cycles in transcription factor activity are a normal feature of cell physiology. Some of this transcriptional activity will contribute to timekeeping, directly or indirectly. If the natural state of a eukaryotic cellular clock revolves around reciprocal interplay between post-translational oscillations and established transcriptional feedback loops, it becomes of great interest to identify at what phases this interconnection is regulated.

*Ostreococcus* cultures are amenable to drug treatment that can be reversed by wash-off, because *O. tauri* grown in liquid culture forms aggregates at the bottom of microplate wells (Fig. 3a). To ascertain at which phases of the circadian cycle gene expression exerts priority over non-transcriptional mechanisms, we performed a 'wedge' experiment<sup>21</sup>,

in which transcription or translation was reversibly inhibited starting at 4-h intervals across the circadian cycle, for increasing durations, in constant light. Resultant phases were determined by the timing of CCA1-LUC expression peaks over the interval following removal of the drug (Fig. 3b). As with the earlier experiments using constant dark, our null hypothesis was that if the clock was immediately arrested by drug treatment then phase would be set by the time of drug wash-off. Phase is described relative to the zeitgeber, or time giver, during entrainment where ZT0 is dawn and ZT12 is dusk (ZT denotes zeitgeber time).

A general trend towards the anticipated wedge shape was observed (Supplementary Fig. 4a, b). However, there were significant exceptions to this pattern: (1) the clock was insensitive to transcriptional inhibition for up to 24 h in treatments starting from ZT8 (Fig. 3b, cordycepin treatment); (2) transcriptional inhibition outside ZT0–ZT8 did not affect phase; (3) after treatments spanning this window, the clock resumed at dusk if treatment began during the subjective night, or at dawn if treatment began during the subjective day (Fig. 3c and Supplementary Fig. 4a, c, d); (4) translational inhibition (cycloheximide treatment) outside ZT4–ZT12 did not affect phase (Fig. 3c and Supplementary Fig. 4b–d).

The simplest interpretation is that transcription of mechanistically relevant clock genes is licensed by post-translational mechanisms and occurs around the first half of the subjective day. These transcripts are translated around the second half of the subjective day and non-transcriptional mechanisms keep time during the subjective night. Presumably, when inhibition of transcription occurs at midday, for example, the resumption of stalled gene expression after wash-off overrides the phase of the non-transcriptional oscillations and the clock resumes from the nearest expected light/dark transition to when inhibition began. This runs contrary to current understanding of clocks in eukaryotes, in which transcription of key clock genes is active almost continuously around the circadian cycle<sup>23</sup>. Even in *O. tauri*, transcription of *TOC1* and *CCA1* would span the full cycle except for the interval ~ZT2–ZT8, after the peak of *CCA1* mRNA and before the rise in *TOC1* mRNA (ref. 4).

The final question of importance is what non-transcriptional mechanisms are involved in sustaining the clock? We hypothesized that the components that sustain these post-translational rhythms are

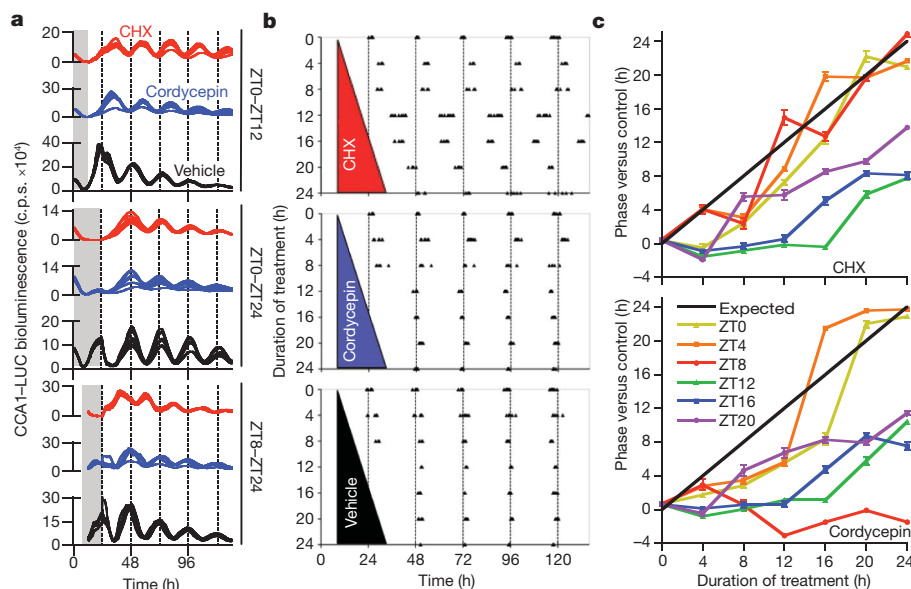


**Figure 3 | Circadian timing can survive the inhibition of cellular transcription, or cytosolic translation.** **a**, Treatment (from top, at ZT0–ZT12, ZT0–ZT24, ZT8–ZT24; shaded) with inhibitors of transcription (10  $\mu\text{M}$  cordycepin, blue lines) or translation (1  $\mu\text{M}$  cycloheximide (CHX), red lines) may shift the phase of reporter expression, compared with vehicle (0.04% DMSO, black lines), depending on the treatment phase and duration. **b**, Peak

times of CCA1-LUC expression from individual wells ( $n > 5$ ) are plotted, after treatments of different durations, starting at ZT8. **c**, Summary of phase shifts ( $\pm$  s.e.m.,  $n > 5$ ) relative to vehicle-treated controls, for all treatment durations (x axis) and starting times (see legend in lower panel). Black line represents the expected result, assuming total resetting by wash-off.

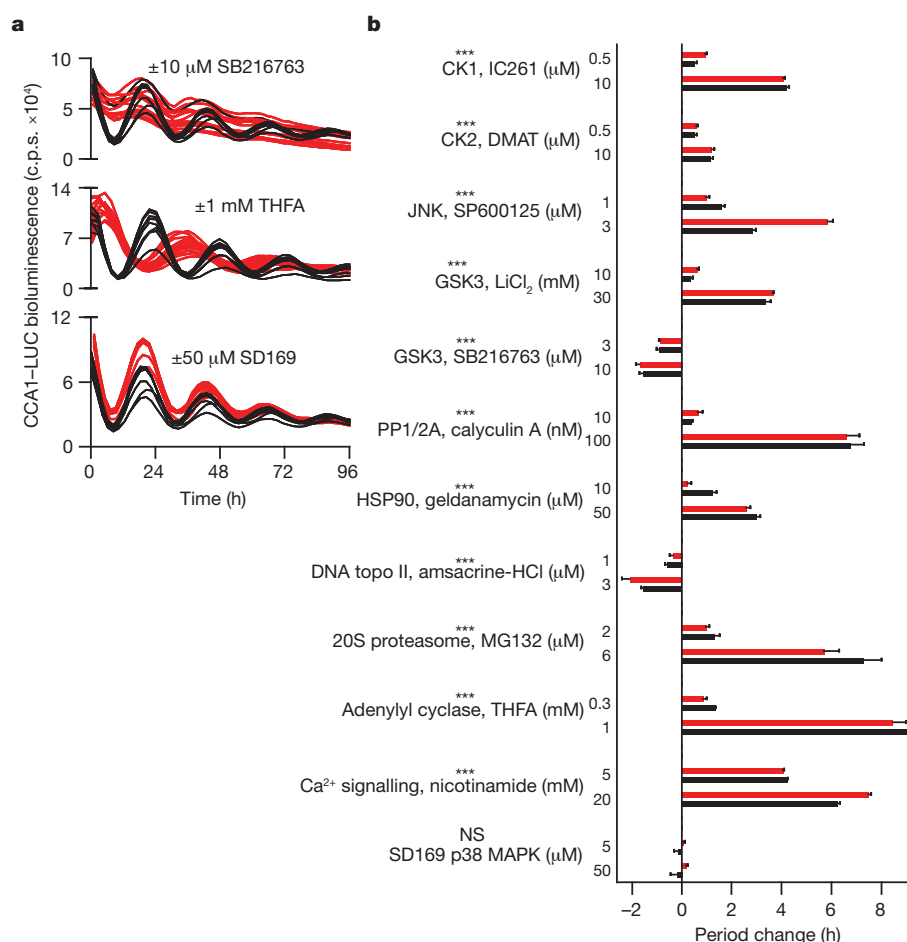


**Figure 4** | Circadian period in *O. tauri* can be modulated pharmacologically in a dose-dependent manner by the application of inhibitors that have been previously validated in other taxa. **a**, Examples of drug effects (red) on CCA1-LUC bioluminescence compared with vehicle controls (black): SB216763 shortens period, 9-(tetrahydro-2-furyl)-adenine (THFA) increases period,

SD169 has no effect. **b**, Summary showing grouped dose-responses on circadian period of transcriptional (red) and translational (black) reporter lines for selected drugs with previously demonstrated action in other taxa ( $\pm$  s.e.m.,  $n \geq 8$ , \*\*\* $P < 0.0001$ , 2-way ANOVA for concentration  $\times$  reporter; not significant (NS) for SD169 negative control,  $n = 8$ ,  $P = 0.90$ ).

likely to be ubiquitous and highly conserved. Certainly the *O. tauri* genome encodes close homologues of enzymes such as casein kinase II that tend to exhibit greater sequence conservation across kingdoms than canonical transcriptional clock genes (Supplementary Table 1). In the last two years a number of high-throughput chemical biology screens on mammalian cellular rhythms in culture have been published, identifying a number of potent modulators of free-running period<sup>12,24–27</sup>. Because many such inhibitors target an enzyme's active site, it seemed plausible that drug action might be similarly conserved. The effects of specific pharmacological inhibitors that have been demonstrated to significantly affect free-running period in mammalian cells, and/or other model organisms (Supplementary Table 2), were therefore tested in *O. tauri*. In all cases, dose-dependent effects were observed on circadian period that correlated with their action in other species such as mouse or *Neurospora* (Fig. 4a, b and Supplementary Fig. 5a). Critically, where tested, such pharmacological perturbations also delayed the timing of transcriptionally incompetent cells, first with respect to the additional cycle of CCA1-LUC expression observed during transcriptional inhibition in constant light (Supplementary Fig. 6a). Second, the period of rhythmic PRX oxidation in constant darkness was also lengthened by the treatments tested (Supplementary Fig. 6b). Although drugs can have pleiotropic effects on cell biology, the drug effects on the clock are conserved across taxa. The parsimonious interpretation is that, both with and without transcription, conserved post-translational mechanisms are necessary to keep biological time.

Although the importance of transcription to circadian rhythms is self-evident, our observation that eukaryotic rhythms persist in the absence of transcription challenges the general model for eukaryotic clocks, indicating a functional equivalent to cyanobacterial timekeeping<sup>28</sup>, although undoubtedly more complex. This is supported by increasing numbers of observations in diverse organisms<sup>5,13,20,29</sup>. Most prominently, the observation of a rhythmic post-translational marker that persists in the absence of transcription in species as diverse as a unicellular green alga and humans<sup>20</sup> raises exciting prospects for our understanding of how circadian clocks evolved. We note that both PRX and cyanobacterial KaiB are clock-relevant members of the thioredoxin-like superfamily<sup>28</sup> that associate into higher molecular mass complexes with catalytic function. We speculate that this may reflect conserved remnants of a proto-clock in the last common ancestor of eukaryotes and prokaryotes.

## METHODS SUMMARY

All materials were purchased from Sigma-Aldrich unless otherwise stated. Transgenic *Ostreococcus tauri* lines<sup>4</sup> were cultured in Keller media-supplemented artificial sea water (Km) under 12/12 h blue (Ocean Blue, Lee lighting filter 724) light/dark cycles ( $17.5 \mu\text{E m}^{-2} \text{s}^{-1}$ ). For recording, cultures were transferred to 96-well microplates (Lumitrac, Greiner Bio-one) at a density of  $\sim 15 \times 10^6$  cells per ml and entrained for 7–10 days. No density effects on clock output were observed under relevant density ranges, and cell division in microplates was found to be close to zero. One day before recording, 150  $\mu\text{l}$  Km was replaced with 150  $\mu\text{l}$  Km containing 333  $\mu\text{M}$  luciferin (Km+). Drugs were made up in DMSO or Km+, diluted in Km+ and added to replicates of 8 or 16 wells immediately before

recording. For incubations in constant darkness, Km+ was supplemented with 200 mM sorbitol and 0.4% glycerol to increase cell viability. Bioluminescent recordings were performed on a TopCount (Packard) under constant darkness or constant red + blue LED light ( $5\text{--}12\ \mu\text{E m}^{-2}$ ). For wash-off of reversible inhibitors, cell aggregates formed in the bottom of the wells were quickly and gently washed twice with Km+, using multi-channel pipettes, and returned to recording conditions. Analysis of period was performed with FFT-NLLS (BRASS 3<sup>30</sup>) using time windows  $\geq 3$  days; mFourfit (BRASS 3) was used to assess phase and confirmed manually. Statistical analysis was performed using GraphPad Prism. For *de novo* RNA synthesis analysis by [ $\alpha$ -<sup>32</sup>P]UTP uptake, 1 ml cell aliquots were either incubated in darkness or light/dark cycles for 4 days. 0.2 MBq of [ $\alpha$ -<sup>32</sup>P]UTP was added, and after incubation cells were collected and washed twice with Km. Incorporation was measured using scintillation counting. Immunoblots were performed as described elsewhere<sup>20</sup>. Sequence alignments were performed using EBI Jalview. BLAST searches were performed using NCBI BLASTp under the default BLOSSUM62 settings.

Received 20 May; accepted 4 November 2010.

- Harmer, S. L. The circadian system in higher plants. *Annu. Rev. Plant Biol.* **60**, 357–377 (2009).
- Reddy, A. B. & O'Neill, J. S. Healthy clocks, healthy body, healthy mind. *Trends Cell Biol.* **20**, 36–44 (2010).
- Lakin-Thomas, P. L. Transcriptional feedback oscillators: maybe, maybe not. *J. Biol. Rhythms* **21**, 83–92 (2006).
- Corellou, F. *et al.* Clocks in the green lineage: Comparative functional analysis of the circadian architecture of the picoeukaryote *Ostreococcus*. *Plant Cell* **21**, 3436–3449 (2009).
- Hastings, M. H., Maywood, E. S. & O'Neill, J. S. Cellular circadian pacemaking and the role of cytosolic rhythms. *Curr. Biol.* **18**, R805–R815 (2008).
- Reddy, A. B. *et al.* Circadian orchestration of the hepatic proteome. *Curr. Biol.* **16**, 1107–1115 (2006).
- Nakajima, M. *et al.* Reconstitution of circadian oscillation of cyanobacterial KaiC phosphorylation *in vitro*. *Science* **308**, 414–415 (2005).
- Roenneberg, T. & Mellow, M. Circadian clocks—the fall and rise of physiology. *Nature Rev. Mol. Cell Biol.* **6**, 965–971 (2005).
- Ueda, H. R. Systems biology flowering in the plant clock field. *Mol. Syst. Biol.* **2**, 60 (2006).
- Mehra, A., Baker, C. L., Loros, J. J. & Dunlap, J. C. Post-translational modifications in circadian rhythms. *Trends Biochem. Sci.* **34**, 483–490 (2009).
- Mellow, M., Mazzotta, G., Chen, Z. & Roenneberg, T. The right place at the right time: regulation of daily timing by phosphorylation. *Genes Dev.* **20**, 2629–2633 (2006).
- O'Neill, J. S., Maywood, E. S., Chesham, J. E., Takahashi, J. S. & Hastings, M. H. cAMP-dependent signaling as a core component of the mammalian circadian pacemaker. *Science* **320**, 949–953 (2008).
- Woolum, J. C. A re-examination of the role of the nucleus in generating the circadian rhythm in *Acetabularia*. *J. Biol. Rhythms* **6**, 129–136 (1991).
- Morse, D. S., Fritz, L. & Hastings, J. W. What is the clock? Translational regulation of circadian bioluminescence. *Trends Biochem. Sci.* **15**, 262–265 (1990).
- Monnier, A. *et al.* Orchestrated transcription of biological processes in the marine picoeukaryote *Ostreococcus* exposed to light/dark cycles. *BMC Genomics* **11**, 192 (2010).
- Moulager, M. *et al.* Light-dependent regulation of cell division in *Ostreococcus*: evidence for a major transcriptional input. *Plant Physiol.* **144**, 1360–1369 (2007).
- Konopka, R. J. Genetic dissection of the *Drosophila* circadian system. *Fed. Proc.* **38**, 2602–2605 (1979).
- Hall, A., Karplus, P. A. & Poole, L. B. Typical 2-Cys peroxiredoxins—structures, mechanisms and functions. *FEBS J.* **276**, 2469–2477 (2009).
- Baier, M. & Dietz, K. J. The plant 2-Cys peroxiredoxin BAS1 is a nuclear-encoded chloroplast protein: its expressional regulation, phylogenetic origin, and implications for its specific physiological function in plants. *Plant J.* **12**, 179–190 (1997).
- O'Neill, J. S. & Reddy, A. B. Circadian clocks in human red blood cells. *Nature* doi:10.1038/nature09702 (this issue).
- Khalsa, S. B., Whitmore, D., Bogart, B. & Block, G. D. Evidence for a central role of transcription in the timing mechanism of a circadian clock. *Am. J. Physiol.* **271**, C1646–C1651 (1996).
- Edwards, K. D. *et al.* FLOWERING LOCUS C mediates natural variation in the high-temperature response of the *Arabidopsis* circadian clock. *Plant Cell* **18**, 639–650 (2006).
- McClung, C. R. Plant circadian rhythms. *Plant Cell* **18**, 792–803 (2006).
- Dodd, A. N. *et al.* The *Arabidopsis* circadian clock incorporates a cADPR-based feedback loop. *Science* **318**, 1789–1792 (2007).
- Eide, E. J. *et al.* Control of mammalian circadian rhythm by CKI $\epsilon$ -regulated proteasome-mediated PER2 degradation. *Mol. Cell. Biol.* **25**, 2795–2807 (2005).
- Hirota, T. *et al.* A chemical biology approach reveals period shortening of the mammalian circadian clock by specific inhibition of GSK-3 $\beta$ . *Proc. Natl Acad. Sci. USA* **105**, 20746–20751 (2008).
- Isojima, Y. *et al.* CKI $\epsilon$ / $\delta$ -dependent phosphorylation is a temperature-insensitive, period-determining process in the mammalian circadian clock. *Proc. Natl Acad. Sci. USA* **106**, 15744–15749 (2009).
- Johnson, C. H., Mori, T. & Xu, Y. A cyanobacterial circadian clockwork. *Curr. Biol.* **18**, R816–R825 (2008).
- Eelderink-Chen, Z. *et al.* A circadian clock in *Saccharomyces cerevisiae*. *Proc. Natl Acad. Sci. USA* **107**, 2043–2047 (2010).
- Edwards, K. D. *et al.* Quantitative analysis of regulatory flexibility under changing environmental conditions. *Mol. Syst. Biol.* **6**, 424 (2010).

**Supplementary Information** is linked to the online version of the paper at [www.nature.com/nature](http://www.nature.com/nature).

**Acknowledgements** CSBE is a Centre for Integrative Systems Biology funded by BBSRC and EPSRC award D019621. C.T. is supported by a BBSRC/ANR joint project F005466 awarded to F.-Y.B. and A.J.M. and by the HFSP. A.B.R. is supported by the Wellcome Trust (083643/Z/07/Z) and the MRC Centre for Obesity and Related metabolic Disorders (MRC CORD).

**Author Contributions** J.S.O'N., G.v.O. and L.E.D. designed and performed the experiments; J.S.O'N., G.v.O., L.E.D., C.T., A.B.R. and A.J.M. analysed data. F.-Y.B. and F.C. generated essential protocols and biomaterials. All authors contributed to writing. J.S.O'N. and G.v.O. contributed equally to this paper.

**Author Information** Reprints and permissions information is available at [www.nature.com/reprints](http://www.nature.com/reprints). The authors declare no competing financial interests. Readers are welcome to comment on the online version of this article at [www.nature.com/nature](http://www.nature.com/nature). Correspondence and requests for materials should be addressed to A.B.R. (areddy@cantab.net) or A.J.M. (Andrew.Millar@ed.ac.uk).

# Structural basis for site-specific ribose methylation by box C/D RNA protein complexes

Jinzhong Lin<sup>1</sup>, Shaomei Lai<sup>1</sup>, Ru Jia<sup>1</sup>, Anbi Xu<sup>1</sup>, Liman Zhang<sup>1,2</sup>, Jing Lu<sup>1,2</sup> & Keqiong Ye<sup>1</sup>

**Box C/D RNA protein complexes (RNPs) direct site-specific 2'-O-methylation of RNA and ribosome assembly<sup>1-4</sup>. The guide RNA in C/D RNP forms base pairs with complementary substrates and selects the modification site using a molecular ruler<sup>5-7</sup>. Despite many studies of C/D RNP structure<sup>8-25</sup>, the fundamental questions of how C/D RNAs assemble into RNPs and how they guide modification remain unresolved. Here we report the crystal structure of an entire catalytically active archaeal C/D RNP consisting of a bipartite C/D RNA associated with two substrates and two copies each of Nop5, L7Ae and fibrillarin at 3.15-Å resolution. The substrate pairs with the second through the eleventh nucleotide of the 12-nucleotide guide, and the resultant duplex is bracketed in a channel with flexible ends. The methyltransferase fibrillarin binds to an undistorted A-form structure of the guide-substrate duplex and specifically loads the target ribose into the active site. Because interaction with the RNA duplex alone does not determine the site specificity, fibrillarin is further positioned by non-specific and specific protein interactions. Compared with the structure of the inactive C/D RNP, extensive domain movements are induced by substrate loading. Our results reveal the organization of a monomeric C/D RNP and the mechanism underlying its site-specific methylation activity.**

Archaeal C/D RNAs possess a bipartite structure with terminal boxes termed C (RUGAUAG, R is purine) and D (CUGA) that form a kink-turn (K-turn) structure<sup>10,11,17,26</sup>, and related internal C' and D' boxes form a second K-turn (Fig. 1a). The two K-turns are connected by dual single-stranded guide sequences that recruit substrates and select the nucleotide paired to the fifth nucleotide upstream of box D/D' for modification. Traditionally, a bipartite C/D RNA is thought to associate with one Nop5 dimer as well as two copies each of L7Ae and fibrillarin into a monomeric RNP (mono-RNP)<sup>14,23</sup>. However, a recent electron-microscope study revealed a dimeric C/D RNP structure (di-RNP) composed of four copies of each of the core proteins and probably two C/D RNAs<sup>24</sup>. In a proposed di-RNP model, each C/D RNA bridges two Nop5 dimers rather than binding to a single Nop5 dimer<sup>24</sup>. Unfortunately, all available C/D RNP crystal structures were obtained with half-mer RNAs containing one copy of box C/D and a free-ended guide<sup>23,25</sup>, and they did not distinguish whether bipartite C/D RNAs bind to one Nop5 dimer or are shared between two Nop5 dimers. To address this question and to study the substrate-loaded conformation of a C/D RNP, we designed a structurally symmetrical RNA resembling an archaeal bipartite C/D RNA (Fig. 1a). We used it to crystallize a complex containing Nop5, L7Ae and fibrillarin from *Sulfolobus solfataricus*<sup>13</sup> as well as two cognate decanucleotide substrates.

Our reconstitution yielded a mixture of RNPs with two major species, RNP1 and RNP2 (Fig. 1b). RNP1 is the crystallized species and corresponds to a mono-RNP as shown by its structure (see below), whereas RNP2 is presumably a dimeric form. The mixture was active in site-specific methylation as it modified a cognate substrate but not a substrate pre-methylated on the target nucleotide (Fig. 1c). Moreover, mono-RNP derived from dissolved crystal, which was stable during the experiment

(Supplementary Fig. 1), was also active (Fig. 1c). To assess the activities of the two RNPs individually, we performed the reaction at 25 °C to inhibit substrate release (Supplementary Fig. 2) and then separated the mixture by native gel electrophoresis. Examination of methyl incorporation into the substrate still bound to the individual RNPs showed that both RNP1 and RNP2 were competent for site-specific methylation (Fig. 1d).

The structure of the substrate-bound C/D RNP was solved by molecular replacement and refined to 3.15-Å resolution with a value of  $R_{\text{work}}/R_{\text{free}}$  of 0.251/0.279 (Supplementary Fig. 3 and Supplementary Table 1). In the structure, the bipartite C/D RNA assembles with a Nop5 dimer and two copies each of L7Ae and fibrillarin, consistent with the classic mono-RNP model<sup>14,23</sup>. The structure has twofold symmetry and resembles a cradle with dimensions of approximately 140 Å × 85 Å × 50 Å that holds RNA components within (Fig. 1d-f).

The structure is built upon the scaffold protein Nop5, which is composed of an amino (N)-terminal domain (NTD), a coiled-coil domain, a tip domain and a carboxy (C)-terminal domain (CTD)<sup>14,22,23</sup>. The coiled-coil domain self-associates and, together with the tip domain, forms a flat platform that supports all the other components in the complex above. The Nop5 CTD and L7Ae constitute an RNA-binding module and sandwich the K-turn formed by box C/D. Consequently, the two K-turns of the bipartite C/D RNA are anchored at opposing sides of the coiled-coil platform, arranging the guide sequences at the centre of the complex. The Nop5 NTD associates with fibrillarin to form a catalytic module. Compared with the half-mer C/D RNP structure<sup>23</sup>, the catalytic and RNA-binding module are unchanged in structure (Supplementary Fig. 4), but they have a very different orientation relative to the coiled-coiled platform (see below). Because of its twofold symmetry, we will only describe the half structure associated with box C/D and the guide between box D and C' (the D-guide).

Residues U14, G15 and A16 in box C and U70, C69 in box D are not required for K-turn formation, but they are often conserved and are important for C/D RNA function<sup>27</sup>. The current structure has higher resolution than the previous half-mer C/D RNP structure<sup>23</sup>, and it suggests that the G15-C69 pair and unpaired A16 are specified by multiple hydrogen bonds from residues Q296 and R339 in the Nop5 CTD (Fig. 2a).

Each substrate forms a 10-base-pair (bp) duplex with nucleotides 2-11 of the 12-nucleotide guide counted from box D/D'. The guide-substrate duplexes are placed in an RNA-binding channel formed by the dimeric coiled-coil domain at the bottom, two opposing Nop5 CTDs at the ends and fibrillarin at the sides. Fibrillarin binds the guide-substrate duplex at the minor groove in such a way that the target nucleotide paired to the fifth nucleotide of the guide is precisely loaded into the active site, indicating that this substrate-loaded structure represents an active conformation of the enzyme. The observation that both substrates are in a fibrillarin-bound active conformation indicates that the two guides of the C/D RNA can function simultaneously. In addition, even though the two guide-substrate duplexes are positioned side by side, they do not contact one another, further suggesting that the two guides can function independently.

<sup>1</sup>National Institute of Biological Sciences, Beijing 102206, China. <sup>2</sup>Graduate Program in Chinese Academy of Medical Sciences and Peking Union Medical College, Beijing 100730, China.

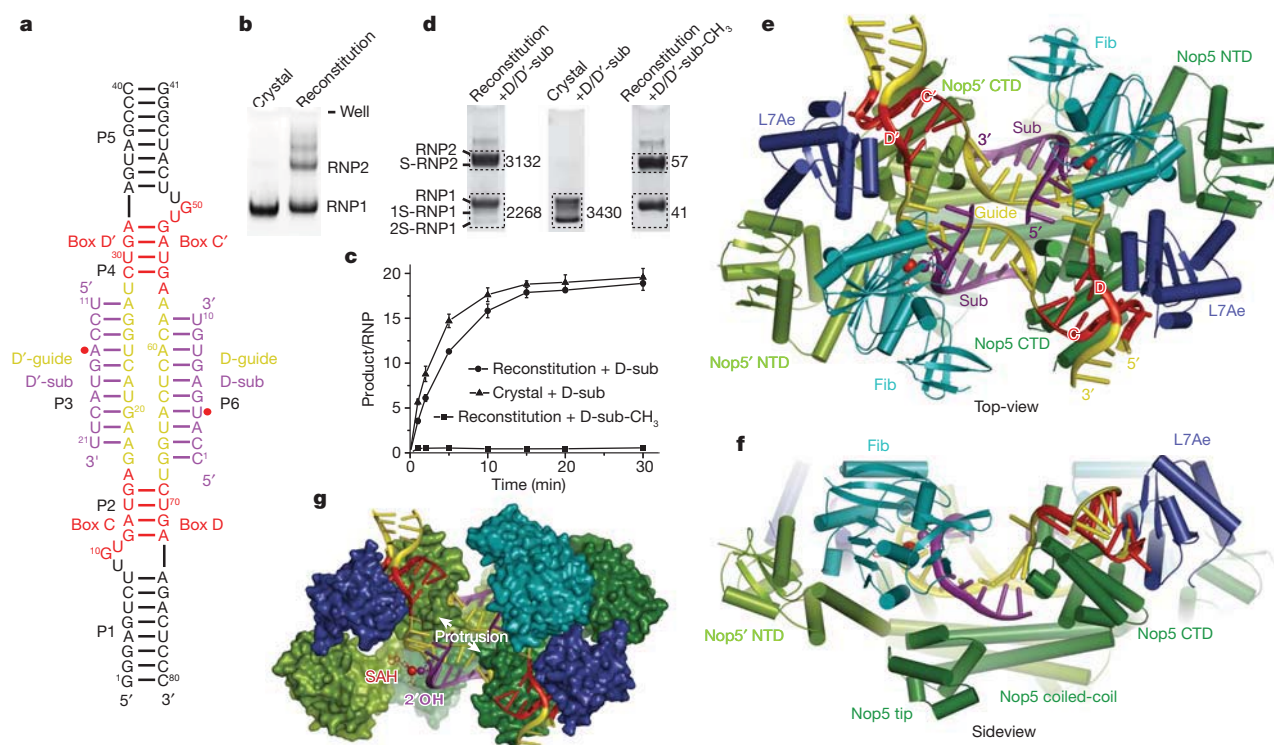


**Figure 1 | Activity and substrate-bound structure of a C/D RNP.**

**a**, Secondary structure of the substrate-bound C/D RNA used for crystallization. Boxes C, C', D and D' (red) are designated as in a natural C/D RNA. Base-paired regions are named P1–P6. The modification targets on the substrates (purple) are marked by red dots. **b**, Ethidium-bromide-stained native gel of reconstituted RNPs and dissolved crystal. **c**, Methylation activity on substrate paired to the D guide (D-sub) or substrate pre-methylated at the target nucleotide (D-sub-CH<sub>3</sub>). The D-sub data are the averages of three replicates  $\pm$  s.d. **d**, Activity of individual RNP fractions. Reconstituted samples or dissolved crystals were assembled with D- and D'-sub or pre-methylated substrates and incubated with [methyl-<sup>3</sup>H]SAM at 25 °C for 5 min before native gel separation. <sup>3</sup>H counts are indicated for RNA extracted from the

The D-guide/substrate duplex (P6) lays over the coiled-coil platform of Nop5 and is bracketed at the D and C' ends by opposing Nop5 CTDs. A highly conserved protrusion in the Nop5 CTD composed of helix  $\alpha$ 9' and its connecting loops to helices  $\alpha$ 9 and  $\alpha$ 10 plays a crucial role in organizing the RNA that links P6 to boxes D and C' (Fig. 2b, c and Supplementary Fig. 5).

The D end of P6 is capped by helix  $\alpha$ 9': the first paired base of the guide (G67) is stacked on the side chain of phenylalanine F305 and the first paired base of the substrate (C1) stacked on the peptide backbone of helix  $\alpha$ 9' (Fig. 2b). P6 is connected to box D by a one-nucleotide linker, which is also the first guide nucleotide U68. Helix  $\alpha$ 9' inserts between P6 and the P2 stem of the K-turn formed by boxes C and D, splay them apart and leaves the one-nucleotide linker unpaired. The first guide residue would be unable to pair to substrate because of the occluding position of helix  $\alpha$ 9', consistent with previous observations<sup>28,29</sup>. The protein–RNA interactions at the guide–box D junction are mainly hydrophobic and occur between residues V279, L304, L308 and F305 and the RNA base and ribose moieties.

At the C' end, P6 docks at the opposing Nop5' CTD with a stacking interaction between the last paired base of the guide (A58) and the side chain of phenylalanine F321 (Fig. 2c). However, the last paired base of

boxed regions. Substrate-bound RNP2 (S-RNP2) and RNP1 bound with one (1S-RNP1) and two substrates (2S-RNP2) are indicated. **e**, Top view of the structure of C/D RNP bound to dual substrates. **f**, Side view. **g**, Top view with proteins in surface representation. One fibrillarin is omitted to show SAH and the target nucleotide. Sub, substrate; Fib, fibrillarin; NTD, N-terminal domain; CTD, C-terminal domain. Nop5 bound to box C/D is green; Nop5' bound to box C'/D' is light green; Fib is cyan; SAH is red; L7Ae is blue; the substrate RNA is purple; boxes C, D, C' and D' are red; the rest of the C/D RNA is yellow. The same colour scheme is used in all subsequent figures. The sulphur atom of SAH and the 2'-OH group of the target nucleotide are shown as red and purple spheres, respectively.

substrate (U10) is not stacked on protein, probably allowing for more flexibility in the guide–substrate pairing at this position. P6 is linked to box C' by the twelfth nucleotide of the guide (A57). This nucleotide projects out with its base stacked on the guanidinium group of R306 in helix  $\alpha$ 9' and its phosphate-ribose backbone intimately contacted by the loop between helices  $\alpha$ 9' and  $\alpha$ 10. In addition, the dimeric coiled-coil domains make contacts with the C' half of P6 at the minor groove by hydrogen bonding and electrostatic interactions, whereas the tip domain has minimal contact with P6 (Fig. 2d).

Fibrillarin transfers a methyl group from S-adenosylmethionine (SAM) to the 2'-hydroxyl group of RNA ribose, yielding S-adenosylhomocysteine (SAH) as a product. In the structure, fibrillarin binds base pairs 1–6 (counted from box D) of P6 at the minor groove (Fig. 3a). This segment of double-stranded RNA (dsRNA), including the target nucleotide, can be well aligned to a standard A-form helix with an root mean squared deviation of 0.53 Å over 12 C1' pairs (Fig. 3b), indicating that fibrillarin accesses the substrate without distorting its helical structure with the guide. The dsRNA-binding region encircles the SAM-binding pocket with a contact area of 907 Å<sup>2</sup>. The guide–substrate dsRNA structure is recognized by a large number of hydrogen bonds directed to the ribose 2'-hydroxyls and phosphates (Figs 2e and 3a), by van der Waals

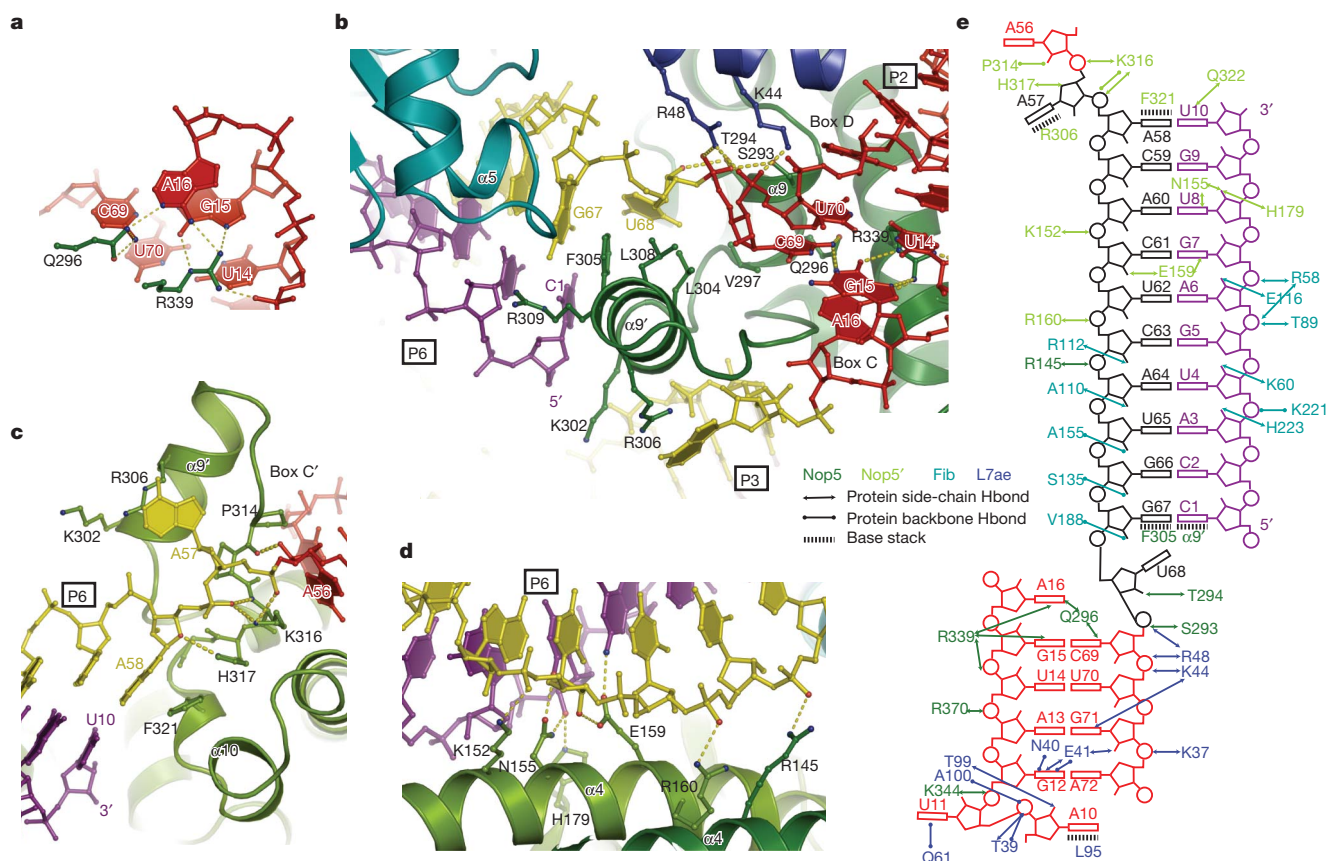


**Figure 2 | Protein-RNA interactions in the substrate-bound C/D RNP.**

**a**, Recognition of boxes C and D by the Nop5 CTD. **b**, RNA interaction around the Nop5 protrusion. **c**, Interaction at the box C' end of the guide-substrate duplex P6. **d**, Interaction between P6 and the Nop5 coiled-coil domains.

**e**, Schematic of protein-RNA interactions, shown for the box C/D half. RNAs and interacting protein residues are shown as balls and sticks, and hydrogen bonds are dashed lines. Oxygen and nitrogen atoms forming hydrogen bonds are coloured red and blue, respectively.

contacts at the minor groove involving helix  $\alpha 5$  (Fig. 2b) and by shape complementarity to the fibrillarin structure (Supplementary Fig. 6). Base pairs 7–10 of P6 are significantly distorted, apparently because of protein interactions and covalent linkage to box C' (Fig. 3b). This region is out of contact with fibrillarin, and the structural distortion may have a minimal effect on activity.

The target ribose remains unmodified in the crystal, probably because the ligand co-purified in the SAM-binding pocket of fibrillarin is SAH in the first place (Fig. 3c). The sulphur atom of SAH is 3.9 Å away from the target 2'-hydroxyl. Three invariant residues (K60, K182 and D153) close to the reaction centre are probably involved in catalysis.

The dsRNA recognition mode would still allow fibrillarin to slide along the minor groove of the guide-substrate duplex. Given that the catalytic module is inherently mobile<sup>14,22,23</sup>, the site specificity of the modification must be determined by other factors in the C/D RNP structure. In this regard, the catalytic module docks against L7Ae at one side (with a contact area of 490 Å<sup>2</sup>) and against the tip domain and a small part of the coiled-coil domain of Nop5' at the other side (with a contact area of 452 Å<sup>2</sup>) (Fig. 3d and Supplementary Fig. 7). These contacts are mostly non-specific, but they could physically prevent fibrillarin from sliding in either direction. Moreover, fibrillarin is stabilized by a specific and highly conserved salt bridge between arginine R112 of fibrillarin and glutamate E163 of Nop5' (Fig. 3e). Lastly, the fixed position of the guide-substrate duplex may also be important for site specificity. Disconnecting the guide from box C'/C was shown to result in non-specific methylation<sup>19</sup>. In this case, the guide-substrate duplex may gain additional dimensions of freedom, allowing fibrillarin to access multiple sites on the substrate. Therefore, the specificity of the modification appears to be jointly determined by fibrillarin's recognition of the dsRNA structure, the restrained mobility

of the catalytic module in the substrate-bound position and the proper positioning of the substrate.

The structure of C/D RNP in the free state is not available, but it may be mimicked by the half-mer RNP structure<sup>23</sup>, wherein fibrillarin is in a resting position and the two K-turns are not covalently connected. To illustrate the conformational change that occurs upon substrate loading, we aligned the structures of the substrate-bound RNP and the half-mer RNP along their dimeric coiled-coil domains (Fig. 4a). The coiled-coil domains can be closely aligned with a root mean squared deviation of 0.522 Å over 112 C $\alpha$  pairs, whereas all other parts of Nop5 show marked domain movement. First, the catalytic module flips about 180° around the junction between Nop5 helices  $\alpha 3$  and  $\alpha 4$  (Fig. 4b). Second, the RNA-binding module and the bound K-turn rotate as a unit about 13° towards the centre of the complex as a result of an upward bend of the last three turns of helix  $\alpha 5$  in the Nop5 coiled-coil domain (Fig. 4a). This movement of the Nop5 CTD was unexpected, as it maintains a fixed orientation to the coiled-coil domain in all previously determined Nop5 structures<sup>14,22,23</sup>. Substrate binding appears to be the primary force driving this movement. Formation of a 10-bp guide-substrate duplex reduces the end-to-end distance of the guide to such a degree that the opposite K-turns are pulled closer. As a result, the distance between the two K-turns (A56 P to C69 P) is reduced by approximately 7 Å upon substrate loading. Alternatively, the RNA-binding module may give way to allow the catalytic module to access the substrate (Fig. 4b). The plasticity of the RNA-binding channel may help accommodate guide and guide-substrate duplexes of variable lengths. Finally, the tip domain undergoes an approximately 6° rotation downward from the platform (Fig. 4a), apparently to make more space for fibrillarin and substrate RNA. These dynamics reveal that the C/D RNP is a modular

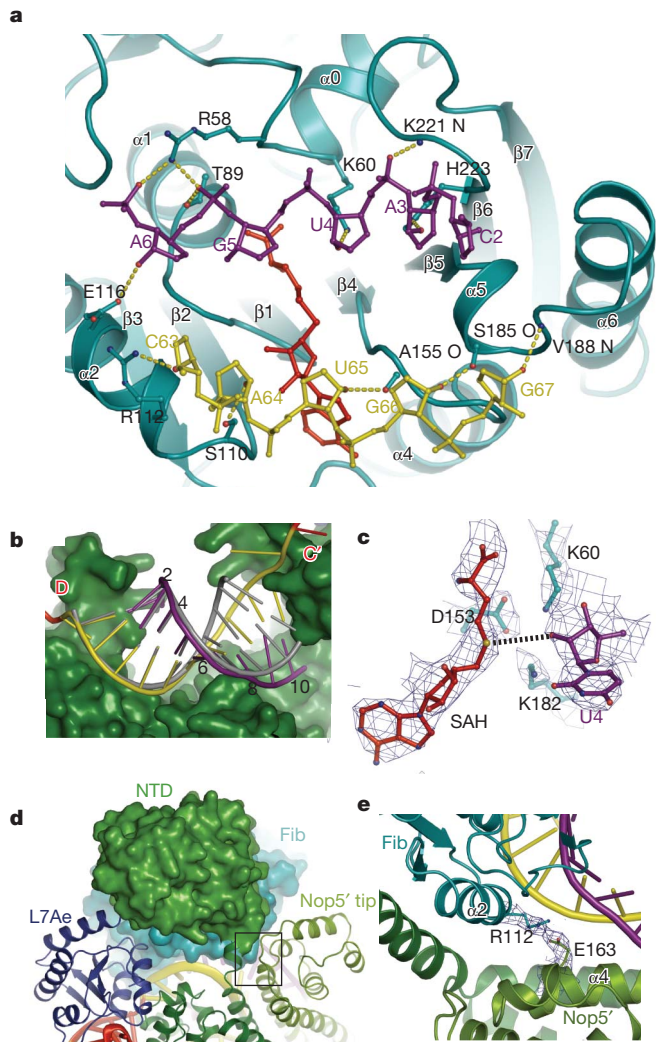


**Figure 3 | Specific substrate recognition by fibrillarlin.** **a**, Fibrillarlin recognition of the minor groove of the guide–substrate duplex. RNA bases are omitted for clarity. Viewed through the major groove. **b**, Alignment of base pairs 1–6 of the guide–substrate duplex with a standard A-form RNA duplex (grey). Every second step is labelled on the substrate strand. **c**, Configuration of the active site. The  $2f_o - f_c$  electron density map is contoured at the  $1\sigma$  level. **d**, The catalytic module at the substrate-bound position is flanked by L7Ae and the tip domain of Nop5'. The box indicates a region shown in **e**. **e**, A salt-bridge interaction linking fibrillarlin to the Nop5' coiled-coil domain.

molecular machine that makes coordinated domain movements during its transformation into a catalytic complex.

Our results depict the organization of a complete monomeric C/D RNP and demonstrate the structural mechanism underlying its site-specific modification activity. The substrate-bound mono-RNP structure suggests that the anchoring of both boxes C/D and C'/D' to the opposite ends of one Nop5 dimer is critical for positioning the guide-substrate duplex in the RNA-binding channel. This explains why archaeal C/D RNAs need a bipartite structure with two sets of boxes C/D and why the dimeric arrangement of Nop5 is important<sup>15,16,19–21</sup>.

Although *in vitro* reconstitution also yields active di-RNPs, further study is needed to understand their structural organization, their relationship to mono-RNPs and their physiological function. If the two C/D RNAs were swapped in a di-RNP<sup>24</sup>, the guide–substrate duplex would be ejected from the RNA-binding channel of Nop5, adopting a very different orientation for fibrillar recognition from that in the mono-RNP structure. It would be unusual if C/D RNPs could specifically modify substrates in two different ways.

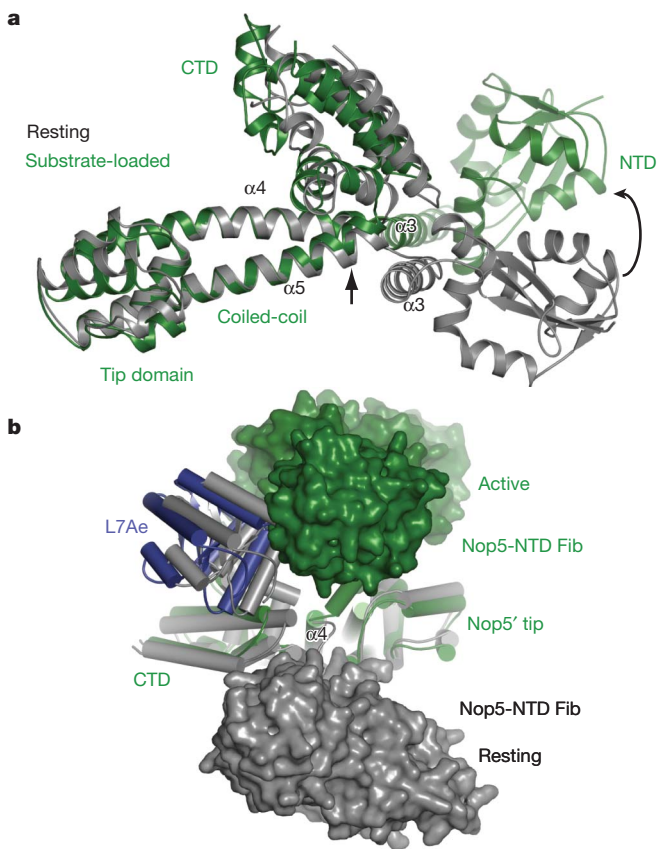


### Figure 4 | Substrate-induced structural changes in the C/D RNP.

**a**, Structural changes of Nop5 upon substrate loading. The structures of the substrate-bound RNP and the half-mer C/D RNP were aligned by their coiled-coil domains. The arrow indicates the bent region in helix  $\alpha 5$ . **b**, Coordinated movement of the catalytic module, RNA-binding module and tip domain upon substrate loading.

## METHODS SUMMARY

A Nop5 fragment (residues 1–380) lacking its C-terminal tail was co-purified with fibrillarin, and L7Ae was purified alone, as previously described<sup>23</sup>. RNAs were prepared by *in vitro* transcription or were chemically synthesized. The two strands of the C/D RNA were annealed at 95 °C for 2 min and then assembled sequentially with two molar equivalents of L7Ae and the fibrillarin–Nop5 (1–380) subcomplex at room temperature. The assembled RNP was concentrated to approximately 10 mg ml<sup>−1</sup> and exchanged to 5 mM HEPES–Na (pH 7.6) buffer. Two decanucleotide substrates, each in a molar ratio of 1.5:1, were added to the RNP before crystallization. The crystal was grown in 2.0 M (NH<sub>4</sub>)<sub>2</sub>SO<sub>4</sub>, 2% PEG-400, 10 mM MgCl<sub>2</sub> and 0.1 M HEPES–Na (pH 6.0) at 20 °C by the hanging drop vapour diffusion method. The crystal was cryoprotected in 2.0 M (NH<sub>4</sub>)<sub>2</sub>SO<sub>4</sub>, 1.0 M Li<sub>2</sub>SO<sub>4</sub>, 0.1 M HEPES–Na (pH 7.5) and 5% glycerol and flash-frozen in liquid nitrogen. The crystal belongs to space group *P*4<sub>1</sub>2<sub>1</sub>2 with cell parameters *a* = *b* = 241.6 Å and *c* = 145.6 Å, and it has one and a half RNPs in the asymmetric unit. The current model includes three copies of Nop5 (residues 3–377), L7Ae (7–128), fibrillarin (5–231), SAH, substrate (1–10) and guide strand (1–35, 9–40 and 6–36). Each half structure of the RNP, as a whole, is superimposable on the other (root mean squared deviation = 0.167–0.325 Å for C $\alpha$  atoms). The Ramachandran plot showed that 95% of the residues are in favoured regions, 4% are in allowed regions and 0.9% are in outlier regions. The structural figures were created in PyMOL<sup>30</sup>.

**Full Methods** and any associated references are available in the online version of the paper at [www.nature.com/nature](http://www.nature.com/nature).

Received 13 July; accepted 19 November 2010.

1. Venema, J. & Tollervey, D. Ribosome synthesis in *Saccharomyces cerevisiae*. *Annu. Rev. Genet.* **33**, 261–311 (1999).

2. Kiss, T. Small nucleolar RNA-guided post-transcriptional modification of cellular RNAs. *EMBO J.* **20**, 3617–3622 (2001).
3. Reichow, S. L., Hamma, T., Ferre-D'Amare, A. R. & Varani, G. The structure and function of small nucleolar ribonucleoproteins. *Nucleic Acids Res.* **35**, 1452–1464 (2007).
4. Henras, A. K. *et al.* The post-transcriptional steps of eukaryotic ribosome biogenesis. *Cell. Mol. Life Sci.* **65**, 2334–2359 (2008).
5. Cavaille, J., Nicoloso, M. & Bachelier, J. P. Targeted ribose methylation of RNA *in vivo* directed by tailored antisense RNA guides. *Nature* **383**, 732–735 (1996).
6. Kiss-Laszlo, Z., Henry, Y., Bachelier, J. P., Caizergues-Ferrer, M. & Kiss, T. Site-specific ribose methylation of preribosomal RNA: a novel function for small nucleolar RNAs. *Cell* **85**, 1077–1088 (1996).
7. Tycowski, K. T., Smith, C. M., Shu, M. D. & Steitz, J. A. A small nucleolar RNA requirement for site-specific ribose methylation of rRNA in *Xenopus*. *Proc. Natl Acad. Sci. USA* **93**, 14480–14485 (1996).
8. Omer, A. D. *et al.* Homologs of small nucleolar RNAs in Archaea. *Science* **288**, 517–522 (2000).
9. Wang, H., Boisvert, D., Kim, K. K., Kim, R. & Kim, S. H. Crystal structure of a fibrillar homologue from *Methanococcus jannaschii*, a hyperthermophile, at 1.6 Å resolution. *EMBO J.* **19**, 317–323 (2000).
10. Vidovic, I., Nottrott, S., Hartmuth, K., Luhrmann, R. & Ficner, R. Crystal structure of the spliceosomal 15.5kD protein bound to a U4 snRNA fragment. *Mol. Cell* **6**, 1331–1342 (2000).
11. Watkins, N. J. *et al.* A common core RNP structure shared between the small nucleolar box C/D RNPs and the spliceosomal U4 snRNP. *Cell* **103**, 457–466 (2000).
12. Cahill, N. M. *et al.* Site-specific cross-linking analyses reveal an asymmetric protein distribution for a box C/D snoRNP. *EMBO J.* **21**, 3816–3828 (2002).
13. Omer, A. D., Ziesche, S., Ebhardt, H. & Dennis, P. P. *In vitro* reconstitution and activity of a C/D box methylation guide ribonucleoprotein complex. *Proc. Natl Acad. Sci. USA* **99**, 5289–5294 (2002).
14. Aittaleb, M. *et al.* Structure and function of archaeal box C/D sRNP core proteins. *Nature Struct. Biol.* **10**, 256–263 (2003).
15. Rashid, R. *et al.* Functional requirement for symmetric assembly of archaeal box C/D small ribonucleoprotein particles. *J. Mol. Biol.* **333**, 295–306 (2003).
16. Tran, E. J., Zhang, X. & Maxwell, E. S. Efficient RNA 2'-O-methylation requires juxtaposed and symmetrically assembled archaeal box C/D and C'/D' RNPs. *EMBO J.* **22**, 3930–3940 (2003).
17. Moore, T., Zhang, Y., Fenley, M. O. & Li, H. Molecular basis of box C/D RNA-protein interactions; cocrystal structure of archaeal L7Ae and a box C/D RNA. *Structure* **12**, 807–818 (2004).
18. Tran, E., Zhang, X., Lackey, L. & Maxwell, E. S. Conserved spacing between the box C/D and C'/D' RNPs of the archaeal box C/D sRNP complex is required for efficient 2'-O-methylation of target RNAs. *RNA* **11**, 285–293 (2005).
19. Hardin, J. W. & Batey, R. T. The bipartite architecture of the sRNA in an archaeal box C/D complex is a primary determinant of specificity. *Nucleic Acids Res.* **34**, 5039–5051 (2006).
20. Omer, A. D., Zago, M., Chang, A. & Dennis, P. P. Probing the structure and function of an archaeal C/D-box methylation guide sRNA. *RNA* **12**, 1708–1720 (2006).
21. Zhang, X. *et al.* The coiled-coil domain of the Nop56/58 core protein is dispensable for sRNP assembly but is critical for archaeal box C/D sRNP-guided nucleotide methylation. *RNA* **12**, 1092–1103 (2006).
22. Oruganti, S. *et al.* Alternative conformations of the archaeal Nop56/58-fibrillar complex imply flexibility in box C/D RNPs. *J. Mol. Biol.* **371**, 1141–1150 (2007).
23. Ye, K. *et al.* Structural organization of box C/D RNA-guided RNA methyltransferase. *Proc. Natl Acad. Sci. USA* **106**, 13808–13813 (2009).
24. Bleichert, F. *et al.* A dimeric structure for archaeal box C/D small ribonucleoproteins. *Science* **325**, 1384–1387 (2009).
25. Xue, S. *et al.* Structural basis for substrate placement by an archaeal box C/D ribonucleoprotein particle. *Mol. Cell* **39**, 939–949 (2010).
26. Klein, D. J., Schmeing, T. M., Moore, P. B. & Steitz, T. A. The kink-turn: a new RNA secondary structure motif. *EMBO J.* **20**, 4214–4221 (2001).
27. Watkins, N. J., Dickmanns, A. & Luhrmann, R. Conserved stem II of the box C/D motif is essential for nucleolar localization and is required, along with the 15.5K protein, for the hierarchical assembly of the box C/D snoRNP. *Mol. Cell. Biol.* **22**, 8342–8352 (2002).
28. Chen, C. L., Perasso, R., Qu, L. H. & Amar, L. Exploration of pairing constraints identifies a 9 base-pair core within box C/D snoRNA-rRNA duplexes. *J. Mol. Biol.* **369**, 771–783 (2007).
29. Appel, C. D. & Maxwell, E. S. Structural features of the guide:target RNA duplex required for archaeal box C/D sRNA-guided nucleotide 2'-O-methylation. *RNA* **13**, 899–911 (2007).
30. DeLano, W. L. *The PyMOL User's Manual* (Delano Scientific, 2002).

**Supplementary Information** is linked to the online version of the paper at [www.nature.com/nature](http://www.nature.com/nature).

**Acknowledgements** We are grateful to the staff at the Shanghai Synchrotron Radiation Facility beamline BL17U for assistance in data collection and to B. Zhu for help with the methylation assay. This research was supported by the Chinese Ministry of Science and Technology (863 grant 2008AA022310) and the Beijing Municipal Government.

**Author Contributions** J. Lin performed sample preparation, biochemical assays, crystallization, data collection and structure determination. S.L., R.J., A.X., L.Z. and J. Lu contributed to sample preparation and crystallization at different stages of the project. J. Lin and K.Y. designed the study, analysed data and prepared the manuscript.

**Author Information** The atomic coordinates and structure factors are deposited in Protein Data Bank under accession number 3PLA. Reprints and permissions information is available at [www.nature.com/reprints](http://www.nature.com/reprints). The authors declare no competing financial interests. Readers are welcome to comment on the online version of this article at [www.nature.com/nature](http://www.nature.com/nature). Correspondence and requests for materials should be addressed to K.Y. (yekeqiong@nibs.ac.cn).

## METHODS

**RNA preparation.** The bipartite box C/D RNA was assembled with two strands, CD45A (5'-GGGAGUCUUGUGAUGAGAAGUACUGGAUCUGAAGUAGC CC-3') and CD45B (5'-GGGCUACUUGUGAUGAAACACUCAUGGUCUGA AGACUCCC-3'). A gene encoding a 5' hammerhead ribozyme<sup>31</sup> and the target RNA was assembled from oligonucleotides and cloned into plasmid pBSK+ downstream of a T7 promoter. The template DNA for transcription was PCR-amplified for 40 cycles from the above plasmid. The sequences of the transcription template are 5'-GCGCGTAATACGACTCACTATAGGGCGAATTGGGTACC CCTCCCTGATGAGAGCGAAAGCTCGAAACTGGAAAGCCAGTCGGG AGTCTTGTGATGAGAACTACTGGATCTGAAGTAGCCC-3' for CD45A, and 5'-GCGCGTAATACGACTCACTATAGGGCGAATTGGGTACCCAGC CCCTGATGAGAGCGAAAGCTCGAAACTGGAAAGCCAGTCGGGCTAC TTGTGATGAAACACTCATGGTCTGAAGACTCCC-3' for CD45B. The sequences of the T7 promoter and the hammerhead are in bold.

The RNA transcription reaction contained 0.1 M HEPES-K (pH 7.9), 35 mM MgCl<sub>2</sub>, 30 mM DTT, 2 mM spermidine, 2.5 mM each of ATP, CTP, UTP and GTP, 0.1 volume of the above PCR product and 80 µg ml<sup>-1</sup> T7 RNA polymerase. After transcription at 37 °C for 4–8 h, the reaction was supplemented with an equal volume of 8 M urea plus 500 mM MgCl<sub>2</sub> and incubated for an additional 2 h to promote self-cleavage of the hammerhead ribozyme. The RNA was precipitated with isopropanol and purified by denaturing polyacrylamide gel and electroelution in Elutrap (Whatman). Two decanucleotide substrate RNAs with the sequences 5'-UCCAGUACUU-3' and 5'-CCAUGAGUGU-3' were purchased from Takara.

**Methylation activity assay.** For activity measurement, four 13-mer RNAs, D-sub (5'-AGACCAUGAGUGU-3'), D'-sub (5'-AGAUCAGUACUU-3'), D-sub-CH<sub>3</sub> (5'-AGACCAU[m]GAGUGU-3') and D'-sub-CH<sub>3</sub> (5'-AGAUCCA[m]GU ACUU-3'), were purchased from Takara. A 200-µl reaction was prepared on ice including 20 pmol C/D RNP, 1,200 pmol substrate, 1,200 pmol unlabelled SAM and 1 µCi [methyl-<sup>3</sup>H]SAM (83 Ci mmol<sup>-1</sup>, PerkinElmer) in a methylation buffer of 20 mM HEPES (pH 7.5), 150 mM NaCl and 1.5 mM MgCl<sub>2</sub>. Aliquots of 20 µl were transferred into PCR tubes and incubated at 70 °C in a PCR machine. One aliquot was saved to quantify total radioactivity. After 1, 2, 5, 10, 15, 20 and 30 min, reaction tubes were removed and frozen in liquid nitrogen. To recover methylated RNA, each sample was mixed with an equal volume of 8 M urea in 1× Tris-borate EDTA buffer and spotted on a 2 cm × 2 cm Hybond-N+ membrane (GE Healthcare). The membranes were baked at 80 °C for 2 h to fix the RNA and were then washed with 8 M urea in 1× Tris-borate EDTA buffer three times for 15 min each and with distilled water three times for 10 min each. The membranes were air-dried, submersed in scintillation fluid and counted in a 1450 MicroBeta TriLux liquid scintillation counter (PerkinElmer). The molar amount of methylated RNA was calculated as the ratio of the counts retained in the membrane to the total counts in a 20-µl reaction, multiplied by the molar amount of SAM.

For methylation analysis of RNP-bound substrate (experiment in Fig. 1d), 100 pmol C/D RNP was assembled with 1,200 pmol each of D-sub and D'-sub 13-mers (or their pre-methylated versions) in 20 µl of methylation buffer at 25 °C for 30 min. The methylation reaction was started by adding 400 pmol unlabelled

SAM and 1.5 µCi [methyl-<sup>3</sup>H]SAM. After incubation at 25 °C for 5 min, the reaction was supplemented with 2 µl loading buffer containing 50% glycerol, 0.25% (w/v) bromophenol blue and 0.25% xylene cyanol FF and loaded onto a 5% native polyacrylamide gel running in Tris-glycine (pH 8.3) buffer. The gel was stained with ethidium bromide. Bands of interest were excised under ultraviolet light and sliced. RNPs were soaked out in 200 µl of soaking buffer containing 0.5 M ammonium acetate, 10 mM magnesium acetate, 1 mM EDTA and 0.1% SDS by 1 h of incubation at 50 °C and additional overnight incubation at 4 °C. The RNA was purified by phenol-chloroform extraction and ethanol precipitation and counted by scintillation.

The RNP concentration was expressed with reference to that of the bipartite guide RNA and was determined by absorbance at 260 nm measured in a NanoDrop 1000 spectrophotometer. The calculated molar extinction coefficient at 260 nm is 854,020 M<sup>-1</sup> cm<sup>-1</sup> for free RNPs and 1,049,820 M<sup>-1</sup> cm<sup>-1</sup> for dual-substrate loaded RNPs (dissolved crystal).

**Structure determination.** Diffraction data were collected at the Shanghai Synchrotron Research Facility beamline BL17U and processed with HKL2000<sup>32</sup>. The structure was solved by molecular replacement with Phaser<sup>33</sup> and Molrep<sup>34</sup>. The structure of the Nop5 NTD and fibrillarin complex<sup>23</sup> (PDB: 3ID6) was first searched for, and three copies were identified in the asymmetric unit. On the basis of this solution, a monomeric Nop5 structure lacking the NTD (PDB: 3ICX) was then searched for, and three copies were found. The arrangement of the three Nop5 molecules is consistent with one and a half Nop5 dimers, with the third molecule forming a dimer with a crystallographically symmetrical Nop5 molecule. Inspection of the electron density revealed movement of the Nop5 CTD. The position of the Nop5 CTD was manually adjusted and rigid-body refined in Refmac. L7Ae and the RNA components were then modelled. The model was built in Coot<sup>35</sup> and refined using Phenix<sup>36</sup> and Refmac<sup>37</sup>. The C/D RNA is asymmetric in sequence and should adopt two orientations in the structure. For simplicity, all three strands of the guide RNA were modelled as 5'-GGGAGUCUUGUGAUG AAACACUCAUGGUCUGAAGACUCCC-3', which is self-complementary between nucleotide residues 1–8 and 33–40, and all three substrates were modelled as 5'-CCAUGAGUGU-3'.

31. Price, S. R., Ito, N., Oubridge, C., Avis, J. M. & Nagai, K. Crystallization of RNA-protein complexes. I. Methods for the large-scale preparation of RNA suitable for crystallographic studies. *J. Mol. Biol.* **249**, 398–408 (1995).
32. Otwinowski, Z. & Minor, W. Processing of X-ray diffraction data collected in oscillation mode. *Methods Enzymol.* **276**, 307–326 (1997).
33. McCoy, A. J. et al. Phaser crystallographic software. *J. Appl. Cryst.* **40**, 658–674 (2007).
34. Vagin, A. A. & Teplyakov, A. MOLREP: an automated program for molecular replacement. *J. Appl. Cryst.* **30**, 1022–1025 (1997).
35. Emsley, P. & Cowtan, K. Coot: model-building tools for molecular graphics. *Acta Crystallogr. D* **60**, 2126–2132 (2004).
36. Adams, P. D. et al. PHENIX: a comprehensive Python-based system for macromolecular structure solution. *Acta Crystallogr. D* **66**, 213–221 (2010).
37. Murshudov, G. N., Vagin, A. A., Lebedev, A., Wilson, K. S. & Dodson, E. J. Efficient anisotropic refinement of macromolecular structures using FFT. *Acta Crystallogr. D* **55**, 247–255 (1999).

# Structure of human O-GlcNAc transferase and its complex with a peptide substrate

Michael B. Lazarus<sup>1,4\*</sup>, Yunsun Nam<sup>2,3\*</sup>, Jiaoyang Jiang<sup>4</sup>, Piotr Sliz<sup>2,3</sup> & Suzanne Walker<sup>4</sup>

The essential mammalian enzyme O-linked  $\beta$ -N-acetylglucosamine transferase (O-GlcNAc transferase, here OGT) couples metabolic status to the regulation of a wide variety of cellular signalling pathways by acting as a nutrient sensor<sup>1</sup>. OGT catalyses the transfer of N-acetylglucosamine from UDP-N-acetylglucosamine (UDP-GlcNAc) to serines and threonines of cytoplasmic, nuclear and mitochondrial proteins<sup>2,3</sup>, including numerous transcription factors<sup>4</sup>, tumour suppressors, kinases<sup>5</sup>, phosphatases<sup>1</sup> and histone-modifying proteins<sup>6</sup>. Aberrant glycosylation by OGT has been linked to insulin resistance<sup>7</sup>, diabetic complications<sup>8</sup>, cancer<sup>9</sup> and neurodegenerative diseases including Alzheimer's<sup>10</sup>. Despite the importance of OGT, the details of how it recognizes and glycosylates its protein substrates are largely unknown. We report here two crystal structures of human OGT, as a binary complex with UDP (2.8 Å resolution) and as a ternary complex with UDP and a peptide substrate (1.95 Å). The structures provide clues to the enzyme mechanism, show how OGT recognizes target peptide sequences, and reveal the fold of the unique domain between the two halves of the catalytic region. This information will accelerate the rational design of biological experiments to investigate OGT's functions; it will also help the design of inhibitors for use as cellular probes and help to assess its potential as a therapeutic target.

The ability to sense and respond to nutrient levels is critical for the growth of all living systems. In eukaryotes, a major mechanism for nutrient sensing involves the essential<sup>11</sup> protein glycosyltransferase OGT, which senses cellular glucose levels via UDP-GlcNAc concentrations, and responds by dynamically O-GlcNAcylating a wide range of nuclear and cytoplasmic proteins<sup>1,12</sup>. These include proteins involved in insulin-like signalling pathways<sup>7</sup> and transcriptional activators that regulate glucose levels by controlling gluconeogenesis<sup>13</sup>. As many known O-GlcNAcylation sites are also phosphorylation sites, OGT is proposed to play a major role in modulating cellular kinase signalling cascades<sup>14</sup>. OGT is also involved in widespread transcriptional regulation<sup>15–17</sup>. Prolonged hyperglycaemia, such as occurs in diabetes, or excessive glucose uptake, such as occurs in cancer cells, results in hyper-O-GlcNAcylation of cellular proteins by OGT, and this increased O-GlcNAcylation has been linked to harmful cellular effects<sup>18</sup>. Thus, strategies to modulate OGT activity may have therapeutic value for treating diabetic complications, cancer, and other diseases<sup>13</sup>.

The lack of a crystal structure has been a major impediment to investigating OGT's molecular mechanisms, understanding substrate recognition, and developing inhibitors. OGT comprises two distinct regions: an N-terminal region consisting of a series of tetratricopeptide repeat (TPR) units<sup>19,20</sup> and a multidomain catalytic region. The TPR domain is proposed to scaffold interactions with other proteins, which may play a role in determining substrate selectivity<sup>21</sup>. A crystal structure comprising 11.5 TPR units of human OGT has been reported<sup>21</sup>, but there have been no structures of the catalytic region. From sequence analysis and structures of bacterial glycosyltransferases<sup>22–26</sup>,

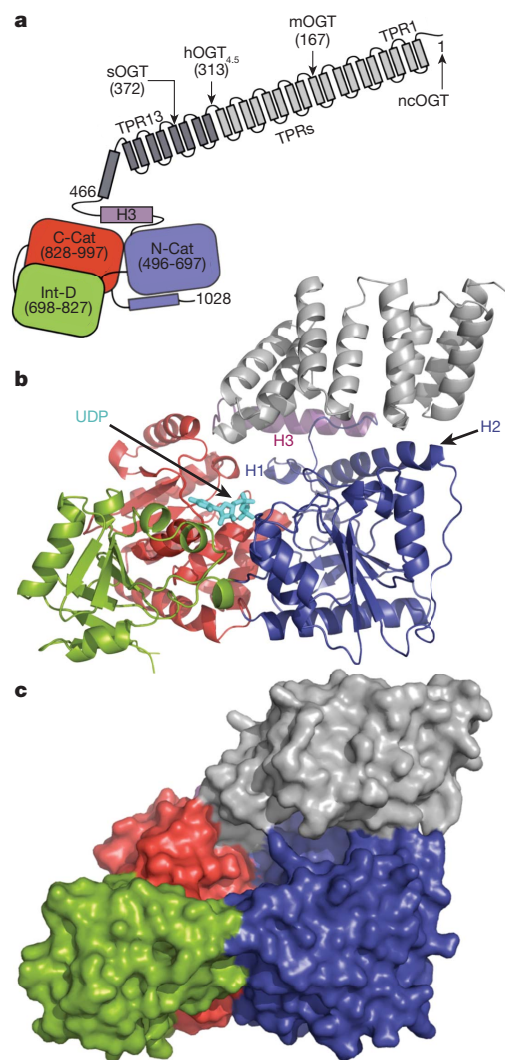


**Figure 1 | Overall structure of human OGT complexed to UDP.**

**a**, Schematic of OGT domain architecture with the TPR units shown in grey, the transitional helix (H3) in purple, the N-Cat domain in blue, the Int-D domain in green, and the C-Cat domain in red. The native isoforms of OGT (sOGT, short OGT; mOGT, mitochondrial OGT; and ncOGT, nucleocytoplasmic OGT) and the crystallization construct differ only in the number of TPRs, as shown. **b**, Overall fold of OGT from the OGT-UDP complex in a ribbon representation. The colouring is the same as the schematic in **a**. The UDP is shown in cyan. The N-Cat domain helices unique to OGT are indicated as H1 and H2. **c**, Surface representation of the OGT-UDP complex. The colouring scheme is the same as in **a** and **b**.

<sup>1</sup>Department of Chemistry and Chemical Biology, Harvard University, Cambridge, Massachusetts 02138, USA. <sup>2</sup>Department of Biological Chemistry and Molecular Pharmacology, Harvard Medical School, Boston, Massachusetts 02115, USA. <sup>3</sup>Laboratory of Molecular Medicine, Children's Hospital, Boston, Massachusetts 02115, USA. <sup>4</sup>Department of Microbiology and Molecular Genetics, Harvard Medical School, Boston, Massachusetts 02115, USA.

\*These authors contributed equally to this work.

including a bacterial homologue of unknown function<sup>25,26</sup>, OGT was predicted to be a member of the GT-B superfamily of glycosyltransferases (Gtfs)<sup>27</sup>. However, OGT is unusual because it is the only known member to glycosylate polypeptides and it contains a long uncharacterized intervening sequence (~120 amino acids) in the middle of the catalytic region. It is also proposed to contain a phosphatidylinositol (3,4,5)-trisphosphate (PIP<sub>3</sub>) binding domain involved in membrane recruitment in response to insulin signalling<sup>7</sup>.

We report two crystal structures of a human OGT construct (hOGT<sub>4.5</sub>) containing 4.5 TPR units and the catalytic domain. The catalytic properties of this construct are similar to those of the full-length enzyme (Supplementary Fig. 1)<sup>28</sup>. One structure (2.8 Å, referred to as OGT-UDP) is a complex with UDP; the other structure (1.95 Å, referred to as OGT-UDP-peptide) is a complex containing UDP and a well-characterized 14-residue CKII peptide substrate<sup>28</sup>. On the basis of currently available experimental data, we also present a model for the full-length enzyme (Supplementary Information). Details of structure determination are presented in Methods and Supplementary Tables 1 and 2.

The OGT-UDP complex is shown in Fig. 1. The catalytic region contains three domains: the amino (N)-terminal domain (N-Cat), the carboxy (C)-terminal domain (C-Cat), and the intervening domain (Int-D) (Fig. 1a, b). The N-Cat and C-Cat domains have Rossmann-like folds typical of GT-B superfamily members; however, the N-Cat domain is distinctive in containing two additional helices, H1 and H2,

which form an essential part of the active site (Fig. 1b). The Int-D domain, which has a novel fold, packs exclusively against the C-Cat domain (Fig. 1c). The UDP moiety binds in a pocket in the C-Cat domain near the interface with the N-Cat domain<sup>27</sup>. This pocket is lined with conserved residues shown to be important for catalytic activity (Supplementary Table 3)<sup>25,26</sup>. A transitional helix (H3) links the catalytic region to the TPR repeats, which spiral along the upper surface of the catalytic region from the C-Cat domain to the N-Cat domain. The TPRs and the catalytic region are demarcated by a narrow horizontal cleft.

The OGT-UDP-peptide complex (Fig. 2), which crystallized in a different space group from the OGT-UDP complex, has a wider cleft between the TPR domain and the catalytic region than the OGT-UDP complex (Fig. 1c and Fig. 2a), and the CKII peptide binds in this cleft. This peptide, YPGGSTPVS\*SANMM, contains three serines and a threonine, but only one serine (underlined; referred to as Ser\*) is glycosylated by OGT<sup>28</sup>. The hydroxyl of Ser\* points into the nucleotide-sugar binding site (Fig. 2b). The two residues N-terminal to Ser\* lie over the UDP moiety; the residues C-terminal to Ser\* traverse towards the back of the cleft along the H2 helix of the N-Cat lobe. Although OGT glycosylates a wide range of target peptides, it prefers sequences in which the residues flanking the glycosylated amino acid enforce an extended conformation (for example, prolines and  $\beta$ -branched amino acids; see Supplementary Fig. 2 and Supplementary Table 4). Consistent with these preferences, the peptide is anchored mainly by contacts from

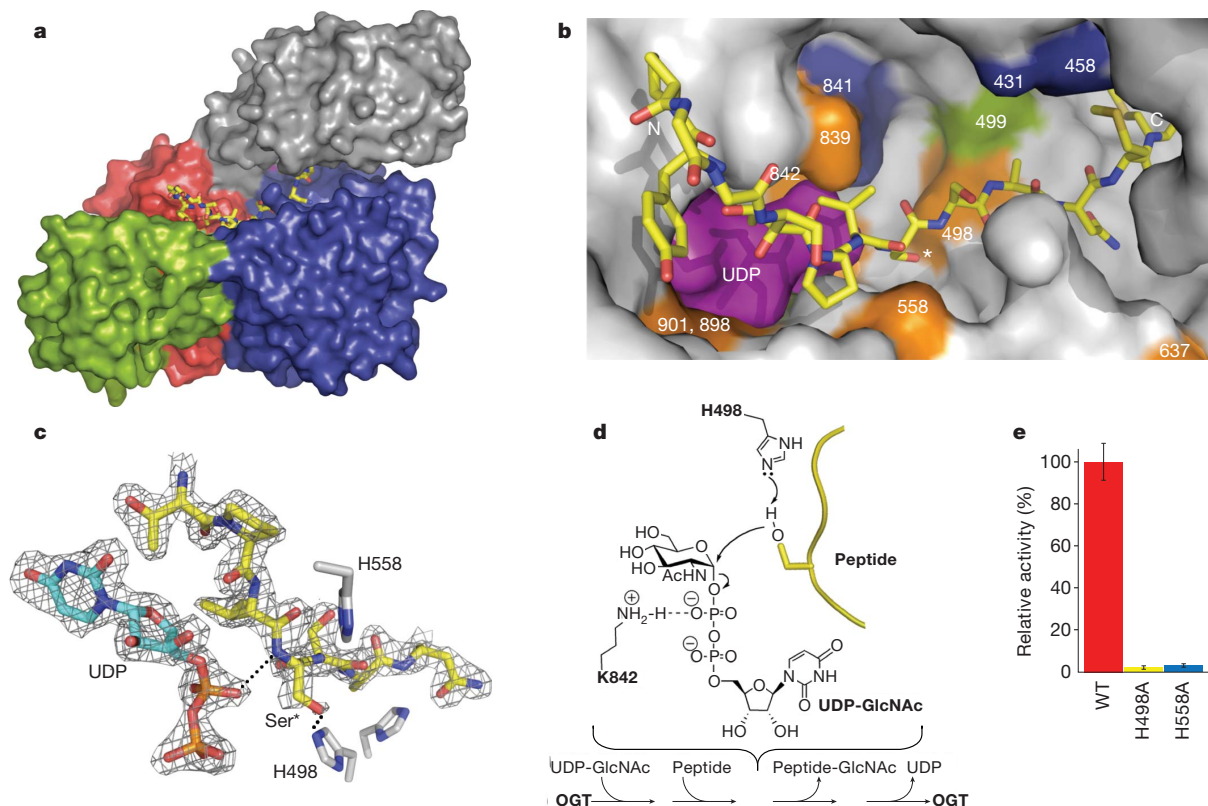


**Figure 2 | Structure of the OGT-UDP-peptide complex.** **a**, Surface rendering of the OGT complex with UDP and the CKII peptide substrate<sup>28</sup>. The view and the colouring is the same as in Fig. 1. The peptide, shown in yellow, lies over the UDP moiety, which is not visible in this orientation. **b**, Close-up surface rendering of the OGT active site (grey) containing the CKII peptide in a stick representation (carbon atoms shown in yellow) with the UDP (purple) in a space filling representation lying directly underneath it. The reactive serine is indicated by an asterisk. The peptide binds in the cleft between the TPR region and the catalytic region, and extends along the interface between the C-Cat and N-Cat domains. Protein residues implicated in catalytic activity are coloured orange, green, or blue in decreasing order of importance based on residual activity after mutation (Supplementary Table 3). Lysine 842 (orange) lies

underneath UDP in this view. **c**, View of UDP (carbon atoms shown in cyan) and part of the CKII peptide (carbon atoms shown in yellow) with selected OGT side chains shown. Dashed lines indicate inferred hydrogen bonds based on distances in the OGT-UDP-peptide complex. The  $2F_o - F_c$  omit map is contoured at the  $1\sigma$  level. **d**, Proposed mechanism of OGT. The ordered sequential bi-bi kinetic mechanism shown is based on the structure of the ternary complex and supporting kinetic experiments (Supplementary Fig. 4). The peptide is depicted in yellow with only the reactive serine hydroxyl shown. H498 is the proposed catalytic base. Lys 842, also shown to be essential for activity<sup>25,26</sup>, stabilizes the UDP moiety. **e**, Histogram showing the relative activities of the H498A and H558A mutants compared to the wild-type (WT) protein (average  $\pm$  s.d.,  $n = 3$ ).

OGT side chains to the amide backbone, with an additional contact from the UDP moiety to the backbone amide of Ser\*. The cleft is also filled with ordered water molecules, enabling it to serve as an adaptable interface to bind a range of polypeptides containing side chains of different sizes, polarity, and hydrogen bonding capabilities. As the peptide substrate is anchored by contacts to its backbone, it is reasonable to infer that protein substrates are glycosylated on flexible regions such as loops or termini that can bind in an extended conformation, exposing the amide backbone.

The closed conformation of the substrate-binding cleft in the OGT–UDP structure is stabilized by a ‘latch’ comprising contacts between TPRs 10/11 and the H2 helix of the catalytic domain (Fig. 2a and Supplementary Fig. 3). Opening of the cleft in the OGT–UDP–peptide complex occurs owing to a hinge-like motion around a pivot point between TPRs 12 and 13. The two structures suggest that glycosylation substrates enter the active site from the face of the enzyme shown in Fig. 2a, with the TPR domain restricting or allowing access, depending on its conformation and its interactions with the catalytic domain. Molecular dynamics simulations indicate that the ‘hinge’ between the catalytic domain and the TPR domain is capable of large motions that fully expose the active site, which would allow protein substrates to approach closely enough for surface loops to enter (Supplementary Movie 1). The molecular mechanisms that facilitate or stabilize opening of the cleft to allow access of protein substrates remain to be determined, but may involve interactions between protein substrates or adaptor proteins and the other regions of OGT.

The OGT–UDP–peptide complex, in addition to revealing how peptide substrates bind, provides unexpected insights into the kinetic mechanism. OGT was previously proposed to have a random sequential ‘bi-bi’ mechanism in which either substrate can bind first<sup>28</sup>. The structure, however, indicates that the peptide substrate binds over the

nucleotide-sugar binding pocket, blocking access to it. Moreover, the  $\alpha$ -phosphate of the UDP moiety contacts the backbone amide of Ser\* (Fig. 2c), which helps orient the peptide. The peptide complex suggests an ordered mechanism in which UDP–GlcNAc binds before the polypeptide substrate. To assess the order of substrate binding, we analysed the product inhibition patterns for UDP. At saturating peptide concentrations, a competitive inhibition pattern was obtained for UDP with respect to UDP–GlcNAc, which is inconsistent with a random mechanism, but supports the ordered sequential bi-bi mechanism implied by the crystal structure (Supplementary Fig. 4).

Another insight from the crystal structure is the identity of the catalytic base. On the basis of analyses of other GT-B family members, including the bacterial OGT homologue, it was proposed that His 558 is the catalytic base. Although we have verified that this residue is critical for catalytic activity, the peptide complex shows that it is more than 5 Å away from the reactive serine hydroxyl and makes an apparent hydrogen bond with the backbone carbonyl of the preceding residue. In contrast, His 498, which is invariant in metazoan OGTs but absent in the homologous bacterial enzyme, protrudes from helix H1 into the active site within 3.5 Å of the Ser\* hydroxyl. As His 498 is critical for activity and is located between the reactive serine hydroxyl and the GlcNAc binding pocket, it is the probable catalytic base in OGT.

We were unable to obtain a crystal of the OGT–UDP–GlcNAc complex owing to hydrolysis of the substrate, but according to the computational docking experiments we performed, the GlcNAc is oriented in a manner that exposes its  $\beta$ -face to the overlying peptide (Supplementary Fig. 5) and places the anomeric carbon near the reactive serine. This conformation is similar to the UDP–GlcNAc conformation observed in a complex of another GT-B family member<sup>23</sup>, and its relevance is supported by evidence that the C2 N-acetyl moiety projects up from the OGT sugar binding pocket<sup>29</sup>. Furthermore, it is consistent with the enzymatic reaction, which

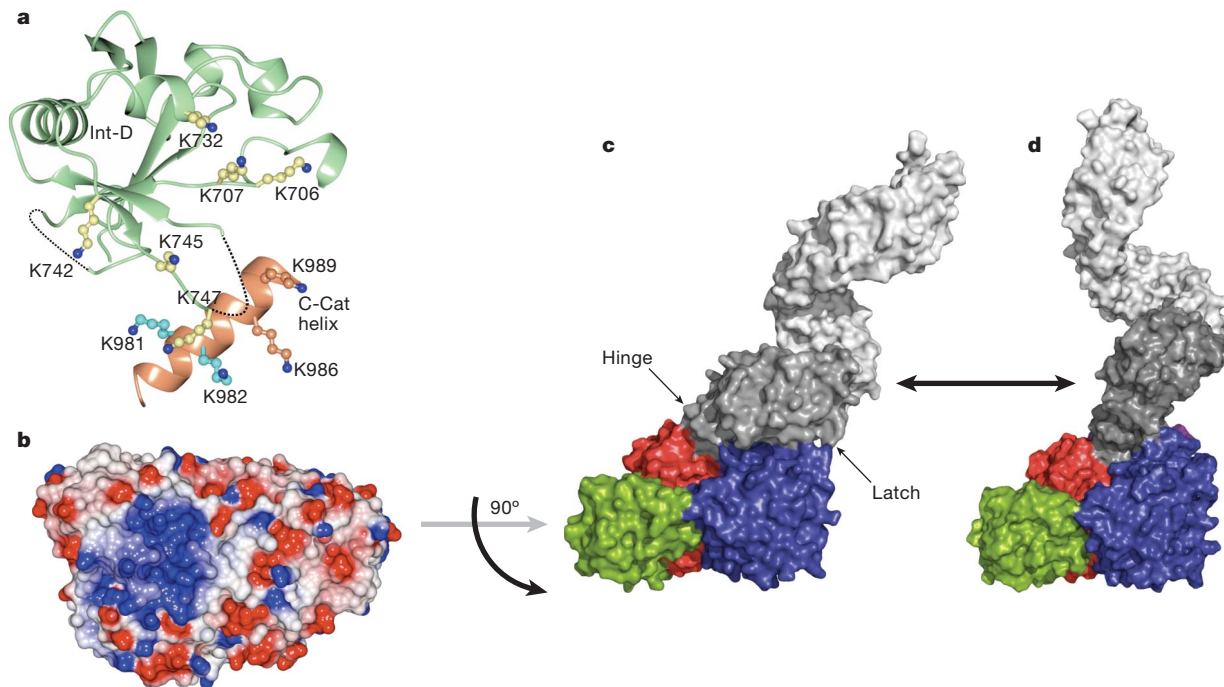


**Figure 3 | Structure of the intervening domain and full-length models of human OGT.** **a**, Ribbon representation of the intervening domain rendered in light green with missing loops represented by dotted lines. Lysine side chains that form an extensive positive surface (see **b**) are displayed in a ‘ball-and-stick’ representation. Shown in coral is a helix from the C-cat domain containing four basic residues that contribute to the positively charged surface<sup>7</sup>. **b**, Surface representation of OGT coloured according to electrostatic potential, with blue representing areas of positive charge and red representing areas of negative charge. The protein is rotated 90° around the *x*-axis from the representation shown in Figs 1, 2 and 3c, exposing the bottom surface of the catalytic region.

**c**, Model of full-length human OGT, shown as a surface rendering and coloured as in Fig. 1a, based on the hOGT<sub>4.5</sub> structures and the previously reported TPR domain structure. The TPRs preceding the boundary of hOGT<sub>4.5</sub> are shown in light grey. The model is shown as a monomer, but OGT may exist in different oligomerization states in cells<sup>21,28</sup>. Hinge and latch regions are indicated by arrows. **d**, Model of full-length OGT opening to accommodate larger substrates. The ‘open’ conformation is based on molecular dynamics simulations (Supplementary Movie 1), as described in Methods. (Atomic coordinates for full-length models are available for download; see Supplementary Information.)

involves displacement of the  $\alpha$ -UDP group to yield an inverted product. On the basis of the accumulated biochemical and structural data, we propose a general mechanism for the reaction (Fig. 2d).

The most unusual feature of OGT is the intervening domain between the catalytic lobes, which is only found in metazoans (Supplementary Figs 6 and 7). This polypeptide adopts a topologically novel fold with a seven-stranded  $\beta$ -sheet core stabilized by flanking  $\alpha$ -helices (Fig. 3a). There are two long unstructured loops for which electron density is missing. An electrostatic surface rendering shows that the intervening domain and an adjacent helix of the C-Cat domain form a large basic surface comprising ten lysine residues (Fig. 3a and b). Among these are K981 and K982, which were previously reported to constitute part of a PIP<sub>3</sub> binding motif that recruits OGT to membranes<sup>7</sup>. We mutated eight of these ten lysines in various combinations (Supplementary Table 3). All mutants were catalytically active (Supplementary Fig. 8), but we were unable to identify a role for the Int-D domain in PIP<sub>3</sub> binding (Supplementary Table 5). We suggest that this domain is involved in other functions *in vivo*. These functions may include substrate selection, cellular localization, or interactions with regulatory factors or receptors. The reported structures and mutant data provide a crucial starting point for investigating the possible roles of the intervening domain.

The structures reported here show how OGT recognizes peptide sequences and provide new information on the enzymatic mechanism as well as a view of the intervening domain. Models of full-length human OGT in its open and closed states, constructed on the basis of crystal structures and molecular dynamics simulations, highlight the conformational changes that may regulate access of substrates to the active site (Fig. 3c and d). Our structures may assist in the development of inhibitors with possible therapeutic value for treating diseases associated with excessive O-GlcNAcylation.

## METHODS SUMMARY

Human OGT residues 313–1031 (CPH...KPVE) were expressed in *Escherichia coli* and purified by nickel affinity chromatography and gel filtration. Protein was then incubated with UDP or with UDP and a 17-residue substrate peptide (KKKYPGGSTPVSSANMM), which was cleaved to YPGGSTPVSSANMM in the crystallization drop (confirmed by mass spectrometry). The OGT–UDP structure was determined using the method of multiple isomorphous replacement with anomalous scattering (MIRAS) (Supplementary Table 2). The OGT–UDP–peptide complex structure was solved by molecular replacement using the refined OGT–UDP structure. The crystal packing for the two complexes is described in Supplementary Fig. 9. Kinetic analysis was performed using UDP-<sup>14</sup>C-GlcNAc and a lysine tagged CKII peptide using our previously described filter binding assay<sup>29</sup>. The molecular dynamics simulation was performed by using the program Desmond<sup>30</sup> on an optimized 64-node Linux-based InfiniBand cluster.

**Full Methods** and any associated references are available in the online version of the paper at [www.nature.com/nature](http://www.nature.com/nature).

**Received 20 April; accepted 3 November 2010.**

**Published online 16 January 2011.**

- Hart, G. W., Housley, M. P. & Slawson, C. Cycling of O-linked  $\beta$ -N-acetylglucosamine on nucleocytoplasmic proteins. *Nature* **446**, 1017–1022 (2007).
- Torres, C. R. & Hart, G. W. Topography and polypeptide distribution of terminal N-acetylglucosamine residues on the surfaces of intact lymphocytes. Evidence for O-linked GlcNAc. *J. Biol. Chem.* **259**, 3308–3317 (1984).
- Haltiwanger, R. S., Holt, G. D. & Hart, G. W. Enzymatic addition of O-GlcNAc to nuclear and cytoplasmic proteins. Identification of a uridine diphospho-N-acetylglucosamine:peptide beta-N-acetylglucosaminyltransferase. *J. Biol. Chem.* **265**, 2563–2568 (1990).
- Yang, X., Zhang, F. & Kudlow, J. E. Recruitment of O-GlcNAc transferase to promoters by corepressor mSin3A: coupling protein O-GlcNAcylation to transcriptional repression. *Cell* **110**, 69–80 (2002).
- Dias, W. B., Cheung, W. D., Wang, Z. & Hart, G. W. Regulation of calcium/calmodulin-dependent kinase IV by O-GlcNAc modification. *J. Biol. Chem.* **284**, 21327–21337 (2009).
- Fujiki, R. *et al.* GlcNAcylation of a histone methyltransferase in retinoic-acid-induced granulopoiesis. *Nature* **459**, 455–459 (2009).
- Yang, X. *et al.* Phosphoinositide signalling links O-GlcNAc transferase to insulin resistance. *Nature* **451**, 964–969 (2008).

- Brownlee, M. Biochemistry and molecular cell biology of diabetic complications. *Nature* **414**, 813–820 (2001).
- Caldwell, S. A. *et al.* Nutrient sensor O-GlcNAc transferase regulates breast cancer tumorigenesis through targeting of the oncogenic transcription factor FoxM1. *Oncogene* **29**, 2831–2842 (2010).
- Liu, F., Iqbal, K., Grundke-Iqbal, I., Hart, G. W. & Gong, C. X. O-GlcNAcylation regulates phosphorylation of tau: a mechanism involved in Alzheimer's disease. *Proc. Natl Acad. Sci. USA* **101**, 10804–10809 (2004).
- Shafi, R. *et al.* The O-GlcNAc transferase gene resides on the X chromosome and is essential for embryonic stem cell viability and mouse ontogeny. *Proc. Natl Acad. Sci. USA* **97**, 5735–5739 (2000).
- Love, D. C. & Hanover, J. A. The hexosamine signaling pathway: deciphering the “O-GlcNAc code”. *Sci. STKE* **2005**, re13 (2005).
- Dentin, R., Hedrick, S., Xie, J., Yates, J. III & Montminy, M. Hepatic glucose sensing via the CREB coactivator CRTC2. *Science* **319**, 1402–1405 (2008).
- Wells, L., Vosseller, K. & Hart, G. W. Glycosylation of nucleocytoplasmic proteins: signal transduction and O-GlcNAc. *Science* **291**, 2376–2378 (2001).
- Gambetta, M. C., Oktaba, K. & Muller, J. Essential role of the glycosyltransferase *sxc*/Ogt in polycomb repression. *Science* **325**, 93–96 (2009).
- Sinclair, D. A. *et al.* *Drosophila* O-GlcNAc transferase (OGT) is encoded by the Polycomb group (PcG) gene, super sex combs (*sxc*). *Proc. Natl Acad. Sci. USA* **106**, 13427–13432 (2009).
- Love, D. C. *et al.* Dynamic O-GlcNAc cycling at promoters of *Caenorhabditis elegans* genes regulating longevity, stress, and immunity. *Proc. Natl Acad. Sci. USA* **107**, 7413–7418 (2010).
- Goldberg, H. J., Whiteside, C. I., Hart, G. W. & Fantus, I. G. Posttranslational, reversible O-glycosylation is stimulated by high glucose and mediates plasminogen activator inhibitor-1 gene expression and Sp1 transcriptional activity in glomerular mesangial cells. *Endocrinology* **147**, 222–231 (2006).
- Kreppel, L. K., Blomberg, M. A. & Hart, G. W. Dynamic glycosylation of nuclear and cytosolic proteins. Cloning and characterization of a unique O-GlcNAc transferase with multiple tetratricopeptide repeats. *J. Biol. Chem.* **272**, 9308–9315 (1997).
- Lubas, W. A., Frank, D. W., Krause, M. & Hanover, J. A. O-Linked GlcNAc transferase is a conserved nucleocytoplasmic protein containing tetratricopeptide repeats. *J. Biol. Chem.* **272**, 9316–9324 (1997).
- Jinek, M. *et al.* The superhelical TPR-repeat domain of O-linked GlcNAc transferase exhibits structural similarities to importin  $\alpha$ . *Nature Struct. Mol. Biol.* **11**, 1001–1007 (2004).
- Ha, S., Walker, D., Shi, Y. & Walker, S. The 1.9 Å crystal structure of *Escherichia coli* MurG, a membrane-associated glycosyltransferase involved in peptidoglycan biosynthesis. *Protein Sci.* **9**, 1045–1052 (2000).
- Hu, Y. *et al.* Crystal structure of the MurG:UDP-GlcNAc complex reveals common structural principles of a superfamily of glycosyltransferases. *Proc. Natl Acad. Sci. USA* **100**, 845–849 (2003).
- Wrabl, J. O. & Grishin, N. V. Homology between O-linked GlcNAc transferases and proteins of the glycogen phosphorylase superfamily. *J. Mol. Biol.* **314**, 365–374 (2001).
- Martinez-Fleites, C. *et al.* Structure of an O-GlcNAc transferase homolog provides insight into intracellular glycosylation. *Nature Struct. Mol. Biol.* **15**, 764–765 (2008).
- Clarke, A. J. *et al.* Structural insights into mechanism and specificity of O-GlcNAc transferase. *EMBO J.* **27**, 2780–2788 (2008).
- Lairson, L. L., Henrissat, B., Davies, G. J. & Withers, S. G. Glycosyltransferases: structures, functions, and mechanisms. *Annu. Rev. Biochem.* **77**, 521–555 (2008).
- Kreppel, L. K. & Hart, G. W. Regulation of a cytosolic and nuclear O-GlcNAc transferase. Role of the tetratricopeptide repeats. *J. Biol. Chem.* **274**, 32015–32022 (1999).
- Gross, B. J., Kraybill, B. C. & Walker, S. Discovery of O-GlcNAc transferase inhibitors. *J. Am. Chem. Soc.* **127**, 14588–14589 (2005).
- Bowers, K. J. *et al.* Scalable algorithms for molecular dynamics simulations on commodity clusters. *Proc. ACM/IEEE Conf. on Supercomputing (SC06)* (ACM Press, 2006).

**Supplementary Information** is linked to the online version of the paper at [www.nature.com/nature](http://www.nature.com/nature).

**Acknowledgements** We thank B. Gross and C. Drennan for advice. We also thank the US National Institutes of Health, the US National Science Foundation, and the Harvard Biomedical Accelerator Fund for financial support. This work is based on research conducted at the Advanced Photon Source (Northeastern Collaborative Access Team beamlines) and Brookhaven National Laboratory (X25 and X29 beamlines).

**Author Contributions** S.W. conceived the project. M.B.L. obtained the crystallization construct and initial diffracting crystals. M.B.L., Y.N. and P.S. determined and refined the crystal structures. J.J. and M.B.L. performed the enzymatic assays. M.B.L., Y.N., J.J., P.S. and S.W. designed experiments, discussed results, and prepared the manuscript.

**Author Information** The structures of the OGT–UDP complex and the OGT–UDP–peptide complex have been submitted to the Protein Data Bank under accession numbers 3PE3 and 3PE4. Atomic coordinates for the full-length models of OGT as well as the docked UDP-GlcNAc structure are available for download from the Walker Laboratory website (see Supplementary Information). Reprints and permissions information is available at [www.nature.com/reprints](http://www.nature.com/reprints). The authors declare no competing financial interests. Readers are welcome to comment on the online version of this article at [www.nature.com/nature](http://www.nature.com/nature). Correspondence and requests for materials should be addressed to S.W. (enzymology; [suzanne\\_walker@hms.harvard.edu](mailto:suzanne_walker@hms.harvard.edu)) or P.S. (structural biology; [piotr\\_sliz@hms.harvard.edu](mailto:piotr_sliz@hms.harvard.edu)).

## METHODS

**Protein purification.** Full length human OGT (ncOGT) was expressed as previously described. The OGT<sub>4.5</sub> construct (spanning residues 313–1031 based on the numbering of the full length human protein) was constructed from our previously reported *E. coli* codon-optimized construct using primers listed in Supplementary Table 6 after being cloned into a pET24b vector (Novagen)<sup>29</sup>. After plasmid transformation into BL21 (DE3), the protein was expressed as a fusion protein with an N terminus consisting of a T7 tag, followed by an 8-His tag, followed by an HRV3C protease cleavage site (LEVLFQGP). Cultures were grown at 37 °C after diluting an overnight culture 1 to 100 in fresh LB media. Cells were grown to an  $A_{600}$  of 1.1, at which point they were transferred to a temperature of 16 °C. After letting the cells grow at 16 °C for 30 min, they were induced with 0.2 mM IPTG and grown overnight at 16 °C for 16 h. Cells were pelleted, resuspended in TBS (20 mM Tris, pH 7.4, 250 mM NaCl) supplemented with 1 mM PMSF and 0.1 mg ml<sup>-1</sup> lysozyme, lysed and the lysate was centrifuged at 5,000g for 20 min to remove unbroken cells. The supernatant was then centrifuged at 100,000g to further clean the lysate. Imidazole was then added to the supernatant to a final concentration of 40 mM before the lysate was incubated with Ni-NTA agarose superflow resin (Qiagen) which was prewashed with TBS + 40 mM imidazole for batch nickel affinity purification. After incubating the lysate and the resin with gentle rocking at 4 °C, the flowthrough was removed and the resin was washed with 10 column volumes of TBS + 50 mM imidazole. The protein was then eluted with 4 column volumes of TBS + 250 mM imidazole. The eluate was supplemented with 0.5 μM THP to prevent aggregation and then concentrated with centrifugal concentrators (Millipore). After protein concentration determination, the N-terminal tags were cleaved by adding HRV 3C protease (EMD) to the concentrated purified protein at a ratio 1 unit/150 μg of protein and incubating at 4 °C for 16 h. Following cleavage, the protein was further purified by gel filtration on a Superdex 200 column (GE Healthcare) in TBS (20 mM Tris, pH 8.0, 150 mM NaCl) + 0.5 μM THP (EMD). The fractions were collected and concentrated using centrifugal concentrators again. The hOGT<sub>4.5</sub> protein was monomeric in solution, as determined by gel filtration and sedimentation equilibrium analytical ultracentrifugation. The protein was then diluted 1:1 in water before setting up crystals.

**Native crystals.** All crystals were grown with the hanging drop method at room temperature. For the UDP structure, 7 mg ml<sup>-1</sup> protein was incubated with 1 mM UDP for several hours at 4 °C. After screening, optimal crystals were obtained when 10 μl of protein was mixed with 5 μl of reservoir solution containing 1.45 M potassium phosphate dibasic, 8 mM EDTA, and 1% xylitol. After several days, hexagonal rod crystals grew, to a maximum size of about 400 × 100 × 100 μm. Crystals were flash frozen using a cryoprotectant consisting of 1.8 M potassium phosphate and 27% xylitol. For the peptide–UDP complex, OGT was incubated with 1 mM UDP and 2 mM CKII3K peptide<sup>28,29</sup> for several hours at 4 °C. Crystals were obtained by mixing 8 μl protein solution with 4 μl reservoir containing 1.6 M Li<sub>2</sub>SO<sub>4</sub> and 0.1 M bis-tris propane-HCl pH 7.0 (1,3-bis(tris(hydroxymethyl)methylamino)propane). Trapezoidal crystals appeared after several days. Crystals were frozen in a cryoprotectant consisting of 1.72 M Li<sub>2</sub>SO<sub>4</sub>, 0.05 M Bis Tris Propane, pH 7.0 and 28% xylitol.

**Heavy metal soaks.** Several heavy metal compounds were screened using the method of ref. 31. After identifying several promising heavy metal compounds, the following conditions gave useful derivatives: K<sub>2</sub>PtCl<sub>4</sub>, 10 mM, 1 h soak; sodium aurothiomalate, 10 mM, 15 min soak; K<sub>2</sub>PtCl<sub>4</sub>, 10 mM, 10 min soak; K<sub>2</sub>PtBr<sub>4</sub>, 1 mM, 1 h soak.

**Data collection.** All the data were collected at NSLS X29 or X25 at Brookhaven National Laboratory except for the gold derivative, which was collected at ID24C at APS at Argonne National Laboratory. The heavy metal derivatives were collected at the following peak wavelengths: gold at 1.0384 Å and platinum at 1.0715 Å. The UDP structure and all the derivatives belonged to the space group P321. The peptide complex crystals were I2. All data sets were processed with iMosflm<sup>32</sup> and scaled using SCALA<sup>33</sup>.

**Structure determination and refinement of the OGT–UDP structure.** The structure of the native OGT–UDP complex was determined by using MIRAS with the program SHARP<sup>34</sup>. The native data set and all the heavy atom derivative data sets were processed with iMosflm and Scala. Heavy atom sites in the K<sub>2</sub>PtCl<sub>4</sub> 1 h soak data set were first determined by using HKL2MAP<sup>35</sup>. SAD phases were then obtained with the CCP4 program Phaser<sup>36</sup> (Experimental Phasing). These initial phases were then used to find the heavy atom sites in the other data sets using the CCP4<sup>37</sup> program FFT. After obtaining all the sites, multiple isomorphous replacement with anomalous scattering (MIRAS) phases to 4.4 Å were obtained using SHARP. The figures of merit at this resolution were 0.46329 (acentric) and 0.47049 (centric). After MIRAS phasing, the map was interpretable, and we confirmed that there were four monomers in the asymmetric unit. Density modification and phase extension to 2.78 Å with NCS averaging were performed using DM, yielding a map with clear side chains. A model was built using as a guide both the structure

of the bacterial homologue (using a homology model generated with Swiss Model) and the heavy atom locations. There are two loops in the intervening domain for which there is no electron density, so these residues are omitted from the model. Twelve residues are missing from one loop and four from the other. The structure was refined with CNS<sup>38</sup>. Initial rigid body refinement optimized the placement of the monomers and then the components of each monomer. After several iterative rounds of simulated annealing, individual B factor refinement, and manual adjustments using COOT<sup>39</sup>, the UDP and waters were added, and the structure refined to an  $R_{\text{work}}$  of 21% and an  $R_{\text{free}}$  of 24%. Refinement was completed in Phenix<sup>40</sup> using TLS refinement<sup>41,42</sup>, minimization, and individual B factor refinement to give a final  $R_{\text{work}}$  of 18.5% and  $R_{\text{free}}$  of 21.8%. Figures were prepared using Pymol<sup>43</sup> and CCP4mg<sup>44</sup>.

### Structure determination and refinement of the OGT–UDP–peptide complex.

Data were processed with iMosflm and Scala, and the structure was determined by molecular replacement. The refined OGT–UDP structure described above was used as a search model using the Phaser molecular replacement module<sup>45</sup> in CCP4. Initial molecular replacement efforts showed that whereas the catalytic domain was nearly identical in the UDP and UDP–peptide complexes, the orientation of the TPRs relative to the catalytic domain was noticeably different. Therefore, the model was broken into three parts: the catalytic domain and two sections of the TPR domains. Using this approach, a good map and model were obtained, which confirmed the twofold NCS present in this structure. The peptide was built by hand, as the side chains were already clear enough at this point to place the residues properly. The peptide in the crystal structure was cleaved from KKKYPGGSTPVS SANMM to YPGGSTPVSSANMM, as confirmed by mass spectrometry. The model was then refined with Phenix. As before, repeated rounds of annealing and individual B factor refinement were interspersed with manual adjustments in COOT. Waters were then added and sulphate ions were added after refining the waters. The structure was completed with cycles of annealing, minimization, TLS and B factor refinement, leading to a final structure with  $R_{\text{work}}$  of 22.4% and  $R_{\text{free}}$  of 25.2%. The crystal packing for the two complexes is described in Supplementary Fig. 9.

**Kinetics.** Mutants were made from the full-length ncOGT using QuickChange mutagenesis and the primers shown in Supplementary Table 6. Kinetic measurements were performed using a previously described filter binding assay<sup>29</sup>. Briefly, reaction mixtures containing 500 μM CKII3K peptide (KKKYPGGSTPVSSANMM), 6 μM UDP-<sup>14</sup>C-GlcNAc (300 mCi mmol<sup>-1</sup> specific activity, American Radiochemicals), 100 nM OGT (WT or mutant protein), and buffer (125 mM NaCl, 1 mM EDTA, 20 mM potassium phosphate, pH 7.4, and 500 μM tris(hydroxypropyl)phosphine) were incubated at room temperature for 30 min. Reactions were then quenched by spotting onto the Whatman P81 phosphocellulose disks, washed three times for five minutes in 0.5% phosphoric acid, and counted by liquid scintillation counting. Reactions proceeded to <10% conversion under these conditions. Positive and negative controls were conducted similarly without enzyme, and positive controls were detected by liquid scintillation counting without the phosphoric acid wash step. Data were analysed based on triplicate experiments. For product inhibition experiments, substrate concentrations were used as described in Supplementary Fig. 2. Reactions were allowed to proceed for either 30 min or 60 min and performed in triplicate and analysed with linear regression using GraphPad Prism5.

**Model preparation.** The hOGT<sub>4.5</sub> construct contains the residues 313–1031 (CPH...KPVE) of the full-length ncOGT protein. Because the first two TPR units of hOGT<sub>4.5</sub> overlap with the last two TPR units of the previously crystallized human TPR domain (PDB code 1W3B)<sup>21</sup>, we superimposed each of the hOGT<sub>4.5</sub> structures (PDB codes 3PE3 and 3PE4) with the TPR domain to create composite models of full length human OGT. Coordinates are provided in Supplementary Data Files 1 and 2.

**Molecular dynamics.** The coordinates of the OGT–UDP–peptide complex were optimized in the Protein Preparation Wizard (Schrodinger 2009) where hydrogens were added; water molecules, UDP and peptide were stripped; and the structure was minimized using the OPLS2001 forcefield. The 1-μm simulation used the CHARM27 forcefield<sup>46</sup>, and the simple point charge model for water<sup>47</sup>. The CHARM27 forcefield was applied to the system using the VIPARR utility. The default Desmond relaxation was performed before simulation, and molecular dynamics were run at constant temperature (300 K) and pressure (1 bar). The simulation was performed by using the program Desmond, version 2.2.9.1.0<sup>30</sup> compiled by SBGrid on an optimized 64-node Linux-based InfiniBand cluster and took 75 days to complete. Molecular dynamics trajectories were processed and animated with VMD<sup>48</sup>.

**Lipid (PIP) binding assays.** Recombinant OGT constructs (His- or GST-tagged full-length human OGT) were overexpressed in *E. coli* and purified by affinity chromatography, using agarose beads conjugated to nickel or glutathione, respectively. PIP binding assays were performed using PIP Strips (Echelon Biosciences). Each membrane was pre-incubated for 2 h at room temperature with a blocking solution

containing 0.1% ovalbumin (for GST fusion constructs) or 3% fatty acid free BSA (for His-tagged constructs) in buffer TBST (20 mM Tris pH 8.0, 50 mM NaCl, 0.1% Tween 20). Purified OGT proteins resuspended in TBST at various concentrations (0.2–2  $\mu$ M) were applied to each membrane. Washing and developing steps were performed as outlined in the manufacturer's protocols, using the same TBST described above, and protein was detected using either anti-His or anti-GST antibodies and HRP-conjugated secondary antibodies.

31. Boggon, T. J. & Shapiro, L. Screening for phasing atoms in protein crystallography. *Structure* **8**, R143–R149 (2000).
32. Leslie, A. G. W. Recent changes to the MOSFLM package for processing film and image plate data. *Joint CCP4 + ESF-EAMCB News. Protein Crystallogr.* **26**, 27–33 (1992).
33. Evans, P. Scaling and assessment of data quality. *Acta Crystallogr. D* **62**, 72–82 (2006).
34. de la Fortelle, E. & Bricogne, G. Maximum-likelihood heavy-atom parameter refinement for the multiple isomorphous replacement and multiwavelength anomalous diffraction methods. *Methods Enzymol.* **276**, 472–494 (1997).
35. Pape, T. & Schneider, T. R. HKL2MAP: a graphical user interface for phasing with SHELX programs. *J. Appl. Crystallogr.* **37**, 843–844 (2004).
36. McCoy, A. J. *et al.* Phaser crystallographic software. *J. Appl. Crystallogr.* **40**, 658–674 (2007).
37. Collaborative Computational Project, Number 4. The CCP4 suite: programs for protein crystallography. *Acta Crystallogr. D* **50**, 760–763 (1994).
38. Brünger, A. T. *et al.* Crystallography & NMR system: A new software suite for macromolecular structure determination. *Acta Crystallogr. D* **54**, 905–921 (1998).
39. Emsley, P. & Cowtan, K. Coot: model-building tools for molecular graphics. *Acta Crystallogr. D* **60**, 2126–2132 (2004).
40. Adams, P. D. *et al.* PHENIX: a comprehensive Python-based system for macromolecular structure solution. *Acta Crystallogr. D* **66**, 213–221 (2010).
41. Painter, J. & Merritt, E. A. TLSMD web server for the generation of multi-group TLS models. *J. Appl. Crystallogr.* **39**, 109–111 (2006).
42. Painter, J. & Merritt, E. A. Optimal description of a protein structure in terms of multiple groups undergoing TLS motion. *Acta Crystallogr. D* **62**, 439–450 (2006).
43. DeLano, W. L. The Pymol Molecular Graphics System. (Delano Scientific, San Carlos, CA, 2002).
44. Pottorff, L. *et al.* Developments in the CCP4 molecular-graphics project. *Acta Crystallogr. D* **60**, 2288–2294 (2004).
45. McCoy, A. J. Solving structures of protein complexes by molecular replacement with Phaser. *Acta Crystallogr. D* **63**, 32–41 (2007).
46. Mackerell, A. D. Jr, Feig, M. & Brooks, C. L. III. Extending the treatment of backbone energetics in protein force fields: limitations of gas-phase quantum mechanics in reproducing protein conformational distributions in molecular dynamics simulations. *J. Comput. Chem.* **25**, 1400–1415 (2004).
47. Berendsen, H. J. C., Postma, J. P. M., van Gunsteren, W. F. & Hermans, J. in *Intermolecular Forces* (ed. Pullman, B.) 331–342 (Reidel, 1981).
48. Humphrey, W., Dalke, A. & Schulten, K. VMD: visual molecular dynamics. *J. Mol. Graph.* **14**, 27–28, 33–38 (1996).

# CAREERS

**COLUMN** Getting the best possible guidance from your adviser **p.570**

**TURNING POINT** How a formative postdoc ignited a neuroscience career **p.571**

**NATUREJOBS** For the latest career listings and advice [www.naturejobs.com](http://www.naturejobs.com)

## INDUSTRY-ORIENTED EDUCATION

# The other path

*The professional science master's degree is growing in popularity but is losing its initial funding. Can it survive?*

BY KAREN KAPLAN

**B**rian Godwin is a group leader in molecular sciences research at the biotechnology company 454 Life Sciences in Branford, Connecticut. But he has never done a postdoc. And he doesn't have a PhD.

Godwin, a biotechnology researcher since 1997, has a professional science master's degree (PSM) in genetics from the University of Connecticut (UConn) in Storrs, where he earned his undergraduate degree in molecular biology. He says that he has never regretted his decision to eschew the conventional route of completing a doctorate, doing a postdoc or two and striving for a tenure-track academic research post. Industry, he says, is the right fit, and his degree provided the right background. "I was asked to stay [to get a PhD at UConn]," he says. "But I was tired of being in school and tired of not earning much money."

## APPLIED SCIENCES

Since the PSM was launched in 1997, some 5,000 degrees have been conferred by more than 100 US universities and academic institutions. About 3,000 students were enrolled in 229 programmes (see 'An alternative degree') for the 2009–10 academic year, according to the US Council of Graduate Schools (CGS), a non-profit organization based in Washington DC that has been promoting the PSM since its inception and certifies PSM degree programmes at US institutions.

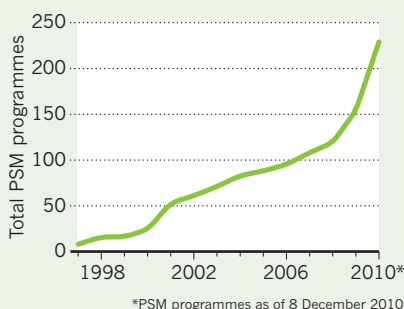
Employers and academics agree that the degree is a good idea — a way to funnel science postgraduates into a practical job track rather than into a PhD system that, even after five or more years of experiments, publications and courses, often fails to deliver the hoped-for research post. But with funding from the PSM's primary supporter, the New York-based Alfred P. Sloan Foundation, about to end, it's unclear whether the degree has sufficient backing and credibility to deliver real job opportunities, despite encouraging indications.

The degree typically comprises two years of academic training in an emerging or interdisciplinary area of science, technology, engineering or maths. The programmes are co-developed by industry and the universities that offer them, and incorporate professional components such as business fundamentals, project management and communication.

It worked well for Godwin, who had thought about a PhD but opted for the PSM and industry. At 454 Life Sciences, a subsidiary of the drug-maker Roche, based in Basel, Switzerland,

## AN ALTERNATIVE DEGREE

Growth of professional science master's (PSM) programmes in the United States.



Godwin is a senior researcher on high-throughput-sequencer development projects. He likes the job's generous compensation and benefits, its team focus, and the possibility that his research will help to treat or prevent disease. Godwin has also co-authored four papers on sequencing, two of which were published in *Nature*. He says that his degree provided relevant and specifically targeted career training. "It gave me the foundation to build upon," says Godwin.

The Sloan Foundation has backed the programme nationwide with US\$22 million in planning and development grants since 1997. Also giving a boost to the PSM in 2009–10

was \$15 million in US National Science Foundation (NSF) grants to about 20 universities to help them create their own programmes. On 4 January, the CGS, which since 2003 has received \$3.8 million from the Sloan Foundation for PSM programme support, announced the latest, and last, round of this funding — \$490,000 for PSM promotion and a data-collection project to compile information on PSM enrolment and degrees, key student characteristics and hiring outcomes for graduates.

Already, managers in industry give holders of PSM degrees high marks for the business-oriented skills that augment their scientific background. "These PSM graduates are trained to walk right into an industrial environment and be ready to go," says Todd Arnold, vice-president of development at 454 Life Sciences, which routinely takes on UConn PSM students as interns and often hires them after graduation. "PhD graduates don't have a clear understanding of how they need to communicate" with non-scientists, Arnold says, noting that scientists at 454 must liaise with colleagues in many different departments. "PSM graduates can work with a whole spectrum of individuals," says Arnold. "And they have the scientific rigour we require."

## UNCERTAIN FUTURE

But the PSM could be headed for a bumpy road as funding ebbs. With the current CGS grant, the Sloan ended its 14 years of support for the programme. "We announced our intention to phase out several years ago," says Michael Teitelbaum, a PSM consultant for Sloan. Potential sources of federal funding remain unclear: neither the NSF nor any other agency has committed funds to the programme, says Carol Lynch, CGS's senior scholar in residence and PSM programme director.

Nevertheless, there is optimism that the programme has gathered enough momentum nationwide to sustain itself. "Local industry likes it," says Stanley Maloy, a biologist and dean of the college of sciences at San Diego State University in California, where biotechnology and biomedical firms are a cornerstone of the regional economy. Maloy points to significant financial support from local companies for his university's PSM programme, which is heavily weighted towards those sectors.

Teitelbaum remains upbeat about the PSM's future. "The momentum is very strong among faculty and institutions," he says. "We believe a critical mass has been established around the country." ■

SOURCE: CGS

## COLUMN

# The care and maintenance of your adviser

Graduate students bear as much responsibility as their mentors for ensuring that they are well guided through their degrees, say **Hugh Kearns** and **Maria Gardiner**.

Ever since the advent of graduate school, students have complained about their advisers. It is almost an article of faith. The adviser is never available or is too available; gives too much feedback or not enough; is too critical or isn't providing enough direction; and so on. Exchanging horror stories with other students is a great way to bond. But advising goes both ways — and if, after careful reflection on their own studies and progress, students determine that they are not getting the guidance they require, they must address the deficiencies.

It is not surprising that advisers figure large in graduate students' conversations. In 2009, the US Council of Graduate Schools in Washington DC reported survey results showing that 65% of the 1,856 doctoral students who responded identified mentoring or advising as a main factor in PhD completion. Our own research at Flinders University in Adelaide, Australia, and our experience at graduate-student workshops across the world suggest that the adviser–student relationship has a big impact on completion time. It certainly influences whether students are still smiling at the end of their degrees!

Students often assume that once they call someone an adviser, he or she automatically acquires all the skills of advising. After all, if your adviser is the world leader in stem-cell technology, he or she must excel at the seemingly simple task of advising — not to mention possess highly developed interpersonal skills and a keen interest in graduate-student development. Sadly, that is not the case.

Sometimes, advising is a weakness of an otherwise very accomplished scientist. This is not surprising. Mentoring tends to be a private business, and often the only model available is an adviser's own experience of having been advised. If it was good, they decide to copy that style and methodology; if it was bad, they do the opposite. There is no guarantee that either approach will provide the student with the guidance he or she needs.

A proactive approach is necessary. If your adviser isn't looking after you in the way you need, then you need to look after them. At some point in the PhD journey, most graduate students come to an important realization: "This is my thesis. My name is written on the front of it. I need to become the driver." The sooner the

candidate does this, the better. If you're not getting feedback, clear direction or the necessary resources, then you must do something about it. What does this mean in practice? Let us take some examples.

## MEETINGS

A comment we often hear at our workshops is, "My adviser is lovely but he/she is just so busy that we never get to talk about my thesis". And our response is, "Yes, your adviser is busy. All advisers are busy and will continue to be busy. Regardless, you need to organize meetings where you can get real face time and talk about your thesis." We're not recommending a quick chat in the coffee room or a brief word in the lab. Nor do we mean a lab meeting.



We mean regularly scheduled meetings focusing on your thesis. You will probably have to schedule them and follow up to make sure that they happen. And when a meeting is cancelled, you will have to reschedule it and persist until it happens.

In our experience, just scheduling the meeting isn't enough. You can't assume that your adviser hosts productive meetings or can intuit what you need to know. You need a specific, uncomplicated agenda that could include such action items as what you've done in the past two weeks; feedback on written work; what you'll

do in the next two weeks; the next meeting.

This all sounds very straightforward. But if more students followed these steps, many adviser–student issues could be resolved.

## FEEDBACK

Again, in an ideal world, your adviser would be skilled at providing supportive comments, delicate in pointing out areas for improvement and deft at intuitively knowing the level of feedback you seek. But this is a fantasy. One student described her feedback experience as similar to being a victim in a drive-by shooting — she handed over her work, it was riddled with bullets and she was left with a bloodied mess as the shooter drove off.

To be fair, e-mailing a chapter to an adviser and saying "Give me feedback" is like walking into a restaurant and saying "Give me food." You need to be a bit more specific. When handing over your work, identify the type of feedback you are looking for. You might say, "This is an early draft, so I just want feedback on the overall direction," or "Please focus on the discussion on page six." If the feedback you get isn't helpful, ask for more detail. Maintaining your adviser means asking for what you need rather than hoping that he or she will know what to provide.

## MANAGING UP

One of the secrets of looking after your adviser is working out what they want — and what most advisers want is a student who comes to them with suggestions and solutions as well as problems, gets things done and makes the job of advising easier. In business this is called 'managing up'. When we work with graduate students we call it the 'care and maintenance' of your adviser.

So although it is natural to complain about your adviser — and can even be cathartic — it is not enough. If your adviser is not giving you what you need, you need to go out and get it. ■

**Hugh Kearns** and **Maria Gardiner** lecture and research in psychology at Flinders University in Adelaide, Australia, and run workshops for graduate students and advisers (see [ithinkwell.com.au](http://ithinkwell.com.au)).

# TURNING POINT

## Jon Simons

*Cognitive neuroscientist Jon Simons is a lecturer in experimental psychology at the University of Cambridge, UK; he arrived at Cambridge after a research fellowship at University College London. Simons recalls two pivotal moments in his career: a move to the United States, and getting his first grant.*

### When did you decide to do research into memory and the brain?

I've known I wanted to do research since high school. A career in research means you have a great deal of freedom to determine the direction of your own work. I don't think I'd be so good at a career in which I was told what to do every day.

As an undergraduate at Aberdeen University, UK, I was lucky to have a psychology lecturer who was very interested in talking about neuropsychology — this idea of studying patients with brain lesions or brain damage and looking to see what effect that damage has on their cognitive function. That's what first got me interested in the field.

### How did going to Harvard University for your first postdoc affect your career?

It was a very formative experience. I was enjoying my PhD at the University of Cambridge, but knew it was a good idea to go somewhere different. An opportunity arose at Harvard with Dan Schacter, who uses imaging to understand how memory works.

Science in the United States is very different from science in the United Kingdom in terms of the opportunities and facilities. Easy access to magnetic resonance imaging scanners and patients with rare lesions or forms of dementia led to several projects related to how memories are stored and retrieved. The people who were expert in these facilities and resources had a strong interest in collaborating. All this resulted in a large number of papers. I got far more out of that year and a half than any similar period in the rest of my career.

### What techniques did you learn?

Functional imaging was a relatively new field then [in 2000], but in Boston there were several fully operational scanners, and loads of people knew how to analyse that data with sophisticated statistics. Learning to use functional magnetic resonance imaging (fMRI) was something I wouldn't have been able to do in Cambridge at that time. I probably wouldn't have got a research fellowship in London without that experience.



### Once you became a lecturer at Cambridge in 2007, how did you get your research started?

It's a big change and responsibility. You feel it is your job to bring money into the department, as well as teach and produce good research.

Getting my first grant was important. It came 18 months after I joined Cambridge. It's a good moment because you feel like you're part of the department and contributing. But then the pressure changes and soon you've got to start thinking about the next one. There's no sitting back on your laurels.

The grant is from the BBSRC [Biotechnology and Biological Sciences Research Council] to try to understand processes involved in memory retrieval. We're trying to combine the spatial resolution from fMRI, which indicates where in the brain these things are happening, with the time resolution from methods such as electroencephalography and magnetoencephalography, which allows you to look very specifically at when things are happening.

### How important is the Experimental Psychology Society prize you won last year?

It probably won't have a huge effect on my career, but it is important — it may affect how much government funding the university gets or how your peers see you. We spend lots of time working hard in the lab, but don't know if others think what we're doing is worthwhile.

### Science funding in Britain has been frozen.

#### Will this affect whether you stay?

A freeze means we'll be behind our international competitors. If the situation gets much worse, I would have to consider moving. ■

INTERVIEW BY KATHARINE SANDERSON

## GRANTS

### Boost for agriculture

Plant geneticists and biologists at the University of California, Davis, have received US\$40 million from the US Department of Agriculture to lead two five-year projects and recruit roughly 65 PhD students and postdocs. Jorge Dubcovsky, a wheat geneticist at Davis, says that he and collaborators at 28 institutions in 21 states will use the funding to recruit around 30 PhD students and 20 postdocs to breed wheat and barley able to resist drought and disease and use nitrogen efficiently. A further 15 graduate students and postdocs will be recruited to help sequence and mine conifer genomes, says project head David Neale. Dubcovsky says that in view of a steady decline in plant-breeding training programmes, the projects will offer recruits a rare opportunity to gain skills in plant physiology, molecular breeding and bioinformatics that are in high demand at agricultural companies.

## DISCRIMINATION

### Employment rights

The eligibility of same-sex partners or spouses for health insurance and other workplace benefits is a major source of concern for gay, lesbian, bisexual and transgendered (GLBT) scientists who work in US states where their relationships are not recognized. The issue emerged at a gathering of 30 GLBT cell biologists at the annual meeting of the American Society for Cell Biology in Philadelphia, Pennsylvania, on 14 December. The participants advised GLBT applicants to seek jobs at private universities not bound by state laws, or negotiate higher salaries to cover partners' insurance costs. Applicants should disclose their marital or partnered status during negotiations, they agreed.

## CONFLICT OF INTEREST

### NIH urged to create rule

The US National Institutes of Health (NIH) in Bethesda, Maryland, has been asked to create regulations for how its grantee institutions handle financial conflicts of interest, in a report released on 10 January by the Office of the Inspector General of the Department of Health and Human Services. The NIH said in a statement that it is considering the recommendation as it drafts rules, but gave no timetable; it has already proposed regulations addressing conflicts for individual researchers. A spokesperson declined further comment.

# INCULTURATION

*A history lesson.*

BY ROBERT SCHERRER

The pupils in Miss Becky Calhoun's Sunday school class trudged behind her on the meandering path that led to the top of Culp's Hill. The sun beat down from a cloudless sky, and Becky stopped briefly to set down her walking stick and adjust her sunbonnet. At the end of the ragged line of students, Jedediah tripped on a root and bumped into Caleb, who turned around and pushed back. "Jedediah, Caleb, behave yourselves!" said Becky. She raised her walking stick. "Do you both need a rap on the head?"

"No, Miss Calhoun," Jedediah said, staring at the ground.

"We'll be good," said Caleb sheepishly.

At the top of the hill, Becky's students gathered in a rough semicircle around an outcropping of pink granite that the locals called the Rooster's Comb. Becky perched on the rock, facing her students. From here she could see all the way to the bend of Waverill Creek and, on the far side of the creek, the small settlement of Pinewood Gulch. Becky smoothed her red-and-white checked gingham dress and began the lesson.

"Pupils," said Becky, "remember our discussion from last week. The Bible was written a long time ago, and many of the things we take for granted today did not exist at the time of the prophets and the patriarchs. Can anyone give me an example of one of our modern inventions that was unknown back in the days of the Bible? Yes, Laura."

"They did not have railroads back then," said Laura.

"That's correct. The railroad is our most important means of transportation, but it did not exist in Biblical times. And conversely, some of the things discussed in the Bible are not in common use today." Becky pointed her walking stick at Abner, who was whispering at the back. "Abner, can you think of an example?"

Abner fidgeted. "Uh, um, scrolls? Parchment scrolls? We don't use those anymore."

Becky smiled. "Yes, Abner. That's a good example. The people in the Bible wrote on parchment scrolls, but we do not." She took off her sunbonnet and adjusted the pin in her auburn hair. "We will begin with Chapter 5 of First Thessalonians, and conclude with the parable of the good shepherd. I will assume that we are all familiar with shepherds. Now who would like to begin reading for us?"

"I would," said Laura. She opened her King James Bible and began. "The day of the



Lord so cometh as a thief in the night." Laura frowned.

"What's wrong, Laura?" asked Becky.

"I'm confused, Miss Calhoun. What is a thief?"

"A thief," said Becky. "Does anybody know what a thief is?" No answer. "A thief is someone who takes something that does not belong to him."

"But that makes no sense," said Abner. "If you wanted something, you could just make it in your fabrikator."

"Oh, I see why you're confused," Becky spread her arms wide. "They did not have fabrikators in Biblical times. And we do not have thieves anymore."

"Miss Calhoun, I still don't understand," said Laura. "It says 'a thief in the night.' What is 'night'?"

"Night," Becky tapped her chin. "Of course, you're all too young to remember. Before they launched the second Sun, it would get very dark once every day, when the Sun dropped below the horizon. That was called 'night.' A few of the students nodded, but others gave her quizzical looks. "Let's continue reading. Caleb, you may read next."

Caleb opened his Bible. "Therefore let us not sleep, as do others." Caleb squirmed and glanced up at Becky.

"What does it mean to 'sleep'?"

"Sleep," said Becky.

She chuckled. "Even I

am too young to remember that. At night, back when there was night, people would lie down, close their eyes and become unconscious for about six to ten hours."

The students giggled. "That sounds very silly, Miss Calhoun," said Jedediah. "Did people really do that?"

"Yes, indeed," said Becky. "We eliminated it with genetic engineering, so nobody need waste such a large portion of the day." Some of the students muttered, but Becky continued. "Let us discuss the meaning of this text. We are instructed to be vigilant, because no one knows the day or the hour when he will die."

"I had an uncle who died," said Caleb.

"Liar," said Jedediah.

"He did too die," insisted Caleb.

"Did not."

"Did too."

"Did not."

Becky smacked the granite with her walking stick. "Silence!" she said. "Jedediah, it's true that death has become rare since we developed antagath and similar drugs. But even though we will never get old, we will all die some day." Caleb smirked at Jedediah.

"I will read our next passage," said Becky. "Please pay attention." She looked down at her Bible. "He that entereth in by the door is the shepherd of the sheep." The students began to murmur. "Who can tell me, what is a shepherd?" asked Becky.

Several students shouted at once: "I know, I know!"

"Laura, what is a shepherd?"

Laura grinned. "You are."

Becky lifted her walking stick and pointed the rounded crook at Laura. "Correct, Laura. And what is a sheep?"

"We are!" shouted all of the students in unison.

"That's right!" said Becky. She smiled at her flock and closed her Bible. "I think we've read enough for today. Let us return to town."

"Miss Calhoun, can we take the railroad back?" asked Caleb.

"Certainly," answered Becky. She gave a mental command, and a shimmering yellow rail appeared at her feet. One by one, the sheep climbed onto the force field and slid, whooping and hollering, down the hill and back home. ■

**Robert Scherrer** is the chair of the Department of Physics and Astronomy at Vanderbilt University. His research area is cosmology. He has also published a number of science-fiction short stories in *Analog*.

► **NATURE.COM**  
Follow Futures on  
Facebook at:  
[go.nature.com/mtoodm](http://go.nature.com/mtoodm)

# Identification of adult nephron progenitors capable of kidney regeneration in zebrafish

Cuong Q. Diep<sup>1,2</sup>, Dongdong Ma<sup>2,3</sup>, Rahul C. Deo<sup>1,2</sup>, Teresa M. Holm<sup>1,2</sup>, Richard W. Naylor<sup>1,2</sup>, Natasha Arora<sup>1</sup>, Rebecca A. Wingert<sup>1,2,4</sup>, Frank Bollig<sup>5</sup>, Gordana Djordjevic<sup>1</sup>, Benjamin Lichman<sup>1</sup>, Hao Zhu<sup>6</sup>, Takanori Ikenaga<sup>7</sup>, Fumihito Ono<sup>7</sup>, Christoph Englert<sup>5,8</sup>, Chad A. Cowan<sup>1,2,4,9</sup>, Neil A. Hukriede<sup>10</sup>, Robert I. Handin<sup>2,3,4</sup> & Alan J. Davidson<sup>1,2,4,†</sup>

Loss of kidney function underlies many renal diseases<sup>1</sup>. Mammals can partly repair their nephrons (the functional units of the kidney), but cannot form new ones<sup>2,3</sup>. By contrast, fish add nephrons throughout their lifespan and regenerate nephrons *de novo* after injury<sup>4,5</sup>, providing a model for understanding how mammalian renal regeneration may be therapeutically activated. Here we trace the source of new nephrons in the adult zebrafish to small cellular aggregates containing nephron progenitors. Transplantation of single aggregates comprising 10–30 cells is sufficient to engraft adults and generate multiple nephrons. Serial transplantation experiments to test self-renewal revealed that nephron progenitors are long-lived and possess significant replicative potential, consistent with stem-cell activity. Transplantation of mixed nephron progenitors tagged with either green or red fluorescent proteins yielded some mosaic nephrons, indicating that multiple nephron progenitors contribute to a single nephron. Consistent with this, live imaging of nephron formation in transparent larvae showed that nephrogenic aggregates form by the coalescence of multiple cells and then differentiate into nephrons. Taken together, these data demonstrate that the zebrafish kidney probably contains self-renewing nephron stem/progenitor cells. The identification of these cells paves the way to isolating or engineering the equivalent cells in mammals and developing novel renal regenerative therapies.

Zebrafish nephrons in the adult kidney are similar to those found in the embryonic kidney<sup>6</sup>, except that they are highly branched and drained by two central collecting ducts (Fig. 1a and Supplementary Fig. 2a–j). We confirmed that zebrafish nephron number increases with age (Fig. 1b), similar to other fish<sup>4,5</sup>. To identify the source of new nephrons in adult zebrafish, we first characterized the effects of gentamicin injection, an established nephrotoxin<sup>7</sup>. Intraperitoneal injection of gentamicin induced nephron damage, downregulated the proximal tubule marker *slc20a1a* and resulted in a failure to take up filtered 40 kDa fluorescent dextran<sup>8</sup> by 1 day post-injection (Fig. 1c–f, *n* = 6/6; Fig. 1j–k, *n* = 8/8; Supplementary Fig. 2k–p). Around 4 days post-injection, partial restoration in nephron function was observed, suggesting some nephrons recovered from the injury (Fig. 1g, l, arrow). At this stage we also detected small, but appropriately proportioned, nephrons that were dextran-positive, proliferating and basophilic, which are characteristic features of immature nephrons<sup>7</sup> (approximately 15 per kidney; Fig. 1i, l inset, n). By 15 days post-injection the damaged nephrons had recovered to near-normal levels, although immature nephrons could still be detected (Fig. 1h, m, arrow).

If the adult kidney contains nephron progenitors responsible for the formation of new nephrons, then these cells might be amenable to transplantation. To test this, we developed a transplantation assay (Fig. 2a and Supplementary Fig. 3a–k) in which recipient fish were

immunocompromised by radiation to prevent graft rejection<sup>9</sup> and then injected with gentamicin. Unpurified whole-kidney marrow cells (WKM), mostly comprising non-tubular interstitial cells<sup>9</sup>, were prepared from Tg(*cdh17:EGFP*)<sup>10</sup> or Tg(*cdh17:mCherry*) donors that express fluorescent reporters in the distal nephron. Injection of approximately  $5 \times 10^5$  of these cells resulted in donor-derived nephrons in 100% of the recipients (*n* = 6) by 18 days post-transplantation (d.p.t.), with an average of 24 donor-derived nephrons (Fig. 2b, arrow, inset). Donor nephron number increased with time, reaching an average of 70 nephrons by 59 d.p.t. (Fig. 2c) and greatly expanded the head kidney on the injected side (Fig. 2d, arrow). At these later time points, we also found donor-derived nephrons in locations distant from the site of injection, which suggests that the transplanted cells are migratory (Supplementary Fig. 3l, arrowheads).

To regenerate damaged tissue successfully, newly created structures must incorporate into existing tissue. To determine whether the donor-derived nephrons were capable of blood filtration, we injected 40 kDa fluorescent dextran into transplant recipients that had received WKM from Tg(*cdh17:mCherry*) donor fish and dissected out individual nephrons. All of the donor-derived nephrons examined (*n* = 5) were dextran-positive (Fig. 2e), indicating that they had integrated into the recipient's blood supply. These results show that nephron progenitors are present in the adult kidney and that after transplantation they are capable of forming new functional nephrons within the host's renal tissue.

Cell transplantation experiments can be confounded by the fusion of donor and recipient cells. To address this, we injected WKM from Tg(*cdh17:mCherry*) donors into Tg(*cdh17:EGFP*) recipients. If fusion occurred, we would expect to find nephrons positive for both mCherry and enhanced green fluorescent protein (EGFP). An analysis of engrafted recipients (*n* = 6) revealed that all of the mCherry-positive nephrons were EGFP-negative, providing evidence that they had not formed by cell–cell fusion. In addition, we identified the connection of the donor-derived nephrons with the host's renal tubules, providing further evidence that the engrafted nephrons had successfully integrated into the recipient's renal system (Fig. 2f).

Lineage labelling studies in the developing mouse kidney have revealed that multiple *Six2*<sup>+</sup> cap mesenchyme cells, the source of nephron progenitors, contribute to a single nephron<sup>11</sup>. To explore this in zebrafish, we transplanted a 1:1 mix of Tg(*cdh17:EGFP*) and Tg(*cdh17:mCherry*) WKM cells into conditioned recipients. Mosaic nephrons containing both EGFP-positive and mCherry-positive cells were found in 27% of the engrafted fish (*n* = 15; Fig. 2g), although the remaining nephrons were either all EGFP-positive or all mCherry-positive. Thus multiple nephron progenitors can contribute to an individual nephron.

<sup>1</sup>Center for Regenerative Medicine, Massachusetts General Hospital, Boston, Massachusetts 02114, USA. <sup>2</sup>Harvard Medical School, Boston, Massachusetts 02115, USA. <sup>3</sup>Hematology Division, Brigham and Women's Hospital, Boston, Massachusetts 02115, USA. <sup>4</sup>Harvard Stem Cell Institute, Cambridge, Massachusetts 02138, USA. <sup>5</sup>Leibniz Institute for Age Research, Fritz Lipmann Institute, Jena D-07745, Germany. <sup>6</sup>Dana-Farber Cancer Institute, Boston, Massachusetts 02115, USA. <sup>7</sup>Section on Model Synaptic Systems, Laboratory of Molecular Physiology, National Institutes of Health/National Institute on Alcohol Abuse and Alcoholism, Bethesda, Maryland 20892, USA. <sup>8</sup>Friedrich-Schiller-University, Jena D-07743, Germany. <sup>9</sup>Department of Stem Cell and Regenerative Biology, Harvard University, Cambridge, Massachusetts 02138, USA. <sup>10</sup>Department of Developmental Biology, University of Pittsburgh, School of Medicine, Pittsburgh, Pennsylvania 15260, USA. <sup>†</sup>Present address: Department of Molecular Medicine and Pathology, School of Medical Sciences, The University of Auckland, Auckland 1142, New Zealand.

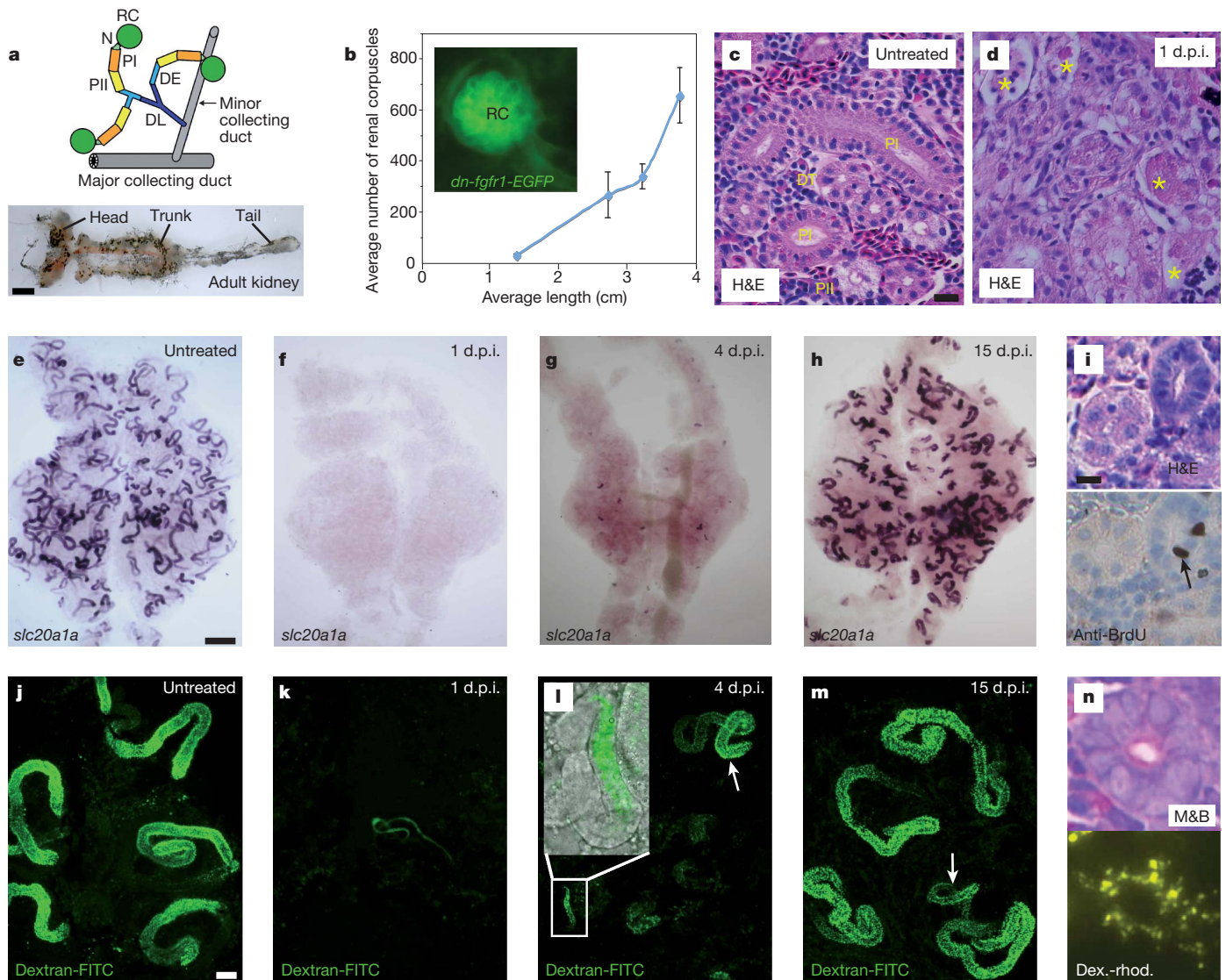


**Figure 1 | The adult zebrafish kidney undergoes nephrogenesis throughout life and after injury.** **a**, Zebrafish kidney and nephron model (scale bar, 1 mm). **b**, Graph showing average number of renal corpuscles (RC) relative to body length (inset shows an RC labelled with *dn-fgfr1-EGFP*<sup>18</sup>) (error bar, one standard deviation;  $n = 3$  fish per time point). RC, renal corpuscle; N, neck; PI, proximal tubule I; PII, proximal tubule II; DE, distal early; DL, distal late. **c, d**, Kidney sections showing gentamicin-damaged nephrons (asterisks; scale bar, 10  $\mu$ m). H&E, haematoxylin and eosin; d.p.i., days post-injection; DT,

distal tubule. **e-h**, Expression of *slc20a1a* in gentamicin-damaged kidneys (scale bar, 0.5 mm). **i**, Immature nephron with dividing cells (arrow) (scale bar, 10  $\mu$ m). **j-m**, Uptake of 40 kDa fluorescein isothiocyanate (FITC)-conjugated dextran by gentamicin-damaged kidneys (inset in **l** shows an immature nephron; arrow in **l** marks a positive nephron; arrow in **m** indicates an immature nephron; scale bar, 30  $\mu$ m). **n**, Serial sections showing that immature nephrons take up 40 kDa dextran-rhodamine. M&B, methylene blue and basic fuchsin.

Mammalian *Six2*<sup>+</sup> cap mesenchyme cells are also characterized by their stem-cell-like self-renewal properties<sup>11</sup>. Serial transplantation is used to distinguish haematopoietic stem cells from progenitors<sup>12</sup>. We investigated whether we could obtain donor-derived nephrons after serial transplantation of WKM from engrafted recipients (Fig. 2h). We transplanted WKM from primary fish containing 2–89 *cdh17:EGFP*<sup>+</sup> donor-derived nephrons and achieved a 48% ( $n = 21$ ) engraftment rate in secondary fish, with the number of donor-derived nephrons ranging from 1 to 53 by 41 d.p.t. The WKM from one of these secondary fish, containing 53 engrafted nephrons, was transplanted again and successfully engrafted a third time, giving rise to 12 donor-derived nephrons in the tertiary recipient at 35 d.p.t. (a total of 135 days from primary to tertiary fish; Fig. 2i–k). These results demonstrate that nephron progenitors possess significant proliferative potential, consistent with self-renewing capabilities.

We next sought to identify the cells responsible for nephron progenitor activity. We noted that approximately 0.1% of the WKM from

Tg(*cdh17:EGFP*) fish is EGFP-positive (Supplementary Fig. 4a). To test whether *cdh17:EGFP*<sup>+</sup> cells could contribute to new nephrons, we sorted and transplanted this fraction (approximately 5,000 cells per fish) but failed to observe engraftment ( $n = 0/7$ ). We subsequently explored other markers of nephron progenitors. In mammals, nephrogenesis initiates with the formation of ‘pre-tubular aggregates’ that undergo a mesenchymal-to-epithelial transition into renal vesicles<sup>13</sup>. These structures express several transcription factors including *Lhx1/Lim1* (ref. 14) and *Wt1* (ref. 15). We therefore examined the Tg(*lhx1a:EGFP*)<sup>16</sup> and Tg(*wt1b:mCherry*) transgenic lines to determine whether these reporters mark nephron progenitors. Kidneys from untreated Tg(*lhx1a:EGFP*) adults were found to contain three distinctive EGFP-positive cell populations: (1) single cells with a mesenchymal morphology (Fig. 3a) that make up approximately 0.02% of the WKM (Supplementary Fig. 4b), (2) homogeneous aggregates of *lhx1a:EGFP*<sup>+</sup> mesenchymal cells ranging from a few to approximately 30 cells (Fig. 3b, c and Supplementary Fig. 4i) (approximately 100 aggregates

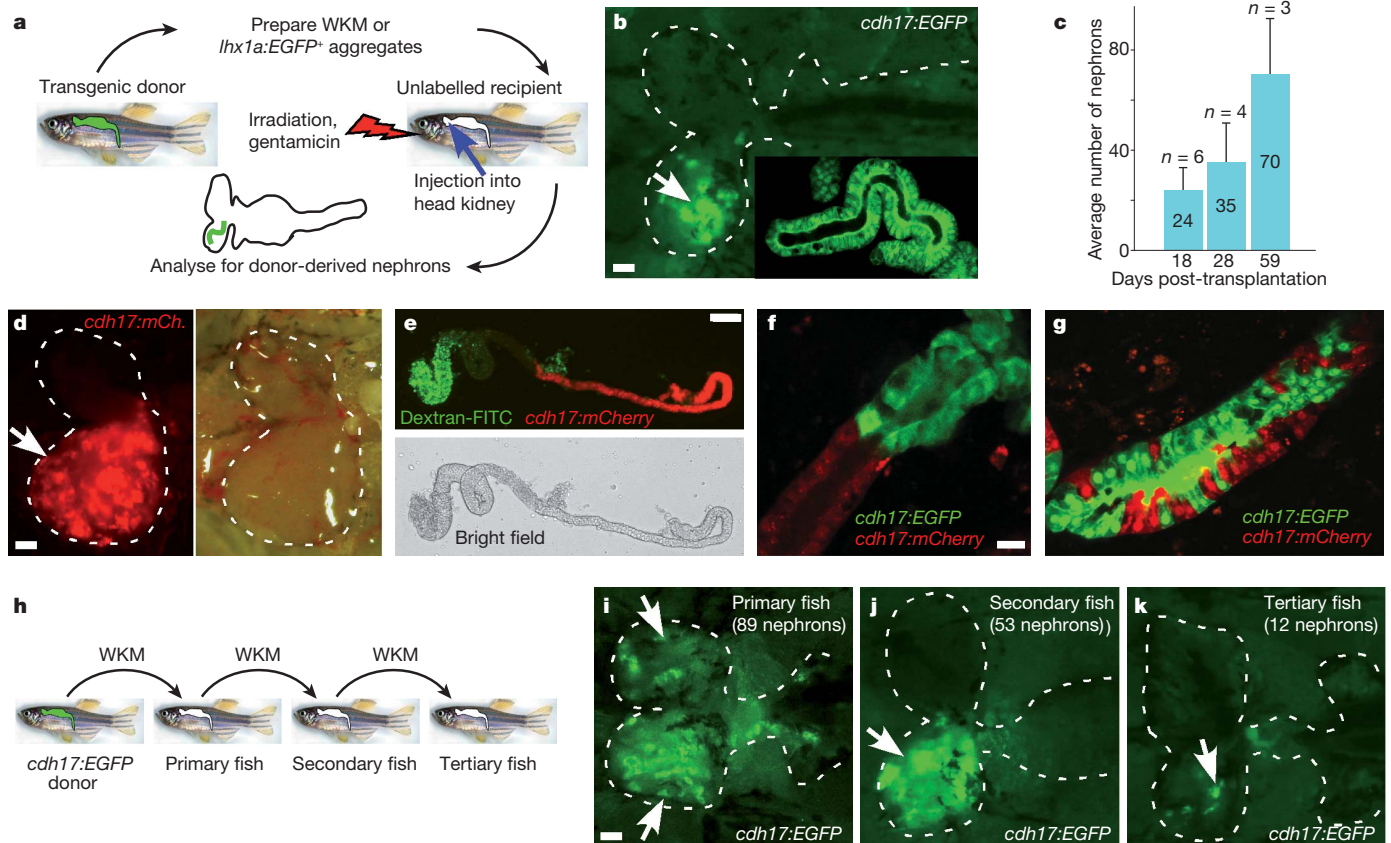


**Figure 2 | The adult zebrafish kidney contains transplantable progenitors that form functional nephrons.** **a**, Overview of the transplantation assay. **b**, A primary transplanted fish at 18 d.p.t. with *cdh17:EGFP*<sup>+</sup> donor-derived nephrons (arrow; inset, higher magnification view; scale bar, 0.5 mm). **c**, Average number of donor-derived nephrons over time (error bar, one standard deviation; *n*, total fish per time point). **d**, Head kidney of a recipient at 34 d.p.t. showing expansion of renal tissue caused by *cdh17:mCherry*<sup>+</sup> donor-derived nephrons (arrow; scale bar, 0.5 mm). **e**, A *cdh17:mCherry*<sup>+</sup> donor-

derived nephron showing functional uptake of 40 kDa FITC-conjugated dextran (scale bar, 30  $\mu$ m). **f**, Connection of donor-derived nephrons (*cdh17:mCherry*<sup>+</sup>) with the *cdh17:EGFP*<sup>+</sup> recipient's renal system (scale bar, 10  $\mu$ m). **g**, A mosaic nephron arising from the co-injection of a mixture of *cdh17:EGFP*- and *cdh17:mCherry*-labelled nephron progenitors. **h**, Overview of the serial transplantation assay. **i–k**, Donor-derived nephrons (*cdh17:EGFP*<sup>+</sup>, arrows) in primary-, secondary- and tertiary-engrafted recipients (scale bar, 0.5 mm).

per kidney) and (3) renal vesicle-like bodies (0–2 per kidney; Fig. 3d). The last two populations were highly reminiscent of pre-tubular aggregates and renal vesicles in mammals.

An examination of Tg(*lhx1a:EGFP*; *wt1b:mCherry*) double transgenic kidneys revealed that only the large aggregates and renal vesicles, but not the other *lhx1a:EGFP*<sup>+</sup> populations, were *wt1b:mCherry*<sup>+</sup> (Fig. 3d). We hypothesized that the *lhx1a:EGFP*<sup>+</sup>/*wt1b:mCherry*<sup>+</sup> renal vesicle-like bodies, which were rare in untreated kidneys, constitute primitive nephrons. Consistent with this, gentamicin treatment greatly induced the formation of *lhx1a:EGFP*<sup>+</sup>/*wt1b:mCherry*<sup>+</sup> double-positive cells (data not shown) and activated the endogenous expression of the early-acting renal genes *pax2a*, *fgf8a*, *wt1a* and *wt1b* in similar structures (Fig. 3e–j and Supplementary Fig. 4c–h). We failed to detect the expression of mature nephron markers in structures resembling either *lhx1a:EGFP*<sup>+</sup> aggregates or *wt1b*<sup>+</sup> renal vesicles (Supplementary Fig. 5a–c and Supplementary Table 1). Similarly, quantitative PCR analysis of purified *lhx1a:EGFP*<sup>+</sup> and *cdh17:EGFP*<sup>+</sup> cells showed that *lhx1a:EGFP*<sup>+</sup> cells express considerably lower levels of mature nephron markers than *cdh17:EGFP*<sup>+</sup> cells (Supplementary Fig. 5d). These findings suggest that *lhx1a:EGFP* labels nephron progenitors and *lhx1a:EGFP*/*wt1b:mCherry* labels early-stage nephrons.

To clarify the lineage relationships between *lhx1a:EGFP*<sup>+</sup> and *lhx1a:EGFP*<sup>+</sup>/*wt1b:mCherry*<sup>+</sup> cells, we took advantage of the optical transparency of larval fish to visualize nephrogenesis *in vivo*. By observing Tg(*cdh17:EGFP*) larvae as well as using wholemount *in situ* hybridization, we found that adult kidney formation initiates at the 5.2-mm stage (approximately 13 days post-fertilization). The first

nephron appears consistently on the embryonic (pronephric) renal tubules just posterior to the swim bladder (Supplementary Fig. 6a–e and data not shown). *lhx1a:EGFP*<sup>+</sup> cells appeared before this, at the 4-mm stage (approximately 10 days post-fertilization) (Fig. 4a, arrow, inset), rapidly migrated along the pronephric tubules (Fig. 4b, arrows), and formed into aggregates (Fig. 4b, arrowheads). An *in vivo* time course of Tg(*lhx1a:EGFP*; *cdh17:mCherry*) and Tg(*lhx1a:EGFP*; *wt1b:mCherry*) larvae showed that the *lhx1a:EGFP*<sup>+</sup> aggregates arose from the coalescence of three or four *lhx1a:EGFP*<sup>+</sup> cells that expanded to form a renal vesicle and activated expression of *wt1b:mCherry* (Fig. 4d and Supplementary Fig. 6f). Similar time courses of Tg(*lhx1a:EGFP*; *cdh17:mCherry*) and Tg(*wt1b:EGFP*; *pax8:DsRed*) larvae demonstrated that the renal vesicle elongated into a *cdh17*<sup>+</sup> nephron, with *lhx1a*<sup>+</sup> cells becoming restricted to the point of fusion with the pronephric tubules, *pax8* initiating in the distal tubule and *wt1b* labelling the glomerulus and proximal tubule (Fig. 4e and Supplementary Fig. 6g). To demonstrate a requirement of *lhx1a:EGFP*<sup>+</sup> cells for nephrogenesis, we ablated single *lhx1a:EGFP*<sup>+</sup> aggregates with a laser (Fig. 4c, arrow), resulting in aborted nephrogenesis in the targeted region without affecting neighbouring nephrons (Fig. 4c, arrowhead) (*n* = 2/2).

Next we tested whether *lhx1a:EGFP*<sup>+</sup> cells had nephron-forming activity. Transplantation of single *lhx1a:EGFP*<sup>+</sup> cells failed to engraft conditioned recipients. However, transplantation of individual *lhx1a:EGFP*<sup>+</sup> aggregates resulted in successful engraftment in 33% (*n* = 15) of transplanted fish (Fig. 4f, g). In one case, a single aggregate contributed to 16 nephrons, 27 aggregates and numerous individual cells (Supplementary Fig. 7a–c), consistent with *lhx1a:EGFP*<sup>+</sup> cells

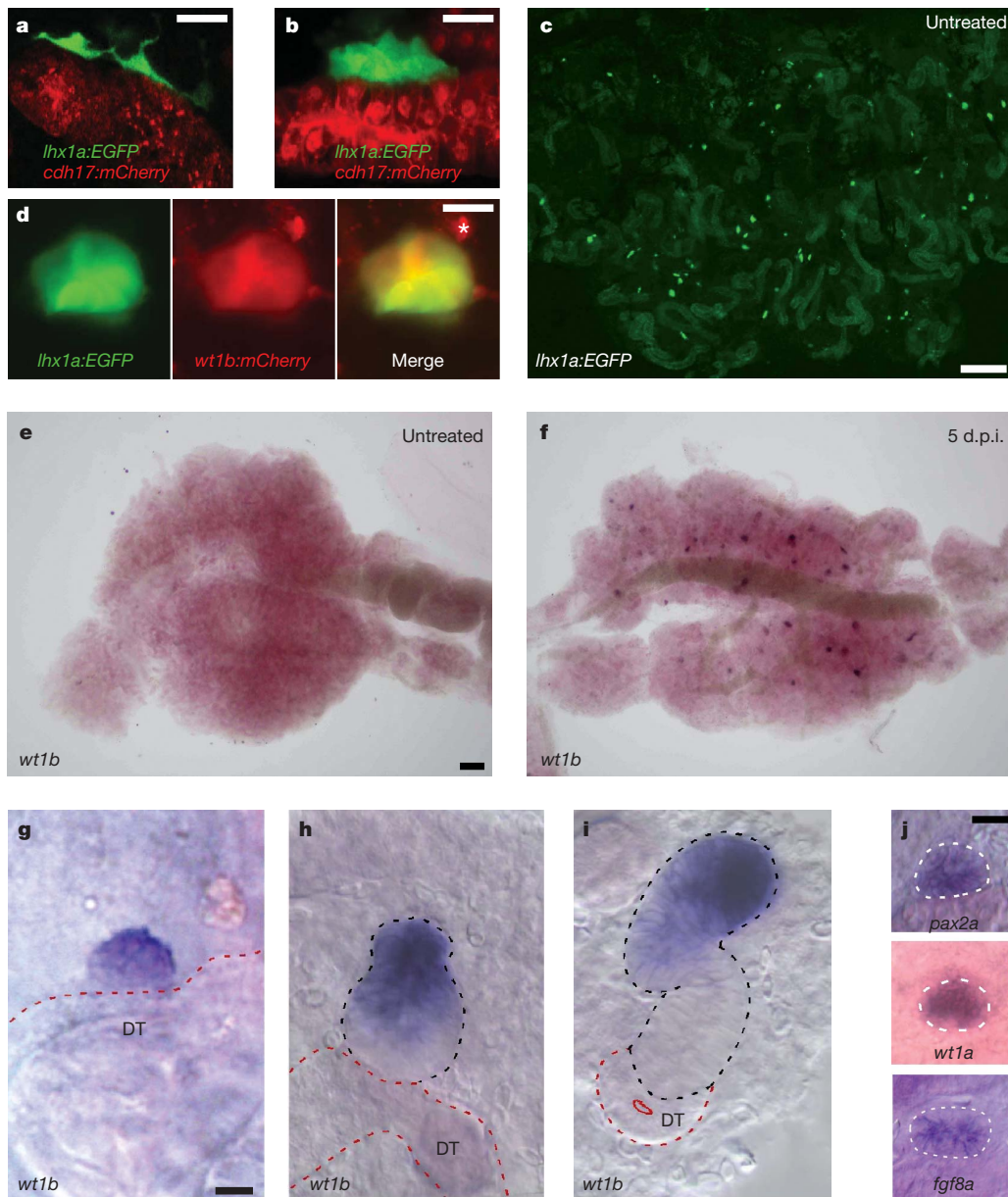


**Figure 3 | Expression of *lhx1a:EGFP* and other renal factors in the adult kidney.** **a**, Single mesenchymal cells labelled with *lhx1a:EGFP* (scale bar, 10  $\mu$ m). **b**, Small aggregates labelled with *lhx1a:EGFP* (scale bar, 10  $\mu$ m). **c**, An untreated kidney showing *lhx1a:EGFP*<sup>+</sup> aggregates in a portion of the trunk region; scale bar, 0.5 mm). **d**, Co-expression of *wt1b:mCherry* and *lhx1a:EGFP* in large aggregates (asterisk, autofluorescence; scale bar, 10  $\mu$ m). **e**, **f**, Expression

having extensive proliferative and self-renewing capabilities. Transplantation of *lhx1a:EGFP*<sup>+</sup>/*wt1b:mCherry*<sup>+</sup> renal vesicles failed to engraft ( $n = 0/10$ ), suggesting that nephron-forming potential is restricted to *lhx1a:EGFP*<sup>+</sup> aggregates. These findings demonstrate that *lhx1a:EGFP*<sup>+</sup> aggregates contain nephron progenitors and support our observation that multiple nephron progenitors are needed to form a nephron.

To determine how similar *lhx1a:EGFP*<sup>+</sup> cells are to *Six2*<sup>+</sup> mouse cap mesenchyme cells, we conducted a microarray analysis, comparing the genes upregulated in *lhx1a:EGFP*<sup>+</sup> cells (relative to *cdh17:EGFP*<sup>+</sup> epithelial cells) with those upregulated in mouse *Six2*<sup>+</sup> cells (relative to mouse proximal tubule epithelial cells). At a global level, the respective gene sets that are upregulated in *lhx1a:EGFP*<sup>+</sup> cells and *Six2*<sup>+</sup> cells are not significantly similar (Supplementary Tables 2–4 and Supplementary Fig. 8a). However, there is conservation of several factors implicated in renal development and/or stem-cell self-renewal. Notably,

of *wt1b* in untreated and gentamicin-damaged kidneys (scale bar, 0.5 mm).

**g–i**, Expression of *wt1b* in a large aggregate (**g**), a comma-shaped body (**h**) and an immature nephron (**i**) in gentamicin-damaged kidneys (scale bar, 10  $\mu$ m). **j**, Expression of *pax2a*, *wt1a* and *fgf8a* in large aggregates or renal vesicles in gentamicin-damaged kidneys (scale bar, 10  $\mu$ m).

orthologues of *Six2* (*six2a*) and *Wt1* (*wt1a*), which are essential for cap mesenchyme maintenance, are upregulated both in *lhx1a:EGFP*<sup>+</sup> cells and in *Six2*<sup>+</sup> cells. Quantitative PCR confirmed that *six2a* and *wt1a* are expressed over 15-fold higher in *lhx1a:EGFP*<sup>+</sup> cells than *cdh17:EGFP*<sup>+</sup> cells (Supplementary Fig. 8b). Several other potentially important regulators were also identified in the comparison, including *Meis2*, *Ezh2* and *Tcf3*, which are implicated in Wnt signalling and/or stem-cell function (Supplementary Table 4). These results suggest that, despite having distinct molecular identities, zebrafish *lhx1a:EGFP*<sup>+</sup> cells and *Six2*<sup>+</sup> cells share a core set of regulatory genes that may be important for conferring renal stem/progenitor cell potential.

In conclusion, we have identified an adult population of nephron progenitors that reside in small aggregates throughout the zebrafish kidney. These cells are uniquely defined by their ability to form new functional nephrons during zebrafish growth, injury and after transplantation. Nephron progenitors can be serially transplanted, consistent

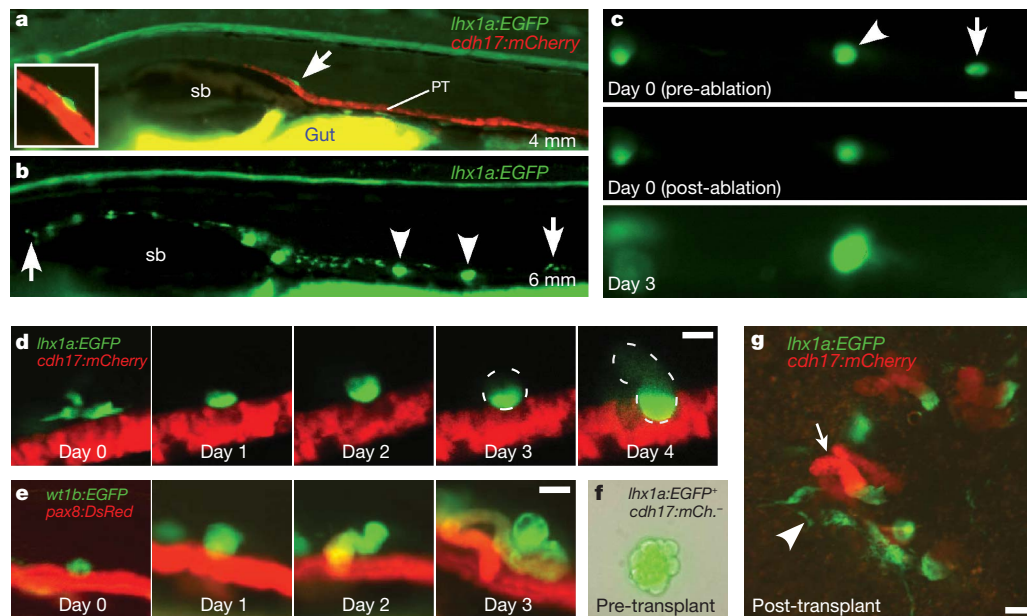


**Figure 4** | *lhx1a:EGFP*<sup>+</sup> cells form nephrons during adult kidney development and after transplantation. **a**, Lateral view of a Tg(*lhx1a:EGFP;cdh17:mCherry*) larva showing the first *lhx1a:EGFP*<sup>+</sup> cell to appear on top of the *cdh17:mCherry*<sup>+</sup> embryonic kidney tubules (arrow and inset). **b**, Lateral view of a Tg(*lhx1a:EGFP*) larva showing the extent of *lhx1a:EGFP*<sup>+</sup> cell migration (arrows) and their aggregation (arrowheads). **c**, Laser-ablation of an *lhx1a:EGFP*<sup>+</sup> aggregate (arrow) inhibits nephron formation without affecting nephrogenesis of an adjacent aggregate (arrowhead). **d**, Time course of a Tg(*lhx1a:EGFP;cdh17:mCherry*) larva

demonstrating that *lhx1a:EGFP*<sup>+</sup> cells coalesce into an aggregate and differentiate into a nephron. **e**, Time course of a Tg(*wt1b:EGFP;pax8:DsRed*) larva showing development of a *wt1b:EGFP*<sup>+</sup> aggregate into a nephron. **f**, Bright field and fluorescent merge of an aggregate from a Tg(*lhx1a:EGFP;cdh17:mCherry*) donor. **g**, Donor-derived *cdh17:mCherry*<sup>+</sup> nephrons (one indicated by arrow) and multiple single *lhx1a:EGFP*<sup>+</sup> cells (arrowhead) resulting from the transplantation of the aggregate shown in **f** (scale bar, 30  $\mu$ m). PT, pronephric tubule; sb, swim bladder; larvae shown with anterior to the left.

with stem-cell capabilities, although confirmation of this awaits direct lineage-tracing experiments. Our *in vivo* imaging of nephrogenesis and chimaeric transplantation results demonstrated that nephrogenic aggregates form by the coalescence of multiple *lhx1a:EGFP*<sup>+</sup> cells (Supplementary Fig. 1). This process is reminiscent of nephrogenesis in mammals and suggests that similar mechanisms govern nephron formation in both species. Consistent with this, *lhx1a:EGFP*<sup>+</sup> cells express *six2a* and *wt1a*, two critical regulators of mammalian nephron progenitors. Our observation that only aggregates of *lhx1a:EGFP*<sup>+</sup> cells, but not single cells, are capable of engraftment suggests that nephron progenitor potential may depend upon a 'community effect'<sup>17</sup>, a phenomenon whereby continued cell contact is necessary for cells to respond to an inductive signal. The failure of renal vesicles to engraft suggests that nephron-forming potential is lost upon epithelial differentiation.

With our data in hand, it is now possible to pursue whether the mammalian adult kidney contains an equivalent population of nephrogenic aggregates. If present, these cells are most probably dormant or their regenerative abilities blocked, given that nephrogenesis ceases around birth. Using zebrafish to understand the molecular identity of nephron progenitors and the pathways that regulate them may lead to therapeutic ways to activate, or artificially engineer, the mammalian counterpart and augment human renal regeneration. With the rise in chronic kidney disease becoming a serious worldwide healthcare issue, a nephron-progenitor-based regenerative therapy will have a major clinical impact.

## METHODS SUMMARY

For WKM transplants, adult recipient fish were conditioned with intraperitoneal injection of gentamicin (80  $\mu$ g g<sup>-1</sup>), then immunocompromised with sub-lethal  $\gamma$ -irradiation (25 Gy) to prevent graft rejection<sup>9</sup>. Unpurified WKM cells were prepared as previously described<sup>9</sup> from Tg(*cdh17:EGFP*)<sup>10</sup> or Tg(*cdh17:mCherry*) donors that express fluorescent reporter proteins in the distal nephron. For the *lhx1a:EGFP*<sup>+</sup> single cell and aggregate transplants, dissected kidneys from

Tg(*lhx1a:EGFP;cdh17:mCherry*) fish were treated with 10% collagenase/dispase for 15 min and cells/aggregates manually transferred with a mouth pipette to a drop of 1X PBS/2% fetal calf serum on a glass slide. A single cell or aggregate was serially passaged through three droplets of PBS/fetal calf serum until free of non-positive cells just before transplantation.

**Full Methods** and any associated references are available in the online version of the paper at [www.nature.com/nature](http://www.nature.com/nature).

Received 19 April; accepted 15 November 2010.

Published online 26 January 2011.

1. Fogo, A. B. Mechanisms of progression of chronic kidney disease. *Pediatr. Nephrol.* **22**, 2011–2022 (2007).
2. Humphreys, B. D. *et al.* Intrinsic epithelial cells repair the kidney after injury. *Cell Stem Cell* **2**, 284–291 (2008).
3. Hartman, H. A., Lai, H. L. & Patterson, L. T. Cessation of renal morphogenesis in mice. *Dev. Biol.* **310**, 379–387 (2007).
4. Reimschuessel, R. A fish model of renal regeneration and development. *ILAR J.* **42**, 285–291 (2001).
5. Zhou, W. *et al.* Characterization of mesonephric development and regeneration using transgenic zebrafish. *Am. J. Physiol. Renal Physiol.* **299**, F1040–F1047 (2010).
6. Wingert, R. A. *et al.* The *cdx* genes and retinoic acid control the positioning and segmentation of the zebrafish pronephros. *PLoS Genet.* **3**, 1922–1938 (2007).
7. Augusto, J., Smith, B., Smith, S., Robertson, J. & Reimschuessel, R. Gentamicin-induced nephrotoxicity and nephroneogenesis in *Oreochromis nilotica*, a tilapia fish. *Dis. Aquat. Organ.* **26**, 49–58 (1996).
8. Kramer-Zucker, A. G., Wiessner, S., Jensen, A. M. & Drummond, I. A. Organization of the pronephric filtration apparatus in zebrafish requires Nephron, Podocin and the FERM domain protein Mosaic eyes. *Dev. Biol.* **285**, 316–329 (2005).
9. Traver, D. *et al.* Effects of lethal irradiation in zebrafish and rescue by hematopoietic cell transplantation. *Blood* **104**, 1298–1305 (2004).
10. Hall, C. *et al.* Transgenic zebrafish reporter lines reveal conserved Toll-like receptor signaling potential in embryonic myeloid leukocytes and adult immune cell lineages. *J. Leukoc. Biol.* **85**, 751–765 (2009).
11. Kobayashi, A. *et al.* Six2 defines and regulates a multipotent self-renewing nephron progenitor population throughout mammalian kidney development. *Cell Stem Cell* **3**, 169–181 (2008).
12. Purton, L. E. & Scadden, D. T. Limiting factors in murine hematopoietic stem cell assays. *Cell Stem Cell* **1**, 263–270 (2007).
13. Dressler, G. R. The cellular basis of kidney development. *Annu. Rev. Cell Dev. Biol.* **22**, 509–529 (2006).

14. Kobayashi, A. *et al.* Distinct and sequential tissue-specific activities of the LIM-class homeobox gene *Lim1* for tubular morphogenesis during kidney development. *Development* **132**, 2809–2823 (2005).
15. Georgas, K. *et al.* Analysis of early nephron patterning reveals a role for distal RV proliferation in fusion to the ureteric tip via a cap mesenchyme-derived connecting segment. *Dev. Biol.* **332**, 273–286 (2009).
16. Swanhart, L. *et al.* Characterization of an *lhx1a* transgenic reporter in zebrafish. *Int. J. Dev. Biol.* **54**, 731–736 (2010).
17. Gurdon, J. B. A community effect in animal development. *Nature* **336**, 772–774 (1988).
18. Lee, Y., Grill, S., Sanchez, A., Murphy-Ryan, M. & Poss, K. D. Fgf signaling instructs position-dependent growth rate during zebrafish fin regeneration. *Development* **132**, 5173–5183 (2005).

**Supplementary Information** is linked to the online version of the paper at [www.nature.com/nature](http://www.nature.com/nature).

**Acknowledgements** We thank E. C. Liao for help with suturing, and R. Ethier and L. Gyr for zebrafish care. A.J.D. was supported by the Harvard Stem Cell Institute, the

American Society of Nephrology and the National Institutes of Health/National Institute of Diabetes and Digestive and Kidney Diseases (P50DK074030).

**Author Contributions** C.Q.D. and A.J.D. designed the experimental strategy, analysed data, prepared the manuscript, and generated and characterized the *Tg(cdh17:EGFP)*, *Tg(cdh17:mCherry)* and *Tg(wt1b:mCherry)* lines. C.Q.D. performed the regeneration, transplants, time course and ablation experiments. C.Q.D., D.M. and R.I.H. made the initial observation that nephron progenitors can be transplanted. N.A.H. generated the *Tg(lhx1a:EGFP)* line (R01DK069403), F.B. and C.E. generated the *Tg(wt1b:EGFP)* line, and T.I. and F.O. provided the *Tg(pax8:DsRed)* line. N.A., R.A.W., G.D. and B.L. analysed kidney expression. H.Z. provided sections of regenerating kidneys. R.C.D., T.M.H., R.W.N., and C.A.C. performed quantitative PCR and microarray analyses. All authors commented on the manuscript.

**Author Information** Reprints and permissions information is available at [www.nature.com/reprints](http://www.nature.com/reprints). The authors declare no competing financial interests. Readers are welcome to comment on the online version of this article at [www.nature.com/nature](http://www.nature.com/nature). Correspondence and requests for materials should be addressed to A.J.D. ([a.davidson@auckland.ac.nz](mailto:a.davidson@auckland.ac.nz)).

## METHODS

**Zebrafish transgenic lines.** Zebrafish were maintained as previously described<sup>19</sup> and according to Institutional Animal Care and Use Committee protocols. The transgenic lines Tg(*wt1b:EGFP*), Tg(*lhx1a:EGFP*) and Tg(*hsp70:dn-fgfr1-EGFP*) were previously reported<sup>16,18,20</sup>. The Tg(*wt1b:mCherry*) line was generated by replacement of EGFP with mCherry in the F47 vector, which contains a shortened version of the *wt1b* promoter that was previously described<sup>20</sup>. The Tg(*cdh17:EGFP*) line was generated by isolation of a 4.3-kb genomic fragment upstream of the Exon 1 5' untranslated region. The promoter fragment was cloned into the XhoI/SalI sites of the Tol2 vector T2AL200R150G<sup>21</sup>. The Tg(*cdh17:mCherry*) line was generated by co-injection of Cre mRNA with the Tol2 vector T2cdh17-loxP-EGFP-loxP-mCherry. The Tg(*pax8:DsRed*) line was generated by gene trap screening. DsRedExpress was inserted into the BamHI/NotI sites of the pT2KSAG Tol2 vector<sup>22</sup> and was used to generate the transgenic line. Mapping of the insertion site by inverse PCR revealed that DsRedExpress was inserted in the intron region between exons 1 and 2 (T.I. and F.O., unpublished observations).

**Adult and larval zebrafish experiments.** Epifluorescent images were taken from a Nikon Eclipse 80i microscope using the Hamamatsu ORCA-ER camera and confocal images were acquired using the A1 high-speed confocal Ti-e inverted microscope system (Nikon).

Adult. Gentamicin (40 µg), BrdU (100 µg) and 40 kDa dextran-FITC or -rhodamine (2 µg) were administered by intraperitoneal injection. Single nephrons were dissected in Ringer's buffer using sharpened tungsten needles. Kidney wholemount *in situ* hybridization was as previously described (<http://zfin.org/ZFIN/Methods/ThisseProtocol.html>) with the addition of 1% dimethyl sulphoxide supplemented to the fixative. Fluorescence-activated cell sorting and analyses were performed using the BD FACSAria (Harvard Stem Cell Institute Flow Cytometry Core Facility). For transplantation of cells directly into the kidney, conditioned recipients were anaesthetized with 0.02% tricaine and a lateral incision was made posterior to the gills and level with the kidney. One microlitre containing approximately  $5 \times 10^5$  WKM cells, or a single *lhx1a:EGFP*<sup>+</sup> cell or a single *lhx1a:EGFP*<sup>+</sup> aggregate was injected directly into the head kidney of recipient fish (3 days after conditioning) using a Hamilton syringe. The incision was closed with a suture and the fish was returned to water (Supplementary Fig. 3a–k).

Larva. Larval wholemount *in situ* hybridization was performed as reported<sup>23</sup>. Ablation of *lhx1a:EGFP*<sup>+</sup> aggregates was performed with the MicroPoint Laser System (Photonic Instruments) in conjunction with the Nikon Eclipse 80i microscope. For the cellular necrosis assay, water control and gentamicin-treated kidneys were incubated for 10 min in  $5 \mu\text{g ml}^{-1}$  of acridine orange (Sigma) in PBS, washed three times with 50 ml PBS and imaged under bright field and epifluorescence (FITC).

**Histology.** Haematoxylin and eosin. Kidneys and larvae were fixed in 4% paraformaldehyde, embedded in paraffin, sectioned and stained with haematoxylin and eosin or antibodies against EGFP and BrdU (Dana-Farber/Harvard Cancer Center Pathology Core Facility).

Methylene blue and basic fuchsin. Kidneys were fixed in 4% paraformaldehyde, embedded in JB4 resin, sectioned and stained with methylene blue and basic fuchsin. **Microarray analysis.** Triplicate samples of approximately 4,000 *lhx1a:EGFP*<sup>+</sup> and *cdh17:EGFP*<sup>+</sup> cells were sorted by fluorescence-activated cell sorting into lysis buffer, complementary DNAs were amplified, labelled with Cy3 (*cdh17:EGFP*<sup>+</sup>) and Cy5 (*lhx1a:EGFP*<sup>+</sup>), and hybridized to the Agilent Whole Zebrafish Genome Oligo Microarray (3 × 44k) by Miltenyi Biotec. All statistical analysis used the R package 2.9.2 (<http://cran.r-project.org/>). Agilent microarrays were processed using the Agilent Feature Extraction software to obtain intensity ratios for each of the 43,803 probes on the array. Intensity ratios from the three separate Agilent

microarrays were subsequently quantile normalized using the normalize Between Arrays function in the affy package and differentially expressed gene between cases and controls determined using the limma package. Given the multiple number of hypotheses tested we selected the qvalue package for false discovery rate (FDR) estimation. RMA normalization, limma and qvalue were used to identify differentially expressed probe sets across the eight GUDMAP mouse kidney microarrays of interest (three for *Six2*<sup>+</sup> cells, five for proximal tubule cells), which were downloaded from the GEO database (GSE12588, GSE6589 and GSE6290). To compare the differentially expressed genes from the two platforms (and species), the microarray probes were matched to gene identities using annotation files provided by the manufacturers. Zebrafish gene identities were then mapped to mouse orthologues using a combination of the InParanoid (<http://inparanoid.sbc.su.se/>) and Ensembl databases. A total of 11,870 Ensembl mouse protein identities were identified that could be compared from both arrays. Given the smaller number of zebrafish arrays, FDR thresholds of 40% (nominal  $P < 0.016$ ), 45% ( $P < 0.048$ ) and 50% ( $P < 0.11$ ) were combined with a minimum twofold change in intensity, which corresponded to 1,635, 3,335 and 5,879 probes, respectively. More stringent FDR thresholds of 5% (nominal  $P < 0.022$ ), 10% ( $P < 0.07$ ) and 15% ( $P < 0.14$ ) were chosen for the mouse probes, leading to 5,250, 5,699, 5,936 probe sets, respectively. Genes that were both significantly upregulated and downregulated in the analysis, as judged by separate probes, were excluded, leaving a total of 10,421 genes for comparison. We used Fisher's exact test for statistical significance over a range of FDR values, yielding a range from  $P = 0.051$  to  $P = 0.86$ . The GEO database record number for the zebrafish microarray data is GSE24803.

**Quantitative PCR.** *lhx1a:EGFP*<sup>+</sup> and *cdh17:EGFP*<sup>+</sup> cells (300–9,000) were purified by fluorescence-activated cell sorting, lysed and complementary DNA generated using the Cells-to-cDNA kit (Ambion). Quantitative PCR was performed in triplicate using SYBR Green chemistry on a Mastercycler RealPlex<sup>2</sup> PCR machine (Eppendorf) using the following primer sets: *slc20a1a* forward 5'-TCTCTG GGACACATTGCATC-3', reverse 5'-AGCAGTTCAGCCATTGAC-3'; *slc13a1* forward 5'-TGCTGGGATTCCTGTTCTTC-3', reverse 5'-AAACCTCCACCAA CAAGCAG-3'; *slc12a1* forward 5'-TCAACGCTCTGAAGAAGCTG-3', reverse 5'-ACGTTGTGTGGGTTTCTTC-3'; *slc12a3* forward 5'-ACAGATCCGGCTG AATGAAG-3', reverse 5'-AGCCAAGCCATGTAAAGAGG-3'; *six2a* forward 5'-AGCTCGGAGGATGAGTTTTC-3', reverse 5'-ATGGTGCCTTGCAGAAG AAG-3'; *wt1a* forward 5'-AGCCAACCAAGGATGTTCAG-3', reverse 5'-AACC TTGATTCCTGGAGCTG-3'. *ef1a* was used as the normalization control: forward 5'-CTGGAGGCCAGCTCAAACAT-3', reverse 5'-ATCAAGAAGAGTAGTAC CGTAGCATTAC-3'. Relative quantification of target gene expression was evaluated using the comparative  $C_T$  method. A mean and standard deviation were determined for the  $\Delta C_T$  value for all genes of interest. The error in fold-change was obtained by considering the effect of an increase or decrease of one standard deviation in  $\Delta C_T$  value.

19. Westerfield, M. *The Zebrafish Book: A Guide for the Laboratory Use of Zebrafish* (Danio rerio) 4th edn (Univ. Oregon Press, 2000).
20. Perner, B., Englert, C. & Bollig, F. The Wilms tumor genes *wt1a* and *wt1b* control different steps during formation of the zebrafish pronephros. *Dev. Biol.* **309**, 87–96 (2007).
21. Urasaki, A., Morvan, G. & Kawakami, K. Functional dissection of the tol2 transposable element identified the minimal cis-sequence and a highly repetitive sequence in the subterminal region essential for transposition. *Genetics* **174**, 639–649 (2006).
22. Kawakami, K. *et al.* A transposon-mediated gene trap approach identifies developmentally regulated genes in zebrafish. *Dev. Cell* **7**, 133–144 (2004).
23. Elizondo, M. R. *et al.* Defective skeletogenesis with kidney stone formation in dwarf zebrafish mutant for *trpm7*. *Curr. Biol.* **15**, 667–671 (2005).

# Transmembrane semaphorin signalling controls laminar stratification in the mammalian retina

Ryota L. Matsuoka<sup>1,3</sup>, Kim T. Nguyen-Ba-Charvet<sup>4,5,6</sup>, Aijaz Parray<sup>4,5,6</sup>, Tudor C. Badea<sup>2,3,†</sup>, Alain Chédotal<sup>4,5,6</sup> & Alex L. Kolodkin<sup>1,3</sup>

**In the vertebrate retina, establishment of precise synaptic connections among distinct retinal neuron cell types is critical for processing visual information and for accurate visual perception. Retinal ganglion cells (RGCs), amacrine cells and bipolar cells establish stereotypic neurite arborization patterns to form functional neural circuits in the inner plexiform layer (IPL)<sup>1–3</sup>, a laminar region that is conventionally divided into five major parallel sublaminae<sup>1,2</sup>. However, the molecular mechanisms governing distinct retinal subtype targeting to specific sublaminae within the IPL remain to be elucidated. Here we show that the transmembrane semaphorin *Sema6A* signals through its receptor *PlexinA4* (*PlexA4*) to control lamina-specific neuronal stratification in the mouse retina. Expression analyses demonstrate that *Sema6A* and *PlexA4* proteins are expressed in a complementary fashion in the developing retina: *Sema6A* in most ON sublaminae and *PlexA4* in OFF sublaminae of the IPL. Mice with null mutations in *PlexA4* or *Sema6A* exhibit severe defects in stereotypic lamina-specific neurite arborization of tyrosine hydroxylase (TH)-expressing dopaminergic amacrine cells, intrinsically photosensitive RGCs (ipRGCs) and calbindin-positive cells in the IPL. *Sema6A* and *PlexA4* genetically interact *in vivo* for the regulation of dopaminergic amacrine cell laminar targeting. Therefore, neuronal targeting to subdivisions of the IPL in the mammalian retina is directed by repulsive transmembrane guidance cues present on neuronal processes.**

Synaptic connections among distinct neuronal cell types are organized in specific laminae within many regions of the nervous system. In the vertebrate retina, RGCs, amacrine cells, and bipolar cells have multiple morphologically distinct subtypes (RGCs, approximately 20; amacrine cells, approximately 30; bipolar cells, approximately 12), and each subtype elaborates a characteristic sublaminal connection pattern within the IPL<sup>1,3</sup>. Recent studies have shown that homophilic cell adhesion molecules, including sidekicks and Dscams, direct sublaminal targeting of distinct amacrine, bipolar and RGC cell types in the developing chicken retina<sup>4,5</sup>. A mutation in mouse *Dscam* disturbs process self avoidance, mosaic spacing and stratification of several amacrine cell subtypes<sup>6,7</sup>; however, it is not clear whether *Dscam* regulates the stratification of these amacrine cell subtypes directly or whether this is a consequence of other abnormalities in the *Dscam* mutant mouse retina, including disorganization of retinal layers and an expanded IPL. Thus, molecular cues that organize specific laminar stratifications in the mammalian retina have yet to be defined.

The semaphorin family of guidance cues includes secreted and membrane-bound proteins that have key roles in various neuronal developmental processes, including axon guidance and branching, neuronal migration and dendritic arborization<sup>8</sup>. Multiple classes of semaphorins have been shown to be expressed in the developing mammalian retina<sup>9,10</sup>; however, whether or how semaphorins function within the retina is not known.

To assess the *in vivo* roles of semaphorins and their receptors in retinal development, we first conducted expression analyses for conventional semaphorin receptors, *neuropilins* (*Npn-1* and *Npn-2*) and *plexins* (*PlexA1–A4*, *B1–B3*, *C1*, *D1*) in the developing mouse retina by *in situ* hybridization. We observed that multiple *plexins* and *neuropilins* are expressed both in overlapping and in distinct locations in the developing retina (data not shown). To investigate physiological functions of these semaphorin receptors in retinal development, we analysed mice harbouring targeted mutations in genes encoding each plexin and neuropilin by immunohistochemistry using various retinal markers, including Pax6, Chx10, Thy-1, TH, calbindin, choline acetyltransferase (ChAT), calretinin and protein kinase C alpha (PKC- $\alpha$ ) (Supplementary Fig. 1 and data not shown)<sup>11–13</sup>. We identified defects in the stereotypic lamina-specific neurite arborization of tyrosine hydroxylase-positive (TH<sup>+</sup>) dopaminergic amacrine cells, and calbindin-positive cells, in the IPL of adult mice homozygous for a targeted mutation in the gene encoding the *PlexA4* receptor<sup>11</sup> (Fig. 1b, d). We used division of the IPL into five parallel sublaminae (S1–S5, S5 being closest to the ganglion cell layer) for our analyses, as previously described<sup>1,2</sup>. We observed that dopaminergic amacrine cells, which predominantly stratify in the S1 sublamina of the IPL in wild-type retinas (Fig. 1a and Supplementary Fig. 2a, c), extend aberrant processes into S4/S5 in the *PlexA4*<sup>−/−</sup> mutant retina (Fig. 1b and Supplementary Fig. 2b, d). Similarly, calbindin-positive cells, which typically establish their projections in three strata at the borders of S1 and S2, S2 and S3, S3 and S4 in the IPL of wild-type retinas<sup>1</sup> (Fig. 1c), showed aberrant targeting of their processes to S4/S5 in the *PlexA4*<sup>−/−</sup> retina (Fig. 1d). These sublaminal targeting defects observed in dopaminergic amacrine cells and calbindin-positive cells show full penetrance and expressivity in *PlexA4*<sup>−/−</sup> mutant retinas (*n* = 10 mutant animals). To determine precisely where the aberrant processes of dopaminergic amacrine cells and calbindin-positive cells are localized within the *PlexA4*<sup>−/−</sup> retina, we performed double-immunolabelling to visualize these two neuronal subtypes and also cells labelled with an antibody directed against calretinin, which marks three strata at the borders of S1 and S2, S2 and S3, S3 and S4 (ref. 1) (the localization of calretinin<sup>+</sup> processes is not disrupted in *PlexA4*<sup>−/−</sup> retinas; Fig. 1e–f). We found that the aberrant processes of both TH<sup>+</sup> and calbindin<sup>+</sup> neuronal subtypes were localized predominantly adjacent to the calretinin<sup>+</sup> S3/S4 stratification band within S4/S5 in *PlexA4*<sup>−/−</sup> retinas (Fig. 1g, h). We confirmed that these two populations of mistargeted retinal neurons labelled by anti-TH and anti-calbindin are different retinal subtypes (Supplementary Fig. 3), demonstrating that *PlexA4* directs distinct retinal subtype targeting in the IPL *in vivo*. We also found that the calbindin<sup>+</sup> cells exhibiting neurite arborization defects in *PlexA4*<sup>−/−</sup> retinas are most probably amacrine cells because these calbindin<sup>+</sup> cells with aberrant processes in the S4/S5 sublaminae are co-immunolabelled by syntaxin, a pan-amacrine cell marker, but not by Brn3a, a marker for a subset of RGCs (data not shown).

<sup>1</sup>The Solomon H. Snyder Department of Neuroscience, The Johns Hopkins University School of Medicine, Baltimore, Maryland 21205, USA. <sup>2</sup>Department of Molecular Biology and Genetics, The Johns Hopkins University School of Medicine, Baltimore, Maryland 21205, USA. <sup>3</sup>Howard Hughes Medical Institute, The Johns Hopkins University School of Medicine, Baltimore, Maryland 21205, USA. <sup>4</sup>Institut National de la Santé et de la Recherche Médicale (INSERM), UMR S968, Institut de la Vision, F-75012 Paris, France. <sup>5</sup>Université Pierre et Marie Curie (UPMC) Paris VI, UMR S968, Institut de la Vision, F-75012 Paris, France. <sup>6</sup>Centre National de la Recherche Scientifique (CNRS) UMR 7210, Institut de la Vision, F-75012 Paris, France. <sup>†</sup>Present address: Retinal Circuit Development & Genetics Unit, Neurobiology-Neurodegeneration and Repair Laboratory, National Eye Institute, Bethesda, Maryland 20892, USA.

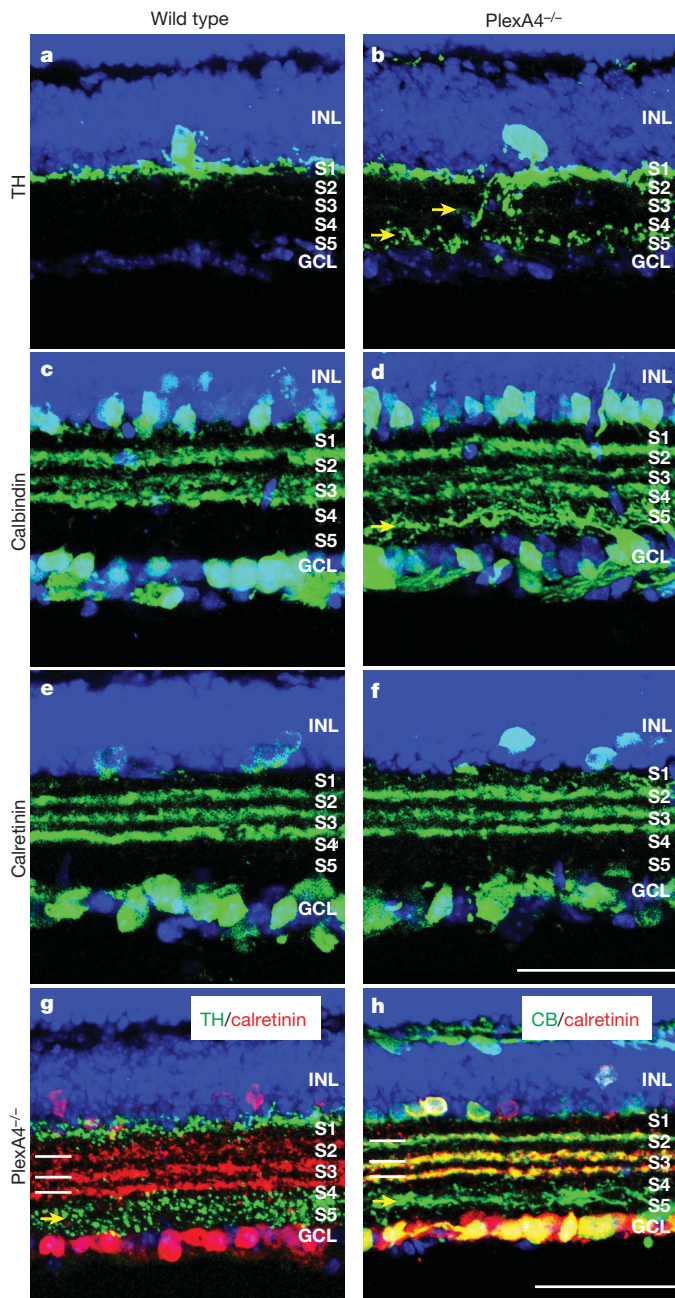


**Figure 1 | PlexinA4 directs lamina-specific neurite arborization of dopaminergic amacrine cells and calbindin-positive cells in the IPL *in vivo*.** **a–f**, Wild-type (**a**, **c**, **e**) and *PlexA4*<sup>−/−</sup> (**b**, **d**, **f**) adult retina sections were immunostained with antibodies against TH (**a**, **b**), calbindin (**c**, **d**) and calretinin (**e**, **f**). INL, inner nuclear layer; GCL, ganglion cell layer. In *PlexA4*<sup>−/−</sup> retinas, TH-positive dopaminergic amacrine cells and calbindin-positive cells exhibit defects in lamina-specific neurite arborization (yellow arrows in **b** and **d**, *n* = 10 *PlexA4*<sup>−/−</sup> animals). In wild-type retinas, dopaminergic amacrine cell processes are observed predominantly in the S1 sublamina of the IPL (**a**). In contrast, aberrant punctate immunostaining is detected in the S4/S5 sublaminae, in addition to S1, in all *PlexA4*<sup>−/−</sup> retinas examined (**b**). The normal stratification of calbindin-positive cells in the IPL (**c**) is disrupted in *PlexA4*<sup>−/−</sup> retinas, resulting in aberrant processes in S4/S5 (**d**). Calretinin-positive cells show normal sublaminal stratification in the IPL of *PlexA4*<sup>−/−</sup> retinas (**e**, **f**). **g**, **h**, *PlexA4*<sup>−/−</sup> adult retina sections double-immunostained with anti-calretinin (white bars) and anti-TH (**g**), or anti-calretinin (white bars) and anti-calbindin (CB) (**h**). Aberrant processes in *PlexA4*<sup>−/−</sup> retinas from dopaminergic amacrine cells, and from calbindin-positive cells, are found closer to the GCL than the calretinin-positive processes that lie between S3 and S4 in the IPL (yellow arrows). Scale bars, 50  $\mu$ m in **h** for **a**, **b**, **g**, **h**, and in **f** for **c–f**.

In contrast, other subtypes of RGCs and amacrine cells, including AII amacrine cells labelled with Disabled-1 (Dab-1), vGlut3-positive amacrine cells, cholinergic amacrine cells labelled with ChAT and R-cadherin-positive cells, show normal neurite arborization in the IPL of *PlexA4*<sup>−/−</sup> mutant retinas (Supplementary Fig. 4). This result further demonstrates that PlexA4 regulation of lamina-specific neurite arborization of retinal neuronal subtypes in the IPL is cell-type specific. Dopaminergic amacrine cell processes, which normally are targeted exclusively to the S1 sublamina (the OFF layer), are misguided in *PlexA4*<sup>−/−</sup> mutants to the S4/S5 sublaminae (a portion of the ON layer), suggesting that PlexA4 contributes to the segregation of ON and OFF layers within the IPL<sup>14</sup>.

Recent studies have shown that dopaminergic amacrine cells co-stratify with, and are synaptically coupled to, M1-type melanopsin intrinsically photosensitive retinal ganglion cells (ipRGCs) in S1 of the mouse IPL<sup>15,16</sup>. Therefore, we asked whether the abnormality in dopaminergic amacrine cell process stratification affects M1-type ipRGC dendritic arborization in the *PlexA4*<sup>−/−</sup> retina. We used an antibody directed against the carboxy (C) terminus of rat melanopsin to label M1-type melanopsin ipRGCs<sup>17,18</sup>, and we observed aberrant dendritic arborization of M1-type ipRGCs in S4/S5, in addition to stratification within S1 of the IPL in *PlexA4*<sup>−/−</sup> retina (Fig. 2a top, b top). We also observed that approximately 75% of aberrant dopaminergic amacrine cell processes (TH-immunoreactive puncta) were co-localized with M1-type ipRGC dendrites (C-terminal melanopsin-immunoreactive puncta) within S4/S5 in *PlexA4*<sup>−/−</sup> mutant retinas (Fig. 2a bottom, b bottom, c, d), suggesting that synaptic connectivity between dopaminergic amacrine cells and M1-type ipRGCs may be still preserved, even though these two neuronal populations have mispositioned processes within the IPL of the *PlexA4*<sup>−/−</sup> mutant retina. Therefore, PlexA4 is required for precise sublaminal targeting of dopaminergic amacrine cell processes and M1-type ipRGC dendrites within the IPL but may not be essential for synaptic target selection between these two neuronal populations. We examined both the cell number and mosaic patterning of dopaminergic amacrine cells and ipRGCs; we observed no significant difference between wild-type and *PlexA4*<sup>−/−</sup> retinas (Supplementary Fig. 5). We also observed no evidence of neuronal process self-avoidance deficits in these cell types in *PlexA4*<sup>−/−</sup> retinas (Supplementary Fig. 5a–b, e–f). In addition, *PlexA4*<sup>−/−</sup> RGC axons do not exhibit major projection defects in their trajectories to image-forming and non-image-forming targets within the brain (Supplementary Fig. 6); nor are errors observed in bipolar cell axon targeting within the IPL (Supplementary Fig. 7).

We next analysed PlexA4 protein expression using a PlexA4-specific antibody<sup>19</sup>. We observed no immunostaining with this antibody in *PlexA4*<sup>−/−</sup> retinas, confirming its specificity (Supplementary Fig. 8a, b). Anti-PlexA4 immunostaining at different postnatal ages shows that PlexA4 is strongly expressed on neuronal processes that predominantly stratify in S1 and S2 of the developing IPL (Fig. 3a left, b). We also observed that dopaminergic amacrine cell processes in S1 co-stratify with the upper PlexA4<sup>+</sup> S1 band (Fig. 3d left, middle and right). To test further if dopaminergic amacrine cells express PlexA4, we performed *in situ* hybridization experiments using a *PlexA4* antisense probe followed by anti-TH immunolabelling. We found that *PlexA4* messenger RNA (mRNA) is localized to the cell bodies of dopaminergic amacrine cells (26 out of 26 dopaminergic amacrine cells analysed showed co-localization of TH and *PlexA4* mRNA; Fig. 3e left, middle and right). Taken together, these results strongly suggest PlexA4 functions cell-autonomously in dopaminergic amacrine cells to regulate stratification of this cell type within the IPL. We did not observe PlexA4 protein expression in M1-type ipRGC cell bodies and dendrites (Fig. 3f left and right). This suggests that the M1-type ipRGC dendritic stratification deficit within the IPL of *PlexA4*<sup>−/−</sup> retinas is a secondary consequence of the developmental defects observed in the IPL of *PlexA4*<sup>−/−</sup> retinas, supporting a primary role for amacrine cells in directing RGC dendritic stratification<sup>3,20,21</sup>. Given our observation that

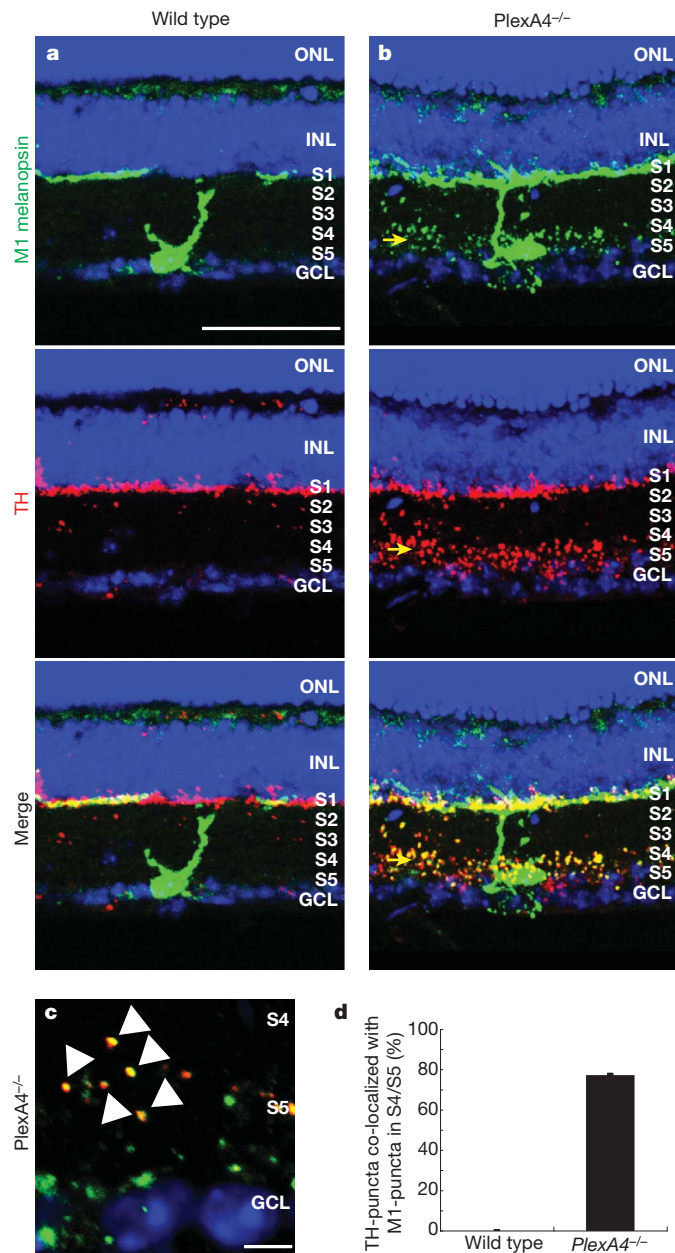


**Figure 2 | PlexinA4 controls dendritic targeting of M1-type ipRGCs within the IPL, but not co-localization of dopaminergic amacrine cell and ipRGC processes.** **a, b,** Top, middle, bottom, double-immunostaining using antibodies directed against the C terminus of rat melanopsin (**a, b,** top, green) and against TH (**a, b,** middle, red) of wild-type (**a,** top, middle, bottom) and *PlexA4*<sup>-/-</sup> (**b,** top, middle, bottom) adult retina sections (merged in **a, b,** bottom). Ectopic dendritic processes of M1-type ipRGCs were observed in the S4/S5 sublaminae of *PlexA4*<sup>-/-</sup> retinas, as were aberrant dopaminergic amacrine processes (yellow arrows, **a,** top, middle, bottom,  $n = 4$  mutant animals). Wild-type M1-type ipRGC dendritic processes and dopaminergic amacrine cell processes are only observed in S1 (**a,** top, middle, bottom). **c,** High-magnification view of S4/S5 in *PlexA4*<sup>-/-</sup> retinas double-immunostained with anti-C-terminal melanopsin and anti-TH. Most TH-positive puncta are co-localized with melanopsin-positive puncta (white arrowheads). **d,** Quantification of ectopic TH-positive puncta co-localized with the ectopic M1-type melanopsin puncta in S4/S5 of *PlexA4*<sup>-/-</sup> retinas. Nearly 76% (194 TH-positive puncta among a total of 254 puncta) of the ectopic TH-positive puncta were co-localized with ectopic M1-type melanopsin puncta in S4/S5 ( $76.4 \pm 1.2\%$  co-localization). In wild-type retinas, almost no TH-positive puncta were observed in S4/S5. Error bar, s.e.m. ( $n = 3$  animals per genotype). Scale bars, 50  $\mu\text{m}$  in **a, b,** top, middle, bottom, 5  $\mu\text{m}$  in **c**.

dopaminergic amacrine cell processes and M1-type ipRGC dendrites are co-localized in the S4/S5 sublaminae of *PlexA4*<sup>-/-</sup> retinas, dopaminergic amacrine cells may provide specific cues used by M1-type ipRGCs to form selective synaptic contacts.

There are two major classes of potential PlexA4 ligand: secreted class 3 semaphorins that bind to neuropilin-obligate co-receptors and form a holoreceptor complex with PlexA4 (ref. 8); and transmembrane class 6 semaphorins that directly bind to PlexA4 in a neuropilin-independent manner<sup>8</sup>. We first analysed neurite arborization of dopaminergic amacrine cells, M1-type ipRGCs and calbindin-positive cells in *Npn-1*<sup>Sema-/-Sema-</sup> (an *Npn-1* allele that generates a variant Npn-1 protein incapable of responding to class 3 semaphorin signalling) and *Npn-2*<sup>-/-</sup> mutant retinas<sup>12,13</sup>. We observed normal neurite stratification patterns in the IPL of all of these three neuronal subtypes in both *Npn-1*<sup>Sema-/-Sema-</sup> and *Npn-2*<sup>-/-</sup> retinas (Supplementary Fig. 9), indicating that secreted class 3 semaphorins are unlikely to act as ligands for PlexA4 in the retina.

Transmembrane class 6 semaphorins, including *Sema6A*, bind directly to PlexA4<sup>19</sup>. *Sema6A* induces growth cone collapse of several neuronal subtypes through the PlexA4 receptor *in vitro* and acts as a repulsive ligand for PlexA4 *in vivo*, regulating hippocampal mossy fibre projections and corticospinal tract decussation<sup>19,22</sup>. To ask whether *Sema6A* is a PlexA4 ligand, required for normal retinal development, we first analysed *Sema6A* protein expression using a *Sema6A*-specific antibody<sup>23</sup> (Supplementary Fig. 8c, c', d, d'). We found that *Sema6A* protein is strongly expressed in retinal S3b–S5 sublaminae (S3b being approximately the lower half of S3), and expressed at much lower levels in the S1–S3a sublaminae (S3a being approximately the upper half of S3) (Fig. 3c). We double-immunolabelled retinal sections with *Sema6A* and PlexA4 antibodies and found that strong *Sema6A* and PlexinA4 protein immunoreactivity is detected in adjacent regions of the developing IPL throughout early postnatal retinal development (Fig. 3a left, middle and right and Supplementary Fig. 10). These results support the hypothesis that *Sema6A* functions as a repulsive barrier within the developing IPL for neuronal processes expressing PlexA4, including dopaminergic amacrine cells. We observed *Sema6A* is not expressed in dopaminergic amacrine cells or M1-type ipRGCs (Fig. 3g, h), consistent with *Sema6A* serving a non-cell autonomous role in constraining the targeting of processes from these neuronal cell types in the IPL. However, immunolabelling experiments revealed that RGC and amacrine cell subtypes, distinct from ipRGCs and dopaminergic amacrine cells, are the major cellular sources of *Sema6A* protein in the developing IPL (see Supplementary Figs 11–13).

Phenotypic analysis of mice homozygous for a targeted gene-trap mutation in the *Sema6A* locus<sup>9</sup> showed that *Sema6A*<sup>-/-</sup> mutants phenocopy the neurite stratification defects in dopaminergic amacrine cells, M1-type ipRGCs and calbindin-positive cells we observe in *PlexA4*<sup>-/-</sup> mutant retinas (with full penetrance and expressivity,  $n = 8$  *Sema6A*<sup>-/-</sup> mutant animals, Fig. 4a–f). This result strongly suggests that *Sema6A* is a functional ligand for PlexA4, required for regulating select aspects of retinal neurite stratification *in vivo*. To assess further the ligand–receptor relationship between *Sema6A* and PlexA4 in retinal development *in vivo*, we investigated genetic interactions between *PlexA4* and *Sema6A* by analysing mice doubly heterozygous for *Sema6A* and *PlexA4* mutations. We quantified the number of TH-positive immunoreactive puncta localized in S4/S5 of *Sema6A*<sup>+/-</sup>;*PlexA4*<sup>+/-</sup> mutant mice (Fig. 4k). In wild-type retinas, TH<sup>+</sup> immunoreactive puncta in S4/S5 were almost undetectable (Fig. 4g). Mice heterozygous for either *PlexA4* or *Sema6A* mutations did not show a significant increase in the number of the TH<sup>+</sup> puncta in S4/S5 (Fig. 4h, i). However, *Sema6A*<sup>+/-</sup>;*PlexA4*<sup>+/-</sup> mutant mice exhibited a markedly increased number of the TH<sup>+</sup> puncta in S4/S5 (Fig. 4j). Therefore, *Sema6A* and *PlexA4* functionally interact *in vivo* and probably act in a common signalling pathway. Together with the complementary expression patterns of *Sema6A* and PlexA4 in specific regions of the developing IPL, these results strongly support a model in

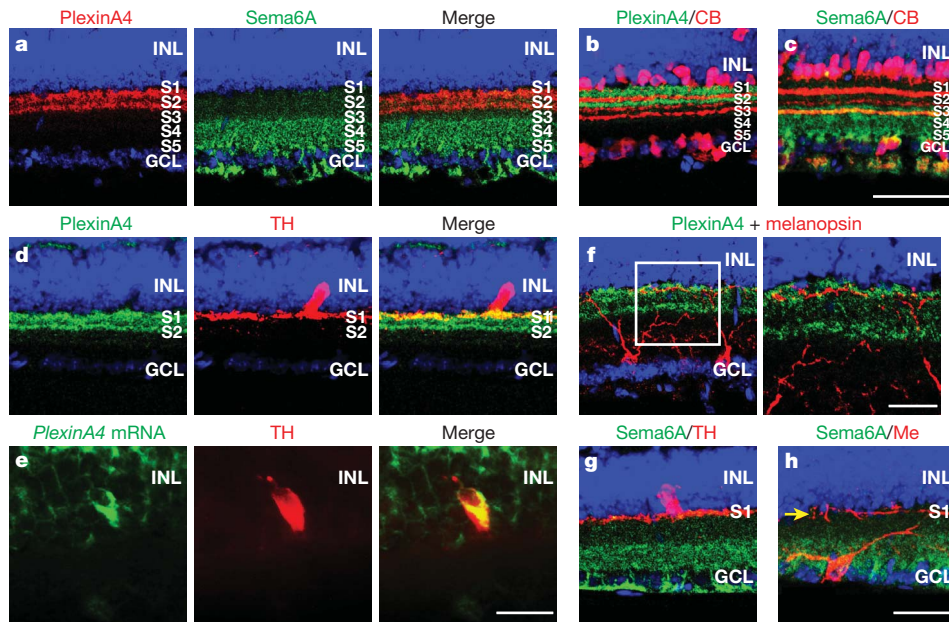


**Figure 3 | PlexinA4 and Sema6A exhibit complementary protein expression in the developing mouse retina.** **a**, Left, middle and right, P14 retina section double-immunostained with anti-PlexA4 (**a**, left, red) and anti-Sema6A (**a**, middle, green) (merged in **a**, right). Strong Sema6A immunoreactivity in the IPL was observed in approximately one-half of S3 and throughout S4 and S5, whereas PlexA4 expression is stratified in two distinct layers in S1 and S2. **b**, P14 retina section double-immunostained with anti-PlexA4 (green) and anti-calbindin (CB, red) shows PlexA4 protein localization in S1/S2 sublaminae relative to calbindin-positive neuronal processes. **c**, P14 retina section double-immunostained with anti-Sema6A (green) and anti-calbindin (CB, red) shows Sema6A protein localization in S3–S5 relative to calbindin-positive neuronal processes. **d**, Left, middle and right, P14 retina section double-immunostained with anti-PlexA4 (**d**, left, green) and anti-TH (**d**, middle, red), revealing colocalization of PlexA4 and TH immunoreactivity in S1 of the IPL (merged in **d**, right). **e**, Left, middle, right, P14 retina section hybridized with *PlexA4*

antisense probe (**e**, left, green) followed by anti-TH immunolabelling (**e**, middle, red, merged in **e**, right). *PlexA4* mRNA is localized to the cell body of dopaminergic amacrine cells (of 26 TH-positive amacrine cells scored, all were positive for *PlexA4* mRNA). **f**, Left and right, P14 retina section double-immunostained with anti-PlexA4 (green) and anti-amino (N)-terminal melanopsin (red), which labels multiple ipRGC subtypes<sup>18</sup> (**f**, left; high magnification of the area in the white square shown in **f**, right). PlexA4 immunoreactivity was not observed in the cell bodies or dendrites of ipRGCs. **g**, **h**, P14 retina sections double-immunostained with anti-Sema6A (green) and anti-TH (**g**, red) or anti-N-terminal melanopsin (Me) (**h**, red). Sema6A protein was not observed in cell bodies, or processes, of dopaminergic amacrine cells and ipRGCs (M1-type ipRGC dendritic processes in the S1 indicated by yellow arrow in **h**). Scale bars, 50 μm in **c** for **a**, left, middle and right, **b**, **c**, 50 μm in **h** for **d**, left, middle and right, **f**, left, **g**, **h**, 20 μm in **e**, right for **a**, left, middle and right, 20 μm in **f**, right.

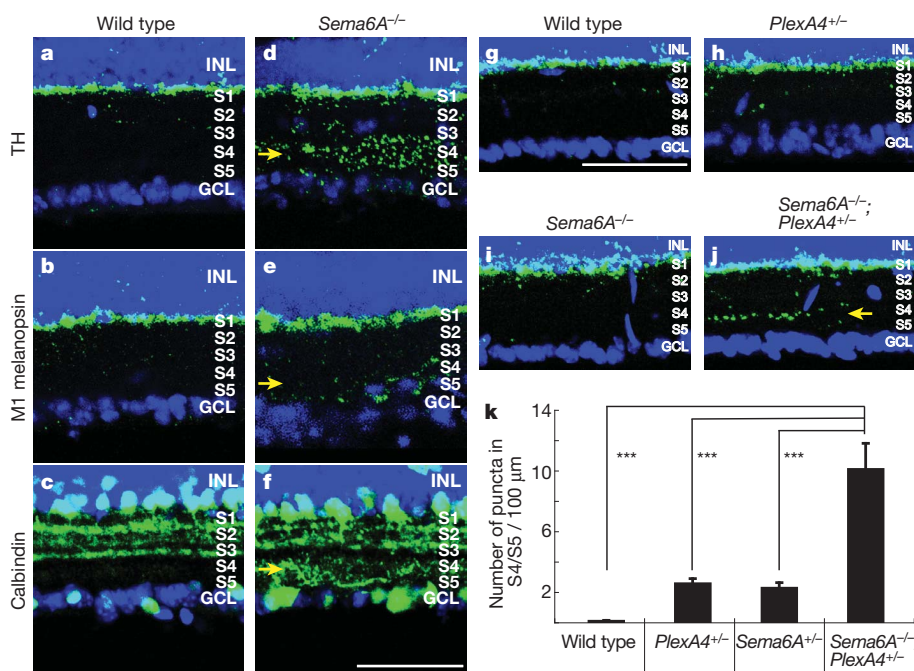


**Figure 4 | Sema6A signalling through the PlexinA4 receptor directs retinal sublamina targeting.** **a–f**, Wild-type (**a–c**) and *Sema6A*<sup>−/−</sup> (**d–f**) adult retina sections were immunostained with antibodies against TH (**a**, **d**), C-terminal melanopsin (**b**, **e**) and calbindin (**c**, **f**). *Sema6A*<sup>−/−</sup> retinas recapitulate the lamina-specific neurite arborization defects of dopaminergic amacrine cells, M1-type ipRGCs and calbindin-positive cells (yellow arrows) observed in *PlexA4*<sup>−/−</sup> retinas ( $n = 8$  *Sema6A*<sup>−/−</sup> animals). **g–j**, Wild-type (**g**), *PlexA4*<sup>+/-</sup> (**h**), *Sema6A*<sup>+/-</sup> (**i**) and *Sema6A*<sup>+/-</sup>; *PlexA4*<sup>+/-</sup> (**j**) adult retina sections were immunostained with anti-TH. **k**, Quantification of ectopic TH-positive puncta detected in the S4/S5 sublaminae in wild-type (**g**), *PlexA4*<sup>+/-</sup> (**h**), *Sema6A*<sup>+/-</sup> (**i**) and *Sema6A*<sup>+/-</sup>; *PlexA4*<sup>+/-</sup> (**j**) sections ( $n = 4$  animals for each genotype). An increased number of TH-positive puncta were observed in S4/S5 in *Sema6A*<sup>+/-</sup>; *PlexA4*<sup>+/-</sup> retinas ( $10.1 \pm 1.7$  puncta per 100 μm, yellow arrow, **j**) compared with the other three genotypes ( $0.1 \pm 0.1$  puncta per 100 μm, wild type;  $2.6 \pm 0.3$  puncta per 100 μm, *PlexA4*<sup>+/-</sup>;  $2.3 \pm 0.4$  puncta per 100 μm, *Sema6A*<sup>+/-</sup>; **g–i**). Error bars, s.e.m. \*\*\* $P < 0.01$  by Tukey's multiple comparison test. Scale bars, 50 μm in **a–f**, and in **g** for **g–j**.

which *Sema6A* acts as a ligand for the *PlexA4* receptor to regulate dopaminergic amacrine cell process targeting in the IPL.

We provide here a demonstration of a molecular cue that directs lamina-specific neurite arborization in the developing mouse retina. We show that *Sema6A* and its receptor *PlexA4* exhibit complementary expression patterns throughout postnatal IPL development, that *Sema6A*<sup>-/-</sup> mutant mice phenocopy defects in lamina-specific neurite stratification of specific retinal neuron subtypes observed in *PlexA4*<sup>-/-</sup> mutant mice, and that they functionally interact *in vivo*. *PlexA4*<sup>-/-</sup> mutant retinas do not exhibit defects in neurite fasciculation of the retinal cell types that show defects in sublaminal targeting in the IPL (Supplementary Fig. 5), further suggesting that sublaminal targeting in the vertical plane of the mouse retina and neurite arborization in the horizontal plane of the mouse retina are governed by separate mechanisms. Our observations of *Sema6A* and *PlexA4* function in retinal development suggest that initial laminar targeting to broad regions within the developing mouse IPL is directed by a transmembrane guidance cue located on neuronal processes that signals through its receptor, present on other neuronal subtypes. This defines a heterophilic interaction distinct from homophilic adhesive interactions mediated by molecules such as sidekicks and Dscams. Neuronal circuitry mediating two parallel ON/OFF visual pathways is spatially segregated in the IPL of the vertebrate retina<sup>1,14</sup>, and this spatial segregation has crucial roles in the effective transmission of distinct light responses to the brain<sup>1</sup>. Determining how the ON and OFF pathways are segregated at the circuit level is fundamental for understanding visual perception: our results suggest that these distinct neuronal pathways are established in the IPL through the action of a transmembrane guidance cue and its receptor. Our elucidation of molecular events critical for lamina-specific targeting in the IPL of the mammalian retina may have general implications for understanding mechanisms that govern the establishment of neuronal connectivity, in particular how laminar organization is achieved during neural development.

## METHODS SUMMARY

The day of birth in this study is designated as postnatal (P) day 0. The *PlexA4*-deficient and *Sema6A* gene-trap mouse lines were previously described<sup>9,11</sup>. Immunohistochemistry and *in situ* hybridization were performed as previously described<sup>13</sup>, and the retinal regions we imaged did not include areas near the peripheral edges or the optic nerve head of retinas. See Methods for additional detailed experimental procedures, including wholemount retina staining, density recovery profile analysis, quantification of anti-TH and anti-C-terminal melanopsin co-localized puncta, genetic interaction analysis, X-gal staining, cholera toxin injection and statistical analysis.

**Full Methods** and any associated references are available in the online version of the paper at [www.nature.com/nature](http://www.nature.com/nature).

**Received 3 September; accepted 17 November 2010.**

**Published online 26 January 2011.**

- Wassle, H. Parallel processing in the mammalian retina. *Nature Rev. Neurosci.* **5**, 747–757 (2004).
- Sanes, J. R. & Zipursky, S. L. Design principles of insect and vertebrate visual systems. *Neuron* **66**, 15–36 (2010).
- Huberman, A. D., Clandinin, T. R. & Baier, H. Molecular and cellular mechanisms of lamina-specific axon targeting. *Cold Spring Harb Perspect Biol* **2**, a001743 (2010).
- Yamagata, M., Weiner, J. A. & Sanes, J. R. Sidekicks: synaptic adhesion molecules that promote lamina-specific connectivity in the retina. *Cell* **110**, 649–660 (2002).

- Yamagata, M. & Sanes, J. R. Dscam and Sidekick proteins direct lamina-specific synaptic connections in vertebrate retina. *Nature* **451**, 465–469 (2008).
- Fuerst, P. G., Koizumi, A., Masland, R. H. & Burgess, R. W. Neurite arborization and mosaic spacing in the mouse retina require DSCAM. *Nature* **451**, 470–474 (2008).
- Fuerst, P. G., Harris, B. S., Johnson, K. R. & Burgess, R. W. A novel null allele of mouse DSCAM survives to adulthood on an inbred C3H background with reduced phenotypic variability. *Genesis* **48**, 578–584 (2010).
- Tran, T. S., Kolodkin, A. L. & Bharadwaj, R. Semaphorin regulation of cellular morphology. *Annu. Rev. Cell Dev. Biol.* **23**, 263–292 (2007).
- Leighton, P. A. *et al.* Defining brain wiring patterns and mechanisms through gene trapping in mice. *Nature* **410**, 174–179 (2001).
- de Winter, F., Cui, Q., Symons, N., Verhaagen, J. & Harvey, A. R. Expression of class-3 semaphorins and their receptors in the neonatal and adult rat retina. *Invest. Ophthalmol. Vis. Sci.* **45**, 4554–4562 (2004).
- Yaron, A., Huang, P. H., Cheng, H. J. & Tessier-Lavigne, M. Differential requirement for Plexin-A3 and -A4 in mediating responses of sensory and sympathetic neurons to distinct class 3 Semaphorins. *Neuron* **45**, 513–523 (2005).
- Gu, C. *et al.* Neuropilin-1 conveys semaphorin and VEGF signaling during neural and cardiovascular development. *Dev. Cell* **5**, 45–57 (2003).
- Giger, R. J. *et al.* Neuropilin-2 is required *in vivo* for selective axon guidance responses to secreted semaphorins. *Neuron* **25**, 29–41 (2000).
- Famiglietti, E. V. Jr & Kolb, H. Structural basis for ON- and OFF-center responses in retinal ganglion cells. *Science* **194**, 193–195 (1976).
- Viney, T. J. *et al.* Local retinal circuits of melanopsin-containing ganglion cells identified by transsynaptic viral tracing. *Curr. Biol.* **17**, 981–988 (2007).
- Zhang, D. Q. *et al.* Intraretinal signaling by ganglion cell photoreceptors to dopaminergic amacrine neurons. *Proc. Natl Acad. Sci. USA* **105**, 14181–14186 (2008).
- Hattar, S., Liao, H. W., Takao, M., Berson, D. M. & Yau, K. W. Melanopsin-containing retinal ganglion cells: architecture, projections, and intrinsic photosensitivity. *Science* **295**, 1065–1070 (2002).
- Pires, S. S. *et al.* Differential expression of two distinct functional isoforms of melanopsin (Opn4) in the mammalian retina. *J. Neurosci.* **29**, 12332–12342 (2009).
- Suto, F. *et al.* Interactions between plexin-A2, plexin-A4, and semaphorin 6A control lamina-restricted projection of hippocampal mossy fibers. *Neuron* **53**, 535–547 (2007).
- Stacy, R. C. & Wong, R. O. Developmental relationship between cholinergic amacrine cell processes and ganglion cell dendrites of the mouse retina. *J. Comp. Neurol.* **456**, 154–166 (2003).
- Kay, J. N. *et al.* Transient requirement for ganglion cells during assembly of retinal synaptic layers. *Development* **131**, 1331–1342 (2004).
- Runker, A. E., Little, G. E., Suto, F., Fujisawa, H. & Mitchell, K. J. Semaphorin-6A controls guidance of corticospinal tract axons at multiple choice points. *Neural Develop.* **3**, 34 (2008).
- Kerjan, G. *et al.* The transmembrane semaphorin *Sema6A* controls cerebellar granule cell migration. *Nature Neurosci.* **8**, 1516–1524 (2005).

**Supplementary Information** is linked to the online version of the paper at [www.nature.com/nature](http://www.nature.com/nature).

**Acknowledgements** We thank K.-W. Yau for the C-terminal melanopsin antibody, F. Suto for the *PlexA4* antibody, B. Howell for the Dab-1 antibody, Y. Yoshida for the *PlexA1*<sup>-/-</sup> eyes, P. Mombaerts for the *PlexB1*<sup>-/-</sup> and *PlexB3*<sup>-/-</sup> mice (unpublished), C. Gu for the *PlexD1*<sup>-lox</sup>, *nestin cre* (unpublished) eyes and M. Tessier-Lavigne for the *PlexA4*<sup>-/-</sup> mice. We also thank J. Nathans, S. Hattar, K. Mandai and M. Riccomagno for comments on the manuscript and discussions, and members of the Kolodkin laboratory for assistance. This work was supported by R01 NS35165 to A.L.K., a predoctoral fellowship from the Nakajima Foundation to R.L.M., the Fondation pour la Recherche Médicale (Programme équipe FRM) to A.C., the Fondation Retina France to K.T.N.-B.-C., and a PhD fellowship from the Paris School of Neuroscience (ENP) to A.P. A.L.K. is an investigator of the Howard Hughes Medical Institute.

**Author Contributions** R.L.M., A.C. and A.L.K. conceived and designed the experiments; R.L.M. performed most of the experiments and data analysis; K.T.N.-B.-C., A.P. and A.C. participated in the phenotypic analyses of *Sema6A* mutant mice and provided *PlexA2*<sup>-/-</sup> and *PlexB2*<sup>-/-</sup> mutants; T.C.B. performed cholera toxin injections and provided suggestions and reagents; R.L.M. and A.L.K. wrote the paper.

**Author Information** Reprints and permissions information is available at [www.nature.com/reprints](http://www.nature.com/reprints). The authors declare no competing financial interests. Readers are welcome to comment on the online version of this article at [www.nature.com/nature](http://www.nature.com/nature). Correspondence and requests for materials should be addressed to A.L.K. (kolodkin@jhmi.edu).

## METHODS

**Animals.** The day of birth in this study is designated as postnatal (P) day 0. The *PlexA4*-deficient and *Sema6A* gene-trap mouse lines were previously described<sup>9,11</sup>. The *PlexA1*<sup>-/-</sup>, *PlexA2*<sup>-/-</sup>, *PlexA3*<sup>-/-</sup>, *PlexB2*<sup>-/-</sup>, *PlexC1*<sup>-/-</sup>, *Npn-1*<sup>Sema-/Sema-</sup> and *Npn-2*<sup>-/-</sup> mice were also described elsewhere<sup>11–13,19,24–27</sup>. The *PlexB1*<sup>-/-</sup> and *PlexB3*<sup>-/-</sup> were obtained from P. Mombaerts (unpublished). The *PlexDI*<sup>-flox</sup>; *nestin cre* mice were generated by G. Gu (unpublished).

**Immunohistochemistry.** Eyes were fixed in 4% paraformaldehyde for 1 h at 4 °C, equilibrated in 30% sucrose/PBS and embedded in OCT embedding media (Tissue-Tek). Retinal sections (20–40 µm) were blocked in 5% fetal bovine serum in 1× PBS and 0.4% Triton X-100 for 1 h at room temperature and then incubated overnight at 4 °C with primary antibodies: rabbit anti-tyrosine hydroxylase (Millipore at 1:1,000), sheep anti-tyrosine hydroxylase (Millipore at 1:400), rabbit anti-N-terminal melanopsin (ATS at 1:2,000), rabbit anti-C-terminal rat melanopsin (a gift from K.-W. Yau at 1:500)<sup>17</sup>, rabbit anti-calbindin (Swant at 1:2,500), rabbit anti-calretinin (Swant at 1:2,500), goat anti-calretinin (Swant at 1:2,500), rat anti-R-cadherin (Developmental Studies Hybridoma Bank at 1:200), goat anti-ChAT (Millipore at 1:100), rabbit anti-Dab-1 (a gift from B. Howell at 1:500), mouse anti-PKCα (Millipore at 1:200), mouse anti-Goz (Millipore at 1:500), goat anti-mouse *Sema6A* (R&D Systems at 1:200), Armenian hamster anti-*PlexA4* (a gift from F. Suto at 1:400)<sup>19</sup>, guinea pig anti-vGlut3 (Millipore at 1:2,500), chicken anti-β-gal (Abcam at 1:100), mouse anti-Brn3a (Millipore at 1:20), rabbit anti-Pax6 (Covance at 1:1,000) and goat anti-Chx10 (Santa Cruz at 1:50). Sections were washed six times for 5 min in 1× PBS and then incubated with secondary antibodies and TO-PRO-3 (Molecular Probes at 1:400) for 1 h at room temperature. Sections were washed six times for 5 min in PBS and coverslips were mounted using Vectashield HardSet Fluorescence Mounting Medium (Vector Laboratories), and confocal fluorescence images were taken using a Zeiss Axioskop2 Mot Plus, LSM 5 Pa confocal microscope. The regions we imaged did not include areas near the peripheral edges or the optic nerve head of retinas.

**Wholemout retina staining.** Enucleated eyes were fixed in 4% paraformaldehyde for 1 h at 4 °C. Whole retina cups were dissected out under a microscope and blocked in PBS containing 5% fetal bovine serum and 0.4% Triton X-100 for 2–3 h at room temperature. Retina cups were then incubated with primary antibodies in PBS containing 5% fetal bovine serum, 0.4% Triton X-100 and 20% dimethyl sulphoxide (DMSO) for 3–4 days at room temperature. Retinas were washed in PBS + 0.4% Triton X-100 for 7–8 h at room temperature and incubated with secondary antibodies in PBS containing 5% fetal bovine serum, 0.4% Triton X-100 and 20% DMSO for 24–36 h at room temperature. Retinas were washed in PBS + 0.4% Triton X-100 for 7–8 h at room temperature and flat mounted for confocal fluorescence images.

**In situ hybridization.** *In situ* hybridization was performed on either fresh frozen or PFA-fixed retina sections (20 µm thickness) as described previously<sup>13</sup>. Digoxigenin-labelled cRNA probes for *PlexA4* and *Sema6A* were used as previously described<sup>28</sup>. Colourimetric *in situ* hybridization was in some cases followed by fluorescence immunohistochemistry and subsequent pseudocolouring of bright field images.

**Quantification of anti-TH and anti-C-terminal melanopsin co-localized puncta.** Confocal images of two selected regions (112 µm × 112 µm field) from

each retina (*n* = 3 retinas from three animals for wild-type and *PlexA4*<sup>-/-</sup> genotypes) were double-immunostained with anti-TH and anti-C-terminal melanopsin, and the number of anti-TH-immunoreactive puncta co-localized with anti-C-terminal melanopsin in the S4/S5 sublaminae of the IPL was quantified.

**Density recovery profile analysis.** Density recovery profile analysis was performed as previously described<sup>6,29,30</sup>. Confocal images of five selected regions (447 µm × 447 µm field) from each wholemount retina (*n* = 3 retinas from three animals for wild-type and *PlexA4*<sup>-/-</sup> genotypes) were used to measure the density recovery profile of dopaminergic amacrine cells or ipRGCs. The retinal regions we used for this analysis did not include the areas near the peripheral edges or the optic nerve head.

**X-gal staining.** Eyes were fixed in 4% paraformaldehyde at 4 °C for 30 min, equilibrated in 30% sucrose/PBS, and embedded in OCT embedding media. Retina sections (20 µm) were stained with 5 mM potassium ferricyanide, 5 mM potassium ferrocyanide, 2 mM MgCl<sub>2</sub> and 1 mg ml<sup>-1</sup> X-gal for 1–2 h at room temperature. Tissue sections were rinsed in PBS and bright-field images were taken.

**Genetic interaction analysis.** Retinal cross sections (40 µm thickness) from adult wild-type, *PlexA4*<sup>+/-</sup>, *Sema6A*<sup>+/-</sup> and *Sema6A*<sup>+/-</sup>; *PlexA4*<sup>+/-</sup> mice were immunostained with anti-TH (*n* = 4 retinas from four animals for each genotype). The number of anti-TH-immunoreactive puncta localized in the S4/S5 sublaminae of the IPL in five selected regions (149 µm × 149 µm field) from each retina was quantified. The retinal regions we used for this analysis did not include the areas near the peripheral edges or the optic nerve head.

**Cholera toxin injection.** Mice were anaesthetized with ketamine. Eyes were injected intravitreally with 1 µl of 2 mg ml<sup>-1</sup> cholera toxin B subunit solution conjugated with Alexa Fluor 488 or 594 (Invitrogen). Four to five days after injection, mice were perfused intracardially with 4% paraformaldehyde in PBS and brains were isolated. Brain sections (100 µm) were cut using a vibratome, and fluorescence images were taken.

**Statistical analysis.** Statistical differences for mean values among multiple groups were determined using Tukey's multiple comparison test. The criterion for statistical significance was set at *P* < 0.05. Error bars, s.e.m.

24. Yoshida, Y., Han, B., Mendelsohn, M. & Jessell, T. M. PlexinA1 signaling directs the segregation of proprioceptive sensory axons in the developing spinal cord. *Neuron* **52**, 775–788 (2006).
25. Cheng, H. J. *et al.* Plexin-A3 mediates semaphorin signaling and regulates the development of hippocampal axonal projections. *Neuron* **32**, 249–263 (2001).
26. Friedel, R. H. *et al.* Plexin-B2 controls the development of cerebellar granule cells. *J. Neurosci.* **27**, 3921–3932 (2007).
27. Pasterkamp, R. J., Peschon, J. J., Spriggs, M. K. & Kolodkin, A. L. Semaphorin 7A promotes axon outgrowth through integrins and MAPKs. *Nature* **424**, 398–405 (2003).
28. Suto, F. *et al.* Plexin-a4 mediates axon-repulsive activities of both secreted and transmembrane semaphorins and plays roles in nerve fiber guidance. *J. Neurosci.* **25**, 3628–3637 (2005).
29. Rodieck, R. W. The density recovery profile: a method for the analysis of points in the plane applicable to retinal studies. *Vis. Neurosci.* **6**, 95–111 (1991).
30. Rockhill, R. L., Euler, T. & Masland, R. H. Spatial order within but not between types of retinal neurons. *Proc. Natl Acad. Sci. USA* **97**, 2303–2307 (2000).

# Observation of scale invariance and universality in two-dimensional Bose gases

Chen-Lung Hung<sup>1</sup>, Xibo Zhang<sup>1</sup>, Nathan Gemelke<sup>1†</sup> & Cheng Chin<sup>1</sup>

The collective behaviour of a many-body system near a continuous phase transition is insensitive to the details of its microscopic physics; for example, thermodynamic observables follow generalized scaling laws near the phase transition<sup>1</sup>. The Berezinskii–Kosterlitz–Thouless (BKT) phase transition<sup>2,3</sup> in two-dimensional Bose gases presents a particularly interesting case because the marginal dimensionality and intrinsic scaling symmetry<sup>4</sup> result in a broad fluctuation regime and an extended range of universal scaling behaviour. Studies of the BKT transition in cold atoms have stimulated great interest in recent years<sup>5–10</sup>, but a clear demonstration of critical behaviour near the phase transition has remained elusive. Here we report *in situ* density and density-fluctuation measurements of two-dimensional Bose gases of caesium at different temperatures and interaction strengths, observing scale-invariant, universal behaviours. The extracted thermodynamic functions confirm the existence of a wide universal region near the BKT phase transition, and provide a sensitive test of the universality predicted by classical-field theory<sup>11,12</sup> and quantum Monte Carlo calculations<sup>13</sup>. Our experimental results provide evidence for growing density–density correlations in the fluctuation region, and call for further explorations of universal phenomena in classical and quantum critical physics.

In two-dimensional (2D) Bose gases, critical behaviour develops in the BKT transition regime, where an ordered phase with finite-range coherence competes with thermal fluctuations and induces a continuous phase transition from normal gas to superfluid with quasi-long-range order<sup>3</sup>. In this fluctuation region, a universal and scale-invariant description of the system is expected through the power-law scaling of thermodynamic quantities with respect to the coupling strength and a characteristic length scale<sup>12,14</sup>—for example, the thermal de Broglie wavelength (Fig. 1a). Especially for weakly interacting gases at finite temperatures, the scale invariance prevails over the normal, fluctuation and superfluid regions because of the density-independent coupling constant<sup>15</sup> and the symmetry of the underlying Hamiltonian<sup>4</sup>.

In this Letter, we verify the scale invariance and universality of interacting 2D Bose gases, and identify BKT critical points. We test the scale invariance of *in situ* density and density fluctuations of 2D gases of <sup>133</sup>Cs at various temperatures. We study the universality near the BKT transition by tuning the atomic scattering length using a magnetic Feshbach resonance<sup>16</sup> and observing a universal scaling behaviour of the equation of state and the quasi-condensate density. Finally, by comparing the local density fluctuations and the compressibility derived from the density profiles, we provide strong evidence of a growing density–density correlation in the fluctuation regime.

We begin the experiment by loading a nearly pure <sup>133</sup>Cs Bose condensate of  $N = 2 \times 10^4$  atoms into a single pancake-like optical potential with strong confinement in the vertical ( $z$ ) direction and weak confinement in the horizontal ( $r$ ) direction<sup>17,18</sup>. The trapping potential,  $V(r, z) = m\omega_r^2 r^2/2 + m\omega_z^2 z^2/2$ , has mean harmonic trapping frequencies  $\omega_r = 2\pi \times 10$  Hz and  $\omega_z = 2\pi \times 1,900$  Hz. Here,  $r$  denotes the radial distance to the trap centre and  $m$  is the caesium atomic mass. In this

trap, the gas reaches temperatures as low as  $T = 15$  nK and a moderate peak chemical potential,  $\mu_0 < k_B T$ . The ratio  $\hbar\omega_z/\mu_0 > \hbar\omega_z/k_B T \approx 6$  indicates that the sample is deeply in the 2D regime with  $<1\%$  population in the vertical excited states. Here,  $\hbar = h/2\pi$ ,  $h$  is the Planck constant, and  $k_B$  is the Boltzmann constant. The 2D coupling constant is evaluated according to  $g = \sqrt{8\pi}a/l_z$  (ref. 15), where  $a$  is the atomic scattering length and  $l_z = 200$  nm is the vertical harmonic oscillator length. We control the scattering length  $a$  in the range 2–10 nm, resulting in weak coupling strengths  $g = 0.05$ – $0.26$ . Here, the density-dependent correction to  $g$  (refs 15, 19) is expected to be small and negligible ( $<2\%$ ).

We obtain *in situ* density distributions of 2D gases by performing absorption imaging perpendicular to the horizontal plane with a commercial microscope objective and a CCD camera<sup>18</sup> (see Fig. 1b for sample images). About 50 images are collected for each experiment condition, and the average density  $n$  and the density variance  $\delta n^2$  are evaluated pixel-wise (Methods). We obtain the radial density  $n(r)$  and variance  $\delta n^2(r)$  profiles (Fig. 2 insets) by accounting for the cloud anisotropy and performing azimuthal averaging<sup>17</sup>.

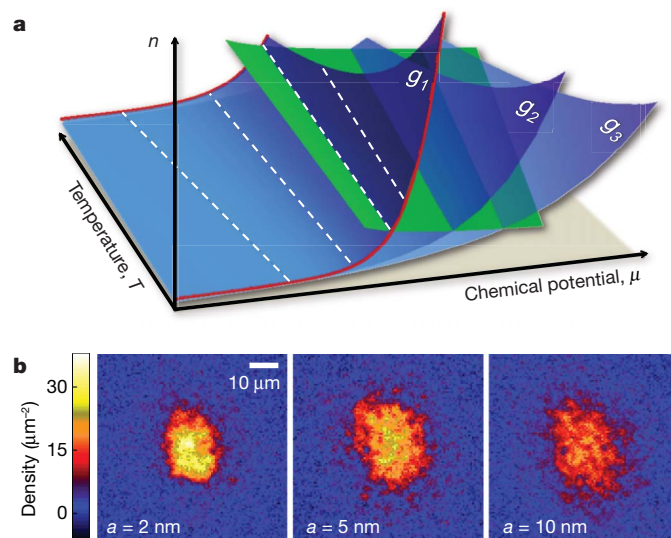


**Figure 1 | Illustration of scale invariance and universality in 2D quantum gases.** **a**, Scale invariance links any thermodynamic observable at different  $\mu$  and  $T$  via a simple power-law scaling. In a 2D Bose gas with coupling constant  $g \ll 1$ , atomic density  $n$  measured at different temperatures (red lines) can be scaled through constant  $\mu/T$  and  $n/T$  contours (dashed lines). Near the BKT phase transition boundary (green plane), systems with different  $g = g_1, g_2, \dots$  (blue planes) scale universally. **b**, *In situ* density measurements of trapped 2D gases provide crucial information to test the hypotheses of scale invariance and universality. Sample images at different scattering lengths  $a$  are obtained from single shots.

<sup>†</sup>The James Franck Institute and Department of Physics, University of Chicago, Chicago, Illinois 60637, USA. <sup>†</sup>Present address: Department of Physics, The Pennsylvania State University, University Park, Pennsylvania 16802, USA.

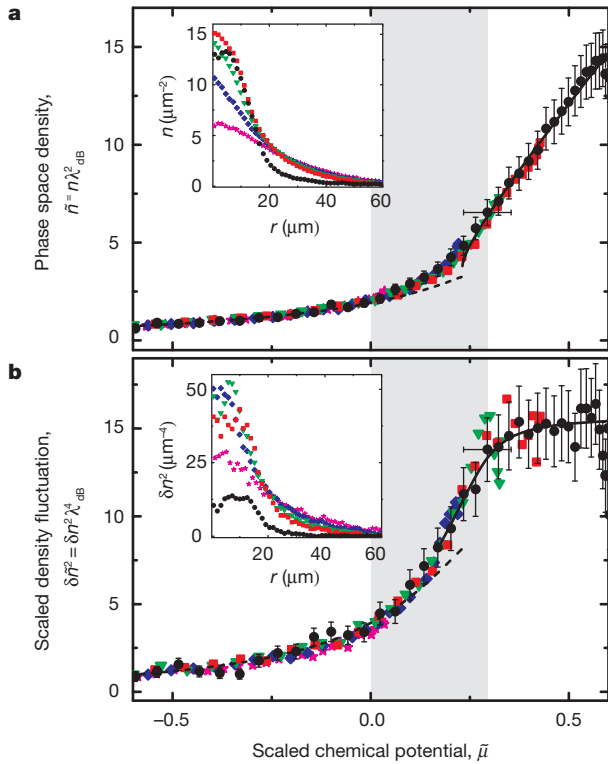


**Figure 2 | Scale invariance of density and its fluctuation.** **a**, Scaled density (phase space density)  $\tilde{n} = n\lambda_{dB}^2$  as a function of the scaled chemical potential  $\tilde{\mu} = \mu/k_B T$  measured at five different temperatures:  $T = 21$  nK (filled black circles), 37 nK (red squares), 42 nK (green triangles), 49 nK (blue diamonds) and 60 nK (magenta stars), and coupling strength  $g = 0.26$ . Mean-field expectations for normal gas (dashed line) and superfluid (solid line) are shown for comparison. Inset, radial density profiles before scaling. **b**, Scaled fluctuation  $\delta\tilde{n}^2 = \delta n^2 \lambda_{dB}^4$  at different temperatures. Dashed line is the mean-field calculation based on the fluctuation-dissipation theorem<sup>25</sup>. Solid line is an empirical fit to the crossover feature from which the critical chemical potential  $\tilde{\mu}_c$  is determined. Inset, radial fluctuation profiles before scaling. The shaded area marks the fluctuation region  $0 < \tilde{\mu} < \tilde{\mu}_c$ . Error bars, s.d. of the measurement.

We obtain the equation of state  $n(\mu, T)$  from the averaged density profile by assigning a local chemical potential  $\mu(r) = \mu_0 - V(r, 0)$  to each point according to the local density approximation. Both  $T$  and  $\mu_0$  can be determined from the low density wing where the sample is assumed normal and the density profile can be fitted to a mean-field formula  $n(\mu, T) = -\lambda_{dB}^{-2} \ln[1 - \exp(\mu/k_B T - gn\lambda_{dB}^2/\pi)]$  (ref. 9), where  $\lambda_{dB} = h/\sqrt{2\pi mk_B T}$  is the thermal de Broglie wavelength.

We confirm the scale invariance of a 2D gas by first introducing the dimensionless, scaled forms of density  $\tilde{n} = n\lambda_{dB}^2$  (phase space density), fluctuation  $\delta\tilde{n}^2 = \delta n^2 \lambda_{dB}^4$ , and chemical potential  $\tilde{\mu} = \mu/k_B T$ , and showing that the equation of state and the fluctuation satisfy the following forms:

$$\tilde{n} = F(\tilde{\mu}) \quad (1)$$

$$\delta\tilde{n}^2 = G(\tilde{\mu}) \quad (2)$$

where  $F$  and  $G$  are generic functions. This suggests that both energy and length scales are set solely by the thermal energy and the de Broglie wavelength, respectively. An example at  $g = 0.26$  ( $a = 10$  nm) is shown in Fig. 2. Here we show that while the original density and fluctuation profiles are temperature dependent (Fig. 2 insets), all profiles collapse to a single curve in the scaled units. At negative chemical potential  $\tilde{\mu} < 0$ , the system is normal and can be described by a mean-field model (dashed lines). In the range  $0 < \tilde{\mu} < 0.3$ , the system enters the fluctuation regime and deviation from the mean-field calculation becomes evident. Crossing from normal gas to this regime, however, we do not observe a

sharp transition feature in the equation of state. At even higher  $\tilde{\mu} > 0.3$ , the system becomes a superfluid and the density closely follows a mean-field prediction<sup>12</sup>  $\tilde{n} = 2\pi\tilde{\mu}/g + \ln(2\tilde{n}g/\pi - 2\tilde{\mu})$ . We notice that the mean-field theory in the superfluid limit cannot also accurately describe the system in the fluctuation regime. Transition into the BKT superfluid phase is most easily seen in the scaled fluctuation  $\delta\tilde{n}^2$ , which crosses over to a nearly constant value due to the suppression of fluctuation in the superfluid regime<sup>20</sup>. In the density profile  $\tilde{n}$ , a corresponding transition feature can be found when one computes the derivative  $\partial\tilde{n}/\partial\tilde{\mu}$ , that is, the scaled compressibility  $\tilde{\kappa}$ , as suggested by the fluctuation-dissipation theorem discussed below. Finally, our measurement suggests that the validity of scale invariance extends to all thermal, fluctuation and superfluid regimes, a special feature of weakly interacting 2D gases<sup>4</sup> which underlies the analysis of a recent experiment<sup>21</sup>.

We associate the crossover feature in the density fluctuations  $\delta\tilde{n}^2$  and the scaled compressibility  $\tilde{\kappa}$  with the BKT transition<sup>20,22</sup>. To estimate the location of the transition point, we apply an empirical fit to this feature and determine the critical chemical potential  $\tilde{\mu}_c$  and the critical phase space density  $\tilde{n}_c$  (Online Methods). Results at different values of  $g$  in the range 0.05 to 0.26 are shown in Fig. 3c, d and compared to the theoretical prediction of  $\tilde{n}_c = \ln(\xi/g)$  and  $\tilde{\mu}_c = (g/\pi) \ln(\xi_\mu/g)$  (ref. 23), where  $\xi = 380$  and  $\xi_\mu = 13.2$  are determined from a classical-field Monte Carlo calculation<sup>11</sup>. Our results show good agreement with the theory, apart from a potential systematic error from the choice of the fit function, which can account for a down shift of 10% in the fitted values of  $\tilde{\mu}_c$  and  $\tilde{n}_c$ .

Further comparison between profiles at different interaction strengths allows us to test the universality of 2D Bose gases. Sufficiently close to the BKT critical point with  $|\tilde{\mu} - \tilde{\mu}_c| < g$ , one expects the phase space density to show a universal behaviour<sup>12</sup>:

$$\tilde{n} - \tilde{n}_c = H\left(\frac{\tilde{\mu} - \tilde{\mu}_c}{g}\right) \quad (3)$$

where  $H$  is a generic function. Here, density and chemical potential are offset from the critical values  $\tilde{n}_c$  and  $\tilde{\mu}_c$ , which remove the non-universal dependence on the microscopic details of the interaction<sup>12,14</sup>.

To test the universality hypothesis, we rescale  $\tilde{\mu}$  to  $\tilde{\mu}/g$  and look for critical values  $\tilde{n}_c$  and  $\tilde{\mu}_c$  such that the equations of state at all values of  $g$  display a universal curve in the phase transition regime (Online Methods). Indeed, we find that all rescaled profiles can collapse to a single curve in the fluctuation region  $-1 < (\tilde{\mu} - \tilde{\mu}_c)/g < 0$  and remain overlapped in an extended range of  $|\tilde{\mu} - \tilde{\mu}_c|/g \leq 2$  (Fig. 3a), which contrasts with the very different equations of state  $\tilde{n}(\tilde{\mu})$  at various  $g$  shown in the inset of Fig. 3a. Our result closely follows the classical-field prediction<sup>12</sup> and quantum Monte Carlo calculations<sup>13</sup> assuming a strictly 2D mean-field contribution; and the fitting parameters (critical density  $\tilde{n}_c$  and chemical potential  $\tilde{\mu}_c$ ) show proper dependence on  $g$  and are in fair agreement with the prediction of theory<sup>11</sup> (Fig. 3c, d). We emphasize that critical values determined from the density fluctuations (Fig. 3c, d) match well with those determined from the universal behaviour, indicating that universality is a powerful tool to determine the critical point from a continuous and smooth density profile. Similar agreement with the theory of critical densities has also been reported on the basis of different experiment techniques<sup>6,8,10</sup>.

Further universal features near the phase transition can be revealed in the growth of the quasi-condensate density  $n_q = \sqrt{n^2 - \delta n^2}$  across the phase transition<sup>11,12,24</sup>. The quasi-condensate density is a measure of the non-thermal population in a degenerate Bose gas. A finite quasi-condensate density does not necessarily imply superfluidity, but can be responsible for a non-Gaussian distribution observed in momentum space<sup>8</sup>. The quasi-condensate density is predicted to be universal near the critical point, following<sup>12</sup>

$$\tilde{n}_q = Q\left(\frac{\tilde{\mu} - \tilde{\mu}_c}{g}\right) \quad (4)$$

where  $Q$  is a generic function and  $\tilde{n}_q = n_q \lambda_{dB}^2$ .

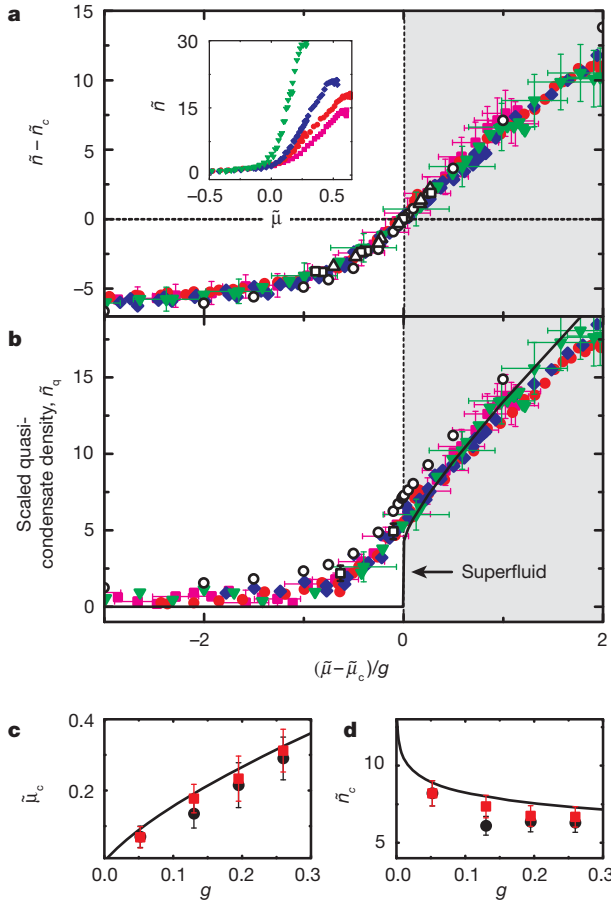


**Figure 3 | Universal behaviour near the BKT critical point.** **a**, Rescaled density profiles  $\tilde{n} - \tilde{n}_c$  measured at various coupling strengths,  $g = 0.05$  (filled green triangles),  $0.13$  (blue diamonds),  $0.19$  (red circles) and  $0.26$  (magenta squares). Inset, original equations of state,  $\tilde{n}(\tilde{\mu})$ . **b**, Scaled quasi-condensate density  $\tilde{n}_q = \sqrt{\tilde{n}^2 - \delta\tilde{n}^2}$  at different interaction strengths. In both plots, Monte Carlo calculations from ref. 12 (open circles) and ref. 13 (**a**, open squares for  $g = 0.07$  and open triangles for  $g = 0.14$ ; **b**, open squares) are plotted for comparison. The shaded area marks the superfluid regime and the solid line in **b** shows the superfluid phase space density calculation<sup>12</sup>. **c**, **d**, Critical values  $\tilde{\mu}_c$  and  $\tilde{n}_c$  determined from the following methods: universal scaling as shown in **a** (see Online Methods; red squares), density fluctuation crossover (see text; black circles), and Monte Carlo calculations from ref. 11 (solid line). Experiment values coincide at  $g = 0.05$  identically, as a result of our analysis (Online Methods). Error bars, s.d. of the measurement.

We use both our density and our fluctuation measurements to evaluate  $\tilde{n}_q$  at various  $g$ . Adopting  $\tilde{\mu}_c$  determined from the universal behaviour of the density profile, we immediately find that all measurements collapse to a single curve in the range  $|\tilde{\mu} - \tilde{\mu}_c|/g \leq 2$  with apparent growth of quasi-condensate density entering the fluctuation region (Fig. 3b). The generic function  $Q$  we determined is in good agreement with the classical-field<sup>12</sup> and quantum Monte Carlo<sup>13</sup> calculations with no fitting parameters. Both our density and fluctuation measurements show universal behaviours throughout the fluctuation region where a mean-field description fails, and confirm universality in a 2D Bose gas near the BKT phase transition<sup>12,13</sup>.

The generic functions we describe above offer new avenues to investigate the critical behaviour of the 2D gas. Following the framework of scale invariance, we compare the dimensionless compressibility  $\tilde{\kappa} = \partial\tilde{n}/\partial\tilde{\mu} = F'(\tilde{\mu})$  and the fluctuation  $\delta\tilde{n}^2 = G(\tilde{\mu})$  extracted from the measurements at  $g = 0.05$  and  $0.26$  (Fig. 4). In the normal gas regime at low phase space density ( $G(\tilde{\mu}), F'(\tilde{\mu}) < 3$ ), a simple equality  $G = F'$  is observed. This result is consistent with the fluctuation-dissipation theorem for a classical grand canonical ensemble<sup>25</sup>, which gives  $k_B T \frac{\partial N}{\partial \mu} = \delta N^2$ , where  $N$  is the particle number in a detection cell.

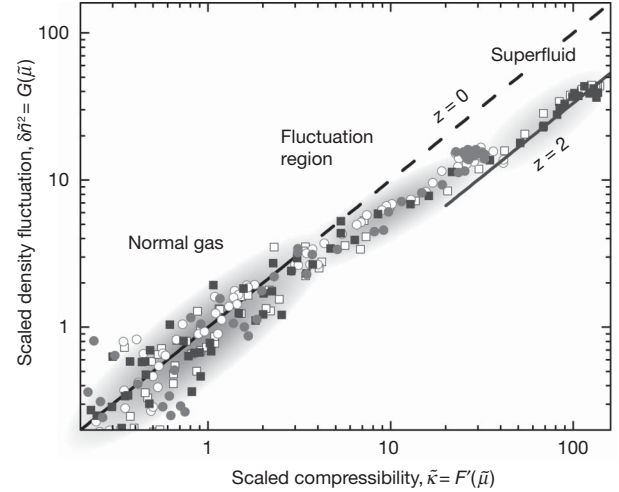


**Figure 4 | Fluctuation versus compressibility.** Scaled compressibility  $\tilde{\kappa} = F'(\tilde{\mu})$  and scaled density fluctuation  $\delta\tilde{n}^2 = G(\tilde{\mu})$  are derived from measurements at two interaction strengths,  $g = 0.05$  (squares) and  $g = 0.26$  (circles), each containing two different temperatures between 20 and 40 nK (filled and open symbols, respectively). Diagonal line shows the expectation of  $G = F'$  in the normal gas region. Solid line shows suppressed fluctuation  $G = F'/(1+z)$  with  $z = 2$ . The grey shaded areas mark the normal (left), fluctuation (middle) and superfluid (right) regimes.

In the fluctuation and the superfluid regimes at higher phase space density, our measurement shows that density fluctuations drop below the compressibility,  $G < F'$ .

Natural explanations for the observed deviation include non-vanishing dynamic density susceptibility at low temperature<sup>26</sup> and the emergence of correlations in the fluctuation region<sup>27</sup>. While the former explanation is outside the scope of this Letter, we show that the correlation alone can explain our observation. Including correlation, the compressibility conforms to<sup>27,28</sup>:

$$\tilde{\kappa}(\mathbf{r}) = \lambda_{\text{dB}}^{-2} \int \langle \delta\tilde{n}(\mathbf{r}) \delta\tilde{n}(\mathbf{r}') \rangle d^2 r' \quad (5)$$

$$= \delta\tilde{n}^2(\mathbf{r})(1+z) \quad (6)$$

where  $\langle \dots \rangle$  denotes ensemble average and  $z = \frac{1 + n(\mathbf{r}) \int [g^{(2)}(\mathbf{r}, \mathbf{r}') - 1] d^2 r'}{\int [g^{(2)}(\mathbf{r}, \mathbf{r}') - 1] d^2 r'}$  is the relative strength of correlation to local fluctuation  $\delta\tilde{n}^2$  (ref. 27). Here  $g^{(2)}$  is the normalized second-order correlation function<sup>29</sup> and  $\nu$  denotes the effective area of the resolution limited spot. When the sample is uncorrelated, we have  $z = 0$ ; non-zero  $z$  suggests finite correlations in the sample. In the fluctuation region shown in Fig. 4, observing a lower fluctuation than would be indicated by the compressibility, with  $z$  approaching 2, suggests that the correlation length approaches or even exceeds our imaging cell dimension,  $\sqrt{\nu} \approx 2 \mu\text{m}$ . This observation is in agreement with the expected growth of correlation when the system enters the fluctuation region. Similar length scales were also observed in the first-order coherence near the BKT phase transition using an interferometric method<sup>8</sup> and near the superfluid phase transition in three dimensions<sup>30</sup>.

In summary, based on *in situ* density measurements at different chemical potential, temperature and scattering length, we have explored and confirmed the global scale invariance of a weakly interacting 2D gas, as well as the universal behaviour near the critical point. Our results provide a detailed description of critical thermodynamics near the BKT transition, and offer new opportunities to investigate other critical phenomena near classical or quantum phase transitions. In particular, we present experimental evidence of the growing correlations in the fluctuation region through the application of the fluctuation-dissipation theorem. Further investigations into the correlations will provide

new insights into the rich critical phenomena near the transition point—for instance, critical opalescence and critical slowing.

## METHODS SUMMARY

Preparation and detection of caesium 2D Bose gases are similar to those described in ref. 18. We adjust the temperature of the sample by applying magnetic field pulses near a Feshbach resonance to excite the atoms. We then tune the scattering length to a designated value, followed by 800-ms wait time to ensure full thermalization of the sample.

Absorption imaging is performed *in situ* using a strong resonant laser beam, saturating the sample to reduce the optical thickness. Atom–photon resonant cross-section and atomic density are independently calibrated. Averaged atom number  $N_i$  and number fluctuation  $\delta N_i^2$  at the  $i$ th CCD pixel are evaluated pixel-wise based on images taken under identical experiment conditions. The photon shot-noise, weakly depending on the sample's optical thickness, is calibrated and removed from the measured number variance. We correct for the effect of finite imaging resolution on the remaining number variance using calibration from dilute thermal gas measurements. The density fluctuation  $\delta n_i^2$  is obtained from the recovered atom number variance using  $\delta n_i^2 \lambda_{\text{dB}}^2 = \delta N_i^2 / A$ , which replaces the dependence on the CCD pixel area  $A$  by a proper area scale  $\lambda_{\text{dB}}^2$  (details in Online Methods).

**Full Methods** and any associated references are available in the online version of the paper at [www.nature.com/nature](http://www.nature.com/nature).

Received 10 September; accepted 1 December 2010.

Published online 26 January 2011.

1. Stanley, H. E. Scaling, universality, and renormalization: three pillars of modern critical phenomena. *Rev. Mod. Phys.* **71**, S358–S366 (1999).
2. Berezinskii, V. L. Destruction of long-range order in one-dimensional and two-dimensional systems possessing a continuous symmetry group — II. Quantum systems. *Sov. Phys. JETP* **34**, 610–616 (1972).
3. Kosterlitz, J. M. & Thouless, D. J. Ordering, metastability and phase-transitions in 2 dimensional systems. *J. Phys. Chem.* **6**, 1181–1203 (1973).
4. Pitaevskii, L. P. & Rosch, A. Breathing modes and hidden symmetry of trapped atoms in two dimensions. *Phys. Rev. A* **55**, R853–R856 (1997).
5. Hadzibabic, Z., Krüger, P., Cheneau, M., Battelier, B. & Dalibard, J. Berezinskii-Kosterlitz-Thouless crossover in a trapped atomic gas. *Nature* **441**, 1118–1121 (2006).
6. Krüger, P., Hadzibabic, Z. & Dalibard, J. Critical point of an interacting two-dimensional atomic Bose gas. *Phys. Rev. Lett.* **99**, 040402 (2007).
7. Schweikhard, V., Tung, S. & Cornell, E. A. Vortex proliferation in the Berezinskii-Kosterlitz-Thouless regime on a two-dimensional lattice of Bose-Einstein condensates. *Phys. Rev. Lett.* **99**, 030401 (2007).
8. Cladé, P., Ryu, C., Ramanathan, A., Helmerson, K. & Phillips, W. D. Observation of a 2D Bose gas: from thermal to quasicondensate to superfluid. *Phys. Rev. Lett.* **102**, 170401 (2009).
9. Hadzibabic, Z., Krüger, P., Cheneau, M., Rath, S. P. & Dalibard, J. The trapped two-dimensional Bose gas: from Bose-Einstein condensation to Berezinskii-Kosterlitz-Thouless physics. *N. J. Phys.* **10**, 045006 (2008).
10. Tung, S., Lamporesi, G., Lobser, D., Xia, L. & Cornell, E. A. Observation of the pre-superfluid regime in a two-dimensional Bose gas. *Phys. Rev. Lett.* **105**, 230408 (2010).

11. Prokof'ev, N., Ruebenacker, O. & Svistunov, B. Critical point of a weakly interacting two-dimensional Bose gas. *Phys. Rev. Lett.* **87**, 270402 (2001).
12. Prokof'ev, N. & Svistunov, B. Two-dimensional weakly interacting Bose gas in the fluctuation region. *Phys. Rev. A* **66**, 043608 (2002).
13. Holzmann, M., Chevallier, M. & Krauth, W. Universal correlations and coherence in quasi-two-dimensional trapped Bose gases. *Phys. Rev. A* **81**, 043622 (2010).
14. Holzmann, M., Baym, G., Blaizot, J.-P. & Laloë, F. Superfluid transition of homogeneous and trapped two-dimensional Bose gases. *Proc. Natl Acad. Sci. USA* **104**, 1476–1481 (2007).
15. Petrov, D. S., Holzmann, M. & Shlyapnikov, G. V. Bose-Einstein condensation in quasi-2D trapped gases. *Phys. Rev. Lett.* **84**, 2551–2555 (2000).
16. Chin, C., Grimm, R., Julienne, P. & Tiesinga, E. Feshbach resonances in ultracold gases. *Rev. Mod. Phys.* **82**, 1225–1286 (2010).
17. Gemelke, N., Zhang, X., Hung, C.-L. & Chin, C. *In situ* observation of incompressible Mott-insulating domains in ultracold atomic gases. *Nature* **460**, 995–998 (2009).
18. Hung, C.-L., Zhang, X., Gemelke, N. & Chin, C. Slow mass transport and statistical evolution of an atomic gas across the superfluid-Mott insulator transition. *Phys. Rev. Lett.* **104**, 160403 (2010).
19. Mora, C. & Castin, Y. Ground state energy of the two-dimensional weakly interacting Bose gas: first correction beyond Bogoliubov theory. *Phys. Rev. Lett.* **102**, 180404 (2009).
20. Simula, T. P., Davis, M. J. & Blakie, P. B. Superfluidity of an interacting trapped quasi-two-dimensional Bose gas. *Phys. Rev. A* **77**, 023618 (2008).
21. Rath, S. P. *et al.* Equilibrium state of a trapped two-dimensional Bose gas. *Phys. Rev. A* **82**, 013609 (2010).
22. Holzmann, M. & Krauth, W. Kosterlitz-Thouless transition of the quasi-two-dimensional trapped Bose gas. *Phys. Rev. Lett.* **100**, 190402 (2008).
23. Popov, V. N. *Functional Integrals in Quantum Field Theory and Statistical Physics* (Reidel, 1983).
24. Bisset, R. N., Davis, M. J., Simula, T. P. & Blakie, P. B. Quasicondensation and coherence in the quasi-two-dimensional trapped Bose gas. *Phys. Rev. A* **79**, 033626 (2009).
25. Huang, K. *Statistical Mechanics* 152–154 (Wiley, 1963).
26. Kubo, R. The fluctuation-dissipation theorem. *Rep. Prog. Phys.* **29**, 255–283 (1966).
27. Toda, M., Kubo, R. & Saitô, N. *Statistical Physics I: Equilibrium Statistical Mechanics* (Springer, 1983).
28. Zhou, Q. & Ho, T.-L. Universal thermometry for quantum simulation. Preprint at <http://arXiv.org/abs/0908.3015v2> (2009).
29. Naraschewski, M. & Glauber, R. J. Spatial coherence and density correlations of trapped Bose gases. *Phys. Rev. A* **59**, 4595–4607 (1999).
30. Donner, T. *et al.* Critical behavior of a trapped interacting Bose gas. *Science* **315**, 1556–1558 (2007).

**Acknowledgements** We thank Q. Zhou, B. Svistunov, T.-L. Ho, Y. Castin, C.-C. Chien, S. Tung, N. Prokof'ev, J. Freerick and D.-W. Wang for discussions. This work was supported by the NSF (grant numbers PHY-0747907, NSF-MRSEC DMR-0213745), the Packard Foundation, and a grant from the Army Research Office with funding from the DARPA OLE program. N.G. acknowledges support from the Grainger Foundation.

**Author Contributions** The data were taken and analysed by C.-L.H. The experimental concept was developed by C.-L.H. and C.C. All authors contributed to discussion of the results and preparation of the manuscript.

**Author Information** Reprints and permissions information is available at [www.nature.com/reprints](http://www.nature.com/reprints). The authors declare no competing financial interests. Readers are welcome to comment on the online version of this article at [www.nature.com/nature](http://www.nature.com/nature). Correspondence and requests for materials should be addressed to C.-L.H. ([clhung@uchicago.edu](mailto:clhung@uchicago.edu)).

## METHODS

### Calibration of the atomic surface density and the atom number fluctuation.

Detection of caesium 2D Bose gases is detailed in ref. 18 and the atomic surface density  $n$  is evaluated with schemes similar to those discussed elsewhere<sup>31</sup>, where the resonant cross-section  $\sigma_0$  is independently calibrated using a thin 3D Bose condensate with similar optical thickness and the known atom number-to-Thomas-Fermi radius conversion. The calibrated value of  $\sigma_0$  can be compared to that determined from the atom shot-noise amplitude in dilute 2D thermal gases, where the noise is evaluated using binned CCD pixels to remove finite resolution effects. For dilute thermal gases, we expect  $\delta N^2 = N$ , where  $N$  is the mean atom number; we compare the fluctuation amplitude to the mean and extract the value of  $\sigma_0$ . Two results agree to within 10% and the residual nonlinearity in the density calibration is negligible.

We evaluate the atom number variance  $\delta N^2$  pixel-wise based on images taken under identical experiment conditions. The photon shot-noise contribution  $\delta N_p^2$ , which weakly depends on the sample's optical thickness  $n\sigma_0$ , is calibrated and removed from the atom number fluctuation using  $\delta N_p^2 = (\delta N_0^2/2)[1 + \frac{(1+\gamma)e^{-n\sigma_0}}{(1+\gamma)^2}e^{n\sigma_0}]$ , where  $\delta N_0^2$  is the photon shot-noise without atoms and  $\gamma$  is the ratio of the imaging beam intensity to the saturation intensity. Both  $\delta N_0^2$  and  $\gamma$  are experimentally calibrated. We then correct for the effect of finite resolution on the number fluctuation<sup>17</sup> by comparing the atom number variance in a dilute thermal cloud to its mean atom number, using  $\delta N^2 = N$ , and applying this calibration to all fluctuations measured at lower temperatures and higher densities.

**Density–density correlation in the fluctuation measurement.** In the fluctuation measurement, we determine  $\delta n^2$  from the pixel-wise atom number variance using the formula  $\delta n^2 \lambda_{dB}^2 = \delta N^2 / A$ , which replaces the dependence on the pixel area  $A$  by a natural area scale  $\lambda_{dB}^2$ . This definition, however, does not fully eliminate the dependence on the imaging resolution spot size  $\nu \approx (2 \mu\text{m})^2$ . In particular, when the density–density correlation length  $\xi$  approaches or exceeds the resolution, the measured fluctuation can depend on the fixed length scale  $\sqrt{\nu}$ , which can complicate

the scaling behaviour. However, we do not see clear deviation of scale invariance and universality within our measurement uncertainties (Figs 2b and 3b). We attribute this to the small variation of the non-scale-invariant contribution within our limited range of sample temperature. Further analysis of the correlations and fluctuations is in progress and the result will be published elsewhere.

**Determination of the BKT critical values from the fluctuation data.** We use a hyperbolic function  $y(\tilde{\mu}) = s(\tilde{\mu} - \tilde{\mu}_c) - \sqrt{s^2(\tilde{\mu} - \tilde{\mu}_c)^2 + w^2}$  to empirically fit the crossover feature of the density fluctuation near the transition region, assuming  $\delta \tilde{n}^2(\tilde{\mu}) = D e^{y(\tilde{\mu})}$ , where the critical chemical potential  $\tilde{\mu}_c$ , the fluctuation in the superfluid regime  $D$ , the slope of the exponential rise  $s$ , and the width of the transition region  $w$  are fitting parameters. The critical phase space density is then determined from the density profile as  $\tilde{n}_c = \tilde{n}(\tilde{\mu}_c)$ . Other choices of fit functions give similar results, contributing only small systematics from the choice of different models.

**Obtaining the universal function.**  $H(x)$ : we use the density profiles in the inset of Fig. 3a to look for critical values  $\tilde{n}_c$  and  $\tilde{\mu}_c$  such that the equations of state at all values of  $g$  collapse to a single universal curve  $H(x) = \tilde{n}(\tilde{\mu}) - \tilde{n}_c$ , where  $x = (\tilde{\mu} - \tilde{\mu}_c)/g$  is the rescaled chemical potential. To do this, we take the profile measured at  $g = 0.05 \equiv g_r$  as the reference, evaluate  $H_r(x) = \tilde{n}(g_r x + \tilde{\mu}_{c,r}) - \tilde{n}_{c,r}$  using the critical values  $\tilde{n}_{c,r}$  and  $\tilde{\mu}_{c,r}$  determined from the fluctuation crossover feature, and smoothly interpolate the data to make a continuous reference curve  $H_r(x)$  in the range of  $|x| \leq 1$ . Using this model, we perform minimum  $\chi^2$  fits to the profiles measured at all other values of  $g$  according to  $\tilde{n}(\tilde{\mu}) = \tilde{n}_c + H_r(\frac{\tilde{\mu} - \tilde{\mu}_c}{g})$ , with only  $\tilde{n}_c$  and  $\tilde{\mu}_c$  as free parameters. This procedure successfully collapses all density profiles (see Fig. 3a), and is independent of any theoretical model. The resulting critical values  $\tilde{n}_c$  and  $\tilde{\mu}_c$  are plotted in Fig. 3c, d.

31. Reinaudi, G., Lahaye, T., Wang, Z. & Guéry-Odelin, D. Strong saturation absorption imaging of dense clouds of ultracold atoms. *Opt. Lett.* **32**, 3143–3145 (2007).

# Cell-type-specific replication initiation programs set fragility of the *FRA3B* fragile site

Anne Letessier<sup>1,2,3</sup>, Gaël A. Millot<sup>1,2,3</sup>, Stéphane Koundrioukoff<sup>1,2,3\*</sup>, Anne-Marie Lachagès<sup>1,2,3\*</sup>, Nicolas Vogt<sup>1,2,3\*</sup>, R. Scott Hansen<sup>4</sup>, Bernard Malfoy<sup>1,2,3</sup>, Olivier Brison<sup>1,2,3</sup> & Michelle Debatisse<sup>1,2,3</sup>

Common fragile sites have long been identified by cytogeneticists as chromosomal regions prone to breakage upon replication stress<sup>1</sup>. They are increasingly recognized to be preferential targets for oncogene-induced DNA damage in pre-neoplastic lesions<sup>2</sup> and hotspots for chromosomal rearrangements in various cancers<sup>3</sup>. Common fragile site instability was attributed to the fact that they contain sequences prone to form secondary structures that may impair replication fork movement, possibly leading to fork collapse resulting in DNA breaks<sup>4</sup>. Here we show, in contrast to this view, that the fragility of *FRA3B*—the most active common fragile site in human lymphocytes—does not rely on fork slowing or stalling but on a paucity of initiation events. Indeed, in lymphoblastoid cells, but not in fibroblasts, initiation events are excluded from a *FRA3B* core extending approximately 700 kilobases, which forces forks coming from flanking regions to cover long distances in order to complete replication. We also show that origins of the flanking regions fire in mid-S phase, leaving the site incompletely replicated upon fork slowing. Notably, *FRA3B* instability is specific to cells showing this particular initiation pattern. The fact that both origin setting<sup>5,6</sup> and replication timing are highly plastic<sup>7,8</sup> in mammalian cells explains the tissue specificity of common fragile site instability we observed. Thus, we propose that common fragile sites correspond to the latest initiation-poor regions to complete replication in a given cell type. For historical reasons, common fragile sites have been essentially mapped in lymphocytes<sup>1</sup>. Therefore, common fragile site contribution to chromosomal rearrangements in tumours should be reassessed after mapping fragile sites in the cell type from which each tumour originates.

Replication forks commonly face sequences intrinsically difficult to replicate such as natural pause sites<sup>9,10</sup>. Various observations have indicated that the sequence of common fragile sites may also constitute a challenge to fork movement. For example, it has been shown that replication is more delayed along common fragile sites than in the rest of the genome following treatment with aphidicolin<sup>11</sup>, a DNA polymerase inhibitor, and that the nucleotide sequences of common fragile sites contain subregions with the potential to form secondary structures<sup>4</sup>. Hence, it was suggested that helicases tend to travel uncoupled from polymerases in common fragile sites, giving rise to long stretches of single-stranded DNA (ssDNA) upon replication stress. In subregions able to adopt secondary structures, ssDNA formed ahead of polymerases may evolve into fork barriers that cause DNA breaks<sup>11</sup>. However, genome-wide analyses have not confirmed that common fragile sites are specifically enriched in sequences prone to form secondary structures<sup>12,13</sup>, and a recent study of the replication dynamics along *FRA6E* did not show fork slowing along the site<sup>14</sup>. The mechanism(s) involved in common fragile site instability thus have remained ill-defined.

We focused on *FRA3B*, the most active common fragile site in human lymphocytes. It overlaps the 1.5-Mb-long *FHIT* (fragile histidine triad)

tumour suppressor gene<sup>15,16</sup>, wherein lies the most fragile subregion of the site. To elucidate the molecular basis of *FRA3B* fragility, we analysed cells pulse-labelled successively with iododeoxyuridine (IdU) and then chlorodeoxyuridine (CldU), two thymidine analogues. We combined the DNA-combing technique with fluorescent detection of newly synthesized DNA and fluorescence *in situ* hybridization (FISH) with probes allowing identification of a 1.6-Mb-long region overlapping the *FHIT* gene (referred to as the *FHIT* locus) (see Methods, Supplementary Figs 1, 2 and Supplementary Table 1). This procedure permitted us to determine replication-fork speed, to search for potential fork stalling, and to map initiation and termination events along this large single-copy sequence (Supplementary Fig. 1).

We studied Epstein-Barr-virus-immortalized human B lymphocytes (JEFF cells) (Supplementary Fig. 3), a cell type that shows a high frequency of breaks at *FRA3B* upon aphidicolin treatment (see later). We compared fork speeds along the *FHIT* locus and in the bulk genome in untreated and aphidicolin-treated cells (Fig. 1a). Statistical analyses show that differences found between treated and untreated cells are significant but not those between the locus and the bulk genome, regardless of the growth conditions. Fork speeds seem to be very heterogeneous along the locus, a phenomenon previously observed in a non-fragile region studied by molecular combing<sup>17</sup>. Plotting the speed of each fork as a function of its position along the locus shows that slow forks do not cluster in any particular subregion (Supplementary Fig. 4), which together indicates that the *FHIT* locus is not a mammalian equivalent of the slow-replicating zones described in yeast cells<sup>18</sup>.

Next we asked whether forks stall along the *FHIT* locus as they do at programmed pause sites in prokaryotes and yeasts<sup>19</sup>. Stalling should lead to asymmetrical forks, namely to individual forks presenting unequal IdU and CldU tracks (see Methods and Supplementary Fig. 1b). Therefore, we calculated asymmetry as the ratio of the longest to the shortest track (Fig. 1b). We found that fork asymmetry increases significantly upon aphidicolin treatment but, again, no differences were found between the locus and the bulk genome regardless of the growth conditions. Moreover, in untreated and aphidicolin-treated cells we found 9 and 22 forks along the locus, respectively, that have an asymmetry factor greater than or equal to 1.5. The mapping of these forks shows that they are evenly distributed (Fig. 1c). Lastly, mapping of all the forks—asymmetrical or not—travelling along the locus showed that no accumulation in particular subregions occurs in either untreated or aphidicolin-treated cells (Supplementary Fig. 5). Thus, forks do not specifically stall along the *FHIT* locus.

We then studied the distribution of initiation and termination events along the locus in untreated cells (Fig. 2a and Supplementary Fig. 1b). Notably, no initiation event maps to within an approximately 700-kb-long region (referred to as the *FRA3B* core) centred on exon 5. In contrast, ten and eight initiation events, respectively, take place in each of the approximately 500-kb-long regions flanking the core. Statistical analysis indicates that the deficit in initiation events in the core is

<sup>1</sup>Institut Curie, Centre de Recherche, 26 rue d'Ulm, 75248 Paris, France. <sup>2</sup>UPMC Univ. Paris 06, F-75005 Paris, France. <sup>3</sup>CNRS UMR 3244, F-75248 Paris, France. <sup>4</sup>Department of Medicine, Division of Medical Genetics, University of Washington School of Medicine, Seattle, Washington 98195, USA.

\* These authors contributed equally to this work.

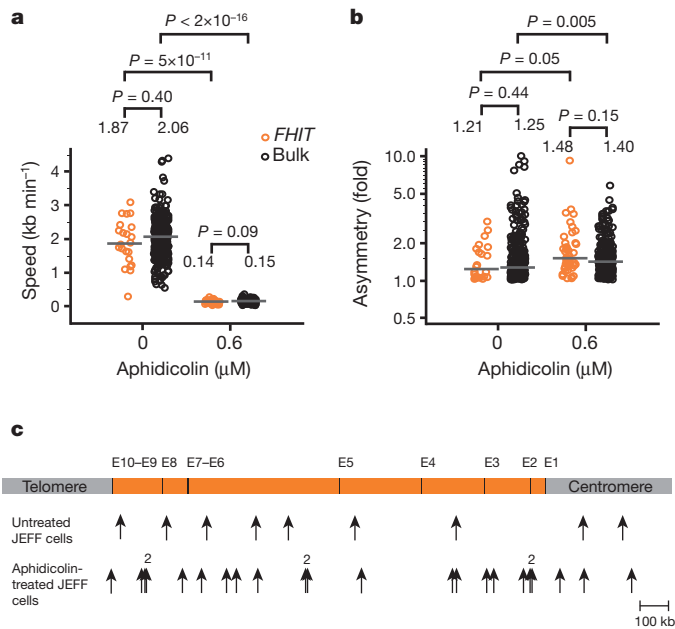


**Figure 1 | Comparison of fork properties in the *FHIT* locus and in the bulk genome in JEFF cells. a, b**, Distributions of fork speed (a) and fork asymmetry (b). Only non-truncated forks (see Supplementary Fig. 1) as determined by DNA counterstaining (see Supplementary Fig. 2) were recorded. Forks travelling in the locus are represented by orange circles (0 μM aphidicolin,  $n = 22$ ; 0.6 μM aphidicolin,  $n = 44$ ) and in the bulk genome by black circles (0 μM aphidicolin,  $n = 283$ ; 0.6 μM aphidicolin,  $n = 216$ ). Horizontal grey lines represent the medians of fork distributions. Medians and  $P$  values are indicated above the distributions. **c**, Upper panel shows *FHIT* gene (orange box) with its exons (E1 to E10). Arrows indicate position of forks with an asymmetry factor greater than or equal to 1.5 (0 μM aphidicolin,  $n = 9$ ; 0.6 μM aphidicolin,  $n = 22$ ). The number above some arrows indicates colocalized forks.

significant (see Methods). Large regions devoid of initiation events have been recently associated with transition zones separating domains with different replication timings. Long-travelling forks move unidirectionally along these zones, from the earliest to the latest domain, leading to progressive establishment of replication delays<sup>7,8,20</sup>. In contrast, forks travel in both directions within the *FRA3B* core (Supplementary Fig. 3) and termination events appear evenly distributed along the entire locus (Fig. 2a). Thus, in most cells, converging forks that emanate from each flanking region merge in the core, indicating that the *FHIT* locus is not a classical transition region.

We also mapped the initiation and termination events along the *FHIT* locus in aphidicolin-treated cells (Fig. 2b). We observed 23 initiation events, the distribution of which confirms the paucity of these events in the core. Despite a lower coverage of the locus the number of initiation events we observed in flanking regions seems comparable to that in untreated cells. Slowing replication speed thus triggers the recruitment of latent origins in flanking regions, as previously observed at other loci<sup>21,22</sup>. In addition, comparable levels of recruitment were observed in flanking regions and in the bulk genome (Supplementary Table 2). Notably, an approximately 900-kb-long region overlapping the core was devoid of any termination events. This deficit is not explained by preferential breakage of fibres bearing X-shaped structures in aphidicolin-treated cells because the density of termination remains normal in flanking regions. Instead, with complete replication of the core taking about 40 h with fork speed decreased to 0.14 kb min<sup>-1</sup>, terminations could occur only in cells that were close to completing replication when aphidicolin was added.

These results indicate that a paucity of initiation events contributes to fragility, which is in line with previous reports showing that the frequency of chromosome rearrangements increases in yeast mutants showing reduced replication-origin efficiencies<sup>23</sup>. In addition, a paucity

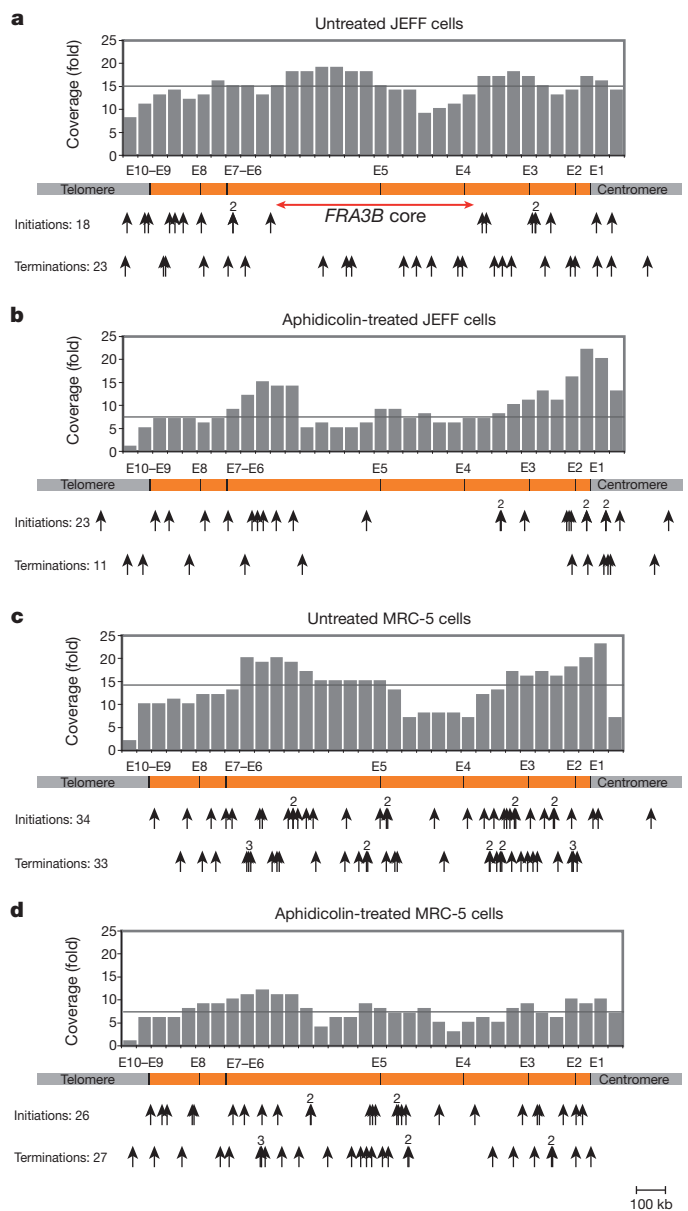


**Figure 2 | Mapping of initiation and termination events along the *FHIT* locus. a–d**, Untreated (a) and aphidicolin-treated (b) JEFF cells and untreated (c) and aphidicolin-treated (d) MRC-5 cells. Upper panels show histograms showing the coverage of the locus per 50-kb window. Each bar represents the number of fibres fully overlapping the corresponding sequence. Horizontal grey lines represent the medians of coverage. Middle panels are as in Fig. 1c. Lower panels, arrows indicate the position of initiation and termination events. The number above some arrows indicates colocalized events. The total number of events observed is indicated on the left.

of initiation events accounts for the *FRA3B* properties reported in the literature, as follows. Firstly, late replication completion, even in cells that go unperturbed through S phase<sup>24,25</sup>, may be due to the long distances that forks coming from flanking regions have to cover before merging. The abnormally long delay to complete replication upon aphidicolin treatment<sup>25</sup> is easily explained by the fact that slowing down fork movement affects long-travelling forks more profoundly than forks that need to cover only short distances. Secondly, increased instability upon inactivation of ATR, which stabilizes stalled forks, has been considered to support the fork barrier hypothesis<sup>11</sup>. Instead, polymerases travelling across long distances may need to be stabilized, notably upon replication stress. Lastly, reduced fragility in cells bearing deletions in the *FHIT* gene has been attributed to removal of sequences

prone to form secondary structures<sup>26</sup>. Alternatively, reducing the size of the core may alleviate incomplete replication in proportion to core shortening.

To characterize further *FRA3B* replication, we took advantage of a recent genome-wide analysis of replication timing by the Repli-Seq technique, which allows reconstitution of fork dynamics during the cell cycle<sup>7</sup>. Several human cell types were studied but information concerning common fragile sites was not exploited. Analysis of a 7-Mb-long region containing the *FHIT* locus (Fig. 3a and Supplementary Fig. 6) showed that the replication profiles along the locus differ notably between fibroblastic (BJ) and lymphoblastoid (GM06990 and H0287) cells. Whereas the profiles observed in lymphoblastoid cells are consistent with the results obtained in JEFF cells by combing, the plateau-shaped profile visible all along the *FHIT* locus in BJ cells indicates that initiation events take place within the *FRA3B* core in these cells. To

confirm and extend this conclusion, we used combing to study the replication profile of the *FHIT* locus in MRC-5 fibroblasts. Our results show that, both in untreated and aphidicolin-treated cells, initiation and termination events are evenly distributed all along the locus (Fig. 2c, d and Supplementary Fig. 7). Together, these observations are consistent with an increasing number of reports showing that both the replication timing<sup>7,8</sup> and the initiation pattern<sup>5,6</sup> of chromosomal domains evolve during differentiation but are conserved among different individuals in a given cell type<sup>27</sup>.

We reasoned that if the initiation-poor core of lymphoblastoid cells is involved in *FRA3B* instability, the site should not be fragile in fibroblasts. We used molecular cytogenetics to determine the frequency of breaks at *FRA3B* in aphidicolin-treated BJ, MRC-5 and JEFF cells (Fig. 3b, Supplementary Fig. 8 and Supplementary Table 3). Notably, the frequency of breaks at *FRA3B* is low in BJ and MRC-5 compared to JEFF cells. Long-travelling forks thus have a key role in *FRA3B* instability. However, this feature alone is insufficient to promote fragility as there are far fewer common fragile sites than initiation-poor regions in the genome. Moreover, it has long been shown that late replication completion contributes to *FRA3B* fragility<sup>25</sup>. Comparison of the replication timing in fibroblastic and lymphoblastoid cells (Fig. 3a and Supplementary Fig. 6) shows that replication of the *FHIT* gene ends very late in both cell types. Thus, late completion per se is also insufficient for fragility. These data indicate that common fragile site fragility results from the combination of late replication completion and paucity of initiation events. To test this prediction, we also analysed the Repli-Seq profiles along *FRA16D*, the second most active common fragile site in lymphocytes<sup>28</sup> (Supplementary Fig. 9a). We found that *FRA16D* shows tissue-specific initiation profiles and replication timing resembling those found at *FRA3B*. We also compared the frequency of breaks at *FRA16D* in aphidicolin-treated JEFF, MRC-5 and BJ cells (Supplementary Fig. 9b and Supplementary Table 4). Again the results look like those obtained for *FRA3B*, which reinforces and generalizes the mechanism we propose.

Tissue-specific reshuffling of the replication program provides a straightforward explanation for the setting of common fragile sites in different cell types, which would be very difficult to explain if nucleotide sequences were responsible for their fragility. In addition, the fact that cell-type-specific initiation profiles are maintained across species in regions of conserved synteny<sup>27</sup> agrees with the observed conservation of common fragile sites in different mammalian species<sup>11</sup>. Thus, we propose that common fragile sites are epigenetically defined loci that correspond to the latest initiation-poor regions to complete replication in a given cell type. The paucity of initiation events might reflect either a cell-type-specific lack of licensed origins<sup>29</sup> or chromatin organization delaying firing so much that cells enter mitosis before it occurs. As previously shown in yeast<sup>9</sup>, the mammalian checkpoint could be unable to delay mitotic onset when only a few long-travelling forks remain at work, which would allow unscheduled condensation of incompletely replicated common fragile sites, resulting in DNA breaks.

## METHODS SUMMARY

For combing experiments, JEFF or MRC-5 cells were grown for 5 h with or without 0.6  $\mu\text{M}$  aphidicolin. Neo-synthesized DNA was labelled with a pulse of IdU followed by a pulse of CldU. After DNA combing, Morse-code probes were hybridized and fibres bearing replication and FISH signals were analysed. The replication fork speed variable was calculated using  $(d_1 + d_{C1}) / (t_1 + t_{C1})$  with  $d_1$  and  $t_1$  being the measured distance (in kb) and labelling time (in min) for IdU incorporation, respectively, and  $d_{C1}$  and  $t_{C1}$  the corresponding parameters for CldU incorporation. The fork asymmetry variable corresponded to  $\max(d_1 / d_{C1}, d_{C1} / d_1)$ , which varies between 1 (no asymmetry) and  $+\infty$  (theoretical maximal asymmetry). Analysis of Repli-Seq data was carried out as described<sup>7</sup>. Breakage at common fragile sites was determined by FISH on metaphases with *FRA3B* or *FRA16D* bacterial artificial chromosome (BAC) probes. The total number of breaks was counted after Giemsa staining of metaphase spreads (see Methods).

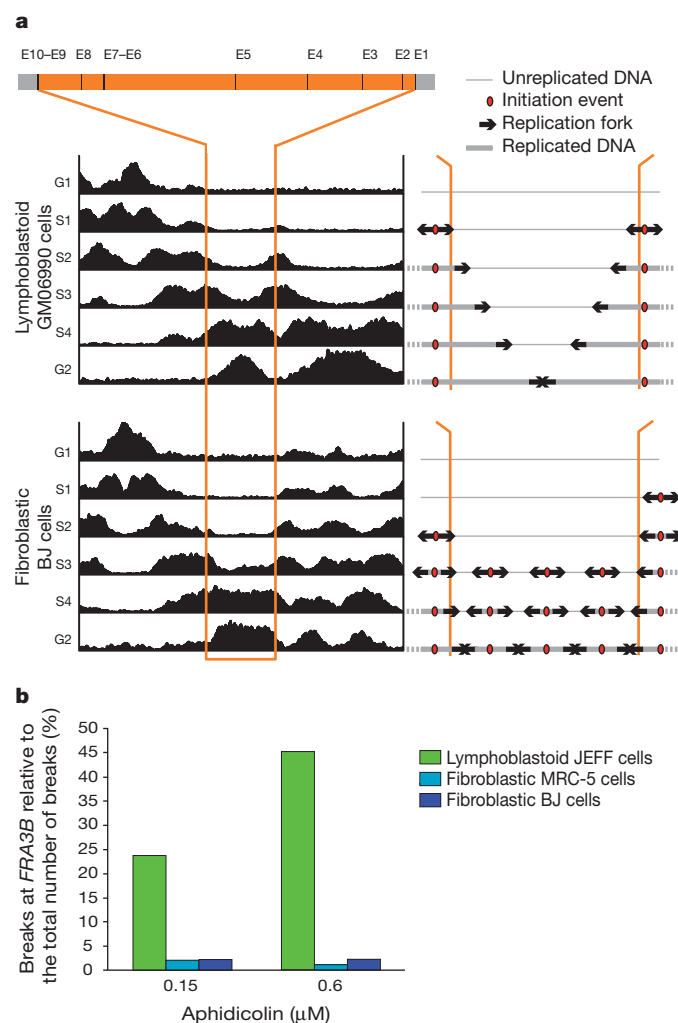


**Figure 3 | Relationship between replication profile of the *FHIT* locus and *FRA3B* fragility in lymphoblastoid and fibroblastic cells.** **a**, Left panel shows Repli-Seq analysis of the replication profiles along a 7-Mb-long region (chromosome 3: 56961124.5–63961124.5; assembly NCBI36 (hg18)) overlapping the *FHIT* gene (delimited by the orange lines) in lymphoblastoid GM06990 cells and fibroblastic BJ cells. Horizontal axis: position along the region. Vertical axis: density of sequence tags in each 50-kb window along the analysed region and for each indicated step of the cell cycle. Right panel shows cartoons illustrating the replication profiles along the *FHIT* locus (*FHIT* gene is delimited by orange lines). **b**, Number of breaks at *FRA3B* relative to the total number of breaks in cells treated with 0.15  $\mu\text{M}$  or 0.6  $\mu\text{M}$  of aphidicolin. Metaphases were prepared after a 3-h treatment with 200 nM nocodazole. See also Supplementary Table 3.

**Full Methods** and any associated references are available in the online version of the paper at [www.nature.com/nature](http://www.nature.com/nature).

**Received 24 September; accepted 8 December 2010.**

**Published online 23 January 2011.**

1. Sutherland, G. R. & Richards, R. I. The molecular basis of fragile sites in human chromosomes. *Curr. Opin. Genet. Dev.* **5**, 323–327 (1995).
2. Negrini, S., Gorgoulis, V. G. & Halazonetis, T. D. Genomic instability—an evolving hallmark of cancer. *Nature Rev. Mol. Cell Biol.* **11**, 220–228 (2010).
3. Bignell, G. R. *et al.* Signatures of mutation and selection in the cancer genome. *Nature* **463**, 893–898 (2010).
4. Schwartz, M., Zlotorynski, E. & Kerem, B. The molecular basis of common and rare fragile sites. *Cancer Lett.* **232**, 13–26 (2006).
5. Grégoire, D., Brodolin, K. & Méchali, M. HoxB domain induction silences DNA replication origins in the locus and specifies a single origin at its boundary. *EMBO Rep.* **7**, 812–816 (2006).
6. Dazy, S., Gandrillon, O., Hyrien, O. & Prioleau, M. N. Broadening of DNA replication origin usage during metazoan cell differentiation. *EMBO Rep.* **7**, 806–811 (2006).
7. Hansen, R. S. *et al.* Sequencing newly replicated DNA reveals widespread plasticity in human replication timing. *Proc. Natl Acad. Sci. USA* **107**, 139–144 (2010).
8. Hiratani, I. *et al.* Global reorganization of replication domains during embryonic stem cell differentiation. *PLoS Biol.* **6**, e245 (2008).
9. Tourrière, H. & Pasero, P. Maintenance of fork integrity at damaged DNA and natural pause sites. *DNA Repair* **6**, 900–913 (2007).
10. Branzei, D. & Foiani, M. Maintaining genome stability at the replication fork. *Nature Rev. Mol. Cell Biol.* **11**, 208–219 (2010).
11. Durkin, S. G. & Glover, T. W. Chromosome fragile sites. *Annu. Rev. Genet.* **41**, 169–192 (2007).
12. Helmrich, A., Stout-Weider, K., Hermann, K., Schrock, E. & Heiden, T. Common fragile sites are conserved features of human and mouse chromosomes and relate to large active genes. *Genome Res.* **16**, 1222–1230 (2006).
13. Tsantoulis, P. K. *et al.* Oncogene-induced replication stress preferentially targets common fragile sites in preneoplastic lesions. A genome-wide study. *Oncogene* **27**, 3256–3264 (2008).
14. Palumbo, E., Matricardi, L., Tosoni, E., Bensimon, A. & Russo, A. Replication dynamics at common fragile site *FRA6E*. *Chromosoma*, (2010).
15. Huebner, K. & Croce, C. M. Cancer and the *FRA3B/FHIT* fragile locus: it's a HIT. *Br. J. Cancer* **88**, 1501–1506 (2003).
16. Pichiorri, F. *et al.* Molecular parameters of genome instability: roles of fragile genes at common fragile sites. *J. Cell. Biochem.* **104**, 1525–1533 (2008).
17. Lebofsky, R., Heilig, R., Sonnleitner, M., Weissenbach, J. & Bensimon, A. DNA replication origin interference increases the spacing between initiation events in human cells. *Mol. Biol. Cell* **17**, 5337–5345 (2006).
18. Cha, R. S. & Kleckner, N. ATR homolog Mec1 promotes fork progression, thus averting breaks in replication slow zones. *Science* **297**, 602–606 (2002).
19. Rothstein, R., Michel, B. & Gangloff, S. Replication fork pausing and recombination or “gimme a break”. *Genes Dev.* **14**, 1–10 (2000).
20. Farkash-Amar, S. *et al.* Global organization of replication time zones of the mouse genome. *Genome Res.* **18**, 1562–1570 (2008).
21. Anglana, M., Apiou, F., Bensimon, A. & Debatisse, M. Dynamics of DNA replication in mammalian somatic cells: nucleotide pool modulates origin choice and interorigin spacing. *Cell* **114**, 385–394 (2003).
22. Courbet, S. *et al.* Replication fork movement sets chromatin loop size and origin choice in mammalian cells. *Nature* **455**, 557–560 (2008).
23. Bielinsky, A. K. Replication origins: why do we need so many? *Cell Cycle* **2**, 307–309 (2003).
24. El Achkar, E., Gerbault-Seureau, M., Muleris, M., Dutrillaux, B. & Debatisse, M. Premature condensation induces breaks at the interface of early and late replicating chromosome bands bearing common fragile sites. *Proc. Natl Acad. Sci. USA* **102**, 18069–18074 (2005).
25. Le Beau, M. M. *et al.* Replication of a common fragile site, *FRA3B*, occurs late in S phase and is delayed further upon induction: implications for the mechanism of fragile site induction. *Hum. Mol. Genet.* **7**, 755–761 (1998).
26. Durkin, S. G. *et al.* Replication stress induces tumor-like microdeletions in *FHIT/FRA3B*. *Proc. Natl Acad. Sci. USA* **105**, 246–251 (2008).
27. Ryba, T. *et al.* Evolutionarily conserved replication timing profiles predict long-range chromatin interactions and distinguish closely related cell types. *Genome Res.* **20**, 761–770 (2010).
28. O'Keefe, L. V. & Richards, R. I. Common chromosomal fragile sites and cancer: focus on *FRA16D*. *Cancer Lett.* **232**, 37–47 (2006).
29. Masai, H., Matsumoto, S., You, Z., Yoshizawa-Sugata, N. & Oda, M. Eukaryotic chromosome DNA replication: where, when, and how? *Annu. Rev. Biochem.* **79**, 89–130 (2010).

**Supplementary Information** is linked to the online version of the paper at [www.nature.com/nature](http://www.nature.com/nature).

**Acknowledgements** We thank E. Blackburn for critical reading of the manuscript. We thank Genomic Vision for making the DNA combing technology available to us. We acknowledge the Nikon Imaging Centre at Institut Curie-CNRS. We thank C. Rouzaud for help in combing experiments. A.L. is supported by a grant from the ARC (Association pour la recherche sur le cancer). The M.D. team is supported by La Ligue Nationale contre le Cancer (LNCC) (Equipe Labellisée EL2008.LNCC/MD), INCa (Institut National du Cancer) (2009-1-PLBI0-10-IC-1) and the PIC Réplication, Instabilité Chromosomique et Cancer (Institut Curie).

**Author Contributions** A.L. performed and analysed combing experiments. G.A.M. performed statistical and Repli-Seq analyses. S.K., A.-M.L. and O.B. performed cytogenetic analyses. N.V. and B.M. designed the Morse code. R.S.H. contributed to Repli-Seq analysis. A.L., G.A.M., O.B. and M.D. wrote the paper. M.D. planned the project.

**Author Information** Reprints and permissions information is available at [www.nature.com/reprints](http://www.nature.com/reprints). The authors declare no competing financial interests. Readers are welcome to comment on the online version of this article at [www.nature.com/nature](http://www.nature.com/nature). Correspondence and requests for materials should be addressed to M.D. ([michelle.debatisse@curie.fr](mailto:michelle.debatisse@curie.fr)).

## METHODS

**Cell culture.** Epstein–Barr-virus-immortalized human B lymphocytes (JEFF cells) were grown in RPMI-1640 plus GlutaMAX-I medium (GIBCO). MRC-5 and BJ cells were grown in MEM plus Earle's salts without L-glutamine medium (GIBCO), 1% MEM nonessential amino acids (GIBCO), 1 mM sodium pyruvate (GIBCO) and 2 mM L-glutamine (GIBCO). In addition, all cells were grown with 10% fetal calf serum (PAN-Biotech GmbH), 100  $\mu\text{g ml}^{-1}$  of penicillin and streptomycin (GIBCO). **FISH on metaphases and Giemsa staining.** JEFF or MRC-5 cells were grown for 16 h with aphidicolin 0.15  $\mu\text{M}$  or 0.6  $\mu\text{M}$  before metaphase preparations. Bacterial artificial chromosomes (BAC) were selected from the human March 2006 (NCBI36 (hg18)) assembly using the UCSC Genome Browser. *FRA3B* was probed with BAC RP11-32J15 (AC104161), RP11-641C17 (AC104164) and RP11-147N17 (AC104300). *FRA16D* was probed with BAC RP11-105F24 (AC106741) and RP11-571O6 (AC092724). Bacterial strains containing BAC were spread on LB agar plates containing 12.5  $\mu\text{g ml}^{-1}$  chloramphenicol and grown overnight at 37 °C. BAC DNA was then extracted according to the manufacturer's instructions (NucleoBond Xtra Midi Plus; Macherey–Nagel). Probes were biotinylated using the BioPrime DNA labelling system (Invitrogen) and purified on Illustra ProbeQuant G-50 Micro Columns (GE Healthcare). FISH on metaphases was performed as described<sup>24</sup> using 150 ng of each *FRA3B* BAC probe or *FRA16D* probe. Immunodetection was performed by successive incubations in the following reagents: (1) Alexa-488-conjugated streptavidin (Invitrogen); (2) biotin-conjugated rabbit anti-streptavidin (Rockland); (3) Alexa-488-conjugated streptavidin (Invitrogen). Chromosomes were counterstained with 4',6-diamidino-2-phenylindole (DAPI) (Vectashield mounting medium for fluorescence with DAPI; Vector Laboratories) and metaphases were observed by fluorescence microscopy. Total breaks, gaps or constrictions on chromosomes were observed on metaphase spreads stained by Giemsa (Giemsa R solution; Reactif RAL) without pre-treatment to obtain a homogeneous staining of chromosomes.

**DNA preparation for molecular combing.** JEFF or MRC-5 cells were grown for 5 h with or without aphidicolin 0.6  $\mu\text{M}$ . Neo-synthesized DNA was labelled as described<sup>21</sup> with the following changes: cells were pulse labelled for 30 min with IdU and for 30 min with CldU when grown in regular medium, or 2 h with IdU and 2 h with CldU when grown in the presence of aphidicolin. Genomic DNA was extracted and combing was performed as described<sup>30,31</sup>.

**FISH on combed DNA and immunofluorescence detection of neo-synthesized DNA.** Morse-code probes were designed as described<sup>17</sup>. Primer pairs and template BAC or fosmid used for PCR are listed in Supplementary Table 1. BAC and fosmid DNA were prepared as described earlier for FISH on metaphases. Hybridization was performed as described<sup>21</sup>. Immunodetection was performed by successive incubations in the following reagents: (1) Alexa-488-conjugated streptavidin (Invitrogen); (2) biotin-conjugated rabbit anti-streptavidin (Rockland); (3) Alexa-488-conjugated streptavidin (Invitrogen), mouse anti-bromodeoxyuridine (BrdU) (BD Biosciences) and rat anti-BrdU (AbD Serotec); (4) biotin-conjugated rabbit anti-streptavidin (Rockland), Alexa-350-conjugated goat anti-mouse (Invitrogen) and Texas-Red-conjugated donkey anti-rat (Jackson ImmunoResearch); (5) Alexa-488-conjugated streptavidin (Invitrogen), Alexa-350-conjugated donkey anti-goat (Invitrogen) and mouse anti-ssDNA (Millipore); (6) Cy5.5-conjugated goat anti-mouse (Abcam); (7) Cy5.5-conjugated donkey anti-goat (Abcam). Antibody incubations, washes and slide mounting were performed as reported previously<sup>21</sup>.

**Image acquisition and treatment.** An Eclipse 90i (Nikon) epifluorescence microscope connected to a CoolSNAP HQ CCD camera and run by Metamorph software (Molecular Devices) was used for image acquisition. A  $\times 100$  objective was used for images of metaphases. A  $\times 60$  objective was used for combed DNA images of the *FHIT* locus and a  $\times 40$  objective for those of the bulk genome. For the locus, two overlays of images were set up for each microscope field. The first one combined the IdU/CldU and FISH signals to identify replicating fibres of interest. The second overlay combined the IdU/FISH and DNA signals to determine the length of the DNA fibre bearing the Morse code. Image analyses were performed with Photoshop and Illustrator (Adobe). Fork positioning along the locus corresponds to the barycentre of the IdU and CldU tracks:  $(d_1 + d_{C1})/2$ , with  $d_1$  and  $d_{C1}$  being the lengths (in kb) of the two tracks of the same fork.

**Repli-Seq analysis.** Analysis of Repli-Seq data was carried out as described<sup>7</sup>.

**Statistical analysis.** The R environment was used for all analyses<sup>32</sup>. Tables, graphical analyses and R code are available on request. Statistical significances were set to  $P \leq 0.05$  and  $\beta \leq 0.1$ . Two-tailed tests were systematically used. Type I and II errors were not controlled by any procedure of correction. The replication fork speed variable was calculated using  $(d_1 + d_{C1})/(t_1 + t_{C1})$ , with  $d_1$  and  $t_1$  being the measured distance (in kb) and labelling time (in min) for IdU incorporation, respectively, and  $d_{C1}$  and  $t_{C1}$  the corresponding parameters for CldU incorporation. The fork asymmetry variable corresponded to  $\max(d_1/d_{C1}, d_{C1}/d_1)$ , which varies between 1 (no asymmetry) and  $+\infty$  (theoretical maximal asymmetry).

Distribution of these two variables in each class was examined using histogram and quantile-quantile plot. In Fig. 1, data were compatible with the Mann–Whitney–Wilcoxon test. Normal approximation due to identical values and continuity correction were applied.

In Fig. 1, for non-significant  $P$  values, the 10% probability of being wrong when considering that the medians are not different is related to: (1)  $\Delta = 0.5 \text{ kb min}^{-1}$  without treatment and  $\Delta = 0.03 \text{ kb min}^{-1}$  in the presence of aphidicolin (Fig. 1a); and (2)  $\Delta = 0.62$  without treatment and  $\Delta = 0.80$  in the presence of aphidicolin (Fig. 1b).  $\Delta$  corresponds to the central parameter difference in the statistical populations verifying  $\beta \leq 0.1$  ( $\mu_{\text{Genome}} = \mu_{\text{FRA3B/FHIT}} + \Delta$ ,  $\mu$  being the central parameter in the population). It gives an estimation of confidence when accepting the  $H_0$  null hypothesis that there is no difference between the two central parameters (means/medians). Let us consider as an example the replication-fork speed in the absence of aphidicolin treatment: if the true difference between the *FRA3B/FHIT* locus median and the genome median is a minimum of  $0.5 \text{ kb min}^{-1}$ , then the probability of being wrong when accepting  $H_0$  is a maximum of 10%. In other words, a difference of  $0.5 \text{ kb min}^{-1}$  or less is considered to be non-relevant in this example when  $H_0$  is accepted. The procedure for getting  $\Delta$  for the replication-fork-speed variable between the two 'FRA3B/FHIT' and 'genome' classes in the absence of aphidicolin is detailed as follows: the two distributions observed were approximately Gaussian, and thus were supposed to be the true distributions in the two statistical populations, except that the mean for 'genome' was set to  $\mu_{\text{FRA3B/FHIT}} + \Delta$ . Using R, two random samples of  $n_{\text{FRA3B/FHIT}} = 22$  and  $n_{\text{Genome}} = 283$  were generated, and the  $W$  statistic calculated. This procedure was repeated 5,000 times to get a  $W$  distribution. A  $\beta$  value was then obtained by determining the proportion of calculated  $W$  inside the  $(W_{0.025}, W_{0.975})$  interval, set by the  $W$  distribution when  $H_0$  is true ( $\Delta = 0$ ). This method was applied for increasing values of  $\Delta$  starting from zero. The whole procedure was repeated ten times and means of  $\beta$  were calculated for each  $\Delta$ . In all cases, the variation coefficient never exceeded 10%. Lastly, the  $\Delta$  minimal value that verifies  $\beta \leq 0.1$  was kept. The same procedure was applied for the fork asymmetry variable, except that observed distributions were approximately exponential (the fitted probability density was  $1/(m-1) \times e^{-(x-1)/(m-1)}$ ,  $m$  being the mean of the observed distribution). Note that for replication-fork-speed data, a Welch test was also used (distributions approximately normal) instead of the Mann–Whitney–Wilcoxon test. However, there was no consequence on the  $P$ -value result because of sample sizes.

The procedure we used to calculate that the deficit in initiation events in the core is significant both in untreated and aphidicolin-treated JEFF cells (Fig. 2a, b) is detailed as follows in the case of the experiment with untreated cells. Let us consider that the region without initiation events extends from the b5 to the d2 probe. The probability for one random initiation event occurring within the b5–d2 region could be defined as the size of this region divided by the size of the *FHIT* gene (from the beginning of E1 to the end of E10), which corresponds to 674,643 bp / 1,502,095 bp = 0.45. However, this calculation does not take into account the coverage of the b5–d2 region and of the rest of the gene by the number of fibres analysed. Therefore, another procedure was chosen to calculate this probability. First, the size of the DNA segment harbouring an initiation event was defined as the distance in kilobases between the two divergent forks (fork sizes included). Thus, 13 measurements corresponding to the 13 initiation events in the *FHIT* gene (from the beginning of E1 to the end of E10) were obtained (range 13–526 kb). The lower value of this range gives an estimation of the minimal size of a DNA segment likely to contain a detectable initiation event. As the 13-kb value is considered low, the first quartile (102 kb) was taken as a threshold value below which a fibre is unlikely to carry such an event. Next, for each fibre, the part overlapping the b5–d2 region was measured and all the values over the 102-kb threshold were added (10,705 kb). The same was done for each fibre covering the rest of the gene (E1–b5 or d2–E10 areas, giving 12,555 kb). Thus, the probability of one random initiation event occurring in the *FHIT* gene localized inside the b5–d2 region was defined as  $10,705 / (10,705 + 12,555) = 0.46$ . Last, the probability of getting  $n$  events or less inside the b5–d2 region when 13 events occur randomly in the *FHIT* gene follows the binomial law  $B(13, 0.46)$ . For zero events,  $P(X = 0) = 3 \times 10^{-4}$ . The same procedure was applied for aphidicolin-treated cells. The threshold obtained was 17.6 kb, the binomial law was  $B(18, 0.36)$  and  $P(X \leq 2) = 0.02$ .

30. Michalet, X. *et al.* Dynamic molecular combing: stretching the whole human genome for high-resolution studies. *Science* **277**, 1518–1523 (1997).

31. Labit, H. *et al.* A simple and optimized method of producing silanized surfaces for FISH and replication mapping on combed DNA fibers. *Biotechniques* **45**, 649–658 (2008).

32. R Development Core Team. *R: A Language and Environment for Statistical Computing* (R Foundation for Statistical Computing, 2006).

# Transient Hoogsteen base pairs in canonical duplex DNA

Evgenia N. Nikolova<sup>1</sup>, Eunae Kim<sup>2</sup>, Abigail A. Wise<sup>1</sup>, Patrick J. O'Brien<sup>3</sup>, Ioan Andricioaei<sup>2</sup> & Hashim M. Al-Hashimi<sup>1</sup>

**Sequence-directed variations in the canonical DNA double helix structure that retain Watson–Crick base-pairing have important roles in DNA recognition, topology and nucleosome positioning. By using nuclear magnetic resonance relaxation dispersion spectroscopy in concert with steered molecular dynamics simulations, we have observed transient sequence-specific excursions away from Watson–Crick base-pairing at CA and TA steps inside canonical duplex DNA towards low-populated and short-lived A•T and G•C Hoogsteen base pairs. The observation of Hoogsteen base pairs in DNA duplexes specifically bound to transcription factors and in damaged DNA sites implies that the DNA double helix intrinsically codes for excited state Hoogsteen base pairs as a means of expanding its structural complexity beyond that which can be achieved based on Watson–Crick base-pairing. The methods presented here provide a new route for characterizing transient low-populated nucleic acid structures, which we predict will be abundant in the genome and constitute a second transient layer of the genetic code.**

Soon after its discovery<sup>1</sup>, it was recognized that the DNA double helix could accommodate a range of conformations that retain Watson–Crick (WC) base-pairing<sup>2</sup>. Sequence-directed variations in duplex DNA structure, shape and flexibility have since been shown to have fundamental roles in biology, including in the indirect readout of DNA sequences by recognition factors<sup>3,4</sup>, nucleosome positioning<sup>4,5</sup> and formation of loops and other large-scale architectures<sup>6</sup> involved in DNA packaging, replication, transcription and recombination. DNA duplexes resiliently maintain WC base-pairing even when supercoiled and wrapped around histone octamers in nucleosomes<sup>7</sup> and when adopting left-handed double-helical conformations known as Z-DNA<sup>8</sup>. Deviations from the WC base-pairing have so far only been observed in duplex DNA bound to proteins<sup>9,10</sup> and small molecule ligands<sup>11,12</sup> and in the context of damaged DNA<sup>13,14</sup>, but never within naked canonical B-DNA duplexes.

Thus far, atomic resolution structural studies of the iconic DNA double helix have exclusively focused on its dominant, experimentally accessible, ground state conformation. Far less is known about other low-energy DNA conformations that may be sampled only transiently in solution. NMR relaxation dispersion experiments<sup>15,16</sup> provide a rare opportunity to detect and characterize such short-lived (< 5 ms) and low-populated species (> 0.1%), often referred to as 'excited states'. This methodology has been widely used to characterize protein excited states that have been implicated in folding<sup>15,16</sup>, recognition<sup>17</sup> and catalysis<sup>18</sup>, culminating in the recent structure determination of a transient protein-folding intermediate<sup>19</sup>. Recent advances in carbon-based relaxation dispersion experiments combined with selective labelling schemes have addressed limitations that have hindered application of this methodology to nucleic acids, allowing detection of excited states in both RNA<sup>20,21</sup> and DNA<sup>21,22</sup>. However, the structures of nucleic acid excited states remain elusive.

## Excited states in CA steps of duplex DNA

We used a recently introduced carbon  $R_{1\rho}$  relaxation dispersion NMR experiment that allows detection of excited states with enhanced time-scale sensitivity<sup>21</sup> to probe for the existence of excited states in canonical

DNA duplexes (Fig. 1a). We uncovered chemical exchange processes directed towards excited states occurring specifically at A•T and G•C base pairs in CA/TG steps (Fig. 1b), which together with TA steps are the most flexible dinucleotide steps in DNA and frequently the confluence point for local structural deformations<sup>23</sup>. In particular, we observed significant  $R_{1\rho}$  relaxation dispersion, indicative of chemical exchange, at the base C8 and sugar C1' carbons of the adenine and guanine residues, and for the C6 carbon of the cytosine residue. No relaxation dispersion was observed for the adenine base C2, the thymine residue, or the cytosine sugar C1' sites (Fig. 1b, Supplementary Fig. 3). The exchange process is enhanced by longer 3' neighbouring A-tracts, modulated by positional context, and for the G•C base pair, is highly pH-dependent (Supplementary Fig. 2). A two-state analysis ( $A \xrightleftharpoons[k_B]{k_A} B$ )

of the off-resonance relaxation dispersion data (Fig. 1c, Supplementary Fig. 2) revealed a single base pair exchange process that is slightly faster for A•T versus G•C and that is directed towards minutely populated ( $p_B \sim 0.64\%$  and  $\sim 0.47\%$  for G•C and A•T in A<sub>6</sub>-DNA, 26 °C) excited states that have exceptionally short lifetimes ( $\tau_B = 1/k_B \sim 1.5$  ms and  $\sim 0.3$  ms for G•C and A•T in A<sub>6</sub>-DNA, 26 °C), and that have downfield-shifted carbon chemical shifts ( $\Delta\omega_{AB(C8)} \sim 2.7$ – $3.2$  p.p.m.,  $\Delta\omega_{AB(C1')} \sim 3.1$ – $3.7$  p.p.m., and  $\Delta\omega_{AB(C6)} \sim 2.2$  p.p.m., Supplementary Table 2).

## Assignment to Hoogsteen base pairs

What is the excited state encoded by CA/TG steps and detected by NMR relaxation dispersion? NMR imino proton exchange measurements<sup>24,25</sup> and computer simulations<sup>26</sup> have shown previously that WC base pairs can spontaneously break open and access extrahelical conformations. Whereas the forward exchange rates ( $k_A$ ) measured by relaxation dispersion ( $\sim 4$ – $20$  s<sup>−1</sup> at 26 °C, Supplementary Table 2) are within an order of magnitude of rates reported previously for base-pair opening ( $\sim 40$ – $400$  s<sup>−1</sup> at 25 °C)<sup>27</sup>, the excited states detected here are at least three orders of magnitude more populated (Supplementary Table 2) and point to more energetically favourable species. To obtain more insights into the excited state, we measured carbon  $R_{1\rho}$  relaxa-

<sup>1</sup>Department of Chemistry and Biophysics, University of Michigan, 930 North University Avenue, Ann Arbor, Michigan 48109, USA. <sup>2</sup>Department of Chemistry, University of California, Natural Sciences 2, Irvine, California 92697, USA. <sup>3</sup>Department of Biological Chemistry, University of Michigan, Ann Arbor, Michigan 48109, USA.

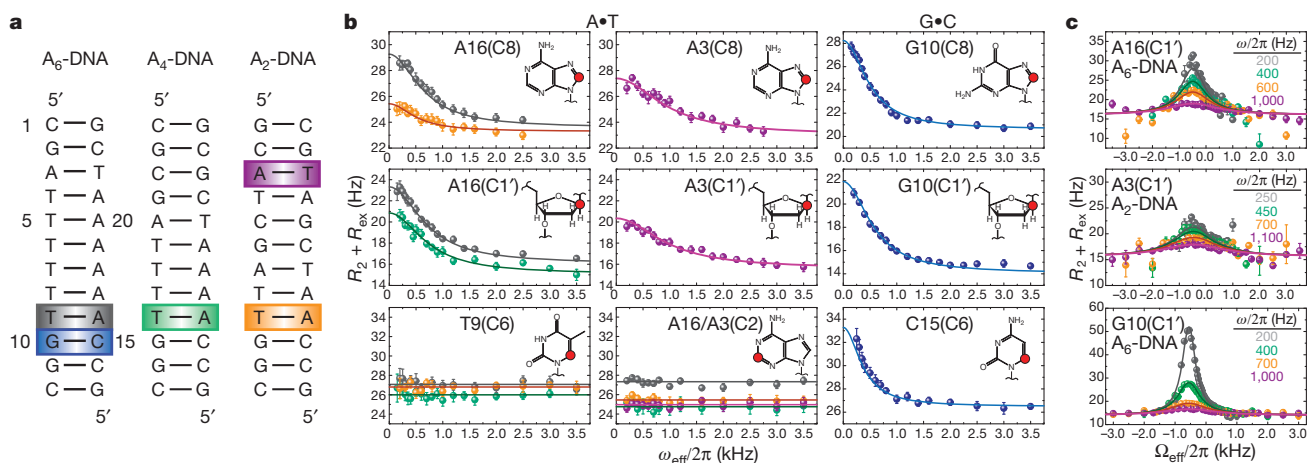


**Figure 1 | Detection of base-pair-specific excited states in CA/TG steps of duplex DNA.** **a**, DNA constructs containing varying length A-tracts with colour-coded A•T and G•C base pairs at CA/TG steps that show carbon chemical exchange. **b**, On-resonance  $^{13}\text{C}$   $R_{1\rho}$  relaxation dispersion profiles for A•T (26.0 °C) and G•C (30.5 °C) showing CA/TG specific chemical exchange at purine base C8 and sugar C1' and at cytosine base C6. Shown are the best

base pair global fits (solid line) to a two-state asymmetric exchange model (Methods, equation 1). **c**, Representative off-resonance relaxation dispersion profiles for corresponding C1' sites and best global fits as in **b**. All error bars represent experimental uncertainty (one s.d.) estimated from mono-exponential fitting of duplicate sets of  $R_{1\rho}$  data and analysis of signal-to-noise.

tion dispersion as a function of temperature (Fig. 2a). We then used transition-state theory and van't Hoff analysis to extract a complete thermodynamic-kinetic description of the two-state equilibria (Supplementary Table 5). Semi-logarithmic van't Hoff plots revealed a linear dependence characteristic of a two-state process for A•T and G•C base pairs (Fig. 2b). The analysis yielded activation free energies ( $\sim 16$  kcal mol $^{-1}$ ) and enthalpies ( $\sim 12$ – $26$  kcal mol $^{-1}$ ) for the forward transition (Fig. 2c) that are comparable to values reported previously for base-pair opening ( $\sim 14$ – $20$  kcal mol $^{-1}$  and  $\sim 8$ – $29$  kcal mol $^{-1}$  respectively)<sup>27,28</sup>. Thus, the transition to the excited state entails disruption of stacking and hydrogen-bonding interactions in the WC base pair. However, for both A•T and G•C, this loss in enthalpy is nearly entirely restored when the excited state is formed. In fact, the excited state is in part destabilized relative to the WC ground state by a less favourable entropy, implying a more 'rigid' excited state conformation and counter to what would be expected for a flexible looped-out state.

Taken together, our data point to an excited state conformation whose creation requires complete disruption of WC base pairs, but

whose thermodynamic stability is comparable to that of a WC base pair. One possibility is that the excited state represents an alternative base pair. Here, the correlated nature of the exchange at purine C8 and C1' nuclei and the large downfield carbon chemical shifts provides important clues. In particular, the magnitude and direction of  $\Delta\omega_{\text{AB(C8)}}$  and  $\Delta\omega_{\text{AB(C1')}}$  are strongly indicative of an *anti-to-syn* transition, as deduced from a survey of carbon chemical shifts<sup>29</sup> and density functional theory (DFT) calculations<sup>30</sup>. Remarkably, an *anti-to-syn* rotation of the adenine or guanine base results in creation of a Hoogsteen (HG) base pair optimally stabilized by two hydrogen bonds (Fig. 3a). The HG G•C base pair would require protonation of cytosine N3 (G•C $^+$ , pK $_a$ (N3)  $\sim 4.2$ , ref. 31), which can in turn explain the relaxation dispersion observed at cytosine C6 at neutral and acidic pH, and the downfield shifted excited state C6 chemical shift, as well as the pH dependence of dispersion measured at carbon sites in the G•C but not in the A•T base pair (see Supplementary Discussion). HG base pairs have been widely observed in non-canonical DNA structures, such as DNA triplexes and quadruplexes, where they

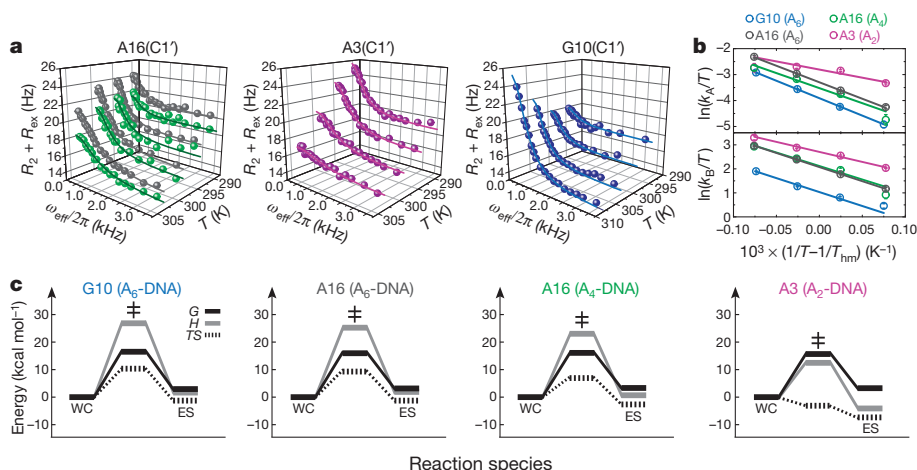


**Figure 2 | Kinetic-thermodynamic analysis of ground-to-excited state transitions.** **a**, Representative on-resonance  $^{13}\text{C}$   $R_{1\rho}$  relaxation dispersion profiles as a function of temperature for A16 (A<sub>6</sub>-DNA and A<sub>4</sub>-DNA), A3 (A<sub>2</sub>-DNA), and G10 (A<sub>6</sub>-DNA) C1'. **b**, Modified van't Hoff plots showing temperature dependence of the forward ( $k_A$ ) and reverse ( $k_B$ ) rate constants for the two-site exchange in A•T and G•C base pairs highlighted in Fig. 1a. Error

bars represent experimental uncertainty (one s.d.) as determined from propagation of errors obtained from mono-exponential fitting of duplicate sets of  $R_{1\rho}$  data and analysis of signal-to-noise. **c**, Corresponding kinetic-thermodynamic profiles for exchange between the WC ground state and the excited state (ES) via a transition state ( $\ddagger$ ), showing activation and net free energy ( $G$ ), enthalpy ( $H$ ), and entropy ( $TS$ ) changes (referenced to 0).



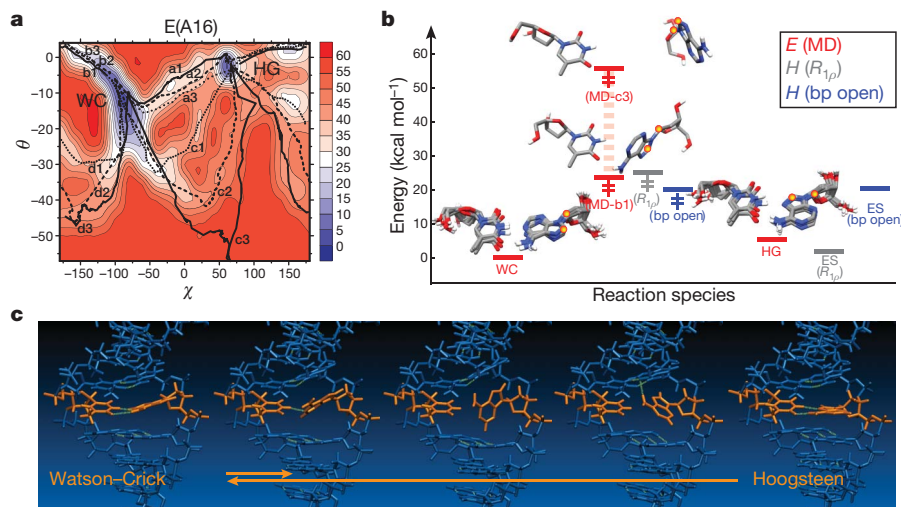


**Figure 4 | Watson-Crick to Hoogsteen base pair transition simulations.** **a**, Pseudo-free-energy ( $E$ , kcal mol<sup>-1</sup>) contour plots as a function of ( $\chi$ ,  $\theta$ ) pairs for A16•T9 obtained from multiple CPR trajectories (a–d). **b**, Initial WC and final excited-state (ES) HG structures and representative lowest-energy (b1) and highest-energy (c3) transition state ( $\ddagger$ ) structures of A16•T9 illustrating the

span of CPR transition barriers, and their relative potential energies (averaged for WC and HG) compared with enthalpies ( $H$ ) derived from NMR  $R_{1\rho}$  relaxation dispersion for chemical exchange or NMR imino proton exchange for A•T base pair opening<sup>27</sup>. **c**, Snapshots from a representative CPR transition pathway (a1) for A16•T9.

### Simulations of WC-to-HG transition

To assess the energetic and stereochemical feasibility of the proposed WC-to-HG transition, as well as obtain insights into the transition pathway, we used conjugate peak refinement (CPR)<sup>41</sup> methods to simulate multiple transition pathways between WC and excited state HG base pairs that sample various glycosidic ( $\chi$ ) and base opening ( $\theta$ ) angles (Fig. 4a). CPR trajectories for A16•T9 and G10•C15 in A<sub>6</sub>-DNA showed smooth WC-to-HG transitions via *anti*-to-*syn* purine rotation around  $\chi$  accompanied by minor adjustments in the complementary pyrimidine residue and neighbouring WC base pairs (Fig. 4a, Supplementary Fig. 7 and Supplementary Movies). Optimal pathways feature purine base-flips at low base pair opening angles into the major groove and transition states, which require complete disruption of WC base-pairing—this is also observed experimentally by relaxation dispersion—in which the purine base is near-orthogonal to its pyrimidine partner. This unusual geometry is well accommodated by the rather large inter-base-pair spacing in the B-form helix (that is, base pair rise  $\sim 3.3$  Å) and its ability to mould without loss of other WC base-pairing. Although a large spread of transition barriers are sampled, the minimal energy barriers and net energy changes are within 2 kcal mol<sup>-1</sup> of NMR-derived ensemble enthalpy terms (Fig. 4b). The final HG state for G10•C15 yields generally lower relative CPR energies—it is observed to adopt variable *syn*-guanine geometry, with either one or no optimal hydrogen bonds to the cytosine due to the lack of N3 protonation that stabilizes the ideal HG base pair, but on occasion forming an intra-residue hydrogen bond to a backbone oxygen (Supplementary Movie 2).

The carbon chemical shifts computed for the WC and lowest-energy HG geometries using DFT also exhibited the characteristic downfield-shifted  $\Delta\omega_{AB(C8)}$  and  $\Delta\omega_{AB(C1')}$  observed experimentally by relaxation dispersion (Fig. 3b and Supplementary Table 4). Conversely, the predicted chemical shifts revealed little and/or random variations between WC and HG base pairs for adenine C2, thymine C6 and cytosine C1', consistent with the lack of observable relaxation dispersion at those sites (Supplementary Fig. 8). Comprehensive DFT calculation of carbon chemical shifts for conformers sampled in various pathways between WC and HG states (Supplementary Fig. 8) yielded a small number of geometries that match the measured excited-state chemical shifts, but that could readily be excluded because they involve barrierless transitions and/or represent high-energy structures that disagree with experimentally derived enthalpies.

Our data strongly indicate that the DNA double helix codes for a preexisting WC-to-HG equilibrium, with HG base pairs representing an accessible and energetically competent alternative to WC base-pairing that present very distinct electrostatic and hydrophobic signatures. This makes it possible to trap HG base pairs by interactions with cellular triggers, thereby expanding the structural and functional diversity of the double helix beyond that which can be achieved based on an alphabet of only WC base-pairing. There are several examples of transcription factors including TBP<sup>9</sup> and p53 tumour suppressor<sup>10</sup> that specifically recognize HG base pairs embedded in different WC contexts, where the modulation in binding affinity, conceivably, by an HG base pair could even be correlated with an essential biological function<sup>40</sup>. In addition, HG base pairs are often trapped by oxidative and alkylation lesions<sup>14</sup>, providing unique recognition signals for repair enzymes in search of damage sites in a sea of undamaged DNA. Transient formation of HG base pairs inside B-DNA may also serve to promote non-canonical structures such as contiguous HG motifs, especially in tandem CA and TA repeats, or more dramatic transformations to Z-DNA<sup>42</sup>, and may well exist in much greater abundance for native genomic DNA, which is under torsional stress in the cellular environment. The methods presented here provide a general strategy for detecting and characterizing excited states in DNA and RNA, which we predict will be abundant in the genome and constitute another transient layer of the genetic code.

### METHODS SUMMARY

Detailed methods on DNA sample preparation and assignment, NMR relaxation dispersion data collection and analysis, MD/CPR simulations, and DFT chemical shift calculations can be found in Methods.

**Full Methods** and any associated references are available in the online version of the paper at [www.nature.com/nature](http://www.nature.com/nature).

Received 4 December 2010; accepted 5 January 2011.

Published online 26 January 2011.

- Watson, J. D. & Crick, F. H. Molecular structure of nucleic acids; a structure for deoxyribose nucleic acid. *Nature* **171**, 737–738 (1953).
- Record, M. T. Jr *et al.* Double helical DNA: conformations, physical properties, and interactions with ligands. *Annu. Rev. Biochem.* **50**, 997–1024 (1981).
- Koudelka, G. B., Mauro, S. A. & Ciubotaru, M. Indirect readout of DNA sequence by proteins: the roles of DNA sequence-dependent intrinsic and extrinsic forces. *Prog. Nucleic Acid Res. Mol. Biol.* **81**, 143–177 (2006).
- Rohs, R. *et al.* The role of DNA shape in protein–DNA recognition. *Nature* **461**, 1248–1253 (2009).

5. Segal, E. *et al.* A genomic code for nucleosome positioning. *Nature* **442**, 772–778 (2006).
6. Saiz, L. & Vilar, J. M. DNA looping: the consequences and its control. *Curr. Opin. Struct. Biol.* **16**, 344–350 (2006).
7. Richmond, T. J. & Davey, C. A. The structure of DNA in the nucleosome core. *Nature* **423**, 145–150 (2003).
8. Wang, A. H. *et al.* Molecular structure of a left-handed double helical DNA fragment at atomic resolution. *Nature* **282**, 680–686 (1979).
9. Patikoglou, G. A. *et al.* TATA element recognition by the TATA box-binding protein has been conserved throughout evolution. *Genes Dev.* **13**, 3217–3230 (1999).
10. Kitayner, M. *et al.* Diversity in DNA recognition by p53 revealed by crystal structures with Hoogsteen base pairs. *Nature Struct. Mol. Biol.* **17**, 423–429 (2010).
11. Ughetto, G. *et al.* A comparison of the structure of echinomycin and triostin A complexed to a DNA fragment. *Nucleic Acids Res.* **13**, 2305–2323 (1985).
12. Seaman, F. C. & Hurley, L. Interstrand cross-linking by bizelesin produces a Watson-Crick to Hoogsteen base-pairing transition region in d(CGTAATTACG)<sub>2</sub>. *Biochemistry* **32**, 12577–12585 (1993).
13. Yang, H., Zhan, Y., Fenn, D., Chi, L. M. & Lam, S. L. Effect of 1-methyladenine on double-helical DNA structures. *FEBS Lett.* **582**, 1629–1633 (2008).
14. Shanmugam, G., Kozekov, I. D., Guengerich, F. P., Rizzo, C. J. & Stone, M. P. Structure of the 1,N<sup>2</sup>-ethanodeoxyguanosine adduct opposite cytosine in duplex DNA: Hoogsteen base pairing at pH 5.2. *Chem. Res. Toxicol.* **21**, 1795–1805 (2008).
15. Palmer, A. G. III. NMR characterization of the dynamics of biomacromolecules. *Chem. Rev.* **104**, 3623–3640 (2004).
16. Korzhnev, D. M. & Kay, L. E. Probing invisible, low-populated states of protein molecules by relaxation dispersion NMR spectroscopy: an application to protein folding. *Acc. Chem. Res.* **41**, 442–451 (2008).
17. Boehr, D. D., Nussinov, R. & Wright, P. E. The role of dynamic conformational ensembles in biomolecular recognition. *Nature Chem. Biol.* **5**, 789–796 (2009).
18. Henzler-Wildman, K. & Kern, D. Dynamic personalities of proteins. *Nature* **450**, 964–972 (2007).
19. Korzhnev, D. M., Religa, T. L., Banachewicz, W., Fersht, A. R. & Kay, L. E. A transient and low-populated protein-folding intermediate at atomic resolution. *Science* **329**, 1312–1316 (2010).
20. Johnson, J. E. Jr & Hoogstraten, C. G. Extensive backbone dynamics in the GCAA RNA tetraloop analyzed using <sup>13</sup>C NMR spin relaxation and specific isotope labeling. *J. Am. Chem. Soc.* **130**, 16757–16769 (2008).
21. Hansen, A. L., Nikolova, E. N., Casiano-Negroni, A. & Al-Hashimi, H. M. Extending the range of microsecond-to-millisecond chemical exchange detected in labeled and unlabeled nucleic acids by selective carbon R<sub>1ρ</sub> NMR spectroscopy. *J. Am. Chem. Soc.* **131**, 3818–3819 (2009).
22. Shajani, Z. & Varani, G. <sup>13</sup>C relaxation studies of the DNA target sequence for HhaI methyltransferase reveal unique motional properties. *Biochemistry* **47**, 7617–7625 (2008).
23. Travers, A. A. The structural basis of DNA flexibility. *Philos. Transact. A Math. Phys. Eng. Sci.* **362**, 1423–1438 (2004).
24. Pardi, A., Morden, K. M., Patel, D. J. & Tinoco, I. Jr. Kinetics for exchange of imino protons in the d(C-G-C-G-A-A-T-T-C-G-C-G) double helix and in two similar helices that contain a G•T base pair, d(C-G-T-G-A-A-T-T-C-G-C-G), and an extra adenine, d(C-G-C-A-G-A-A-T-T-C-G-C-G). *Biochemistry* **21**, 6567–6574 (1982).
25. Guéron, M., Kochoyan, M. & Leroy, J. L. A single mode of DNA base-pair opening drives imino proton exchange. *Nature* **328**, 89–92 (1987).
26. Pérez, A., Luque, F. J. & Orozco, M. Dynamics of B-DNA on the microsecond time scale. *J. Am. Chem. Soc.* **129**, 14739–14745 (2007).
27. Coman, D. & Russu, I. M. A nuclear magnetic resonance investigation of the energetics of basepair opening pathways in DNA. *Biophys. J.* **89**, 3285–3292 (2005).
28. Song, K. *et al.* An improved reaction coordinate for nucleic acid base flipping studies. *J. Chem. Theory Comput.* **5**, 3105–3113 (2009).
29. Greene, K. L., Wang, Y. & Live, D. Influence of the glycosidic torsion angle on <sup>13</sup>C and <sup>15</sup>N shifts in guanosine nucleotides: investigations of G-tetrad models with alternating *syn* and *anti* bases. *J. Biomol. NMR* **5**, 333–338 (1995).
30. Xu, X. & Au-Yeung, S. Investigation of chemical shift and structure relationships in nucleic acids using NMR and density functional theory methods. *J. Phys. Chem. B* **104**, 5641–5650 (2000).
31. Izatt, R. M., Christensen, J. J. & Rytting, J. H. Sites and thermodynamic quantities associated with proton and metal ion interaction with ribonucleic acid, deoxyribonucleic acid, and their constituent bases, nucleosides, and nucleotides. *Chem. Rev.* **71**, 439–481 (1971).
32. Ghosal, G. & Muniyappa, K. Hoogsteen base-pairing revisited: resolving a role in normal biological processes and human diseases. *Biochem. Biophys. Res. Commun.* **343**, 1–7 (2006).
33. Abrescia, N. G., Thompson, A., Huynh-Dinh, T. & Subirana, J. A. Crystal structure of an antiparallel DNA fragment with Hoogsteen base pairing. *Proc. Natl Acad. Sci. USA* **99**, 2806–2811 (2002).
34. Nair, D. T., Johnson, R. E., Prakash, L., Prakash, S. & Aggarwal, A. K. Human DNA polymerase  $\epsilon$  incorporates dCTP opposite template G via a G.C+ Hoogsteen base pair. *Structure* **13**, 1569–1577 (2005).
35. Powell, S. W., Jiang, L. & Russu, I. M. Proton exchange and base pair opening in a DNA triple helix. *Biochemistry* **40**, 11065–11072 (2001).
36. Sau, A. K. *et al.* Evidence for A<sup>+</sup> (*anti*)-G(*syn*) mismatched base-pairing in d-GGTAAGCGTACC. *FEBS Lett.* **377**, 301–305 (1995).
37. Lu, L., Yi, C., Jian, X., Zheng, G. & He, C. Structure determination of DNA methylation lesions N<sup>1</sup>-meA and N<sup>2</sup>-meC in duplex DNA using a cross-linked protein-DNA system. *Nucleic Acids Res.* **38**, 4415–4425 (2010).
38. Gilbert, D. E., van der Marel, G. A., van Boom, J. H. & Feigon, J. Unstable Hoogsteen base pairs adjacent to echinomycin binding sites within a DNA duplex. *Proc. Natl Acad. Sci. USA* **86**, 3006–3010 (1989).
39. Hoopes, B. C., LeBlanc, J. F. & Hawley, D. K. Contributions of the TATA box sequence to rate-limiting steps in transcription initiation by RNA polymerase II. *J. Mol. Biol.* **277**, 1015–1031 (1998).
40. Meyer, T., Carlstedt-Duke, J. & Starr, D. B. A weak TATA box is a prerequisite for glucocorticoid-dependent repression of the osteocalcin gene. *J. Biol. Chem.* **272**, 30709–30714 (1997).
41. Fischer, S. & Karplus, M. Conjugate peak refinement: an algorithm for finding reaction paths and accurate transition-states in systems with many degrees of freedom. *Chem. Phys. Lett.* **194**, 252–261 (1992).
42. Segers-Nolten, G. M., Sijtsma, N. M. & Otto, C. Evidence for Hoogsteen GC base pairs in the proton-induced transition from right-handed to left-handed poly(dG-dC)•poly(dG-dC). *Biochemistry* **36**, 13241–13247 (1997).

**Supplementary Information** is linked to the online version of the paper at [www.nature.com/nature](http://www.nature.com/nature).

**Acknowledgements** We thank A. L. Hansen, S. Horowitz and J. Feigon for valuable discussions and suggestions, A. V. Kurochkin for NMR expertise, and C.L. Brooks III for access to a supercomputing cluster. We gratefully acknowledge the Michigan Economic Development Cooperation and the Michigan Technology Tri-Corridor for support in the purchase of a 600 MHz spectrometer. This work was supported by NSF CAREER awards (MCB 0644278 to HMA and CHE-0918817 to I.A.) and an NIH grant (R01GM089846). E.N.N. acknowledges support by a Rackham International and Predoctoral Fellowship awarded by the University of Michigan.

**Author Contributions** E.N.N. prepared DNA samples assisted by A.A.W. and performed/analysed all NMR experiments and DFT calculations; E.N.N. and H.M.A. conceived the idea of an HG excited state base pair and approaches to investigate its formation; I.A. and E.K. performed and analysed the MD/CPR simulations; P.J.O. provided expertise and guidance for damaged DNA studies along with critical manuscript revisions; H.M.A. and E.N.N. with help from P.J.O., E.K. and I.A. wrote the paper.

**Author Information** Reprints and permissions information is available at [www.nature.com/reprints](http://www.nature.com/reprints). The authors declare no competing financial interests. Readers are welcome to comment on the online version of this article at [www.nature.com/nature](http://www.nature.com/nature). Correspondence and requests for materials should be addressed to H.M.A. ([hashimi@umich.edu](mailto:hashimi@umich.edu)) or I.A. ([andricio@uci.edu](mailto:andricio@uci.edu)).

## METHODS

**Preparation and NMR resonance assignment of unlabelled and  $^{13}\text{C}/^{15}\text{N}$ -labelled DNA.** Isotopically labelled DNA dodecamers (Fig. 1a) were synthesized by *in vitro* primer extension using a template hairpin DNA (IDT), Klenow fragment DNA polymerase (NEB), and uniformly  $^{13}\text{C}/^{15}\text{N}$ -labelled dNTPs (Isotec, Sigma-Aldrich). Single-stranded DNA products were purified by 20% denaturing polyacrylamide gel electrophoresis (PAGE), isolated by passive elution and desalted on a C18 reverse-phase column (Sep-pak, Waters). Oligonucleotides were lyophilized and resuspended in NMR buffer (15 mM sodium phosphate pH 6.8, 25 mM sodium chloride, 0.1 mM EDTA, 10%  $\text{D}_2\text{O}$ ). Complementary oligonucleotides were annealed at an equimolar ratio typically at 0.5–1.0 mM for NMR studies. Unlabelled DNA oligonucleotides were purchased from IDT ( $\text{A}_2$ -DNA,  $\text{A}_4$ -DNA,  $\text{A}_6$ -DNA in Fig. 1a, and E-DNA in Supplementary Fig. 6), Exiqon, Inc. ( $\text{A}_6$ -DNA $^{\text{A16LNA}}$  and  $\text{A}_2$ -DNA $^{\text{A16LNA}}$  in Supplementary Fig. 4) and Midland Certified, Inc. ( $\text{A}_6$ -DNA $^{\text{mA16}}$  and  $\text{A}_6$ -DNA $^{\text{mG10}}$  in Supplementary Fig. 5). Unlabelled DNA constructs including equivalent samples to  $^{13}\text{C}/^{15}\text{N}$ -labelled DNA were prepared as described<sup>21</sup> at 2.0–4.0 mM concentrations and assigned using conventional  $^1\text{H}$ - $^1\text{H}$  nuclear Overhauser effect spectroscopy (NOESY) in 10%  $\text{D}_2\text{O}$  at 5 °C and/or 26 °C. The 2:1 complex between echinomycin (Selleck Chemicals) and E-DNA was prepared as described previously<sup>38</sup>. All NMR experiments were performed on a Bruker Avance 600 MHz NMR spectrometer equipped with a 5 mm triple-resonance cryogenic probe.

**Selective  $^{13}\text{C}$   $R_{1\rho}$  relaxation dispersion.** Rotating frame ( $R_{1\rho}$ ) relaxation dispersion profiles were measured at a single field (14.1 T) using a selective carbon experiment with a one-dimensional acquisition scheme<sup>21</sup> that extends the sensitivity to chemical exchange into millisecond timescales relative to conventional two-dimensional relaxation dispersion methods. On-resonance data were recorded at variable (100 to 3,500 Hz) effective spinlock field strength ( $\omega_{\text{eff}}$ ) (Supplementary Tables 1 and 3) for various sites in  $^{13}\text{C}/^{15}\text{N}$ -labelled and unlabelled DNA constructs. For  $^{13}\text{C}/^{15}\text{N}$ -labelled DNA samples (Supplementary Fig. 2) and E-DNA octamer (Supplementary Fig. 6), off-resonance dispersion data were collected in a temperature dependent manner at variable spinlock offset frequencies ( $\Omega_{\text{eff}} \approx \Omega_{\text{ave}}$ , see below) and at three to four different spinlock powers ( $\omega_1$ ) (Supplementary Table 1 and 3). In each case, the following relaxation delays were used: {0, 4, 8, 12 (2×), 16, 20, 26, 32 (2×) ms} for C2/C6/C8 and {0, 4, 8, 12 (2×), 18, 26, 34, 42 (2×) ms} for C1' in  $^{13}\text{C}/^{15}\text{N}$ -labelled DNA constructs; {0, 40 (2×) ms} for C8 and {0, 48 (2×) ms} for C1' at 17 °C, {0, 48 (2×) ms} for C8 and {0, 60 (2×) ms} for C1' at 26 °C in E-DNA; {0, 30 (2×) ms} for C8 in  $\text{A}_6$ -DNA $^{\text{A16LNA}}$ . Data points corresponding to Hartmann–Hahn matching conditions were omitted from the data fits as described previously<sup>21</sup>. Data were processed using nmrPipe<sup>43</sup> and the  $R_{1\rho}$  or the effective transverse relaxation rates ( $R_{2\text{eff}} = R_2 + R_{\text{ex}}$ ) were computed by fitting the resonance intensities to monoexponential decays using Mathematica 6.0 (Wolfram Research).

Measured relaxation dispersion profiles with on- and off-resonance data were fit by equation (1) (below) that assumes a two-state equilibrium ( $\text{A} \rightleftharpoons \text{B}$ ) with an asymmetric population distribution ( $p_{\text{A}} \gg p_{\text{B}}$ )<sup>44</sup> using Mathematica 6.0 (Wolfram Research):

$$R_{1\rho} = R_1 \cos^2 \theta + R_2 \sin^2 \theta + \sin^2 \theta \frac{p_{\text{A}} p_{\text{B}} \Delta\omega_{\text{AB}}^2 k_{\text{ex}}}{\Omega_{\text{B}}^2 + \omega_1^2 + k_{\text{ex}}^2} \quad (1)$$

where  $R_1$  and  $R_2$  are the intrinsic longitudinal and transverse relaxation rates, respectively (assumed to be identical for A and B species),  $\Omega$  is the resonance offset from the spinlock carrier,  $\omega_1$  is the spinlock strength;  $\tan \theta = \omega_1 / \Omega_{\text{ave}}$ ,  $\Delta\omega_{\text{AB}} = \Omega_{\text{B}} - \Omega_{\text{A}}$ ,  $\Omega_{\text{ave}} = p_{\text{A}} \Omega_{\text{A}} + p_{\text{B}} \Omega_{\text{B}}$ , where  $p_{\text{A}}$  ( $p_{\text{B}}$ ) is the major (minor) state fractional population ( $p_{\text{A}} + p_{\text{B}} = 1$ );  $k_{\text{ex}} = k_{\text{A}} + k_{\text{B}}$  is the exchange rate constant for a two-state equilibrium, where  $k_{\text{A}} = p_{\text{B}} k_{\text{ex}}$  and  $k_{\text{B}} = p_{\text{A}} k_{\text{ex}}$  are the forward and reverse rate constants respectively. Similar results were obtained when fitting relaxation dispersion profiles against more complex two-state exchange models including the Laguerre approximation<sup>45</sup> that do not assume a skewed population distribution (data not shown) and statistical analysis implied that application of the more complex model here was not justified. Temperature-dependent data for base/sugar resonances within the same nucleotide or base pair were fit individually and globally with shared parameters ( $k_{\text{ex}}$  and  $p_{\text{B}}$  for each temperature) (Supplementary Tables 2 and 3). The best-fit model was assessed using F-test statistics (data not shown), which uses chi-square ( $\chi^2$ ) and F-distribution analysis to determine the feasibility of a complicated model (that is, individual fits) versus a more simple model (that is, shared-parameter fits) nested inside the first model. The chemical shift difference  $\Delta\omega_{\text{AB}}$  was assumed to be invariant over the narrow temperature range investigated. On-resonance  $R_{1\rho}$  profiles were fit by a simplified two-state fast exchange expression<sup>44</sup> ( $k_{\text{ex}} \gg \Delta\omega_{\text{AB}}$ ):

$$R_{1\rho} = R_2 + R_{\text{ex}} = R_2 + \frac{\Phi_{\text{ex}} k_{\text{ex}}}{\omega_1^2 + k_{\text{ex}}^2}; \Phi_{\text{ex}} = p_{\text{A}} p_{\text{B}} \Delta\omega_{\text{AB}}^2 \quad (2)$$

where all parameters are as described above.

**Thermodynamic analysis.** The observed temperature dependence of the forward ( $k_{\text{A}}$ ) and reverse ( $k_{\text{B}}$ ) rate constants (Supplementary Table 2) was fit by a modified van't Hoff equation that accounts for statistical compensation effects and assumes a smooth energy surface<sup>27</sup>:

$$\ln \left( \frac{k_i(T)}{T} \right) = \ln \left( \frac{k_{\text{B}} \kappa}{h} \right) - \frac{\Delta G_i^{\ddagger}(T_{\text{hm}})}{RT_{\text{hm}}} - \frac{\Delta H_i^{\ddagger}}{R} \left( \frac{1}{T} - \frac{1}{T_{\text{hm}}} \right) \quad (3)$$

where  $k_i$  ( $i = \text{A}, \text{B}$ ) is the rate constant,  $\Delta G_i^{\ddagger}$  and  $\Delta H_i^{\ddagger}$  are the free energy and enthalpy of activation respectively,  $R$  is the universal gas constant,  $T$  is temperature, and  $T_{\text{hm}}$  is the harmonic mean of the experimental temperatures computed as  $T_{\text{hm}} = n / \sum_{i=1}^n (1/T_i)$ ;  $k_{\text{B}}$  is Boltzmann's constant,  $h$  is Planck's constant,  $\kappa$  is the transmission coefficient (assumed to be 1) in the pre-exponential factor of Eyring's theory. The entropy of activation ( $\Delta S_i^{\ddagger}$ ) was calculated as follows:

$$T \Delta S_i^{\ddagger} = \Delta H_i^{\ddagger} - \Delta G_i^{\ddagger}(T_{\text{hm}}) \quad (4)$$

Semi-logarithmic plots are included in Fig. 2b and best-fit thermodynamic parameters are reported in Supplementary Table 5.

An alternative interpretation of the thermodynamic parameters is given by the phenomenological Ferry law<sup>46,47</sup>, which incorporates a lower energy barrier with a rough enthalpic surface:

$$\ln(k_i) = \ln C - \frac{\Delta H_i^{\ddagger}}{RT} - \frac{\langle H_i^{\ddagger} \rangle}{(RT)^2} \quad (5)$$

where  $C$  is a constant, where  $\langle H_i^{\ddagger} \rangle^{1/2}$  represents the enthalpy due to ruggedness of the barrier. The maximum  $\langle H_i^{\ddagger} \rangle^{1/2}$  values were calculated by taking the smooth Arrhenius-like enthalpic barrier to be vanishing ( $\Delta H_i^{\ddagger} = 0$ ) and are reported in Supplementary Table 4.

**Molecular dynamics simulations of WC-to-HG base pair transition pathways.**

An initial duplex DNA in standard B-form with Watson–Crick (WC) base-pairing corresponding to  $\text{A}_6$ -DNA was generated using 3DNA<sup>48</sup>. Hoogsteen (HG) base pairs were generated at A16•T9, A3•T22 and G10•C15 positions using known X-ray coordinates<sup>49,50</sup>, where the purine adopts a *syn* conformation, whereas the complementary pyrimidine retains an *anti* conformation (see Fig. 3a). Initially, all conformers with WC or HG base-pairing were equilibrated through a series of energy minimizations using the Adopted Basis Newton–Raphson (ABNR) algorithm. Canonical (NVT) ensemble MD were performed with the CHARMM27 all-atom force field<sup>51</sup> and the generalized Born molecular volume (GBMV) implicit solvation model (GBMV II)<sup>52–54</sup>. The velocity–Verlet algorithm was used with a time step of 2 fs. A temperature of 300 K was kept constant with a Nosé–Hoover thermostat<sup>55,56</sup>. The cutoff for non-bonded list generation was set to 21 Å, the cutoff for non-bonded interactions was set to 18 Å, and the onset of switching for non-bonded interactions was set to 16 Å. The SHAKE algorithm was used to constrain vibrations of covalent bonds to hydrogen atoms involved. To conserve the duplex DNA structure during pre-equilibration, flat-bottom distance restraints were applied, which prevented the hydrogen-bond donor from moving more than 2.0 Å. The simulations ran for a total of 6.0 ns (Supplementary Fig. 7).

For the collection and analysis of equilibrium data, the initial 1 ns simulation data were discarded. We constructed a two-dimensional free-energy map using the following two reaction coordinates: the DNA backbone root mean square deviation (r.m.s.d.) and the potential energy value; the minimization of this approximate free energy surface permitted us to choose the most populated structure in the canonical ensemble ( $F = -k_{\text{B}} T \ln P(X, Y)$ ,  $X$  and  $Y$  are reaction coordinates,  $k_{\text{B}}$  is Boltzmann's constant,  $T$  is the absolute temperature (Supplementary Fig. 7)). The DNA backbone r.m.s.d. is defined by selecting the P-O5'-C5'-C4'-C3'-O3' atoms. The reference structure was a standard B-form DNA (twist angle  $\Omega = 36.0^\circ$ , rise per base pair along helix axis = 3.3 Å) without minimization. In order to probe the transition pathway between a WC and a HG base pair conformer, we used the conjugate peak refinement (CPR) method<sup>41</sup> applicable to the study of complex isomerization reactions, including allosteric transitions in proteins and more general conformational changes in macromolecules. The resulting paths follow the adiabatic energy surface without applying any constraints and path-points between saddle-points ensure the continuity of the path, not necessarily constrained to find the absolute bottom of the energy valley. The initial WC-to-HG pathways were generated using a targeted molecular dynamics method that applied a holonomic constraint, which decreased gradually the r.m.s.d. to the final target structure. In each CPR cycle, a heuristic procedure was used to modify the path by improving, removing, or inserting one path-point, so that the new path avoids the maximum energy peak. Finally, to refine the CPR path further, we used a synchronous chain minimization method of all path-points, under the constraint that the points move within hyperplanes orthogonal to the path. The most populated structures with the WC base

pair or with the HG base pair from the normal MD simulations corresponded to 'reactant' and 'product' wells, respectively, on the energy surface. In order to sample a wider range of possible transition pathways, additional putative intermediates that differed in either the flip-over or flip-out angle were added by modifying, respectively, the glycosidic angle,  $\chi$  (O4'-C1'-N9-C4), of the purine base and a centre-of-mass pseudo-dihedral angle,  $\theta^{28}$ , which describes the extent to base opening. CPR data are reported in Supplementary Fig. 7.

**Density functional theory calculations of carbon chemical shifts.** DFT chemical shift calculations were conducted on a high-performance computing cluster using Gaussian 03 (ref. 57). DNA conformations of the target A•T and G•C base pair that represent a range of ( $\chi$ ,  $\theta$ ) pairs were selected from each simulated WC-to-HG transition pathway and capped by 3'OH/5'OH (UCSF Chimera<sup>58</sup>) for DFT calculations (Supplementary Fig. 8) without further geometry optimization. NMR <sup>13</sup>C chemical shift calculations were conducted using the GIAO method with the B3LYP/6-311+G(2d,p) basis set. The isotropic carbon chemical shifts ( $\sigma_{\text{ISO}}$ ) were referenced to TMS ( $\sigma_{\text{TMS}} = 182.759$  p.p.m.) using the relationship  $\delta_{\text{ISO}} = \sigma_{\text{TMS}} - \sigma_{\text{ISO}}$ , where the structure of TMS was optimized at the same level of theory. Computed carbon chemical shifts were referenced to the most stable WC conformer in a given transition pathway and matched with NMR excited-state chemical shift differences ( $\Delta\omega_{\text{AB}}$ ) in Supplementary Table 4. For benchmarking, similar DFT calculations were performed on single guanosine nucleotides with *anti* and *syn* glycosidic conformations from crystal structures of *Oxytricha nova* telomeric G-quadruplex (5'-(G)<sub>4</sub>(T)<sub>4</sub>(G)<sub>4</sub>; PDB ID: IJPQ, IJRN, 2GWQ, 2GWE and 2NPR) with added hydrogen atoms (UCSF Chimera<sup>58</sup>) and no further geometry optimization, and compared to observed NMR C8 chemical shifts for the same G-quadruplex (courtesy of M. Gill and P. Loria) (Supplementary Fig. 8). Similar calculations were performed for unmodified and N1-methyladenine modified HG base pairs and control WC base pairs using existing crystal structures (PDB ID: 1K61, 3IGK, 3IGL, 3KZ8, 3H8O and 2ATA).

43. Delaglio, F. *et al.* NMRPipe: a multidimensional spectral processing system based on UNIX pipes. *J. Biomol. NMR* **6**, 277–293 (1995).

44. Palmer, A. G. III & Massi, F. Characterization of the dynamics of biomacromolecules using rotating-frame spin relaxation NMR spectroscopy. *Chem. Rev.* **106**, 1700–1719 (2006).
45. Miloushev, V. Z. & Palmer, A. G. III.  $R_{1\rho}$  relaxation for two-site chemical exchange: general approximations and some exact solutions. *J. Magn. Reson.* **177**, 221–227 (2005).
46. Ferry, J. D., Grandine, L. D. & Fitzgerald, E. R. The relaxation distribution function of polyisobutylene in the transition from rubber-like to glass-like behavior. *J. Appl. Phys.* **24**, 911–916 (1953).
47. Denisov, V. P., Peters, J., Horlein, H. D. & Halle, B. Using buried water molecules to explore the energy landscape of proteins. *Nature Struct. Biol.* **3**, 505–509 (1996).
48. Olson, W. K. *et al.* A standard reference frame for the description of nucleic acid base-pair geometry. *J. Mol. Biol.* **313**, 229–237 (2001).
49. Abrescia, N. G., Gonzalez, C., Gouyette, C. & Subirana, J. A. X-ray and NMR studies of the DNA oligomer d(ATATAT): Hoogsteen base pairing in duplex DNA. *Biochemistry* **43**, 4092–4100 (2004).
50. Aishima, J. *et al.* A Hoogsteen base pair embedded in undistorted B-DNA. *Nucleic Acids Res.* **30**, 5244–5252 (2002).
51. MacKerell, A. D. Jr, Banavali, N. & Foloppe, N. Development and current status of the CHARMM force field for nucleic acids. *Biopolymers* **56**, 257–265 (2000).
52. Chocholoušová, J. & Feig, M. Implicit solvent simulations of DNA and DNA-protein complexes: agreement with explicit solvent vs experiment. *J. Phys. Chem. B* **110**, 17240–17251 (2006).
53. Feig, M. *et al.* Performance comparison of generalized born and Poisson methods in the calculation of electrostatic solvation energies for protein structures. *J. Comput. Chem.* **25**, 265–284 (2004).
54. Lee, M. S., Feig, M., Salsbury, F. R. Jr & Brooks, C. L. III. New analytic approximation to the standard molecular volume definition and its application to generalized Born calculations. *J. Comput. Chem.* **24**, 1348–1356 (2003).
55. Nosé, S. A unified formulation of the constant temperature molecular-dynamics methods. *J. Chem. Phys.* **81**, 511–519 (1984).
56. Hoover, W. G. Canonical dynamics: equilibrium phase-space distributions. *Phys. Rev. A* **31**, 1695–1697 (1985).
57. Frisch, M. J. *et al.* Gaussian 03, Revision C.02. (Gaussian, 2004).
58. Pettersen, E. F. *et al.* UCSF Chimera—a visualization system for exploratory research and analysis. *J. Comput. Chem.* **25**, 1605–1612 (2004).